Pulse Pattern Formation in V-shaped External Cavity Mode-locked Lasers: Modelling Strategies and Bifurcation Analysis

vorgelegt von

M. Sc.
Jan Philipp Hausen

an der Fakultät II – Mathematik und Naturwissenschaften

der Technischen Universität Berlin

zur Erlangung des akademischen Grades

Doktor der Naturwissenschaften
– Dr. rer. nat. –

genehmigte Dissertation

Promotionsausschuss:

Vorsitzender:	Prof. Dr. Michael Lehmann
Gutachterin:	Prof. Dr. Kathy Lüdge
Gutachter:	Dr. Bryan Kelleher

Tag der wissenschaftlichen Aussprache: 21. Oktober 2021

Berlin 2021

Abstract

Passively mode-locked semiconductor vertical external cavity surface emitting lasers (VECSELs) have been subject to intense research in the last decades due the comparably cheap and flexible semiconductor manufacturing process. This led to a great enhancement of the performance figures of the pulsed laser output, namely the pulse width and pulse amplitude. Hence, semiconductor based mode-locked VECSELs have become competitive to their well established solid state based counter-parts for applications such as spectroscopy, material processing and eye surgery.
The main constituents of such a laser are a semiconductor gain chip, a semiconductor saturable absorber mirror and a highly reflective outcoupling facet. To enable an efficient beam guiding within the resonator and convenient optical pumping, the disk lasers are often configured in a V-shaped cavity geometry. Recent experiments on these devices have shown that despite the good performance figures interesting physics in terms of various pulsed states can appear.
In this work, firstly a delay differential equation model is derived in order to enable a detailed theoretical investigation of the V-shaped VECSEL device in a broad parameter regime with a strong focus on the effect of the cavity geometry.
In the following, a bifurcation analysis is performed to unravel the emergence of pulse cluster states in a regime of intermediate cavity lengths (0.625 ns round-trip time). The cluster states appear due to the characteristic gain depletion scenario in the V-shaped cavity. Specifically, the gain is passed twice by each pulse per round-trip. The pulse clusters are characterized as temporally non-equidistant clusters of pulses, which are periodic with a period approximately equalling the cold cavity round-trip time. Pulse clusters with an increasing number of pulses are born in cusps of saddle-node bifurcations along the fundamental solution branch at characteristic round-trip times. Their upper stability boundary can be shifted to higher pump powers, if the relative length of the cavity arms is adjusted.
The pulse clusters are further investigated in the long cavity regime (round-trip time longer than 2 ns). In this regime, the pulses can become temporally localized as they do not interact via the exponential tails of the gain relaxation, due to the complete gain recovery between pulse passes. Interestingly, the pulses within one cluster remain globally bound by the gain depletions but become locally independent, which is shown via a Floquet analysis. As the pulses maintain a random phase relationship, the cluster states can be referred to as incoherent photonic molecules.
By deriving a non-local Haus master equation model for the V-shaped VECSEL, the influence of second-order dispersion on the pulse clusters is investigated. On that account, a new dynamical boundary condition enabling the correct treatment of the long-term carrier memory is introduced. The investigation unravels that the interplay of amplitude-phase coupling and dispersion can be beneficial in terms of the performance figures and regions of stability. Additionally, the effect of third-order dispersion is examined utilizing a delay algebraic equa-

tion model for the V-shaped VECSEL. On that account, a correspondence of all parameters to the DDE models is found. Comparing the results obtained using both models, it is possible to illustrate the emergence of third-order dispersion instabilities that can especially arise, if the gain chip has a high quality top-side distributed Bragg reflector.
Finally, the delay differential equation model is extended by a more complex modelling of the gain. Namely, the usage of submonolayer quantum dots as the active medium is discussed. The detailed numerical analysis of different parameters illustrates that the amplitude phase coupling can have stronger destabilizing influence, as determined in experiments on similar devices.

Deutsche Zusammenfassung

Passiv modengekoppelte oberflächenemittierende Halbleiterlaser mit vertikalem externem Resonator (Vertical External Cavity Surface Emitting Laser, VECSEL) wurden in den letzten Jahrzehnten intensiv erforscht, was besonders auf den vergleichsweise kostengünstigen und flexiblen Halbleiterherstellungsprozess zurückzuführen ist. Dies führte zu einer erheblichen Verbesserung der Leistungsdaten des gepulsten Laseremission, insbesondere der Pulsbreite und der Pulsamplitude. Daher sind halbleiterbasierte modengekoppelte VECSEL für Anwendungen wie Spektroskopie, Materialbearbeitung und Augenchirurgie zu ihren etablierten festkörperbasierten Pendants konkurrenzfähig geworden .
Die Hauptbestandteile eines solchen Lasers sind ein Halbleiter-Verstärkerchip, ein sättigbarer Halbleiter-Absorberspiegel und eine hochreflektierende Auskopplungsfacette. Um eine effiziente Strahlführung innerhalb des Resonators und ein optisches Pumpen zu ermöglichen, werden die Scheibenlaser häufig in einer V-förmigen Kavitätsgeometrie konfiguriert. Jüngste Experimente mit diesen Lasern haben gezeigt, dass neben den guten Leistungsdaten interessante physikalische Effekte in Form von verschiedenen gepulsten Zuständen auftreten können.
In dieser Arbeit wird zunächst ein Verzögerungsdifferentialgleichungsmodell abgeleitet, um eine detaillierte theoretische Untersuchung eines V-förmigen VECSELs in einem breiten Parameterbereich zu ermöglichen, wobei der Schwerpunkt auf dem Effekt der Kavitätsgeometrie liegt.
Im Folgenden wird eine Bifurkationsanalyse durchgeführt, um das Auftreten von Puls-Cluster-Zuständen in einem Bereich mittlerer Kavitätslängen (0,625 ns Umlaufzeit) zu entschlüsseln. Die Cluster-Zustände treten aufgrund des charakteristischen Puls-Verstärkungsszenarios in der V-förmigen Kavitätsgeometrie auf: Der Verstärkerchip wird von jedem Puls zweimal pro Umlauf passiert. Die Pulscluster werden als zeitlich nicht äquidistante, periodisch auftretende Cluster von Pulsen charakterisiert, deren Periode ungefähr der Kavitätsumlaufzeit entspricht. Cluster mit zunehmender Anzahl von Pulsen entstehen in Cusps von Sattelknoten-Bifurkationen entlang des fundamentalen Lösungszweigs bei charakteristischen Umlaufzeiten. Ihre obere Stabilitätsgrenze kann mittels einer Anpassung der relativen Länge der Kavitätsarme zu höheren Pumpleistungen verschoben werden.
Die Pulscluster werden des Weiteren im Regime einer langen Kavität (Umlaufzeit länger als 2 ns) untersucht. In diesem Bereich sind die Pulse zeitlich lokalisiert, da sie nicht über den exponentiellen Verlauf der Ladungsträgerrelaxation im Verstärkerchip wechselwirken, weil sich der Verstärkerchip zwischen den Pulsdurchgängen vollständig erholt. Interessanterweise bleiben die Pulse innerhalb eines Clusters global durch die Ladungsträgerabräumungen gebunden, werden aber lokal unabhängig, was durch eine Floquet-Analyse gezeigt wird. Da die Pulse eine zufällige Phasenbeziehung beibehalten, können die Clusterzustände als inkohärente photonische Moleküle bezeichnet werden.
Mit Hilfe eines neu hergeleiteten nichtlokalen Haus-Master-Gleichungsmodells für V-förmige

VECSEL wird der Einfluss der Dispersion zweiter Ordnung auf die Pulscluster untersucht. Dafür wird eine neue dynamische Randbedingung eingeführt, die eine korrekte Behandlung der Langzeit Ladungsträgerdynamik ermöglicht. Die Untersuchung zeigt, dass das Zusammenspiel von Amplituden-Phasen-Kopplung und Dispersion sich vorteilhaft auf die Leistungswerte und Stabilitätsbereiche auswirken kann.
Zusätzlich wird der Effekt der Dispersion dritter Ordnung mit Hilfe eines algebraischen Verzögerungsgleichungsmodells für den V-förmigen VECSEL untersucht. Dabei wird eine Übereinstimmung aller Parameter mit dem DDE-Modell gefunden. Der Vergleich der mit beiden Modellen erzielten Ergebnisse zeigt das Auftreten von Dispersionsinstabilitäten dritter Ordnung, die insbesondere dann auftreten können, wenn der Verstärkerchip einen hochreflektiven Bragg-Reflektor auf der Oberseite hat.
Schließlich wird das Verzögerungsdifferentialgleichungsmodell um eine komplexere Modellierung der Verstärkung erweitert. Insbesondere wird die Verwendung von submonolayer Quantenpunkten als aktives Medium diskutiert. Die detaillierte numerische Analyse verschiedener Parameter zeigt, dass die Amplituden-Phasen-Kopplung einen stärkeren destabilisierenden Einfluss haben kann, wie in Experimenten an submonolayer basierten VECSELs festgestellt wurde.

Acknowledgements

I firstly want to thank Kathy Lüdge for supervising my thesis, keeping up an enjoyable and motivating work environment despite the pandemic situation, introducing me to many aspects non-linear laser dynamics and always having an open door for discussion for any kind of problem. I would like to thank Bryan Kelleher for taking the time to be the external reviewer on the examining board for this thesis and Michael Lehmann for being the chairman of the examination board.
In addition to that, I would like to thank my collaborators Svetlana V. Gurevich and Julien Javaloyes for hosting me at the UIB, for all their patience while explaining many numerical and physical concepts, great pizza lunch breaks and a successful cooperation. Also thank you to Christian Schelte for many scientific discussions at UIB.
Furthermore, I want to thank Nina Owschimikow, Bastian Herzog and Alexander Nelde for the nice experimental results in our collaboration and an enjoyable cooperation.
Additionally, I would like to thank Andrea Schulze for always finding a solution for any bureaucratic problem.
A special thanks to Stefan Meinecke and Felix Köster for countless coffee breaks, patiently answering every stupid question, our fun conference visits, proof reading this manucscript and many planking sessions.
Thank you to the members of the nonlinear laser dynamics work group Andre Röhm, Lina Jaurigue, Benjamin Lingnau and David Hering for an enjoyable work environment and scientific discussions. Furthermore, thank you to my bachelor students Victor Rosty, Tobias Rattmann, and Marcella Marggraf.
I am grateful for being part of the SFB910 and the SFB787 and the many seminars and conference I was able to attend.
Furthermore, I would like to thank Aris Koulas-Simos, Lucas Bremer and Marcel Hohn for many funny lunch breaks under pandemic conditions.
I would like to thank Oliver Kohn, Katharina Kohn, Nora Hausen, Raphael Kalender, Aris Koulas-Simos and Lucas Bremer for proof reading this manuscript.
I want to thank my close friends and family for all their emotional support. Thank you to Lara for all her unconditional love and support. Finally, thank you to my parents Ines and Klaus and and my sister Nora for always believing in me and for getting me started with math and physics.

To Dad

Contents

1 Introduction

The foundation of today's laser devices was laid long before the first experimental demonstration. Published in 1899, the French physicists C. Fabry and A. Pérot came up with the idea of an "interference apparatus" to enhance interference phenomena by repeatedly reflecting light between a pair of mirrors [PER99]. In the history of laser devices and in modern applications, this interferometer is a prominent choice to enclose the gain medium and form the laser resonator/cavity, because it is easy to implement or even naturally results in the fabrication of semiconductor laser diodes. About 20 years after this invention, a second landmark was set by A. Einstein, who postulated the stimulated emission of radiation when investigating the quantum nature of light [EIN16, EIN17]. It took another two decades until in 1940 W. Fabrikant had the idea of applying the effect of stimulated emission to amplify radiation [HEC10]. Delayed by the second world war and the complexity of finding the right gain media to be used inside a resonator to achieve the necessary population inversion, which was not well understood, it still took several decades for the first laser to be realised [BER15, HEC10].
At the start of the 1950s, the idea of amplifying microwaves, leading to the so-called maser (microwave amplification by stimulated emission of radiation) device, was independently brought up in the US by C. Townes as well as in Russia by A. M. Prochorow together with N. G. Bassow [HEC10]. All three physicists later received the Nobel Prize in 1964 for their groundbreaking work [NOB98]. Another related Nobel Prize was awarded two years later to A. Kastler for his works on optical pumping at the start of the 1950s [NOB98, COH66], which was a fundamental building block for achieving the amplification of light and microwaves. The premier demonstrations of maser devices were published some years later by J. P. Gordon and C. Townes, who achieved the required population inversion in the gain medium by using a gas filled with excited molecules [GOR54, GOR55, BER15]. In the meantime, solid-state active media were proposed as gain media, marking an important step in the development of solid-state lasers [BLO56]. After the successful application in the microwave regime, C. Townes together with A. L. Schawlow introduced the idea of an optical maser [SCH58], for which slowly the acronym laser (light amplification by stimulated emission of radiation) pushed through inside the research community. Ultimately, the first laser, based on ruby as the active medium, was constructed by T. Maiman, whose initial submission of the results to Phys. Rev. Lett. got rejected in 1960 [HEC10], but was published later in the year with details following in subsequent publications [MAI60, MAI61]. The initial report was the onset of the development of various devices in the following years [SCH61]. Importantly, P. Sorokin and M. Stevenson established lasers based on a four level system as the gain medium, relying on doped calcium fluoride crystals [SOR60, SOR61, HEC10]. These early-stage devices all were operated with a pulsed intensity output, which is necessary for many applications, but for others a constant intensity is vital. Thus, the presentation of a gas laser (Helium-Neon mixture), concurrently being the first device operating in the

continuous-wave regime, i.e. with constant intensity [JAV61], was a further major breakthrough.
Having probably the greatest impact for modern photonic technology, the demonstration of lasing from a semiconductor p-n junction (Gallium Arsenide) was achieved only two years after the ruby laser [HAL62, NAT62, HEC10]. This was the foundation for the invention of a cavity setup that is still the basis of many modern laser setups, namely the vertical cavity surface emitting laser (VCSEL), emitting vertically to the semiconductor plane [MEL65].
Although the first laser devices already delivered a pulsed output, the quest for optimising the performance figures of the pulsed output is still ongoing 60 years later. For example, this includes the optimisations of the pulse duration, repetition rates, production costs, wavelength tuning or timing-jitter (timing stability) of the output. These improvements are aimed at by many diverse innovations regarding the gain material, cavity setup or dispersion control [SPE91, FAI94, STI95, LED98, INN03, KEL03, LI09, HEC10]. Hence, applications such as frequency comb generation for spectroscopy [SCH12c, YE03], different forms of material processing and deposition [BOO04, GRE13d, YAP15, KER16] or optical communications [AVR00, YAR97, LI09] were accomplished. A well-established method for generating a pulsed laser output is the phase-locking of the individual longitudinal lasing modes, which is termed "mode-locking" [WEI09].
One of the most influential researchers on this topic was H. Haus, who introduced the "Haus master equation" for mode-locking. In his famous article "Mode-locking of lasers" [HAU00], he reviewed that the initial theoretical and experimental works on the topic of active mode-locking were established by various groups in 1964 [DID64, HAR64, YAR65, HAU00]. These observations all tackled the active form of mode-locking relying on "internal loss modulation" [HAU00], which can be introduced by an intra-activity electro-optic modulator for example [WEI09]. As its name suggests, the passive mode-locking technique achieves the locking effect by passively modulating the radiation inside the cavity. Examples of passive modulations are saturable absorbers or the exploitation of the optical Kerr effect [WEI09], i.e. Kerr-lens mode-locking. Early-stage realisations of passive mode-locking were obtained with ruby lasers utilising saturable filters/dye, only one year after the active counterpart [MCC65, HER65, MOC65]. However, it took more than a decade until this knowledge was successfully transferred to semiconductor lasers making it possible to generate pulses in the (sub-)picosecond range applying active [HO78, IPP80, HOL80] and passive mode-locking [ZIE81].
For the optimisation of the pulse duration an external cavity configuration with the gain placed inside an external resonator has been found to be very beneficial [SPE91, KEL03], as for example additional dispersion compensation can easily be included into the laser setup [STI95]. Although it was already possible to generate pulses in the 10 fs regime relying on solid state gain media [SPE91, STI95], the introduction of saturable absorbers based on semiconductors was a real breakthrough since it reduced the complexity of laser devices [KEL92, KEL03]. One very prominent realisation is the semiconductor saturable absorber mirror (SESAM) [KEL92, KEL96], which consists of a top side active absorbing section, which can be reversed biased to control the absorption, and a back-side distributed Bragg reflector to ensure a high reflectivity.
Although SESAMs were first applied to the best performing solid state lasers [KEL92], their invention led to the development of passively mode-locked vertical external cavity surface emitting lasers (VECSELs) purely based on semiconductors [HOO00, KEL06, GAA16]. In these setups, also referred to as disk lasers, the gain consists of a highly reflective bottom-

side DBR, an active section, which can be based on different forms of nanometric semiconductor hetero-structures, e.g. quantum wells, and a top side anti-reflection coating [KEL06, TIL15, WAL16, GAA16].
This work aims at theoretically investigating the dynamics of passively mode-locked VECSELs, whose single components are arranged in a V-shaped cavity setup as experimentally presented in Reference [WAL16]. However, the modelling techniques can be easily adapted to describe other VECSEL arrangements. Two landmarks in the theoretical investigation of passive mode-locking were set by G. New and H. Haus in 1974 and 1975 respectively. When investigating how a pulse width below the relaxation time of the absorber can be established, New delivered the explanation of a short open net gain (accumulated gain and losses) window in the vicinity of the pulse. The window opens when the absorber is sufficiently bleached. Consequently, the gain overcomes the losses so that a pulse can be amplified until the gain is sufficiently depleted and the losses dominate again, i.e. the net gain window closes again. In the meantime Haus provided the first closed form analysis for active mode-locking as well as passive mode-locking with a fast and slow saturable absorber [NEW74, HAU75, HAU75a, HAU75b]. Not only because of their intuitiveness, these concepts are still of much value today. In particular the Haus master equation approach [HAU00] allows an analysis of the dynamics at low computational costs. However, with the increase of computational capacity, more complex models have been developed to explain the behaviour of devices for which Haus and New's approximations fail. These comprise for example travelling-wave approaches to capture details of the device geometry and spectral field [FLE68, AGR89, MUL06, JAV10, RAD11a, ROS11c, MEI19], fully microscopic models suitable to investigate the generation of pulses in the femtosecond regime [HAD99, KIL17, KIL18, MCL20], models based delay-algebraic equations to describe resonance effects in the semiconductor micro-cavities [MUL05a, SCH19b], delay differential equation systems to effectively reproduce the dynamics while circumventing the approximations of small gain and loss [VLA04, VLA09, VIK06, JAU16] or extended master equation approaches based on partial differential equations to investigate coherent effects or dispersion [DIN09, PER20, CAM16, HAU20a]. The advantages and disadvantages of the latter three approaches (delay algebraic model, delay differential model, extended Haus master equation) are elaborated in this work by applying them to a V-shaped passively mode-locked VECSEL. This is done in the context of getting a better understanding of these devices in different operation regimes, e.g. long and short cavity limit, and therefore deliver a theoretical framework to enhance the performance of such devices for applications such as frequency comb generation for spectroscopy or super-continuum generation [KLE14, WAL16, COD16, LIN17e, WAL19], optical frequency metrology [UDE02] or two photon microscopy [AVI11a, VOI17].
This work is structured as follows: In chapter 2, a brief introduction to the basic physical background is given, which comprises semiconductor lasers, passive mode-locking and bifurcations. Following in chapter 3, a delay differential equation model for a passively mode-locked V-shaped semiconductor VECSEL based on quantum well active media is derived. The model represents the starting point of a large part of the results presented in this manuscript. In chapter 4, the emergence of specific pulse patterns, resulting from the influence of the cavity geometry, is discussed in detail considering all relevant parameters of the systems. Furthermore, the impact of the cavity configuration on the laser output in the intermediate- and long-cavity regime is elaborated. Additionally, a nonlocal Haus master equation for the V-shaped laser system is derived. In chapter 5, dispersion effects are dis-

cussed requiring the introduction of two further mathematical models. Namely, these are an extension of the Haus master equation to adequately reproduce the dynamics in the regime of strong gain modulations and a delay algebraic system, which enables the investigation of third-order dispersion. Chapter 6 deals with the impact of the gain structure. The influence of using submonolayer quantum dots as the gain medium in comparison to quantum wells is explored. On that account, the delay differential equation model is extended by a more complex description of the charge carrier dynamics in the gain, enabling the investigation of the coupling between different energy states of the semiconductor material, i.e. the active submonolayer quantum dot states and the 3D semiconductor bulk. A summary and conclusion is given in chapter 7.

2 Theory

To theoretically explore the parameter dependence of the laser emission state and its key performance figures, the most commonly applied framework is the description of the device as a (nonlinear) dynamical system. A dynamical system is defined as the mathematical formulation of a time-dependent deterministic process, which can be used to predict the temporal evolution of the characteristic system variables [KUZ98a]. This type of modelling stretches across many different disciplines such as biology, economics, chemistry and physics [GUC83, STR94a, KUZ98a]. Lasers are typically described by means of differential equation systems. These can be derived by finding adequate equations for the evolution of the electric field and the charge carriers in the gain medium while also including their interaction. For semiconductor lasers, this is often based on a semi-classical approach, in which Maxwell's wave equations are coupled to a Schroedinger equation describing the charge carrier dynamics [OHT08, ERN10b]. The latter strongly depends on the characteristics of the gain configuration, which can be effectively varied due to the well-established semiconductor growth techniques.
From an experimental perspective, a practical technique to establish a pulsed output from a semiconductor laser is the application of *mode-locking*. It includes an active or passive loss modulation of the lasing modes and therefore leads to a formation of a pulsed state, if applied correctly. Consequently, a multi-mode approach as well as the correct inclusion of the loss modulation into the dynamical system, is necessary to describe mode-locked lasers.
One key approach to investigate dynamical systems and to classify their temporal behaviour at different parameters is a linear stability analysis [GUC83, STR94a, KUZ98a]. This technique is based on determining the response of the system in a close vicinity of a fixed-point or periodic solution, so that it can be approximated to be linear. The stability information opens up the possibility to unravel changes in phase space that occur when altering the laser parameters. The characteristic parameter points at which these qualitative changes of the state occur are mathematically referred to as bifurcations. Close to these critical parameter points, dynamical systems can be described by generic normal forms and it is therefore possible to easily compare systems across different disciplines. Most famous is the occurrence of deterministic chaos mediated by different bifurcations among a variety of systems [AHL02, AHL06, BLA04a, CLA09, HUE91a, COU87]. Furthermore, this enables the prediction of the lasing state of a system by investigating the dependence of the critical bifurcation points on the parameters of interest.
In order to provide an overview of the basic theoretical concepts applied in this work, this chapter firstly introduces semiconductor lasers and the characteristics of different gain designs in section 2.1. Secondly, the concept of mode-locking is shortly discussed with a special focus on passive mode-locking, as the basis of the lasers discussed in this work (section 2.2). Lastly, the fundamentals of bifurcation theory as well as the most important bifurcations that are part of this work are outlined in a descriptive manner in section 2.3.

2.1 Semiconductor Lasers

Characteristic for semiconductors is the structure of their electronic states. They are defined as bands, which have a continuous shape, relating the allowed electronic energy and momentum of a charge carrier in the ionic lattice [CHO99]. The highest energy band that is completely filled at zero temperature is known as the valence band, while the next higher band is referred to as the conduction band. In between bands an energy interval exists in which no electronic states are allowed. It is known as the bandgap. Equal to the characteristics of the bands, it results from the lattice structure and is therefore characteristic for the semiconductor material. If the valence band maximum and the conduction band minimum lie at the same electron momentum, the bandgap is defined to be direct [HAK86, CHO99]. A direct bandgap greatly enhances the probability of radiative transitions, which are defined by the relaxation of an electron in the conduction band to an unoccupied valence band state (hole) via the emission of a photon. In case of indirect bandgaps, the radiative transitions further require electron-phonon interactions, which makes them less probable. Therefore, a direct bandgap is a required property of a semiconductor laser gain material. The occupation of the electronic states across the different bands is determined by a Fermi-function [CHO99].
The physical bases of every semiconductor laser device are the fundamental types of quantum mechanical light-matter interactions. Namely, these are the absorption, spontaneous emission and stimulated emission of a photon. Their basic concept is visualised in the context of the semiconductor band structure in Fig. 2.1. Sketched is the energy of valence and conduction band and their dependence on the electron momentum with electron and hole states along the bands indicated by red circles.
The absorption process is defined as the excitation of an electron from the valence to the conduction band mediated by a photon that has an energy larger than the bandgap $h\omega > E_{\mathrm{gap}}$. This process is exploited when optically pumping semiconductor lasers. In these pumping schemes, valence band electrons are excited by the usage of a second laser device that emits photons with an energy far above the bandgap. The excited electrons then relax back to the bandgap edge via electron and phonon scattering processes.
The reversion of (spontaneous) absorption is represented by the occurrence of spontaneous emission. In this process a photon is emitted, if an electron from the conduction band recombines with a hole state in the valence band. The emitted photon exhibits a random polarisation and direction.
As postulated by Einstein, stimulated emission is defined as the process in which a photon triggers the radiative relaxation of an excited electron. As a part of the relaxation, a second photon is emitted that has the same polarisation, energy and phase as the incoming photon. The requirement to the incoming photon however is that its energy matches the bandgap energy.
Lasing is defined as the continuous exploitation of stimulated emission to amplify light. This requires maintaining a situation in which stimulated emission exceeds the absorption processes and other losses. On that account, a population inversion in the semiconductor material is necessary, i.e. the number of states occupied in the conduction band has to exceed the number of occupied states in the valence band. This is connected to the fact that the probability of the optical transitions (stimulated absorption and emission) are proportional to the population of the initial and final state of the electron that is excited or recombines. A population inversion can be achieved by means of electrically or optically pumping the

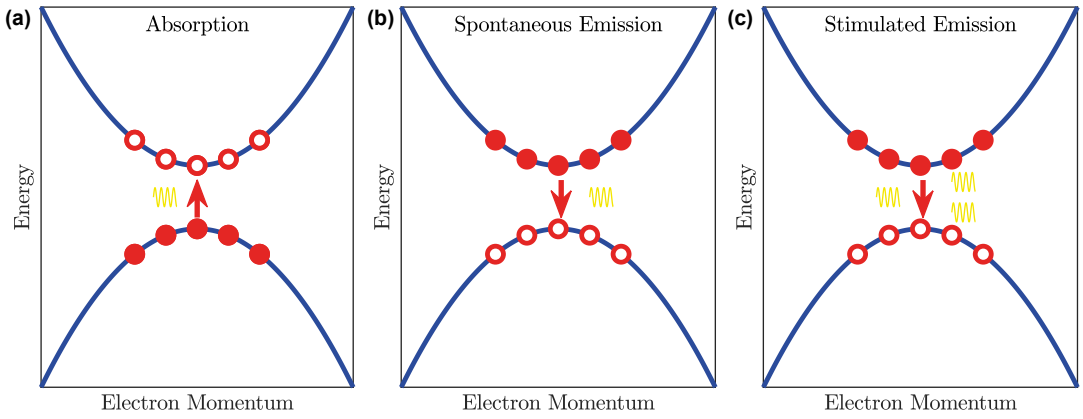

Figure 2.1.: Fundamental types of light-matter interaction. The blue curves denote the valence and conduction band of a semiconductor, the filled red (hollow) circles denote electrons (holes). (a) Absorption of an incoming photon (yellow) that leads to the excitation of an electron from the valence to the conduction band. (b) Spontaneous emission of a photon, mediated by the radiative recombination of an electron-hole pair. (c) Stimulated emission of a photon; an incoming photon triggers the radiative recombination of an electron-hole pair that leads to the emission of a photon equalling the incoming photon in polarisation, energy and direction. Figure based on Fig. 1.2 in [LIN15b].

semiconductor gain medium. The onset of light amplification by stimulated emission of radiation (lasing) is defined as the point at which the generation of coherent photons exceeds the optical losses. A very effective way to reduce the optical losses is to position the gain medium inside a resonator. The simplest form of a resonator consists of two highly reflective mirrors at the two ends of the semiconductor medium, known as a Fabry–Pérot cavity.
The first realisations of lasing from a semiconductor were reported in 1962 [HAL62, NAT62, HOL62, HEC10]. The semiconductor gain medium in these laser setups was based on a p-n homojunction. In these structures, the p-type section is doped with additional atoms from a lower element group, resulting in an excessive number of holes, while the n-type section is doped with atoms from a higher group so that excessive electrons are present. In the area around the connection point, the excess charge carriers recombine and consequently no free carriers remain. The system can be driven from equilibrium by applying an external voltage, which leads to a continuous radiative recombination in the interface region [EIC10]. However, lasing with this type of gain structures was only possible at cryogenic temperatures and in pulsed operation mode [CHO99, HEC10], leading to a very low efficiency not suitable for any type of applications. One of the most important developments on the way towards today's highly efficient semiconductor laser devices at micrometer sizes, was the successful introduction of semiconductor hetero-structure growth [ALF69, ALF96, CHO99]. Exploiting the characteristics of different bandgap materials lead to a much higher carrier and optical confinement and therefore greatly enhanced the efficiency [CHO99].
Another great progress was marked by the establishing of quantum well heterostructures growth [DIN74, DIN76]. Quantum well heterostructures are defined as semiconductor layers, whose spatial extension is reduced to the order of roughly one De Broglie wavelength in one dimension. The spatial localisation of the charge carriers in one dimension drastically changes the dependence of the density of electronic states on the energy compared to the typical square root dependence in a semiconductor 3D-bulk structure as presented in Fig. 2.2

[CHO99]. The advantages of the quantum confinement are not only the increased efficiency, due to the higher modal gain, but also a tailorability of the transition energies as well as the time scales of the carrier dynamics [GOE83, HAD04, ALF96, OHT08, COL12]. The first quantum well laser was realised in 1975 [ZIE75], but it took several more years to achieve lasing with good performance figures [ALF96]. Nowadays, they are commercially available and included into many applications, of which the most important one is probably optical fibre communication [COL12]. Multi-layered quantum wells are also part of quantum cascade lasers, which are based on intersubband transitions [GMA01, YAO12]. These offer the possibility to conveniently achieve lasing from semiconductors in the mid-infrared regime.
As technology advanced, the further reduction of the spatial dimensions was made possible, paving the way for lasers based on quantum wires [YAC96, HAR05, LEL07, MAY13] or quantum dot heterostructures [BIM97, BIM99, BIM08a]. As the quantum confinement in all three spatial dimensions leads to a discrete density of states (see Fig. 2.2(c)), quantum dots are also referred to as artificial atoms [CHO13a]. Due to their high efficiency, quantum dot lasers are interesting candidates for nano-laser technology [CHO14b, DEK20]. However, in the field of disk lasers quantum dot gain media still cannot compete with the well-established quantum well lasers [GER08a, SCH09h, NEC19, GAA16, GUI17].
Semiconductor lasers are often modelled by means of rate equations describing the temporal evolution of the number of laser photons $S(t)$ and the number of charge carriers carriers $N(t)$ (electrons and holes) [LIN15, ERN10b]. In its simplest form such a rate equation model reads [LIN15, ERN10b]

$$\frac{dS(t)}{dt} = 2g\,[N(t) - N_0]\,S(t) - \frac{1}{T_{\mathrm{ph}}}S(t), \tag{2.1}$$

$$\frac{dN(t)}{dt} = J - \frac{1}{T_{\mathrm{C}}}N(t) - 2g\,[N(t) - N_0]\,S(t), \tag{2.2}$$

where N_0 is the charge carrier number needed to achieve a population inversion (transparency), T_{ph} is the photon life-time mediated by outcoupling losses and T_{C} represents the excited charge carrier life-times [ERN10b]. The optical or electrical pumping of the active section is accounted for by the term J. The influence of the nonlinear term, representing the stimulated emission, is given by the linear gain coefficient g.
Although the system is defined only by a few parameters, it is sufficient to model a wide range of dynamical phenomena, especially if it is extended to model the influence of optical feedback or an external optical injection induced by a second laser [LAN80b, YAN10, ROT07, ERN95a, ALS96, HEN83, HEN80].
In this work, a delay differential equation approach is followed (see chapter 3) to adequately describe the characteristics of a passively mode-locked vertical external-cavity surface-emitting laser, arranged in a V-shaped cavity geometry. Its active sections are embodied by multilayered semiconductor quantum wells.

2.2 Mode-locking of Lasers

Definition

Mode-locking is a technique to generate ultra-short laser pulses. It is mostly established among solid-state and semiconductor laser devices [IPP94, HAU00, KEL06]. The Fourier transform of the pulsed laser output as indicated in Fig. 2.3 [IPP94], helps understanding

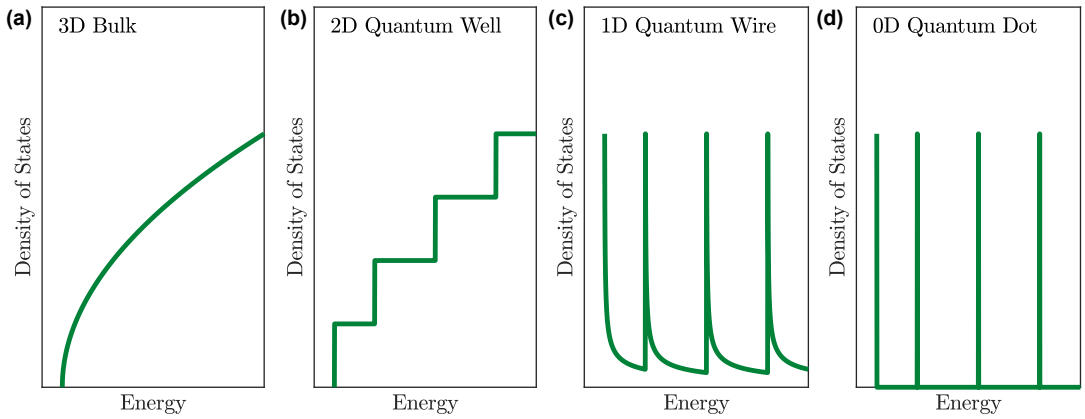

Figure 2.2.: Sketched density of states for different semiconductor structures with differing spatial localisation of the charge carriers. The spatial localisation occurs due to the reduction of the structure in one or several dimensions to a spatial extension of the order of roughly one De Broglie wavelength, as indicated by the sketches in the upper part of the subpanels. Figure based on Fig. 1.3 in [LIN15b].

the terming of the technique. One directly notices that opposed to CW emission, many different longitudinal modes (blue lines Fig. 2.3(b)) are amplified in the emission process [HAU00]. The fundamental mode-locking state is defined as a pulsed laser emission in which the temporal distance between the pulses roughly equals the cold-cavity round-trip time T as shown in Fig. 2.3(a). The splitting of the modes in the power spectrum of the pulses is approximately given by the inverse round-trip time $\Delta f = 1/T$, characteristic of a Fabry–Pérot resonator [IPP94]. Slight deviations from this splitting occur, due to nonlinear light-matter interactions. The amplification of each mode is characterised by the laser's gain spectrum. It is mainly determined by the properties of the gain material and the configuration of the active gain section. The latter includes the geometrical design and arrangement of localisation centres (e.g. quantum wells) as well as additional structures such as distributed Bragg reflectors to increase the reflectivity. The often-used Lorentzian approximation of the gain spectrum is indicated by the red line in Fig. 2.3(b) and its bandwidth is denoted as γ [HAU00, VLA04]. In an ideal case without dispersion and further nonlinear effects, the inverse spectral bandwidth would directly translate to the pulse width $PW \approx 1/\gamma$.
For a better understanding of the mode-locking mechanism in the time domain, a single longitudinal mode can be referred to as a plane wave with the relative phase ϕ_n, amplitude A_n and frequency ω_n. The temporal evolution of the mode can then be written as[1]

$$A_n e^{i(\omega_n t + \phi_n)}. \tag{2.3}$$

As indicated in the pulse spectrum before, the axial modes are approximately separated by $\Delta\omega = \frac{2\pi}{T}$, where T is the round-trip time of the laser [HAU00]. Precisely, standing waves are only supported in the laser resonator, if they fullfill the boundary condition $\frac{n\lambda}{2} = L$, where L is the cavity length and n is the refractive index. An example of the temporal evolution of two longitudinal cavity modes with relative phase ϕ_n is shown in Fig. 2.4(a). Utilising the approximation for the frequency spacing, one can rewrite the frequency of the modes in terms of the mode spacing and the central optical frequency ω, which gives $\omega_n = \omega_0 + \frac{2\pi n}{T}$.

[1] Please note that the interpretation of the longitudinal modes as independently oscillating plane waves in a cavity is not always meaningful. However, it is a common way to support the explanation of mode-locking.

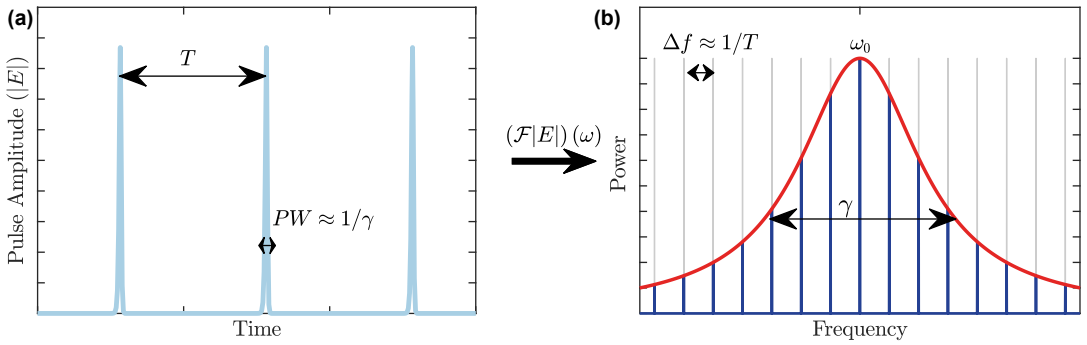

Figure 2.3.: Time-series of a pulsed laser output and corresponding power spectrum in the frequency domain. (a) Time series of the electric field amplitude in the fundamental mode-locking state. Characteristically, the pulses are separated by approximately the cold-cavity round-trip time T. The pulse width is approximately given by the inverse bandwidth of the power spectrum, which is shown in (b). The blue lines denote the different longitudinal (axial) cavity modes. The red curve depicts the gain spectrum of the laser, approximated by an Lorentzian lineshape. The cavity modes are separated by approximately the inverse round-trip time $\Delta f \approx 1/T$ and the full width at half maximum (FWHM) of the spectrum is given by γ. Figure based on [MEI21a].

The superposition of an arbitrary number of longitudinal modes can therefore be expressed as

$$\mathcal{E}(t) = \sum_{n}^{N} A_n e^{i\left(\frac{2n\pi}{T}t+\phi_n\right)}, \tag{2.4}$$

where the optical component $\exp(i\omega_0 t)$ was factored out and $\mathcal{E}(t)$ is the slowly varying complex electric field envelope. From the superposition, one can deduce that for a pulsed output the modes are required to be coherent, i.e. maintain a fixed relationship of the relative phases ϕ_n in time [IPP94, HAU00]. However, as indicated in Fig. 2.4(b)-(c), this is not the only requirement. If the relative phases are randomly distributed, their superposition does not yield the formation of pulses as presented in Fig. 2.4(c). In contrast, the ideal case of perfectly synchronised modes, i.e. $\phi_n = 0$, leads to a formation of a train of narrow pulses. Yet, other adequate distributions of ϕ_n (e.g. quadratic) also lead to the formation of pulses, which are understood to be chirped [FON83].

Techniques

In experiments, mode-locking can be achieved by introducing a modulation of the optical losses [IPP94, HAU00]. This can be applied actively or passively.
As its name suggests, active mode-locking is based on the active modulation of the losses, often realised by introducing an electro-optic modulator (EOM) inside the laser cavity. The formation of the pulses occurs, if the EOM device modulates the central mode at the frequency of the inverse round-trip time [HAU00]. In turn, the modulation leads to the formations of side-bands in the optical spectrum, which injection lock with adjacent modes. This process continues to further neighbouring modes [NEW74, IPP94, HAU00].
In contrast, Passive mode-locking relies on a loss modulation induced by a passive component, such as a saturable absorber. The first theories to explain passive mode-locking were introduced by Haus and New [NEW74, HAU75a, HAU75b]. News's work unravelled a famous stability criterion, which still provides a widely used framework to understand

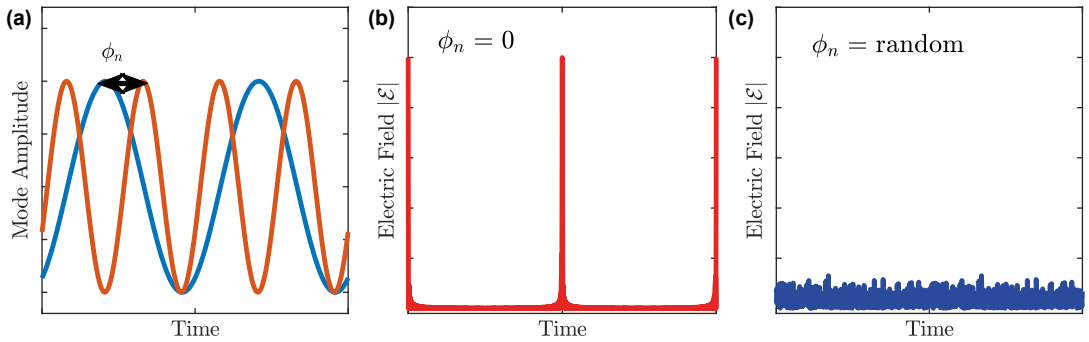

Figure 2.4.: (a) Two single oscillating plane waves with differing frequency and relative phase ϕ_n. (c) Superposition of 500 modes with a constant frequency splitting $\omega_n = n\omega_0$ and with $\phi_n = 0$ across all modes. (c) Same superposition as in (b), but with randomly distributed relative phases ϕ_n.

mode-locking instabilities [NEW74, MAR14c, OTT13, JAU17a]. He pointed out that the duration of the pulse does not only depend on the fast recovery of the absorber but also on its saturation relative to the gain. For a semiconductor mode-locked laser, this can be best understood from investigating the time-series of the electric field as well as the gain and loss as indicated in Fig. 2.5(a)-(b). Subtracting gain and losses leads to a quantity introduced as the **net-gain**. If this quantity is above 0, the pulse experiences an amplification, otherwise the light output is suppressed. As indicated in the time-series of the net gain in Fig. 2.5(c), the pulses always coincide with an open net gain window (net-gain > 0). If one investigates the dynamics in the vicinity of the pulse (Fig. 2.5(a)-(c)), the mechanism of the opening net-gain window becomes evident. As the pulse saturates the absorber, the gain becomes greater than the losses and the pulse can be amplified as long as this situation is maintained (the net-gain window is open), indicated by the green shaded area in Fig. 2.5(d)-(e). However, as the gain is fully depleted or the absorber recovers quickly, the open net-gain window closes again, suppressing the further amplification of light. Hence, the introduction of a saturable absorber leads to the formation of a regular pulse train that is robust against perturbations due to the negative net-gain in between pulses.

Passively mode-locked lasers have been realised based on different gain materials as well as cavity configurations. In the early-stages of mode-locking, dye gain media were a widely spread choice in the realisation of external cavity lasers [NEW74, SHA74, HER78, FON83, PEN92]. However, with regard to the very low timing jitter and extremely low pulse lengths in the femtosecond regime, external cavity lasers based on solid-state materials became the most successful devices and are commercially available for different applications today, with Ti:Sapphire lasers being the most prominent gain material [SHE02, SCH03i, FOR03, KIM07]. Next to external cavity setups, passively mode-locked solid-state fibre lasers have been successfully established for different wave-lengths and with narrow line-widths suitable for specific spectroscopy applications [ORS04, KUE17, ZOU20]. With the ongoing improvement and better understanding of epitaxial growth, semiconductor materials have become an attractive choice as gain media in external cavity devices as well as monolithic devices. The latter have been shown to exhibit excellent performance figures at different cavity layouts [ROS11f, WEB15, MEI19] and can be based on various localisation centres (heterostructures) in the active section, e.g. quantum dots [RAF07, MEE14, NOR19], quantum wells [KAI07b, MUL05a, WEB18a] or quantum dashes [VUJ15, ZEB21]. Due to their exceptional scalability, which ultimately aims at on-chip integration, monolithic mode-locked

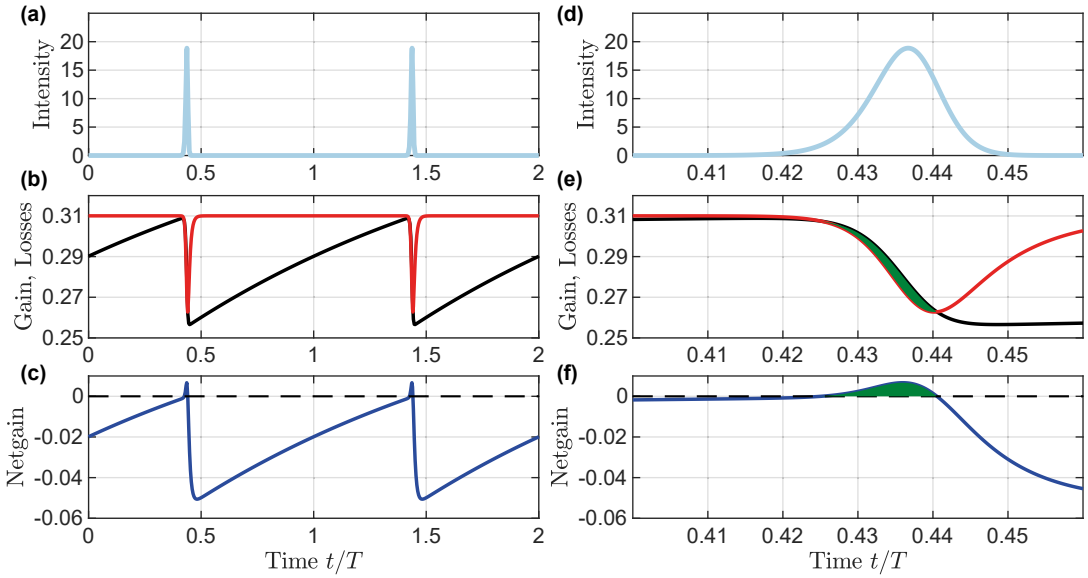

Figure 2.5.: (a) Intensity time-series in the regime of the pulsed fundamental mode-locking state. (b) Dynamics of the charge carriers in the gain (black) and the saturable absorber (red). (c) Net-gain dynamics calculated from subtracting the gain and the total losses at every point in time. (d)-(e) Show the same dynamics as in (a)-(c) but zoomed to the vicinity of a single pulse. Figure based on [JAU17a].

lasers are ideal candidates for data transmission, e.g. in optical communication systems [KAI07b, SCH10g, ZEB21, ROS11g], data centres [VUJ15] or for the realisation of on-chip artificial neurons [MES16]. The invention of the semiconductor saturable absorber mirror [KEL96], lead to a lot of progress in the research of mode-locked disk lasers based on semiconductor chips [HOO00, KEL06, GAA16]. Similar to their solid-state counterparts, these devices can be used to generate ultra-short pulses and very broad frequency combs [WAL16, WAL19, GAA16]. Specifically, passively mode-locked vertical-external cavity surface-emitting lasers are the subject of this work and the setup is elaborated in detail in section 3.2. Other mentionable applications that require broad frequency combs or ultra short pulses are distance measurements [JAN18a], measurements of the optical frequency via analysis of beat signals [REI99b], frequency synthesizers [CUN01], super-continuum generation [MAY15a, WAL16, WIL13b], eye surgery [JUH99, NAG09], meteorology [UDE02, DID10] or dual comb spectroscopy [LIN17e].

It has to be mentioned that hybrid mode-locking techniques (combination of active and passive techniques) also exist and have been successfully realised in various experiments [THO03, FIO10, KUN07a, AHM08]. One primary advantage includes the reduction of noise and its influence on the temporal fluctuations of the repetition rate (Timing Jitter) [FIO10, HAB14, JAU17a]. Furthermore, for many applications it is desirable to synchronise the pulse repetition rate with an external electrical signal that can be realised by a small modulation of the absorber section [KUN07a]. However, hybrid mode-locking techniques are seldomly applied in semiconductor disk lasers and therefore not discussed in this work.

As already visible from the dynamics in Fig. 2.5, the dynamical models for passively mode-locked lasers have to include the dynamics of the saturable absorber. A helpful tool to learn more about the influence of the additional time scales in the dynamical system and the interplay between gain and absorber is given by a bifurcation analysis. In simple terms,

this technique offers a mathematical approach to investigate critical parameter points of the system at which the dynamics change their characteristics.

2.3 Bifurcations

In a generic framework, a dynamical system can be described by a system of ordinary differential equations with respect to time[2]

$$\frac{d}{dt}\mathbf{x}(t) = \mathbf{f}(\mathbf{x}), \tag{2.5}$$

here the vector $\mathbf{x}(t) = (x_1(t), ..., x_n(t))$ contains the time-dependent variables of the system. With regard to a laser, $\mathbf{x}(t)$ at least contains a variable related to the electric field and the gain charge carrier dynamics, as priorly discussed. However, the system can be of higher dimension, if the occupation numbers of different quantum dot subgroups are modelled separately or the dynamics of the microscopic polarisation states are included for example [LIN15b, MCL20, KIL17]. The functions $\mathbf{f} = (f_1, ..., f_n)$ are characterised by the investigated problem and mediate the evolution of the system variables with respect to time. Typically, this evolution is analysed by representing the variables in the vector space $(x_1, .., x_n)$ at each point in time during the time interval of interest. In a graphical representation, the resulting line of $(x_1(t_0), ..., x_n(t_0)) \rightarrow (x_1(t_{\text{end}}), ..., x_n(t_{\text{end}}))$ is referred to as a trajectory and the vector space is referred to as the phase space. The course of a trajectory in phase space depends on the initial conditions of the system $\mathbf{x}_0$ as well as the attractors and repellers of the system. As their name suggests, attractors (repellers) can be simply understood as characteristic points in phase space, which attract (repel) a trajectory. The simplest type of these points are fixed-point solutions $\mathbf{x}^*(t)$, which are characterised by the condition

$$\frac{d}{dt}\mathbf{x}^*(t) = \mathbf{f}(\mathbf{x}^*(t)) = 0. \tag{2.6}$$

Thus, if a system (trajectory) is in a fixed-point, the dynamics remain unchanged forever, if no external perturbation is applied. How a system reacts to a perturbation, while being in a fixed-point solution, determines if the solution is classified as stable or unstable, i.e. is attracting or repelling. In a stable fixed-point, small perturbations are damped out and the system remains in the fixed-point [STR01a]. In contrast, already the smallest possible perturbation drives the system away from an unstable fixed-point. However, unstable fixed-points are still of significance as their repelling character can have a large influence on the behaviour of the system, especially if noise is present. A very prominent example are low frequency fluctuations in laser systems subject to feedback, which can be understood as excursions of the trajectories around unstable external cavity modes (fixed-points) [MOR88, HEI98c, VIK00]. Furthermore, unstable solutions can turn stable, if the parameters of the system are altered. For example, in an optical feedback scheme the stabilisation of pulsed solutions when increasing the optical feedback strength can be observed [TYK16, KEL17b, HAU21].
The parameter points at which the character of an attractor (or repeller) changes or additional solutions are born (or vanish) are mathematically referred to as bifurcation points. They can be subdivided into the classes of global or local bifurcations. To investigate the

[2]The author highlights that the introduction given in this chapter is based on the books [STR01, KUZ98a]. The former is recommended for a general introduction to dynamical systems and the latter for a rigorous mathematical description of dynamical systems and bifurcation theory.

former, it is not sufficient to only examine the phase space in a close vicinity of a fixed-point solution to unravel the change in dynamics. Rather, a global investigation of neighboring bifurcation points is required as several local bifurcations can be part of a global bifurcation scenario. These are, however, not part of this work and an introduction can be found in Reference [KUZ98a]. As their name suggests, local bifurcations can be discovered by determining the reaction of the system to perturbations in a close vicinity of a fixed-point. The commonly applied method to asses the local stability is based on a linearisation of the system around the fixed-point. Following the linearisation, one can recover a dynamical equation for the temporal evolution of the deviation $\delta\mathbf{x}(t)$ from the fixed-point $\mathbf{x}^*$, i.e. its reaction to a perturbation

$$\frac{d}{dt}\delta\mathbf{x}(t) = \mathbf{J}|_{x*}\,\delta\mathbf{x}(t). \tag{2.7}$$

The entries of the Jacobian matrix $\mathbf{J}|_{x*}$, evaluated at the investigated fixed-point, read $J_{i,j} = \frac{df_i}{dx_j}\Big|_{x*}$. The stability can finally be determined by calculating the eigenvalues λ of the Jacobian. If all eigenvalues have a negative real part $\mathrm{Re}(\lambda) < 0$, perturbations are damped out and therefore the fixed-point is stable. However, if one eigenvalue has a positive real part $\mathrm{Re}(\lambda) > 0$, the solution $\delta x(t)$ diverges, which means that the derivation from the fixed-point growth in time. Therefore, the fixed-point[3] is unstable.

Bifurcations of Fixed-Points

Performing a linear stability analysis at continuously varied parameter values can be applied to unravel bifurcations. The bifurcation points can be identified as the parameter points at which the sign of one or several eigenvalues change. In this work, three types of bifurcations of fixed-points are encountered, for which the behaviour of the eigenvalues and their appearance in 1D-bifurcation diagrams is presented in Fig. 2.6.
Firstly, a saddle-node bifurcation[4] can be understood as the transition from an unstable to a stable solution, which appears as a fold of the solution branch. The bifurcation point is characterised by a single eigenvalue crossing the imaginary axis in Fig. 2.6(a_1) and is marked by the dashed line in Fig. 2.6(a_{2-3}). The stable and unstable part of the branch is plotted in a 1D-bifurcation diagram in Fig. 2.6(a_{2-3}), where the x-axis denotes the bifurcation parameter and the y-axis the value of one system variable in the fixed-point (this could be e.g. the intensity in laser systems). Thick lines denote a stable fixed-point and thin lines an unstable fixed-point. The supercritical form of the bifurcation is shown in Fig. 2.6(a_2) and the subcritical form is presented in Fig. 2.6(a_3). The square root dependence of the fixed-point is characteristic for the saddle-node bifurcation and can always be recovered close to such a

[3] For the delayed systems investigated in this work the technique works analogously. The dynamical system can be defined as

$$\frac{d}{dt}x(t) = \mathbf{f}(\mathbf{x}(t), \mathbf{x}(t-\tau)), \tag{2.8}$$

and the delay then leads to another contribution in the linearisation

$$\frac{d}{dt}\delta\mathbf{x}(t) = \mathbf{J}|_{x*}\,\delta\mathbf{x}(t) + \mathbf{B}|_{x*}\,\delta\mathbf{x}(t-\tau), \tag{2.9}$$

where $J_{i,j} = \frac{df_i}{dx_j}$ and $B_{i,j} = \frac{df_i}{dx_j(t-\tau)}$ [JAU17a].

[4] Per se, the saddle-node bifurcation is strictly no bifurcation, as two fixed-points appear "from nothing" and do not bifurcate from another solution. However, in the literature it is anyhow referred to as a bifurcation.

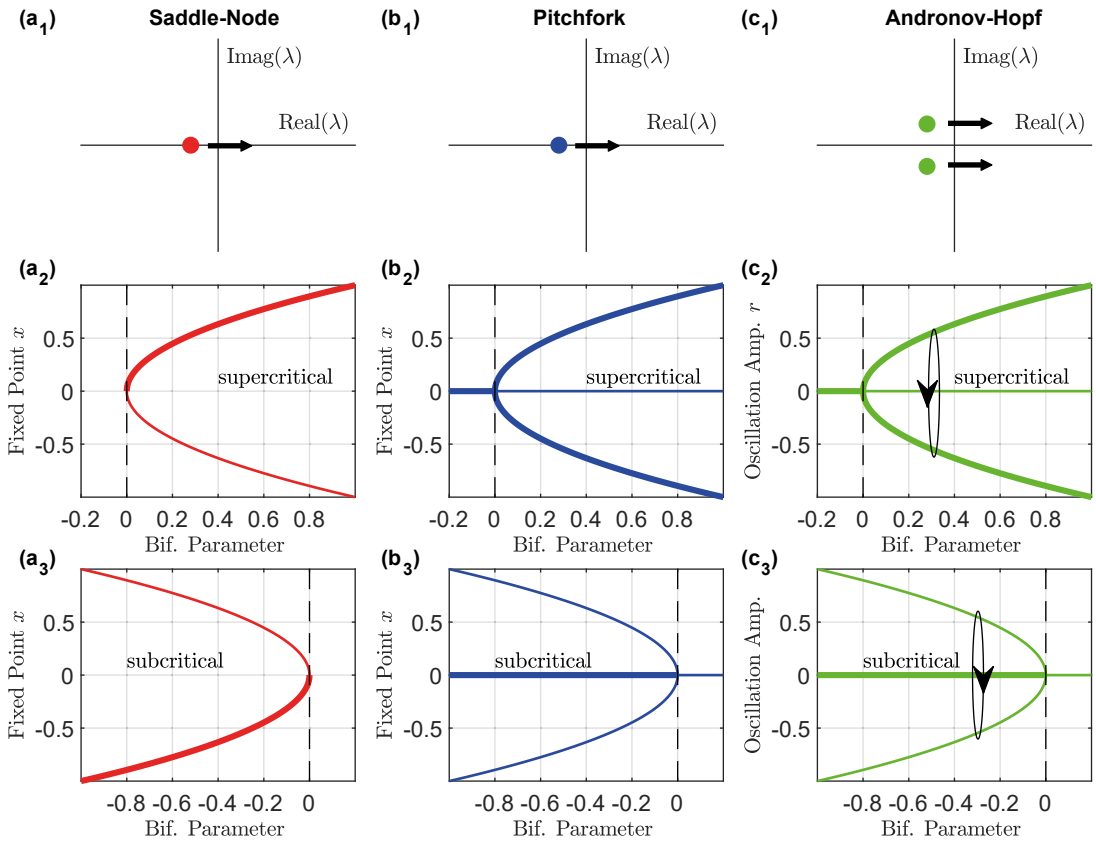

Figure 2.6.: Characteristics of different bifurcations of fixed-points: (a) Saddle-Node bifurcation, (b) Pitchfork bifurcation and (c) Andronov-Hopf bifurcation. (a_1)-(c_1) Behaviour of the critical eigenvalue at the bifurcation point in the complex plane. (a_2)-(c_2) 1D-bifurcation diagram showing the characteristic dependence of the fixed-point value on the bifurcation parameter close to the bifurcation points (dashed vertical line) for supercritical bifurcations. Thick (thin) lines denote stable (unstable) dynamics. (a_3)-(c_3) 1D-bifurcation diagram for the subcritical case of all bifurcations.

bifurcation point independent of the specifics of the system. Alternative to the understanding of the stable and unstable solution belonging to a single branch, one can interpret the bifurcation point as a collision of the stable and unstable fixed-point solutions, which causes both solutions to vanish.

At a supercritical pitchfork bifurcation, one fixed-point becomes unstable and two additional stable fixed-points are born with a symmetrical evolution of their fixed-point values (see Fig. 2.6(b_2)). Hence, one eigenvalue of the central fixed-point crosses the imaginary axis at the bifurcation point as depicted in Fig. 2.6(b_1). A 1D-bifurcation diagram of the subcritical case is shown in Fig. 2.6(b_2).

An Andronov-Hopf bifurcation marks the birth of a periodic orbit (limit cycle solution). This type of solutions is different from a fixed-point solution as they describe an "isolated closed trajectory" [STR01a] instead of a single point in phase space. If a dynamical system falls onto a limit cycle attractor, its temporal dynamics is given by a periodic oscillation with period $\tau_p > 0$ in phase space so that $A^*(t) = A^*(t + \tau_p)$ for all t [LUZ02]. Below the bifurcation point, only a fixed-point solution exists (left of the dashed line in Fig. 2.6(c_2)). The limit cycle is born as a pair of complex conjugate eigenvalues (with non-zero imaginary part) of the fixed-point solution crosses the y-axis in the complex plane (see Fig. 2.6(c_1)) at

the bifurcation point. The oscillation frequency is approximately determined by the imaginary part of these eigenvalues. To present a 1D-bifurcation diagram, only the maxima and minima of the oscillation in one variable are plotted in Fig. 2.6(c_{2-3})) with the ellipses indicating the oscillation. In consequence, the upper and lower branch correspond to the same solution, in contrast to the pitchfork bifurcation giving birth to two additional solutions. Andronov-Hopf bifurcations play a central role in the onset of pulsed mode-locking oscillations [VLA04, VLA05, JAU17a, HAU19] or oscillations induced by laser feedback [MOR92, HEL90b, RIT93a, PIE01].

Bifurcations of Limit Cycles

As discussed for fixed-point solutions, the stability of limit cycles and their appearance can also change when the system parameters are altered. These parameter points are defined as limit cycle bifurcations. To obtain the stability of limit cycles, a similar linearisation technique as for fixed-points can be applied to find a differential variational equation (linearised system giving the behaviour of the perturbations)[LUZ02]. The framework used to determine a set of eigenvalues of a characteristic integration operator matrix (monodromy operator $\mathcal{M}$), that describe the stability, is known as Floquet theory. A detailed introduction and techniques of numerical calculation are presented in References [LUZ02, ENG02, KLA08, JAU17a].
An intuitive understanding of the monodromy operator $\mathcal{M}$ as the time integration operator of the variational equation, can be deduced from a simple numerical calculation approach. Usually $\mathcal{M}$ is a square matrix of size $\tau_p/\delta t$, where δt is the temporal resolution used in the numerical approximation and τ_p is the period of the limit cycle solution[5]. A column vector of the operator can be calculated by selecting one point in the period of the limit cycle and then solitary perturb each point along the meshed limit cycle. For each perturbation a propagation of the perturbed solution along one period is then applied. Determining the difference between the initial (unperturbed limit cycle) and final values of the selected point for each perturbation then gives a column of the operator (vector of $\tau/\Delta t$; see appendix B of [MAR15d]). This has to be repeated for all points along the limit cycle, leading to a total of $\tau/\Delta t$ column vectors for the monodromy matrix. The eigenvalues can then be calculated by diagonalising the resulting matrix.
The eigenvalues of the monodromy operator are known as Floquet multipliers μ and the corresponding eigenvectors represent the Floquet modes. If the system is perturbed in one of the eigendirections (Floquet modes) and the absolute value of the corresponding Floquet multiplier is below unity ($|\mu| < 1$), the perturbation is damped out and the system is stable in the corresponding direction. Thus, if all $|\mu| < 1$, the limit cycle solution is stable. However, always one trivial Floquet multiplier at $|\mu| = 1$ exists for autonomous systems, which represents a neutral mode, i.e. an invariance against a perturbation in the corresponding eigendirection. In this case, it belongs to the translation of the time origin [LUZ02, ENG02] or in other words a longitudinal perturbation along the limit cycle.
Three different types of limit cycle bifurcations are encountered in this work, namely saddle-node bifurcations, period-doubling bifurcations and torus bifurcations. Characteristic for a

[5] It has to be mentioned that in delayed systems, the boundary integration domain of the monodromy operator is either defined by the maximum delay time or by the period of the solution, depending on which one is shorter. Due to the infinite dimension of the phase space, the operator has infinite dimensions but can be approximated very well with a fine temporal resolution [MAR15d].

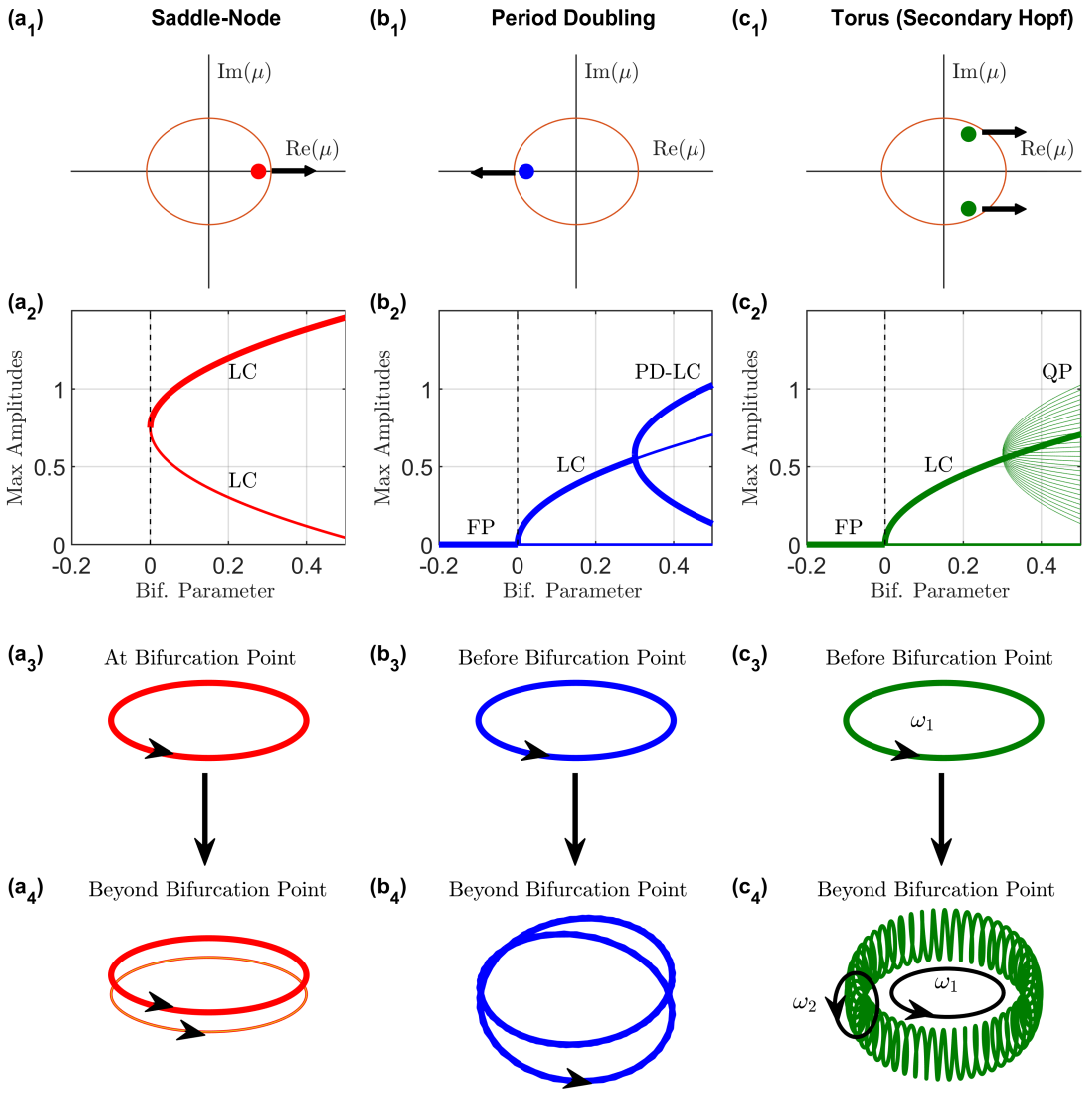

Figure 2.7.: Characteristics of different limit cycle bifurcations: (a) Saddle-Node, (b) Period Doubling and (c) Torus bifurcation. (a_1)-(c_1) Behaviour of the critical Floquet multiplier μ at the bifurcation point in the imaginary plane. The circle denotes the unit circle. If all multipliers are inside the circle, the dynamics is stable. (a_2)-(c_2) 1D-bifurcation diagram showing the characteristic dependence of the maxima of the limit cycle oscillations on the bifurcation parameter close to the bifurcation points (dashed vertical line). Thick (thin) lines denote stable (unstable) dynamics. FP denotes a fixed-point, LC a limit cycle, PD-LC a period doubled limit cycle and QP quasi-periodic dynamics. (a_3)-(c_3) Phase space portrait at/before the bifurcation point, showing a stable limit cycle.(a_4)-(c_4) Phase space portrait beyond the bifurcation point, showing: (a_4) a stable and unstable limit cycle; (b_4) A period double solution; (c_4) Quasi periodic oscillating torus.

saddle-node bifurcation of limit cycles[6], a single Floquet multiplier leaves the unit circle as depicted in Fig. 2.7(a_1). The 1D-bifurcation diagram in Fig. 2.7(b_1) looks identical to the fixed-point situation, with the difference being that the y-axis corresponds to the maximum amplitudes of the oscillation in one variable and not the fixed-point value. Again, thick lines denote stable dynamics. In phase space, the bifurcation can be understood as a birth of two limit cycles, which is presented in Fig. 2.7(a_{3-4}).
As its name suggests, the period doubling bifurcation leads to the emergence of a limit cycle solution oscillating at a doubled period compared to the initial limit cycle. It is characterised by a single Floquet multiplier of a limit cycle solution leaving the unit circle as illustrated in Fig. 2.7(b_1). A plot of the dynamics in phase space is presented in Fig. 2.7(b_{3-4}). Before the bifurcation point, a single limit cycle exists, which then turns unstable. Beyond the bifurcation point, the attractor appears as a once flipped version of the initial limit cycle, which is why the bifurcation is also referred to as flip bifurcation. For its occurrence the system has to be at least three dimensional.
Lastly, the torus bifurcation has to be mentioned as it leads to most of the quasi-periodic dynamics discussed in this work. It is also referred to as secondary Andronov-Hopf bifurcation, as an additional oscillation frequency is born. Similar to the Andronov-Hopf bifurcation of fixed-point solutions, a pair of complex conjugate eigenvalues leaves the unit circle (see Fig. 2.7(c_1)). Due to the second oscillation frequency, which can lead to quasi-periodic dynamics, many more oscillation maxima can be found as demonstrated in the bifurcation diagram in Fig. 2.7(c_2), where the bifurcation point is indicated by the dashed black line. In phase space, the dynamics transition from a regular periodic orbit to an oscillation that has the appearance of a torus. The transition is sketched in Fig. 2.7(c_2). The two oscillation frequencies are displayed as black arrows. The ratio of the two frequencies determines, if the torus trajectory reconnects to itself. If $\frac{\omega_1}{\omega_2} \in \mathbb{Q}$ the trajectory closes, which leads to another periodic solution, else it is quasi-periodic. Prominent examples of torus bifurcations are the onset of the Q-switching instability [VLA04, JAU17a, HAU20a].

[6] It has to be highlighted again that the saddle-node bifurcation of limit cycles strictly is no local bifurcation. On the one hand, it is a global bifurcation as it corresponds to the global transition of corresponding manifolds [STR94a]. On the other hand it can be characterised via a Floquet analysis (local theory).

3 Delay Differential Equation System

3.1 Introduction

Two of the most influential schemes to model lasers based on delay differential equations (DDE) are the Ikeda equation [IKE79, ERN17] and the Rozanov-Lang-Kobayashi equations [ROS75a, LAN80b], which both aim at describing the dynamics of lasers subject to optical feedback. In these DDE systems, the delay naturally occurs due to the out-coupled field being fed back into the laser cavity after the delay time τ. The delay time corresponds to the time of flight of the light to a feedback mirror and back towards the laser device.
The work on this type of model system greatly enhanced the understanding of many different effects such as the laser operation in a regime of deterministic chaos [CHO84, ALB11, ALN09, OHT99], phase locking effects generating periodic or quasi-periodic intensity dynamics [MOR92, HEL90b, RIT93a, PIE01, ERZ06], high frequency intensity oscillations in the regime of short feedback times [TAG94], oscillations of the laser frequency [FIS04, ERZ06], or stochastic low frequency oscillations [HOH95, HEI98c].
The investigation of these laser related problems as well as the research on related topics, e.g. feedback control [PYR92, AHL04, ATA03, BAB02, BON12] or oscillator networks [NIE91, CRO97a, GOL99], lead to a deep understanding of the dynamics in DDE systems. This made the development of a DDE system to analyse a passively mode-locked semiconductor laser additionally appealing. It was introduced by A.G. Vladimirov and D.V. Turaev in 2004 [VLA04, VLA04a]. However, the most important reasons for its development were the limitations of existing theoretical models with regard to an investigation of different dynamical regimes. The master partial differential equation systems developed by H. Haus [HAU75a, HAU75b, HAU00], were successfully applied to explain a variety of effects and specially pulse shaping as. e.g., given in References [HAU93a, IPP94, HAU95, NAM97, WUN00, AVR00, JIA01]. Nevertheless, these relied on the assumptions of small gain and losses, which do not always hold in passively mode-locked semiconductor lasers. Alternatives are represented by extended travelling-wave models [BIS95a, SCH96n, BIS97a, MUL06] or fully microscopic models based on the many body semiconductor Bloch equations [HAD99, KIL17, MCL20]. The former were firstly established for the analysis of monolithic semiconductor lasers [SCH88j, AGR89, AGR91, TRO94] and describe the evolution of the slowly varying electric field envelopes along the cavity. Yet, both approaches have the downside of very high computational demands, especially for the large external cavity lasers of interest in this work.
The derivation of the DDE model starts from the travelling-wave equations, which are coupled to rate equations representing the charge carrier dynamics in a semiconductor laser with quantum-well gain and absorber medium [MAR83]. The carrier dynamics are modelled in terms of integrated carrier densities in gain and absorber, neglecting diffusion and approximating the distribution along the transverse dimension to be constant [AGR89, VLA04].

The most important assumption for the development of the DDE system is that the field is considered to propagate unidirectionally in a ring cavity consisting of a gain, absorber and passive section as well as a spectral filter. Incorporating the wavelength dependence of the gain via a Lorentzian spectral filter at the output, together with the unidirectional propagation, leads to the final DDE for the electric field. Despite the unidirectional propagation, this DDE system was successfully applied to theoretically recover experimental findings related to feedback effects [OTT12a, OTT14b, JAU16, JAU17], large external cavity mode-locked lasers [MAR14c, CAM16] or extension to further gain media [VIK06, VLA10, VIK14]. In the limit of small gain and absorption, the DDE model can be recast into a Haus master equation partial differential equation [KOL06, SCH18e, SCH18f, HAU20a].
Nevertheless, the assumption of unidirectional propagation leads to problems when modelling external cavity lasers with a V-shaped external cavity geometry, as the gain is passed twice per round-trip by each pulse. Hence, it is important to include the backwards propagating field as proposed in Reference [VLA09]. Based on this approach, a DDE system is derived in this chapter, to unravel the dynamics of a passively mode-locked vertical external cavity surface-emitting laser with a V-shaped cavity geometry. First, the experimental realisation of such devices is described in more detail in section 3.2. Then a detailed derivation of the DDE model starting from Maxwell's equations in matter is elaborated in section 3.3 and finally a discussion of the model with regard to other modelling techniques and the parameter values used is outlined (section 3.4).

3.2 V-shaped VECSEL Setup

The type of laser investigated in this work is a passively mode-locked vertical external cavity surface-emitting laser for which the components are arranged in a way so that the cavity geometry is formed as a V. A sketch of the V-shaped cavity geometry, as experimentally realised in References [HOO00, WIL13b, KLO11a, WAL16, GRO20, MEY20], is shown in Fig. 3.1. There are three central components to this type of laser device: A semiconductor gain-chip, a semiconductor saturable-absorber mirror and an outcoupling facet.
The semiconductor gain-chip consists of a back-side distributed Bragg reflector (DBR) and an active section composed of several quantum-well layers (QWs). The topside of the chip is characterised by a confining overgrowth layer as well as an additional antireflection coating and a protective fused silica layer [WAL16]. Due to their advantages such as a low lattice mismatch, sufficient thermal conductivity and the well-established epitaxial growth techniques [KEL06, GAA16] leading to high quality DBR mirrors, III-V semiconductors are a very popular choice of the gain material in state of the art devices [KEL06, GAA16, LAU18]. The composition of the semiconductors in the active section can be adjusted for different needs (e.g. emission wavelength), but the usage of InGaAs quantum well layers ($\approx 5-20$ layers [TIL15]) was among the most successful applications with regard to pulse duration and pulse intensity [WAL16, GAA16]. To achieve the population inversion, the gain can be optically pumped by an additional commercial laser diode with an operating wavelength usually far above the bandgap of the semiconductor bulk material [WAL16, GAA16, GUI17]. Alternatively, electrical pumping can be applied, if the active region is enclosed into additional contacts and is grown in a p-i-n configuration with an optional current spreading layer [JIA93a, MUL05a, CHI20].
The second important component of the VECSEL is a semiconductor saturable absorber mirror (SESAM). Its composition is similar to the gain-chip, with the major difference being

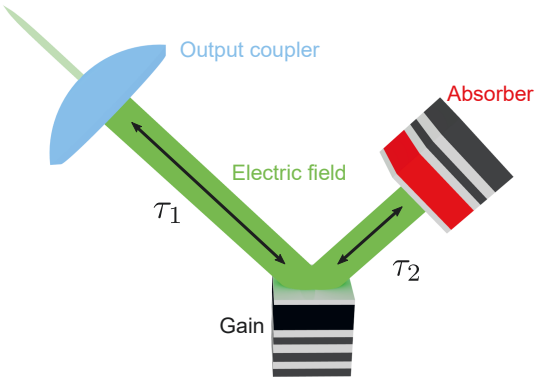

Figure 3.1: Setup of a passively mode-locked vertical external cavity surface-emitting laser with a V-shaped cavity geometry, as experimentally realised in [WAL16]. The three central components are an output coupler (light blue) with high reflectivity and two semiconductor chips with back-side DBR, representing the gain and absorber. The active region of the gain is shown in black, whereas the absorber is indicated in red. The times of flight needed for the electric field (green) to pass the length of the cavity arms are given by τ_1, τ_2.

firstly that a lower number of quantum-wells is used (e.g. only one in the realisations in Reference [WIL13b, WAL16]) so that the saturation energy is lower than in the gain. Secondly, the semiconductor chip is grown at a lower temperature, with additional barriers enclosing the quantum-well region (e.g. AlAs [WAL16, FIN20]) to ensure a fast carrier recovery to the ground state, which is necessary for narrow pulse mode-locking [TIL15]. Other possibilities to achieve a faster recovery are selective doping and inherent material defects [TIL15]. Potentially, the carrier relaxation can be actively controlled by applying a reverse bias, if the chip is designed in a way that contacts can be attached [LAG05, LIU10b].
The usage of active components different to quantum wells can be beneficial with regard to the performance figures (e.g. pulse amplitude, pulse width, wavelength tunability). Consequently, the gain and absorber active sections of mode-locked semiconductor VECSELs were realised using quantum dots [HOF08a, HOF11a, NEC19, FIN20], submonolayer quantum dots [ALF18] or semiconductor membranes [KAH16, BEK17a] as the active sections. Furthermore, it is to say that the topside of the gain and absorber-chip can be overgrown with a distributed Bragg reflector, which is useful for the generation of localised structures as presented in the experimental demonstrations outlined in References [MAR14c, CAM16]. The concept of localised states is discussed further in section 4.3.1, whereas the effects resulting from the additional micro-cavity are outlined in section 5.4.1.
The third essential element for the VECSEL is an outcoupling facet with a suitable reflectivity/transmissivity. In most experimental realisations, only about 1 % of the light is coupled out per round-trip, enabling a high amplification and appropriate saturation of the absorber [KEL06, WIL13b, WAL16, KLO11a, GRO20].
Applications of passively mode-locked VECSEL devices include frequency comb generation for spectroscopy or super-continuum generation [KLE14, WAL16, COD16, LIN17e, WAL19], optical frequency metrology [UDE02] or two photon microscopy [AVI11a, VOI17]. Compared to solid-state lasers, semiconductors are appealing due to their comparatively cheap production costs as well as the potential to access priorly not available wavelength ranges, which are especially appealing for spectroscopy applications [LIN17e]. Further fields of applications requiring ultra short laser pulses are the field of eye surgery [JUH99, NAG09] or laser material processing [KER16].

3.3 Delay Differential Equation Model - Derivation

The derivation of the delay differential equation (DDE) model for a passively mode-locked laser with a V-shaped cavity geometry based on quantum-well active sections follows the

ideas outlined in Reference [VLA09] and is similar to the derivation of the unidirectional DDE model of mode-locking, which was first published in References [VLA04, VLA04a] and is further presented in detail in References [OTT14, JAU17a].
Since the electric field is described classically in the description of laser devices due to the high light intensity, one can start the derivation from Maxwell's equations in matter. Assuming no free charge densities and no free current, these can easily be transformed to the following wave equation, describing the evolution of the electric field $\boldsymbol{E}(\boldsymbol{r},t)$ in the semiconductor medium

$$\nabla^2\boldsymbol{E}(\boldsymbol{r},t)-\frac{n^2}{c_0^2}\frac{\partial^2}{\partial t^2}\boldsymbol{E}(\boldsymbol{r},t)=\mu_0\frac{\partial^2}{\partial t^2}\boldsymbol{P}(\boldsymbol{r},t), \tag{3.1}$$

where $\boldsymbol{P}$ is the macroscopic polarisation, c_0 is the speed of light, n refers to the (piece-wise constant) refractive index and μ_0 is the permeability of free space. This wave-equation can be simplified by utilising different approximations that hold well for the investigation of a semiconductor laser device. In the following, the coordinate system is defined in a way that the z-axis corresponds to the optical axis of the laser and the transverse components are neglected, due to the flat transverse emission profile of mode-locked VECSELs [WAL16]. Furthermore, the electric field is assumed to consist of forward- (+) and backward-propagating (-) plane waves related to the optical frequency/wavelength and of the slowly varying envelope functions $\psi_{\mathcal{E}}^{+}(\boldsymbol{r},t)$ and $\psi_{\mathcal{E}}^{-}(\boldsymbol{r},t)$. This slowly varying envelope approximation holds well for a laser, due to the narrow line-width. Hence, the decomposed expression for the electric field reads

$$\boldsymbol{E}(\boldsymbol{r},t)=\frac{1}{2}\boldsymbol{e}\left[\psi_{\mathcal{E}}^{+}(\boldsymbol{r},t)e^{ikz}+\psi_{\mathcal{E}}^{-}(\boldsymbol{r},t)e^{-ikz}\right]e^{-i\omega t}+c.c. \tag{3.2}$$

Here, the linear dispersion relation $k\equiv\frac{\omega}{v}$ relates the optical frequency of the laser ω, the group velocity v and the wavenumber k. Furthermore, $\boldsymbol{e}$ is the unit vector in the direction of the field polarisation.
The same decomposition is applied for the polarisation with envelope functions $\psi_{\mathcal{P}}^{\pm}(\boldsymbol{r},t)$. Inserting these expression into eq. (3.1) and utilising that the envelopes vary much slower than the other oscillations (in time and space) [HAK85, TAR98a] leads to

$$\left[\pm\partial_z+\frac{1}{v}\partial_t\right]\psi_{\mathcal{E}}^{\pm}(\boldsymbol{r},t)=\frac{i\omega\mu_0 v}{2}\psi_{\mathcal{P}}^{\pm}(\boldsymbol{r},t). \tag{3.3}$$

This equation can be simplified to only depend on the longitudinal direction z and time, which necessitates a further decomposition of the envelope functions. First eq. (3.3) is multiplied by $\psi_{\mathcal{E}}^{\pm *}(\boldsymbol{r},t)$ and then the complex conjugate of the equation is added. As a next step, one integrates over the transverse dimension. The envelope function of the electric field can be decomposed into the instantaneous electric field strength $\mathcal{E}_s^{\pm}(z,t)$ and the mode profile $m_{\mathcal{E}}^{\pm}(\boldsymbol{r},t)$ according to

$$\psi_{\mathcal{E}}^{\pm}(\boldsymbol{r},t)=m_{\mathcal{E}}^{\pm}(\boldsymbol{r},t)\mathcal{E}_s^{\pm}(z,t). \tag{3.4}$$

A similar Ansatz is applied for the polarisation and both decompositions are inserted into the transversely integrated equations. One can simplify the integrals over the transverse dimension by assuming that the mode profiles of electric field and polarisation vary much

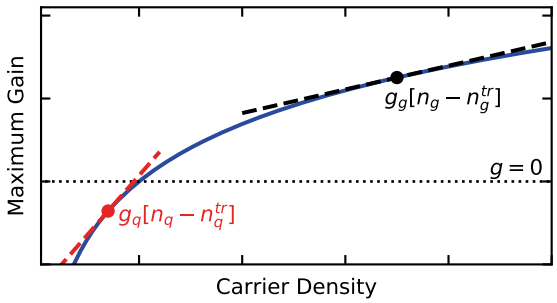

Figure 3.2: Sketch of the relationship between maximum optical gain and carrier density in a quantum-well material. Exemplary operation points with corresponding linear fit of the gain curve (dashed lines) are indicated in black and red for the gain and absorber respectively. Figure adapted from [JAU17a].

slower than the electric field strength in z. The integrals over the mode-profiles are then summarised by the confinement factor $\Gamma(z)$ [COL12a, LIN15b][1] and one is left with a travelling-wave equation for the intensity $|\mathcal{E}(z,t)|^2$. Transforming this equation from the intensity to a complex field equation[2] then leads to the following travelling-wave equation relating the instantaneous electric field strength $\mathcal{E}(z,t)$ and the instantaneous polarisation strength $\mathcal{P}(z,t)$

$$\left[\pm\partial_z + \frac{1}{v}\partial_t\right]\mathcal{E}^{\pm}(z,t) = \frac{i\omega\mu_0 v\Gamma(z)}{2}\mathcal{P}^{\pm}(z,t). \tag{3.5}$$

To arrive at a model suitable to model semiconductor laser dynamics, the light matter interaction has to be described correctly, which is embodied in the right hand side of eq. (3.1) by the derivative of the polarisation. In order to explore this interaction for different types of quantum-well gain structures, calculations based on modelling the band-structures on different levels of complexity have been conducted in the past[ASA84, YAM85, ARA86, AHN90]. This included reproducing the relationship between the optical gain and charge-carrier density, which is heavily influenced by the band-structure. For a fully microscopic description, the energy states can be described to behave like a superposition of many coupled two-level systems [HES96a, CHO99, KIL16, MCL20]. Anyhow, this leads to very high computational demands and makes it almost impossible to determine time-series of the dynamics longer than several 100 ns [MCL20].
This made analytic approaches for the gain and susceptibility, incorporating microscopic calculation results, feasible [BOW95, BAL95a, MAK96a, BAL98a]. Additionally, these were applied for the description of mode-locked devices [MUL05a, MUL06].
One of the simplest approximations of the relationship of gain and charge-carrier density is a logarithmic dependence [WIL88a, MAK96a, COL12a]. It matches very well with more complex theories [ASA84, YAM85, ARA86, AHN90] and is indicated by the blue line in Fig. 3.2. However, a more commonly used approximation is the one of a linear relationship between these two quantities [AGR89, BAN01, BIS95a, VLA04, VLA09], shown by the linear fits (dashed lines) to the logarithmic dependence in Fig. 3.2. For bulk-semiconductors, this phenomenological estimate can be rigorously derived from microscopic approaches under certain conditions [CHO99]. Nevertheless, this approximation is mostly valid for Class-B semiconductor lasers in which the polarisation changes on a much faster time scale than the charge carrier relaxation. Therefore the polarisation can be adiabatically eliminated, leading to the linear gain approximation. Combining the approximations for the electric field and the linear fit of the gain with respect to the carrier density, leads to the so-called travelling-wave equations [FLE68, AGR91, TRO94, BAN01, OTT14] These describe the evolution of

[1] This part of the derivation was done by Stefan Meinecke and is published in Reference [MEI21a].
[2] Here the intensity equation results first, due to the initial multiplication with $\psi_{\mathcal{E}}^{\pm *}(\boldsymbol{r},t)$.

the complex electric field envelope in the semiconductor active sections. The charge-carrier density in the different sections is modelled in terms of rate equations [SCH88j, TAR98a], also considering a faster relaxation of the polarisation compared to charge carrier excitation and neglecting lateral diffusion [SCH88j, TAR98a]. Furthermore, the carrier gratings resulting from the interference of forward and backward propagating field are assumed to have a negligible influence due to the short active section in the semiconductor chips. The equation system expressing dynamics of the electric field strength $\mathcal{E}_s^{\pm}$ of the forward and backward propagating field and the carrier densities $n_s(z,t)$ reads

$$\Big[\pm\partial_z + \frac{1}{v}\partial_t\Big]\mathcal{E}_s^{\pm}(z,t) = \Big\{-\frac{\beta_s}{2} + \frac{1-i\alpha_s}{2}g_s\Gamma_s\Big[n_s(z,t) - n_s^{tr}\Big]\Big\}\mathcal{E}_s^{\pm}(z,t), \tag{3.6}$$

$$\begin{aligned}\partial_t n_s(z,t) =& j_s(z,t) - \gamma_s n_s(z,t)\\ &- v g_s\Gamma_s\Big[n_s(z,t) - n_s^{tr}\Big] \times \Big[|\mathcal{E}_s^{+}(z,t)|^2 + |\mathcal{E}_s^{-}(z,t)|^2\Big].\end{aligned} \tag{3.7}$$

Here, n_s^{tr} is the effective carrier density at transparency resulting from the linear fit of the gain curve (see Fig. 3.2), Γ_s denotes the transverse optical confinement factor, $j_s(z,t)$ refers to the pump parameter, β_s corresponds to the linear losses, γ_s describes the carrier relaxation rate via non-radiative scattering processes and v represents the group velocity, which is estimated to be constant along all sections. It is assumed that the parameters are piece-wise constant in each section of the laser. The different type of sections are two passive sections p, a gain section g and an absorber section q. They are indicated by the index $s \in \{p, g, q\}$. As mentioned above, the interplay between charge carriers in the quantum-well and the electric field is modelled by the linear term

$$\frac{1-i\alpha_s}{2}g_s\Gamma_s\Big[n(z,t) - n^{tr}(z)\Big], \tag{3.8}$$

where g_s is the differential gain, resulting from the linear fit of the gain curve with respect to the carrier density as indicated in Fig. 3.2. The two linear fits represent two typical operation points in terms of charge-carrier density for the absorber and the gain. On the one hand, the absorber is reversed biased or designed in a way that the carriers relax very fast, hence exhibits a negative gain i.e. absorption. On the other hand, the gain is pumped electrically or optically which leads to a high charge-carrier density and positive gain.
An additional imaginary contribution to the field-carrier interaction is included via $i\alpha_s$. This factor was firstly applied by C. H. Henry [HEN82] to correctly reproduce the linewidth enhancement induced by semiconductor gain media, which he quantified to be close to $1+\alpha^2$. It is a phenomenological description of the relationship of charge carriers and the refractive index. The linewidth enhancement is defined as $\alpha = \frac{\partial_N \chi_r}{\partial_N \chi_i}$, with the index denoting the real r and imaginary part i of the electric susceptibility, and the carrier density N [HEN82, HAR83, HAD99]. As can be deduced from its imaginary contribution, the factor models an additional change in the phase of the electric field resulting from the carrier induced alteration of the refractive index during the gain depletion, i.e. the carrier dependent response of the medium.
In order to solve the first-order partial differential equation (3.6), a coordinate transformation $(z,t) \mapsto (\zeta, t^*)$ to the co-moving frame is applied, i.e. an appropriate characteristic

curve to transform the equation into an ordinary differential equation is found. The applied coordinate transformation reads

$$z(\zeta) = \zeta, \tag{3.9}$$

$$t(\zeta) = t^* \pm \frac{z}{v} = t^* \pm \frac{\zeta}{v}. \tag{3.10}$$

with the derivatives transforming according to

$$\frac{\partial}{\partial t} = \frac{\partial \zeta}{\partial t}\frac{\partial}{\partial \zeta} + \frac{\partial t^*}{\partial t}\frac{\partial}{\partial t^*} = \frac{\partial}{\partial t^*}, \tag{3.11}$$

$$\frac{\partial}{\partial z} = \frac{\partial \zeta}{\partial z}\frac{\partial}{\partial \zeta} + \frac{\partial t^*}{\partial z}\frac{\partial}{\partial t^*} = \frac{\partial}{\partial \zeta} \mp \frac{1}{v}\frac{\partial}{\partial t^*}. \tag{3.12}$$

This leads to the ODEs

$$\frac{d}{d\zeta}\mathcal{E}_s^{\pm}(z(\zeta), t(\zeta)) = \pm\Big[-\frac{\beta_s}{2} + \frac{1 - i\alpha_s}{2} N_s(z(\zeta), t(\zeta))\Big]\mathcal{E}_s^{\pm}(z(\zeta), t(\zeta)), \tag{3.13}$$

where the charge-carrier density $n_s(z(\zeta), t(\zeta))$ in the quantum-well active medium is rescaled according to $N_s(z(\zeta), t^*(\zeta)) = g_s\Gamma_s[n_s(z(\zeta), t^*(\zeta)) - n_s^{tr}]$. It is now possible to integrate eq. (3.13) for the forward (backward) propagating field from z_s to z_{s+1} (z_{s+1} to z_s) along the characteristic. Applying a separation of variables to solve the integrals leads to

$$\begin{aligned}\mathcal{E}_s^+\left(z_{s+1}, t^* + \frac{z_{s+1}}{v}\right) = &\mathcal{E}_s^+\left(z_s, t^* + \frac{z_s}{v}\right) \\ &\times \exp\left(-\frac{\beta_s}{2}\Delta z_s + \frac{1 - i\alpha_s}{2}\int_{z_s}^{z_{s+1}} d\zeta N_s\left(\zeta, t^* + \frac{\zeta}{v}\right)\right),\end{aligned} \tag{3.14}$$

$$\begin{aligned}\mathcal{E}_s^-\left(z_s, t^* - \frac{z_s}{v}\right) = &\mathcal{E}_s^-\left(z_{s+1}, t^* - \frac{z_{s+1}}{v}\right) \\ &\times \exp\left(-\frac{\beta_s}{2}\Delta z_s + \frac{1 - i\alpha_s}{2}\int_{z_s}^{z_{s+1}} d\zeta N_s\left(\zeta, t^* - \frac{\zeta}{v}\right)\right).\end{aligned} \tag{3.15}$$

The time is then shifted according to $t' = t^* + \frac{z_{s+1}}{v}$ in eq. (3.14) and according to $t' = t^* - \frac{z_s}{v}$ in eq. (3.15). In order to find an equalling expression for integrals over the carrier densities in the two equations, it is assumed that the time of flight $\Delta t = \frac{\Delta z}{v}$ between the two ends of the sections is short and therefore both integrals are expressed by means of the carrier intensity after half the section is passed[3]. This leads to the following equations modelling the alteration of the electric field induced by the propagation through the active medium

$$\mathcal{E}_s^+(z_{s+1}, t') = \mathcal{E}_s^+(z_s, t' - \Delta t_s)e^{-\frac{\beta_s \Delta z_s}{2} + \frac{1 - i\alpha_s}{2}\mathcal{N}_s(t')}, \tag{3.16}$$

$$\mathcal{E}_s^-(z_s, t') = \mathcal{E}_s^-(z_{s+1}, t' - \Delta t_s)e^{-\frac{\beta_s \Delta z_s}{2} + \frac{1 - i\alpha_s}{2}\mathcal{N}_s(t')}, \tag{3.17}$$

with the integrated carrier densities $\mathcal{N}_s$ defined according to

$$\mathcal{N}_s(t') = \int_{z_s}^{z_{s+1}} d\zeta N\left(\zeta, t' - \frac{\Delta t_s}{2}\right). \tag{3.18}$$

[3]For the forward and backward propagating field the integrals are transformed according to

$$\int_{z_s}^{z_{s++1}} d\zeta N\left(\zeta, t^* + \frac{\zeta}{v}\right) = \int_{z_s}^{z_{s+1}} d\zeta N\left(\zeta, t' + \frac{\zeta - z_{s+1}}{v}\right) \approx \int_{z_s}^{z_{s+1}} d\zeta N\left(\zeta, t' - \frac{\Delta t_s}{2}\right),$$

$$\int_{z_s}^{z_{s+1}} d\zeta N\left(\zeta, t^* - \frac{\zeta}{v}\right) = \int_{z_s}^{z_{s+1}} d\zeta N\left(\zeta, t' + \frac{z_s - \zeta}{v}\right) \approx \int_{z_s}^{z_{s+1}} d\zeta N\left(\zeta, t' - \frac{\Delta t_s}{2}\right).$$

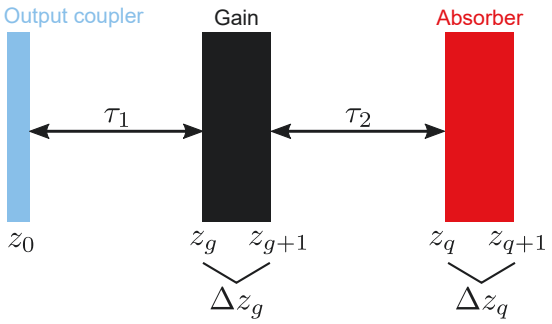

Figure 3.3: Sketch of the linearised cavity used for finding the boundary conditions (3.19)-(3.27). The output coupler is positioned at $z = z_0$ and the gain (g) and absorber (q) stretch out from $z_{g,q}$ to $z_{g+1,q+1}$ over a spatial width of $\Delta z_{g,q}$.

From this point, eq. (3.16)-(3.17) can be applied to formulate the boundary conditions induced by the setup of the V-shaped external laser cavity. On that account, the reflection at the gain-chip is approximated by a transmission through a section of width Δz_g. A sketch of the linearised cavity is indicated in Fig. 3.3. Four sections that are passed during one cavity round-trip can be identified. Starting from the outcoupling facet (z_0), a passive section of optical length $\Delta z_{p1} = \tau_1 \cdot v$ is passed first, which has no effect on the electric field as it is characterised by free space. As indicated in Fig. 3.3, the light subsequently passes the gain (black area from Δz_g to Δz_{g+1}) and then a second passive section ($\Delta z_{p2} = \tau_2 \cdot v$) with the absorber positioned at the end of it (red area from Δz_q to Δz_{q+1}). The light is reflected at the back-side DBR of the absorber (marked as Δz_{q+1} in Fig. 3.3) and then passes back through the cavity to the outcoupling facet. Coalescing these cavity boundary conditions with eq. (3.16)-(3.17) the following set of equations can be found

$$\mathcal{E}_g^+(t', z_g) = \mathcal{E}^+(t' - \tau_1, z_0), \tag{3.19}$$

$$\mathcal{E}_g^+(t', z_{g+1}) = \mathcal{E}_g^+(t' - \Delta z_g/v, z_g) e^{-\frac{\beta_g \Delta z_g}{2} + \frac{1-i\alpha_g}{2}\tilde{G}(t')}, \tag{3.20}$$

$$\mathcal{E}_q^+(t', z_q) = \mathcal{E}_g^+(t' - \tau_2, z_{g+1}), \tag{3.21}$$

$$\mathcal{E}_q^+(t', z_{q+1}) = \mathcal{E}_q^+(t' - \Delta z_q/v, z_q) e^{-\frac{\beta_q \Delta z_q}{2} + \frac{1-i\alpha_q}{2}\tilde{Q}(t')}, \tag{3.22}$$

$$\mathcal{E}_q^+(t', z_{q+1}) = \mathcal{E}_q^-(t', z_{q+1}), \tag{3.23}$$

$$\mathcal{E}_q^-(t', z_q) = \mathcal{E}_q^-(t' - \Delta z_q/v, z_{q+1}) e^{-\frac{\beta_q \Delta z_q}{2} + \frac{1-i\alpha_q}{2}\tilde{Q}(t')} \tag{3.24}$$

$$\mathcal{E}_g^-(t', z_{g+1}) = \mathcal{E}_g^-(t' - \tau_2, z_q), \tag{3.25}$$

$$\mathcal{E}_g^-(t', z_g) = \mathcal{E}_g^-(t' - \Delta z_g/v, z_{g+1}) e^{-\frac{\beta_g \Delta z_g}{2} + \frac{1-i\alpha_g}{2}\tilde{G}(t')}, \tag{3.26}$$

$$\mathcal{E}_p^-(t', z_0) = \mathcal{E}_g^-(t' - \tau_1, z_g), \tag{3.27}$$

where $\mathcal{N}_g(t') = \tilde{G}(t')$ and $\mathcal{N}_q(t') = \tilde{Q}(t')$ define the carrier densities in the gain and absorber respectively. It has to be highlighted, that the reflection losses at the gain and absorber chip are neglected due to the high quality DBRs on the bottom and the antireflection coatings at the top [WAL16]. The time of flight through the gain and the absorber active sections $\frac{\Delta z_{g,q}}{v}$ is much smaller than other time scales of the system. The fastest time scale is represented by the gain bandwidth γ and hence $\frac{\Delta z_{g,q}}{v} \ll \gamma^{-1}$ justifies the approximations $z_{g,q} \approx z_{g+1,q+1}$ and $t - \frac{\Delta z_{g,q}}{v} \approx t$. Additionally, the linear loss terms are neglected as $\beta_{g,q}\Delta z_{g,q} \ll 1$. It has to be pointed out that, if a pulse travels the spatial distance of one cavity length L inside the laser cavity, it arrives at its initial position, which gives the following spatial boundary condition

$$\mathcal{E}_s^{\pm}(t', z) = \mathcal{E}_s^{\pm}(t', z + L), \tag{3.28}$$

with the relationship of the cavity length L and the cold-cavity round-trip time T given by $L = \frac{T}{v} = 2\tau_1 + 2\tau_2$. Here, $\tau_{1,2}$ are defined as indicated in Fig. 3.3 and Fig. 3.1. The longitudinal lasing modes can be deduced from the round-trip time via the standing wave condition $\omega_L = \frac{2\pi n}{T}$, with the integer n. Nonetheless, due to the nonlinear influence of the field-carrier interaction, the mode-locking frequency slightly differs from this value, which is further discussed in section 4.2.
To find a single expression for the alteration of the electric field during one round-trip, the boundary conditions (3.19)-(3.27) can be iteratively inserted into each other to express the field $\mathcal{E}_p^-(z_0, t')$ at the outcoupling facet (z_0) by the forward propagating field one round-trip in the past $\mathcal{E}_p^+(z_0, t' - 2\tau_1 - 2\tau_2) = \mathcal{E}_p^+(z_0, t' - T)$. The iterative combination of the BCs leads to the following expression

$$\begin{aligned}\mathcal{E}_p^-(z_0, t') = &\mathcal{E}_p^+(z_0, t' - 2\tau_1 - 2\tau_2) \\ &\times e^{\frac{1-\alpha_g}{2}[\tilde{G}(t'-\tau_1)+\tilde{G}(t'-2\tau_2-\tau_1)]} \\ &\times e^{(1+i\alpha_q)\tilde{Q}(t'-\tau_1-\tau_2)}.\end{aligned} \tag{3.29}$$

This algebraic equation gives the amplification of a pulse during one round-trip. Yet, each mode is amplified equally as the expression is frequency independent. A further important aspect that has to be included into the model is the finite bandwidth of the gain or the DBR depending on the gain-chip design. It is included by a lumped element approach, embodied by a Lorentzian spectral filter at the outcoupling facet, which in the frequency domain can be expressed as [VLA04, VLA05]:

$$f(\omega) = \frac{\gamma}{\gamma + i\omega}, \tag{3.30}$$

with the filter bandwidth γ and the angular frequency ω. Due to the required continuity, this leads to the following boundary condition for the electric field in the spectral domain:

$$\mathcal{E}_p^+(z_0, \omega) = \mathcal{E}_p^-(z_0, \omega) f(\omega)\sqrt{\kappa}, \tag{3.31}$$

where κ represents the non-resonant losses accumulated over one round-trip, which are predominately determined via the outcoupling losses at the facet. The boundary condition can be transferred to the time-domain required for numeric simulation purposes by utilising the inverse Fourier transform, while making use of the convolution theorem[4]. The resulting equation reads[5]

$$\mathcal{E}_p^+(z_0, t') = \sqrt{\kappa}\int_{-\infty}^{t'} d\tau f(t' - \tau)\mathcal{E}_p^-(z_0, \tau) = \sqrt{\kappa}\int_{-\infty}^{t'} d\tau \gamma e^{-\gamma(t'-\tau)}\mathcal{E}_p^-(z_0, \tau). \tag{3.32}$$

[4]The convolution theorem for the inverse Fourier transform $\mathcal{F}^{-1}$ reads

$$\mathcal{F}^{-1}\Big\{\mathcal{E}_p(\omega) \cdot f(\omega)\Big\} = \mathcal{F}^{-1}\Big\{\mathcal{E}_p(\omega)\Big\} * \mathcal{F}^{-1}\Big\{f(\omega)\Big\}.$$

Where $\cdot$ denotes the multiplication and $*$ denotes the convolution of the two functions.

[5]The inverse Fourier transformation of the Lorentzian filter is defined as follows

$$\mathcal{F}^{-1}\Big\{f(\omega)\Big\}(t) = f(t) = \gamma e^{-\gamma t}.$$

with $t' > 0$ due to causality.

The upper limit of the integral is given by t due to causality, which implies that $\mathcal{E}(\sigma, z) = 0$ for $\sigma > t$. To reformulate the integral equation into a differential equation, the total derivative with respect to ζ is applied on both sides and the Leibniz integral rule is applied[6]. This yields the following differential equation

$$\begin{aligned}\frac{d}{dt'}\mathcal{E}_p^+(z_0,t') &= \sqrt{\kappa}\gamma\mathcal{E}_p^-(z_0,\tau) + \sqrt{\kappa}\int_{-\infty}^{t'} d\tau \frac{\partial}{\partial t'}\gamma e^{-\gamma(t'-\tau)}\mathcal{E}_p^-(z_0,\tau) \\ &= \sqrt{\kappa}\gamma\mathcal{E}_p^-(z_0,t') - \gamma\mathcal{E}_p^+(z_0,t'). \end{aligned} \tag{3.33}$$

Inserting the expression for the backwards propagating field (3.29) makes it possible to find a DDE that only depends on the forward propagating field at the outcoupling facet

$$\begin{aligned}\frac{d}{dt'}\mathcal{E}(t') =& -\gamma\mathcal{E}(t') + \gamma\sqrt{\kappa}\mathcal{E}(t'-2\tau_2-2\tau_1) \\ &\times e^{\frac{1-i\alpha_g}{2}(\tilde{G}(t'-\tau_1-2\tau_2)+\tilde{G}(t'-\tau_1))} \\ &\times e^{(1-i\alpha_q)\tilde{Q}(t'-\tau_1-\tau_2)}, \end{aligned} \tag{3.34}$$

where the notation $\mathcal{E}_p^+(z_0,t') \equiv \mathcal{E}(t')$ is used for simplicity.
To complete the DDE system, equations describing the dynamics of the integrated carrier densities have to be found. On that account, eq. (3.7) is rescaled as before and the coordinate transformation given in eq. (3.9)-(3.10) is applied

$$\begin{aligned}\partial_t N_s(z(\zeta),t(\zeta)) =& \mathcal{J}_s(z(\zeta),t(\zeta)) - \gamma_s N_s(z(\zeta),t(\zeta)) \\ &- r_s N(z(\zeta),t(\zeta))\left[|\mathcal{E}_s^+(z(\zeta),t(\zeta))|^2 + |\mathcal{E}_s^-(z(\zeta),t(\zeta))|^2\right], \end{aligned} \tag{3.35}$$

with the charge-carrier density rescaled according to $N((z(\zeta),t(\zeta)) = g_s\Gamma_s[n_s(z(\zeta),t(\zeta)) - n_s^{tr}]$, the pump term $\mathcal{J}_s(z(\zeta),t(\zeta)) = g_s\Gamma_s(j(z(\zeta),t(\zeta)) - \gamma_s n^{tr})$ and the differential gain $r_s = g_s\Gamma_s v$. Integrating this equation from z_s to z_{s+1} in ζ and inserting the definition[7] for the integrated carrier densities (3.18) gives

$$\begin{aligned}\partial_{t'}\mathcal{N}_s(t') =& J_s(t') - \gamma_s\mathcal{N}_s(t') - r_s\int_{z_s}^{z_{s+1}} d\zeta N_s(z(\zeta),t(\zeta))|\mathcal{E}_s^+(z(\zeta),t(\zeta))|^2 \\ &- r_s\int_{z_s}^{z_{s+1}} d\zeta N_s(z(\zeta),t(\zeta))|\mathcal{E}_s^-(z(\zeta),t(\zeta))|^2, \end{aligned} \tag{3.36}$$

where $J_s(t')$ is the integrated current density. In order to find a simplification for the integral terms, the coordinate transformed travelling-wave equation (3.13) is multiplied with the complex conjugate of the electric field (for the forward and backward direction). The real part of the resulting equations reads

$$\frac{d}{d\zeta}|\mathcal{E}_s^\pm(z(\zeta,t(\zeta))|^2 = \pm\Big[-\beta_s + N_s(z(\zeta),t(\zeta))\Big]|\mathcal{E}_s^\pm(z(\zeta)|^2. \tag{3.37}$$

[6] The Leibniz integral rule reads

$$\frac{d}{dt}\left[\int_{\xi(t)}^{\rho(t)} f(\tau,t)d\tau\right] = f(\rho(t),t)\frac{d}{dt}\rho(t) - f(\xi(t),t)\frac{d}{dt}\xi(t) + \int_{\xi(t)}^{\rho(t)}\frac{\partial}{\partial t}f(\tau,t)d\tau.$$

[7] Again, the time is shifted according to $t' = t^* + \frac{z_{s+1}}{v}$ and $t' = t^* - \frac{z_s}{v}$, which is included in the $t(\zeta)$ expressions.

Integrating both sides over ζ and separating linear and nonlinear contributions then gives

$$\int_{z_s}^{z_{s+1}} d\zeta \left[\beta_s |\mathcal{E}_s^{\pm}(z(\zeta),t(\zeta))|^2 \pm \frac{d}{d\zeta}|\mathcal{E}_s^{\pm}(z(\zeta,t(\zeta))|^2\right] = \int_{z_s}^{z_{s+1}} d\zeta N_s(z(\zeta),t(\zeta))|\mathcal{E}_s^{\pm}(z(\zeta),t(\zeta))|^2. \tag{3.38}$$

The integral over $\beta|\mathcal{E}_s^{\pm}(z(\zeta),t(\zeta))|^2$ can be approximated by the trapezoidal rule[8], since Δz is assumed to be small. Inserting the coordinate transformations eq. (3.9)-(3.10) for the forward and backward propagating field and shifting the time as before, leads to the following result for the (+) direction

$$\begin{aligned}
&\int_{z_s}^{z_{s+1}} d\zeta \left[\beta_s |\mathcal{E}_s^{+}(z(\zeta),t(\zeta))|^2 + \frac{d}{d\zeta}|\mathcal{E}_s^{+}(z(\zeta,t(\zeta))|^2\right] \\
\approx &|\mathcal{E}_s^{+}(z_{s+1},t')|^2 - |\mathcal{E}_s^{+}(z_s,t'-\Delta t_s)|^2 + \frac{\beta_s \Delta z_s}{2}\left[|\mathcal{E}_s^{+}(z_s,t'-\Delta t_s)|^2 + |\mathcal{E}_s^{+}(z_{s+1},t')|^2\right] \\
= &|\mathcal{E}_s^{+}(z_s,t'-\Delta t_s)|^2 \left\{e^{-\beta_s \Delta z_s + \mathcal{N}_s(t')} - 1 + \frac{\beta_s}{2}\Delta z_s (e^{-\beta_s \Delta z_s + \mathcal{N}_s(t')} + 1)\right\} \\
\approx &|\mathcal{E}_s^{+}(z_s,t'-\Delta t_s)|^2 e^{-\frac{\beta_s}{2}\Delta z_s}\left(e^{\mathcal{N}_s(t')} - 1\right).
\end{aligned} \tag{3.39}$$

For the (-) direction the approximations lead to

$$\begin{aligned}
&\int_{z_s}^{z_{s+1}} d\zeta \left[\beta_s |\mathcal{E}_s^{-}(z(\zeta),t(\zeta))|^2 \pm \frac{d}{d\zeta}|\mathcal{E}_s^{-}(z(\zeta,t(\zeta))|^2\right] \\
\approx &|\mathcal{E}_s^{+}(z_s,t')|^2 - |\mathcal{E}_s^{-}(z_{s+1},t'-\Delta t_s)|^2 + \frac{\beta_s \Delta z_s}{2}\left[|\mathcal{E}_s^{+}(z_s,t')|^2 + |\mathcal{E}_s^{+}(z_{s+1},t'-\Delta t_s)|^2\right] \\
= &|\mathcal{E}_s^{+}(z_s,t'-\Delta t_s)|^2 \left\{e^{-\beta_s \Delta z_s + \mathcal{N}_s(t')} - 1 + \frac{\beta_s}{2}\Delta z_s (e^{-\beta_s \Delta z_s + \mathcal{N}_s(t')} + 1)\right\} \\
\approx &|\mathcal{E}_s^{-}(z_{s+1},t'-\Delta t_s)|^2 e^{-\frac{\beta_s}{2}\Delta z_s}\left(e^{\mathcal{N}_s(t')} - 1\right).
\end{aligned} \tag{3.40}$$

For the last line, it is assumed that the linear losses accumulated during the pass of the narrow sections are small $\beta_s \Delta z \ll 1$. Therefore, the exponentials can be expanded. Applying the found simplifications for the integrals to eq. (3.36) yields

$$\begin{aligned}
\partial_{t'}\mathcal{N}_s(t') = &J_s(t') - \gamma_s \mathcal{N}_s(t') \\
&- r_s e^{-\frac{\beta_s}{2}\Delta z_s}\left(e^{\mathcal{N}_s(t')} - 1\right)\left[|\mathcal{E}_s^{-}(z_{s+1},t'-\Delta t_s))|^2 + |\mathcal{E}_s^{+}(z_s,t'-\Delta t_s))|^2\right].
\end{aligned} \tag{3.41}$$

As the passive sections consist of free space, the carrier dynamics are only modelled for the gain $\mathcal{N}_g(t') = \tilde{G}(t')$ and for the absorber $\mathcal{N}_q(t') = \tilde{Q}(t')$. At this point, the boundary conditions (3.19)-(3.27) are utilised to express the forward and backward propagating field in eq. (3.41) by the altered forward propagating field at the outcoupling facet. Furthermore, the notation $\mathcal{E}_p^{+}(z_0,t') \equiv \mathcal{E}(t')$ is used for simplicity. Additionally neglecting the influence

[8] The trapezoidal rule reads: $\int_a^b f(x)dx \approx (b-a)\frac{f(a)+f(b)}{2}$.

of the losses β_s, leads to the following two equations for the carrier dynamics in gain and absorber, respectively

$$\begin{aligned}\frac{d}{dt'}\tilde{G}(t') =& J_g(t') - \gamma_g\tilde{G}(t') - r_g\left(e^{\tilde{G}(t')} - 1\right)\\ &\times\left[|\mathcal{E}(t'-\tau_1)|^2 + |\mathcal{E}(t'-\tau_1-2\tau_2)|^2 e^{2\tilde{Q}(t'-\tau_2)+\tilde{G}(t'-2\tau_2)}\right],\end{aligned} \tag{3.42}$$

$$\begin{aligned}\frac{d}{dt'}\tilde{Q}(t') =& J_q(t') - \gamma_q\tilde{Q}(t') - r_q\left(e^{\tilde{Q}(t')} - 1\right)\\ &\times\left[|\mathcal{E}(t'-\tau_1-\tau_2)|^2 e^{\tilde{G}(t'-\tau_2)} + |\mathcal{E}(t'-\tau_1-\tau_2)|^2 e^{\tilde{Q}(t')+\tilde{G}(t'-\tau_2)}\right].\end{aligned} \tag{3.43}$$

To arrive at a dimensionless formulation for simulation purposes, the electric field is normalised according to $E = \sqrt{Tr_g}\mathcal{E} = \sqrt{Tvg_g\Gamma_g}\mathcal{E}$ and the time according to $t' = \frac{\tilde{t}}{T}$, where T is the cold-cavity round-trip time. Additionally, all rates are rescaled applying a multiplication by T and all times by a division by T [JAU17a]. The delay differential equation system then reads

$$\begin{aligned}\frac{d}{d\tilde{t}}E(\tilde{t}) =& -\gamma E(\tilde{t}) + \gamma\sqrt{\kappa}E(\tilde{t}-2\tau_2-2\tau_1)\\ &\times e^{\frac{1-i\alpha_g}{2}(\tilde{G}(\tilde{t}-\tau_1-2\tau_2)+\tilde{G}(\tilde{t}-\tau_1))}e^{(1-i\alpha_q)\tilde{Q}(\tilde{t}-\tau_1-\tau_2)},\end{aligned} \tag{3.44}$$

$$\begin{aligned}\frac{d}{d\tilde{t}}\tilde{G}(\tilde{t}) =& J_g - \gamma_g\tilde{G}(\tilde{t}) - (e^{\tilde{G}(\tilde{t})} - 1)\\ &\times\left[\mid E(\tilde{t}-\tau_1)\mid^2 + \mid E(\tilde{t}-\tau_1-2\tau_2)\mid^2 e^{2\tilde{Q}(\tilde{t}-\tau_2)+\tilde{G}(\tilde{t}-2\tau_2)}\right],\end{aligned} \tag{3.45}$$

$$\frac{d}{d\tilde{t}}\tilde{Q}(\tilde{t}) = J_q - \gamma_q\tilde{Q}(\tilde{t}) - s(e^{2\tilde{Q}(\tilde{t})} - 1)e^{\tilde{G}(\tilde{t}-\tau_2)}\mid E(\tilde{t}-\tau_1-\tau_2)\mid^2, \tag{3.46}$$

where the ratio proportional to the differential gain coefficients and the confinement factors is defined as $s = \Gamma_q g_q(\Gamma_g g_g)^{-1} = r_q r_g^{-1}$ and the current densities are assumed to be constant in time. In order to reduce the number of delayed variables in the DDE system, the time in the carrier equations is shifted according to the transformations $\tilde{t} = t + \tau_1$ for eq. (3.45) and $\tilde{t} = t + \tau_1 + \tau_2$ for eq. (3.46). Additionally, two new variables are introduced for the carrier densities, which are defined as

$$\tilde{G}(t+\tau_1) = G(t), \quad \tilde{Q}(t+\tau_1+\tau_2) = Q(t). \tag{3.47}$$

Inserting the new variables leads to the final DDE system describing the passively mode-locked semiconductor VECSEL with a V-shaped cavity geometry and quantum-well active sections

$$\frac{d}{dt}E(t) = -\gamma E(t) + \gamma E(t-T)R(t-T), \tag{3.48}$$

$$\begin{aligned}\frac{d}{dt}G(t) =& J_g - \gamma_g G(t) - \left[e^{G(t)} - 1\right]\\ &\times\left[\mid E(t)\mid^2 + \mid E(t-2\tau_2)\mid^2 e^{2Q(t-2\tau_2)+G(t-2\tau_2)}\right],\end{aligned} \tag{3.49}$$

$$\frac{d}{dt}Q(t) = J_q - \gamma_q Q(t) - s\left[e^{2Q(t)} - 1\right]e^{G(t)}\mid E(t)\mid^2, \tag{3.50}$$

$$R(t-T) = \sqrt{\kappa}e^{\frac{1-i\alpha_g}{2}[G(t-2\tau_1)+G(t-T)]+(1-i\alpha_q)Q(t-T)}, \tag{3.51}$$

where the pump current and unsaturated absorption can be expressed in terms of the integrated carrier densities G_0 and Q_0 according to $J_g = G_0\gamma_g$ and $J_q = Q_0\gamma_q$ [SCH18e]. These integrated carrier densities are related to the equilibrium charge carrier densities at the lasing threshold, which is discussed in section 4.2.1.

3.4 Parameters and Discussion

The parameters most easily varied in an experiment are the pump of the gain $\mathcal{J}_g$, the total round-trip time T and the relative length of the two cavity arms, which manifests itself in the length of the delays τ_1 and τ_2. As the pump is simply expressed in terms of a variation in the equilibrium level of the gain, the system is sufficient to qualitatively model electrically or optically pumped VECSELs. However, it has to be pointed out that the pump power (unsaturated absorption) and the integrated carrier density G (Q) are normalised so that they are relative to the value at transparency of the gain (absorber), which is defined as the integrated carrier density at which the reflectivity of the semiconductor chip becomes unity ($r = 1$). This means that $J_g = 0$ ($J_q = 0$) corresponds to the transparency of the gain (absorber) chip [JAU17a]. Therefore, the pump value at the lasing threshold represents the excess pump power needed to reach the threshold starting from transparency. In this parameter normalisation, a numerical pump current of $J = 30J_{th}$ could still be realisable in experiments, as the difference between threshold and transparency pump power often is way smaller than their absolute physical values [WAL16, HAU19].
The influence of a potential reverse bias applied to the absorber is described by the equilibrium carrier density Q_0 in the absorber and the non-radiative carrier relaxation rate γ_q ($J_q = \gamma_q Q_0$). As an applied bias has a heavy influence on the band quasi Fermi-levels, it can have an effect on both quantities. Nevertheless, for state of the art VECSELs the required absorber properties are achieved by a proper adjustment of the epitaxial growth process and therefore no reverse bias is necessary [WAL16, FIN20]. In consequence, the non-radiative relaxation rates in the gain γ_g and absorber γ_q as well as the unsaturated absorption Q_0 are mainly influenced by the structure and composition of the respective semiconductor chips. For the gain relaxation rate, values between $\gamma_g = 0.3\,\mathrm{ns}^{-1}$ $-10\,\mathrm{ns}^{-1}$ and for the absorber relaxation rate values between $\gamma_q = 0.02\,\mathrm{ps}^{-1}$-$0.6\,\mathrm{ps}^{-1}$ are in accordance with experimental results [KAR94, JON95b, MUL05a, SIE13b, WAL16, ALF18]. Due to its fast relaxation compared to the round-trip time in VECSELs $\gamma_q T \gg 1$, the absorber usually asymptotically relaxes to its equilibrium value Q_0 in between pulse interactions, whereas for the gain this is only true for comparably long cavities of several metres.
The bandwidth of the spectral filter γ refers to the limited bandwidth of the gain or an additional (narrower) filtering element, such as distributed Bragg reflectors. For a top and bottom distributed Bragg reflector surrounding the active section, the Lorentzian line shape approximation is especially valued. However, a value of $\gamma = 3500\,\mathrm{ns}^{-1}$ [WAL18, MEI21a] would be more realistic to quantitatively describe the filtering. Yet, due to its strongly narrowing effect on the laser pulses, it makes numerical calculations computationally very demanding and path-continuation techniques at close to realistic pulse widths (100 fs - 1 ps) almost impossible. Therefore, a value of $\gamma = 240\,\mathrm{ns}^{-1}$ is utilised in most calculations presented in this work. The low value of γ has no drastic effect on the qualitative appearance of the dynamical output in the investigated parameter regime, as outlined in section 4.2. It has to be highlighted that although pulse width of 100 fs seconds can be reproduced by enlarging the filter (gain bandwidth) far enough, one has to keep in mind that in such a

case the slowly varying envelope approximation is not necessarily valid. Furthermore, the assumption of a negligible active section width breaks down at very low pulse width as the time of flight in the active sections becomes of the same time scale as the pulse width. In consequence, the DDE model is suitable to describe qualitative dynamics of mode-locked lasers but is subject to strong limitations when it comes to a quantitative reproduction of the pulse width. Interestingly, the DDE model of mode-locking produces the qualitatively same bifurcation structure in certain regions as the Yamada model, if $\gamma = 1$ [TER18].
The factor proportional to the ratio of the differential gain and absorption s, which is also referred to as the ratio of the saturation energies [VLA04, JAU17a], has to fulfill the condition $s = \frac{E_g}{E_q} > 1$ for mode-locking to occur. Otherwise the absorber saturates slower than the gain. Values used in recent works on monolithic and external devices range from $s = 2 - 30$ [VLA04, VLA05, OTT14b, JAU16, MAR14c, SCH18f, HAU19, HAU20]. Since this ratio comprises the confinement factors, it can be altered by changing the saturation energies or post chip fabrication via the introduction of lenses in the external cavity. Additionally, the differing micro-cavity enhancement in gain and absorber-chip can be an influential factor.
A parameter that was subject to a lot of scientific discussions is the linewidth enhancement factor α. As a reminder, the linewidth enhancement is defined as $\alpha = \frac{\partial_N \chi_r}{\partial_N \chi_i}$, with the index denoting the real r and imaginary part i of the electric susceptibility, and the carrier density N [HEN82, HAR83, HAD99]. For quantum-well gain media, experimental data indicated values of $\alpha = 2 - 7$ [RID90, UKH04, FOR07, WAL16]. However, the phenomenological approach comes to a limit for ultra short pulses (fs regime) or high excitation powers [AGR93a, WAN07, LIN12b]. In this regimes the variation of the refractive index (depending on the charge-carrier density) is a temporally evolving quantity during the interaction of the medium and the pulse. Hence, the α-factor is not constant in time on the very fast time scales [UKH04, AGR93a, HER16] and furthermore omits a frequency dependence [UKH04, RID90]. Additionally, it was shown that for quantum dots the influence of the α-factor can be modelled well by $\alpha = 0$ [LIN14, CHO20b] and experiments on quantum well based mode-locked lasers have been excellently qualitatively reproduced by using $\alpha_g = \alpha_q = 0$ [PIM14, JAU16, NIK16]. This agreement can be reasoned by the fact that effects counteracting the impact of the α-factors are not considered in the DDE model (or also other models), such as the influence of group velocity dispersion [PIM17]. Thus, the analysis of the most dynamical regimes in this work starts at $\alpha_{g,q} = 0$, as it drastically simplifies the bifurcation analysis and provides a good first overview of the dynamical regimes. From this starting point, the influence of the $\alpha_{g,q}$ is investigated in a regime of $\alpha_{g,q} < 2$ for quantum-wells, which is oriented to the experimentally determined data in Reference [WAL16]. Anyhow, slightly lower values compared to the experimental data are chosen in the discussion presented in this work due to the multi-mode nature of the DDE system in which $\alpha_{g,q}$ impact all modes equally. In consequence, taking the maximum value would lead to an overestimation, due to the frequency dependence of the α-factor in experiments.
As mentioned before, the parameters are scaled to the cold-cavity round-trip time for simulation purposes. The values used a large part of this work are given in the overview shown in Table 3.1. A round-trip time of $T = 625\,\text{ps}$ is used, which is typical for mode-locked VECSELs [GAA16, WAL16]. Nonetheless, the investigation is started from a lower round-trip time of 220 ps to get a first overview. The slight adjustments made to the parameter values in order to investigate different dynamical regimes are discussed at the start of each section.

The introduced DDE model is subject to several advantages and disadvantages. Firstly, the

Symbol	Value	Dimensionless	Meaning
T	0.625 ns	1	Cold cavity round-trip time
$\tau_{1,2}$	0.15625 ns	0.25	Length of the cavity arms
γ	240 ns^{-1}	150	Gain/filter Bandwidth
J_g	1 ns^{-1}	0.625	Pump rate in the gain
J_q	-104 ns^{-1}	-65	Pump rate in the absorber
γ_g	1 ns^{-1}	0.625	Gain non-radiative relaxation rate
γ_q	180 ns^{-1}	112.5	Absorber non-radiative relaxation rate
α_g	0	0	Gain line-width enhancement factor
α_q	0	0	Absorber line-width enhancement factor
κ	0.99	0.99	Intensity losses at the output coupler
s	2	2	Ratio of the differential gain

Table 3.1.: Parameter values used for the numerical calculations in the high performance mode-locking regime. Parameters chosen to adapt experimental values [WAL16][WAL18].

carrier-field interaction is simplified to a linear relationship between gain and carrier density as well as a constant line-width enhancement factor. This can be circumvented at the highest level by describing the carrier dynamics utilising a fully microscopic model, which is especially well suited for the investigation of ultra-short pulse generation [KIL17, KIL19, MCL20]. Alternatively, a more complex approach for the macroscopic polarisation can be included [MUL05a, JAV10, JAV11], which is not as complex. However, due to the resulting large systems of equations in microscopic models and the high resolution necessary to describe effects on time scales of 10 fs magnitude, numeric calculations become computationally very demanding and even with up to date servers the lengths of the calculated time series are restricted to several 100 ns [MCL20]. As elaborated at the start of this section, another option of including a more complex field-carrier interaction lies in the usage of a travelling-wave approach, which circumvents the simplification of infinitely narrow active sections. In this case, the field depends on space and time, which can be of use when investigating the role of cavity geometry influences on a micrometer scale [MEI19] or complex gain effects not requiring a fully microscopic approach [MUL06, ROS11c]. Furthermore, the influence of differing gain structures, as quantum dots for example, can be introduced in detail into the DDE system [VIK06, VLA10, RAG13, SIM14], which is discussed for a gain system based on submonolayer quantum-dots in section 6.3. Another extension of the ring DDE model is presented in Reference [PIM19] to account for inhomogeneous broadening by including the polarisation dynamics. Yet, all these alternatives come with additional computational demands and therefore have to be chosen with care.

It has to be underlined that the spectral filtering and internal losses in the DDE system are introduced via the lumped element approach, which means that the losses occur at one fixed point in the cavity and are not accumulated during propagation as in the travelling-wave or fully microscopic models. Consequently, the electric field strength can be over- or underestimated at some points of the cavity, which influences the field carrier interaction. Nevertheless, this assumption greatly reduces the computational demands.

Another simplification that has to be pointed out is that the spectral filtering and the gain level are introduced independently in the DDE model. An alternative relatively simple approach accounting for the complex interplay between filtering and nonlinearity inside the active sections is based on delay algebraic equations (DAE) and presented in Refer-

ences [MUL05a, SCH19b, AVR19]. In this set of DAEs the VECSEL is modelled by two coupled micro-cavities (gain and absorber), which is especially appealing if the semiconductor chips are single vertical-cavity surface-emitting lasers with a highly reflective top-side DBR [MAR14c, CAM16, SCH19b]. Furthermore, the DAE approach delivers an option to investigate third-order dispersion effects, which are often overwhelmed by second-order diffusion in DDE systems [SCH19b]. A DAE system for the V-shaped passively mode-locked VECSEL is discussed in section 5.4, with a special focus on third-order dispersion effects.
Although third-order dispersive effects arise naturally in DDE systems, it is very cumbersome to introduce group velocity dispersion [PIM17, PIM20]. A method to investigate the influence of dispersion effects is to transform the DDE system into Haus master partial differential equation [HAU00, KOL06, CAM16, SCH18e, SCH18f, HAU20a] as outlined in section 4.3.3. This has the advantage that the influence of the cavity geometry occurs intuitively as a nonlocal term. Yet, Haus master equation approaches are usually used to describe mode-locked lasers in the regime of a complete gain recovery between pulses (i.e. long-cavity regime) [CAM16] or high-speed mode-locking [HAU00, KOL06], where the gain can be approximated to be constant during one round-trip. To apply a Haus master equation in a regime of incomplete gain recovery between pulse passes, i.e. when the gain recovery time is the range of the cavity round-trip time, requires the introduction of additional boundary conditions. A sufficient boundary condition and an investigation of the group velocity dispersion in the passively mode-locked VECSEL is elaborated in sections 5.2 and 5.3.

4 Cavity Effects

4.1 Introduction

In this chapter, the influence of the cavity geometry on the laser dynamics in a passively mode-locked VECSEL, as introduced in the previous chapter, is examined. Accordingly, the DDE model incorporating the cavity geometry via the introduction of three delay times (τ_1, τ_2, T) is analysed via direct numerical integration applying a Runge-Kutta algorithm of fourth order [PRE07]. These findings are complemented by a bifurcation analysis based on numerical path-continuation utilising the software DDE-biftool [ENG02, SIE14a]. The software package relies on the Newton method to enable the continuation of solution branches and linear stability analysis/Floquet analysis to unravel the stability of the found solutions [ENG02, SIE14a].
The chapter is structured as follows, in the first section 4.2 a regime of intermediate-cavity length of $L \approx 20\,\text{cm}$ usually utilised for high performance mode-locking is discussed ($T \approx 625\,\text{ps}$). Firstly, the transition from the *off*-state to the continuous-wave lasing state and the fundamental mode-locking solution is elaborated in comparison to the conventional DDE system. Secondly, subsection 4.2.2 includes the discussion of the emergence of temporally non-equidistant pulse cluster solutions, characteristic for the cavity geometry. Subsequently, the effect of enlarging or shortening the cavity length is discussed in subsection 4.2.3 and finally the role of the cavity geometry is analysed.
In the second main section 4.3, the long-cavity regime with a cavity length of $L > 60\,\text{cm}$ ($T > 1.8\,\text{ns}$) is investigated. In this regime, the single pulses become temporally localised as they do not interact via the gain, which is explained in detail in subsection 4.3.1. The following subsection 4.3.2 discusses the emergence of phase incoherent photonic molecules as a consequence of the characteristic influence of the cavity geometry. In the two final subsections a nonlocal Haus master equation model is derived (subsection 4.3.3), which is subsequently used to discuss the effect of introducing an asymmetry in the cavity geometry and how this influences the distance of pulses in one photonic molecule (subsection 4.3.4).

4.2 Intermediate-Cavity Regime

Before analysing the dynamics emerging in a V-shaped VECSELs at intermediate-cavity lengths, it is first of all important to define the term "intermediate". The cavity length is classified to be "intermediate" at about 20 cm [WAL16], as it is longer than most monolithic devices with cavity lengths ranging from hundred microns to a few millimeters [JON95b, GRI09, VLA09, WEB18, AVR00], but shorter than the long-cavities required for localised states to occur. The localisation manifests at cavity lengths of several metres [MAR14c, CAM16]. Another possibility to classify the cavity length is utilising its relation to the relaxation rate of the gain γ_g. In the long-cavity regime, the gain relaxation is on a much faster time scale than the cold-cavity round-trip time, i.e. $\gamma_g T \gg 1$. Accordingly, an intermediate length can

be defined as a regime, where the gain relaxation and the round-trip time are of the same time scale $\gamma_g T \approx 1$. Finally, in a short cavity regime the gain almost does not relax during one round-trip $\gamma_g T \ll 1$.
The analysis of the intermediate-cavity regime is motivated by the experimental works presented in References [WAL16, WAL18]. These reported the occurrence of non-equidistant pulses, as a performance limiting instability. To obtain an overview of the full bifurcation scenario, i.e. all stabilising dynamics, the simplest solutions, namely the *off*-state and the continuous-wave (CW) lasing state are investigated first (subsection 4.2.1). From this starting point the emergence of pulse-clusters is examined (subsection 4.2.2) and the role of different gain/absorber parameters and cavity parameters is discussed (subsection 4.2.3).

4.2.1 Lasing Threshold and Fundamental Solution

A parameter point critical for the classification and comparison of lasers with respect to their efficiency is the lasing threshold. It corresponds to the critical pump current value (or optical pump power) that has to be overcome to achieve lasing with constant intensity (continuous-wave lasing). From a bifurcation analysis perspective, it is the bifurcation point in which the *off* steady state solution becomes unstable and the continuous-wave (CW) solution emerges. The threshold value is often used to put the applied pump current into a comparable perspective. In terms of the delay differential equation model (3.48)-(3.51), it corresponds to the transition

$$(0, G_0, Q_0) \rightarrow (E_0 e^{i\omega t}, G_0, Q_0), \tag{4.1}$$

where the left-hand side refers to the *off*-state and the right-hand side to the continuous-wave state. Directly at the bifurcation point, the electric field is yet very small and therefore the constant amplitude of the electric field in the gain and absorber equation is $E_0 = 0$. The equilibrium integrated charge carrier densities in the gain and absorber at threshold are given by G_0 and Q_0 respectively. Furthermore, ω is the angular oscillation frequency of the electric field with respect to the optical frequency, i.e. $\omega = 0$ describes the maximum gain mode. Hence, in a fixed coordinate system, the CW solution is a limit cycle solution due to the complex oscillation of the electric field.
An analytic expression for the lasing threshold can be found by exploiting the fact that close to the bifurcation point both solutions are approximately equal as done in References [VLA05, JAU17a]. Inserting the *off*-solution into the carrier equations of the DDE model (3.49)-(3.50) and the CW solution into the electric field equation (3.48) of the DDE model, then leads to the following equations

$$\begin{aligned} i\omega =& -\gamma + \gamma\sqrt{\kappa} e^{(1-i\alpha_g)G_0 + (1-i\alpha_q)Q_0 - i\omega T}, && (4.2)\\ 0 =& J_g - \gamma_g G_0, && (4.3)\\ 0 =& J_q - \gamma_q Q_0. && (4.4) \end{aligned}$$

Taking the real and imaginary part of eq. (4.2) then gives

$$\begin{aligned} \omega =& -\gamma\sqrt{\kappa} e^{G_0+Q_0} \sin(\alpha_g G_0 + \alpha_q Q_0 + \omega T), && (4.5)\\ \gamma =& \gamma\sqrt{\kappa} e^{G_0+Q_0} \cos(\alpha_g G_0 + \alpha_q Q_0 + \omega T). && (4.6) \end{aligned}$$

These conditions can be simplified by dividing (4.5) by (4.6) and adding the squared equations. The two resulting equations read

$$\omega^2 + \gamma^2 = \gamma^2 \kappa e^{2G_0 + 2Q_0}, \tag{4.7}$$

$$\frac{\omega}{\gamma} = -\tan\left(\alpha_g G_0 + \alpha_q Q_0 + \omega T\right). \tag{4.8}$$

Rearranging eq. (4.7) for G_0 and inserting equations (4.3) and (4.4) for the equilibrium integrated carrier densities then leads to an expression for the threshold current:

$$J_{\mathrm{th}} = \gamma_g \left[\frac{1}{2}\ln\left(\frac{\omega^2}{\gamma^2} + 1\right) - \frac{1}{2}\ln\left(\kappa\right) - \frac{J_q}{\gamma_q}\right]. \tag{4.9}$$

The set of transcendental equations (4.8) and (4.9) can be solved to find the threshold pump current for the different CW modes. They are defined by their frequency shift ω with respect to the maximum gain mode[1] ($\omega = 0$). Thus, one can deduce that the α factors can cause the emission of another mode being favoured (see eq. (4.8)), and therefore a higher threshold current is necessary to compensate for the lower gain [VLA05, JAU17a].
It is possible to apply a coordinate transformation into a rotating coordinate system in which the rotation of the complex electric field with oscillation frequency ω is cancelled out. Hence, the limit cycle turns into a fixed-point/equilibrium in the new coordinate system. Consequently, the CW solution can be referred to as a relative equilibrium. The transformation to rotating coordinates is necessary for a bifurcation analysis of the mode-locked solutions, since these occur as periodically repeating pulses in intensity with a period approximately given by $f = (nT + \frac{1}{\gamma})^{-1}$. Without the coordinate transformation, the mode-locking and the optical frequency would lead to two superposed oscillations in phase space. In order to enable the numerical path-continuation of pulsed solutions, the phase-symmetry is exploited in the software package DDE-biftool utilised to conduct the bifurcation analysis presented in this work [ENG02, SIE14a]. In rotating coordinates, the mode-locked solutions appear as relative limit cycles, meaning that they only oscillate at the frequency f. Anyhow, applying the transformation leads to more time-consuming calculations as the oscillation speed ω is determined numerically in each path-continuation step and convergence problems can occur. For the simple case of $\alpha_g = \alpha_q = 0$ without detuning, only the real part of the electric field equation eq. (3.48) can be investigated because there is no influence on the phase remaining. In consequence, the rotational coordinate transformation is not required here due to the fact that all the dynamics can be investigated in terms of the electric field amplitude and the charge carriers. This is exploited for all path-continuation results for $\alpha_g = \alpha_q = 0$ presented in this work, and essentially has a similar effect as transforming the system into rotating coordinates.
As mentioned before, the coordinate transformation converts limit cycles into relative equilibria, which has an effect on the found bifurcation points. Although the bifurcation points are not shifted in parameter space, some bifurcations can appear differently. This is the case for the Andronov-Hopf bifurcation giving birth to the CW solution along the *off*-state equilibrium. In the rotating coordinates (or when using a real electric field at $\alpha_g = \alpha_q = 0$), the CW state is a constant steady state solution. Therefore, it is not born in an Andronov-Hopf,

[1] Please note that the maximum gain mode is shifted to 0 by the choice of the rotating frame, canceling out the optical frequency.

but in a Pitchfork bifurcation[2]. As depicted in the 1D-bifurcation diagram in Fig. 4.1(a) obtained utilising DDE-biftool, the Pitchfork bifurcation (black circle) leads to the emergence of a symmetric CW solution pair with negative and positive electric field amplitude E (orange lines). The pump current value of this bifurcation point perfectly matches the previously determined analytical result of the threshold current. As previously outlined, the found solutions are steady states in the amplitude picture as displayed by the temporal dynamics of the *off*- and CW-state in Fig. 4.1(b_{1-2}). The presence of a Pitchfork bifurcation can be deduced from examining the eigenvalues obtained from a linear stability analysis performed utilising DDE-biftool. The eigenvalue spectrum along the *off*-state is depicted in Fig. 4.1(c), with the eigenvalue spectrum below the threshold (stable *off*-solution) denoted in red and above the threshold in green (unstable *off*-solution). It is important to say that only the dominant eigenvalues are shown, since the phase space of delay systems is of infinite dimensions. As expected for a Pitchfork bifurcation, one eigenvalue crosses the y-axis (black-line) and obtains a positive real-part at the bifurcation point. In its further course, the CW solution turns unstable in an Andronov-Hopf bifurcation (AH_{FML}), as signaled by the black squares in Fig. 4.1(a). The found bifurcation structure for the symmetric cavity configuration is similar to the results obtained from a path-continuation of the ring DDE model [VLA04, JAU17a], which is not surprising because for the continuous-wave solution the gain and absorber are continuously depleted. In the CW case, the second gain pass only increases the gain by a factor of two compared to the ring model and the absorption is doubled due to the assumption of the double pass of the active section. This further becomes evident when comparing eq. (4.2) to the expression for the threshold current obtained in [JAU17a], as eq. (4.2) contains a further factor of 1/2.

An extended continuation of the positive amplitude CW branch in pump current is indicated in Fig. 4.2(a). The first Andronov-Hopf bifurcation point (AH_{FML}) gives birth to the stable fundamental mode-locking (FML) solution[3], of which the electric field and carrier dynamics for two round-trips are displayed in Fig. 4.2(b_1). Characteristic for the V-shaped cavity, the gain (black) is depleted twice by each pulse per round-trip, whereas the absorber (red) is only depleted once, due to its position at the end of the cavity. This marks a fundamental difference to the behaviour of the ring-cavity DDE in which only one propagation direction is considered [VLA04, VLA05, JAU17a] and therefore only one gain depletion per pulse occurs. The type of bifurcation is deduced from the eigenvalue spectrum of the CW solution, which is presented in Fig. 4.2(c) for the pump power below ($J_g < J_{ML}$) and above ($J_g > J_{ML}$) the bifurcation point. Typical for an AH bifurcation, it is clearly visible that a pair of complex conjugate eigenvalues crosses the y-axis.

Performing a linear stability analysis along the unstable part of the CW branch, unravels that successive super-critical AH bifurcations appear, which give birth to unstable limit cycles. At these bifurcation points, an additional pair of complex conjugate eigenvalues crosses the y-axis and obtain a positive real part, leading to a higher instability of the system. The emerging limit cycles correspond to the harmonic mode-locking solutions (HML_n) oscillating at an integer multiple n of the fundamental mode-locking frequency. In other words, n temporally equally spaced pulses propagate around the cavity. As an example, the dynamics of the second-order harmonic mode-locking solution HML_2 is displayed in Fig. 4.2(b_2). For

[2] This can be deduced from the normal form of the Hopf bifurcation, which can be split into a phase and modulus contribution. If the phase rotation is canceled out, the modulus contribution equals the normal form of a Pitchfork bifurcation.

[3] Please note that the investigation presented here is performed at a round-trip time $T = 220\,\mathrm{ps}$, which is slightly below the experimentally used values, to obtain a first simple overview of the bifurcation scenario.

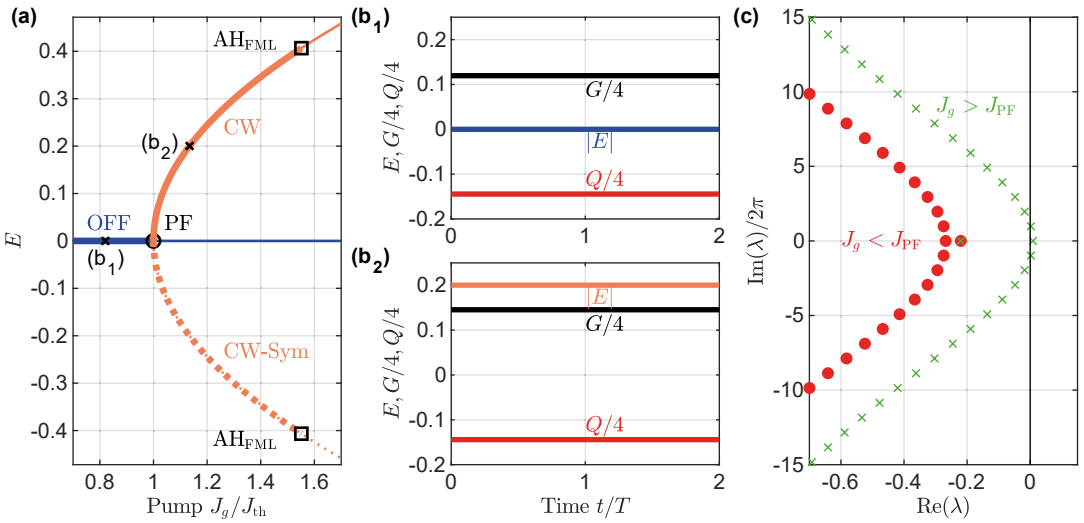

Figure 4.1.: (a) 1D-Bifurcation diagram along the pump current J_g, with the electric-field amplitude E along the symmetric continuous-wave solutions (CW) in orange and along the *off*-solution in blue. Thick (thin) lines denote stable (unstable) dynamics. The black circle indicates a pitch-fork bifurcation (PF) and the black squares an Andronov-Hopf bifurcation ($\mathrm{AH_{FML}}$). ($\mathrm{b_{1+2}}$) Electric field amplitude $|E|$, gain G, and absorber Q dynamics at the points marked by the black crosses in (a). (c) Dominant eigenvalues resulting from the linear stability analysis along the *off* solution, for J_g below (red) and above the CW threshold (green). Parameters as in Table 3.1 and $T = 220\,\mathrm{ps}$.

a symmetric cavity configuration in the mode-locking regime, the Andronov-Hopf bifurcations of the HML_n solutions occur ordered from low to large n along the CW branch in J_g. However, this can change if the cavity is tuned to be asymmetric or a localised state regime is investigated.

Investigating the FML solution, the double gain pass in the V-shaped system manifests itself in a second gain depletion induced by each pulse (see Fig. 4.2($\mathrm{b_1}$)). However, this is different for the harmonic mode-locking solution with two pulses ($\mathrm{HML_2}$), which at first sight only leads to a single gain depletion per pulse, as can be drawn from comparing the electric field and gain dynamics in Fig. 4.2($\mathrm{b_2}$). Yet, in the $\mathrm{HML_2}$ state the pulses are spaced by $\Delta = T/2$, equalling the time difference between the two gain-depletions of a single pulse for a symmetric cavity with $\tau_1 = \tau_2 = T/2$. Hence, the two pulses of the $\mathrm{HML_2}$ solution collide in the gain and deplete it simultaneously. As this amplification of the pulses is energetically not favourable, the $\mathrm{HML_2}$ solution only becomes stable with much lower pulse energies compared to the FML solution in the symmetric cavity configuration and was not visible in experiments [WAL18]. The requirements for the $\mathrm{HML_2}$ solution to become stable are discussed in sections 4.2.2 and 4.2.4. The same reasoning can be applied to explain the instability of all further even numbered harmonic mode-locking solutions in the symmetric cavity. The stabilisation of multi-pulse solutions is substantially different from the Ring DDE model, where the harmonic solutions become stable successively at higher pump powers [VLA04, JAU17a].

4.2.2 Emergence of Pulse Clusters

When increasing the pump power of a mode-locked laser, often the situation occurs that the laser switches to an operation regime with multiple pulses in the cavity as enough gain is

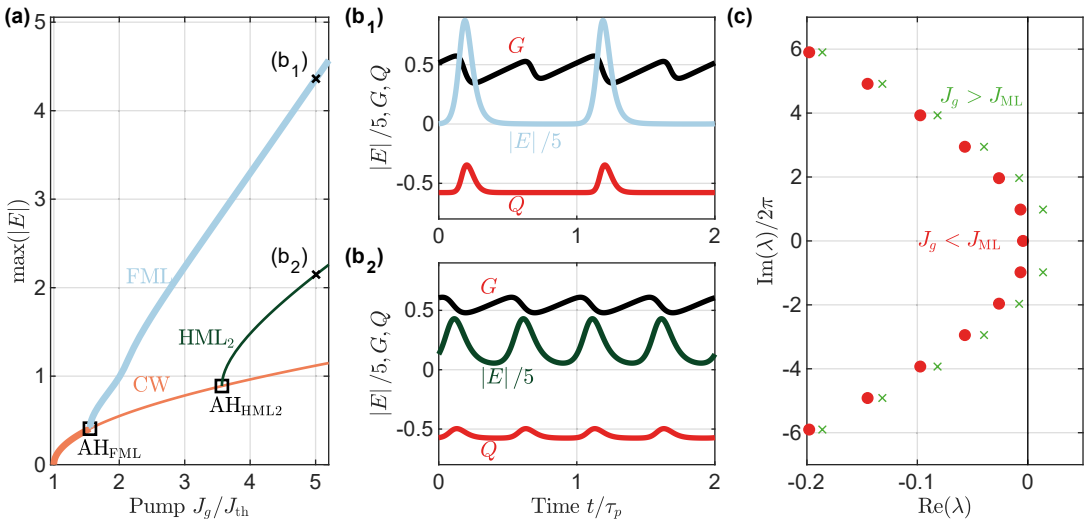

Figure 4.2.: (a) 1D-Bifurcation diagram along the pump current J_g, with the maximum electric field amplitude of the symmetric continuous-wave solutions (CW) in orange, the fundamental mode-locking solution in light blue (FML) and the second harmonic mode-locking solution in green (HML_2). Thick (thin) lines denote stable (unstable) dynamics. The black squares indicate Andronov-Hopf bifurcations along the CW branch (AH_{FML}). (b_{1+2}) One period (τ_P) of the electric field amplitude $|E|$, gain G, and absorber Q dynamics at the points marked by the black crosses in (a). (c) Eigenvalues from the linear stability analysis along the CW solution, found for J_g below (green) and above the bifurcation point of the fundamental mode-locking branch J_{ML} (red). Parameters as in Table 3.1 and $T = 220\,\text{ps}$.

"available" to amplify multiple pulses [SAN90, VLA04, VLA09, MAR14c, WAL18]. With regard to the solutions shown in the bifurcation analysis in the previous section, this means that a multi-pulse solution (e.g. HML_2) turns stable in a certain bifurcation point, characteristic for the investigated system. In the case of passive mode-locking with a saturable absorber, this is naturally connected to an adequate balance between amplification and losses [NEW74, IPP94]. As external cavities are investigated here, with a comparably long distance between the semiconductor chips, the absorber recovers completely between two pulse passes, due to the fact that it is usually designed so that it recovers on a much faster time scale than the gain [WAL16, GAA16]. Combining a lower saturation energy and faster relaxation rate for the absorber (compared to the gain) can be beneficial in terms of the length of the optical pulses [IPP94]. The complete recovery of the absorber (in the chosen modelling approach) is depicted by the time traces of the absorber dynamics (red) in Fig. 4.2(b_{1-2}). However, the depletion/saturation of both, the gain and absorber, depend on the intensity of the pulses in a strong nonlinear way, which makes an intuitive prediction of the stable states and the emergence of instabilities very difficult. Furthermore, multistabilities of the different solutions can occur. This means that e.g. a multi-pulse solution can be stable at the same parameter-set as the FML solution [VLA04, MAR14c]. In experiments, it can be observed as a hysteresis in the P-I curve when tuning up and down the pump power in small steps [WAL18, MAR14c]. In this subsection, the emergence and multistability of multi-pulse states is outlined for the V-shaped VECSEL making use of a bifurcation analysis as well as direct numerical integration.

As discussed before, the HML_2 dynamics is mostly unstable in a V-shaped cavity at a sym-

metric cavity configuration and a low bandwidth γ. Nevertheless, the dynamics of the laser switches to a multi-pulse solution as the pump power is increased. Namely, these multi-pulse states can be referred to as "pulse cluster" (PC_n) solutions with n unequally spaced pulses in the cavity [HAU19]. The emergence of the PC_2 solution is depicted in Fig. 4.3 with an exemplary time-trace of the electric field and gain dynamics displayed in panel (b_3). As the investigation is started at low cavity round-trip times of $T = 220\,\text{ps}$ to get a first overview of the bifurcation structure, the pulses still appear to be very broad. This can be influenced by increasing the filtering γ, which is discussed later in this section.

Bifurcation Structure

At low round-trip times the stable fundamental mode-locking branch (thick blue line in Fig. 4.3 (a)) emerges from the first Andronov-Hopf bifurcation (AH_{FML}) along the continuous-wave branch. The stability of the limit cycles is obtained via the frame-work of Floquet theory in DDE-biftool [KAL08, SIE14a]. The stability determining Floquet multipliers can be computed from the linear stability analysis of the periodic orbits and are the eigenvalues of the monodromy matrix, which describes the system's reaction on perturbations to the investigated limit cycle (see section 2.3). A limit cycle solution is considered to be stable, if the absolute value of all Floquet multipliers is $|\mu| \leq 1$. It has to be considered that one Floquet multiplier is always located at $\mu = 1$. It is referred to as the trivial multiplier and represents the system's invariance to a perturbation in the direction connected to a translation of the time origin [KAL08, HAU20]. Exemplary for the first stable region of the FML branch, the limit cycle dynamics and the largest 100 Floquet multipliers are presented in Fig. 4.3(b_1)-(c_1) for the operation point marked by the black cross in Fig. 4.3 (a).
At a critical pump current marked by the upper saddle-node bifurcation $SN_{1,U}$ (red circle)[4], the fundamental mode-locking solution turns unstable. Due to the induced loop, the branch extends to lower pump powers again. One period of the dynamics in this part of the solution branch is exemplary visualised in Fig. 4.3 (b_2), with the Floquet multipliers indicating the transition of a single multiplier to the unstable region of $|\mu| > 1$ in Fig. 4.3 (c_2). The visible side pulse already begins to grow shortly before the $SN_{1,U}$ bifurcation and continues its growth along the reversed unstable part of the branch. In the further course of the branch, the main pulse decreases in amplitude until at the minimum $SN_{1,L}$ both pulses are of approximately the same height. At this turning point, both pulses begin to grow simultaneously along the branch, forming the pulse cluster PC_2 solution with a pulse distance of $\Delta_{PC2} = 0.25$ (see Fig. 4.3 (b_3)). The PC_2 solution becomes stable in the torus bifurcation T_2 marked by a green circle in Fig. 4.3(a) at the transition from a thin to a thick green line. Subsequently, the same bifurcation scenario as for the FML region can be observed. First a small satellite pulse grows shortly before the $SN_{2,L}$ bifurcation, as already slightly visible in Fig. 4.3 (b_3). Thereafter, the dynamics turns unstable and the branch loops back to lower pump currents until a second saddle-node bifurcation ($SN_{2,U}$) is reached, embodying a local minimum in pulse amplitude. Due to the low round-trip time, the pulses merge together at the lower saddle-point and a very wide pulse emerges, turning stable at the torus bifurcation $T_{\mathcal{R}}$. It can be understood as a result of a continuous saturation of the absorber in the regime of high pump power and wide pulses. As the absorber is not able to recover between pulses,

[4] Here, the first subscript refers to the number of pulses in one round-trip and the second refers to the position on the branch with U-upper and L-lower.

the pulses of the cluster "merge" to form a wide pulse. In the regime of very high bandwidth, the fat pulses occur as almost rectangular. The continuous transformation of the pulse shape along the branch is further elaborated in the next section 4.2.3.
Experimentally, qualitatively similar results with respect to the occurrence and formation of the different dynamical regimes at increased pump powers were obtained [WAL18]. In these experiments, the FML state also first turned unstable at elevated pump powers with a side-pulse appearing in the autocorrelation measurements[5]. Subsequently, a transition to pulse cluster dynamics at higher pump powers was investigated, which was followed by an unstable state characterised by a pulse cluster state (PC_2) accompanied by a satellite pulse in the autocorrelation measurements. It has to be noted that the side-pulse in the autocorrelation measurement could be caused by an instability. More details on the reproduction of the experimentally found dynamics can be found in chapter 5 of Reference [MEI21a].
Physically the stabilisation of the pulse cluster solution PC_2 over the harmonic mode-locking state HML_2 can be reasoned by the energetically more favourable pulse amplification. As visible in Fig. 4.3 (b_3), the formation of a pulse cluster leads to four equidistant gain depletions. In contrast, only two gain depletions occur in the HML_2 state (see Fig. 4.2(b_2)) due to the collision of the pulses in the gain. Thus, more energy is transferred to the pulses of the PC_2 state compared to the pulses of the HML_2 solution. At this point, it has to be highlighted that also odd numbered harmonic mode-locking solutions can stabilise in the symmetric cavity due to the equidistant gain depletion in the V-shaped cavity [MEI21a].
The generation mechanism via Andronov-Hopf bifurcations along the CW branch is very similar to that observed in the Ring DDE model [JAU17a] and is therefore not discussed in detail for the mode-locking regime. Nevertheless, the impact of the asymmetry for HML_n and PC_n states is elaborated in detail for the localised state regime in section 4.3.4.
Taking into account the bifurcation scenario of the PC_2 solution, a very similar bifurcation structure was recovered in the investigation of liquid drops sliding down an inclined plate in Reference [WIL17b], with a focus on the interdependency of sliding velocity and the drop volume. In this system, additional "side-drops" close to the upper saddle-node bifurcation appear and split into two drops, which again underlines the possibility to unravel similarities in the behaviour of very different systems utilising bifurcation analysis.

Characteristics of the Pulse Cluster Solution

In order to illustrate the distinct features of the PC_2 solution, the dynamics are further investigated in different representations in Fig. 4.4, with the data obtained from a direct numerical integration of the DDE system[6]. In panel (a) of Fig. 4.4, the dynamics of the electric field amplitude (colour code) is shown in a pseudo space-time plot. The investigation of the pseudo space-time plot originates from the idea to separate the dynamics of the delay system into a fast and a slow time scale [GIA96, HAU00, YAN17b]. On the one hand, the fast time scale (x-axis) corresponds to changes that happen within one round-trip, i.e. the emergence of one single pulse or the depletion of the absorber. On the other hand, the slow time scale (y-axis) refers to alterations of the dynamics from round-trip to round-trip, e.g. a drift of the pulse with respect to the cold-cavity round-trip time or a slow modulation

[5] In these experiments the pulse width was at about 100 fs and therefore applying autocorrelation measurements is the standard technique to investigate the dynamics as real-time oscilloscopes cannot be utilised [WAL16, WAL18].
[6] It has to be highlighted that for these calculations the round-trip time is increased to $T = 625$ ps, as used in experiments [WAL16].

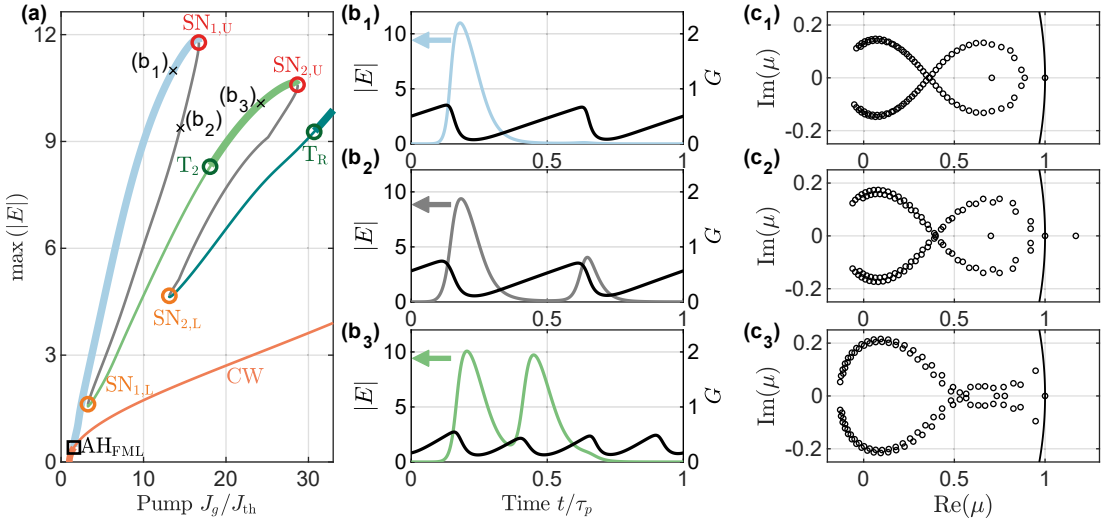

Figure 4.3.: (a) 1D-Bifurcation diagram in pump current J_g, displaying the maximum electric field amplitude along the fundamental mode-locking branch. The different colours refer to the different dynamics continuously evolving along the branch with fundamental mode-locking in light blue, pulse clusters with two pulses in green (PC_2) and a fat pulse regime in teal. The grey regions refer to unstable dynamics with satellite pulses. The amplitude along the continuous-wave solution is indicated in orange. Thick (thin) lines denote stable (unstable) dynamics. The circles represent different types of bifurcations, with saddle-node bifurcations at the upper (U) loop of the branch marked by red circles and denoted $SN_{n,U}$ with n referring to the number of pulses at the bifurcation point. At the lower (L) loop of the branch, the saddle-node bifurcations are marked by orange circles ($SN_{2,L}$). Green circles denote torus bifurcations T_n and the black square (AH_{FML}) refers to the Andronov-Hopf bifurcation giving birth to the fundamental solution branch. (b_{1-3}) Electric field amplitude (coloured) and gain (black) dynamics in one period (τ_p) of the mode-locking solutions at different parts of the branch depicted by black crosses in (a). (c) Largest 100 Floquet multipliers found from the linear stability analysis of the limit cycle solution at the points marked by the black crosses in (a). The black line denotes the unit circle. Parameters as in Table 3.1 and $T = 220\,\mathrm{ps}$.

leading to quasi-periodic dynamics. The separation of time scales can further be exploited to derive a Haus master partial differential equation (PDE) system starting from the DDE system, which is outlined in section 4.3.3. In the resulting PDE, the fast time scale can be understood as a representation of the electric field amplitude in (pseudo) space via the relation $cT = L$, where c is the speed of light, L the cavity length, and T is the cavity round-trip time. The pseudo space-time plot presented here indicates that the found PC_2 solution is stable over more than 200 round-trips and that no quasi-periodic dynamics or instabilities appear. It has to be noted that the x-axis is normalised to approximately one period τ_p of the periodic PC_2 solution. For the investigated solution, the period ($\tau_p = 1.002\,T$) is slightly larger than the cold-cavity round-trip time. In consequence, a slight drift of the pulses to the right would be visible without the normalisation of the slow time scale with respect to τ_p. The drift occurs as a consequence of the time lag induced by the filtering in the DDE system, which leads to the enlarging of the period [MAR14c]. Although causality arguments require the period to be larger than the round-trip time [MAR14c], it can happen that in a regime of large gain, absorption and cavity losses the period is slightly below the cold-cavity round-trip time ($\tau_p < T$) [JAU17a].
Investigating the trajectories of the PC_2 dynamics in the (G,$|E|$)-plane of the phase space,

one can again deduce the role of the second gain depletion as demonstrated in Fig. 4.4(c). At $|E| = 0$, the gain performs an excursion, while the electric field remains unchanged. This corresponds to the second gain depletion of the pulses, which is not accompanied by a pulse in the intensity time-series (see Fig. 4.3 (b_3)), as the DDE model describes the electric field amplitude at the outcoupling facet of the VECSEL. Furthermore, the phase space representation of the dynamics (Fig. 4.4(c)) indicates that the pulses in one pulse cluster are not always perfectly equal, which is connected to the fact that the gain does not fully relax between the pass of the two subsequent pulses, as already shown in Fig. 4.3(b_3). This contradicts to the HML_2 dynamics, in which the two pulses in one round-trip are perfectly equal.

A quantity that often is used to classify the mode-locking stability, is the so-called (intensity) net-gain [NEW74, HAU00, JAU17a]. It is defined by the sum of the gain and the losses at each point in time during one round-trip. In case of the DDE model, one obtains the following expression for the net-gain $\mathcal{G}(t)$ when taking into account the gain and loss terms resembling the field carrier interaction terms in the electric field equation

$$\mathcal{G}(t) = G(t - 2\tau_1) + G(t - T) + 2Q(t - T) + \ln(\kappa). \tag{4.10}$$

If the net-gain is strongly positive, small perturbations can be amplified and therefore lead to a destabilisation of the system. In contrast, if the net-gain is negative, perturbations die out. The temporal course of the net-gain in case of the PC_2 solution is depicted in Fig. 4.4(d). It indicates two strongly open net-gain windows at the position of the two pulses, resulting from the saturation of the absorber. The other two net-gain windows indicate the position of the second gain depletion. At the investigated pump power, they are slightly larger than 0. As no noise is present, the low positive amount of net-gain at this position is not sufficient to support a further pulse or destabilise the system. Nevertheless, these open net-gain windows lead to a destabilisation of the PC_2 solution into a quasi-periodic regime, if the pump is further increased.

A power spectrum obtained from applying a fast Fourier transform to a time-series of the PC_2 intensity dynamics is displayed in Fig. 4.4(b). Two striking features compared to a power spectrum of the fundamental solution (continuously decreasing peaks at each frequency $1/\tau_p$) are that firstly every fourth spectral line is close to 0. Secondly, every second line is modulated compared to an FML spectrum where a continuous decrease of the spectral lines can be observed. These modulations can be deduced from approximating the Fourier components of the periodic PC_2 solution.
Starting at an arbitrary periodic signal

$$E(t) = E(t + \tau_p), \tag{4.11}$$

the Fourier series and the single Fourier components $\tilde{E}_n$ are defined by

$$E(t) = \sum_n \tilde{E}_n e^{in\omega_0 t}, \tag{4.12}$$

$$\tilde{E}_n = \mathcal{F}(E) = \frac{1}{\tau_p} \int_0^{\tau_p} E(t) e^{-i\omega_0 t} dt. \tag{4.13}$$

In turn, the power spectral density $S_E(\omega)$ (power spectrum) can be written as a sum of all single components

$$S_E(\omega) = \sum_n \left|\tilde{E}_n\right|^2 \delta(\omega - n\omega_0). \tag{4.14}$$

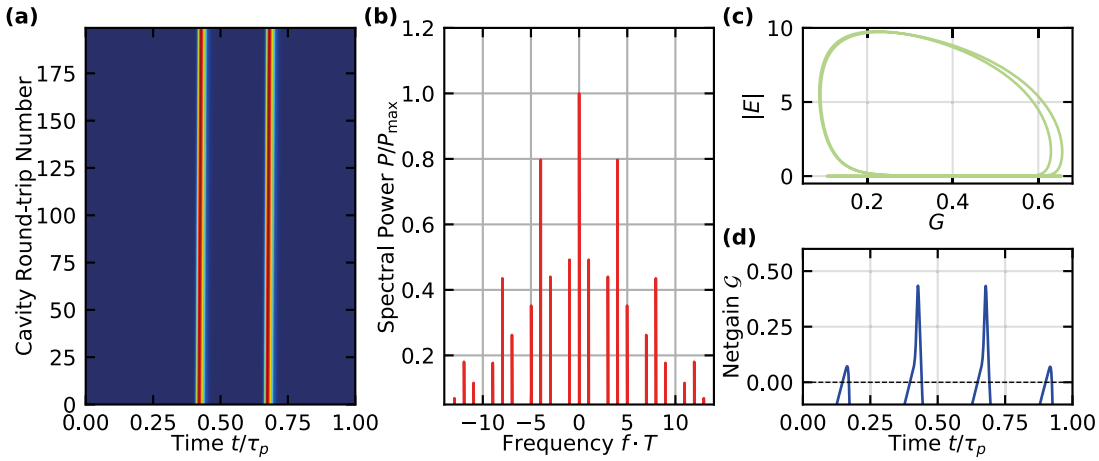

Figure 4.4.: (a) Pseudo space-time plot of the electric field amplitude of the PC_2 mode-locking dynamics, depicting 200 round-trips. The fast time scale, referring to changes during one round-trip, is shown on the x-axis whereas the slow time scale that corresponds to changes from round-trip to round-trip is on the y-axis. It has to be noted that the x-axis is normalised to one period τ_p of the PC_2 limit cycle, which is $\tau_p = 1.002\,T$. (b) Power-spectrum of the PC_2 solution without noise. (c) PC_2 dynamics in the $(G, |E|)$ plane of the phase space. (d) Net-gain in one round-trip of the PC_2 solution, calculated according to eq. (4.10). All parameters were chosen according to Table 3.1 and $T = 625\,\text{ps}$ and $J_g/J_{\text{th}} = 8$.

One can utilise these definitions to find an expression for the power spectral density of the PC_2 solution in the simplest case of two identical pulses. The periodic solution in this case can be expressed by the superposition of two periodic pulse trains. The temporal evolution of the relative phase of the pulses is denoted as the function $\phi(t)$ and the temporal distance is defined by $\theta(t)$. Finally, the resulting periodic function can be expressed as

$$\mathcal{E}(t) = E(t) + E(t + \theta(t))e^{i\phi(t)}. \tag{4.15}$$

In a stable mode-locking state, one can assume that $\theta(t)$ and $\phi(t)$ both evolve very slowly in time and therefore deduce the Fourier coefficients of $\mathcal{E}(t)$ in terms of the coefficients of the single function

$$\tilde{\mathcal{E}}_n(t) = \tilde{E}_n \left[1 + e^{i[n\omega_0\theta(t)+\phi(t)]}\right]. \tag{4.16}$$

Utilising these Fourier-coefficients, one can again deduce the power spectral density

$$S_{\mathcal{E}}(\omega) = \sum_n \left|\tilde{E}_n\right|^2 \left|1 + e^{i[n\omega_0\theta(t)+\phi(t)]}\right|^2 \delta(\omega - n\omega_0). \tag{4.17}$$

In experiments as well as in the numeric integration, the power-spectral density results from an average over a time τ_a, which is much larger than a single round-trip. Applying this average with respect to time leads to the following simplified expression for the power-spectral density

$$\langle S_{\mathcal{E}}(\omega)\rangle = 2\sum_n \left|\tilde{E}_n\right|^2 [1 + C_n]\,\delta(\omega - n\omega_0), \tag{4.18}$$

where the amplitudes C_n give the influence of the time shift and the phase shift according to

$$C_n = \langle \cos\left(n\omega_0\theta(t) + \phi(t)\right)\rangle = \frac{1}{\tau_a}\int_0^{\tau_a} \cos\left(n\omega_0\theta(t) + \phi(t)\right). \tag{4.19}$$

In the case of no noise and $\alpha_g = \alpha_q = 0$, the pulses are perfectly coherent and therefore $\phi(t) = 0$. Furthermore, the temporal spacing of the pulses $\theta(t) = T/4$ is constant, as no noise is included. With $\omega = \frac{2\pi}{T}$ this leads to

$$C_n = \langle \cos\left(\frac{n}{2}\pi\right)\rangle = \begin{cases} 0, & n = 1 + 2i, i \in \mathbb{N}, \\ 1, & n = 4 + 4i, i \in \mathbb{N}, \\ -1, & n = 2 + 4i, i \in \mathbb{N}, \end{cases} \tag{4.20}$$

which recovers the same modulation of the spectral lines found in the numerically obtained power spectrum presented in Fig. 4.4(c). In contrast, the spectral lines are modulated according to $C_n = (-1)^n$ in the HML_2 case, which leads to an elimination of every second spectral line as compared to the FML dynamics. This can be predicted intuitively from the fact that the period of the HML_2 is halved compared to the FML solution and therefore the distance between the spectral lines is doubled. At this point, it has to be noted that including the influence of the amplitude-phase coupling and noise strongly influences the appearance of the spectra. The former leads to a shift of the optical spectrum with respect to the centre of the Lorentzian filter (see page 51 of Reference [JAU17a] or subsection 4.3.2 of this work), whereas the power spectrum is only altered very slightly. The inclusion of noise leads to an incoherence between pulses within one pulse cluster, meaning that $\phi(t)$ becomes an uniformly distributed statistical quantity and therefore $C_n = 0$, which is discussed in more detail in section 4.3.2.
In order to illustrate the influence of further parameters, the next two subsections include a discussion of the gain bandwidth γ and the unsaturated absorption J_q as well as the influence of the carrier relaxation rates $\gamma_{g,q}$. Motivated by experimental values, this is presented for a round-trip time of $T = 625\,\mathrm{ps}$. A detailed bifurcation analysis unravelling the role of the round-trip time is presented in section 4.2.3.

Influence of the Unsaturated Absorption

Additional to the pump power J_g, the unsaturated absorption J_q is a second parameter that can potentially be easily controlled post-fabrication [JAU17a]. This can be achieved e.g. by applying a reverse bias or temperature control. Nonetheless, in the investigated VECSELs the quantities of the absorber chip are mainly determined by the composition of the active section and consequently the details of the growth process [WAL16]. Yet, the unsaturated absorption is a crucial parameter as it mainly characterises the equilibrium carrier density level in the absorber and therefore the amount of absorption induced by the SESAM. Hence, it is important to investigate its interplay with the available gain, i.e. the pump power. In Fig. 4.5, a 2D-bifurcation diagram is presented, displaying the different dynamical regimes in the (J_g,J_q) parameter plane[7]. The subpanels are obtained performing an (a) upsweep and (b) downsweep in pump power via direct numerical integration. A 'sweep' corresponds

[7] Please note that the pump power is not normalised to the threshold due to the threshold dependence on J_q as given in (4.9).

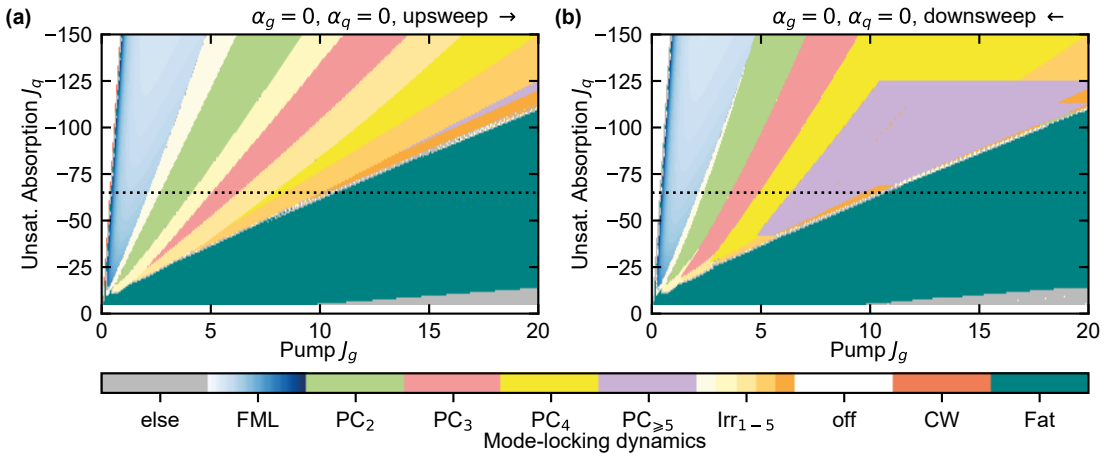

Figure 4.5.: 2D-bifurcation diagram in the parameter plane of pump power (normalised to the threshold J_{th}) and unsaturated absorption (J_g, J_q). The different dynamical regimes are classified according the intensity time-series and are distinguished by the colour code. FML refers to fundamental mode-locking and is displayed in blue, with the shading corresponding to the pulse width normalised to the maximum found in the FML region (light shading depicts to narrow pulses). PC_n corresponds to pulse clusters with n pulses and is displayed in green, red, yellow and purple. The different shades of light orange (Irr_{1-5}) represent quasi-periodic irregular pulse cluster solutions in which the pulse at the leading edge of the cluster dies out and a pulse at the trailing edge of the pulse cluster grows. continuous-wave dynamics are indicated in dark orange and and the teal coloured regions mark a regime of fat pulses with a pulse width exceeding $PW > 0.2T$. For illustration purposes, pseudo space-time plots of the dynamics are depicted in Fig. 4.6. (a) Displays an upsweep in pump current, whereas (b) displays a downsweep in pump current. All parameters are chosen according to Table 3.1 and $T = 625\,\mathrm{ps}$. The dotted line marks the corresponding value of J_q used in the further course of this section.

to continuously increasing (decreasing) the pump parameter in small increments, utilising the stabilised dynamics of the previous calculation as the initial condition for the next parameter point. Thus, it is ensured that the operation regime of the laser only changes if a stability boundary (bifurcation point) is passed. Sweeping in both directions is necessary to determine the upper and lower stability boundaries of the found solutions. The operation regimes are distinguished by analysing the intensity time-series with regard to the number of pulses in one pulse cluster and the stability (periodicity) of the solution. The blue shaded regions represent fundamental mode-locking and the shading indicates the pulse width (determined as the full width at half maximum) normalised to the maximum pulse width in the FML regime, with light regions indicating narrow pulses. Consequently, it is possible to deduce that the pulses are very broad (similar to sinusoidal oscillations) close to the transition between the CW (orange) and FML state, but are narrowing as the pump power is increased. This behaviour does not change when the unsaturated absorption is varied. A pseudo space-time representation of the FML state is displayed in Fig. 4.6(a), where the x-axis is (approximately) normalised to the period of the pulsed solution τ_p so that only a negligible drift appears.

To further classify the dynamics in the (J_g, J_q) parameter plane displayed in Fig. 4.5, stable pulse clusters (PC_n) with n pulses in the cavity are specified by light green, red, yellow and purple. The dynamics of these states is illustrated Fig. 4.6(c,e,g). Analysing the time-series unravels that the distance between the pulses can always be approximated by $\Delta \approx \tau_p/2n$ in

the case of a symmetric cavity ($\tau_1 = \tau_2 = T/4$). From comparing the up- and downsweep depicted in Fig. 4.5(a,b), it is possible to deduce a multistability of the different states, which was already evident at a lower round-trip time in the continuation of the fundamental solution branch displayed in Fig. 4.3. Nevertheless, in between the stable periodic pulse cluster solutions quasi-periodic states appear, which are marked in different shades of orange representing the number of pulses in one round-trip (Irr_{1-5}). These states cannot be determined applying DDE path-continuation techniques. Anyhow, transforming the DDE system into a Haus master partial differential equation model would potentially allow for a path-continuations, as quasi-periodic states appear as periodic states in the PDE framework. Such a PDE model is derived in section 4.3.3. The quasi-periodic nature of the irregular pulse cluster states becomes visible in the pseudo-space time plots of these states in Fig. 4.6(b,d,f,h). Every fifty to more than hundred round-trips (depending on the state) the leading pulse in one round-trip dies out and a second pulse (that becomes present as a small satellite first) grows to again complete the pulse-cluster. This exchange takes place on a time scale of approximately ten round-trips. In between two pulse exchanges, the solution is very similar to the stable PC_n state with slightly thicker pulses. The basis of this instability is an additional widely opening net-gain window (see Fig. 4.4(d)) at the temporal position of the second gain depletion of the leading pulse (leftmost in the space-time plots). In case of a symmetric cavity, this position is given by adding half a round-trip to the original position. A small pulse slowly grows at this position until it depletes all the gain of the leading pulse, which therefore dies out. Details on these type of instabilities and a thorough investigation of their dependence on the cavity geometry are given in Reference [MEI21a].
From the 2D-bifurcation diagrams in Fig. 4.5(a,b), it can be drawn that the laser switches to a regime with extremely wide pulses, if the pump current exceeds the absorption above a critical threshold. The plateaus of these wide pulses are not flat, but modulated in intensity (teal coloured). As already presented in Fig. 4.3(a), these pulses stabilise along the fundamental branch in a torus bifurcation. A pseudo space-time plot of such a broad pulse is visualised in Fig. 4.6(i). It has to be noted that in the situation in which the pulse width exceeds half the length of the cavity $PW > T/2$ the gain is continuously depleted (in the symmetric configuration) due to the double gain pass. Anyhow, this regime occurs at pump powers far above the threshold ($J_g/J_{\mathrm{th}} > 30$) and is therefore very difficult (maybe impossible) to access experimentally.
Generally, it has to be noted that a change of the unsaturated absorption elevates the threshold (see eq. (4.9)), as it increases the losses that have to be compensated by the gain. This is evident from the growth of the white region in Fig. 4.5 corresponding to the *off*-state with increasing absolute value of J_q. Comparing the behaviour with results presenting the bifurcation structure in the ring DDE model [VLA05, JAU17a, HAU20a], it is visible that the general appearance stays very similar, although especially the parameters for the cavity losses κ and the ratio of the saturation coefficients s differ strongly. Namely, these similarities are that multi-pulse solutions with an increasing number of pulses emerge at higher unsaturated absorption, which are characterised by HML_n in the ring and PC_n in the V-shaped cavity. Furthermore, a broad continuous depletion of the gain occurs at a high pump power. The depletion is characterised by a CW solution in the ring and broad pulse solution in the V-shape model. As already discussed for the PC_2 solution, the pulse cluster solutions do not appear in additional Andronov-Hopf bifurcations as the HML_2 states. This is discussed in more detail later in this section. Furthermore, the Q-switched mode-locking instability [RAC06, KOL06], characterised by an additional slow modulation of the gain (see section

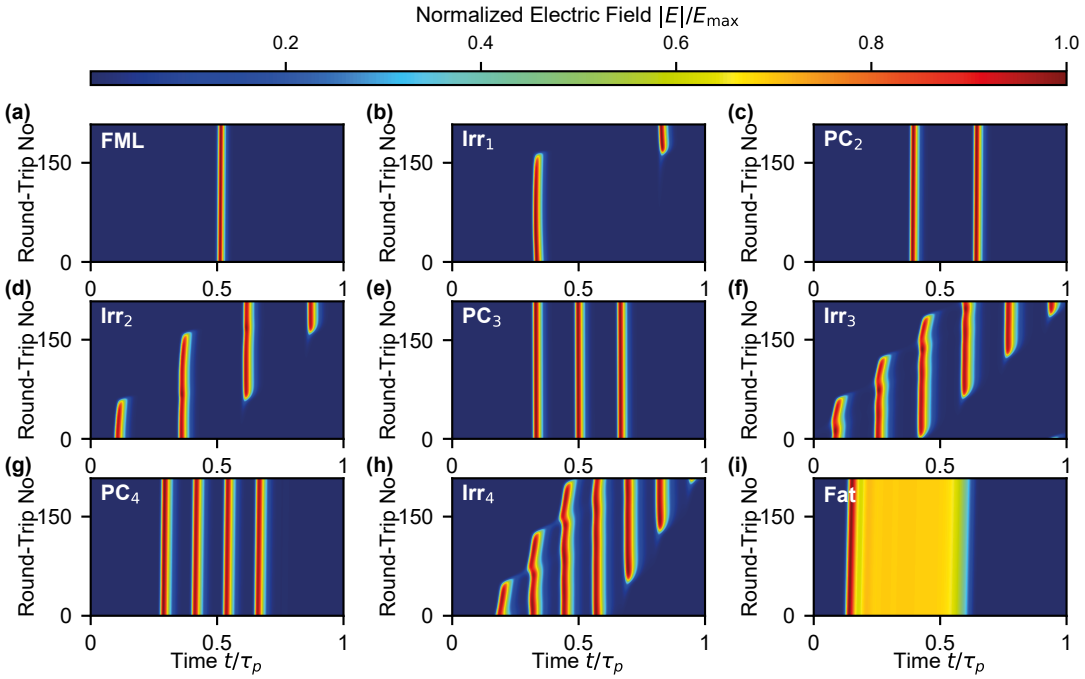

Figure 4.6.: Pseudo space-time representation of pulsed regimes found in a symmetric cavity configuration of the V-shaped VECSEL. The y-axis corresponds to the slow time scale and represents the number of round-trips, the x-axis refers to the fast-time scale indicating changes within one round-trip. The fast time scale is normalised to the period ($\tau_p \approx T + \gamma^{-1}$) of the respective solution so that no drift appears. All parameters are chosen according to Table 3.1 and $T = 625\,\mathrm{ps}$. The different pump currents J/J_{th} used are (a) 4.0 (b) 5.0 (c) 9.9 (d) 11.9 (e) 15.2 (f) 19.8 (g) 21.8 (h) 25.1 (i) 32.3. Figure adapted from [HAU19].

5.2) is not evident in the investigated parameter regime, due to a low value of the saturation energy ratio of $s = 2$ ($s = 25$ in [VLA05] and $s = 5$ in [VLA04]) and comparably low unsaturated absorption ($Q_0 = -1.33$ for $J_q = -150$).
Physically the occurrence of higher-order pulse cluster solutions with increasing unsaturated absorption can be reasoned by the pulse narrowing effect of the absorber at larger values of J_q. At increased J_q, the absorber is able to absorb a larger fraction of the leading edge of the pulses. Hence, the gain is able to recover more between pulses. Due to the narrower pulse shape, more pulses can be supported in the pulse clusters. They can exist closer together without gain competition and letting the gain relax sufficiently long till the pass of the next pulse. Nevertheless, the absorber needs to fully recover between pulse passes so that the pulses are sufficiently narrowed. Otherwise the pulses of one cluster merge (intensity does not drop to 0 in between pulses) and one obtains the wide pulse dynamics. Nonetheless, the increased absorption makes a higher amount of gain necessary, which is why the lower bifurcation lines shift to higher pump currents, if J_q is increased.
The upper stability boundaries shift to higher pump powers more quickly, leading to a broadening of the stable PC$_n$ regions in pump power (c.f. Fig. 4.5). This can be reasoned by the fact that the destabilisation of a PC$_n$ solution is caused by the emergence of the respective quasi-periodic instability based on the opening of an additional widely opening net-gain window. In case the absorption is increased, a higher amount of pump power is required to exceed the critical gain level and therefore the bifurcation boundary shifts accordingly.

Influence of the Bandwidth

The bandwidth of the gain is introduced by the parameter γ (see section 3.4) and experimentally mainly determined by the Bragg reflectors, antireflection coating of the gain-chip and the bandwidth of the quantum well active section [CHO98a, VLA04, WAL16]. In the DDE model, it is included independent of the pump power, which is not always a valid approximation as in experiments the pump can strongly influence the gain spectrum, due to the alteration of the charge-carrier density. Nevertheless, in the case of a broad resonance as designed in experiments to circumvent unwanted effects of a limited bandwidth [WAL16] the Lorentzian approximation included in the DDE model is sufficient (see section 3.3). A model system including the interplay of bandwidth and pump power is discussed in section 5.4.

As γ determines the width of the gain spectrum, it has a strong influence on the pulse shape. The result of a numerical path-continuation along γ for the PC_2 solution at a pump current of $J/J_{\mathrm{th}} = 8$ is indicated in Fig. 4.7(a). Plotted is the maximum pulse amplitude in one round-trip $\max(|E|)$ and the average pulse width of the pulses in the cluster with respect to γ. As expected from the relation via the Fourier transform, an increase in the gain bandwidth γ, leads to a decrease of the pulse width. The altered nonlinear pulse shaping further leads to an increase in the pulse maximum (green line Fig. 4.7(a)). As outlined in Reference [VLA05], the pulse width can be approximated by a dependence of $\Delta_p \propto \gamma^{-1}$ and the amplitude by $E_0 \propto \sqrt{\gamma}$, if no additional dispersion is present and the gain bandwidth is very large [VLA05, JAU17a]. In consequence, the pulse energy $\approx E_0^2 \Delta_p$ remains approximately constant when altering γ. Yet, in a highly nonlinear regime, i.e. strong gain and absorption, the pulse width can strongly deviate from this behaviour [MEI21a]. The change of the pulse shape along the PC_2 branch with increasing γ is depicted in Fig. 4.7(b), illustrating the narrowing of the pulses. Furthermore, it has to be noted that the change of the pulse shape is very similar for both pulses in one cluster.

In order to investigate the influence of the gain bandwidth on the stability boundaries of the different mode-locked states, a 2D-bifurcation diagram in the (J_g, γ) plane is calculated performing a numerical upsweep in J_g, which is shown in Fig. 4.7(c). It indicates that the upper bifurcation points of the PC_n solutions as well as of the FML solution only shift very slightly when increasing the gain bandwidth towards experimentally obtainable values [WAL18, MEI21a]. The small alterations of the bifurcation lines can be ascribed to the only slightly affected pulse energy with increasing γ. This underlines that utilising a small value of $\gamma = 150 = 0.25\,\mathrm{ps}^{-1}$ to drastically lower the computation time of the bifurcation analysis is a feasible approximation to unravel the bifurcation landscape at high bandwidths. Nonetheless, a change that has to be accounted for is the occurrence of a HML_2 solution above a critical bandwidth, marked by a dark green area at $\gamma > 1.25\,\mathrm{ps}^{-1}$ in Fig. 4.7(c). It can be reasoned by the fact that the broader gain spectrum leads to a narrowing of the pulses, while their amplitude is increased (see Fig. 4.7(a))[8]. A higher electric field amplitude causes a stronger bleaching of the absorber and therefore a net-gain window can open although the pulses deplete the gain simultaneously. Consequently, the HML_2 solution stabilises.

Furthermore, the stable regimes of the PC_n solutions shrink, if γ is further decreased. This is caused by a broadening of the pulses at low gain bandwidths. If a very wide pulse is

[8] It has to be highlighted that the gain bandwidth is modelled via a Lorentzian filter in a lumped element approach in the DDE framework. Therefore, increasing the gain-bandwidth in the model corresponds to a reduced filtering as initially the gain is frequency independent.

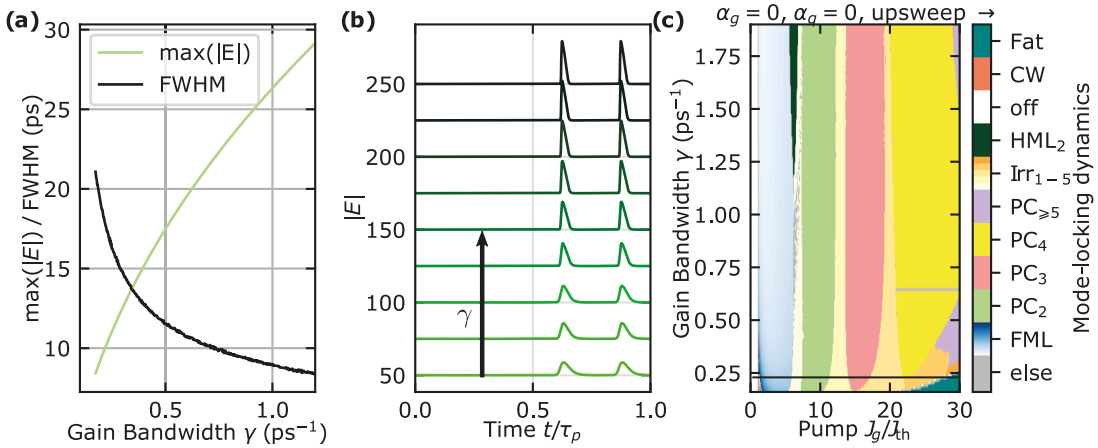

Figure 4.7.: (a) Path continuation of the PC_2 solution ($J/J_{th} = 8$) in bandwidth γ. The y-axis corresponds to the maximum pulse amplitude (light green line) and average pulse width (black line) in the pulse cluster at each point in γ. (b) Evolution of the electric field amplitude along the solution branch shown in (a). The bandwidth increases in steps of $\Delta\gamma = 0.16\,\mathrm{ps}$ from bottom to top. (c) 2D-bifurcation diagram in the plane of pump power (normalised to the threshold) and unsaturated absorption (J_g, γ), obtained performing an upsweep in J_g. The different dynamical regimes were classified according to the intensity time-series and can be distinguished via the colour code as defined previously (see Fig. 4.5 and Fig. 4.6 for details). The dark green area here denotes second-order harmonic mode-locking (HML_2). All parameters were chosen according to Table 3.1 and $T = 625\,\mathrm{ps}$. The dotted line marks the corresponding value of γ used in the further course of this section.

amplified, the gain is depleted for a longer duration and hence the time of exponential relaxation till the arrival of the subsequent pulse is shortened. However, the parameter value for $\gamma = 0.24\,\mathrm{ps}^{-1}$ (depicted by the black line in Fig. 4.7(c)) chosen for the further course of this work is as low as possible, while avoiding the regime of very broad pulses regime.

Influence Carrier Relaxation Rates

Two further parameters that can have a substantial influence on the dynamics are the carrier relaxation rates in the gain γ_g and the absorber γ_q. In experimental devices, they are mainly determined by the applied current/bias and the composition and design of the semiconductor chips. Although it can be necessary to account for the current dependence of different scattering rates to reproduce certain phenomena [LIN16, MEI19, HAU21], the carrier relaxation rates in absorber and gain are included as independent quantities in many theoretical works on passively mode-locked lasers [BIS95a, VLA04, VLA05, MUL05a, SCH19b, HAU19] as already outlined in section 3.4. Nevertheless, when investigating the dynamics in the parameter plane of the pump current and the gain relaxation rate (J_g, γ_g) one has to keep in mind the normalisation of the pump current which includes the transparency carrier density multiplied by the relaxation rate (see eq. (3.13)). Thus, it is feasible to use the definition of the pump current found when deriving an expression for the threshold current in section section 4.2.1 giving $J_g = \gamma_g G_0$. It is often used in the derivation of a Haus master equation [KOL06, SCH18e, SCH18f, HAU20a]. Here, G_0 denotes the equilibrium integrated carrier density at threshold. Making use of this expression it is possible to independently investigate the influence of the pump level and the relaxation rate in the (G_0, γ_g) parameter plane as

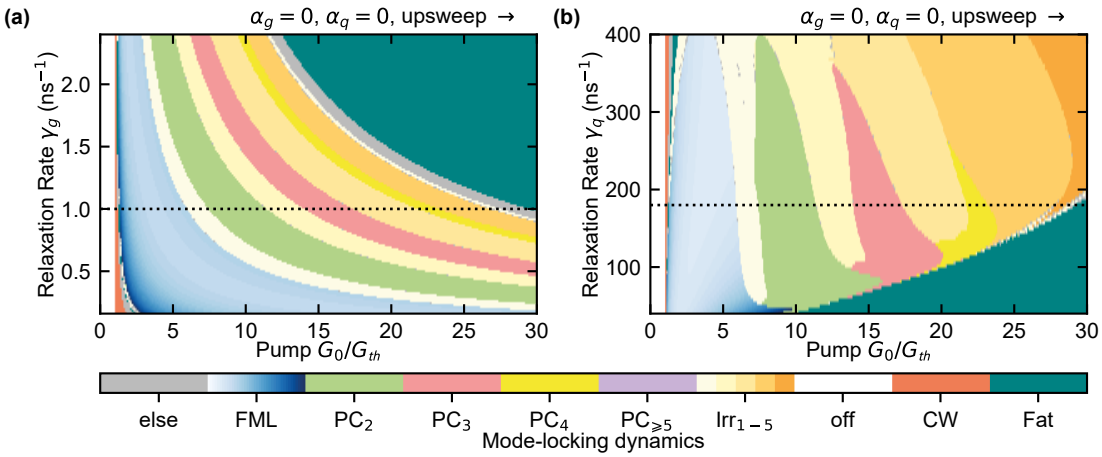

Figure 4.8.: 2D-bifurcation diagrams in the parameter plane of the equilibrium carrier density and the carrier relaxation rate of the gain (G_0, γ_g) in (a) and in the parameter plane of the equilibrium carrier density and the carrier relaxation rate of the absorber (G_0, γ_q) in (b). Both bifurcation diagrams were obtained performing an upsweep in J_g. The different dynamical regimes were classified according to the intensity time-series and can be distinguished via the colour code as defined previously (see Fig. 4.5 and 4.6 for details). All parameters were chosen according to Table 3.1 and $T = 625\,\mathrm{ps}$. The dotted lines denote the corresponding values of γ_g and γ_q used in the further course of this section. For both panels $Q_0 = J_q\gamma_q^{-1} = -0.577$ is kept fixed.

depicted in the 2D-bifurcation diagram in Fig. 4.8(a). Plotted is an upsweep in the pump parameter G_0.

From the bifurcation diagram, it is possible to deduce that the relaxation rate does not impact the type of dynamical regimes occurring above threshold for the investigated parameter values, i.e. no further instabilities are induced. Anyhow, it can be seen that although the succession of the dynamical regimes does not change, their stable pump current interval decreases in width and shifts to lower values of G_0. Furthermore, the area of fat pulses emerges at much lower pumping rates (with respect to the threshold). This can be reasoned by the fact that due to the enlarged relaxation rate γ_g, the gain relaxes faster to its equilibrium after a depletion. Consequently, more gain is available at the subsequent pulse pass compared to the situation of lower γ_g (at the same value of G_0) because in the intermediate-cavity regime ($\gamma_g T \approx 1$) the gain never fully relaxes to its equilibrium in between pulse passes (see Fig. 4.3(b_1). Thus, multi-pulse solutions already stabilise at lower pump powers due to the increased amplification. In the next section, it is outlined that increasing the round-trip time T has a similar effect as elevating the relaxation rate because the factor $\gamma_g T$ mainly determines the amount of the available gain at a subsequent pulse pass (if J_g is constant).

The impact of altering the carrier relaxation rate in the absorber is shown in Fig. 4.8(b). Plotted is an upsweep in the pump parameter G_0 for different values of the absorber relaxation rate. It has to be pointed out that for the unsaturated absorption the relation to the equilibrium carrier density at threshold $\gamma_q Q_0 = J_q$ is used and Q_0 is kept fixed for all scans in order to illustrate the sole effect of γ_q. In contrast to the gain, the absorber always recovers to an equilibrium in between two subsequent pulse passes in the intermediate-cavity regime at realistic relaxation rates. Yet, the absorber has a strong influence on the stability boundaries of the stable and irregular pulse cluster regimes. If the relaxation rate is reduced very drastically to values below $\gamma_q < 50\,\mathrm{ns}^{-1}$, the absorption is decreased to an extent that

the system does not support the emergence of multi-pulse solutions anymore. In this regime, mainly the fat pulse solution emerges, due to the reduced narrowing effect of the absorber. On the other hand, a strong increase of the absorber relaxation rate leads to a favouring of irregular pulse clusters, due to the destabilising effect of the increased absorption. This can be reasoned by the faster closing of the net-gain window, due to the faster relaxation of the absorber. Additionally, it is visible that an increase in the carrier relaxation rate in the absorber decreases the pulse width, as can be seen from the shading of the FML region.
In general, it is to conclude that an increase or decrease of the chosen relaxation rates adapted from experimental values [WAL16, HAU19] and marked by black dotted lines in Fig. 4.8(a,b), does not lead to an emergence of additional dynamical regimes in the performed upsweeps in pump power. Furthermore, the general bifurcation structure is unaffected by a change of $\gamma_{g,q}$ in this range with regard to succession of the pulse cluster states.

4.2.3 Enlarging the Cavity

When setting up a VECSEL device, the cold-cavity round-trip time is a crucial parameter as it mainly determines the period of the pulsed laser output. The period of the fundamental mode-locking solution is approximately[9] given by $\tau_p \approx T + \gamma^{-1}$ and the period of the harmonic solutions with n pulses results as $\tau_{\mathrm{p,HML}} = \tau_p n^{-1}$. Hence, the role of the cavity round-trip time T is investigated in detail in this section, with a special focus on the alteration of the bifurcation scenario leading to the emergence of pulse clusters. In the case of a V-shaped cavity geometry, the round-trip time is related to the length of the two cavity arms via $T = 2\tau_1 + 2\tau_2$. Anyhow, a symmetric arrangement is investigated first in order to obtain a simple overview. This means that the length of the two cavity arms is adjusted equally, i.e. the condition $\tau_1 = \tau_2$ is always fullfilled. The introduction of a slight asymmetry ($\tau_1 \neq \tau_2$) is discussed in section 4.2.4.
For the sake of unravelling the changes in the bifurcation structure induced by an alteration of the total cavity length, the fundamental solution branch emerging from the first Andronov-Hopf bifurcation along the CW branch ($\mathrm{AH_{FML}}$), is continued in pump power for different round-trip times. The resulting 1D-bifurcation diagrams are depicted in Fig. 4.9($\mathrm{a_{1-3}}$) with thick (thin) lines denoting stable (unstable) dynamics. Plotted is the normalised maximum pulse amplitude $\max(|E|)$ in one round-trip against the normalised pump power. The general bifurcation scenario of the branches at different round-trip times does not differ significantly. Nonetheless, with increasing round-trip time a more pronounced recurrent looping behaviour can be recovered, with higher-order pulse cluster solutions (PC_n) stabilising during each additional loop, depicted by the different colours along the branches Fig. 4.9($\mathrm{a_{1-3}}$). Each upper loop attributes the upper stability boundary of the respective PC_n solution and is characterised by a saddle-node bifurcation denoted as $\mathrm{SN_{n,U}}$ (red circles in Fig. 4.9($\mathrm{a_{1-3}}$)). Similarly the lower (additional) loops are embodied by saddle-node bifurcations and are denoted $\mathrm{SN_{n,L}}$ as before (orange circles). Here, the first subscript n refers to the number of pulses in the cluster and the second to the position on the branch[10]. As found for the $\mathrm{PC_2}$ solution at low round-trip times (see Fig. 4.3), the higher-order pulse cluster solutions stabilise in torus bifurcations indicated by green circles and denoted as T_n in Fig. 4.9($\mathrm{a_{1-3}}$).

[9] In the regime of strong gain and absorption in monolithic devices the period can be lower than the round-trip time [JAU17a, VLA11]. Nonetheless, for the chosen parameter set the given approximation holds well, as the DDE model can be transformed to a PDE, in which the drift is given by $1/\gamma$. A derivation is presented in Appendix A.2.
[10] "L" corresponds to the *lower* loop and "U" to the *upper* loop.

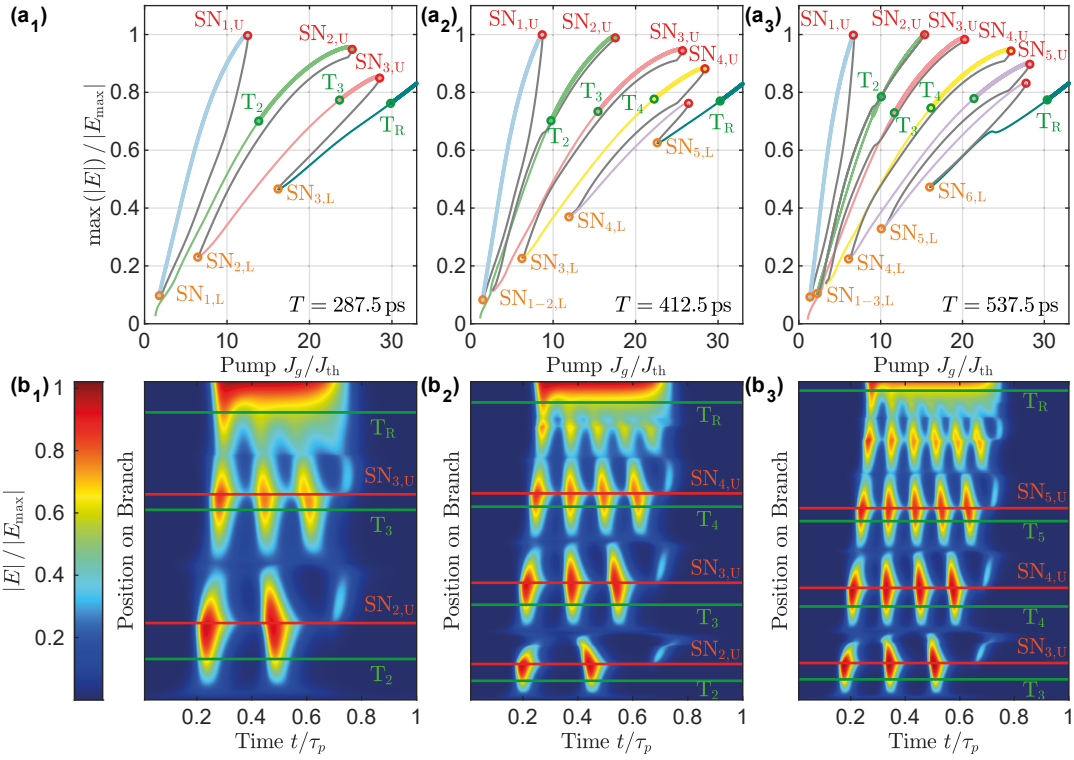

Figure 4.9.: (a_{1-3}) 1D-Bifurcation diagram along the pump current J_g (normalised to the threshold), showing the maximum electric field amplitude max ($|E|$) (normalised to the global maximum in the investigated regime $E_{\max}$) along the fundamental mode-locking branch and detached branches. The three panels show the branches for the displayed cold-cavity round-trip times T. The different colours refer to the different dynamics, with fundamental mode-locking in light blue, pulse clusters (PC_2) with two pulses in green, PC_3 in light red, PC_4 in yellow, PC_5 in purple and a fat pulse regime in teal. The grey regions refer to unstable dynamics with satellite pulses. Thick (thin) lines denote stable (unstable) dynamics. The saddle-node bifurcations at the upper part of the branch are marked by red circles and denoted by $SN_{n,U}$, with n referring to the number of pulses observable at the bifurcation point. Saddle-node bifurcations at the lower part are marked in orange ($SN_{2,L}$). Green circles denote torus bifurcations T_n, with the torus bifurcation stabilising the fat pulse regime denoted by $T_{\mathcal{R}}$. (b_{1-3}) One period (τ_p) of the electric field dynamics (colour code) along the fundamental solution branch born in the first Andronov-Hopf bifurcation along the CW branch and shown in the respective upper panel. The bifurcation points governing the stability are indicated by the same colours and labels. The x-axis corresponds to one period of the electric field dynamics, whereas the y-axis corresponds to the position along the branch (starting from the bottom). All other parameters as in Table 3.1. Figure adapted from [HAU19].

The torus bifurcation giving rise to a stable mode-locked solution characterised by a very wide pulse (teal), is depicted as $T_{\mathcal{R}}$ at the rightmost position of the branch.
The different PC_n dynamics along the branch are distinguished by the colour code as in the 2D-bifurcation diagrams presented before (e.g. see Fig. 4.5) with light blue denoting fundamental mode-locking, green referring to pulse clusters with two pulses (PC_2), red corresponding to the PC_3 solution, yellow to the PC_4 solution and purple to pulse clusters with more than 4 pulses. The grey parts of the branch indicate regions in which the solution continuously transitions from a PC_n to PC_{n+1} solution. To visualise this continuous transition, the dynamics of the electric field amplitude along each branch is illustrated in Fig. 4.9(b_{1-3}). Here, the y-axis corresponds to the continuation points along the branch (position on branch) and the colour code represents the normalised electric field amplitude in one period of the found solution at the respective branchpoint. The green and red lines stand for the (de-)stabilising torus and saddle-node bifurcations as indicated in (a). From the plots of the dynamics, it is possible to deduce that after the stabilising torus bifurcation T_n the pulses in one cluster grow in amplitude along the branch until a critical maximum at which they destabilise in the $SN_{n,U}$ bifurcation. Shortly before this point a side-pulse emerges, which can be identified as a light yellow regime to the right of each pulse cluster, directly above the red SN lines in Fig. 4.9(b_{1-3}). The behaviour of all PC_n solutions and the side-pulses is very similar after the $SN_{n,U}$ bifurcation point and almost independent of the number of pulses in the cluster. First the side-pulse dissociates itself from the cluster, while the amplitude and temporal distance of the pulses in the cluster decreases until a critical minimum. After the minimum, the side-pulse rapidly adjusts its temporal distance to the pulse cluster and grows as an additional pulse of the continuously forming PC_{n+1} solution. The temporal distance within the pulse clusters is given by $\Delta_{PCn} \approx \tau_p/2n$ in the stable regions [HAU19].
Regardless of the round-trip time, a transition to a mode-locking state characterised by a wide-pulse (wide red area at the top of Fig. 4.9(b_{1-3})) can be found after the highest order pulse cluster. As discussed before, the wide pulse dynamics results from the pulses of a cluster being too close together, while exhibiting a broad pulse width. In consequence, they merge at higher pump powers instead of the forming of higher-order pulse cluster. This also can be drawn from the yellow regions indicating a non-zero electric field amplitude in between the pulses of a cluster before the stabilisation of the fat pulse in Fig. 4.9(b_{1-3}). Initially, the higher-order pulse clusters emerge as unstable solutions. This is shown by the appearance of the PC_6 solution in Fig. 4.9(b_3) for which no stable regime can be found although the corresponding loop along the branch already exists (see Fig. 4.9(a_3)). The stabilisation is mediated via the simultaneous emergence of two torus bifurcations along the respective loop, which is discussed in more detail later in this section. It has to be pointed out that although solutions appear well separated along the branches they actually exist at similar pump currents (see Fig. 4.9(a)). Consequently, the pulse clusters can be multistable for different points of operation [HAU19].
It can be concluded that the continuous emergence of the pulse cluster with two pulses as discussed in section 4.2.2 can be generalised to PC_n solutions emerging with an increase of the round-trip time. Their birth is connected to the appearance of additional loops along the fundamental solution branch, born in the first Andronov-Hopf bifurcation along the CW branch. These loops are embodied by a pair of saddle-node bifurcations $SN_{n,U}$ and $SN_{n,L}$, of which the upper bifurcation represents the upper stability boundary. The lower stability boundary of each PC_n solution is given by a torus bifurcation.

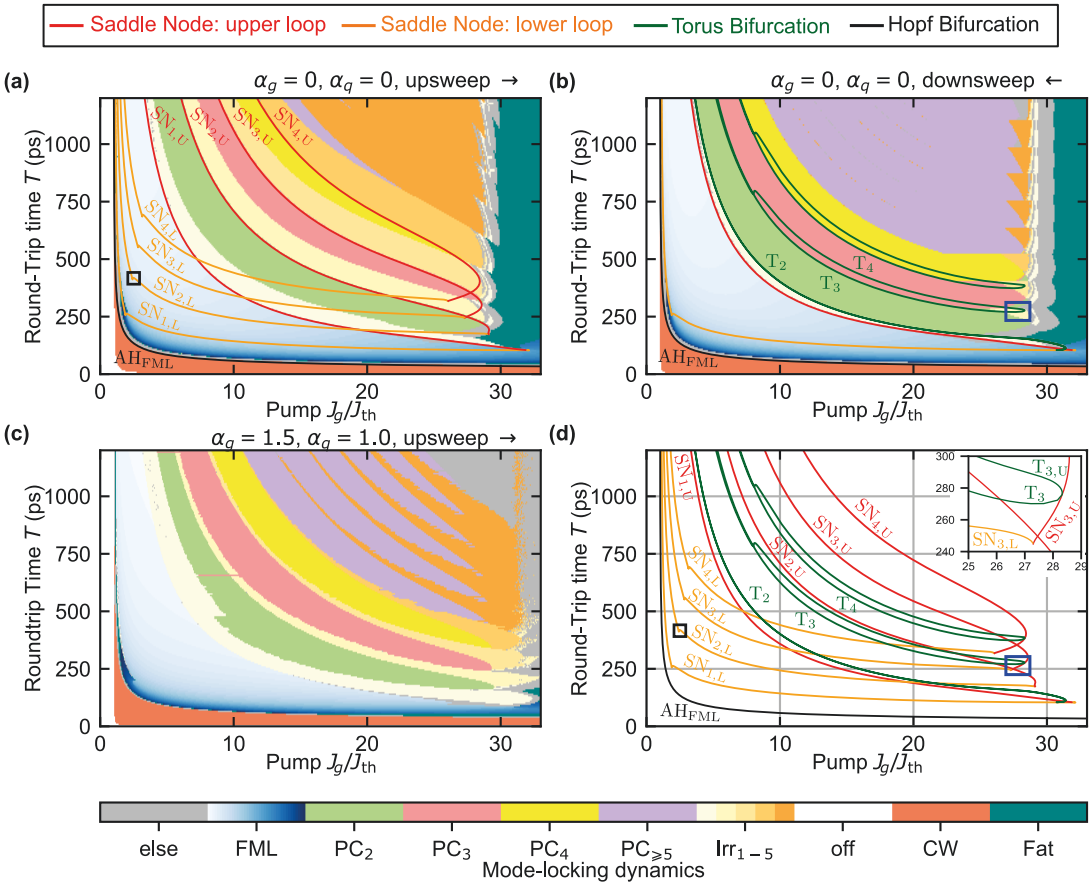

Figure 4.10.: 2D-bifurcation diagrams in the parameter plane of pump power (normalised to the threshold) and the cavity round-trip time (J_g, T). An upsweep in pump current is performed to obtain the diagram in (a) whereas a downsweep is performed for (b). Subpanel (c) indicates an upsweep with $\alpha_g = 1.5$ and $\alpha_q = 1.0$. The different dynamical regimes are classified according to the intensity time-series and are distinguished via the colour code as defined previously (see Fig. 4.5 and 4.6 for details). The red lines in (a) represent the saddle-node bifurcation lines $SN_{n,U}$ marking the upper stability boundary of the pulse cluster solutions and the FML solution (see Fig. 4.9). They are connected to the $SN_{n,L}$ bifurcations at the lower loops of the branch (orange) in cusps. The green lines in (b) denote the bifurcation lines of the torus bifurcations T_n characterising the lower stability boundaries. The lower stability boundary of the FML solution is given by the $SN_{1,L}$ bifurcation (see Fig. 4.9(a_1)). The black line indicates the first Andronov-Hopf bifurcation along the CW branch AH_{FML} (d) Indicates a combination of all saddle-node and torus bifurcation lines displayed in (a)-(b), with the inset showing a zoom of the area marked by the blue square. The black square marks the cusp in which the PC_2 solution detaches from the branch. The laser parameters are presented in Table 3.1. Figure adapted from [HAU19].

A further notable development induced by the increase of the round-trip time, is the detaching of lower order solutions from the main fundamental solution branch, as presented for the FML and the PC_2 solution in Fig. 4.9. Already at the lowest round-trip time shown, the PC_2 instead of the FML solution emerges at the start of the fundamental solution branch as depicted in the dynamics in Fig. 4.9(b_1). From the 1D-bifurcation diagrams in Fig. 4.9(a), one can deduce that there is no connection between the fundamental solution branch emerging from the AH_{FML} bifurcation and the FML solution branch for all investigated round-trip times. Instead the FML solution exists as a solitary branch. After the detaching, the lower stability boundary of the FML solution is not characterised by the AH_{FML} bifurcation anymore, but the newly emerging $SN_{n,L}$ bifurcation. Yet, the stability intervals of the FML and PC_2 solutions do not change significantly during the detaching process. Consequently, the fundamental solution branch (starting as the green line in Fig. 4.9(a_1)), is only stable in a very small interval in J_g after its emergence from the AH_{FML} Andronov-Hopf bifurcation at the bottom of the branch. This is followed by an unstable region, characterised by the PC_2 solution (thin green line), while the solitary FML solution remains stable (thick blue lines in Fig. 4.9(a_{1-3})). A stable pulsed PC_2 regime does not exist until the T_2 tours bifurcation, although it directly emerges from the first Andronov-Hopf bifurcation at the round-trip times investigated for Fig. 4.9(a_{1-2}).
When further increasing the round-trip time to $T = 537.5\,\mathrm{ps}$, the PC_2 solution also detaches from the main fundamental solution branch (Fig. 4.9(a_3)). This again manifests in the respective dynamics along the branch, demonstrated in Fig. 4.3(b_3). Instead of the PC_2 solution, the PC_3 solution emerges directly at the start of the branch and a continuous transition to higher-order pulse clusters follows (see Fig. 4.3(b_3)). Yet, the stability of all stable PC_n solutions is not affected by the detaching and thus it is a crucial information for discussing the origin of the branches, but would not be visible in an experiment.
A deeper insight into the bifurcation structure governing the emergence of higher-order pulse clusters can be gained by a path-continuation of the bifurcations characterising the branch structure in the (J_g, T) parameter plane, namely the $SN_{n,U}$, $SN_{n,L}$ and T_n bifurcations. Plotted in Fig. 4.10(a) are the bifurcation lines corresponding to the upper ($SN_{n,U}$ red) and the lower ($SN_{n,L}$ - orange) saddle-node lines. Comparing the red $SN_{n,U}$ lines to the underlying numerical upsweep of the dynamics (same colour code as before), emphasises that in the investigated parameter regime the type of the bifurcation characterising upper stability boundary is not influenced by altering the round-trip time, as already suggested by the path-continuation of the single branch in Fig. 4.9(a). Interestingly, the bifurcation lines of the upper and lower saddle-node bifurcations $SN_{n,U}$ and $SN_{n,L}$ collide in a cusp bifurcation point[11] at a critical round-trip time, which is depicted by the intersection of the red and orange lines in Fig. 4.10(a). A zoom of the bifurcation lines in the region of a cusp (blue square Fig. 4.10(b)) is displayed in the inset of Fig. 4.10(d). These cusp bifurcation points characterise the emergence of the loops along the solution branch as they give birth to the two saddle-node bifurcations enclosing each loop along the fundamental solution branch (see Fig. 4.9(b_{1-3})). Thus, the $SN_{n,U}$ and $SN_{n,L}$ bifurcations are born at the same parameter pair in the (J_g, T) plane. Yet, they rapidly separate in pump power as the round-trip time is increased from the cusp, which embodies the extension of the respective loop along the

[11] A cusp bifurcation point is a codimension two bifurcation point at which two saddle-node bifurcations collide tangentially. In this case, the dimension of the centre manifold stays at $\dim(W_c) = 1$ but a normal form coefficient becomes 0. A detailed explanation of the bifurcation diagram, the behaviour of the eigenvalues and normal form can be found in chapter 8.2 (pages 304, 305) of Reference [KUZ98a].

branch. A second characteristic point along the saddle-node lines is a second cusp bifurcation point at lower pump powers, which is exemplary marked along the $SN_{2,L}$ line by a black square in Fig. 4.10(a). This point defines the detaching of the branches and is elaborated in detail in the further course of this section.
All pulsed solutions are enclosed by the AH_{FML} Andronov-Hopf bifurcation line, which is plotted as a black line in Fig. 4.10(a). At very low round-trip times, this Andronov-Hopf bifurcation is not present and hence only CW operation is possible. This is related to the fact that compared to the total cavity round-trip the pulses get very broad in this regime, as exemplarily depicted by the shading of the FML region[12], due to the differing pulse shaping effects at the large mode-spacing. Consequently, the gain recovery between pulse passes is very short due to the comparably long depletion time. In contrast, the absorber still almost fully recovers in between pulse passes due to the much higher relaxation rate. Therefore, the energy in the cavity is too low to compensate for the losses and enable a stable pulsing regime. It is also noticeable that the FML solution is always the first pulsed solution to stabilise, although it detaches from the AH_{FML} Andronov-Hopf point at $T \approx 250\,\mathrm{ps}$. The reason underlying this stabilisation mechanism was discussed before and lies within the unchanged stability in the detaching process as revealed by the large stable FML region at low pump powers (thick light blue line in Fig. 4.9(a)). Opposing to the wide pulses in the fundamental mode-locking region at low round-trip times, the pulses in the teal region at high pump powers ("fat") exhibit a modulation on-top of the pulses. However, both solutions have a period close to $\tau_p \approx T + \gamma^{-1}$. The modulation of the wide pulses in the fat pulse regime is visualised in the pseudo space-time representation of the fat pulse regime in Fig. 4.6(i), where the amplitude at the leading edge of the pulse is much higher and then followed by an almost constant plateau.
The shifting of the upper bifurcation boundaries to lower pump powers with increasing T is very similar to the influence of the gain relaxation time γ_g. This can be explained by the fact that enlarging either of the two quantities leads to an enhanced exponential gain relaxation ($\propto G_0[1-\exp(-\gamma_g T/2)]$) between pulses. In case of increasing the gain relaxation rate this is caused via a steepening of the exponential relaxation, whereas the increase of the round-trip time leads to a longer relaxation period. Thus, the maximum pulse amplitude $\max(|E|)$ is elevated almost equally, if γ_g or T are increased as shown by the 1D-bifurcation diagram in Fig. 4.11(a). The diagram is obtained by applying path-continuation to the PC_2 solution with the continuation parameter once set to T (black line) and to γ_g (blue) and finally comparing both lines at an equal gain relaxation parameter $\gamma_g T$. As a consequence of the increased available gain, the multi-pulse solution already turns stable at lower pump powers as illustrated in Fig. 4.10(b). This is further embodied by a shift of the corresponding torus bifurcations (green lines Fig. 4.10(b)). Vice versa the shift of the upper bifurcation boundaries ($SN_{n,U}$) to lower pump powers is caused by the destabilising influence of the excessive gain, as it leads to additional widely opening net-gain windows inducing the quasi-periodic dynamics (orange shading in Fig. 4.10(a)) [IPP94].
The transition point to wide-pulses dynamics almost does not shift in J_g when alternating T. In contrast, γ_g induces a strong shift of the bifurcation point (see Fig. 4.8(a)). The reason of this behaviour may lie within the influence of γ_g on the pulse width (relative to the round-trip time) that is contrary to T in the investigated region as indicated in Fig. 4.11(b). Plotted is the (average) relative pulse width along the PC_2 solution branch continued in

[12] The shading gives the relative pulse width normalised to a maximum of $0.35T$. A light shading corresponds to narrow pulses.

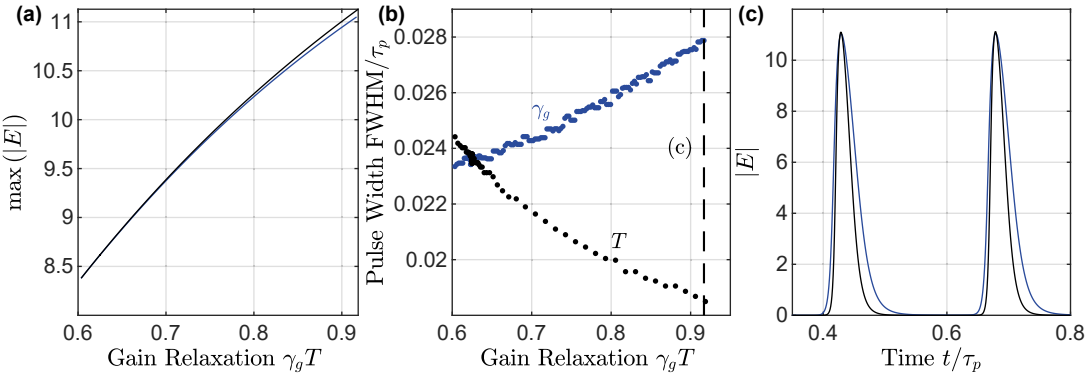

Figure 4.11.: (a) 1D-bifurcation diagram showing the development of maximum electric field amplitude max (|E|) within one period of the PC_2 solution, if the factor determining the amount of the gain relaxation $\gamma_g T$ is varied. The blue line is obtained by continuing the PC_2 solution in γ_g whereas for the black line the round-trip time T is the continuation parameter. (b) Average pulse width within the PC_2 solution along the same solution branches as in (a). The pulse width is defined as the full width at half maximum (FWHM) and normalised to the period of the solution. Shown in (c) are profiles of the electric field amplitude of the PC_2 solution along both branches at the $\gamma_g T$ value indicated by the dashed line in (b). All parameters are chosen according to Table 3.1 and $J/J_{\mathrm{th}} = 6.8335$.

γ_g (blue) and in T (black) at a constant pump power. The absolute pulse width growth in both cases, due to the increased gain relaxation. Nevertheless, the absolute pulse width does not grow proportional to the cavity length T as it is elevated due to the nonlinear increase of the gain relaxation. Therefore, the relative pulse width decreases as shown by the black dots in Fig. 4.11(b). Finally, the longer cavity length leads to a lower relative pulse width than an elevation of γ_g, although the factor determining the gain relaxation time $\gamma_g T$ is equal. Exemplary pulse profiles of the PC_2 solution obtained by a separate path-continuation along γ_g (blue) and T (black) starting from $\gamma_g T = 0.625$ to $\gamma_g T \approx 0.91$ are displayed in Fig. 4.11(c). The profiles illustrate the enlargement of the relative pulse width with γ_g. The increase in the relative pulse width furthermore leads to a suppression of the birth of additional higher-order pulse clusters, if only γ_g is elevated, because the pulses become too broad relative to the fixed round-trip time of $T = 625\,\mathrm{ps}$ used to generate the 2D-bifurcation diagram in Fig. 4.8(a). Consequently, instead of additional pulse clusters, the region of fat pulses shifts to lower pump powers. Opposing to that, the narrowing effect of the increased round-trip time, caused by the higher number of amplified modes leading to an altered nonlinear pulse shaping, enables the stabilisation of higher-order pulse clusters (see Fig. 4.10). It has to be noted that in experiments the pulse widths are much lower than investigated here [WAL16, WAL18]. Taking into account the highly nonlinear field carrier interaction of ultra-short pulses can lead to a decrease of the pulse width with increasing cavity length. A method to investigate this behaviour in detail would be the integration of fully microscopic models [KIL17, MCL20], which however is subject to high computational demands.

The introduction of non-zero line-width enhancement factors (α-factors) does not severely influence the qualitative appearance of the bifurcation scenario as displayed for an J_g-upsweep in the (J_g, T) parameter plane in Fig. 4.10(c). Here, $\alpha_g = 1.5$ and $\alpha_q = 1.0$ are chosen to be close to experimental values [WAL16, WAL18]. It is evident that the irregular

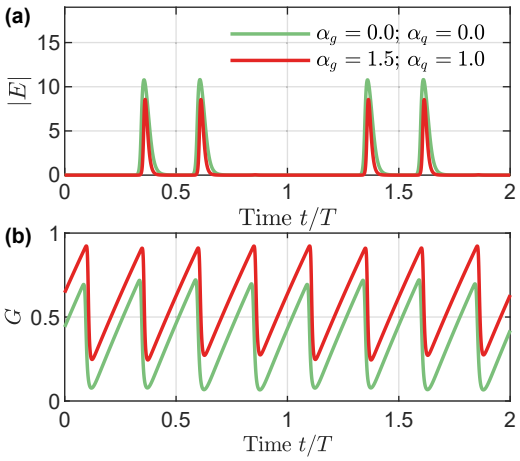

Figure 4.12: (a) Time-series of the electric field amplitude calculated with zero line-width enhancement (green) and with the line-width enhancement factors set to $\alpha_g = 1.5$; $\alpha_q = 1.0$ (red). (b) Time-series of the gain corresponding to the solution plotted in (a). All parameters are chosen according to Table 3.1 and $T = 625\,\mathrm{ps}$ and $J_g/J_{\mathrm{th}} = 10.7$.

solutions become less pronounced and the boundaries of the pulse cluster regimes appear close together in pump power in the upsweep. This can be reasoned by the upper stability boundary of the irregular PC solutions that is shifting to lower pump powers. Furthermore, upper stability boundary of all pulse clusters slightly shifts to lower pump powers, which can be deduced from comparing (e.g.) the transition from the red to yellow shaded regions in Fig. 4.10(a) and Fig. 4.10(c) for the highest round-trip times. As the α-factors shift the optical spectrum away from the resonance of the spectral filter (see page 51 of Reference [JAU17a]), the pulses experience a higher filtering and hence exhibit a lower intensity. This is exemplarily illustrated by the intensity time-series in Fig. 4.12(a) calculated at the same pump power, but with zero (green) and non-zero line-width enhancement factors (red). The increased filtering leads to a less efficient depletion of the gain as shown by the gain level of the two time-series of the gain dynamics in Fig. 4.12(b). Therefore, a destabilisation of the respective regimes occurs earlier in the upsweep along J_g, as the critical gain level at which the respective dynamics destabilises requires a lower pump power. In other words, less pump power is required for an additional net-gain window to open wide enough to destabilise the solution.

At this point it is important to highlight, that the influence of the linewidth enhancement factor (amplitude-phase coupling) in the DDE model can be overestimated when utilising the values determined in experiments [WAL16], due to the multi-mode nature of the DDE system in combination with the neglection of the frequency dependence of $\alpha_{g,q}$ [UKH04]. A further simplification in the used model is the assumption of time-independent α-factors [AGR93a, HER16]. In principle, the lower pulse intensity induced by the non-zero α-factor explained above is mainly resulting from the role of the α-factors in the multi-mode DDE model and not necessarily related to a physical effect. From measurements and microscopic approaches it becomes clear, that the value of α is not independent of the gain spectrum as it is mainly determined by the carrier densities. Nonetheless, effects counteracting the influence of the linewidth enhancement such as group velocity dispersion are not included in the DDE model either [PIM17]. Therefore, a good qualitative agreement to experimentally determined dynamics can be achieved by utilising zero or low values for $\alpha_{g,q}$ [PIM14, JAU16, NIK16, MAR14c], without directly neglecting its presence as the counteracting effects are neglected as well.

On the account of studying the dependence of the lower stability boundaries on the round-trip time, a path-continuation of the torus bifurcation lines T_n (green lines) in the (J_g,

T)-plane is displayed in Fig. 4.10(b) and complemented by a numerical downsweep. Again, the bifurcation lines perfectly match the numerically found transitions. As the $SN_{n,U}$ and T_n bifurcation lines similarly shift to lower pump powers, the stable region of the PC_n solution is only decreased slightly with increasing round-trip times (see red and green lines in Fig. 4.10(d)). The 2D-bifurcation lines again indicate the multistability of the PC_n solutions as the lower stability boundary of the PC_{n+1} (green lines) always lies at lower pump currents than the upper stability boundary of the PC_n solution (red lines). A multistability of the irregular and stable pulse cluster solutions becomes evident when comparing the up- and downsweep, i.e. Fig. 4.10(a) and Fig. 4.10(b). In the downsweep, a direct transition between the PC_n states is evident whereas in the upsweep the stable PC solutions are always separated by irregular PC pulsations (see Fig. 4.6 for plots of the solutions). In the upsweep, these intermediate transitions occur because the attractor of the PC_n solution at upper stability boundary lies closer to that of the corresponding irregular solution than to that of the next higher-order PC_{n+1} state. In contrast, the attractor of PC_{n+1} solution is multistable with the PC_n solution and its attractor lies closer to the regular lower order pulse cluster than to that of the lower order irregular counterpart. Thus, no transition to irregular occurs in the downsweep and a wide region of stable pulse clusters with more than 4 pulses can be found marked by the large violet region in Fig. 4.10(b). The only irregular solution that is visible in the downsweep is the one related to the FML solution, due to the fact that the FML state is not multistable to the PC_2 solution.

As discussed before, the higher-order pulse cluster solutions initially emerge as unstable solutions, as the cusp of saddle-node bifurcations (collision of $SN_{n,L}$ and $SN_{n,U}$ lines) giving birth to the corresponding loop along the branch, emerges at a lower round-trip time than the respective stabilising torus bifurcations. This can be deduced from comparing the minimum of the T_n line with respect to the round-trip time to the position of the respective cusp in Fig. 4.10(d). Nonetheless, the PC_2 state is an exception in this scenario as the comparison shows that the T_2 bifurcation already exists at a lower round-trip time than the cusp. The T_2 bifurcation appears from a 1:1 resonance scenario close to the cusp at which $SN_{1,L}$ and $SN_{1,U}$ collide ($J_g/J_{\mathrm{th}} \approx 30.8$, $T \approx 105\,\mathrm{ps}$). This cusp marks the emergence of the first Andronov-Hopf bifurcation along the fundamental solution branch. Directly after its appearance, the T_2 torus represents the boundary between an unstable FML regime with a side-pulse and fat-pulse emission. Yet, with increasing cavity round-trip times, further torus points emerge along the fundamental solution branch and take the place as the stabilising bifurcation of the wide pulse regime. Thus, the T_2 bifurcation becomes the lower stability boundary of the PC_2 solution, as it is shifted along the branch during the formation of the PC_2 loop.

The generation mechanisms of the T_3 and T_4 torus are similar to each other, as they both emerge from a torus-torus connection point, which occurs for the T_3 bifurcation in the region marked by a blue square in Fig. 4.10(b,d). A zoom of the bifurcation lines in this region is presented in Fig. 4.13(a), where the torus-torus point (T-T point) is marked by green square. The other subpanels of Fig. 4.13 indicate zooms of the upper loop of the fundamental solution branch, indicating the position of the bifurcations (along the PC_3 region) in the 1D-bifurcation diagram of pump power and maximum electric field amplitude (compare light red region in Fig. 4.9(a_1)). The respective round-trip times are marked by black lines in (a). At round-trip times between the emergence of the saddle-node cusp and the torus-torus point ($245\,\mathrm{ps} < T < 270\,\mathrm{ps}$ in (a)), the loop exists with an unstable PC_3 region as depicted in Fig. 4.13(b). As the round-trip time is increased the two torus bifurcations,

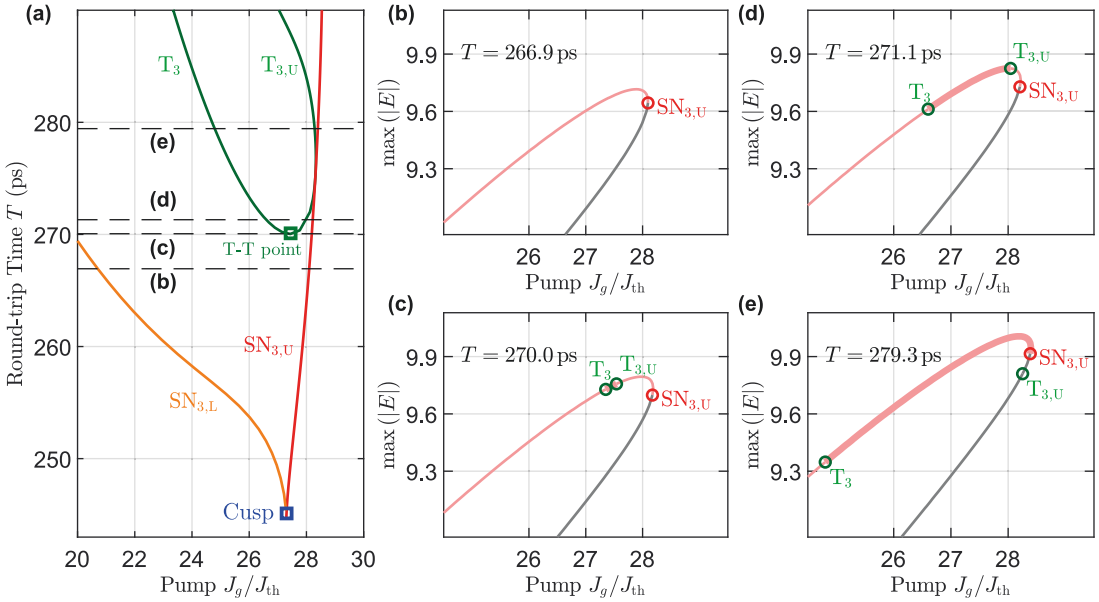

Figure 4.13.: (a) Close up of the path-continuation of the $SN_{3,U}$-$SN_{3,L}$ (red and orange) and the T_3 (green) bifurcations in the (J_g, T) parameter plane, indicated by the blue square in Fig. 4.10(b,d). (b)-(e) Close up of the 1D-Bifurcation diagram (see Fig. 4.9(a)) along the pump current J_g, with the maximum electric field amplitude in one period of the PC_3 solution on the y-axis. The four panels show the branches for the cold-cavity round-trip times marked by the dashed lines in (a). PC_3 mode-locking is depicted by light red lines and the grey regions correspond to unstable PC_3 dynamics with satellite pulses. The torus bifurcations corresponding to the torus line in (a) are marked by green circles, whereas the saddle-node bifurcation is marked by a red circle (red line in (a)). Thick lines denote stable regions, whereas thin lines mark unstable dynamics. All other parameters as in Table 3.1.

labelled as T_3 and $T_{3,U}$, emanate from the torus-torus point and enclose a stable PC_3 region, c.f. Fig. 4.13(c). This mechanism is very similar to the emergence of the Andronov-Hopf bifurcations along the CW branch, giving birth to the mode-locked solutions. These also emerge in pairs and split (in J_g) if J_q is enlarged [VLA04, JAU17a]. Already at round-trip times slightly above the torus-torus point, the two bifurcations split along the branch (Fig. 4.13(d)) until the upper torus bifurcation passes the $SN_{n,U}$ bifurcation as shown in Fig. 4.13(e). This is tangential passing of the green torus and the red SN line in Fig. 4.13(a). At further increased round-trip times, the two torus bifurcations lie close to each other in the (J_g, T) parameter plane, but are situated on opposite sides of the solution branch as displayed in Fig. 4.13(e).

As discussed before, a detaching of the FML regime and the different PC solutions from the fundamental solution branch, generated in the AH_{FML} bifurcation, can be observed with increasing round-trip times. The underlying mechanism can be understood by investigating the second cusp along the $SN_{n,L}$ lines in the (J_g, T)-plane, which has the same structure for all investigated SN bifurcation lines (see Fig. 4.10(a,d)).

A zoom of the cusp along the $SN_{2,L}$ in the area marked by a black square in Fig. 4.10(a) is illustrated in Fig. 4.14. At low round-trip times below the cusp, depicted by the yellow region in Fig. 4.14(a), only the $SN_{2,L}$ bifurcation exists. At these round-trip times, it represents the lower loop along the AH_{FML} branch, separating the PC_2 and the PC_3 dynamics,

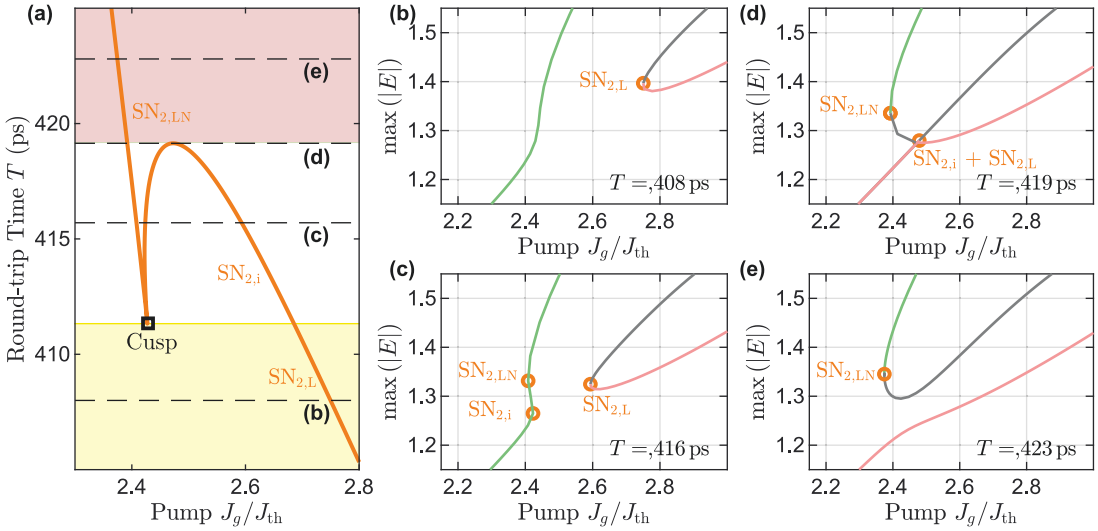

Figure 4.14.: (a) Close up of the path-continuation of the $\mathrm{SN}_{2,\mathrm{L}}$ saddle-node-bifurcation in the (J_g, T) parameter plane, indicated by the black square in Fig. 4.10(a). The red-shaded background corresponds to a detached PC_2 solution branch. In contrast, the branch is connected to the FML branch in the yellow region. The cusp is marked by the black square and corresponds to the point where the $\mathrm{SN}_{2,\mathrm{LN}}$ and $\mathrm{SN}_{2,\mathrm{i}}$ merge. The dashed black lines mark the round-trip times for which the solution branch is shown in the other panels. (b)-(e) Close up of the 1D-Bifurcation diagram (see Fig. 4.9(a)) along the pump current J_g, with the maximum electric field amplitude (max ($|E|$)) in one round-trip on the y-axis. The different colours refer to the different dynamics, with PC_2 in green and PC_3 in light red. The grey regions correspond to unstable dynamics with satellite pulses. All shown branches belong to unstable dynamics. The orange circles refer to the saddle-node bifurcations found in (a). All other parameters as in Table 3.1.

as displayed by the orange circle in the zoom of the 1D branch in Fig. 4.14(b). For comparison, the whole branch is plotted at a similar round-trip time in Fig. 4.9(a_2). In the cusp bifurcation point marked by the black square in Fig. 4.14(a)), two additional saddle-node bifurcations denoted as $\mathrm{SN}_{2,\mathrm{LN}}$ and $\mathrm{SN}_{2,\mathrm{i}}$ are born[13] at the lower end of the branch marked by the two additional orange circles in Fig. 4.14(c). At a round-trip time of $T \approx 419\,\mathrm{ps}$, the $\mathrm{SN}_{2,\mathrm{i}}$ and $\mathrm{SN}_{2,\mathrm{L}}$ bifurcations collide. The corresponding shape of the branch in this situation is presented in Fig. 4.14(d). Above the collision point, the two saddle-node bifurcations disappear (red area in Fig. 4.14(a)) and only the $\mathrm{SN}_{2,\mathrm{LN}}$ is left, representing the lower existence boundary of the PC_2 solution (see Fig. 4.14(e)). It has to be pointed out that a difference between the collision point ($T \approx 419\,\mathrm{ps}$) and the cusp ($T \approx 412\,\mathrm{ps}$) is the number of existing solutions. Only three solutions merge at the cusp, which are located below the $\mathrm{SN}_{2,\mathrm{i}}$ bifurcation, above the $\mathrm{SN}_{2,\mathrm{LN}}$ bifurcation and in between the two points as demonstrated in Fig. 4.14(c)[14]. Opposing, four different solutions collide in the saddle-node collision point as shown in Fig. 4.14(d). In conclusion, the combined effect of the cusp bifurcation point and the saddle-node collision point leads to the detaching of the branch in J_g. Due to the same appearance of the saddle-node lines corresponding to higher-order PC solutions, the

[13] Here, the subscript LN refers to "lower new", due to the fact that this saddle-node bifurcation adopts the role as the lower boundary and the i refers to "intermediate" as the corresponding SN bifurcation only exists for a very small region of round-trip times.

[14] This can be deduced from the normal form of the cusp, given on pages 303, 304 of Reference [KUZ98a].

detaching process is equal for all PC_n solutions.

4.2.4 Impact of Asymmetry

In order to investigate the impact of the asymmetry, the bifurcation lines characterising the stability boundaries are continued in the (J_g, τ_2)-parameter plane while fulfilling the additional condition $2\tau_1 + 2\tau_2 = T = \text{const}$. Thus, the sole influence of the cavity geometry can be studied. In experiments, this would correspond to re-positioning the gain chip closer to the outcoupling facet or the absorber. The upper stability boundaries given by the saddle-node bifurcations on the upper loops (see Fig. 4.9(a)) are presented as red lines in Fig. 4.15(a) and are labelled $SN_{2,U}$. Complementary to the bifurcation lines a numerical upsweep in pump current indicating the detected dynamics by means of the colour code is plotted. The numerically found stability boundaries fit well to the path-continuation results, as the bifurcation lines lie directly on the transitions between the different dynamical regimes. It is noticeable that the fundamental mode-locking solution (FML) as well as the pulse cluster solutions (PC_n) stretch to higher pump currents, if a slight asymmetry is introduced to the cavity geometry. Following the bifurcation analysis, this is induced by a shift of the saddle-node bifurcations. This shift unravels a symmetry with respect to the symmetric cavity configuration $\tau_2 = T/4$. A reason for that lies in the fast relaxation rate of the absorber so that it fully relaxes although the gain chip is shifted closer to it. Hence, shifting the gain chip to either of the sides has a very similar influence in the investigated regime. From a physical perspective, the shift of the stability boundary can be reasoned by a varied gain landscape (amplification of the pulse), which leads to the destabilising net-gain windows opening at higher pump powers. The variation of the gain landscape is induced by the adjusted temporal distance between the first and second gain depletion. Consequently, a time window of long and shorter gain relaxation phase exists. It furthermore has to mentioned that the amplitude of the pulses becomes unequal at a slight asymmetry, due to the altered gain relaxation. This is in qualitative agreement with experiments, in which the best FML performance with regard to pulse amplitude was achieved with a slightly asymmetric positioning of the semiconductor chips [WAL16].
Plotted in Fig. 4.15(b) are the lower stability boundaries of the FML and PC_n solutions in the (J_g, τ_1)-parameter plane, i.e. the torus bifurcation lines T_n and $SN_{1,U}$ for the FML solution. In contrast to the upper stability boundaries, these bifurcation lines are not affected by the introduction of a slight asymmetry. A detailed investigation of the cavity asymmetry and the destabilising mechanisms at stronger variations of τ_1, τ_2 can be found in Reference [MEI21a].

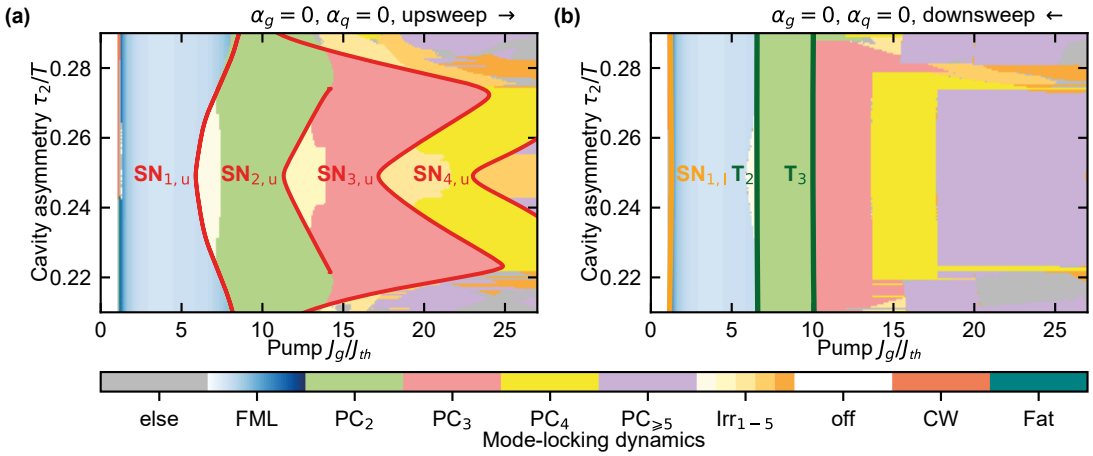

Figure 4.15.: 2D-bifurcation diagrams in the parameter plane of pump power (normalised to the threshold) and the cavity geometry (J_g, τ_2). An upsweep in pump current is shown in (a) whereas a downsweep is indicated in (b). The different dynamical regimes are classified according to the intensity time-series and can be distinguished via the colour code as defined previously (see Fig. 4.5 and 4.6 for details). The red lines in (a) represent the saddle-node bifurcation lines ($SN_{n,U}$) marking the upper stability boundary of the pulse cluster solutions and the FML solution (see Fig. 4.9). The green lines in (b) denote the bifurcation lines of the torus bifurcations T_n characterising the lower stability boundaries. The lower stability boundary of the FML solution is given by the $SN_{1,L}$ bifurcation (see Fig. 4.9(a_1)). All parameters are chosen according to Table 3.1 and $T = 625\,\mathrm{ps}$. Figure adapted from [HAU19].

4.3 Long-cavity Regime

So far, the cold-cavity round-trip times of interest in this chapter ($T < 0.7\,\mathrm{ns}$) were chosen to adapt experiments conducted for the sake of optimising the performance figures of the mode-locked laser output, i.e. the pulse width and pulse amplitude [WAL16, WAL18]. However, when further increasing the round-trip time and fulfilling experimental stability requirements by introducing the correct imaging conditions between gain and absorber [CAM18], the mode-locked solutions can become multistable to the laser *off*-state. Thus, regular mode-locked pulsations can be excited below the continuous-wave threshold [MAR14c, CAM16]. In the long-cavity regime, the round-trip time is by far the slowest time scale of the system. Therefore, the gain relaxation is comparably fast with respect to the round-trip time, i.e. $\gamma_g T \gg 1$. Consequently, a complete recovery of the gain towards its equilibrium carrier density takes place in between two subsequent pulse passes in this regime, so that the pulses do not influence each other by the tails of the exponential gain relaxation [MAR14c]. Due to their temporal independence and their multistability to the homogeneous *off*-state, the mode-locked pulses can be referred to as localised structures or temporal dissipative solitons [MAR14c]. The occurrence of these states in a mode-locked VECSEL with a V-shaped cavity geometry is discussed in this section and is based on Reference [HAU20].
In this section first a short introduction of the term temporal dissipative soliton is given in the context of mode-locked lasers, followed by an explanation of the bifurcation scenario leading to the emergence of soliton states in the mode-locked VECSEL (subsection 4.3.1). In subsection 4.3.2, the analysis is extended to the emergence of localised pulse clusters, in which the pulses are globally bound but locally independent. Thus, the pulse clusters can be referred to as photonic molecules [HAU20, JAV17]. A Haus master equation describing the V-shaped VECSEL in the long-cavity regime is derived in subsection 4.3.3. Based on this model, an analytical prediction for the distance of pulse cluster states and the lower bifurcation boundary in the long-cavity regime is determined in subsection 4.3.4.

4.3.1 Temporally localised States

From a mathematical perspective, conservative solitons originally were defined as localised solutions of nonlinear, exactly integrable partial differential equations [HAS89, AKH08, GRE12b]. A widely known example of such an equation is the nonlinear Schrödinger equation [AKH08, BUL79, BOY08, KRU11, SCH19b], which can be rigorously derived from Maxwell's equations. Therefore, it can be utilised to describe the propagation of electromagnetic waves (optical pulses) in different media [BOY08]. In physical terms, the soliton solutions describe an excitable wave-packet that remains unaltered in shape and amplitude during its propagation, due to the mutual cancellation of nonlinear and dispersive effects [HAS89, AKH08, GRE12b]. The first known observation of a soliton structure was a solitary water-wave, maintaining a constant width and amplitude during its propagation in a canal [DAV85, REM94].
In the 1990s, it was realised that similar localised structures can emerge in non-conservative systems in which the dissipation is compensated by a constant supply of energy, additional to the balance of nonlinearity and dispersion [AKH05, AKH08, AKH09, WU84, MOS87, FAU90, PIC91, GRE12b]. When investigating these systems, the integrability of the underlying mathematical models often falls victim to the higher complexity of the equation systems required [HAS89]. Therefore, the strict mathematical definition of solitons cannot always be applied to describe localised structures in dissipative systems. Nonetheless, the

analogy of the dominant physical properties, i.e. the balance of counteracting physical effects as basis for their solitary existence, between original solitons and solitary waves in dissipative systems remains. This led to the extension of the initial (conservative) soliton concept towards dissipative solitons [AKH09, GRE12b]. Combining the soliton concept with that of nonlinear systems, dissipative solitons can be understood as stable equilibria or limit cycle solutions [WAN20f]. Hence, their properties are determined by the system parameters and a bifurcation analysis can be applied to investigate their behaviour [GRE12b].
Examples of dissipative solitons in systems of different nature comprise plasma spots in a gas discharge system [AST01], localised excitations in a vertically vibrated granular layer [UMB96], self-replicating spots in a reaction-diffusion system [LEE94], hydrodynamic surface-wave solitons [WU84] or dissipative optical solitons [VAN94]. The latter manifest in different forms in driven photonic nonlinear systems such as ring resonators [JAN15, GUS15], microcavities [YI18], external cavities fed by a vertical-cavity surface-emitting lasers [TAN08b] or mode-locked lasers [MAR14c, GRE12b].
In photonic systems, the localisation can be observed transverse to the light propagation axis [LUG03, ACK09, MAR15d] or in the direction of the propagation axis [BAR17a, HER14b, MAR14c, MAR15b]. The latter is referred to as temporal localisation. A combination of both localisation types would potentially lead to structures introduced as light bullets [BRA04, PIM13, JAV16, GUR17]. Anyhow, the structures discussed in this work are solely localised in the longitudinal direction.
Mode-locked laser pulses were interpreted as temporally localised structures, especially in solid-state fibre lasers [GRE12b], as in these systems the slowly evolving gain can be approximated as a constant and New's background stability criterion[15] is satisfied [MAR14c]. Dissipative solitons in fibre laser systems are therefore often described by the complex cubic-quintic Ginzburg-Landau equation [MAR14c, GRE12b, AKH08]. Due to the comparably fast gain relaxation times in passively mode-locked semiconductor VECSELs discussed here, they can be tuned to a regime in which the round-trip time is the slowest time scale of the system [MAR14c] while strong gain depletions are present. As described in Reference [MAR14c], mode-locked pulses can be referred to as localised states in these long-cavity devices as they become individually addressable and are multistable to the laser *off*-state. The authors of Reference [MAR14c] further state that the multistability is crucial for the localisation, as it compensates the fact that New's stability criterion is not necessarily fullfilled for the investigated long-cavity devices.
Since the gain relaxation takes place on a much faster time scale than the round-trip time ($\gamma_g T \gg 1$), the temporal independence of each solitary pulse can be identified by the full gain relaxation in between pulses [MAR14c, CAM16]. This is visualised by the black lines in Fig. 4.16(c)-(d), denoting the gain dynamics in different pulsed solutions in the long-cavity regime of a V-shaped VECSEL. As the gain (almost) completely relaxes between two depletions, the pulses do not interact via the exponential tails of the gain relaxation[16]. If two localised pulses are excited close together in the short/intermediate-cavity regime, the interaction leads to a temporal drift of the pulses, as the system strives towards the energetically most favourable pulse amplification scenario. In this case, the gain interaction can be

[15] The background stability criterion is fulfilled, if in between the mode-locked pulses the accumulation of absorption and cavity losses are greater than the gain [NEW74, MAR14c].
[16] It has to be stated that the relaxation follows an exponential rule, and therefore the gain value only asymptotically approaches the equilibrium value. Yet, the effect of the residual exponential tail of the gain depletion only becomes visible on time scales much larger than the stability of the system in experiments or numerically feasible integration times and therefore is neglected here.

Table 4.1: Parameter values used for numerical calculations to model the localised states in a V-shaped passively mode-locked VECSEL [HAU20].

Symbol	Value	Symbol	Value
T	1.8725 ns	γ	240 ns^{-1}
J_g	5 ns^{-1}	γ_g	1 ns^{-1}
J_q	-32 ns^{-1}	γ_q	180 ns^{-1}
α_g	0	α_q	0
κ	0.99	s	20

understood as a form of repulsive force [CAM16].
In principle, it would be possible to arrive in a long-cavity regime by lowering the gain relaxation time γ_g^{-1} to achieve a full gain recovery in between pulse passes at shorter cavity lengths. Nonetheless, this would require to redesign the active section configuration and therefore adjusting the epitaxial growth process. Furthermore, it is limited by the material properties and is not as flexible as adjusting the cavity length.
The experimental reports on localised states in passively mode-locked semiconductor VECSELs in the long-cavity regime so far relied on coupling the gain and absorber chip in a face-to-face (linear) cavity configuration [MAR14c, MAR15b, CAM16, CAM18, SCH19b]. In opposition to the V-shaped cavity setup discussed in this work, the gain is only depleted once per round-trip in these configurations. As the ring delay differential equation model for passively mode-locked lasers [VLA04] includes all relevant time scales to describe the formation of localised states, it was widely used for their theoretical investigation [MAR14c, MAR15b, CAM16, SCH18e]. In consequence, it is reasonable to utilise the previously introduced DDE model (see section 3.3) to investigate the V-shaped VECSEL in the localised state regime and to analyse the role of the cavity geometry on the formation of bound localised states.
Two critical parameters that are increased in comparison to the previously described mode-locking regime (see Table 3.1) are the ratio of the differential gain coefficients in the gain and absorber s and the cold-cavity round-trip time T. Enlarging the value of s leads to a stronger modulation of the absorber in the DDE equations, as it elevates the magnitude of the field-carrier interaction term in the absorber equation (see eq. (3.50)). From an experimental perspective, an increase in s can be realised by the usage of lenses [CAM18] or the adjustment of the chip design to alter the quasi-equilibrium carrier density (see Fig. 3.2) or the transverse confinement factors. In comparison to the investigation of the mode-locking regime presented in the first part of this chapter, the carrier relaxation rate in the gain γ_g is slightly increased for computational convenience in accordance with experimental realisability in order to reach the localised regime at lower round-trip times. Furthermore, the unsaturated absorption J_q is slightly decreased, as the laser is operated in the subthreshold regime, which only requires a low amount of absorption. Furthermore, a low absorption is required in order to be able to compare the DDE model to a Haus master equation system, which is derived in section 4.3.3. Nevertheless, both quantities (J_q and γ_g) do not drastically change emergence of the different localised states and the investigated bifurcation scenario as their effect is very similar to that discussed in the previous chapter (in the intermediate-cavity regime). A full set of the parameter values utilised in this section is given in Table 4.1. The analysis is started at a symmetric cavity configuration, i.e. $\tau_1 = \tau_2$.
Examples of mode-locking dynamics in the localised regime of the V-shaped VECSEL are depicted in Fig. 4.16. In panel (a) the fundamental mode-locking (FML) state is displayed with the electric field dynamics coloured in light blue and the gain dynamics in black. Due

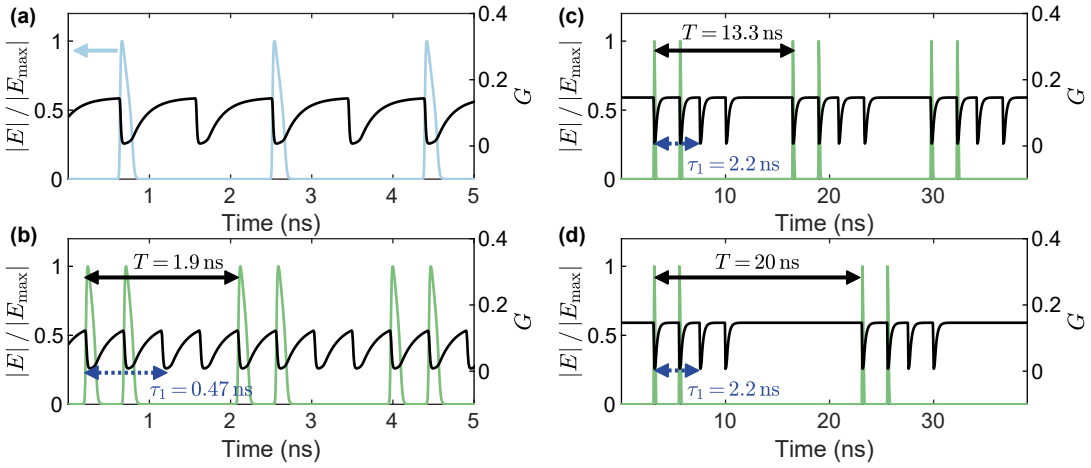

Figure 4.16.: Time-series of the electric field amplitude and the gain integrated carrier density in the localised state regime. (a) Indicates the fundamental mode-locking solutions (blue) whereas subpanels (b)-(d) display the PC_2 (green) solution in the intermediate and long-cavity regime. The blue arrows specify the distance between the two gain depletions of a single pulse given by $\min(\tau_1, \tau_2)$. The chosen round-trip times were $T = 1.875\,\mathrm{ns}$ in (a)-(b), $T = 13.3\,\mathrm{ns}$ in (c) and $T = 20\,\mathrm{ns}$ in (d). The cavity geometry is set to $\tau_1 = \tau_2 = T/4$ in (a)-(b). In (c) $\tau_1 = 0.165T$, $\tau_2 = 0.335T$ and in (d) $\tau_1 = 0.11T$, $\tau_2 = 0.39T$ were used. All other parameters as given in Table 4.1 and $J_g/J_{\mathrm{th}} = 0.8$. Figures adjusted from [HAU20].

to the double gain depletion of each pulse, the chosen round-trip time of $T = 1.875$ is not long enough to ensure a complete gain recovery in between pulse passes (see black lines in Fig. 4.16(a)). Thus, this regime can be referred to as an intermediate-cavity regime ($T\gamma_g > 1$). Yet, it has to be pointed out that the shown pulsed states are all multistable to the *off*-solution, as the pump value is set to $J_g/J_{\mathrm{th}} = 0.8$ and therefore the dynamics can be clearly distinguished to the mode-locking states discussed in the first part of this chapter.
As mentioned before, the main difference of the states presented here to the localised states in face-to-face coupled cavity discussed in References [MAR14c, MAR15b, CAM16] is that each pulse induces a second gain depletion as it propagates backwards through the V-shaped cavity. As indicated in Fig. 4.16(b), this leads to the stabilisation of localised pulse cluster solutions (PC_2). In the intermediate-cavity regime, the pulses in one cluster are strongly bound due to the enclosure of each pulse between the two gain depletions of the preceding pulse (marked by the blue arrow in Fig. 4.16(b)).
If the round-trip time is elevated far enough above the gain relaxation time, the gain relaxes completely in between pulse passes as illustrated in Fig. 4.16(c)-(d). Here, the cold-cavity round-trip time is set to $T = 13.3\,\mathrm{ns}$ (c) and $T = 20\,\mathrm{ns}$ (d). The absolute length of the shorter cavity arm is fixed at $\tau_1 = 2.2\,\mathrm{ns}$ in an asymmetric cavity configuration. Furthermore, the blue arrows in Fig. 4.16(c)-(d) indicate the temporal distance between the two gain depletions induced by the first pulse of the cluster in one round-trip, which remains constant due to the fixed length of the cavity arm. In both cases, the second pulse in the cluster is trapped in between the preceding and successive gain depletions. Interestingly, the second pulse can locally drift in between the two depletions because of the flat gain landscape. Consequently, the two pulses in the cluster are globally bound due to the two gain depletions, but are at the same time locally independent. The transition from the strongly bound state as pictured in Fig. 4.16(b) to the locally independent state (see Fig. 4.16(d)) is elaborated in the next

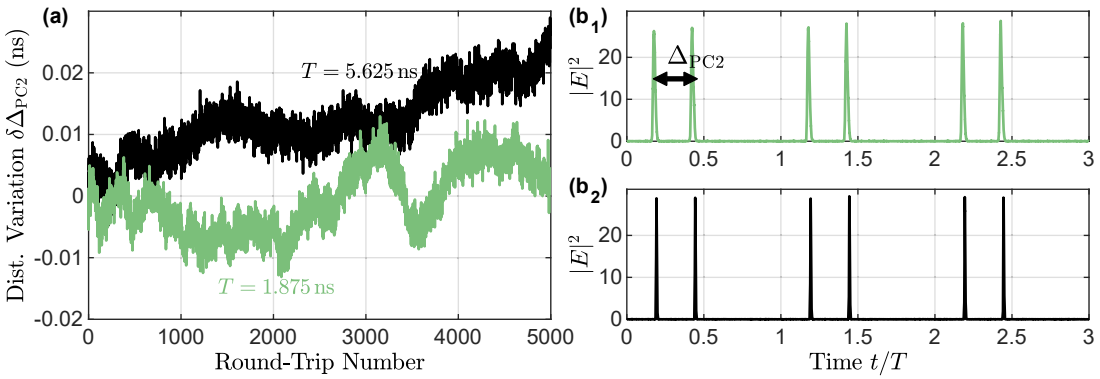

Figure 4.17.: (a) Noise induced variation of the Pulse distance Δ_{PC2} within one pulse cluster as indicated in (b). The green line corresponds to a round-trip time of $T = 1.875$ ns and the black line to $T = 5.625$ ns. (b_{1-2}) Excerpt of the electric field time-series utilised to compute the pulse distance variation with the same colours as in (a). All parameters are given in Table 4.1, $J_g/J_{th} = 0.7$ and $\alpha_g = 1.5$, $\alpha_q = 0.5$. The noise strength is set to $\sqrt{\eta} = 10$ (normalised to $T = 0.625$ ps) and added as an additive noise contribution to the electric field equation in each integration step $+\sqrt{\eta/dt}\xi$, where ξ is a Gaussian white noise term.

section 4.3.2 by the means of Floquet theory. The locally independent pulse cluster in the localised regime is very similar to the nested photonic molecules discussed in References [JAV17, MAR15d, WAN19e]. In a simple picture, they can be understood as two interlaced rings, which are locally shiftable, but not separable on a global scale (catenane molecules) [JAV17]. Comparing the gain landscape in Fig. 4.16(c) and (d) illustrates, that the size of the pulse clusters (photonic molecule) is solely given by the temporal distance between the two gain depletions of the first pulse within one round-trip. This quantity is defined by the length of the shorter cavity arm, i.e. $\min(\tau_1, \tau_2)$. Therefore, the size of the photonic molecule is independent of the total cavity length and in a very long-cavity it would be possible to excite several coexisting photonic molecules. In addition to that, the DDE system can be transferred to a Haus master equation system in which the second gain depletion is embodied by a nonlocality inducing the global binding of the two pulses [HAU20], which is further examined in section 4.3.3. The absolute fluctuation $\delta\Delta_{PC2}$ of the pulse distance within one molecule relative to the equilibrium value of $\Delta_{PC2} = T/4$ is demonstrated in Fig. 4.17(a) for two different round-trip times. It is possible to deduce that the pulse distance does not drift far away from the equilibrium values of $\Delta_{PC2} = 0.46875$ ns (green) and $\Delta_{PC2} = 1.40625$ ns (black) on the investigated time scale of several thousand round-trips. Furthermore, it is possible to recover this behaviour for different noise realisations. To visualise the effect of the noise, excerpts of the electric field time-series used to compute the pulse distances are plotted in Fig. 4.17(b). Since the noise strength is scaled so that it has the same influence for both round-trip times, the absolute fluctuation of Δ_{PC2} with regard to the round-trip number is very similar. However, due to the flat gain landscape in larger cavities, the pulses position can deviate more strongly from the equilibrium position (black line). In other words, the interaction of the pulses via the exponential tails of the gain relaxation is reduced and therefore they can drift more strongly until they experience the repelling influence of the other pulse.

To achieve localisation, the mode-locked pulses have to be stable below the lasing threshold, i.e. multistable to the *off*. Consequently, they cannot be established by solely ramping up the

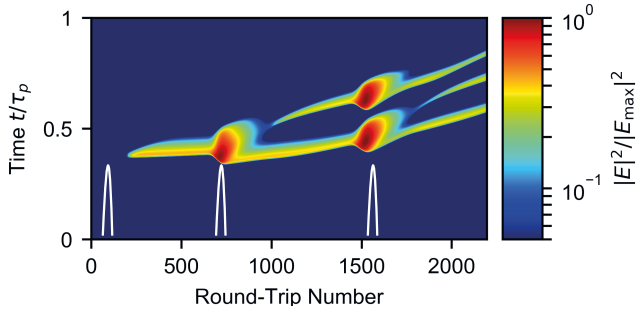

Figure 4.18.: Pseudo space-time plot of the electric field amplitude in the localised state regime. The white pulses mark the temporal positions (round-trips 100, 700, and 1500) at which Gaussian pulses are additionally applied to the constant base pump current. The first two excitation pulses have an amplitude of $J_g = 2.20J_{\text{th}}$ and a full width at half maximum of FWHM $= 47T$ while for the third an amplitude of $J_g = 2.75J_{\text{th}}$ and width of FWHM $= 59T$ are used. The round-trip time is $T = 1.875$ and the cavity is slightly asymmetric with $\tau_1 = 0.15$,$\tau_2 = 0.35$. All other parameters are given in Table 4.1 and $J_g/J_{\text{th}} = 0.85$. Figure adapted from [HAU20].

laser pump current. In experiments, there are two possibilities to generate a stable pulsed lasing state that is multistable to the off solution. The first option is to increase the pump current above the lasing threshold and once a pulse solution has stabilised, decrease the pump to the stability region of the *off*-state, i.e. below the threshold. Due to the multistability, the pulsed state remains stable below the threshold [MAR14c]. The second option is to apply a perturbation to the pump current, which is characterised by increasing it drastically above the threshold for a short period of time. Figure 4.18 indicates how the latter method can be used to excite the localised pulse clusters. Plotted is a pseudo space-time representation of the electric field amplitude (colour code) with the slow time scale on the x-axis and the fast time scale on the y-axis. At the round-trips marked by the white pulses, Gaussian-shaped pulses are applied to the otherwise constant pump J_g. The first perturbation leads to the excitation of a single localised mode-locked pulse. Subsequently, the additional perturbations to the pump power lead to an increase of the optical pulse number, if the amplitude and full-width at half maximum of the perturbation are chosen adequately [CAM16, HAU20]. Here, the amplitude of the first two Gaussian perturbations is set to $J_g = 2.20J_{\text{th}}$ with a full width at half maximum of FWHM $= 47T$. To generate the third optical pulse, the excitation has to be slightly increased in amplitude ($J_g = 2.75J_{\text{th}}$) and width (FWHM $= 59T$). As priorly discussed, the two gain interactions of each pulse lead to a stabilisation of the pulse cluster solutions at the intermediate-cavity length of interest here. This contrasts the observations in face-to-face coupled VECSELs in which harmonic mode-locking solutions stabilise [MAR14c, CAM16]. Nevertheless, pulse-cluster like solutions can be excited in linear cavities by applying a current modulation [MAR15b].

The excitability of the localised pulses, combined with the flat gain landscape in the long-cavity regime indicated in Fig. 4.16(d), leads to an individual addressability of the pulse cluster solutions.

The individual addressability of the localised pulses makes them interesting candidates for several applications since their properties can be exploited to realise arbitrary trains of optical pulses [GRE12b, MAR14c, HAU20]. For example, the pulses can be utilised to store information, if they are interpreted as optical bits and therefore the cavity could potentially be used as an all-optical buffer as discussed for different types of dissipative solitons in Ref-

erences [GEN08, LEO10, MAR14c, GAR15, PAN16e]. Exploiting the multi-pulse structure of photonic molecules, they were suggested to represent a more complex form of bits and therefore extent the binary alphabet in a way that each molecule transfers two bits of information. This could potentially enhance optical data transfer because the Shannon limit can be circumvented by transmitting two bits at once [ROH12a, YUS14, MIT16].
As the localised pulses are incoherent, they could be applied in future spectroscopy applications demanding dense frequency combs and a variable distribution of the comb power [CHE10d, COI14, TLI17, HAU20]. The frequency comb resulting from an arbitrary train of localised pulses is not spectrally modulated as the pulses do not generate a coherent beating. The intensity of the comb teeth can then be controlled by the number of pulses in the cavity, while the resolution decrease resulting from a coherent beating can be avoided. This potential control of the frequency comb power might find applications in pump-probe sensing of material properties [PED08]. Finally, tailoring a certain pattern of stable optical pulses at a controllable repetition rate makes localised pulses an interesting candidate for material processing applications [KER16].

4.3.2 Phase Incoherent Photonic Molecules

As mentioned in the previous section, (localised) pulse clusters in the long-cavity regime can be referred to as photonic molecules due to their binding features making them locally independent but globally bound. The subject of this section is the underlying bifurcation structure, giving rise to the pulse cluster dynamics in the long-cavity regime. From this starting point it is possible to investigate the transition from bound pulse clusters to phase incoherent photonic molecules by performing a Floquet analysis of the states at increasing round-trip times.
Compared to the 'usual' mode-locking case as presented in section 4.2, the general bifurcation mechanism giving birth to the pulsed solutions does not change. As plotted in the 1D-bifurcation diagram in Fig. 4.19, the fundamental (light blue) and harmonic mode-locking solutions (green and red) still emerge from Andronov-Hopf bifurcations (AH) along the continuous-wave branch. The Andronov-Hopf bifurcations along the CW branch are depicted by black squares and labelled as AH with the subscript referring to the emerging solution. It has to be noted that the $\mathrm{AH}_{\mathrm{HML2}}$ and the $\mathrm{AH}_{\mathrm{HML3}}$ exchange their order in J_g with respect to the situation at intermediate-cavity lengths.
Although the AH bifurcations seem to be subcritical in the zoom presented in Fig. 4.19, they are in fact not. A saddle-node bifurcation appears very close to each AH point (not visualised here), leading to the shown branch structure. Hence, the FML solution is born stable and immediately gains one unstable eigenvalue in a saddle-node bifurcation. The branch remains unstable till a second characteristic saddle-node bifurcation along the branch appears. Similarly, the HML_n solutions are born with $2n_i$ unstable eigenvalues, where n_i indicates the position of the AH bifurcation along the branch starting at 1. The HML solutions receive an additional unstable eigenvalue in a saddle-node bifurcation, turning the course of the branches to lower pump powers.
In comparison to the investigation of face-to-face coupled cavities, no detaching of the solution branches from the CW solution is visible as a clear connection to the CW branch can be found here [MAR14c, SCH18e]. However, it has to be noted that a slightly different set of parameters was used in the different investigations of the linear cavity system and that qualitatively the stability analysis remained very similar to the one presented here.

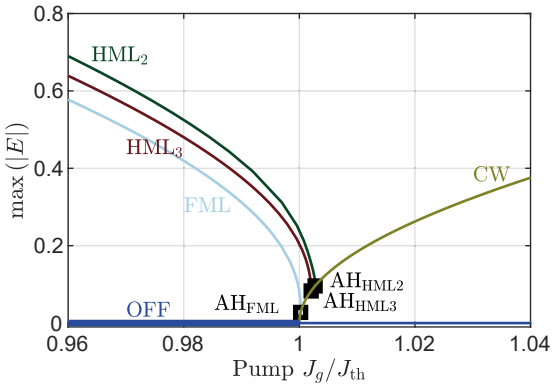

Figure 4.19: 1D-Bifurcation diagram in pump power (J_g/J_{th}) displaying the evolution of the maximum electric field amplitude max($|E|$) along the constant intensity continuous-wave solution (orange), the laser *off*-state (dark blue), the fundamental mode-locking solution (light blue) and the harmonic mode-locking solutions of second order HML_2 (green) and third-order HML_3 (red). Exemplary electric field dynamics along the pulsed branches are indicated in Fig. 4.20(a). Thick (thin) lines denote stable (unstable) dynamics. All parameters are given in Table 4.1.

Branch Structure in the localised State Regime

An extended continuation of the fundamental and harmonic solution branches in the localised state regime is illustrated in Fig. 4.20(a_1). As observed in previous works on linear cavities [MAR14c, SCH18e], the branches all stretch out below the CW threshold and then are subject to a loop, induced by a saddle-node bifurcation (depicted by a black square SN for the FML solution in Fig. 4.20(a_1)). Examples of the electric field and gain dynamics along the branch are indicated for a pump power of $J_g/J_{\mathrm{th}} = 0.85$ in Fig. 4.20(a_{2-4}). The time is normalised to n-periods of the solution, where n refers to the number of pulses in the HML_n solution. The fundamental and third-order harmonic mode-locking solution both become multistable to the *off*-solution (horizontal dashed line at $|E| = 0$) in the investigated regime as indicated by the thick lines. The FML branch gains its stability in a saddle-node bifurcation (SN - black square), whereas the HML_3 solution stabilises in a torus bifurcation (T - black circle). In contrast, the HML_2 solution does not become stable for the symmetric cavity configuration investigated here.
The reason for the instability of the even order HML solutions can be understood by investigating the gain dynamics depicted in Fig. 4.20(a_{2-4}). For the solutions with an odd number of pulses, twice as many equidistant gain depletions as pulses are observable in one cavity round-trip (Fig. 4.20(a_{2+4})). As discussed before, this results from the double gain pass of each pulse in the V-shaped cavity configuration. For the even numbered HML_2 solution, only as many gain depletions as pulses are visible at first sight Fig. 4.20(a_3). In this situation, the temporal distance between the pulses is as long as the time of flight between the two gain passes of each single pulse. Therefore, the two pulses of the HML_2 state pass the gain simultaneously and is depleted by two pulses simultaneously. This situation is energetically unfavourable with regard to the amplification and therefore the solution remains unstable. Higher order even numbered mode-locking solutions remain unstable due to the same reason. How the cavity geometry influences the stability due to the changed gain depletion scenario is elaborated in section 4.3.4.
Two major differences in the bifurcation scenario of the (symmetric) V-shaped cavity VECSEL and the linear cavity can be determined. Firstly, the even numbered HML solutions only remain unstable in the symmetric cavity regime in the V-shaped cavity in contrast to the face-to-face coupled situation [MAR14c]. Secondly, the stabilisation of higher-order harmonic solutions is mediated by torus bifurcations and not by saddle-node bifurcations [MAR14c].
Investigating the dominant eigenvalues at each point of the HML_2 solution in detail, it is

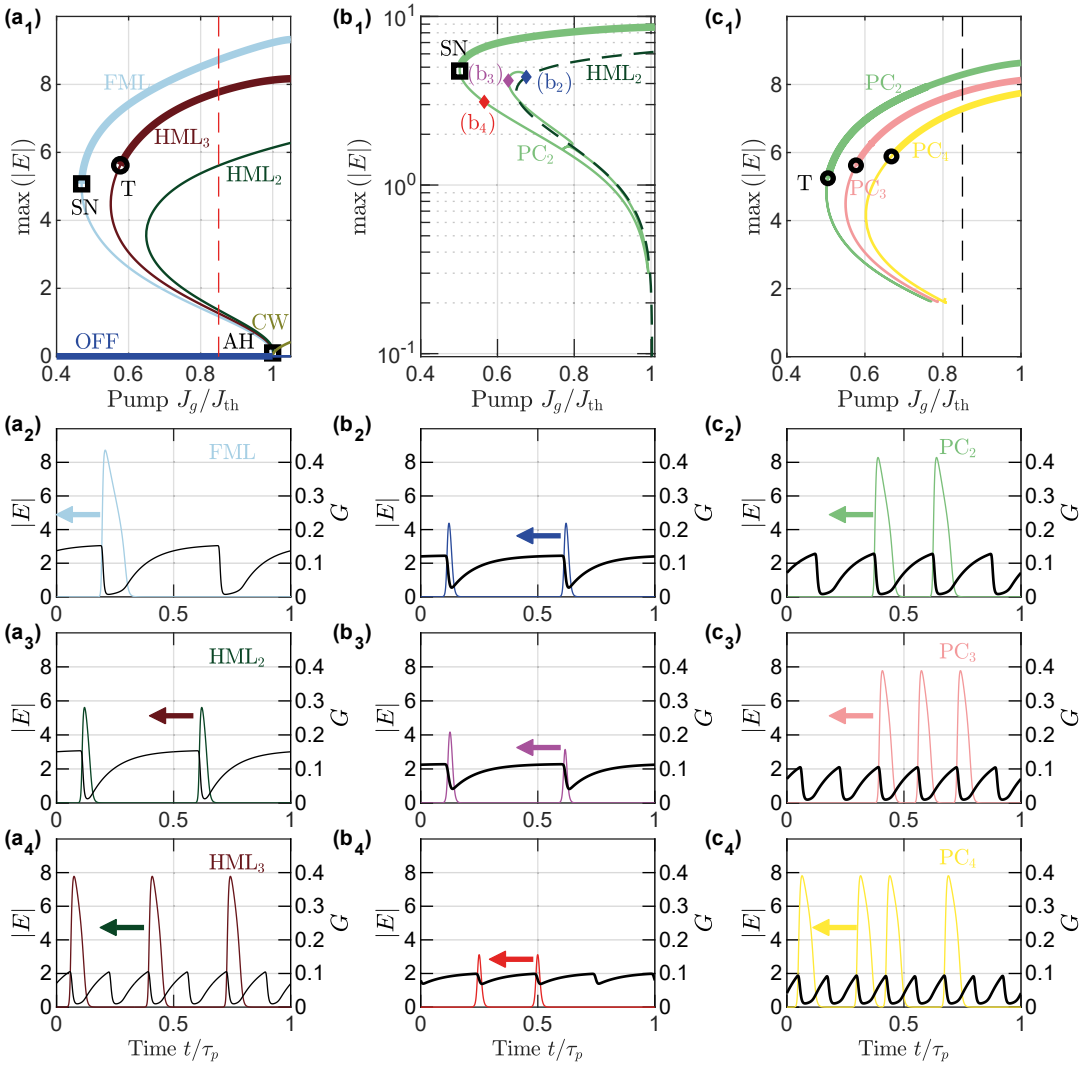

Figure 4.20.: (a_1)-(b_1) 1D-Bifurcation diagrams displaying the evolution of the maximum electric field amplitude max(E) along the different harmonic mode-locking (HML$_n$) and pulse cluster (PC$_n$) solution branches continued in pump power (J_g/J_{th}). Stable (unstable) dynamics are depicted by thick (thin) lines. Black squares label saddle-node bifurcations (SN), black circles denote torus bifurcations (T). The colours and labelling of the branches correspond to the electric field and gain dynamics shown in the lower sub-panels. (a_2)-(a_4) Dynamics of the electric field and the gain (right y-axis) at the pump power indicated by the vertical black dashed dashed line in (a_1). The time is normalised to the period of the FML solution τ_p. The different panels display the fundamental mode-locking solution (FML) and the two lowest-order harmonic mode-locking solutions HML$_2$ and HML$_3$. (b_2)-(b_4) One period τ_p of the field amplitude dynamics and the gain (right y-axis) along the pulse cluster PC$_2$ solution branch (light green) at the points marked by the coloured diamonds in (b_1). (c_2)-(c_4) Gain and electric field dynamics at the pump current marked by the black line in (c_1) for the PC$_2$ (light green) and PC$_3$ (light red) pulse cluster solutions and the irregular PC$_4$ pulse cluster. All parameters are given in Table 4.1. Figure adapted from [HAU20].

possible to find a period doubling bifurcation in the upper part of the branch at $(J_g/J_{\mathrm{th}}) \approx 0.71$. Its position along the HML_2 branch (dark green) is shown by the blue diamond in Fig. 4.20(b_1). At this point, an unstable solution with a period of $\tau_p \approx T + \gamma^{-1}$ emerges. By definition of the period doubling bifurcation, the emerging solution is equal to the HML_2 solution with a doubled period at the bifurcation point, as visualised in Fig. 4.20(b_2). As one continues the newly emerged solution (light green in Fig. 4.20(b_1)), the amplitudes of the two pulses successively decreases as indicated in Fig. 4.20(b_3). After reaching a minimum in amplitude, the pulses adjust their position so that in the further course of the branch a localised pulse cluster solution is formed, as plotted in Fig. 4.20(b_4). Similar to the HML_2 branch, the PC_2 solution is subject to a loop, marking the minimum power at which the solution exists. Again, the turning point is characterised by a saddle-node bifurcation (SN - black square). Due to the more optimal gain depletion scenario, the maximum pulse amplitude along the PC_2 branch is higher compared to the HML_2 solution.
As in the super threshold mode-locking regime, the PC_2 solution is stabilised in a torus bifurcation displayed as a black circle in Fig. 4.20(c_1). Additional to the PC_2 solution, the panel further visualises the course of the PC_3 (light red) and an irregular PC_4 (yellow) solution branch in pump power and maximum electric field amplitude. Both higher-order branches behave very similar to the multi-pulse HML_n and PC_n branches described before: A loop at a minimum in pump power can be observed at which the branch turns to higher amplitudes via a saddle-node bifurcation. A stable regime then manifests via torus bifurcations along the branches (black circles in Fig. 4.20(c_1)).
Due to the crucial influence of the gain depletions on the stabilisation, it is worth investigating the gain dynamics of the PC_n solutions. For a pump power of $J_g/J_{\mathrm{th}} = 0.85$, the temporal evolution of the integrated carrier densities are shown in black lines together with the coloured electric field dynamics in Fig. 4.20(c_{2-4}). As discussed in the previous section, all pulse cluster solutions exhibit an equidistant gain depletion, which in turn explains their formation: The pulse distances adjust to the cavity configuration so that an optimal (equidistant) depletion of the gain is maintained. For an odd number of pulses in the cavity, the harmonic and the PC solutions lead to the same gain landscape. This becomes visible when comparing the gain dynamics of the PC_3 solution depicted in Fig. 4.20(c_3) and of the HML_3 solution visualised in Fig. 4.20(a_4). The two solutions can be transformed into each other by permuting the position of the central pulse of the PC_3 solution with the position of its second ('ghost') gain depletion (i.e. shifting the central pulse by $2\tau_2 = 0.5\tau_p$).
The permutation of the pulse position with the position of the ghost depletion leaves the gain dynamics unaffected and consequently irregular pulse patterns can become stable, as illustrated by the irregular PC_4 solution in Fig. 4.20(c_4). It has to be noted that the absorber saturation points shift in time but have no influence on the stabilisation due to the full relaxation in between pulses.

Binding Mechanism of the Pulse Clusters

From the gain time-series of the PC_2 solution, it becomes evident that at the chosen round-trip time and gain relaxation rate ($\gamma_g = 3.125\,\mathrm{ns}^{-1}$,$T = 1.875\,\mathrm{ns}$), no complete relaxation between pulses is possible (see Fig. 4.20(c_2)). Thus, the pulses still interact via the tails of their exponential gain relaxation [MAR14c] and the PC_2 solution can therefore be described as locally bound. This binding can be assessed by investigating the Floquet multipliers of the periodic solutions. An introduction of how the Floquet multipliers can be computed

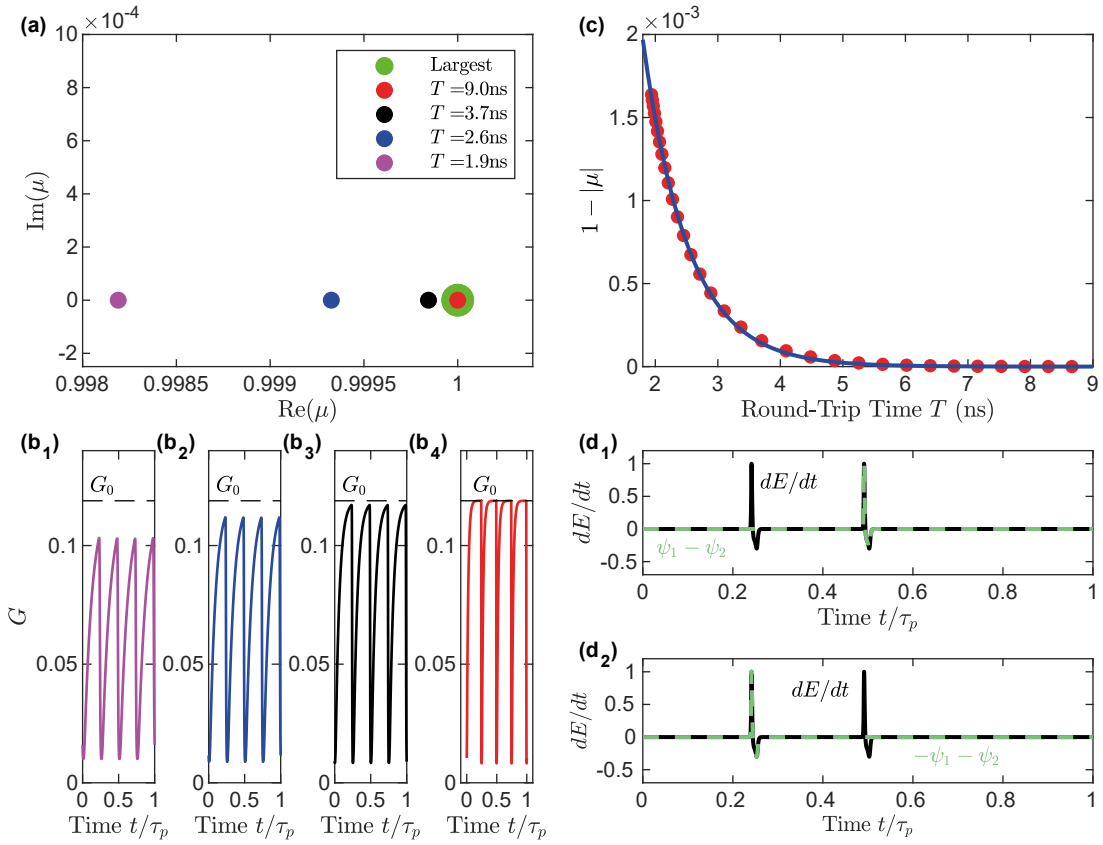

Figure 4.21.: (a) Maximum (large green circle) and second largest Floquet multiplier (μ) of the PC_2 solution calculated at different cold-cavity round-trip times as given by the legend and plotted in the complex plane. (b_{1-4}) Gain dynamics of the PC_2 solution at the different round-trip times depicted in (a). The vertical dashed line visualises the equilibrium integrated charge-carrier density G_0, which is unaltered for all sub-panels. (c) Difference of the absolute value of the second largest Floquet multiplier (μ) to unity (red dots) with respect to the cold-cavity round-trip. An exponential fit is indicated by a blue line. (d_{1-2}) Superposition of the eigenvectors (green) belonging to the largest (ψ_1) and second largest (ψ_2) eigenvalue (Floquet multiplier) of the monodromy operator of the PC_2 solution obtained utilising DDE-biftool. The black lines indicate the derivative of the electric field dynamics with respect to time in one period (τ_p) of the PC_2 solution. Both quantities are normalized to the maximum. All parameters are given in Table 4.1 and $J_g/J_{\mathrm{th}} = 0.65$. Figure adapted from [HAU20].

as the eigenvalues of the monodromy matrix can be found in section 2.3 or in References [LUZ02, ENG02, JAU17a]. Briefly, the Floquet multipliers are the eigenvectors of the (time-integration) mondoromy matrix. They can be understood as a measure of how the system (oscillating in a periodic orbit) reacts to a perturbation in the direction of corresponding eigenvector (Floquet mode). As the phase space of a DDE system has infinite dimensions, one has to restrict the analysis to the maximum Floquet multipliers. This also occurs naturally since the monodromy matrix has finite dimensions due to required time discretisation. If the absolute all Floquet multipliers is $|\mu| \leq 1$, the system is stable because all perturbations are damped out.

The two maximum Floquet multipliers μ of the PC_2 solution for different round-trip times are indicated in the complex plane in Fig. 4.21(a). As no multiplier with $|\mu| > 1$ can be found, the solution is stable. A trivial multiplier $|\mu| = 1$ represents a neutral mode of the system (large green dot). This means that the system is invariant to a perturbation in the corresponding eigendirection. In this case, the eigendirection corresponds to a translation of the time origin [HAU20]. As expected, the trivial multiplier is maintained when the round-trip time is increased since it remains at the position of the large green dot in Fig. 4.21(a) for all round-trip times. Opposing to that, the second largest multiplier is subject to a change, if T is elevated, as it approaches $\mu = 1$. This is depicted by the coloured dots in Fig. 4.21(a) that represent the second largest Floquet multiplier at the round-trip times given by the legend. The same colour code is used to plot the gain dynamics at the respective round-trip times in Fig. 4.21(b). One notices quickly that the closer the gain relaxes to its equilibrium value (dashed line G_0), the closer does the Floquet multiplier approach unity ($|\mu| = 1$). In fact, the asymptotic approach is found to behave exponentially as demonstrated in Fig. 4.21(c). Plotted by red dots is the distance of the absolute value of the second largest Floquet multiplier to unity (1-$|\mu|$) with respect to the cold-cavity round-trip time. The blue line indicates an exponential fit with the fit parameters given in the caption. The fit matches the data points very well, underlining the exponential behaviour.

The continuous development of a second trivial Floquet multiplier demonstrates that the PC_2 solution gains a second neutral mode with increasing round-trip time. In order to determine the eigendirection of the neutral modes, the eigenvectors corresponding to the two trivial multipliers are computed. Their electric field[17] components are displayed as green lines in Fig. 4.21(d). For comparison, the time derivative of the electric field profile of the PC_2 periodic orbit is plotted in black.

As the eigenvectors both match the derivative of a single pulse of the PC_2 pulse cluster, one can conclude that the two neutral modes each correspond to a perturbation in the direction of a single pulse solution. The system becomes invariant to a perturbation in the two eigendirections as $|\mu| = 1$, which means that the pulses are locally independent. However, the pulses are still globally bound as each pulse is trapped in between the two gain depletions of the other pulse. Yet, this can not be assessed by the Floquet analysis due to its local nature. Furthermore, it has to be pointed out that the neutral mode of the pulse cluster at low round-trip times corresponds to the complete cluster, highlighting their existence as a locally bound structure.

Based on recent research terming localised multi-pulse structures "soliton molecules" [GRE12b, JAV17, KRU17b, MAR15d, WAN19e, KUR19], justifies referring to the pulse clusters in the

[17] It has to be noted that a linear combination of the two eigenvectors is shown here as the basis of the vector space results from the numerical diagonalisation of the monodromy matrix and not necessarily matches the required basis.

long-cavity regime as soliton or photonic molecules. Anyhow, the fundamental difference to real molecules is the required constant energy supply to maintain their existence [AKH08].

Coherence of the Pulse Cluster Solutions

A widely investigated property of soliton molecules is the phase relationship of the two (or more) pulses. It is usually determined as the difference of the phases at the electric field amplitude related to the pulse maximum $\Delta\phi(t) = \phi_1(t) - \phi_2(t)$ [LED99a, SOT99, ZAV09, ORT10]. Generally, the pulses can either maintain a (quasi) constant phase relationship [LED99a, ROH13], exhibit phase flipping events [ZAV09] or evidence an independent motion of the phases, which includes a 'chaotic' or periodic evolution of the phase difference [SOT99, ZAV09, ORT10, WAN19e]. Most recently single solitons were found to be incoherent [WAN20f].
For the localised pulse clusters in the V-shaped VECSEL, the phases of the pulses within the PC_2 pulse cluster remain constant, if no amplitude-phase coupling is present, i.e. $\alpha_g = \alpha_q = 0$ and no noise is present. The reason for this lies within the characteristics of the electric field equation (3.48) in the used DDE model. If both α-factors are zero, the phase remains unaltered during one round-trip. Hence, the values $\alpha_g = 1.5$ and $\alpha_q = 0.5$ are introduced during investigation of the phase-relationship [SCH18f, SCH18e]. In absence of noise, the α-factors lead to a simultaneous drift of the phase at the maximum pulse amplitudes and hence a constant phase difference between the pulses within one cluster.
By analysing the optical spectrum of the PC_2 state, it is further possible to asses the coherence of the pulses within the solution in the absence of noise. The corresponding optical spectrum is presented in the green lines in Fig. 4.22(c). As derived from a simple analysis of the spectral components in section 4.2.2, the modulation of the spectrum with respect to the fundamental situation is a clear indication of coherent pulses in the PC_2 solution. As expected, the amplitude-phase coupling induces a shift of the optical spectrum but introduces no incoherence [JAU17a]. A zoom of the spectrum presented in green in Fig. 4.22(d) allows for a better visibility of the modulation of the coherent spectrum (no noise).
However, if noise is added to the system, the phase difference exhibits a random walk[18] as displayed for several noise realisations[19] in Fig. 4.22(a). To underline the presence of a random walk, the ensemble variance[20] is plotted in Fig. 4.22(b). Its linear evolution with increasing round-trip number (time) clearly indicates the underlying random walk. Therefore, it can be concluded that the pulses in the PC_2 localised pulse cluster are incoherent in the presence of noise [VIK14, KEL17a]. This is further supported by the appearance of the optical spectrum of the PC_2 solution including noise. It is plotted in black in Fig. 4.22(c). The spectrum is subject to no modulation[21] compared to the fundamental spectrum and it

[18] A random walk in the most simple description corresponds to a person taking successive random steps to either the left or right with a constant probability [GAR02]. The steps are of equal length and are temporally equally spaced. In the case of a continuous time variable, the random walk is connected to the Wiener process [GAR02]. Characteristic for the random walk is a zero mean and a linearly increasing variance [GAR02].
[19] Note that a transient time of 1000 round-trips is used, starting from the stable PC_2 solution. This leads to the different starting points of the random walks.
[20] The ensemble variance is computed as the variance of the phase difference across 50 noise realisation in each round-trip.
[21] A slight modulation is still visible due to the limited numerical accuracy. The spectrum is computed as an average of 50 spectra. Each spectrum is computed from a converged time-series of the PC_2 solution with a length of 20000 round-trips applying the fftw3 C++ library.

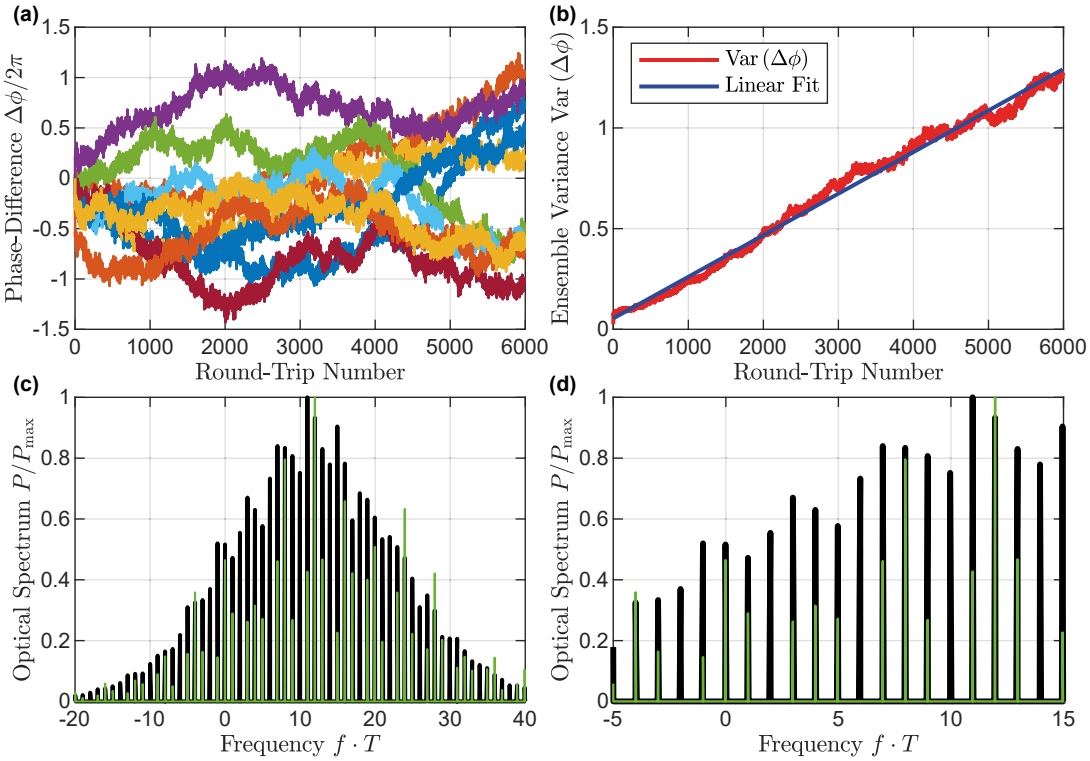

Figure 4.22.: (a) Temporal evolution of the phase difference $\Delta\phi$ between the two pulses within the PC_2 solution. The phase is determined at the maximum pulse amplitude. The colours indicate different noise realisations. (b) Ensemble variance across different noise realisations of the phase difference shown in (a) with respect to the round-trip time. The blue line indicates a linear fit $y = m \cdot x + b$ with $m = 0.0002$ and $b = 0.0543$. (c) Optical spectrum of the PC_2 solution with (black) and without noise (green). (d) Zoom in of the optical spectrum to the region indicated by the blue lines in (c). All parameters are given in Table 4.1 and $J_g/J_{\text{th}} = 0.7$. The noise strength is set to $\sqrt{\eta} = 20$ (see caption of Fig. 4.17).

can therefore be assessed that it results from the combination of two incoherent pulses.
In conclusion, photonic molecules, that are globally bound but locally independent, can be found in the long-cavity regime of passively mode-locked V-shaped VECSELs. Their local independence can be determined via the analysis of the largest Floquet exponents, which indicate the continuous development of a second neutral mode. Despite the global binding mechanism induced by the secondary gain depletion, the pulses in one molecule are phase incoherent. This can be assessed by analysing the phase difference across the two pulses and the optical spectrum of the solution.

4.3.3 Nonlocal Haus Master Equation Model

The Haus master partial differential equation (PDE) was first introduced for the description of "forced mode-locking" [HAU75] and shortly after for passively mode-locked lasers with a slow [HAU75a, KAE95] or fast [HAU75b] saturable absorber. It describes the evolution of the pulsed electric field at the laser output by means of two time scales. The slow time scale θ is related to the changes a pulse experiences from round-trip to round-trip, e.g. the filter induced temporal drift with respect to the round-trip time. Secondly, the fast time scale σ describes the changes of the electric field as well as charge carriers in gain and absorber within one round-trip. The fast time scale can be interpreted as a representation of the cavity in space and therefore to a spatial distribution of the pulse therein [GIA96, YAN17b]. This description of the pulse propagation with respect to the slow and fast time scale was exploited in sections 4.2.3 and 4.3.2 when showing the pseudo space-time representations of pulsed states as in Fig. 4.18 and Fig. 4.6.
Initially the Haus master equation was derived phenomenologically by additively combining the influences experienced by a pulse during one cavity round-trip (e.g. dispersion, gain or Kerr nonlinearity) and thereby finding an approximation for the evolution of the pulse from round-trip to round-trip [HAU75a]. The approach includes the assumption of weak gain and losses (uniform field limit), which is of importance for the derivation presented in this section. The resulting partial differential pulse propagation equation can be understood as a coordinate transformed nonlinear Schroedinger equation, which is extended by a suitable modelling of the gain and absorption processes [HAU00, BOY08, MAR14c]. The level of complexity at which the gain and absorber dynamics are modelled as well as the selection of nonlinear influences (e.g. dispersion) in the electric field equation, strongly depends on the investigated laser device and operation regime [HAU00, IPP94]. Additional to the situation of fast and slow saturable absorbers, different variants of the Haus master equation were successfully introduced to describe additive pulse mode-locking in fibre lasers, Kerr-lens mode-locking, the role of different orders of dispersion or coherent effects [HAU95, IPP94, HAU00, PER20, SCH20d, HAU20a]. For the description of solid-state lasers, the gain and absorption processes can be strongly simplified due to their very slow and fast evolution. Based on this time scales, the Haus master equation can be transformed to the complex cubic-quintic Ginzburg-Landau equation, which is often used to investigate dissipative solitons [MAR14c, LED99a, GRE12b, AKH08, GUS15]. However, to model the V-shaped VECSEL discussed here, it is necessary to include the evolution of the carrier densities in gain and absorber by means of dynamical equations as their relaxation rates can neither be classified as much faster or slower compared to the other time scales of the system. Furthermore, the carrier densities are subject to strong modulations. Nonetheless, in the intermediate-cavity regime ($\gamma_g^{-1} \propto T$) problems can occur following this approach, due to the necessity to introduce proper boundary conditions to maintain the long-term carrier memory essential for quasi-periodic dynamics. A method to address this problem is discussed in detail in section 5.2.
The initial derivation of the Haus master equation (HME) starts with the Lorentzian approximation of the gain spectrum of the longitudinal lasing modes in a mode-locked laser [HAU00]. It proceeds with finding an expression for the alteration (via gain, loss and modulation) of the spectral fringes during each round-trip along the cavity. The resulting transfer function is then Fourier transformed leading to a master equation in the time-domain [HAU75, HAU75a, HAU00]. Yet, to derive a HME for a passively mode-locked V-shaped

VECSEL, a different approach is utilised in the following[22]. Namely, it is possible to derive a HME from the delay differential equation model based on a multiple time-scale analysis [KOL06, SCH18f, SCH18e, CAM16]. Putting aside the fact that utilising the V-shaped DDE model as a starting point enables a derivation of the HME from first principles, it ensures a correct treatment of the additional influences introduced by the V-shaped cavity geometry. It has to be noted that it would be possible to follow the functional mapping method introduced in References [SCH18f, SCH20d], but the multiple time scale approach provides a simpler treatment of the additional delayed terms during the derivation.

Preparation Steps

As mentioned before, the derivation starts with the DDE model (3.48)-(3.51) for the passively mode-locked laser with a V-shaped cavity geometry derived in section 3.3. To follow the approach outlined in Reference [KOL06], some changes to the priorly introduced normalisation of the parameters and variables are required before starting the actual derivation. The time $\tilde{t}$ remains normalised to the round-trip time according to $t = \frac{\tilde{t}}{T}$. However, the electric field and the parameters are not scaled to the round-trip time in the following derivation. In consequence, the electric field is normalised so that $E = \sqrt{T}\gamma_g A$ and the ratio of the differential gain and absorption is defined as $\tilde{s} = s\frac{\gamma_g}{\gamma_q}$ during the derivation. Thus, the DDE model can be written as

$$\varepsilon\frac{dA(t)}{dt} = -A(t) + A(t-1)\sqrt{\kappa}e^{\frac{1}{2}\left[G(t-\frac{2\tau_1}{T})+G(t-1)\right]+Q(t-1)}, \tag{4.21}$$

$$\frac{dG(t)}{dt} = \gamma_g T\left[G_0 - G(t) - \left[e^{G(t)}-1\right]\left\{|A(t)|^2 + \left|A\left(t-\frac{2\tau_2}{T}\right)\right|^2 e^{2Q\left(t-\frac{2\tau_2}{T}\right)+G\left(t-\frac{2\tau_2}{T}\right)}\right\}\right], \tag{4.22}$$

$$\frac{dQ(t)}{dt} = \gamma_q T\left[Q_0 - Q(t) - \tilde{s}\left[e^{2Q(t)}-1\right]e^{G(t)}\left|A\left(t\right)\right|^2\right]. \tag{4.23}$$

Where the product of round-trip time and gain bandwidth is expressed by $\varepsilon = \gamma^{-1}T^{-1}$, and the α-factors are left out for convenience. As the central approximation of the HME, an uniform field limit is required. This means that the modifications of pulse induced by the gain, absorption, outcoupling and filtering losses are small in the investigated regime [HAU75a]. The localised structures discussed in this section emerge in the subthreshold regime. Therefore, this requirement is certainly fullfilled for the amplification as $G_0 \approx 0.1$. Furthermore, the low unsaturated absorption $Q_0 \approx 0.18$ and outcoupling losses $1-\kappa = 0.01$ as well as the broad filter $\gamma = 240\,\mathrm{ns}$ meet this requirement. It has to be noted that in the high performance mode-locking regime, the experimentally determined chip reflectivities (small signal gain) of $\approx 103\%$ and the small outcoupling losses hint at a situation in accordance with this requirement [WAL16]. This is underlined by the success of the Haus master equation for high performance mode-locked solid-state lasers [HAU00]. The applicability of the Haus master equation in this regime of semiconductor VECSELs is further elaborated in section 5.2.

[22] The derivation of the HME for V-shaped cavities was published in Reference [HAU20] and is based on the multi time-scale approach presented in Reference [KOL06].

Multiple Time-Scale Analysis

The application of a multiple time scale approach starting from the DDE model is motivated by the natural division of the dynamics into two time scales in the target HME. In a first step, it is therefore necessary to define the additional time scales[23]. With respect to the DDE model, which only includes the time scale t, this necessitates a split of t into a slow θ and a fast σ time scale, as well as treating them independently [BEN99c]. The second main constituent of a multiple time scale approach is a perturbation expansion of the system variables. On that account, the system variables are expressed in terms of a power series in a smallness parameter ε. Exemplarily expanding the electric field $A(\theta, \sigma)$ to second-order in ε yields[24]

$$A(\theta, \sigma) = A_1(\theta, \sigma) + \varepsilon A_2(\theta, \sigma) + \varepsilon^2 A_3(\theta, \sigma) + O(\varepsilon^3). \tag{4.24}$$

The smallness parameter chosen here is $\varepsilon = \gamma^{-1} T^{-1}$, as it is physically related to the fastest time scale of the system and is proportional to the pulse width [VLA05]. It is furthermore a natural choice because it scales the derivative in the electric field equation, which can be understood as a resonant forcing term. Consequently, if $\varepsilon \to 0$ and the charge carrier contributions are negligibly small, the solution of the system is just periodic in the electric field as $A(t-1) = A(t)$ (see eq. (4.21)).
Based on the uniform field limit (low gain and absorption), the small variables and parameters can be redefined with respect to the smallness parameter [BEN99c]

$$G(t) = \varepsilon^2 \tilde{G}(t) \ , \ Q(t) = \varepsilon^2 \tilde{Q}(t), \tag{4.25}$$

$$G_0 = \varepsilon^2 G_m \ , \ Q_0 = \varepsilon^2 Q_m, \tag{4.26}$$

$$\kappa = \exp -\varepsilon^2 k. \tag{4.27}$$

The relaxation rates $\gamma_{g,q}$ are not rescaled for the investigated laser system, as the gain and absorber relax fully between pulse passes and therefore the factors $\gamma_g T$ and $\gamma_q T$ are not of a small magnitude. In contrast, the factor $\gamma_g T$ is of the order ε^2 in the short cavity regime investigated in Reference [KOL06], due to the small gain relaxation during each round-trip. However, a long-cavity is investigated here and therefore $\gamma_g T \gg 1$.
The rescaled variables/parameters are utilised to simplify eq. (4.21)-(4.23) as the exponentials can be expanded to the first-order in ε^2, which yields

$$\begin{aligned} \varepsilon \frac{dA(t)}{dt} =& - A(t) + A(t-1) \left[1 + \frac{\varepsilon^2}{2} \left\{ \tilde{G}\left(t - \frac{2\tau_1}{T} \right) + \tilde{G}(t-1) + 2\tilde{Q}(t-1) - k \right\} \right] \\ &+ O\left(\varepsilon^4\right), \end{aligned} \tag{4.28}$$

$$\frac{d\tilde{G}(t)}{dt} = \gamma_g T \left[G_m - \tilde{G}(t) - \tilde{G}(t) \left\{ |A(t)|^2 + \left| A\left(t - \frac{2\tau_2}{T} \right) \right|^2 \right\} \right] + O\left(\varepsilon^2\right), \tag{4.29}$$

$$\frac{d\tilde{Q}(t)}{dt} = \gamma_q T \left[Q_m - \tilde{Q}(t) - 2\tilde{s}\tilde{Q}(t) \, |A(t)|^2 \right] + O\left(\varepsilon^2\right). \tag{4.30}$$

[23] In a general multiple time scale approach it is possible to introduce more than two time scales, but here it is convenient to only chose two, based on the target model and especially the underlying physics.
[24] Please note that in the conventional notation the index in the expansion starts at 0 [HAU20, KOL06]. However, here it starts at 1 to circumvent any confusion with the equilibrium carrier densities in the gain G_0 and absorber Q_0.

This simplified equation system now serves as the staring point of the multiple time-scale analysis [KOL06]. Firstly, the fast σ and slow time scale θ with respect to ε are defined, followed by the perturbation expansion as a series in ε.
Based on the physical properties of the system (and the well known form of the Haus master equation), the fast time scale σ refers to changes within one round-trip and the slow θ time scale to alterations from round-trip to round-trip. They can be defined as

$$\sigma = \omega t, \tag{4.31}$$

$$\theta = \varepsilon^2 t. \tag{4.32}$$

Choosing $O(\varepsilon^2)$ for the slow time scale is motivated by the time scale of amplitude (gain) fluctuations [HAU20]. Contrary to most simple application of the multiple time-scale analysis, the fast time scale depends on t [BEN99c]. The choice of the time scales is motivated by the period of the pulsed solutions. As mentioned before, the system exhibits a one-periodic solution in the electric field $A(t) = A(t-1)$, if $\varepsilon \to 0$, and the charge carrier contributions are negligible. Similar to the Poincaré-Linstedt method [VER96], one can therefore find the period of the pulsed solutions (τ_p) of the full system by an increase of the period of the unforced system ($\tau_{\text{p,unf.}} = 1$). Physically it can be understood by the fact that the time needed for one pulse to pass through the cavity is enlarged with respect to the cold-cavity round-trip time, due to the finite interaction time with the intracavity elements[25] [CAM16, SCH18e]. In the uniform field limit, the Lorentzian filter modelling the gain bandwidth has a dominant influence on the electric field and induces an increase of the round-trip time of $\approx \frac{1}{\gamma}$ [VLA05]. The mathematical calculations of transforming the simplest form of the DDE system into a PDE unravelling the drift, are described in Appendix A.2. Therefore, it is possible to approximate the altered period τ_p by [CAM16, SCH18e]

$$\tau_p \approx T + \frac{1}{\gamma} = T(1+\varepsilon), \tag{4.33}$$

which just gives $\tau_p = 1 + \varepsilon$, if the time is normalised to the round-trip T. By utilising the inverse period one can obtain an expression for ω in eq. (4.31) so that the scaling of the fast time scale includes the increased period, caused by the time lag of the filter. The factor can then be approximated as

$$\omega = \frac{1}{\tau_p} = \frac{1}{1+\varepsilon} \approx 1 + \omega_1 \varepsilon + \omega_2 \varepsilon^2. \tag{4.34}$$

Where the second term is expanded with respect to small ε and the introduction of the adjustable parameters ω_1 and ω_2 is important to later simplify the solvability conditions given by the multiple time-scale analysis. Expanding up to the second-order is necessary as the drift is not strictly linear with ε. Hence, the final definition of the slow and fast time scale utilised in the further derivation reads

$$\sigma = \left(1 + \omega_1 \varepsilon + \omega_2 \varepsilon^2\right) t, \tag{4.35}$$

$$\theta = \varepsilon^2 t. \tag{4.36}$$

[25] This approximation is on the basis of the uniform field limit. If the absorption, mirror losses and gain become large, it is possible to find solutions with $\tau_p < T$ as outlined in Reference [JAU17a].

On the account of adequately including the two time scales into the model, the total derivative $\frac{d}{dt}$ is transformed according to

$$\frac{d}{dt} = \frac{\partial\sigma}{\partial t}\frac{\partial}{\partial t} + \frac{\partial\theta}{\partial t}\frac{\partial}{\partial\theta} = (1 + \omega_1\varepsilon + \omega_2\varepsilon^2)\partial\sigma + \varepsilon^2\partial\theta. \tag{4.37}$$

Furthermore, the delayed terms have to be transferred to the new coordinates, which gives $A(t-1) \Rightarrow A(\theta - \varepsilon^2, \sigma - \omega)$. To reduce the delay to one time scale, a Taylor expansion up to second-order in ε is utilised for the electric field, which yields

$$\begin{aligned} A\left(\theta - \varepsilon^2, \sigma - 1 - \omega_1\varepsilon - \omega_2\varepsilon^2\right) \approx & A(\theta, \sigma - 1) - \varepsilon\omega_1\partial_\sigma A(\theta, \sigma - 1) \\ & - \varepsilon^2\left[\partial_\theta + \omega_1^2\partial_\sigma^2 + \omega_2\partial_\sigma\right] A(\theta, \sigma - 1) + O(\varepsilon^3). \end{aligned} \tag{4.38}$$

Here, the power series expansion of the electric field eq. (4.24) is left out at first, for a better readability. The delayed terms of the integrated charge carrier densities are only Taylor expanded up to $O(1)$ in ε, due to the pre-factor of order $O(\varepsilon^2)$. The pre-factor results from the rescaling of the gain and absorber variables in the electric field equation (4.28) based on the uniform field limit. Furthermore, only terms of order $O(1)$ are considered in the gain and absorber equations (4.29)-(4.30). The expansion for the gain variable then yields

$$\tilde{G}\left(\theta - \varepsilon^2, \sigma - 1 - \omega_1\varepsilon - \omega_2\varepsilon^2\right) \approx \tilde{G}(\theta, \sigma - 1). \tag{4.39}$$

This is analogously performed for the second delayed gain term and the delayed absorber term.
Combining the power series expansion (4.24), the introduction of the new time scales (4.36)-(4.35), the transformation of the derivative (4.37) and the expansion of the delayed terms (4.38)-(4.39), one can now search for a solution of the form $A(\theta, \sigma, \varepsilon)$, $G(\theta, \sigma, \varepsilon)$ and $Q(\theta, \sigma, \varepsilon)$. On that account, the system is split into problems of order $O(1)$, $O(\varepsilon)$ and $O(\varepsilon^2)$.
Using the notation $A(\theta, \sigma) \widehat{=} A$ and $A(\theta, \sigma - 1) \widehat{=} A(\sigma - 1)$ for simplicity, one arrives at the following equations for the $O(1)$ problem

$$A_1 = A_1(\sigma - 1), \tag{4.40}$$

$$\partial_\sigma\tilde{G}_1 = \gamma_g T\left[G_m - \tilde{G}_1 - \tilde{G}_1\left\{|A_1|^2 + \left|A_1\left(\sigma - \frac{2\tau_2}{T}\right)\right|^2\right\}\right], \tag{4.41}$$

$$\partial_\sigma\tilde{Q}_1 = \gamma_q T\left[Q_m - \tilde{Q}_1 - 2\tilde{s}\tilde{Q}_1|A_1|^2\right]. \tag{4.42}$$

Again, it has to be highlighted that the derivative with respect to the slow time scale θ in the carrier equations is of $O(\varepsilon^2)$ and therefore is not considered here. The same is true for all higher-orders in the expansion of the delayed electric field term in the gain eq. (4.41), so only the zeroth order of the expansion remains ($A(\sigma - 2\frac{2\tau_2}{T})$). From the solvability condition eq. (4.40), one finds the requirement that A_1 is of period 1 on the fast time scale.
As a next step, one proceeds to $O(\varepsilon)$ for the electric field equation, which yields

$$\begin{aligned} A_2 - A_2(\sigma - 1) &= -\omega_1\partial_\sigma A_1(\sigma - 1) - \partial_\sigma A_1 \\ \Rightarrow A_2 - A_2(\sigma - 1) &= -(1 + \omega_1)\partial_\sigma A_1. \end{aligned} \tag{4.43}$$

Since the derivative term would introduce a resonant forcing, i.e. divergence, it is required to be 0. Therefore, the condition that A_2 is of period 1 can be deduced, which is assured by

setting $\omega_1 = -1$. Note that the higher-orders for the gain and absorber equations are not considered as these equations are only investigated on $O(1)$, motivated by the time scale of their evolution.
Proceeding with $O(\varepsilon^2)$ one finds

$$\begin{aligned} A_3 - A_3(\sigma-1) = &- \omega_1\partial_\sigma A_1 - \partial_\sigma A_2 - \partial_\theta A_1(\sigma-1) \\ &+ \frac{1}{2}\omega_1^2\partial_\sigma^2 A_1(\sigma_0-1) - \omega_2\partial_\sigma A_1(\sigma-1) - \omega_1\partial_\sigma A_2(\sigma-1) \\ &+ \frac{1}{2}\left[\tilde{G}_1\left(\sigma - \frac{2\tau_1}{T}\right) + \tilde{G}_1(\sigma-1) + 2\tilde{Q}_1(\sigma-1) - k\right] A_1(\sigma-1). \end{aligned} \tag{4.44}$$

This expression can be simplified by utilising that A_1 and A_2 are periodic in σ with a period of 1 (as σ is normalised to T), as well as $\omega_1 = -1$. Consequently, one finds that $\omega_2 = 1$ with the same reasoning as before. Thus, the remaining solvability condition yields

$$\begin{aligned} A_3 - A_3(\sigma-1) = &-\partial_\theta A_1 + \frac{1}{2}\partial_\sigma^2 A_1 \\ &+ \frac{1}{2}\left[\tilde{G}_1\left(\sigma - \frac{2\tau_1}{T}\right) + \tilde{G}_1(\sigma-1) + 2\tilde{Q}_1(\sigma-1) - k\right] A_1. \end{aligned} \tag{4.45}$$

To find a one-periodic solution in A_3 (and circumvent a resonant forcing) requires the right hand side of this equation to be equal to 0. Combining the carrier equations with the solvability condition for the electric field then leads to the final PDE system

$$\partial_\theta A_1 = \frac{1}{2}\partial_\sigma^2 A_1 + \frac{1}{2}\left[\tilde{G}_1\left(\sigma - \frac{T-2\tau_2}{T}\right) + \tilde{G}_1 + 2\tilde{Q}_1 - k\right] A_1, \tag{4.46}$$

$$\partial_\sigma \tilde{G}_1 = \gamma_g T\left[G_m - \tilde{G}_1 - \tilde{G}_1\left\{|A_1|^2 + \left|A_1\left(\sigma - \frac{2\tau_2}{T}\right)\right|^2\right\}\right], \tag{4.47}$$

$$\partial_\sigma \tilde{Q}_1 = \gamma_q T\left[Q_m - \tilde{Q}_1 - 2\tilde{s}\tilde{Q}_1|A_1|^2\right]. \tag{4.48}$$

As only the first-order of the power expansion is left, the index of the variables A_1, G_1, Q_1 can be dropped in the following.

Final Model and Boundary Condition

A final nonlocal HME exhibiting the same variable and parameter normalisations as the DDE system, is found by reverting the normalisations introduced at the start of the derivation. Firstly, these include $E = \sqrt{T}\gamma_g A$ and $\tilde{s} = s\frac{\gamma_g}{\gamma_q}$. Furthermore, the old charge carrier variables and parameters prior to the introduction to the smallness parameter according to eq. (4.25)-(4.27) are reintroduced. Additionally, the slow time scale is rescaled with respect to the smallness parameter according to $\theta/\varepsilon^2 = \theta$ (the same symbol is kept for simplicity). Finally,

all rates are normalised to the round-trip time. The final nonlocal Haus master partial differential equation model for the V-shaped VECSEL reads

$$\partial_\theta E(\theta,\sigma) = \frac{1}{2\gamma^2}\partial_\sigma^2 E(\theta,\sigma) + \left\{\frac{1}{2}\left[1-i\alpha_g\right]\left[G\left(\theta,\sigma-\frac{T-2\tau_2}{T}\right)+G(\theta,\sigma)\right] + \left[1-i\alpha_q\right]Q(\theta,\sigma)+\frac{1}{2}\log(\kappa)+i\omega\right\}E(\theta,\sigma), \tag{4.49}$$

$$\partial_\sigma G(\theta,\sigma) = J_g - \gamma_g G(\theta,\sigma) - G(\theta,\sigma)\left[|E(\theta,\sigma)|^2 + \left|E\left(\theta,\sigma-\frac{2\tau_2}{T}\right)\right|^2\right], \tag{4.50}$$

$$\partial_\sigma Q(\theta,\sigma) = J_q - \gamma_q Q(\theta,\sigma) - 2sQ(\theta,\sigma)|E(\theta,\sigma)|^2, \tag{4.51}$$

where ω is introduced as a parameter to adjust the rotating frame. The pump power and unsaturated absorption are expressed by means of $J_g = G_0\gamma_g$ and $J_q = Q_0\gamma_q$ to achieve a closer resemblance with the DDE model. However, this has to be kept in mind when varying the relaxation rates. Note that Q and Q_0 are negative quantities here, as in the DDE system. Interestingly, the time delayed terms in the DDE system transform to a nonlocal influence in the Haus master equation system, if the delay does not equal one cavity round-trip. This opens up the possibility to interpret the second gain depletion as a nonlocal influence on the electric field, which can be altered via the cavity geometry. The global binding mechanism of the photonic molecules hence also stems from the gain nonlocality, trapping a pulse between the first and second (nonlocal) gain depletion of its predecessor, similar to the nested molecules discussed in Reference [JAV17]. The influence of shifting the cavity arms and therefore altering the nonlocal contribution is discussed in the next section.
The numerical integration of the system is performed by applying the Fourier split-step algorithm introduced in the Appendix of Reference [GUR17], which is outlined in detail in Appendix B.1. For each round-trip θ, one finds a solution for all points in σ in one round-trip, i.e. σ ranging from 0 to 1. To correctly model the transition from round-trip to round-trip $\theta \to \theta+1$ while maintaining the long-term charge-carrier memory, one has to connect the last point of the integration domain $(\theta, \sigma = 1)$ to the first point of the subsequent round-trip $(\theta+1, \sigma = 0)$. In the long-cavity regime, the gain is able to completely relax to the equilibrium value in between two pulse passes. Therefore, the simple boundary condition $G(\theta+1, 0) = G_0$ can be utilised for the path-continuation as well as direct numerical integration, if the round-trip time is very long. For the absorber $G(\theta+1, 0) = Q_0$ can always be used, as it recovers much faster than the gain.
However, the gain does not necessarily relax fully till the end of the round-trip, for the relaxation rates and round-trip times in the intermediate-cavity regime. Consequently, a different boundary condition maintaining the carrier memory in the gain is required. The natural boundary condition is the asynchronous map boundary condition $G(\theta+1, \sigma = 0) = G(\theta, \sigma = 1)$ arising from assuring the continuity of the solution. Nevertheless, utilising an asynchronous boundary condition is not always convenient. A solution to this problem is presented in section 5.2, where a dynamical boundary condition for the gain is derived.

Agreement of Haus Master Equation and DDE Model

To assess the agreement of the DDE and HME partial differential equation model in the localised regime, a bifurcation analysis of the pulsed states is performed. Depicted in Fig. 4.23(a) is a 1D-bifurcation diagram showing the maximum pulse amplitude $\max(|E|)$

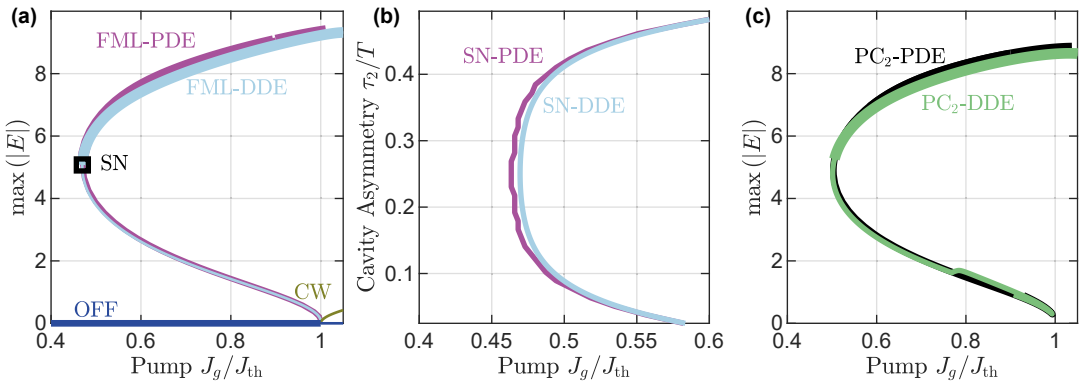

Figure 4.23.: (a) 1D-Bifurcation diagram displaying the evolution of the maximum electric field amplitude max(E) along the fundamental mode-locking solution (FML) continued in pump power (J_g/J_{th}). The magenta coloured line is obtained utilising the Haus master partial differential equation model (PDE) and the path-continuation software PDE-2-Path, whereas the light blue bifurcation line is found using the DDE model of mode-locking (3.48)-(3.51) applying the software DDE-biftool. (b) 2D-bifurcation diagram in the (J_g, τ_2)-plane of the saddle-node bifurcation point marked by SN in (a) for both models. The DDE line is determined by applying DDE-biftool, whereas the PDE line is determined by direct numerical integration. (c) Same 1D-bifurcation diagram as in (a) but for the PC$_2$ solution in the Haus master PDE (black) and the DDE model (green). All parameters are given in Table 4.1. Figure adapted from [HAU20].

along the fundamental mode-locking (FML) solution branch continued in J_g. The light blue line corresponds to the FML solution in the DDE model. It is the same as already discussed in Fig. 4.20(a$_1$). The magenta coloured line (FML-PDE) represents the fundamental solution branch obtained from the PDE model. To continue this solution branch, the software package pde2path [UEC14] is utilised[26]. Starting from the lowest amplitudes in the lower unstable part of the branches, their course almost matches perfectly until the minimum in J_g. It is marked by a black square (SN) and is given by a saddle-node bifurcation at which the fundamental solution turns stable. The type of the bifurcation point is equal for both models and the stabilising dynamics are depicted by thick lines. In the upper part of the branch, the solutions slightly differ in pulse amplitude, but both remain stable. The slight deviation might be caused by the simple boundary condition $G(\theta, \sigma = 0) = G_0$, as the gain does not relax completely for the round-trip time of $T = 1.875\,\text{ns}$ utilised here. Therefore, the pulses experience a slight excess gain in the PDE model compared to the DDE model as the gain is always set to the equilibrium level G_0 at the start of the round-trip. A further reason for the deviation may lie within the linearisation applied in the derivation of the HME model, which becomes of more importance at increasing field amplitudes.
Plotted in Fig. 4.23(b) is a 2D-bifurcation diagram of the SN point (black square in (a)) in the parameter plane of the pump power and cavity asymmetry (J_g, τ_2). It shows how the lower stability boundary of the FML solution shifts in pump power, if the cavity geometry is altered while the round-trip time T is left constant[27]. Again, the magenta line is obtained using the Haus master PDE model and the light blue line corresponds to the result of the DDE model. In contrast to the DDE model, the PDE line is determined by direct numerical

[26] The path-continuation utilising pde2path was performed by Svetlana V. Gurevich from WWU Münster.
[27] How the cavity geometry is represented by the delays τ_1 and τ_2 can be looked up in section 3.2 and 3.3. Experimentally, the shift can be understood as a repositioning of the gain chip inside the cavity, i.e. closer to the outcoupling facet or absorber chip.

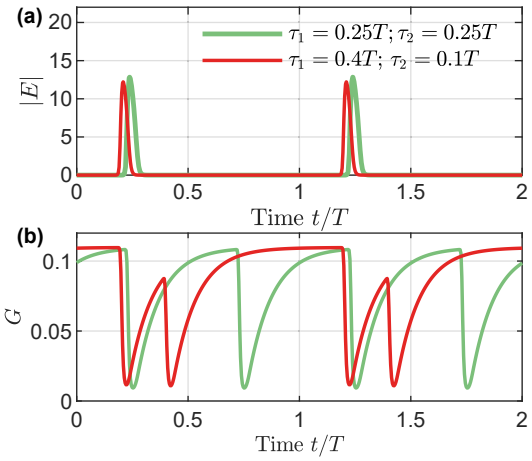

Figure 4.24: (a) Time-series of the FML electric field amplitude calculated at a symmetric cavity configuration of $\tau_1 = \tau_2 = T/4$ (green) and at cavity configuration of $\tau_1 = 0.4T$; $\tau_2 = 0.1T$ (red). (b) Time-series of the gain corresponding to the solution plotted in (a). Laser parameters according to Table 4.1 and $J_g/J_{\mathrm{th}} = 0.6$.

integration and not path-continuation. Nonetheless, the two lines indicated a very similar behaviour. The slight roughness of the SN-PDE line can be reasoned by the accuracy of the direct numerical integration. Furthermore, it is evident that the SN-PDE line is situated at slightly lower pump currents, especially for a symmetric cavity ($\tau_2 = 0.25T$). As before, this can be reasoned by the increased gain induced by the use of the boundary condition. It has to be noted that for the direct numerical integration the boundary condition outlined in sec 5.2 is used.

The general course of the saddle-node bifurcation line to higher pump powers with increasing cavity asymmetry (shifting τ_1, τ_2 away from the symmetric position) can be reasoned by the adjusted gain depletion scenario. If τ_1 is altered while maintaining a constant round-trip time fullfilling the boundary condition $T = 2\tau_1 + 2\tau_2 = \text{const}$, it effectively leads to an adjustment of the distance between the two gain depletions. A visualisation of the changed gain depletion and electric field dynamics induced by an increase of τ_1 (and simultaneous decrease in τ_2) is shown in Fig. 4.24. The red curve in Fig. 4.24(b) represents the gain dynamics in the asymmetric case ($\tau_1 = 0.4T$; $\tau_2 = 0.1T$), whereas the green line corresponds to the symmetric cavity situation. It becomes evident that the distance between the first and second gain depletion decreases with respect to the symmetric case in which all gain depletions are spaced equidistantly. However, after the pulse has passed the gain chip twice in the asymmetric cavity, there is a long relaxation period (increase at $t \approx 1$ in Fig. 4.24(b)). It is caused by the enlargement of the second cavity arm caused by the condition of a constant cavity length $T = 2\tau_1 + 2\tau_2$. The asymmetry in the gain relaxations leads to less available gain, because the gain relaxes most effectively shortly after the depletion due to its exponential recovery. Therefore, a higher pump power is necessary to achieve the same amplification/ level of available gain, which manifests in a shift of the lower stability boundary, i.e. SN bifurcation point. Additionally, the pulse amplitude slightly decreases in the asymmetric cavity as indicated in Fig. 4.24(a). An in-depth investigation of the influence of the cavity asymmetry on the stabilisation multi-pulse structures and the pulse distance within the PC solutions is given in the next section.

The 1D-bifurcation lines of the PC_2 solution along J_g match very well across the two models as visualised by the black (PDE) and green line (DDE) in Fig. 4.20(a_3). Again, the minimum in J_g is represented by a saddle-node bifurcation in both models and its position in J_g lies very close. The slight deviation of the maximum pulse amplitude in the upper part of the branch is again related to the boundary condition and the linearisation of the exponential

terms.
At this point it has to be noted, that the application of pde2path is much more cumbersome than that of DDE-biftool. In the stability analysis (of the PC_2) obtained using pde2path, several bifurcation points of unclear origin occurred. Anyhow, they were not further investigated, due to the beta stadium of the software.

4.3.4 Impact of Asymmetry

In both models used investigate the passively mode-locked V-shaped VECSEL, the cavity geometry is described by means of the delay times τ_1 and τ_1, as described in the derivation of the DDE model (section 3.3) and the Haus master PDE model (section 4.3.3). The two delay parameters represent the time a pulse needs to pass the respective cavity arm. As outlined before, the delayed terms in the DDE model transform to nonlocal terms in the Haus master PDE, if the delay does not equal the cavity round-trip time. Changing the cavity geometry can have a substantial influence on the stability boundaries of the different mode-locking states and hence on the stabilising laser dynamics. This is mainly induced by the changed gain depletion scenario, because a strongly asymmetric cavity configuration primarily leads to unequidistantly distributed gain depletions. For the high performance mode-locking regime, the introduction of a slight asymmetry is discussed in section 4.2.4. It has to be highlighted that the term "asymmetric" here only refers to the unequal length of the cavity arms. In this section the initial investigation of the influence of an asymmetric cavity configuration on the single-pulse FML state in the localised state regime is extended to the PC_n and HML_n multi-pulse solutions[28].
As presented for the fundamental localised mode-locking solution in Fig. 4.23(b), the examination of the stability regions of harmonic mode-locking is performed by a bifurcation analysis. On that account, the critical bifurcation points are continued in the parameter plane of the cavity asymmetry and pump power (J_g/J_{th}, τ_2/T). As outlined previously, the total cavity length is kept constant by oppositely varying the length of the cavity arms, i.e. maintaining the boundary condition $2\tau_1 + 2\tau_2 = T = \mathrm{const}$. Namely, the critical bifurcation points are the saddle-node bifurcations (SN) representing the characteristic curvature of the solution branches as well as the minimum pump power value required for the existence of the corresponding solution and the stabilising torus bifurcation. The SN and torus bifurcation (T) are both exemplarily depicted in Fig. 4.20(a_1).
The obtained 2D-bifurcation lines of the saddle-node and torus bifurcations in the (J_g/J_{th}, τ_2/T)-plane are plotted in Fig. 4.25 for the harmonic mode-locking solutions up to fourth order (four equal and temporally equidistant pulses in the cavity). From the course of the bifurcation lines, one can clearly identify a resonance behavior with respect to the cavity asymmetry τ_2 [HAU20]. For the saddle-node bifurcations in Fig. 4.25(a), it is embodied by the occurrence of local maxima and minima in pump power at characteristic cavity geometries (values of τ_2). This effect critically depends on the number of pulses in the cavity as the number of resonance points (pump power minima) linearly increase with the number of pulses in the corresponding solution. The torus bifurcations almost display the same resonance structure. Yet, instead of local maxima in pump power no stabilising torus bifurcation can be found for certain cavity configurations and the curves in Fig. 4.25(b) are discontinuous. These parameter points in τ_1, τ_2 are characterised by a collision of two pulses in the gain chip. They occur if the temporal distance between the pulses in the harmonic mode-locking

[28] Most parts of this section were published in [HAU20].

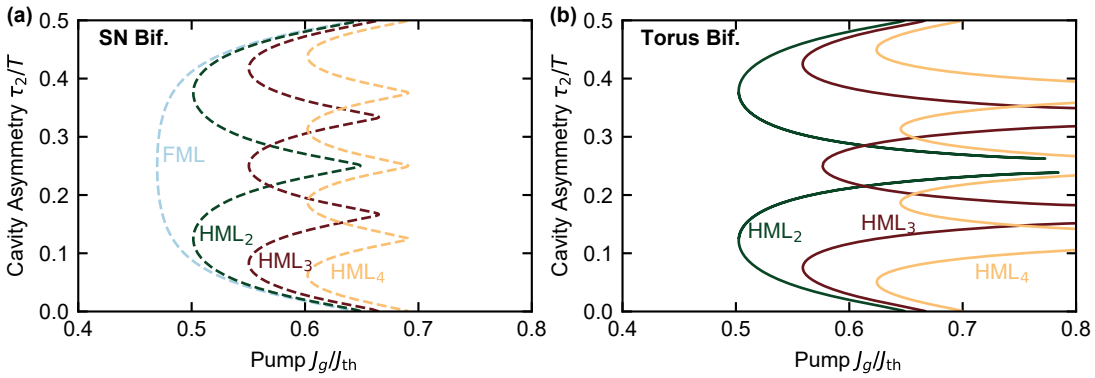

Figure 4.25.: (a) Bifurcation lines in the parameter plane of pump power and cavity asymmetry (J_g, τ_2). The cavity asymmetry is varied, while maintaining a constant round-trip time. Shown are the saddle-node (SN) bifurcations representing the minimum pump power at which the localised fundamental (FML) and harmonic mode-locking solutions (HML$_n$) exist. The SN point is marked by a black square in Fig. 4.20(a$_1$) exemplarily for the FML solution and embodies the characteristic curvature of the solution branches. (b) Bifurcation lines of the torus bifurcations (T) at the lower stability boundaries of the localised harmonic mode-locking solutions (HML$_n$). The torus point is marked by a black circle in Fig. 4.20(a$_1$) exemplarily for the HML$_3$ solution. Laser parameters according to Table 4.1. Figure adapted from [HAU20].

solution equals the propagation time between the two gain passes (e.g. $2\tau_2 = T/2$ for HML$_2$ or $2\tau_2 = 0.33T$ for HML$_3$) [HAU20]. This scenario can be found once for the HML$_2$ solution as it contains two pulses that can collide. However, for the HML$_3$ solution a further possibility of a pulse collision opens up due to the additional pulse and their resulting reduced temporal distance in the cavity (e.g. the first and second or the first and third pulse can collide). Therefore, an additional unstable point can be found. This behaviour continues with an increasing number of equidistant pulses.

Oppositely, the local minima in pump current of saddle-node and torus bifurcation lines correspond to the most favourable situation in terms of the pulse amplification. Due to the pulse-passes happening at the largest possible temporal interval, the maximum gain saturation can be achieved at these cavity configurations for the harmonic mode-locking solutions. The increased gain relaxation between pulse passes leads to a higher available gain and consequently the solutions can exist (stably) at lower pump powers. The maximised pulse amplification also explains why in a symmetric cavity the PC$_2$ solution is stable, while the HML$_2$ is not. As indicated by the gain landscape of the respective solutions shown in Fig. 4.20(a$_3$) and Fig. 4.20(c$_2$), the PC$_2$ solution induces four gain depletion whereas the HML$_2$ only creates two.

In order to obtain a broader overview of the multistability of the localised states, the bifurcation scenario is investigated by means of direct numerical integration. In the subthreshold regime of localised states, the *off*-solution cannot serve as the initial condition to start the laser, because it is stable and therefore the laser would just remain in this state. Furthermore, due to the large multistability unravelled by the previously presented bifurcation analysis, the choice of the initial condition has a large influence on the stabilising dynamics. As discussed in section 4.3.2, different pulsed states can be excited by applying perturbations to the pump current. This technique is followed to excite selected stable dynamics at characteristic cavity configurations based on the bifurcation analysis in Fig. 4.25. Subsequently, these stable states can be used as the initial condition of the direct numerical integration at each

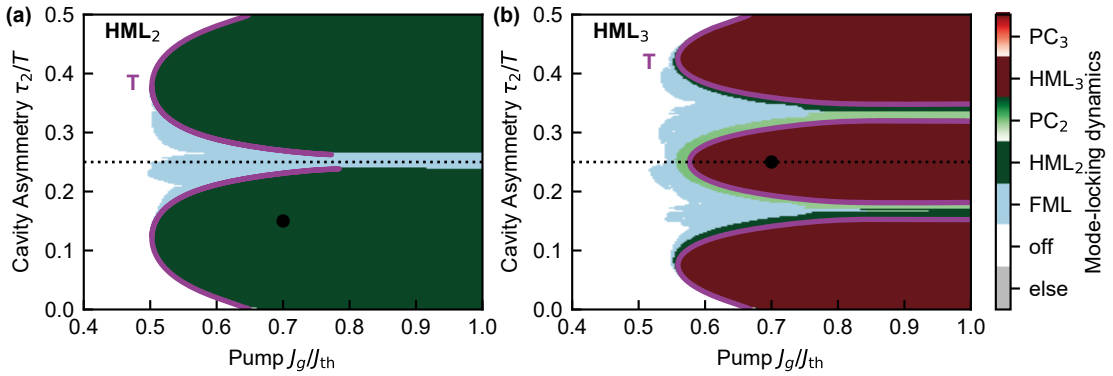

Figure 4.26.: 2D-bifurcation diagrams in the (J_g, τ_2) parameter plane in the localised regime indicating the stabilising dynamics. The cavity asymmetry is varied, while maintaining a constant round-trip time, which is assured by fulfilling the boundary condition $T = 2\tau_1 + 2\tau = \text{const}$. The colour code distinguishes between fundamental mode-locking (FML), pulse cluster solutions (PC_n) and harmonic mode-locking solutions (HML_n) with n referring to the number of pulses. The white coloured region represents the laser *off*-state. At each parameter pair (J_g, τ_2), a stable solution is utilised as the initial condition of the direct numerical integration ($3 \cdot 10^4$ round-trips). The utilised solutions are (a) HML_2 and (b) HML_3. The initial conditions are determined as the stable solutions after $3 \cdot 10^4$ transient round-trips at the parameter pairs $(J_g/J_{\text{th}}, \tau_1) = (0.7, 0.15)$ for (a) and $(J_g/J_{\text{th}}, \tau_1) = (0.7, 0.25)$ for (b). The shading of the red and green colour code represents the distance between the pulses in the PC solution with the darkest region corresponding the maximum possible distance (transition to HML solution). The other laser parameters are chosen according to Table 4.1.

parameter point of interest in the parameter plane of cavity asymmetry and pump power (J_g, τ_2). After a transient time of $3 \cdot 10^4$ round-trips, the converged state is evaluated with respect to the pulse properties and pulse distance. Experimentally, this would correspond to "seeding" the laser with a certain pulse pattern and observe its reaction, i.e. the resulting stable emission state at varied cavity configurations.

The 2D-bifurcation diagrams obtainable by seeding the HML_2 and HML_3 solution as the initial condition is depicted in Fig. 4.26. The stabilising dynamics are depicted by the colour code with blue corresponding to the fundamental mode-locking solution, dark green indicating HML_2, and dark red indicating HML_3. The shading of the red and green colours illustrates the temporal pulse distance within one pulse cluster PC_n. The darkest colour corresponds to the transition from a PC_n to a HML_n state as the latter represents the largest possible pulse distance within the cavity[29]. However, starting from the HML solutions leads to a case where almost no PC solutions stabilise. This changes if PC solutions are seeded into the cavity, which is discussed later in this section. The symmetric cavity configuration is depicted by the black dotted line and the black circles in (a) and (b) depict the parameter points at which the initial condition is initially stable ($J_g = 0.7 J_{\text{th}}$).

The previously discussed stabilising torus bifurcations (see Fig. 4.25) of the respective HML_n solution are plotted as magenta lines in Fig. 4.26(a,b). These match the direct numerical integration result very well. Once more, the resonance effect with respect to the cavity asymmetry is clearly visible as the HML_n solutions destabilise at the previously discussed characteristic cavity configurations at which the pulses collide at the gain chip. These points fall together with the discontinuity of the torus lines. The irregularities at the boundaries of the FML solution can be explained by the initial condition being closer to the attractor of

[29] Here, only the smaller distance within the pulses is investigated.

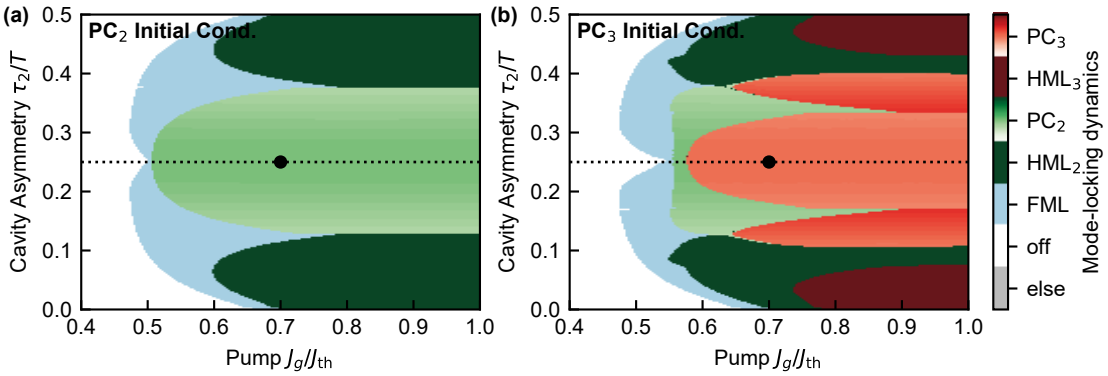

Figure 4.27.: Numerical 2D-bifurcation diagrams in the (J_g, τ_2) parameter plane in the localised regime indicating the stabilising dynamics when seeding PC_n solutions. The cavity asymmetry is varied, while maintaining a constant round-trip time, which is assured by fulfilling the boundary condition $T = 2\tau_1 + 2\tau = \text{const}$. The colour code is the same as in Fig. 4.26 with the difference that here at each parameter pair (J_g, τ_2) a stable (a) PC_2 and (b) PC_3 solution are used as the initial conditions. They can be found as the stable solutions after $3 \cdot 10^4$ transient round-trips at a symmetric cavity configuration (black dashed line) and $J_g/J_{\mathrm{th}} = 0.7$. Laser parameters according to Table 4.1. Figure adapted from [HAU20].

the *off*-solution than to the FML solution. Thus, the system stabilises in the *off*-state.
As the continuation of the characteristic bifurcations of the PC solutions is very cumbersome at high round-trip times, the influence of the cavity asymmetry is investigated only by means of direct numerical integration. On that account, the same technique of using a stable solution as the initial condition is applied. Nevertheless, in this case different PC_n solutions are chosen as the starting point of the direct numerical integration in order to unravel their multistability.
The resulting dynamics from seeding the PC_2 and the PC_3 solution into the laser as the initial condition is plotted in Fig. 4.27. The colour code distinguishes the dynamics equally as in Fig. 4.26. Importantly, the shading of the red and green colours illustrates the temporal pulse distance within one pulse cluster with ascending pulse distance from bright to dark colours. The darkest shading corresponds to the maximum pulse distance and therefore to the transition from PC to HML dynamics. Again, the black dotted line indicates the symmetric cavity configuration and the black circles show the origin of the stable solutions ($J_g = 0.7 J_{\mathrm{th}}$).
Similar to the behaviour of the HML_n states, a resonance with respect to the cavity configurations can be found for the PC_n solutions. The symmetric cavity configuration represents the energetically most favourable situation in terms of pulse amplification due to the equidistant gain depletion. Therefore, the minimum in pump current at which the solutions stabilise coincides with this characteristic point for the PC_2 and PC_3 pulse cluster.
If the cavity is shifted away from the symmetric arrangement, the pulses adapt to the changed gain depletion scenario by adjusting their temporal distance within the cluster as an additional degree of freedom. This is visible from the brightening shading in Fig. 4.27 when τ_2 deviates from the central position. An example of the distance adjustment in the electric field dynamics are plotted in Fig. 4.28(a), showing two differently spaced pulse clusters at a symmetric (green) and asymmetric cavity configuration (red). The associated gain dynamic is plotted in Fig. 4.28(b). The gain dynamics in the shifted cavity (red) unravels that an

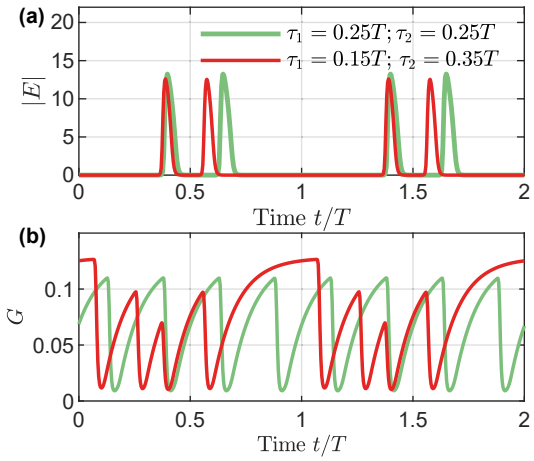

Figure 4.28: (a) Time-series of the electric field amplitude calculated at a symmetric cavity configuration $\tau_1 = \tau_2 = T/4$ (green) and at cavity configuration of $\tau_1 = 0.15T$; $\tau_2 = 0.35T$ (red). (b) Time-series of the gain corresponding to the solution plotted in (a). Laser parameters according to Table 4.1 and $J_g/J_{\mathrm{th}} = 0.7$.

adjustment of τ_2 shortens the temporal distance between the four gain depletions in one round-trip, but leads to a very long relaxation period after the complete pulse cluster has passed the gain. Because of its exponential behaviour, the gain relaxes much less at the end of the long period, than in the steep region shortly after the depletion. This energetically less favourable redistribution of the relaxation leads to slightly smaller pulses (c.f. red and green pulses in Fig. 4.28(a)) and is the reason for the shifting of the lower stability boundary to higher pump currents.
Furthermore, it is possible to deduce that at strongly asymmetric cavity configurations only HML_n solutions stabilise although PC_n solutions are seeded into the cavity. In the strongly asymmetric case, the two gain depletions of a single pulse lie very close together. Hence, it is not favourable for an additional pulse to fit in between these to depletions to form a cluster, because it would result in three very short gain relaxation periods and one very long one (see Fig. 4.28(b)). As discussed before, long gain relaxation periods are energetically much less favourable with respect to the pulse amplification.
Although the cavity setup itself is asymmetric with an output coupler at the one end and the absorber on the other end, this does not make an impact in the investigated regime. The changes in dynamics as well as the adjustment of the temporal distance occur in a symmetric fashion around $\tau_2 = T/4$, i.e. the symmetric configuration (see dashed line in Fig. 4.27). This can be reasoned by the time scales of the system. The absorber recovers on several magnitudes faster than the round-trip time $\gamma_q T > 300$. Thus, a notable difference between the gain-chip being situated close to the outcoupling facet ($\tau_2 \to T/2$) or the absorber chip ($\tau_2 \to 0$) is only to be expected, if the distance is on the time scale of the order of the absorber relaxation. Furthermore, it has to be noted that the unsaturated absorption $J_q = -20$ ($Q_0 = -0.177$) is small in the investigated regime, which leads to a reduced influence of the absorber. It has to be mentioned that the introduction of low non-zero line-width enhancement factors only has a very slight influence on the bifurcation lines in the investigated parameter regime. A 2D-bifurcation diagram for $\alpha_g = 1.5$,$\alpha_q = 0.5$ is shown in Appendix C. In this case, the adjustment of the pulse distance with changing cavity geometry is maintained. The only striking difference in case of non-zero α-factors is the stabilisation of the PC_4 solution at higher pump currents, which is related to the PC_4 attractor basin being closer to the used initial condition.

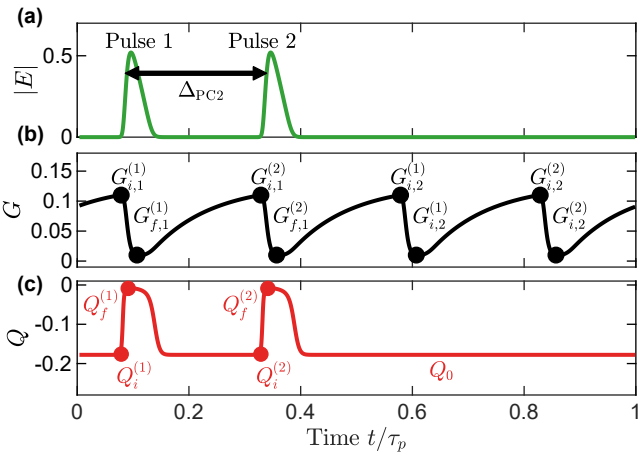

Figure 4.29: (a) Dynamics of the electric field amplitude in one period τ_p of the PC_2 solution. The black arrow indicates the analytically determined pulse distance Δ_{PC}. (b) One period of the gain dynamics of the PC_2 solution. The critical points at the start of the fast and slow stage, that are approximated using eqs. (4.52)-(4.60), are marked by black circles. (c) One period of the absorber dynamics of the PC_2 solution. Red circles mark the critical points approximated by eqs. (4.61)-(4.64). Figure adapted from [HAU20].

Analytic Determination of the Pulse Distance

From an application point of view, the adjustment of the temporal distance within a pulse clusters opens up the possibility to tailor distinct pulse patterns by means of altering the cavity geometry. Due to their incoherence, these pulsed structures would exhibit an unmodulated spectrum (see Fig. 4.22) and therefore could be used for spectroscopy implementations in chemistry or biology [DEM14]. In consequence, the underlying physical mechanisms are not only of interest from a fundamental perspective. In this subsection, a simple analytical expression describing the nonlinear dependence of the pulse distances Δ_{PC_n} on the cavity geometry (T, τ_1, τ_2) is determined. It reveals that the dominant influences on the pulse distance can be approximated by the slow time scales of the gain relaxation rate and length of the cavity arms[30]. The searched distance Δ_{PC_n} is illustrated for the PC_2 solution in Fig. 4.29(a).

As a starting point, the gain and absorber dynamics are decomposed into slow and fast stages. The former correspond to the relaxation of the carriers, whereas the latter refer to the interaction of the carriers with the electric field, i.e. depletion (saturation) of the gain (absorber). The gain and absorber values at the start of the fast stage are indicated by the filled circles at the higher absolute gain and absorber levels in the time-series presented in Fig. 4.29(b)-(c). They are labelled as $G_{i1,2}^{(n)}$ and $Q_i^{(n)}$, where n refers to the pulse (see 4.29(a)) causing to the following depletion/saturation. The subscript i points out that the charge carrier value is the "initial" value before a depletion. The number in the subscript of the gain expression corresponds to the interaction being the first 1 or second 2 of pulse n in one round-trip [HAU20]. As the absorber is only passed once by each pulse, the indexing is not necessary.

The end of the fast stage is depicted by the circles close to 0 in the time-series of the gain and absorber dynamics in Fig. 4.29(b)-(c). The labelling is as before ($G_{f1,2}^{(n)}$ and $Q_f^{(n)}$) with the only difference being that the first subscript is f, which refers to the "final" value after the depletion/saturation.

To find algebraic expressions for the characteristic points in the gain and absorber dynamics shown in Fig. 4.29(b)-(c), three simple initial approximations are made. Firstly, an exponential recovery of the gain in between pulses passes is assumed. Secondly, the amount of depletion is modelled to be proportional to the pulse energy P according to $\propto e^{-P}$ [IPP94].

[30] The derivation was published in [HAU20].

Here, the pulse energy is defined as $P = \int_{-\varepsilon}^{+\varepsilon} |E|^2 d\sigma$ with the pulse width ε. Finally, the pulse width is assumed to be very narrow $\varepsilon \to 0$.
Applying these three assumptions one can recover the following sequence of algebraic equations approximating the gain dynamics at the critical points in one round-trip

$$t = -\varepsilon \quad , \quad G_{i1}^{(1)}, \tag{4.52}$$

$$t = +\varepsilon \quad , \quad G_{f1}^{(1)} = G_{i1}^{(1)} e^{-P_1}, \tag{4.53}$$

$$t = \Delta - \varepsilon \quad , \quad G_{i1}^{(2)} = G_{f1}^{(1)} e^{-\gamma_g \Delta} + G_0[1 - e^{-\gamma_g \Delta}], \tag{4.54}$$

$$t = \Delta + \varepsilon \quad , \quad G_{f1}^{(2)} = G_{i1}^{(2)} e^{-P_2}, \tag{4.55}$$

$$t = 2\tau_2 - \varepsilon \quad , \quad G_{i2}^{(1)} = G_{f1}^{(2)} e^{-\gamma_g (2\tau_2 - \Delta)} + G_0[1 - e^{-\gamma_g (2\tau_2 - \Delta)}], \tag{4.56}$$

$$t = 2\tau_2 + \varepsilon \quad , \quad G_{f1}^{(2)} = G_{i2}^{(1)} e^{-P_1}, \tag{4.57}$$

$$t = 2\tau_2 + \Delta - \varepsilon \quad , \quad G_{i2}^{(2)} = G_{f2}^{(1)} e^{-\gamma_g \Delta} + G_0[1 - e^{-\gamma_g \Delta}], \tag{4.58}$$

$$t = 2\tau_2 + \Delta + \varepsilon \quad , \quad G_{f2}^{(2)} = G_{i2}^{(2)} e^{-P_2}, \tag{4.59}$$

$$t = T \quad , \quad G_{i1}^{(1)} = G_{f2}^{(2)} e^{-\gamma_g (T - 2\tau_2 - \Delta)} + G_0[1 - e^{-\gamma_g (T - 2\tau_2 - \Delta)}], \tag{4.60}$$

where Δ refers to the distance of the pulses and the index of the pulse power P distinguishes pulse 1 and 2. As before, γ_g is the gain relaxation rate.
To find a sequence of algebraic equations for the absorber, two further simplifications can be made. As the absorber recovers on a much faster time scale than the gain, it relaxes to the equilibrium Q_0 between each pulse pass and therefore the exponential recovery does not need to be modelled. Furthermore, the absorber chip is only passed once per round-trip, leading to less critical points in the dynamics. Finally, the sequence of equations for the absorber can be written as

$$t = -\varepsilon \quad , \quad Q_i^{(1)} = Q_0, \tag{4.61}$$

$$t = +\varepsilon \quad , \quad Q_f^{(1)} = Q_0 e^{-2sP_1}, \tag{4.62}$$

$$t = \Delta - \varepsilon \quad , \quad Q_i^{(2)} = Q_0, \tag{4.63}$$

$$t = \Delta + \varepsilon \quad , \quad Q_f^{(2)} = Q_0 e^{-2sP_2}, \tag{4.64}$$

where the normalisation factor s is proportional to the ratio of the differential gain coefficients in gain and absorber, scaling the absorber modulation in the DDE and HME model and γ_q is the absorber relaxation rate.
The found system of algebraic equations can now be solved to find an expression for Δ. On that account, the pulses within one cluster are assumed to be equal, which is a valid approximation in the localised state regime close to the symmetric cavity. It can be assessed by means of the autocorrelation. For the pulses to be equal, they require to experience the same effective gain, which yields the condition

$$G_{i1}^{(1)} + G_{i2}^{(1)} = .. = G_{i1}^{(n)} + G_{i2}^{(n)}, \tag{4.65}$$

relating the gain depletions of all pulses (here only $n = 2$ is required). Solving the whole system of algebraic equations then leads to the following relation between the pulse power P and the temporal pulse distance Δ

$$e^{2P} = \frac{2e^{\gamma_g \Delta} - e^{\gamma_g (2\tau_2 - \Delta)} - e^{\gamma_g (T - \Delta - 2\tau_2)}}{2e^{\gamma_g (T - \Delta)} - e^{\gamma_g (2\tau_2 + \Delta)} - e^{\gamma_g (T + \Delta - 2\tau_2)}}. \tag{4.66}$$

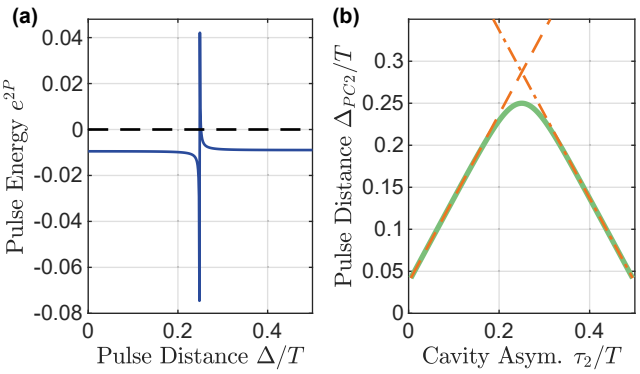

Figure 4.30: (a) Pulse energy as a function of the pulse distance obtained from the expression eq. (4.66). The black dashed line marks a pulse energy of $P > 0$, which is only physically relevant. (b) Analytically determined pulse distance Δ_{PC} within the PC_2 solution (green) as a function of the cavity asymmetry under the boundary condition $T = 2\tau_1 + 2\tau_2 = \text{const}$. The orange lines determine the asymptotic behaviour of the pulse distance for $\tau_2 \to 0$ and $\tau_2 \to T/2$ according to eq. (4.69) and (4.70). Figure adapted from [HAU20].

Analysing this expression one finds that it is negative across almost all pulse distances Δ as indicated in Fig. 4.30(a). The only exception is the region close to the singular point labelled as Δ_{PC2}. As a negative pulse energy is not possible, physical arguments restrict the solution of eq. (4.66) to be at Δ_{PC2}. At this point, e^{2P} is positive valued and all values of the pulse energy are spanned rapidly. Hence, one can solve eq. (4.66) for the pole to incorporate the conditions imposed by physical arguments. This yields the following expression

$$2e^{\gamma_g(T-\Delta_{\mathrm{PC2}})} - e^{\gamma_g(2\tau_2+\Delta_{\mathrm{PC2}})} - e^{\gamma_g(T+\Delta_{\mathrm{PC2}}-2\tau_2)} = 0. \tag{4.67}$$

Rearranging with respect to Δ_{PC2} then leads to the function

$$\Delta_{\mathrm{PC2}}(\gamma_g, T, \tau_1, \tau_2) = \frac{T-2\tau_2}{2} - \frac{1}{2\gamma_g}\log\left(\frac{1+e^{\gamma_g(T-4\tau_2)}}{2}\right). \tag{4.68}$$

This function relates the pulse distance within the PC_2 solution to the gain relaxation and the cavity geometry. The resulting behaviour of the pulse distance with respect to the cavity geometry at fixed round-trip times $T = 1.875\,\mathrm{ns}$ and $\gamma_g = 5\,\mathrm{ns}$ is visualised by the green line in Fig. 4.30(b). Close to the symmetric cavity configuration at $\tau_2 = \tau_1 = T/4$, the pulse distance responds nonlinearly to changes in the cavity geometry with an approximately quadratic dependence on τ_2. However, in the limit of small and large τ_2, i.e. the gain chip being positioned closely to the absorber chip or outcoupling facet, the behaviour becomes approximately linear. This can recovered by recovering the asymptotic behaviour of equation (4.68) in the limit of large and small τ_2, which reads

$$\lim_{\tau_2\to 0}\Delta_{\mathrm{PC2}} = \tau_2 + \frac{\log(2)}{2\gamma_g}, \tag{4.69}$$

$$\lim_{2\tau_2\to T}\Delta_{\mathrm{PC2}} = \frac{T-2\tau_2}{2} + \frac{\log(2)}{2\gamma_g}. \tag{4.70}$$

These linear relationships are displayed by orange lines in Fig 4.30(b) and already match the full expression very well for small deviations from the symmetric configuration.
The same procedure can be followed to find an analytic expression for the pulse distance within the PC_3 pulse cluster Δ_{PC3}. The only adjustment that has to be conducted is that the gain (absorber) has to be approximated at four (two) additional points, resulting from

the interaction with the additional pulse in the cavity. Therefore, the following expression for Δ_{PC3} can be determined

$$\Delta_{\mathrm{PC3}}(\gamma_g, T, \tau_1, \tau_2) = \frac{T - 2\tau_2}{3} - \frac{1}{3\gamma_g} \log\left(\frac{1 + e^{\gamma_g(T-4\tau_2)}}{2}\right). \tag{4.71}$$

Thus, one can deduce that Δ_{PC2} and Δ_{PC3} follow the same nonlinear dependence on the cavity asymmetry, with the only difference between the two expressions eq. (4.68) and eq. (4.71) being a different factor in the denominators. The two analytic expressions are plotted as black lines in Fig. 4.31(a). The coloured lines represent the pulse distance found along the path continued PC_2 (green) and PC_3 solution (red) obtained utilising DDE-biftool[31]. The varied parameters in the path-continuation are τ_1 and τ_2 with the boundary condition $2\tau_1 + 2\tau_2 = T = \text{const}$. The pulse distance is determined from the electric field profile at each continuation point. Stable regimes along the branches are depicted by thick lines. In the stable regions, the analytic expressions (4.68) and (4.71) accurately match the path-continuation results.

The solution branches both become unstable, if the cavity geometry is shifted too far away from the symmetric configuration. Shortly after the destabilisation point (given by torus bifurcations) both branches loop back and cease to exist beyond a critical value of τ_2. Specifically, the pulse distance along the unstable parts beyond the looping point of the PC_2 solution grows again until the branch reconnects with the HML_2 solution at $\tau_2 \approx T/4$. The connection point can be found at the open ends in Fig. 4.31(a)-(b). Close to this point at $\tau_2 \to T/4$ the pulses deplete the gain almost simultaneously ($\Delta_{\mathrm{PC2}} \to T/2$). As outlined before, this is energetically less favourable in terms of the pulse amplification and leads to an unstable solution in this regime of the branch.

In contrast, the path-continuation of the PC_3 solution along τ_2 unravels a closed loop. It can be clearly identified when plotting the maximum pulse amplitude along the branch in a 1D-bifurcation diagram as shown by the red line in Fig. 4.31(b). One can deduce that the pulse distances are equal in the stable and unstable regions of the PC_3 solution as the regimes overlap in Fig. 4.31(a). Nevertheless, the maximum pulse amplitude varies strongly across the regimes. The same is true for pulse width given by the full width at half maximum plotted in Fig. 4.31(c).

The path-continuation results are in accordance with the previously discussed numeric result presented in Fig. 4.27(a)-(b) as the branches indicate the same decrease of the pulse distance with increasing cavity asymmetry. Furthermore, the branches reflect the less energetically favourable situation at shifted cavity configurations as the pulse width as well as the maximum amplitude decreases, which indicates a decrease in the pulse energy.

In summary, the pulse distance within the pulse clusters can be recovered by a simple analytical expression only depending on the cavity geometry (τ_1, τ_2, T) and the gain relaxation rate (γ_g). The expressions were validated by comparing them to a well matching path-continuation result. Finally, the results allow for the conclusion that the pulse distance within one cluster decreases, to adapt to the differing gain depletion scenario that is mainly determined by the cavity asymmetry and gain recovery time.

[31] Potentially this could also be recovered using the Haus master equation model with pde2path.

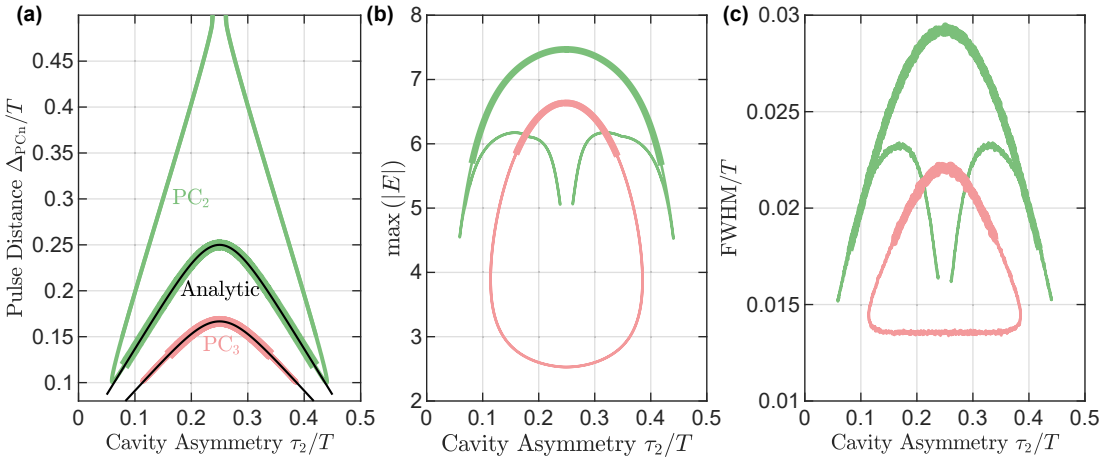

Figure 4.31.: (a) Pulse distance within the PC_2 (green) and PC_3 (red) solutions. The solutions are by determined continuing the respective solution branch in τ_2 using DDE-biftool, while maintaining a constant cavity round-trip time, i.e. $T = 2\tau_1 + 2\tau_2 = \text{const}$. Thick (thin) lines indicate stable (unstable) dynamics. The black lines indicate the analytic results according to eq. (4.68) and (4.71). (b) Maximum electric field amplitude in one period of the PC_2 (green) and PC_3 solution (red) along the same solution branch shown in (a). (c) Average full width at half maximum (FWHM) of the pulses within the PC_2 (green) and PC_3 solution (red) along the solution branch shown in (a). All parameters are given in Table 4.1 and $J_g/J_{\text{th}} = 0.65$. Figure adapted from [HAU20].

Analytic Determination of the Branch Structure

Using the nonlocal Haus master equation model (4.49)-(4.51) as a starting point, it is possible to derive an analytic approximation for the branch structure of the PC_2 solution and therefore of the characteristic saddle-node bifurcation defining the minimum pump power at which the PC_2 solution exists (see Fig. 4.20(c_1)). On that account, one combines the electric field equation with the decomposition of the gain (4.52)-(4.60) and absorber (4.61)-(4.64) as well as the found expression for the pulse distance eq. (4.68).
To simplify the electric field equation of the nonlocal Haus master equation model (4.49), the phase effects are neglected due to the small influence of realistic line-width enhancement factors on the boundaries of the PC_2 regime (see Appendix C). Additionally, New's approximation is applied [NEW74], which implies neglecting the spectral filtering embodied by the second derivative ∂_σ^2. This approximation is sufficient in the subcritical strongly nonlinear LS regime, if the outcoupling losses dominate [MAR14c, HAU20]. Hence, the electric field equation (4.49) can be transformed to a simplified equation for the intensity $|E|^2$, which reads

$$\frac{1}{2}\partial_\theta |E(\theta,\sigma)|^2 = \left\{\frac{1}{2}\left[G\left(\theta, \sigma - \frac{T-2\tau_2}{T}\right) + G(\theta,\sigma)\right] + Q(\theta,\sigma) + \frac{1}{2}\log(\kappa)\right\}|E(\theta,\sigma)|^2. \tag{4.72}$$

This equation is integrated over the fast time scale σ around the vicinity of each pulse within the PC_2 cluster, in order to find an expression for the relationship between pulse power and pump current. The position of pulse n on the fast time scale is written as σ_n. The integral $\mathcal{I}_n$ over each pulse n then gives

$$\mathcal{I}_n = \int_{\sigma_n-\varepsilon}^{\sigma_n+\varepsilon} \left[\frac{1}{2}\left[G\left(\theta, \sigma - \frac{T-2\tau_2}{T}\right) + G(\theta,\sigma)\right] + Q(\theta,\sigma) + \frac{1}{2}\log(\kappa)\right]|E|^2 d\sigma. \tag{4.73}$$

Where it is exploited that the derivative with respect to the slow time scale θ and the integration with respect to the fast time scale σ are exchangeable according to the Leibniz rule. Utilising the definition of the pulse power, one then obtains $\frac{dP}{d\theta}$ on the left hand side of the equation (4.72), which is 0 for the PC_2 steady state[32]. Based on New's stability criterion [NEW74, IPP94], equation (4.73) yields that the position of each pulse is given by the zeros of the integral $\mathcal{I}_n = 0$ as they represent the position of an opening net-gain window. This is defined as the point at which gain and losses exactly cancel out, closely before the net-gain becomes positive and the pulse is amplified.
Utilising the connection of the pump current (unsaturated absorption) and the equilibrium integrated carrier density in the gain $\gamma_g G_0 = J_g$ (in the absorber $\gamma_q Q_0 = J_q$), one can write the carrier equations of the Haus master equation model as

$$\partial_\sigma G(\theta,\sigma) = \gamma_g \left[G_0 - G(\theta,\sigma)\right] - G(\theta,\sigma)\left[|E(\theta,\sigma)|^2 + \left|E\left(\theta,\sigma - \frac{2\tau_2}{T}\right)\right|^2\right], \tag{4.74}$$

$$\partial_\sigma Q(\theta,\sigma) = \gamma_q \left[Q_0 - Q(\theta,\sigma)\right] - 2sQ(\theta,\sigma)|E(\theta,\sigma)|^2. \tag{4.75}$$

Assuming that the gain and the absorber have relaxed to their equilibrium close at the leading edge of a pulse implies $G_0 - G(\theta,\sigma) \approx 0$ and $Q_0 - Q(\theta,\sigma) = \approx$. In order to simplify the gain equation with regard to the nonlocality, one can make use of the characteristics of the investigated PC_2 solution. As no pulse exists at a distance of $\frac{2\tau_2}{T}$ to the pulse of interest and only the vicinity of the pulse is looked at, the nonlocal term in the gain equation becomes zero $\left|E\left(\theta,\sigma_n - \frac{2\tau_2}{T}\right)\right|^2 = 0$. Hence, the gain and absorber equations can be simplified to

$$\partial_\sigma G(\theta,\sigma) = -G(\theta,\sigma)I(\theta,\sigma), \tag{4.76}$$

$$\partial_\sigma Q(\theta,\sigma) = -2sQ(\theta,\sigma)I(\theta,\sigma). \tag{4.77}$$

To find an approximation for the nonlocal term in the integral (4.73), one can apply the same reasoning and furthermore assume a T-periodicity of the gain in the long-cavity regime

$$G\left(\theta,\sigma - \frac{T-2\tau_2}{T}\right) \approx G\left(\theta,\sigma - \frac{T-2\tau_2}{T} + \frac{T}{T}\right) = G\left(\theta,\sigma + \frac{2\tau_2}{T}\right). \tag{4.78}$$

The transformation of the nonlocal gain term enables to the following approximation, if one considers the carrier equation (4.76) at a time shifted by $+2\tau_2$

$$\partial_\sigma G\left(\theta,\sigma + \frac{2\tau_2}{T}\right) = -G\left(\theta,\sigma + \frac{2\tau_2}{T}\right) I(\theta,\sigma). \tag{4.79}$$

Inserting these simplified carrier equations into eq. (4.73) and using the previously introduced notation[33] for the carrier values at the boundaries of the pulse, one can solve the integral according to

$$\begin{aligned}&\int_{\sigma_n-\varepsilon}^{\sigma_n+\varepsilon} \left[\frac{1}{2}\left[G\left(\theta,\sigma + \frac{2\tau_2}{T}\right) + G(\theta,\sigma)\right] + Q(\theta,\sigma) + \frac{1}{2}\log(\kappa)\right]|E|^2 d\sigma. \\ &= G_{i1}^{(n)} - G_{f1}^{(n)} + G_{i2}^{(n)} - G_{f2}^{(n)} - \frac{1}{2s}\left[Q_f^{(n)} - Q_0\right] + \frac{1}{2}\log(\kappa)P_n.\end{aligned} \tag{4.80}$$

[32] Here, it has to be noted that periodic solutions in the DDE system become steady state solutions in the Haus master PDE model. Therefore, the pulse energy does not vary from round-trip to round-trip.

[33] First subscript refers to the carrier value before (i) and after (f) the depletion, the second subscript indicates the first and second interaction with the respective pulse.

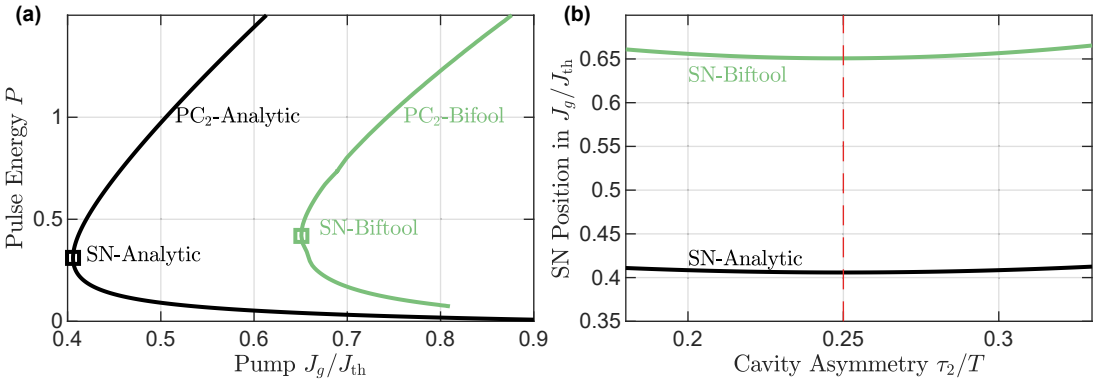

Figure 4.32.: (a) 1D-bifurcation diagram indicating the pulse energy along PC_2 branch with respect to the pump power. The green line indicates the DDE-biftool result, whereas the black line corresponds to the branch found according to the analytic expression (4.82). The black squares indicate the saddle-node bifurcation at the minimum point in pump power. A 2D-bifurcation diagram of these saddle-node bifurcation points in the (τ_2, J_g)-plane is indicated in (b). The parameter point (symmetric cavity) used in (a) is marked by the dashed line. Again, the green line indicates the DDE-biftool result and the black line is computed by applying eq. (4.82) for different cavity configurations. All parameters are given in Table 4.1 and $\kappa = 0.87$, $\gamma = 480\,\text{ns}$.

Furthermore, the relationship between the carrier value before and after the gain depletion (4.53) depletion and absorber saturation (4.62) can be applied, which yields

$$\mathcal{I}_n = \frac{G_{i1}^{(n)} + G_{i2}^{(n)}}{2}(1 - e^{-P_n}) + \frac{Q_0}{2s}(1 - e^{-2sP_n}) + \frac{1}{2}\log(\kappa)P_n. \tag{4.81}$$

Inserting the equations for the gain before the first and second depletion ($G_{i1}^{(n)}$, $G_{i2}^{(n)}$) found from the system of algebraic equations (see eq. (4.52)-(4.60)) and the expression for Δ_{PC2} eq. (4.68) into eq. (4.81) and solving for the normalised gain $g = \frac{G_0}{G_{th}}$, results in the following equation relating pulse power and the gain value

$$\begin{aligned} g(x) = &-4\left[e^{\gamma_g T}x^2 - 1\right]\left[\frac{-Q_0(1-x^{-s})}{2s} - \frac{1}{4}\log(x)\log(\kappa)\right] \\ &/\Big\{\left[\sqrt{x}-1\right]\left[-2Q_0 - \log(\kappa)\right] \\ &\times\Big[2 + \frac{\sqrt{2}(\sqrt{x}-1)2e^{\frac{1}{2}\gamma_g(T-2\tau_2)}}{\sqrt{1+e^{\gamma_g(T-4\tau_2)}}} + \frac{\sqrt{2}(\sqrt{x}-1)xe^{\frac{3}{2}\gamma_g(T-2\tau_2)}}{\sqrt{1+e^{\gamma_g(T-4\tau_2)}}} \\ &+ \frac{\sqrt{2}(\sqrt{x}-1)xe^{\frac{1}{2}\gamma_g(T+2\tau_2)}}{\sqrt{1+e^{\gamma_g(T-4\tau_2)}}} - 2e^{\gamma_g T}x^{\frac{3}{2}} + (x-\sqrt{x})\left(e^{\gamma_g(T-2\tau_2)} + e^{\gamma_g 2\tau_2}\right)\Big]\Big\}, \end{aligned} \tag{4.82}$$

where $x = e^{2P}$ and all other parameters are defined according to the explanation in section 3.4. The found equation represents an analytic approximation of the branch structure.
A comparison of the found analytic formula for the PC_2 branch structure (4.82) to the PC_2 solution branch computed using DDE-biftool is shown in Fig. 4.32(a). The general characteristic of the branch is well reproduced by the analytic expression (black). Furthermore, the folding point (SN) occurs at similar pulse energies for both results. Nevertheless, the analytically determined solution branch appears to be strongly shifted in the pump power

compared to the path-continuation result. The reason for that lies in the application of New's approximation, which reaches its limit, if the outcoupling losses $1-\kappa$ are low compared to the losses induced by the Lorentzian filter (gain bandwidth). Hence, for the computed branches in Fig. 4.32(a) already a reduced value of $\kappa = 0.87$ and an enlarged value of the bandwidth $\gamma = 300\,\mathrm{ns}$ are used to find a better agreement. Shifting the parameters further to a regime in which New's approximation is valid, would potentially lead to a better accordance. Yet, the path-continuation using DDE-biftool becomes cumbersome if γ is increased due to the narrower pulses.
By applying expression (4.82) for different values of τ_2 and determining the minimum point in pump power, the 2D saddle-node line can be reproduced in the parameter plane of cavity asymmetry and pump power (J_g, τ_2). The result is plotted in black Fig. 4.32(b), together with the saddle-node line obtained using DDE-biftool (green). Again, the qualitative behaviour is well reproduced, but a shift in pump power is evident. The reason for the deviation of the lines is the same as before.

4.4 Summary

In this chapter the dynamics of a passively mode-locked V-shaped VECSEL were investigated in two different regimes by means of direct numerical integration and path-continuation of the delay differential equation model derived in chapter 3. The two regimes are mainly distinguished via the cavity length and are motivated by experiments leading to the formation of interesting pulsed structures. Firstly, an intermediate-cavity length, used for high performance mode-locking is investigated and secondly the long-cavity regime leading to the emergence of localised structures is examined.

In the high performance mode-locking regime, the fundamental mode-locking solution branch is born from an Andronov-Hopf bifurcation along the CW branch at low cavity round-trip times ($T = 220\,\mathrm{ps}$). Due to the double gain pass of each pulse in the V-shaped system, the output does not transition to a harmonic mode-locking solution at increased pump powers (in a symmetric cavity arrangement). Instead pulse cluster solutions become evident, in which the temporal distance of the n pulses is given by $\Delta = T/2n$ with the cold-cavity round-trip time T. These pulse clusters form as they allow for an equidistant gain depletion and are therefore energetically favourable with regard to the maximum amplification of the pulses. The clusters are periodic with a frequency of approximately the inverse cold-cavity round-trip time.
The behaviour of the stability boundaries of the pulse cluster solutions was investigated in a large range of parameters. It was outlined that an increase of gain bandwidth γ decreases the pulse-width, but almost does not affect the position of the bifurcation boundaries of the PC_n solutions in pump power. In contrast, an increase of the unsaturated absorption shifts the stability boundaries of the solution to higher pump powers, as a higher amount of absorption has to be compensated for the pulses to stabilise. Furthermore, the stable regions of the PC_n solutions stretch over a larger pump power interval at a higher unsaturated absorption.
Increasing the relaxation rate of the absorber γ_q leads to a decrease of the stable regions, while a quasi-periodic pulse cluster solutions are favoured. An alteration of the gain relaxation rate causes a very similar behaviour compared to an increase of the round-trip time. In both cases, the stable regions of the FML and PC_n solutions shift to lower pump powers. This can be reasoned by the fact that altering each quantity leads to an equal change of the

amount of gain relaxation. However, an increase of the round-trip time leads to an alteration of the nonlinear pulse shaping effects due to the increased number of longitudinal modes supported by the gain spectrum. These decrease the pulse width and hence higher-order pulse clusters emerge as the round-trip time is increased.
By performing a path-continuation of the pulse cluster solution, it was unravelled that the PC_n solutions emerge in additional loops along the fundamental solution branch, generated in the first Hopf bifurcation along the continuous-wave solution. The additional loops are characterised by the occurrence of a pair of saddle-node bifurcations embodying the loops along the fundamental bifurcation branch. The upper saddle-node bifurcation represents the upper stability boundary of the corresponding PC_n solution, whereas the lower stability boundary is given by a torus bifurcation for each PC_n state. The torus bifurcations appear in a torus-torus collision point at a critical round-trip time slightly above the emergence of the respective solution. It furthermore became evident that the FML and lower order PC_n solutions detach from the main solution branch in a cusp of saddle-node bifurcations as the round-trip time is increased.
Applying path-continuation and direct numerical integration, it was possible to unravel the influence of an asymmetric cavity configuration. In the used DDE model, this was done by varying the delay times τ_1 and τ_2 corresponding to the length of the two cavity arms. The investigations indicate that the lower bifurcation boundaries (torus bifurcations) are not affected by the asymmetry. Anyhow, introducing a slightly asymmetric configuration can lead to a shift of the upper stability boundary to higher pump powers.

In the second part of the chapter, the long-cavity regime was discussed. It is characterised by the round-trip time being much larger than the gain relaxation time. Hence, the gain is allowed to (almost) fully relax between pulse passes. In this regime, the pulsed solutions can become multistable to the laser *off*-state (if the ratio of differential gain s is elevated). Due to the combination of the stable background embodied by the *off*-state and the vanishing interaction of the pulses via the exponential tails of the gain relaxation, the pulses can be understood as localised states, i.e. dissipative solitons.
Similar to the case of linear cavity configurations discussed in previous works, the fundamental mode-locking solution and harmonic mode-locking solutions, characterised by equidistant pulse separation, emerge from Andronov-Hopf bifurcations along the CW branch. Shortly after their birth, the branches loop to lower pump powers in a saddle-node bifurcation to stretch below the lasing threshold. Due to the characteristics of the cavity geometry, only odd numbered harmonic solutions stabilise in a symmetric cavity, as these enable an equidistant gain depletion. For even numbered harmonic mode-locking solutions, the pulses collide in the gain, which is energetically not favourable in terms of the amplification. Hence, these solutions only become stable at asymmetric cavity configurations.
Interestingly, pulse cluster solutions emerge in the localised state regime and exhibit a similar branch structure as the HML solutions. The PC_2 solution is born in a period doubling bifurcation along the HML_2 branch. Applying a Floquet analysis, it was possible to show that at intermediate-cavity lengths, the pulses of the PC_2 solutions are still bound as only one neutral mode of the system was obtained. However, as the round-trip time is increased, the absolute value of a second Floquet multiplier asymptotically approaches 1. Hence, two neutral modes exist, corresponding to the two locally independent pulses of the cluster. Due to the double gain depletion, the pulses are still globally bound. This binding mechanism is similar to catenane molecules and therefore the pulse clusters can be referred to as photonic

molecules.
Investigating the phase difference at the maximum of the two pulses in one cluster, one finds that the pulses are incoherent despite the global binding mechanism. The incoherence can further be assessed by calculating the optical spectrum of the pulses, that exhibits no modulation, which would occur in case the pulses are coherent.
Furthermore, it was found that the cavity geometry (determined by the delays τ_1, τ_2) has a strong influence on the stabilising solutions and the temporal distance of the pulses. As the temporal distance between the gain depletions varies with the relative length of the two cavity arms, a resonance behaviour with regard to the stabilising HML_n dynamics becomes evident in the parameter plane of pump power and cavity asymmetry. At the cavity geometry at which the equidistant pulses collide at the gain chip, the solutions become unstable. Vice versa the stability boundary of the solutions, given by a torus bifurcation, stretches to the lowest pump power in case the gain is depleted equidistantly.
The examination of the PC_n solutions at a varied cavity geometry indicates that the pulses within a cluster alter their temporal distance as the length of the cavity arms is changed, in order to maintain the maximum amplification. By deriving a nonlocal Haus master equation starting from the DDE model for the V-shaped VECSEL in combination with several simple assumptions, it was possible to recover an analytic prediction of the temporal pulse distance. The found expressions for the PC_2 and PC_3 solutions only depend on the round-trip time, the length of the cavity arms and the relaxation rate of the gain. Comparing the analytic formula to results obtained using DDE-biftool, a perfect agreement was determined. Making use of the analytic approximation of the pulse distance, an analytic formula for the PC_2 branch structure was acquired. It exhibited a good qualitative agreement and made it possible to find an expression for the position of the saddle-node bifurcation (in the (J_g, τ_1) plane) embodying the loop of the solution branch.

In future works, it could be interesting to further validate the accordance of theory and experiment. On that account, a detailed experimental investigation of the bifurcation scenarios at different cavity geometries would be of use. The basis of these experimental findings could serve as a starting point to further adjust the used mathematical models. Especially a quantitative modelling of pulses with a length of 100 fs would require a more microscopic approach such as presented in [KIL17, MCL20]. Hence, one could use the experimental data and a fully microscopic approach in order to find new models that include all relevant physical processes, but are simple enough to allow for reasonable computation times.
Two alternatives to the applied DDE and PDE models in this section are discussed in the next two sections. Firstly, a delay differential equation model is introduced that allows to investigate the influence of a carrier grating and the angle of incidence at the gain chip. Secondly, the delay differential equation model is extended by not only modelling the active states, but also including the scattering between different semiconductor states.

5 Dispersion Effects

5.1 Introduction

In optics, *chromatic-dispersion* is referred to as a frequency dependent change of the phase velocity of an electromagnetic wave. The alteration of the phase velocity is induced by the frequency dependent response of the medium in which the wave propagates. In other words, it is based on the frequency dependence of the refractive index caused by the interaction of the electromagnetic wave with the electrically charged particles in the material [HEC01, AGR01, PAS21]. Hence, the amount of dispersion is determined by the properties of the (dielectric) medium in which the wave propagates [HAK86, HEC01, AGR01]. Short optical pulses are especially influenced by dispersion, as they can be understood as a superposition of many longitudinal lasing modes (electromagnetic waves) which requires a broad optical gain spectrum stretching over several tens of nanometers [BOY08, HEA16, CHE18b, WOO18, WAL16]. Both, the active material dispersion induced by a homogeneous medium and the passive characteristics of a wave-guide (semiconductor laser cavity) can contribute to the dispersion experienced by a light pulse. The wave guides or mirrors (distributed Bragg reflectors) utilised are usually composed of heterogeneous materials and designed in various geometries [AGR01, MOR10a, PAS21].
Anyhow, there are several other effects which are identified as a form of dispersion in the research related to the propagation of light in lasers and optical fibres. Firstly, the nonlinear wavelength dependence of the gain is specified as *gain dispersion* [AGR91, SIE98, BAN01]. It is connected to the frequency dependence of the refractive index via the Kramers-Kronig relation. The gain dispersion can have a significant influence on the occurrence of self-pulsations in DFB lasers [SIE98, BAN01] or lead to the onset of regular oscillation bursts in lasers with saturable absorption [CAL14]. This form of dispersion is relevant to model the amplification of ultra-short pulses due to their broad spectral properties [AGR91]. In the DDE and the Haus partial differential equation (PDE) models discussed in this work, it is embodied by the introduction of a Lorentzian shaped filter (see sections 3.3 and 4.3.3). This type of modelling reaches its limits for pulses in the 100 fs regime, as in that case the pulses are of shorter extent than the propagation time in the active sections. Therefore, the spatial width of the latter is not negligible, which is a central simplification in the derivation of the DDE and HME models due to the slowly varying envelope approach. If a (quantitative) modelling of ultra-short pulses is of interest, a complete microscopic modelling is necessary, but cumbersome due to the very long integration times with modern computers [KIL17, KIL19, MCL20]. Therefore, the assumption of a Lorentzian gain bandwidth can be justified as a valid approximation to assure reasonable computation times delivering a broad overview of the dynamics in broad parameter regimes.
In addition to that, higher-order transverse modes can propagate at a varying group-velocity depending on the properties of the wave-guide. This effect is referred to as intermodal

dispersion [HEC01, PAS21, AGR01] and can have a substantial influence on the output of multi-mode lasers or optical fibres [PAS21]. Nevertheless, it is neglected in this work as the investigated lasers operate close to transverse single-mode operation [RUD08, TIL15, WAL16] with a Gaussian beam profile and hence transverse effects are not taken into account.
Thirdly, polarisation mode dispersion becomes relevant when transmitting optical pulses in optical communication schemes [AGR01]. Polarisation mode dispersion occurs, due to a breaking of the mode degeneracy of the x- and y-polarised modes, i.e. the birefringence of the waveguide. This degeneracy breaking results from the natural birefringence of the material as well as (material and geometry related) imperfections of the waveguide and causes varying group velocities across different polarisation directions. Nevertheless, the induced difference in the propagation time can be relevant for laser applications such as dual comb spectroscopy [AGR01, SHT05, LIN17e].
Outside the field of optics, chromatic-dispersion phenomena are especially studied in the research of solitary waves (solitons), which form based on a balance of dispersion and nonlinear effects [DAV85, HAS89, REM94, AKH08] as discussed in section 4.3. A very prominent and probably first observed example is a water wave propagating in a canal while preserving its width and amplitude [DAV85, REM94].
In the field of optical solitons, chromatic-dispersion plays a crucial role as temporal optical solitons are often embodied as ultra-short optical (laser) pulses [AKH05, AKH08, GRE12b]. Some of the most prominent theoretical models to analyse the propagation of these pulses are the Ginzburg-Landau equations [SOT97, ARA02, GUR19], the Lugiato-Lefever equations [LUG87, LEO13a] and the nonlinear Schrödinger equation [BUL79, BOY08, KRU11, SCH19b]. Due to the partial differential equation nature of these models, chromatic-dispersion of different order is embodied by a time derivative of the corresponding order in the electric field equation. In this case, the magnitude of the dispersion contributions is determined by the respective pre-factor of the derivative term. The sign of the pre-factor indicates whether a regime of normal or anomalous dispersion is investigated [PIM17]. The method of including the dispersion is motivated by the definition of dispersion in the general partial differential pulse propagation equation (nonlinear Schrödinger equation) in dispersive media that can be derived from Maxwell's wave equation [BOY08]. Here, the distinction of the dispersion into different orders stems from a power series expansion of the propagation constant $k(\omega)$ of the electro-magnetic wave with respect to its frequency dependence [BOY08]

$$k(\omega) \approx k_0 + \Delta k_{\mathrm{NL}} + k_1(\omega - \omega_0) + \frac{1}{2}k_2(\omega - \omega_0)^2, \tag{5.1}$$

where the pre-factors are given by the derivative of the propagation constant with respect to the frequency $k_n = \left(\frac{d^n k}{d\omega^n}\right)_{\omega=\omega_0}$ and Δk_{NL} is a nonlinear contribution depending on the intensity [BOY08]. The different powers of the frequency transform into derivatives with respect to the time when applying a Fourier transform[1].
Pulse propagation models enabled the investigation of the nature of temporal solitons (optical pulses) in various systems such as fibre amplifiers [AKH98, KRU11], optical fibres [HAS89, KOD94, HAU13] or different types of mode-locked lasers [KAL08, ORT10, GRE12b, WOO18, LIU09, PEN19a].
chromatic-dispersion becomes an important parameter when investigating the performance of mode-locked lasers in the regime of non-solitary mode-locked pulses [MAR84, PEN92,

[1] A detailed derivation for a pulse propagation equation for solitons and ultra-short optical pulses in semiconductor media is given in reference [BOY08] in sections 7.5.2 and 13.2.

CHE99c, ORT07, WIL09, ROS12a]. Especially with regard to the pulse width and pulse energy, the interplay of dispersion and nonlinearity has to be considered carefully in order to achieve the best performance [WAL16, MEY20] and to realise wavelength tunable devices with an appropriate emission stability [CHE18b]. Recently, it was found that a certain amount of second and third-order dispersion induced by the gain chip can enhance the performance figures in passively mode-locked semiconductor VECSELs [SIE13b, HEA16, WAL16]. The first theoretical investigations of the influence of dispersion on the output pulses of passively mode-locked lasers relied on the Haus master equation approach with an additional dispersion contribution [MAR85a, CHE99c, HAU00]. However, modelling the influence of different orders of dispersion is still a demanding question, as fully microscopic approaches and travelling-wave models require an excessive amount of computational resources for an analysis of the long-term dynamics in VECSELs [SIE98, JAV10, KIL17, MCL20]. This limits their applicability, although the especially microscopic models have the advantage that the dispersion occurs from microscopic interactions and not as individually adjustable parameters. Similar to the other pulse-propagation models, the drawback of the Haus master equation approach is the inadequate modelling of the gain dynamics when the relaxation time of the gain is of the magnitude of the cavity round-trip time and the gain is strongly depleted [HAU00, PER20, HAU20a]. In opposition, models based on DDEs deliver the opportunity to correctly model the long-term gain dynamics in this regime, while including dispersion effects is not straightforward [PIM17, PIM20].
In this chapter, two alternative approaches to study the effect of second and third-order dispersion in passively mode-locked semiconductor VECSELs with a V-shaped cavity geometry are discussed. First, a generalised form of the Haus master equation with a dynamic boundary condition is derived in section 5.2. The generalisation is then combined with the nonlocal Haus master equation for the V-shaped VECSEL to study the influence of group-velocity dispersion in section 5.3. On the account of examining the effect of third-order dispersion, a delayed algebraic equation (DAE) system for the V-shaped VECSEL is introduced in section 5.4. The advantage of the DAE formulation is that in contrast to DDE models, the third-order dispersion contribution is not overwhelmed by the diffusive influence of the gain bandwidth [SCH19b].

5.2 Boundary Condition Problem

As mentioned before, investigating the chromatic-dispersion contributions of different order is straightforward using pulse propagation partial differential equations such as the Haus master equation (HME) [BUL79, BOY08, SOT97, LUG87, HAU00]. In these PDE systems, the different orders of dispersion appear as time derivatives of the respective order [MAR85a, HAU00, PIM17]. Hence, the Haus master equation of mode-locking [HAU00, KOL06] is a feasible choice to investigate dispersion phenomena. This is supported by the limited computationally feasible alternatives, as it can be challenging to correctly include dispersive effects in time delayed systems [PIM17, PIM20, SCH19b, SCH20d, HES21], such as the DDE model presented in section 3.3.
Nevertheless, the Haus master equation approach was originally developed for gain media that recover slowly compared to the cold-cavity round-trip time ($\gamma_g^{-1} \gg T$) [HAU00, KOL06, HAU20a]. This was motivated by the aim of modelling the variation of the electric field strengths from round-trip to round-trip at low computational cost and thus was limited to the vicinity of the pulse. It is based on splitting the mode-locking dynamics into two time

scales, as outlined in detail for the derivation of the nonlocal Haus master equation in section 4.3.3. Namely, the slow time scale θ is an integer and refers to changes from round-trip to round-trip, whereas the fast time scale σ describes the dynamics within one round-trip and is normalised to the round-trip time.
In the situation of a relatively slow carrier relaxation, it is sufficient to model the gain via its average value within the round-trip (over the fast time scale σ), as it remains quasi uniform due to weak depletions [HAU00, KOL06, HAU20a]. Hence, the evolution of the average gain is modelled only on the slow time scale (θ from round-trip to round-trip) and no additional boundary condition connecting the gain value at the end of one round-trip to the start of the next round-trip is needed. Details on the origin of the time scales can be found in section 4.3.3, where a nonlocal Haus master equation is derived via a multiple time scale approach from the V-shaped DDE model.
As discussed in section 4.3.3, finding a boundary condition for the HME approach is relatively simple in the long-cavity regime ($\gamma_g^{-1} \ll T$), despite the strong gain depletions. In this regime, the gain always recovers (almost) fully to its equilibrium value G_0 in between pulse passes. The choice of the boundary condition describing the gain value $G(\theta+1, 0)$ at the start of the consecutive round-trip $(\theta + 1)$ is thus naturally given by the full relaxation $G(\theta + 1, 0) = G_0$.
In the intermediate-cavity regime, the gain relaxation is evolving on the same time scale as the cold-cavity round-trip time ($\gamma_g^{-1} \approx T$). Therefore, the gain does not fully recover until a consecutive pulse pass. In this situation, the gain depletion in the previous round-trip has an influence on the subsequent pulse pass due to the incomplete recovery of the charge carriers, which can be described as "carrier memory". This memory effect is of particular importance to model semiconductor lasers, because γ_g^{-1} is in the nanosecond range, such as the cavity round-trip time. Furthermore, taking into account carrier memory is essential to model the onset of quasi-periodic regimes. An example of such an quasi-periodic output is the well known Q-switched mode-locking (QSML) instability in passively mode-locked lasers [ERN00c, FLY04, VLA05, TER18, HAU20a]. This instability is embodied by a pulse train that is strongly modulated over a slow time scale of several hundreds of round-trips [HAU20a]. In addition to that, the inclusion of carrier memory is crucial to model the harmonic transitions of passive mode-locking, characterised by the transition of the lasing output from N to $N + 1$ equally spaced pulses in one round-trip. Finally, long-term gain dynamics are essential for an adequate modelling of the transient dynamics, i.e. drifts, of localised pulses [MAR14c] as discussed in the last section 4.3. These can repel each other via the exponential tails of the gain relaxation, if they are excited temporally close to each other within the cavity.
One approach to account for a strong gain depletion and incomplete carrier recovery can be rigorously included in a *coherent* Haus master equation approach. It starts from the Maxwell-Bloch equations and results in an additional integro-differential equation for the deviation of the gain from its average on the fast time scale within one round-trip [PER20]. Yet, in this section a simpler technique is introduced as previously published in Reference [HAU20a]. It relies on finding an appropriate boundary condition to connect the gain at the end of one round-trip to the start of the next round-trip. It is embodied by an ordinary differential equation for the gain at the start of the round-trip, which is on the slow time scale and therefore leaves the computational costs almost unaffected. As mentioned before, this technique is especially useful to model passively mode-locked semiconductor lasers in

the intermediate-cavity regime. Examples of such devices are long-cavity monolithic devices [FLY04], VECSELs [KEL06, WAL16, MAR14c, HAU20] or ring cavities [PER20].

5.2.1 Boundary Conditions of the Haus Master Equation Model

To firstly discuss the boundary condition problem and the importance of the long-term carrier effects without the complicated influences of the gain nonlocality, the investigation is started using the simpler DDE and HME models of mode-locking based on the assumption of a ring cavity instead of the V-shaped cavity geometry[VLA04, VLA04a, VLA05, KOL06, HAU00]. In these models, the electric field and charge carriers in the active sections are described according to the same principles as in the V-shape models. The main difference is the influence of the cavity geometry, incorporated by the additional delay (nonlocal) terms in the V-shape model. The ring delay differential equation model of mode-locking was introduced in References [VLA04, VLA04a] and reads

$$\frac{d}{dt}E(t) = -\gamma E + \gamma\sqrt{\kappa}e^{\frac{1}{2}[(1-i\alpha_g)G(t-T)+(1-i\alpha_q)Q(t-T)]}E(t-T), \tag{5.2}$$

$$\frac{d}{dt}G(t) = \gamma_g G_0 - \gamma_g G(t) - e^{-Q(t)}(e^{G(t)}-1)|E(t)|^2, \tag{5.3}$$

$$\frac{d}{dt}Q(t) = \gamma_q Q_0 - \gamma_q Q(t) - s(e^{Q(t)}-1)|E(t)|^2. \tag{5.4}$$

The derivation of the model, despite the assumption of a ring cavity, is very similar to the one outlined for the V-shaped cavity geometry in section 3.3. Here, the electric field E and the integrated carrier densities in the gain G and absorber Q are scaled exactly as before and the parameters are the same as for the V-shape model. For a discussion of the parameters see section 3.4. It has to be noted that $\gamma_g G_0 = J_g$ and $\gamma_q Q_0 = J_q$ are used in order to be able to vary the relaxation rates and the equilibrium carrier densities independently. Note that Q and Q_0 are defined as negative quantities.
The derivation of the corresponding Haus master equation model (HME) can be performed by starting from the ring DDE model (5.2)-(5.4) and following the same procedure as outlined in section 4.3.3. A detailed derivation can be found in References [HAU00, KOL06, CAM16]. Alternatively, a functional mapping approach can be followed [SCH18f]. The ring Haus master equation model then reads

$$\partial_\theta E(\theta,\sigma) = \frac{1}{2\gamma^2}\partial_\sigma^2 E(\theta,\sigma) + \frac{1}{2}\left[[1-i\alpha_g]\,G(\theta,\sigma) + [1-i\alpha_q]\,Q(\theta,\sigma) + \frac{1}{2}\log(\kappa)\right]E(\theta,\sigma), \tag{5.5}$$

$$\partial_\sigma G(\theta,\sigma) = \gamma_g G_0 - \gamma_g G(\theta,\sigma) - G(\theta,\sigma)|E(\theta,\sigma)|^2, \tag{5.6}$$

$$\partial_\sigma Q(\theta,\sigma) = \gamma_q Q_0 - \gamma_q Q(\theta,\sigma) - sQ(\theta,\sigma)|E(\theta,\sigma)|^2. \tag{5.7}$$

Equations (5.5)-(5.7) describe the electric field evolution from round-trip to round-trip $\partial_\theta E$, and the variation of the carrier densities G and Q on the fast time scale σ. The meaning of all parameters is the same as for the V-shape DDE and PDE systems (sections 3.4 and 4.3.3). The solutions of the systems are determined by means of direct numerical integration applying the split-step algorithm introduced in the Appendix of Reference [GUR17], which is outlined in detail in Appendix B.1.

Asynchronous Map Boundary Condition

The carrier memory in the gain, i.e. the variation of the gain value at the start of each round-trip, is especially important when investigating quasi-periodic regimes. To illustrate its role, the long-term dynamics of the quasi-periodic Q-switched mode-locking instability is shown in Fig. 5.1[2]. From the electric field time-series plotted in Fig. 5.1(a), one clearly notices the quasi-periodic modulation of the pulse amplitude by a second frequency, which is slower than the mode-locking frequency. It arises from a secondary Andronov-Hopf (torus) bifurcation along the fundamental mode-locking solution branch [JAU17a]. The modulation of the mode-locked pulses is related to carrier memory effects as can be seen in the long-term gain dynamics visualised in Fig. 5.1(c). In between pulse passes, the gain does not recover to an equal level, as the pulse grows from round-trip to round-trip driven by the energetically favourable situation of a completely bleached absorber. Therefore, the gain is depleted more strongly from round-trip to round-trip as the pulse is increasingly amplified. This continues until the gain is almost completely depleted. At this point, not enough gain is available to maintain the high pulse amplitude against the losses. Consequently, the pulse amplitude starts to decrease while the gain is able to relax up to a critical level at which the pulse growth starts again [HAU20a].
As discussed before, the gain value at the start of each round-trip $G(\theta, \sigma = 0)$ varies on the slow time scale θ and is (quasi-)periodic on a time scale of ≈ 160 round-trips in the shown Q-switched mode-locking (QSML) regime. A zoom of the gain dynamics in two consecutive round-trips during the growth stage of the pulse is displayed in Fig. 5.1(b,d). The gain value at the end of each round-trip (start of the next round-trip) is marked by red circles in Fig. 5.1(d)). In the Haus master equation, the gain values at the domain boundaries are given by $G(\theta, \sigma = 1)$ for the end of the round-trip and $G(\theta + 1, \sigma = 0)$ for the start of the next round-trip as indicated in the figure.
Nonetheless, the variation of the gain at the round-trip boundary cannot be described by means of the standard form of the Haus master equation, because either the gain is modelled as a constant over the fast time scale, which is not sufficient for strong depletions [KOL06], or via a complete recovery [SCH18e, CAM16]. In consequence, an adequate boundary condition has to be found that sufficiently incorporates these long-term carrier "memory" effects.
Inspecting the gain dynamics $G(\theta, \sigma)$ at the transition of two consecutive round-trips (see Fig. 5.1(d)) already delivers an intuitive boundary condition for the Haus master equation, that can be drawn from the requirement of a continuous solution. This requirement can be met by the condition equating the previously introduced gain values at the start $G(\theta+1, \sigma = 0)$ and end $G(\theta, \sigma = 1)$ of two consecutive round-trips [GIA96, HAU20a]

$$G(\theta, \sigma = 1) = G(\theta + 1, \sigma = 0). \tag{5.8}$$

The resulting asynchronous map boundary condition (MBC) can be applied to extend the ring HME (5.5)-(5.7) by a description of the long-term carrier effects. Using a numerical integration step of $d\theta = 1$ (see Appendix B.1 for the integration scheme), it is possible to successfully reproduce the previously discussed quasi-periodic Q-switched mode-locking (QSML) regime.

[2] The time-series is obtained by applying a direct numerical integration of the generalised ring HME model that is introduced in this section (equations (5.5)-(5.7) together with (5.11)). The utilised parameter set is chosen similar to the coupled VCSELs discussed in Reference [MAR14c, CAM16] and is given in the caption of Fig 5.1.

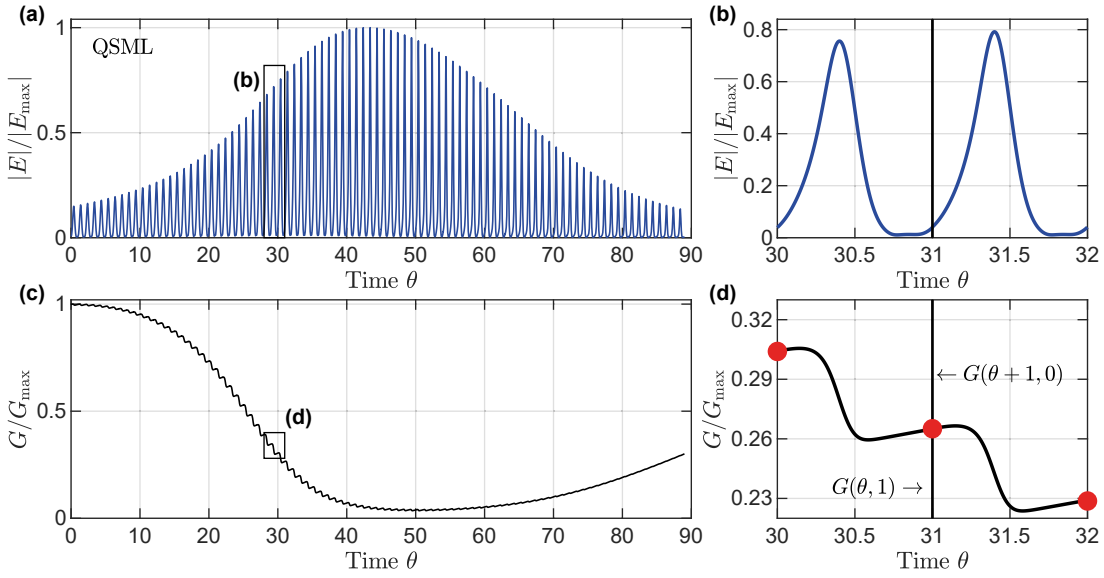

Figure 5.1.: QSML in HME with dynamic boundary condition: (a) Time-series of the electric field amplitude $|E|$ and (c) integrated carrier density in the gain G in the quasi-periodic QSML regime over 90 round-trips. Black squares mark the close ups shown in panels (b) and (d), which correspond to two cavity round-trips. The border between two round-trips is indicated by the black vertical line. The chosen laser parameters used for the integration of the generalised HME system and normalised to the round-trip time are $(\kappa, \gamma, \gamma_g, \gamma_q, \alpha_g, \alpha_q, Q_0, s, T) = (0.99, 80, 0.02, 2, 1.5, 1.0, -0.3, 30, 1)$.

In order to classify the results of the extended Haus model, a 1D-bifurcation diagram in the regime of QSML is compared to the well-established DDE model in Fig. 5.2. Plotted with blue dots are all pulse maxima within 500 round-trips at each point in pump power found using the DDE model. The maximum and minimum pulse amplitudes found at each parameter value using the HME model are depicted by red lines.
The qualitative accordance of the maxima in Fig. 5.2(a) shows, that applying the map boundary condition (5.8) enables to recover the Q-switched mode-locking dynamics. However, using the HME model leads to an increased QSML region with respect to the pump value G_0, as visible from the red lines in Fig. 5.2(a). The lower stability boundary of the QSML solution is shifted to smaller pump currents and the upper bifurcation point is shifted to higher pump currents. The reason for that most likely lies in the insufficient resolution with respect to $d\theta$, which is set to $d\theta = 1$. Yet, when refining the resolution, the boundary condition ceases to deliver the QSML result. This is illustrated by the red lines in Fig. 5.2(b), which indicate that the maximum and minimum pulse amplitudes in the investigated regime are almost identical for all pump currents. Hence, no quasi-periodic QSML regime is detectable at a refined resolution, which can be generalised to all values of $d\theta < 1$. Furthermore, a QSML regime is evident for $d\theta > 1$, but it exhibits an even stronger discrepancy of the bifurcation points and pulse maxima compared to the DDE result.
The dependence of the emerging dynamics on the resolution $d\theta$ strongly limits the applicable numerical integration techniques when using the map boundary condition. Applying an explicit integration scheme such as the finite differences method (instead of the previously used split-step method) would require a small resolution of $d\theta$ due to the Courant–Friedrichs–Lewy (CFL) condition [COU28]. Specifically the CFL condition would require $d\theta < (\gamma d\sigma)^2$, which is clearly smaller than 1, as $d\sigma < 1/\gamma$ is necessary to maintain an adequate resolution of

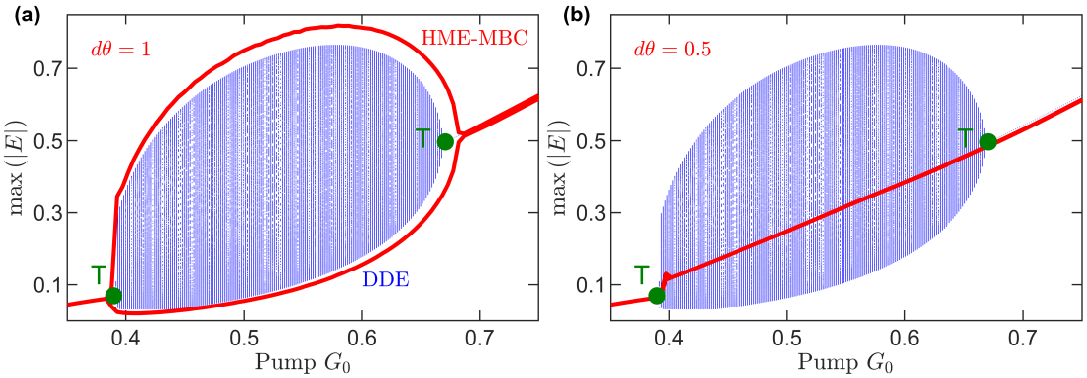

Figure 5.2.: Ring-Cavity MBC: 1D-bifurcation diagrams showing the maximum pulse amplitudes as a function of the pump power G_0 in the Q-switched mode-locking regime. The temporal dynamics in the QSML regime is exemplarily shown in Fig. 5.1. The blue dots indicate all pulse amplitudes obtained in 500 round-trips of direct numerical integration of the Ring DDE; The red lines indicate the absolute maximum and minimum electric field amplitudes found in 500 round-trips integrating the HME, extended by the map boundary condition (MBC) (5.8). Resolution set to (a) $d\theta = 1$ and (b) $d\theta = 0.5$ and $d\sigma = \frac{1}{1024}$ for both panels. The chosen laser parameters normalised to the round-trip time are $(\kappa, \gamma, \gamma_g, \gamma_q, \alpha_g, \alpha_q, Q_0, s, T) = (0.99, 80, 0.02, 2, 1.5, 1.0, -0.3, 30, 1)$.

the pulses (pulse width $\approx 1/\gamma$ [VLA05]). Thus, a quasi-periodic modulation of the intensity cannot be detected when integrating the system applying an integration based on the finite differences method, because of the malfunctioning asymmetric boundary condition. Consequently, the result of a 1D sweep using the finite differences method looks almost identical to Fig. 5.2(b), which is obtained applying the split-step algorithm outlined in Appendix B.1.

Ordinary Differential Equation Boundary Condition

A possibility to include the long-term carrier correlations without the inconveniences of the asynchronous BC eq. (5.8), is to transform the "map" boundary condition into a dynamical BC. This is done by reformulating eq. (5.8) as a *synchronous* ordinary differential equation (ODE).
As a first step, the gain eq. (5.6) of the Haus master equation model is integrated over the cavity length in σ to yields

$$G(\theta, 1) - G(\theta, 0) = \gamma_g G_0 - \int_0^1 \gamma_g G(\theta, \sigma) - G(\theta, \sigma)|E(\theta, \sigma)|^2 d\sigma. \tag{5.9}$$

In order to find an expression only depending on the gain at the start of the round-trip $\sigma = 0$, the asynchronous boundary condition eq. (5.8) is inserted on the left-hand side of the equation. This gives

$$G(\theta + 1, 0) - G(\theta, 0) = \gamma_g G_0 - \int_0^1 \gamma_g G(\theta, \sigma) - G(\theta, \sigma)|E(\theta, \sigma)|^2 d\sigma. \tag{5.10}$$

The gain value at the start of each round-trip is defined as a new variable that only changes on the slow time scale: $G(\theta, 0) = \mathcal{G}(\theta)$. To transform the boundary condition, a slow temporal evolution of $\mathcal{G}(\theta)$ is assumed, which is true in most quasi-periodic solutions. Hence, one can

use the first-order approximation[3] $\mathcal{G}(\theta+1)-\mathcal{G}(\theta) \approx d\mathcal{G}/d\theta$ for the left hand side of equation (5.10). This leads to the following dynamical equation representing the boundary condition complementing the HME system (5.5)-(5.7):

$$\frac{d\mathcal{G}(\theta)}{d\theta} = \gamma_g G_0 - \int_0^1 \gamma_g G(\theta,\sigma) - G(\theta,\sigma)|E(\theta,\sigma)|^2 d\sigma. \tag{5.11}$$

A boundary condition for $Q(\theta,\sigma)$ can be found by applying the same steps to the absorber equation and defining $Q(\theta,0) = \mathcal{Q}(\theta)$. The complete system is again integrated using the split step integration scheme outlined in Appendix B.1 using $(\mathcal{G},\mathcal{Q})$ as inhomogeneous Dirichlet BCs [HAU20a].
Due to the time lag induced by the Lorentzian filter as well as the nonlinear gain and absorber effects, the physical round-trip time of a pulse is slightly elevated from the round-trip time[4]. This results in a temporal drift of the pulse position when integrating the HME from one round-trip to the next $\theta \to \theta+1$. In order to maintain a constant pulse position during the integration, the translation operator $(v_0\partial_\sigma)$ is added to eq. (5.5). Here, v_0 is defined as the correction needed to match the actual pulse round-trip time (period of the solution) $\tau_p = T + \frac{1}{\gamma} + v_0$, and is updated every round-trip. Details on the calculation of v_0 are given in Appendix B.1. Furthermore, the drift can be taken into account when defining the boundary conditions, which is presented in Appendix B.2. Nevertheless, extended tests applying the second-order boundary condition with drift, lead to almost identical results compared to the first-order boundary condition (5.11). In consequence, the boundary condition (5.11) is used to compute all presented further results.

5.2.2 Verification of the Boundary Condition

This section aims at demonstrating the applicability of the ODE dynamic boundary (DBC) condition in a proof of principle, by comparing the results of a numerical analysis of the generalised Haus master equation and the DDE system. This is performed in the regimes of Q-switched mode-locking (QSML) and the transitions between harmonic mode-locking (HML) solutions, which are both not obtainable using the standard HME approach. Furthermore, the boundary condition is used to reproduce the dynamics of the V-shaped VECSEL applying the generalisation to the nonlocal HME derived in section 4.3.3.

Ring Haus Master Equation

As discussed in the previous section, already the map boundary condition is sufficient to qualitatively reproduce the 1D-bifurcation scenario of the QSML regime (see Fig. 5.2). However, it is not possible to refining the resolution $d\theta$, without strongly influencing the detected dynamics. Applying the dynamic BC (5.11) solves this problem. A 1D-bifurcation diagram with respect to the pump power in the regime of QSML is shown in Fig. 5.3(a). Illustrated by the colours is a comparison of the DDE system (blue) and the generalised Haus master PDE with dynamic boundary condition (HME-DBC). For the PDE system, only the absolute maximum and minimum pulse amplitudes found at each pump power are plotted, whereas for the DDE system all detected maxima (in 3000 round-trips) are visualised. Although

[3] An alternative boundary condition including the usage of a higher-order expansion is discussed in Appendix B.2.

[4] In case of strong gain and absorption, the period can be lower than the round-trip time [JAU17a, VLA11]. However, this regime is not investigated here.

a resolution of $d\theta = 0.25$ is used, both models exhibit an excellent agreement, with only a slight variation of the bifurcation points. The onset and end of the Q-switching regime are determined by torus (secondary Andronov-Hopf) bifurcations in the DDE system (green circles in Fig. 5.3(a)), which appear as Andronov-Hopf bifurcations in the PDE system. This is caused by the nature of the pulsed mode-locking solutions in both systems. In the PDE system, the fundamental mode-locking state manifests as a steady state solution, because a constant pulse shape can be found in each integration domain. In contrast, the FML solution is characterised as a periodic orbit in the DDE system, due to the periodic oscillation of the variables with time.
In order to determine the accordance of the models in a wider range of parameters the bifurcation boundaries are compared. The torus bifurcations in the DDE system (green circles in Fig. 5.3(b)) can be continued in the (G_0, Q_0) parameter plane using DDE-biftool. The result is plotted as a green line in Fig. 5.3(b). It is compared to the dynamics obtained from a direct numerical integration of the Haus master PDE performing an upsweep in G_0 and evaluating the different mode-locking states according to their characterising features. The obtained dynamics are depicted by the colour code (see caption of Fig. 5.3) and specifically the QSML region is indicated in pink. Its boundaries match the bifurcation line of the DDE system very well. As known from previous works [VLA05, JAU17a], the QSML dynamics vanishes at low Q_0 as the torus bifurcations collide and vanish below a critical point in Q_0. Aside the torus bifurcation point, the first Andronov-Hopf bifurcation along the CW branch, that gives birth to the FML state before the onset of the Q-switched regime, matches well between the two models. The Andronov-Hopf bifurcation line (DDE) is shown as a black dashed line in Fig. 5.3(b).
To further evaluate the boundary condition, the attention is now turned to another critical parameter regime. Namely, the transition between harmonic mode-locking states (HML_n) of different order when continuously increasing (up-sweeping) the pump current. These transitions require to adequately model the variation of the gain at the start of each round-trip. A comparison of the pulse maxima found in a 1D scan across the pump parameter using the generalised Haus PDE (red) and the DDE system (blue) is indicated in Fig. 5.4(a). The transitions towards the different states can be identified as changes of the determined pulse amplitudes $\max(|E|)$. The drop of the amplitude is always reasoned by the emergence of an additional pulse and therefore a redistribution of the available gain. Although the pulse amplitudes slightly differ across the models, the transition points match well. The difference in the electric field amplitude can either be caused by the linearisation performed in the derivation of the HME or by a slight underestimation of the gain at the domain boundary.
Once more, the transition points are characterised by torus bifurcations along the solutions (Andronov-Hopf bifurcations in the PDE system), which lead to very small regions of quasi-periodic dynamics (many different maxima found at one pump value) until the system stabilises on the next higher HML_n solution (when the pump current is increased). The path-continuation (DDE) of the torus bifurcation points T_n in the (G_0, γ_g) plane is plotted in green lines Fig. 5.4(b). For comparison, the direct numerical Haus PDE result is depicted by the underlying colour code. It becomes evident that the upper stability boundaries of the mode-locking states are well reproduced by the generalised Haus PDE, as the DDE bifurcation lines are in accordance with the direct numerical integration result. The course of the bifurcation lines to lower pump currents at increased gain relaxation rates, stems from the higher available gain due to the accelerated gain recovery. Hence, multi-pulse solutions can stabilise at lower pump powers. The same mechanism is discussed for pulse-clusters in the

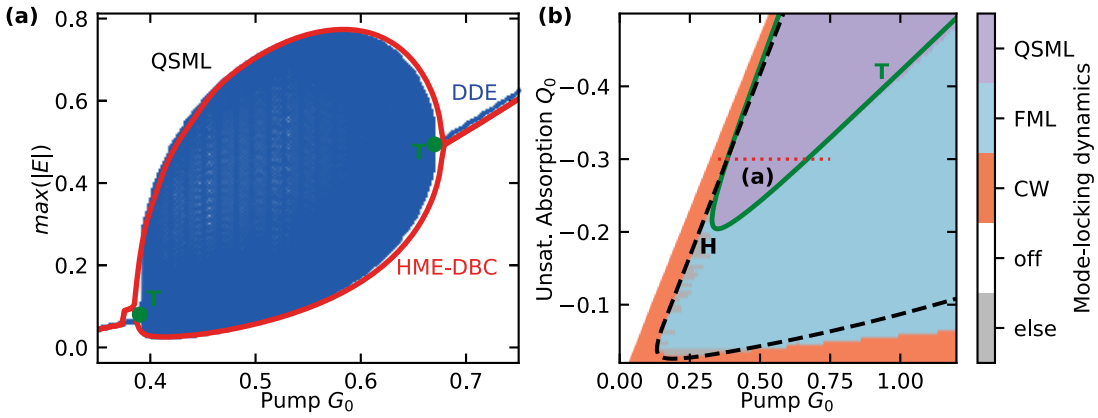

Figure 5.3.: Ring-Cavity DBC: 1D-bifurcation diagram showing the maximum pulse amplitudes (max (|E|)) as a function of the pump power G_0 in the Q-switched mode-locking regime. The temporal dynamics are exemplarily shown in Fig. 5.1. The blue dots indicate all pulse intensities obtained in 500 round-trips of direct numerical integration of the Ring DDE; The red lines indicate the absolute maximum and minimum pulse intensities found using the generalised ring Haus master PDE system with dynamical boundary condition (HME-DBC), given by eq. (5.11). (b) 2D-bifurcation diagram depicting the different dynamic regimes in the parameter plane of pump power and unsaturated absorption (G_0, Q_0) obtained performing a numerical upsweep in G_0 using the generalise HME model. The colours indicate fundamental mode-locking (FML; blue), Q-switched mode-locking (QSML; pink), and continuous-wave operation (CW; orange). The green line marks the torus (T) bifurcations indicated by green dots in (a). The black dashed line corresponds to the Andronov-Hopf (H) bifurcation giving birth to FML dynamics. The bifurcation lines are obtained utilising the Ring DDE model. The dotted red line marks the $Q_0 = -0.3$ value used in (a). The chosen laser parameters are the same as in Fig. 5.2. Figure adapted from [HAU20a].

V-shaped cavity in section 4.2.2. Since no second gain depletion is evident in the ring laser model, harmonic mode-locking states appear instead of the pulse-cluster solutions.
As a further validation, the comparison of the models is performed in the (G_0, Q_0) parameter plane comprising the harmonic transitions. The corresponding 2D-bifurcation diagram is presented in Fig. 5.4(c). Once more, the torus bifurcation lines characterising the stability boundaries of the HML$_n$ states are visualised by green lines (DDE) and the first Andronov-Hopf bifurcation along the CW branch is plotted as a black dashed line. All bifurcation lines exhibit an excellent agreement to the transitions in the colour code, that represents the dynamics classified from the direct numerical integration of the generalised Haus master PDE. Yet, it has to be noted that at higher values of G_0 and Q_0 (not shown), the integration results of the Haus master equation become increasingly unstable. This results from the decreasing validity of the linerisation of the exponential terms made in the derivation of the Haus master PDE from the DDE model (see section 4.3.3).
The dynamical boundary condition (DBC) is not only of use in the short/intermediate-cavity regime. As discussed in section 4.2.3, it is often sufficient to utilise the long-cavity boundary condition $\mathcal{G}(\theta) = G_0$ when investigating localised states in the long-cavity regime. Anyhow, in order to unravel the transient dynamics of multiple localised pulses in the cavity [MAR14c, CAM16, HAU20], it is crucial to correctly model the gain at the beginning of each round-trip. This is required to adequately model the interaction of the pulses via the exponential tail of the gain relaxation, before the pulses settle in an equilibrium state. The deviation in the transient dynamics caused by the usage of the long-cavity boundary condi-

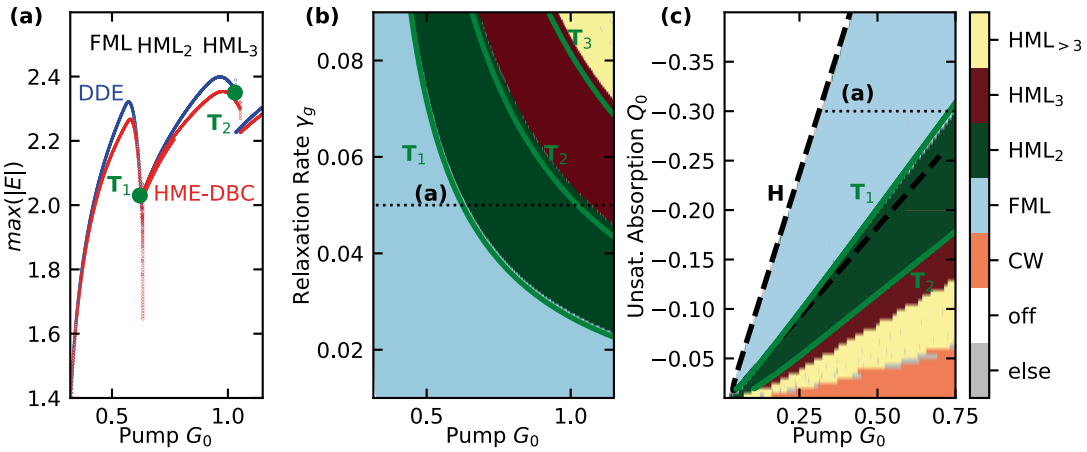

Figure 5.4.: Ring-Cavity DBC: (a) 1D-bifurcation diagram in pump power G_0 showing all unique pulse maxima ($\max(|E|)$) obtained in 250 round-trips in the regime of fundamental (FML) and harmonic mode-locking (HML_n). The blue dots correspond to the result determined via the DDE model and the red dots to the generalised Haus master equation with dynamical boundary condition (HME-DBC). (b) 2D-bifurcation diagram in the parameter plane of the pump power and the gain relaxation rate (G_0, γ_g) obtained by direct numerical integration of the Haus master PDE (upsweep in G_0) with dynamical boundary condition (HME-DBC). The different colours refer to the following dynamics: Fundamental mode-locking (FML;blue), harmonic mode-locking of second-order (HML_2; green), third-order (HML_3; red) and above third-order ($\mathrm{HML}_{>3}$; yellow), continuous-wave lasing (CW; orange) and unclassified dynamics (grey). (c) 2D-bifurcation diagram in the parameter plane of the pump power and unsaturated absorption (G_0, Q_0) obtained applying the same procedure and with the same colour code as in (b). The green lines in (b)-(c) represent torus bifurcations (T_n) determined utilising DDE-biftool for the Ring DDE model. The black line corresponds the first Andronov-Hopf bifurcation along the CW branch. The chosen laser parameters normalised to the round-trip time are $(\kappa, \gamma, \gamma_g, \gamma_q, \alpha_g, \alpha_q, Q_0, s, T) = (0.99, 300, 1.5, 30, 0, 0, -0.3, 3, 1)$. Figure adapted from [HAU20a].

tions is presented in Fig. 5.5. Plotted is a pseudo space-time representation [GIA96] of the electric field dynamics of three pulses in the long-cavity regime. To obtain the transients in Fig. 5.5(a), the long-cavity boundary condition $\mathcal{G}(\theta) = G_0$ is used, whereas the result in Fig. 5.5(b) is computed using the dynamical BC (5.11). The most prominent deviation between the two results is the temporal drift of the leftmost pulse. In Fig. 5.5(a), the pulse does not change its position as the gain is always fully relaxed at the start of each round-trip due to the boundary condition. In other words, the pulse does not experience a repulsive force to later times caused by incomplete gain recovery following the depletion of the last pulse in the previous round-trip. Nonetheless, the dynamical boundary condition (5.11) correctly models the gain relaxation across the round-trip boundary and therefore the repulsive interaction of the last pulse on the first is recovered. Consequently, a drift to the right is evident. This transient behavior again underlines the importance of the correct modeling of the carrier memory.

V-shaped Cavity

The attention is now turned towards the V-shaped cavity, outlined in the intermediate and long-cavity regime in the previous chapter. In order to describe the differing gain landscape induced by the double gain pass of each pulse per round-trip, the derived Haus master PDE

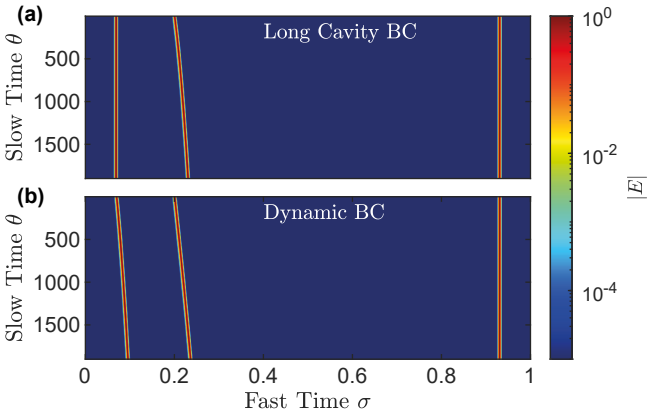

Figure 5.5: Ring Cavity: Pseudo space-time representation of the transient dynamics of the electric field amplitude in the localised state regime (Ring HME model). The x-axis corresponds to the fast time scale σ, and the y-axis to the slow time scale θ. (a) Long-cavity boundary condition $\mathcal{G}(\theta) = G_0$. (b) Dynamical boundary condition eq. (5.11). The laser parameters normalised to the round-trip time are $(\kappa, \gamma, \gamma_g, \gamma_q, \alpha_g, \alpha_q, Q_0, s, T) = (0.99, 300, 16, 400, 0, 0, -0.3, 3, 1)$. Figure adapted from [HAU20a].

includes additional nonlocal terms. As examined in section 4.3.3, the nonlocal Haus master equation provides results that are in accordance with the V-shaped DDE in the localised state regime when applying the long-cavity boundary condition $G(\theta, 0) = G_0$. However, investigating shorter cavity lengths leads to incomplete gain relaxations in between round-trips and therefore necessitates the use of the dynamical boundary condition eq. (5.11).

The analysis of the generalised nonlocal Haus master PDE is started by examining the transitions between pulse-cluster states of different order (PC_n) as discussed in section 4.3.1. Here, the same parameter set as in the previous investigation of the V-shaped VECSEL is used (Table 3.1), with a slight decrease of the unsaturated absorption to $J_q = -39.375$ ($Q_0 = -0.35$). This adjustment is done to achieve a better validity of the linearisation performed in the derivation of the Haus master equation (see section 4.3.3). As presented in Fig. 4.5, a slight change of J_q does not cause to a qualitative difference in the observed dynamical states.

A 1D scan (numerical upsweep) across the pump power is presented in Fig. 5.6(a). Plotted are all pulse maxima obtained at each pump power. Again, the DDE result is coloured in blue and the Haus PDE result in red. The upper bifurcation boundaries match well. In the DDE model, they are characterised by saddle-node bifurcations ($\mathrm{SN}_{n,U}$) as the branch structure is still the same as discussed in section 4.2.2 (see Fig. 4.3). Yet, a slight mismatch in the pulse amplitudes, especially in the quasi-periodic regimes (around $G_0 \approx 2.5$ and $G_0 \approx 5$) is detected. The origin of the deviation lies within the previously elaborated linearised exponential terms in the Haus master equation (see section 4.2.3). At large values of the integrated carrier density in the gain (produced by $G_0 > 1$), an expected mismatch therefore occurs from the inaccuracy of the linearisation. Furthermore, the dynamical boundary condition can be slightly inaccurate at high pump currents due to the strong gain depletions and therefore lead to a slightly elevated or decreased average gain. This is especially visible in the quasi-periodic regimes where the intensity does not drop to as far.

Once more, the bifurcation lines obtained using the DDE model are compared to the dynamics determined by the generalised Haus PDE, which is shown in Fig. 5.6(b). An excellent agreement is found for small Q_0 and the pulse-cluster dynamics are well reproduced. Nevertheless, an increasing separation of the DDE bifurcation lines from the transitions found using the HME systems is visible at higher Q_0 and G_0. This can be again reasoned by the validity of the linearisation.

In the results presented in Fig 5.6(b), the bifurcation lines do not match as well as in the previously presented ring model (e.g. Fig. 5.4(c)). This can mainly be ascribed to the used

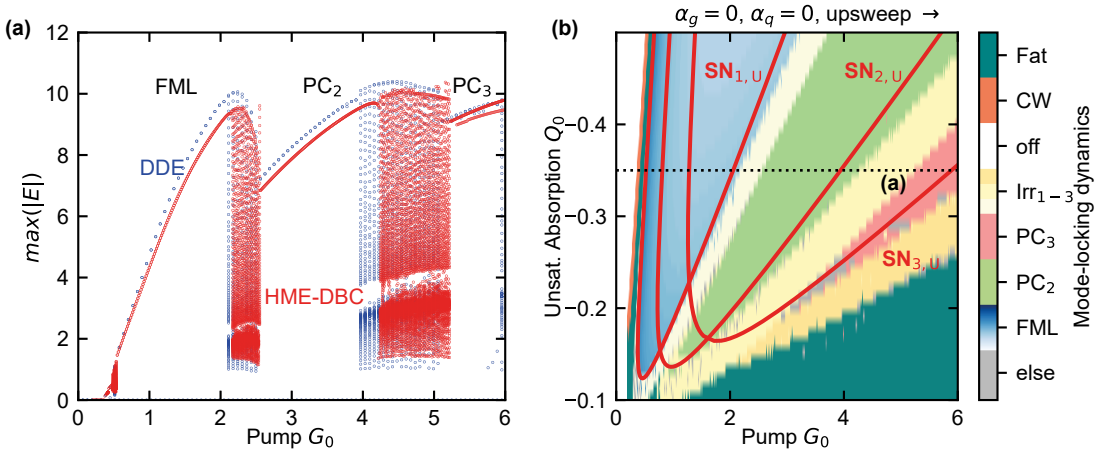

Figure 5.6.: V-shaped Cavity DBC: (a) 1D-bifurcation diagram in pump power G_0 showing all unique pulse maxima ($\max(|E|)$) obtained in 2000 round-trips in the regime of fundamental (FML) and pulse-cluster mode-locking (PC_n). The blue dots correspond to the result determined via the V-shaped DDE model and the red dots to the V-shape Haus master equation PDE with dynamical boundary condition (HME-DBC). (b) 2D-bifurcation diagram in the parameter plane of the pump power and unsaturated absorption (G_0, Q_0) obtained by direct numerical integration of the Haus master PDE (upsweep in G_0) with dynamical boundary condition (HME-DBC). The different colours refer to the following dynamics: Fundamental mode-locking (FML) the shading indicating the pulse width (normalised to the maxium), pulse-cluster dynamics with n pulses (PC_n), quasi-periodic pulse-cluster dynamics with n pulses (Irr_{1-5}), continuous-wave lasing (CW; orange), unclassified dynamics (grey) and fat pulses with a width of $> T/4$. The black dotted line indicates the Q_0 value used for the 1D scan in (a). The red lines represent the saddle-node bifurcations at the upper stability boundary (u) of the FML ($\mathrm{SN}_{1,u}$) and PC_n solutions ($\mathrm{SN}_{n,u}$) in the DDE model (see Fig. 4.9 for details). Laser parameters as given in Table 3.1.

parameter values. The round-trip time at which the V-shaped system is investigated initially leads to very narrow pulses. Thus, a lower value of γ is chosen to counteract the narrowing effect and to enable the path-continuation based on DDE-biftool. In consequence, the losses induced by the filtering are larger when using the parameter set of the V-shaped system and therefore the stable regimes of the solutions shift to higher pump powers (c.f. x-axis of Fig. 5.6(b) and Fig. 5.4(c)). This again favours the discrepancy caused by the linearisation. The shift of the bifurcation lines to higher G_0 results from the higher necessary gain at the increased level of absorption. Additionally, higher-order pulse-clusters are supported with increasing Q_0, due to the pulse narrowing effect of the absorption at the leading edge of the pulse. A more detailed physical interpretation of the 2D-bifurcation diagram in the (Q_0, G_0) plane is given in section 4.2.3. The 2D-bifurcation diagram presented there is obtained using the DDE model and qualitatively produces the same result (see Fig. 4.5).
As presented for the ring model, the accordance of the DDE and PDE models in the parameter plane of the pump power and gain relaxation rate (G_0, γ_g) is assessed for the V-shaped system. Plotted in Fig. 5.7 is the corresponding 2D-bifurcation diagram. The red lines indicate the saddle-node bifurcations (DDE) and the colour code distinguishes the mode-locking dynamics (Haus PDE). Although the unsaturated absorption is slightly varied, the 2D-bifurcation diagram obtained using the Haus master eq. qualitatively looks very similar to the DDE result presented in Fig. 4.8. A physical interpretation of the influence of the gain relaxation rate and its similarity to the variation of the cavity round-trip time is given

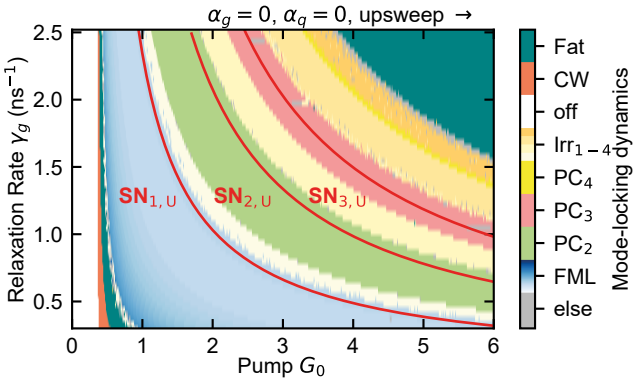

Figure 5.7: V-shaped Cavity DBC: 2D-bifurcation diagram in the parameter plane of the pump power and gain relaxation rate (G_0, γ_g) obtained by direct numerical integration of the Haus master PDE (upsweep in G_0) with dynamic boundary condition (HME-DBC). The colour code refers to the same dynamics as in Fig. 5.6. The red lines again represent saddle-node bifurcations determined applying DDE-biftool to the V-shaped DDE model (see Fig. 5.6 and section 4.2.3). Laser parameters as given in Table 3.1, and $J_q = -39.375$ ($Q_0 = -0.35$).

in sections 4.2.2-4.2.3.

Despite the slight discrepancy of the transition points and bifurcation lines in Fig. 5.7, the qualitative trend matches well. Furthermore, the mismatch does not increase when varying γ_g. This supports the claim of the linearisaton being the main source of deviations in the comparison of the DDE and PDE models.

In an alternative approach, a Haus master equation maintaining the exponentials in the electric field equation is presented in Reference [CAM16]. It could potentially solve the discrepancy problem at higher G_0 and Q_0. Anyhow, the separation of the different contributions according to the multiple time scale analysis in the derivation is not easily applicable, if no linearisation is performed. Therefore, a rigorous derivation of a nonlocal HME for the V-shaped system including the exponentials could be cumbersome. At this point, this question is left open for further research.

It is possible to conclude the generalised Haus model enables the investigation of harmonic transitions as well as quasi-periodic QSML regimes. This was demonstrated for the ring Haus master PDE as well as for the nonlocal V-shape Haus master PDE. In both cases, the pulse amplitudes as well as the stability boundaries of the investigated dynamics were in accordance with the results obtained using the corresponding DDE model. The most significant discrepancies between the DDE model and the generalised DDE model were not related to the new dynamic boundary condition, but rather to the linearisation performed in the derivation of the Haus model. After the proof of principle it is now possible to take advantage of the Haus model and study the influence of a second-order dispersion contribution.

5.3 Second order Dispersion

Following the embodiment of the second-order dispersion in pulse-propagation models [BOY08], the group-velocity second-order dispersion (GVD) is added as an additional imaginary contribution of $i\delta\partial_\sigma^2$ to the electric field equation of the Haus master equation. For the ring cavity, the field equation then reads

$$\partial_\theta E = \left[\frac{1}{2\gamma^2} - i\delta\right]\partial_\sigma^2 E + \frac{1}{2}[(1-i\alpha_g)G + (1-i\alpha_q)Q + \frac{1}{2}\log\kappa]E. \tag{5.12}$$

For the nonlocal HME describing the V-shaped cavity this can be performed accordingly. To distinguish between normal and anomalous dispersion effects, the sign of the dispersion constant δ can be altered. Here, $\delta > 0$ corresponds to anomalous dispersion [SCH18e]. The amount of dispersion is considered to be strong, if the value of the dispersion parameter exceeds the filtering effect determined by the factor $\frac{1}{2\gamma^2}$. Hence, δ is normalised to this value in the following investigations to provide a better comparability. At this point it has to be pointed out, that a transformation of an experimentally determined value of the second-order dispersion to an adequate dispersion parameter value δ is very difficult. Firstly, other counteracting dispersion effects (e.g. third-order dispersion) are not included into the model and therefore the sole influence of the GVD can quickly be overestimated. Furthermore, the influence of the amplitude-phase coupling (α-factors) in multi-mode models can only be qualitatively reproduced as its wavelength dependence is not included. The same is true for the group-velocity dispersion factor here, which in reality also depends on the applied pump power (charge-carrier density). Yet, the strength of the Haus master PDE is to provide a qualitative overview of the influence of different laser parameters and resulting properties of the output [IPP94, HAU00]. This is aimed at here, as the general influence of the GVD on the stabilising dynamics is investigated rather than a quantitative examination of the pulse properties. For a quantitative reproduction of the pulse-shape in the regime of ultra-short pulses, the best results could be obtained using a fully microscopic model as performed in [KIL17, MCL20, MCL21]. In this case, the dispersion naturally results from the microscopic effects rather than a fixed parameter. At a lower modelling complexity, travelling-wave and delay algebraic equation models deliver the possibility to account for a more complex wavelength dependence of the gain effects via different treatments of the macroscopic material polarisation [MUL05a, JAV10a, JAV10]. The disadvantage of these approaches are their large computational demands, making a long-term analysis of the dynamics impractical.
The investigation presented here firstly focuses on the qualitative effect of the group-velocity dispersion on the QSML regime modelled by the ring Haus PDE system. Secondly, the pulse-cluster transitions in the V-shaped VECSEL and their dependence on GVD are investigated.

Ring Cavity

The quasi-periodic QSML dynamics are often considered as a detrimental effect due to the inconsistent pulse amplitudes. Thus, the behaviour of its upper stability boundary, which describes the transition to stable fundamental mode-locking, is studied with respect to the pump current in the following. Here, it is of interest whether a slight influence of the GVD can be beneficial to shrink the QSML regime.
The group-velocity dispersion (GVD) as well as the line-width enhancement factors both strongly effect the phase of the electric field. From a mathematical point of view they are incorporated as imaginary contributions in the electric field equation (5.12). In order to un-

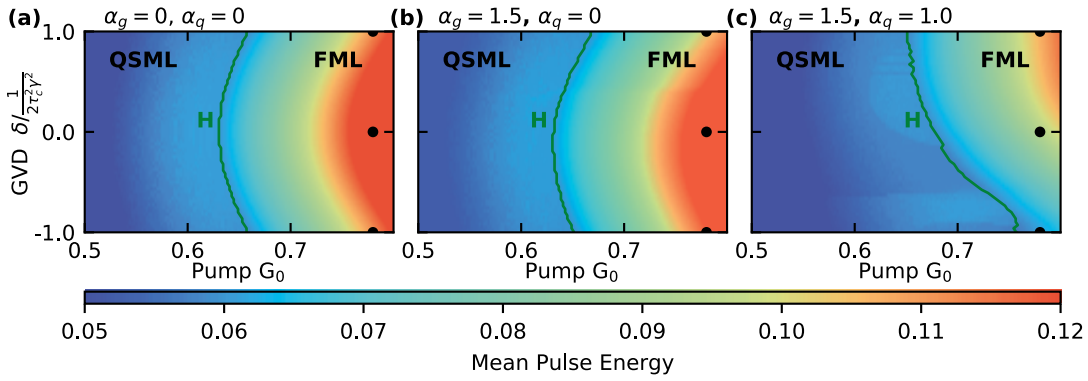

Figure 5.8.: Ring-Cavity DBC: Mean pulse energy in the parameter plane of pump power and group-velocity dispersion (G_0, δ). The group-velocity dispersion is normalised to the factor determining the influence of the gain bandwidth/spectral filtering for a better comparability. The green line indicates the Andronov-Hopf bifurcation (torus in the DDE) at the transition from Q-switched mode-locking (QSML) to fundamental mode-locking (see Fig. 5.3(a)). The direct numerical integration is performed as a downsweep in G_0, starting in the FML regime. (a)-(c) indicate the influence of the line-width enhancement factors, with the parameter values given on top of the respective panels. The other chosen laser parameters are given in the caption of Fig. 5.2. Figure adapted from [HAU20a].

ravel the interplay of both quantities, 2D scans in the parameter plane of the group-velocity dispersion and the pump current are performed (downsweep in G_0). For each parameter point, the mean pulse energy[5] across 300 round-trips is calculated and the dynamics are evaluated according to the characteristics of the time series. The result for three different combinations of α_g,α_q is depicted in Fig. 5.8, with the mean pulse energy indicated by the colour code. The green line corresponds to the Andronov-Hopf bifurcation[6] (upper bifurcation point in Fig. 5.3(a)) separating the QSML (left) and the FML (right) region, which is given by a torus bifurcation in the DDE model.
In absence of the amplitude-phase coupling ($\alpha_g = \alpha_q = 0$), the Andronov-Hopf bifurcation line shifts symmetrically around $\delta = 0$ to higher pump powers. The reason for that lies within the chirp that is induced to the pulse at large values of $|\delta|$. The chirp leads to an excess bandwidth and hence incurs stronger spectral filtering. In turn, the increased filtering losses lead to a drop in pulse energy and consequently the pulse is amplified less efficiently. Finally, the reduced net amplification leads to a higher pump current required for the FML dynamics to stabilise. The pulse shape in the FML regime ($G_0 = 0.78$) for $\delta = 0$ and $\delta = \pm 1$ is depicted in Fig. 5.9(a). The reduced pulse energy is clearly visible and furthermore an increased width of the pulses, caused by the GVD, is evident. Additionally, the pulses at $\delta = 1$ and $\delta = -1$ are identical (red and blue line perfectly overlap in Fig. 5.9(a)), which highlights the symmetric influence of the dispersion, if $\alpha_g = \alpha_q = 0$. It has to be highlighted that in the investigated system, the GVD does not solitarily impact the pulse, but in combination

[5] The pulse energy is defined as the temporal integration over the pulse intensity.
[6] As the transition between QSML and FML in the (G_0, δ) parameter space is only determined via direct numerical integration it is potentially possible that the transition is embodied by another bifurcation at varied δ. However, an investigation of the appearance of the bifurcation boundaries in the 1D scans did not evidence any characteristic changes of the bifurcation structure. Furthermore, the transition line between QSML and FML states only shows very smooth changes in 2D (Fig. 5.8), which further does not hint at a change of the bifurcation scenario. This strongly suggests the torus bifurcation is sustained. Ultimately, it could be assessed by continuing the bifurcation line using Pde2path [UEC14].

with the laser nonlinearities. Hence, the pulse shapes differ from the simply broadening or compressing effect of normal or anomalous dispersion. Furthermore, one has to account for differing influence of the absorber on pulses of different width. Broader pulses with a lower intensity usually experience higher losses, due to the fast recovery of the absorber.
The symmetric impact of the GVD around $\delta = 0$ can be explained by the complex conjugate symmetry of the electric field equation in the Haus master PDE (5.12) in absence of other phase effects ($\alpha_g = \alpha_q = 0$). Nevertheless, if a non-zero amplitude-phase coupling is considered ($\alpha_g \neq 0$) the symmetry is lost. This is indicated in Fig. 5.8(b) illustrating the 2D-bifurcation diagram in the (G_0, δ) plane for $\alpha_g = 1.5$, $\alpha_q = 0$. The interplay of the amplitude-phase coupling and GVD shifts the most beneficial situation with regard to the pulse energy towards slightly negative values of δ (red area in Fig. 5.8(b)). In consequence, a slight asymmetry with respect to $\delta = 0$ is introduced. Examples of the pulse shapes at a positive, negative and zero dispersion parameter are presented in Fig. 5.9(a). Due to the influence of α_g, a negative dispersion value does not decrease the pulse amplitude as much as a positive value of δ (see Fig. 5.9(b)). However, the pulse is also strongly broadened at $\delta = -1$.
The asymmetry of the Andronov-Hopf bifurcation line with respect to $\delta = 0$ is strongly enhanced, if additionally $\alpha_q \neq 0$, which is depicted in Fig. 5.8(c). In this case, it becomes evident, that at constant pump powers the pulse energy in the FML regime is higher for dispersion values $\delta > 0$ (yellow region in Fig. 5.8(c)). The higher pulse energies hint at lower filtering or absorber induced losses, resulting from the altered nonlinear pulse formation, which lets the FML solution stabilise at lower pump powers as compared to $\delta < 0$. The difference is also strongly visible in the pulse shapes in Fig. 5.9(c). Comparing the pulse shape across the panels, one notices that already at $\delta = 0$ (black lines) the amplitude is reduced by the influence of the α-factors. In the negative as well as in the positive dispersion regime, the pulses broaden with respect to $\delta = 0$. The interplay of the α-factors and the positive dispersion lead to a more enhanced broadening effect, while maintaining a high pulse amplitude and therefore the pulse energy is strongly increased. In contrast, the additional influence of negative dispersion leads to a decrease in pulse energy.
It can be concluded that at the investigated values of the α-factors, the group-velocity dispersion mainly favours the extension of the QSML regime and shifts the onset of stable FML dynamics to higher pump currents. Anyhow, in presence of an already weak amplitude-phase coupling anomalous dispersion ($\delta > 0$) can be beneficial as the boundary between FML and QSML states does not shift as strongly to higher pump powers as for normal dispersion ($\delta < 0$).

V-shaped Cavity

The attention is now turned to the influence of the GVD on the pulse-cluster states emerging in a V-shaped VECSEL setup in the intermediate-cavity regime as discussed in section 4.2.3. On that account, the dispersion contribution $i\delta\partial_\sigma^2$ is added to the electric field equation of the generalised nonlocal Haus master equation (4.49).
As previously presented for the ring model, scans in pump power (upsweep) are performed for different values of the GVD (δ). A comparison of the 1D-bifurcation scenario at GVD values of $\delta = 0$ and $\delta/\frac{1}{2\gamma^2} = 0.425$ is plotted in Fig. 5.10(a). It reveals the unique pulse amplitudes (collected in 100 round-trips) found at each pump power value. The normalisation of the GVD to the filter constant is again used for a better comparability of the dispersion

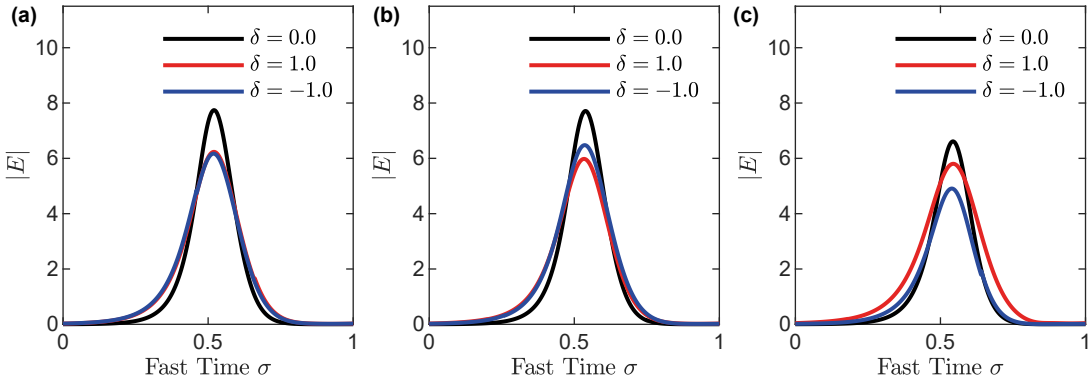

Figure 5.9.: Ring-Cavity DBC: Pulse shape in the FML regime at different values of the group-velocity dispersion δ. The subpanels correspond to different combinations of the α-factors: (a) $\alpha_g = 0$,$\alpha_q = 0$, (b) $\alpha_g = 1.5$,$\alpha_q = 0$, (c) $\alpha_g = 1.5$,$\alpha_q = 1.0$, with the parameter points shown by black dots in Fig. 5.8. The pump parameter is set to $G_0 = 0.78$ and the other laser parameters are given in the caption of Fig. 5.2.

strength.
Although the general bifurcation scenario is not changed when including GVD in case of $\alpha_g = \alpha_q = 0$, one observes a decrease of the maximum pulse amplitude at all pump powers. At the start of each dynamical regime, the pulses exhibit very similar amplitudes for $\delta = 0$ and $\delta = 0.425$, but an increasing difference is evident at higher pump currents in Fig. 5.10(a). This can be ascribed to the increased filtering losses induced by the excess bandwidth of the pulses caused by the GVD. Furthermore, the inclusion of the GVD leads to a further influence on the nonlinear pulse shaping mechanisms priorly only determined by the gain and absorber. This leads to an altered amplification and absorption of the pulse.
The occurrence of two maxima in the PC_2 and PC_3 regime for $\delta = 0.425$ hints at an uneven amplification of the pulses in the cluster. Combined with the decreased pulse amplitude it hints at a less effective amplification at non-zero dispersion, which causes the regimes of FML and PC_n solutions stretching out to slightly higher pump currents at $\delta = 0$.
A broader overview of the stabilising dynamics in the parameter plane of the pump power and GVD is illustrated in the 2D-bifurcation diagram in Fig. 5.10(b). Indicated by the colour code are the stabilising FML and (irregular) pulse-cluster dynamics. As no amplitude-phase coupling is included ($\alpha_g = \alpha_q = 0$), the upper bifurcation boundaries (saddle-node bifurcations) of the fixed-point[7] FML ($G_0 \approx 2.1$) and PC_2 ($G_0 \approx 4.1$) solutions shift symmetrically to lower pump powers around $\delta = 0$. This symmetry is again related to the complex conjugate symmetry of the electric field equation. The upper bifurcation points of the irregular solutions (orange shaded regions) are almost unaffected by the group-velocity dispersion, which is also true for the lasing threshold at very low pump currents (transition to white region in Fig. 5.10(b)). To unravel the behaviour of the lower stability boundaries of the PC solutions a numerical downsweep in pump power has to be performed. It is illustrated in Fig D.2 of Appendix D and reveals that the lower bifurcation points are not affected by the GVD.
The behaviour of the upper and lower stability boundaries can be better understood, by investigating the influence of the GVD on the mean pulse width (FWHM) and the mean

[7]These states are periodic in the DDE but become fixed-points in the PDE formulation.

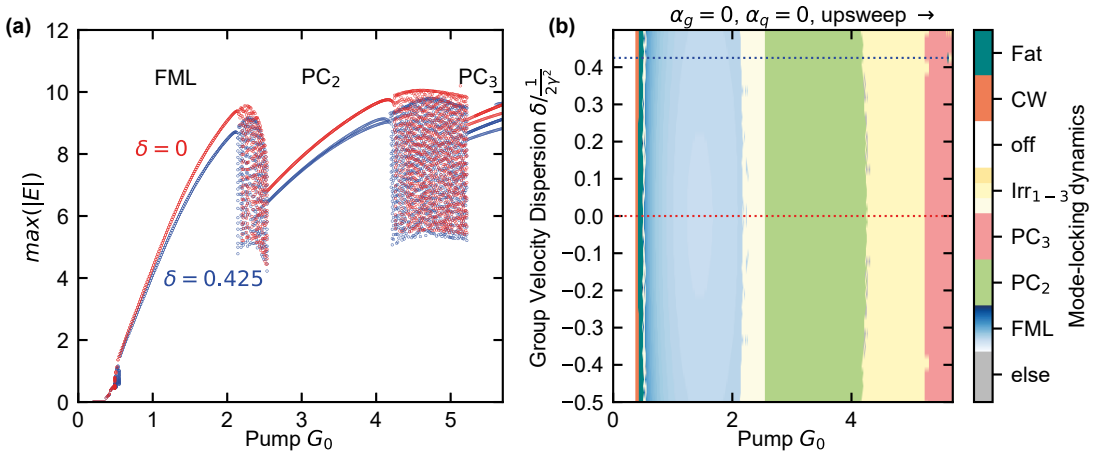

Figure 5.10.: V-shaped Cavity DBC: (a) 1D-bifurcation diagram in pump power G_0 showing all unique pulse maxima ($\max(|E|)$) obtained in 100 round-trips in the regime of fundamental (FML) and pulse-cluster mode-locking (PC_n). The blue dots correspond to a group-velocity dispersion of $\delta/\frac{1}{2\gamma^2} = 0.425$ and the red dots to $\delta/\frac{1}{2\gamma^2} = 0$. (b) 2D-bifurcation diagram in the parameter plane of the pump power and the group-velocity dispersion (G_0, δ) obtained by direct numerical integration of the generalised nonlocal Haus master PDE (upsweep in G_0). The different colours refer to the same dynamics as in Fig. 5.6. Laser parameters as given in Table 3.1, and $J_q = -39.375$ ($Q_0 = -0.35$).

pulse area[8]. Both quantities are plotted for the fixed-point solutions in the (G_0, δ) parameter plane in Fig. 5.11. Close to the lower transition points of the FML and PC_n states (upper stability boundaries of the irregular solutions), one notices that the pulse energy is almost unaffected by the GVD (Fig. 5.11(a)). Furthermore, the change of the pulse width is only marginal close these points. Consequently, the pulse amplification and gain depletion is very similar along the transition for all values of the GVD and therefore the bifurcation scenario remains unchanged.
In contrast, close to the upper bifurcation boundaries of the FML and PC_2 state, the mean pulse energy is not constant across the different values of group-velocity dispersion at a constant G_0. Close to $\delta = 0$ the pulse energy is much higher than at high absolute values of δ (e.g. see shading for $G_0 \approx 4$ in Fig. 5.11(a)). Additionally, the pulse width is slightly lower at $\delta = 0$ compared to non-zero dispersion at $G_0 \approx 4$ (see Fig. 5.11(b)). It has to be noted that the pulse width is calculated as the FWHM and therefore the edges of the pulses are not taken into account in this quantity. Nonetheless, the investigation of the time-series indicated an additional strong broadening at the edges of the pulses (see Fig. 5.9), which elevates the electric field amplitude above 0 in between the pulses of a cluster. Hence, the electric field in between the pulses is further amplified, stealing gain from the pulses. This is also evident from the lower pulse amplitudes in the 1D scan in Fig. 5.10(a). Consequently, the combination of the less effective amplification (lowered pulse amplitude/energy) and the broadening of the pulses lets the regular solutions destabilise at lower pump powers.

As discussed for the ring model (c.f. Fig 5.8), the interplay of the dispersion and the α-factors strongly influences the stability boundaries as visible from the bifurcation diagrams in Fig. 5.12. Plotted in (a) and (b) are the same 1D and 2D-bifurcation diagrams as before, but with $\alpha_g = 0.25$, $\alpha_q = 0$. In contrast to the completely symmetric influence of the disper-

[8]Here, the mean is calculated over all pulses in 100 round-trips.

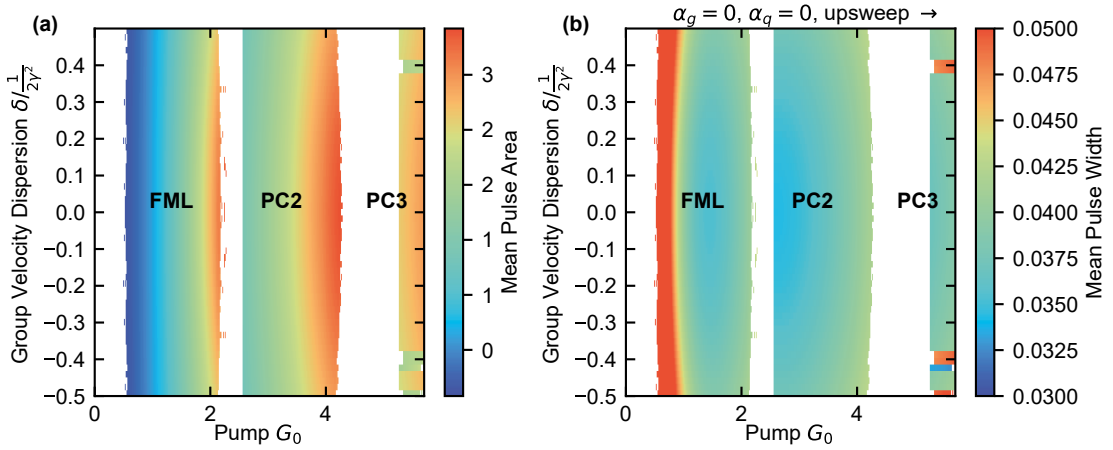

Figure 5.11.: V-shaped Cavity DBC: (a) Mean pulse width in the parameter plane of the pump power and the group-velocity dispersion (G_0, δ) obtained by direct numerical integration of the Haus master PDE (upsweep in G_0). (b) Mean Pulse width in the same parameter plane. Both quantities are shown only for the fixed-point solutions (white indicates a (quasi-)periodic solution). The underlying dynamics are plotted in Fig. 5.10 and given by the labels. Laser parameters as given in Table 3.1 and $J_q = -39.375$ ($Q_0 = -0.35$).

sion at zero α-factors, a variation of the pulse amplitudes becomes evident when comparing the 1D scans obtained at positive and negative dispersion values (see Fig. 5.12(a)). Furthermore, the shift of the bifurcation points becomes asymmetric with respect to $\delta = 0$ as the stability boundaries shift differently in G_0, despite the same absolute value of the dispersion. Additionally, further PC_n instabilities occur for $\delta = -0.35$ as visible from the many different maxima present at $G_0 > 4$ in Fig. 5.12(a).

The 2D-bifurcation diagram in Fig. 5.12(b) again reveals that, although only a small linewidth enhancement factor of $\alpha_g = 0.25$ is included, the upper bifurcation lines do not shift symmetrically with respect to δ anymore. From a mathematical perspective this can once more be reasoned by the loss of the complex conjugate symmetry of the electric field equation. The stronger shift of upper boundary of the PC_2 solution in comparison to the FML boundary can be explained by the fact that it occurs at a higher pump current and therefore the elevated gain level $G(\theta, \sigma)$ increases the influence of α_g in the equations. Yet, the position of the lower transition points towards the FML and PC solutions remain almost unchanged, which can be interpreted with respect to the previously discussed unchanged pulse energy and pulse width. Close to the transition points, both quantities are almost unaffected by the inclusion of the small α_g (see Fig. D.1).

The asymmetric shift of the upper bifurcation boundary is caused by the differing filtering and absorber losses (i.e. differing nonlinear pulse shaping) induced by the interplay of positive or negative dispersion with α_g. Again, the highest pulse energy (i.e. most effective amplification) coincides with the transition point being at the highest pump power (see Fig. D.1(a)).

The strong influence of already a very small α_g factor compared to the ring model can be ascribed to the double gain interaction of a pulse in the V-shaped cavity. Hence, the α_g-factor influences the pulse twice per round-trip. It has to be highlighted that the inclusion of higher α-factors quickly leads to a vastly increasing number of instabilities. This may result from the strong interplay of the phase effects. Furthermore, the comparably high average gain,

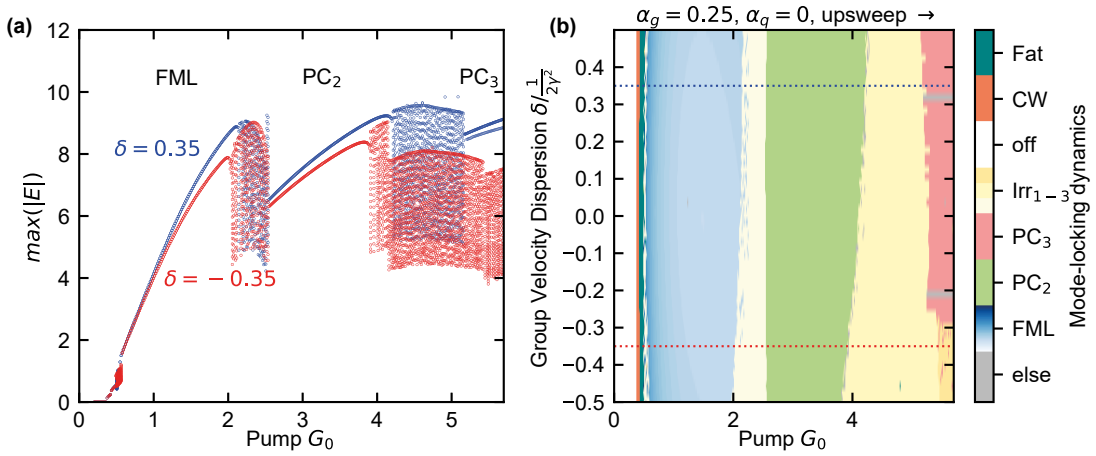

Figure 5.12.: V-shaped Cavity DBC: (a) 1D-bifurcation diagram in pump power G_0, showing all unique pulse maxima as in Fig. 5.10. The blue dots correspond to a dispersion of $\delta/\frac{1}{2\gamma^2} = 0.35$ and the red dots to $\delta/\frac{1}{2\gamma^2} = -0.35$. (b) 2D-bifurcation diagram in the (G_0, δ) parameter plane obtained by a direct numerical integration (upsweep in G_0). The different colours refer to the same dynamics as in Fig. 5.10. Laser parameters as given in Table 3.1, and $J_q = -39.375$ ($Q_0 = -0.35$) and $\alpha_g = 0.25$,$\alpha_q = 0.0$.

induced by the large pump parameter G_0, strongly enhances the influence of α_g due to the multiplication in the electric field equation (4.49). Thus, using experimentally determined values for ($\alpha_g \approx 2.5$ [WAL16]) would most likely correspond to an overestimation of the amplitude-phase coupling in this regime. To conclude, it was elaborated that it is possible to model the influence of second-order dispersion on the output of a V-shaped VECSEL using a generalised nonlocal Haus master equation. The V-shaped VECSEL was investigated at an intermediate-cavity length, producing fundamental mode-locking and pulse-cluster states. In accordance with previous works and experiments, it was found that due to the interplay with amplitude-phase coupling effects (modelled by constant α-factors) second-order dispersion can have a positive effect [SIE13b, HEA16, WAL16] on the laser output. These are embodied by higher mean pulse energies or the possibility to drive the laser with a higher pump current, while maintaining a stable FML or PC_2 state. The downside of the presented modelling approach, is the qualitative nature of the predictions due to the wide range of simplifications. Furthermore, the pulse-width is much larger than in experiments, in which 100 fs pulses are produced [WAL16]. A clear analysis of the accuracy of the dispersion analysis presented here could be done with greatly enhanced computational capabilities in the future, allowing to integrate fully microscopic models over several round-trips at realistic cavity lengths [KIL17, MCL20].

5.4 Third order Dispersion

Next to second-order dispersion discussed in the last section, third-order dispersion (TOD) can become a factor of impact when investigating pulsed laser emission. It can be a limiting factor in the optimisation of the duration of ultra-short pulses in the femtosecond regime, generated in mode-locked solid state (Ti-sapphire) lasers [CUR93, ZHO94, BRA93a] and fibre lasers [DEN94, OLI06]. Furthermore, the interplay of TOD and GVD plays an important role in the design of semiconductor chips for passively mode-locked VECSELs and can have a positive influence [SIE13b, WAL16]. Externally, a possibility to compensate TOD is given by applying an appropriate phase modulation [HEL03]. Nevertheless, it can be exploited as a beneficial effect counteracting nonlinear phase shifts [ZHO05]. Furthermore, TOD can play an important role when investigating the propagation of optical solitons in different (driven) nonlinear resonators [AKH08, GRE12b, LEO13a]. In these systems, TOD can either lead to instabilities [KOD94], can have an effect on pulse compression [CHA94], can cause the generation or destabilisation of bound states [GRE12b, CHE16f, SAK18] or can aid the stabilisation of various soliton states [TLI10, PAR14, MIL14b]. Additionally, TOD can have a substantial effect on the occurrence of dark solitary waves [PAL99, YOU17a].
Based on the modelling of the electromagnetic wave propagation in different structures such as mode-locked laser-, fibre- or micro-cavities, the influence of dispersion has mainly been investigated within partial differential equation frameworks [SOT97, ARA02, AKH08, GRE12b, LEO13a, GUR19], due to the straightforward phenomenological inclusion of the dispersive terms. Hence, it is possible to investigate the role of third-order dispersion within the dynamics of the V-shaped passively mode-locked VECSEL by the application of the Haus master equation framework presented in the previous section. The only change required would be an added third-order dispersion term embodied by a third-order derivative with respect to the fast time scale as presented in Reference [HAU93b].
However, another approach is pursued in this work, as only recently it was suggested that third-order dispersion can be described as a "simple, robust, and unitary transformation" in delayed systems [SCH19b]. This makes it possible to describe the effect of TOD, while taking advantage of the previously mentioned properties of delayed systems such as reduced memory requirements for long cavities and the possibility of a complete bifurcation analysis. The approach applied in References [SCH19b, SCH20d, HES21] to investigate TOD effects in external cavity mode-locked lasers, is based on the usage of a delay algebraic equation model and was originally introduced in References [MUL05a, MAR15c]. This approach follows the idea of describing the gain and absorber chip as two coupled mico-cavities and including the cavity geometry by the description of the fields in the macro-cavity. An adjusted model for the V-shaped cavity is derived from the starting point given by the models describing face-to-face coupled micro-cavities [SCH19b, HES21] in subsection 5.4.1. It is similar to the work presented in [AVR19]. Furthermore, to asses the contribution of the TOD, a transformation of all parameters from the DAE to the DDE model is elaborated in subsection 5.4.2. In subsection 5.4.3 the influence of third-order dispersion on different regimes is discussed by comparing the two models, making use of the parameter transformations.

5.4.1 V-shaped Delay Algebraic Equation Model

As a starting point for the derivation of a delay algebraic equation system to model a passively mode-locked V-shaped VECSEL, the DAE model for face-to-face coupled gain and absorber chip presented in [MAR15c, SCH19b] is taken into account. As described in section 4.3.1, this

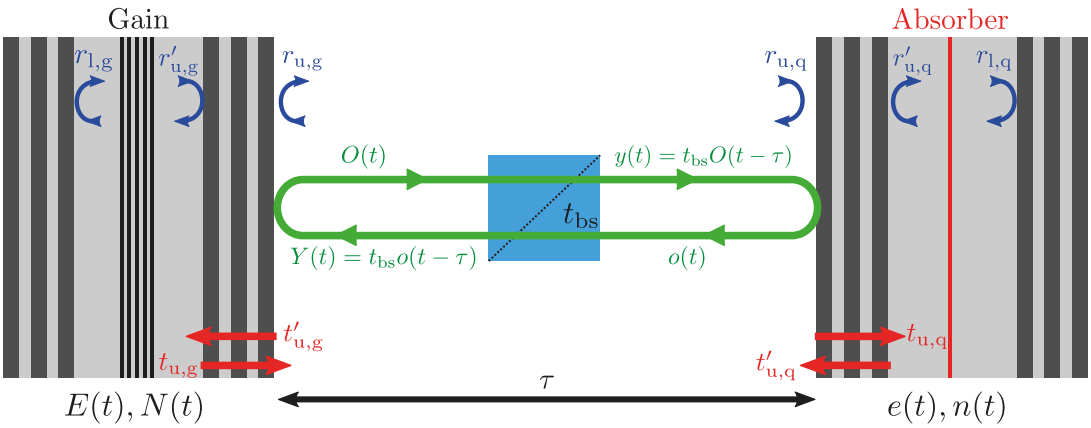

Figure 5.13.: Sketch of face-to-face coupled gain and absorber chip in an external cavity of length τ. The thin black (red) lines indicate the active region in the gain (absorber) micro-cavity. The reflectivities (r) at the different surfaces/DBRs are indicated in blue and transmittances (t) are indicated in red with the arrow pointing into the direction of the transmission. The blue square indicates a beam splitter with transmissivity t_{BS}. The green circle refers to the light propagating around the cavity and indicates how the output fields $O(t)$ and $o(t)$ of the micro-cavities are related to the fields incident on the other micro-cavities $Y(t), y(t)$. Figure adapted from [SCH19b].

type of linear[9] cavity setup can be utilised to generate temporally localised states in the long-cavity regime. Similar to the derivation of the DDE model, the derivation initially starts at Maxwell's wave equation (3.1) describing the evolution of the monochromatic electromagnetic field in a semiconductor medium [MAR15c]. In this case, the medium is embodied by the gain and absorber micro-cavities. A sketch of the linear external cavity setup (coupled microcavites) is indicated in Fig. 5.13. Displayed are the different electric fields in the different sections of the device as well as the important reflectivities and transmittances used to establish the boundary conditions. The figure illustrates the relationship between the intracavity fields $E(t)$,$e(t)$, the micro-cavity self emission fields $O(t), o(t)$ and the fields injected into the micro-cavities $Y(t), y(t)$. The basic steps of the derivation include relating the fields in the external cavity and the electric fields inside the different sections of the micro-cavities[10] by finding the correct boundary conditions in the Fourier domain and subsequently transforming back into time domain (for details see Appendix I of [MAR15c]). In the DAE equation system discussed in this section, the charge-carrier dynamics and the light-matter interaction are modelled via the linear gain approximation as in the travelling-wave approach (eq. (3.7)) discussed at the start of section 3.3. As mentioned before, the linear gain term stems from the adiabatic elimination of the macroscopic polarisation of the semiconductor medium [MAR15c, SCH19b]. Approaches based on describing the field carrier interaction via dynamically calculating the macroscopic polarisation, can be found in References [MUL05a,

[9] Here, the term "linear cavity" is used to simply describe the case of two face-to-face coupled micro-cavities (see Fig. 5.13).

[10] The intracavity field $E(t)$ can be decomposed into the fields in the upper and lower part of the semiconductor chips as well as in the quantum well region. For details see [MAR15c].

JAV10, JAV12]. Thus, the differential equations for the final model for the face to face coupled system read [MAR15c, SCH19b]

$$\frac{1}{\kappa_g}\frac{\partial}{\partial t}E(x,y,t) = \Big[\,[1-i\alpha_g]\,N(x,y,t) - 1 + i\omega_0 + (i+d_g)\,\Delta_\perp\Big]E(x,y,t) + h_g Y(x,y,t), \tag{5.13}$$

$$\frac{\partial}{\partial t}N(x,y,t) = \gamma_g\,[N_0 - N(x,y,t)] - N(x,y,t)|E(x,y,t)|^2 + \mathcal{D}_g\Delta_\perp N(x,y,t), \tag{5.14}$$

$$\frac{1}{\kappa_q}\frac{\partial}{\partial t}e(x,y,t) = \Big[\,[1-i\alpha_q]\,n(x,y,t) - 1 + (i+d_q)\,\Delta_\perp\Big]e(x,y,t) + h_q y(x,y,t), \tag{5.15}$$

$$\frac{\partial}{\partial t}n(x,y,t) = \gamma_q\,[n_0 - n(x,y,t)] - sn(x,y,t)|e(x,y,t)|^2 + \mathcal{D}_q\Delta_\perp n(x,y,t), \tag{5.16}$$

$$\tag{5.17}$$

complemented by the delay algebraic equations

$$y(x,y,t) = t_{\mathrm{bs}}O(x,y,t-\tau) = t_{\mathrm{bs}}\big[E(x,y,t-\tau) - Y(x,y,t-\tau)\big], \tag{5.18}$$

$$Y(x,y,t) = t_{\mathrm{bs}}o(x,y,t-\tau) = t_{\mathrm{bs}}\big[e(x,y,t-\tau) - y(x,y,t-\tau)\big]. \tag{5.19}$$

The electric fields inside the gain and absorber micro-cavities are given by $E(x,y,t)$ and $e(x,y,t)$ respectively. Furthermore, $N(x,y,t)$ and $n(x,y,t)$ describe the charge carrier densities in gain and absorber. Furthermore, $Y(x,y,t)$ is the field incident on the gain, whereas $y(x,y,t)$ is the field coupled into the absorber micro-cavity as displayed in Fig. 5.13. The delay τ describes the distance between the two semiconductor chips. The fields at the output of the micro-cavities $O(x,y,t), o(x,y,t)$ are given by superposition of the reflection of the incident field at the micro-cavity surface and the self-emission of the micro-cavity, i.e. $o(x,y,t) = e(x,y,t) - y(x,y,t)$ and $O(x,y,t) = E(x,y,t) - Y(x,y,t)$. It is important to note that initially the expressions for $O(x,y,t)$ and $o(x,y,t)$ include pre-factors taking to into account the reflection and transmission losses as well as the reflection induced phase changes. Nevertheless, it is feasible to apply a proper normalisation to the electric fields to simplify all expressions. The normalisation of the DAE system and all parameters is given in appendix A.1. It has to be highlighted that for the normalisation of the transmittances and reflectivities, Stokes relation is applied. Assuming a passive section in between the cavities, the field injected into one of the cavities is defined as the output field of the opposite cavity, delayed by the cavity length τ and multiplied by the transmittance of the beam splitter t_{bs}, as given in equations (5.18)-(5.19).
The normalised photon life-times in the gain and absorber micro-cavities are given by $\kappa_{g,q}^{-1}$ and the carrier life-times are denoted as $\gamma_{g,q}^{-1}$, respectively. The amplitude-phase coupling is included via the constant line-width enhancement factors $\alpha_{g,q}$, and s is the saturation parameter describing the ratio of the saturation energies in gain and absorber (see Appendix A.1 for details). The carrier diffusion coefficients in the gain and absorber sections, scaled to the diffraction length, are given by $\mathcal{D}_{g,q}$. In addition to that, the transverse field diffusion coefficients $d_{g,q}$ describe the variation of cavity losses with the angle of incidence. The equilibrium carrier densities are given by N_0 and n_0, which can be interpreted as the pump and the unsaturated absorption ($n_0 < 0$, and $N_0 > 0$). The detuning between the cavities is given

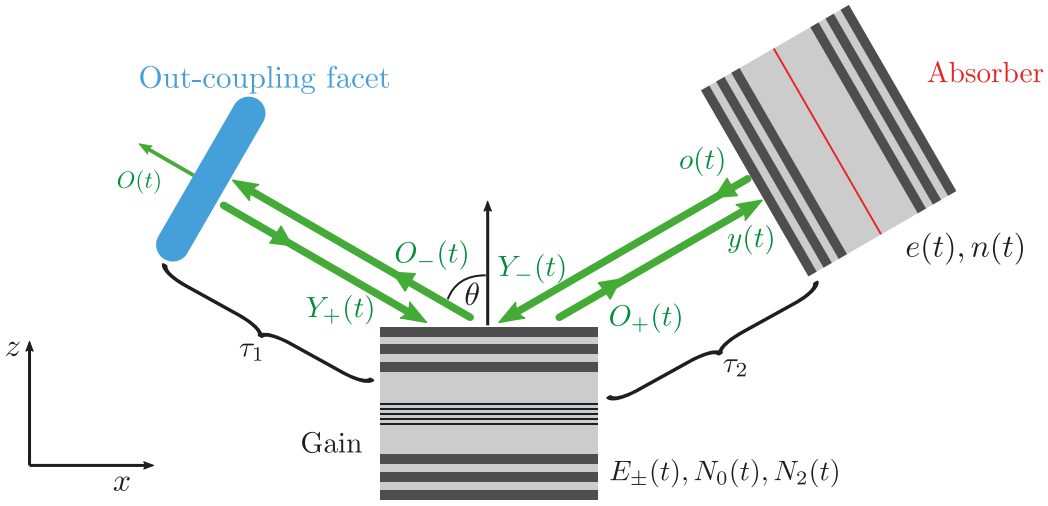

Figure 5.14.: Sketch of a passively mode-locked VECSEL in a V-shaped cavity configuration. Here, gain and absorber chip are sketched with top and bottom DBR, as usually used for experiments in the localised state regime [MAR15c]. The cavity arms have a length of τ_1 and τ_2. The thin black (red) lines indicate the active region in the gain (absorber) micro-cavity. The reflectivities at the different surfaces/DBRs are defined as in Fig. 5.13, but are not show here. The outcoupling facet with a reflectivity of η is coloured in blue. The green arrows refer to the light propagating around the macro-cavity and illustrate how the output fields of the micro-cavities $O_\pm(t), o(t)$ are related to the fields incident on the other micro-cavities $Y_\pm(t), y(t)$.

by ω_0. The factors $h_{g,q}$ describe the coupling of the incident field into the micro-cavities and depend on the reflectivity of the upper and lower DBR of the micro-cavities according to

$$h_i = \frac{(1 + |r_{l,i}|)\,(1 - |r_{u,i}|)}{(1 - |r_{u,i} r_{l,i}|)}, \tag{5.20}$$

where $r_{u,i}$ is the reflectivity of the upper Bragg mirror, and $r_{l,i}$ is the reflectivity of the lower Bragg mirror, with the subscript $i \in \{g, q\}$ referring to the gain (g) and absorber (q), as shown in Fig. 5.13.

If the top-mirror is perfectly reflective ($r_{u,i} = 1$), no light enters the micro-cavity and consequently $h_i = 0$ [SCH19b]. However, the devices investigated here consist of two highly reflective DBRs at the top and bottom of which the lower mirror is slightly more reflective, which is typical for VCSEL micro-cavities [LI03]. Thus, the reflectivities are approximated by $r_{u,i} \approx 0.99$ at the top and $r_{u,i} \to 1$ at the bottom [SCH19b], leading to $h_i = 2$. In case of an empty cavity, this regime can be understood as a Gires-Tournois interferometer, which consists of a bottom mirror with a reflectivity close to unity and a top mirror of lower reflectivity [GIR64]. This type of interferometer is a well-established technique to induce an adjustable amount of second and third-order dispersion [SCH19b], that depends on the reflectivities and the detuning of the cavity and the incident light.

In order to transform the model from the case of a face-to-face coupled cavity to a V-shaped external cavity, three major differences between the cavities have to be taken into account[11]. Firstly, there are two cavity arms in the V-shaped configuration and thus a second delay defining the cavity geometry has to be included when coupling the fields as shown in Fig. 5.14.

[11] The original derivation of the model was performed by Svetlana V. Gurevich and Julien Javaloyes and submitted to the author in a private communication in April 2019.

Secondly, the gain is injected bidirectionally as illustrated by the green arrows arriving at the gain chip in Fig. 5.14. This can lead to carrier gratings due to interference of the incident beams [PER10d, LAU17]. As indicated by the angle θ, normal incidence of the injected fields at the gain is not always given, which is the third major difference.
Due to the fact that the incidence at the absorber is considered as mono-directional and normal to the chip-surface, the equations for the carrier density and the electric field describing the absorber (5.16)-(5.15) remain unchanged. Anyhow, in the following a flat transverse electric field profile is assumed and it is therefore possible to neglect the diffraction/diffusion terms in the carrier and field equations for the absorber (partial derivatives with respect to x and y). In contrast, it is necessary to retain the transverse contribution to account for the non-normal incidence at the gain micro-cavity, which breaks the x-y symmetry of the Gaussian mode. However, a 1D transverse problem can be assumed to treat the distortion of the mode in which the x-axis refers to the micro-cavity surface plane. Therefore, only the contribution ∂_x^2 remains in the electric field and carrier equations for the gain. The z-axis is chosen to be normal to the micro-cavity plane (see bottom left of Fig. 5.14). Additionally, the field diffusion $d_{g,q}$ can be neglected as it has a minor influence in case of the investigated VECSELs, as it is constructed to have a stable transverse mode-profile. Consequently, the starting point for the micro-cavity differential equations for the gain are the following two equations

$$\frac{1}{\kappa_g}\frac{\partial}{\partial t}E(x,t) = \left[\left[1-i\alpha_g\right]N(x,t) - 1 + i\omega_0 + i\partial_x^2\right]E(x,t) + h_g Y(x,t), \tag{5.21}$$

$$\frac{\partial}{\partial t}N(x,t) = \gamma_g\left[N_0 - N(x,t)\right] - N(x,t)\left|E(x,t)\right|^2 + \mathcal{D}\partial_x^2 N(x,t), \tag{5.22}$$

where a transverse Gaussian mode $\phi(x,y)$ is factored out, so that the field only has the remaining fast variation along the x-axis due to the angle of incidence.
When an incident electric field is reflected by the micro-cavity, the x-component of the corresponding wave vector is conserved, whereas the z-component is inverted. Furthermore, only the x-component of the wave vector is different for the bidirectionally incident fields, whereas the z-component is equal (see Fig. 5.14). Accordingly, a transverse wave vector decomposition can be applied to distinguish between the fields incident from the left (Y_+, E_+) and from the right (E_-,Y_-). The transverse wave vector decomposition for injected and intracavity fields reads

$$Y(x,t) = Y_+(x,t)e^{iq_x x} + Y_-(x,t)e^{-iq_x x}, \tag{5.23}$$

$$E(x,t) = E_+(x,t)e^{iq_x x} + E_-(x,t)e^{-iq_x x}. \tag{5.24}$$

The wave vector is defined as $q_x = q_0 \sin(\theta)$, with the angle of incidence with respect to the normal axis θ (see Fig. 5.14), the angular wavenumber $q_0 = \frac{2\pi n}{\lambda}$ and the wavelength λ. The interference of the two waves leads to a carrier density grating with a wavelength that depends on the angle of incidence, as can be seen from the wave vector/wavenumber. Originally a similar grating effect was observed when applying a density matrix formulation to calculate the distribution of moving two level atoms in a gas, encountered by two counter-propagating electro-magnetic waves [HAR72, PER10d, JAV10a]. The two fields induce a spatial modulation (or temporal modulations in the "atom rest frame" [HAR72]) of the density matrix, which occurs at all harmonics of the wave vector [HAR72]. Motivated by these observations, a similar description of the spatial modulation was pursued to describe spatial

hole-burning resulting from the bidirectional wave propagation in semiconductor ring cavities and Fabry-Pérot cavities [JAV09, JAV10a, PER10d, JAV10]. Yet, for semiconductor media only the first harmonic ($2q_x$) is considered in the modulation due to the increased damping of the high-order terms resulting from spatial diffusion [JAV09, PER10d]. Motivated by previous works on the formation of carrier gratings, the following decomposition is applied for the carrier densities [JAV10, JAV10a]

$$N(x,t) = N_1(x,t) + N_{+2}(x,t)e^{2iq_x x} + N_{-2}(x,t)e^{-2iq_x x}, \tag{5.25}$$

where N_1 is the quasi-homogeneous contribution to the charge-carrier density and N_{+2}, N_{-2} are the (slowly varying) complex amplitudes of the carrier density grating, with $N_{-2} = N_{+2}^*$ and the wave vectors as defined before [JAV10]. The factor of 2 in the exponentials compared to the spatial modulation of the fields can be deduced from the interference pattern of two incoming fields [LAU17]. In turn, the population grating (spatial hole burning) leads to a coupling between the counter-propagating incoming fields via the saturation terms [JAV10]. The transverse decomposition of the variables given by eq. (5.23)-(5.25) is now inserted into eq. (5.21)-(5.22). The resulting equations read[12]

$$\begin{aligned}
\frac{1}{\kappa_g}\frac{\partial}{\partial t}\left[E_+ e^{iq_x x} + E_- e^{-iq_x x}\right] =& e^{iq_x x}\Big\{ [1 - i\alpha_g]\,[N_1 E_+ + N_{+2} E_-] - E_+ \\
&+ i(\partial_x + iq_x)^2 E_+ + h_g Y_+ \Big\} \\
&+ e^{-iq_x x}\Big\{ [1 - i\alpha_g]\,[N_1 E_- + N_{-2} E_+] - E_- \\
&+ i(\partial_x - iq_x)^2 E_- - h_g Y_- \Big\} \\
&+ [1 - i\alpha_g]\left[e^{3iq_x x} N_{+2} E_+ + N_{-2} E_- e^{-3iq_x x}\right], \qquad (5.26) \\
\frac{\partial}{\partial t}\left[N_1 + N_{+2}e^{2iq_x x} + N_{-2}e^{-2iq_x x}\right] =& \gamma_g\,[N_0 - N_1] - N_1\left[|E_+|^2 + |E_-|^2\right] \\
&+ \mathcal{D}\partial_x^2 N_1 + 2\mathrm{Re}\left(N_{+2} E_- E_+^*\right) \\
&+ e^{2iq_x x}\Big\{ - \gamma_g N_{+2} - N_1 E_-^* E_+ \\
&- \left[|E_+|^2 + |E_-|^2 - \mathcal{D}\,(\partial_x + 2iq_x)^2\right] N_{+2} \Big\} \\
&+ e^{-2iq_x x}\Big\{ - \gamma_g N_{-2} - N_1 E_- E_+^* \\
&- \left[|E_+|^2 + |E_-|^2 - \mathcal{D}\,(\partial_x - 2iq_x)^2\right] N_{-2} \Big\} \\
&+ N_{+2} E_+ E_-^* e^{4iq_x} + N_{-2} E_+^* E_- e^{-4iq_x}. \qquad (5.27)
\end{aligned}$$

From this point, it is possible to identify the coefficients of the different oscillating contributions $e^{\pm imq_x}$. It is assumed that the exponential terms vary much faster than the slowly varying amplitudes. Therefore, terms with $m > 2$ can be neglected, as they average out over

[12] The coordinates are left out for better readability, the dependencies are as before $E_\pm(x,t), Y_\pm(x,t), N_{\pm 2}(x,t), N_1(x,t)$.

their high number of periods in space. In order for this to be a valid approximation, the period of the carrier grating $(2q_x)^{-1}$ has to be much smaller than the diameter of the laser beam L. Using the definition of q_x, this leads to the condition

$$\frac{\lambda}{4\pi n \sin(\theta)} \ll L \Rightarrow \frac{\lambda}{4\pi n L} \ll \sin(\theta). \tag{5.28}$$

As the beam radius in similar devices is in the region of several 100 µm [WAL16, LAU17] and the wavelength is close to ≈ 1 µm [GAA16], this is fullfilled for an incident angle of a few degrees. Identifying the remaining oscillations then leads to the following set of equations

$$\frac{1}{\kappa_g}\frac{\partial}{\partial t}E_\pm = [1 - i\alpha]\left[N_1 E_\pm + N_{\pm 2}E_\mp\right] - E_\pm + i\left(\partial_x + iq_x\right)^2 E_\pm + h_g Y_\pm, \tag{5.29}$$

$$\frac{\partial}{\partial t}N_1 = \gamma_g\left[N_0 - N_1\right] - N_1\left[|E_+|^2 + |E_-|^2\right] - 2\mathrm{Re}\left(N_{+2}E_- E_+^*\right), \tag{5.30}$$

$$\frac{\partial}{\partial t}N_{+2} = -\left[\gamma_g + 4\mathcal{D}q_x^2 + |E_+|^2 + |E_-|^2\right]N_{+2} - N_1 E_+ E_-^*, \tag{5.31}$$

where it is further applied that $q_x\partial_x N_{\pm 2}$ and $\partial_x^2 N_{\pm 2}$ are negligible compared to $q_x^2 N_{\pm 2}$ [JAV09, PER10d]. Due to the relation $N_{+2} = N_{-2}^*$ it is only necessary to keep one equation for the carrier grating in the final set of equations.
Although the resulting equation system is already quite simple, further simplifications are possible for the sake of computational costs and intuitiveness. The population grating only exists, if two fields are incident on the gain chip, and it can be therefore assumed to be a small cross saturation term in the regime of mode-locking dynamics. Furthermore the damping term $\mathcal{D}_g q_x^2$ is large for semiconductor gain media [JAV09]. In consequence, an adiabatic elimination of $N_2(t)$ can be justified and reads

$$N_{\pm 2} = -\frac{N_1 E_\pm E_\mp^*}{\gamma_g + 4\mathcal{D}q_x^2 + |E_+|^2 + |E_-|^2}. \tag{5.32}$$

For a further simplification the saturation parameter $\varepsilon_c = \left(\gamma_g + \mathcal{D}_g q_x^2\right)^{-1}$ can be defined and again it is assumed that the transverse electric field profile is large, i.e. the diffraction contributions ∂_x^2 are neglected. Furthermore, it becomes evident that the detuning of the cavities $\omega_0 = q_x^2$ has a contribution stemming from the angle of incidence. The simplified equations for the rightward and leftward propagating intracavity fields $E_\pm(t)$ and quasi-homogeneous contribution to the charge-carrier density $N_1(t)$ in the gain micro-cavity read

$$\frac{1}{\kappa_g}\frac{d}{dt}E_\pm(t) = \left[\left[1 - i\alpha_g\right]N_1(t)\left[1 - \varepsilon_c|E_\mp(t)|\right] - 1 + i\omega_0\right]E_\pm(t) + h_g Y_\pm(t), \tag{5.33}$$

$$\frac{d}{dt}N_1(t) = \gamma_g\left[N_0 - N_1(t)\right] - N_1\left[|E_+(t)|^2 + |E_-(t)|^2\right]. \tag{5.34}$$

In the next step, algebraic equations that couple the micro-cavity dynamics are found. Making use of the boundary conditions resulting from the V-shaped VECSEL setup to determine the relationship between the injected and emitted fields, makes it possible to account for the cavity geometry via the two delay times τ_1,τ_2. These refer to the time of flight needed to pass the two cavity arms respectively, as displayed in Fig. 5.14. The different fields are indicated along the green arrows representing the electric field propagation in Fig. 5.14. $O_\pm(t)$

describes the field emitted to the left (−) and right (+) from the gain chip, $Y_{\pm}(t)$ are the injected fields from the left and right, and $y(t)$ and $o(t)$ are the injected and emitted field at the absorber chip. This leads to the following three delay algebraic equations relating the injected and emitted fields

$$y(t) = O_{+}(t - \tau_2), \tag{5.35}$$
$$Y_{-}(t) = o(t - \tau_2), \tag{5.36}$$
$$Y_{+}(t) = \eta O_{-}(t - 2\tau_1), . \tag{5.37}$$

As the emitted field to the left of the gain chip ($O_{-}(t)$) needs to pass the left cavity arm twice to return to the gain chip again, a factor of 2 is included in front of the delay τ_1 in eq. (5.37). Furthermore, η describes the losses at the outcoupling facet. Defining the fields $O_{\pm}$,o as the superposition of the reflected incident field and the emitted part of the intracavity field with the same normalisation as before ($O_{\pm}(t) = E_{\pm}(t) - Y_{\pm}(t)$ and $o(t) = e(t) - y(t)$) leads to the final set of coupled differential and delay algebraic equations for the V-shaped cavity geometry

$$\frac{1}{\kappa_g}\frac{d}{dt}E_{\pm}(t) = \Big[\left[1 - i\alpha_g\right] N(t) \left[1 - \varepsilon_c \left|E_{\mp}(t)\right|^2\right] - 1 + i\omega_0\Big] E_{\pm}(t) + h_g Y_{\pm}(t), \tag{5.38}$$
$$\frac{d}{dt}N(t) = \gamma_g \left[N_0 - N(t)\right] - N(t)\Big[\left|E_{+}(t)\right|^2 + \left|E_{-}(t)\right|^2\Big], \tag{5.39}$$
$$\frac{1}{\kappa_q}\frac{d}{dt}e(t) = \Big[\left[1 - i\alpha_q\right] n(t) - 1\Big] e(t) + h_q y(t), \tag{5.40}$$
$$\frac{d}{dt}n(t) = \gamma_q \left[n_0 - n(t)\right] - s n(t) \left|e(t)\right|^2, \tag{5.41}$$
$$y(t) = E_{+}(t - \tau_2) - Y_{+}(t - \tau_2), \tag{5.42}$$
$$Y_{-}(t) = e(t - \tau_2) - y(t - \tau_2), \tag{5.43}$$
$$Y_{+}(t) = \eta\left[E_{-}(t - 2\tau_1) - Y_{-}(t - 2\tau_1)\right], \tag{5.44}$$

where the equations for the absorber are defined as for the face-to-face coupled cavity. All parameters are defined as described for the "linear" cavity DAE system in eq. (5.13)-(5.19). The subscript of N_1 is dropped as N_2 is adiabatically eliminated. In the further course of this section, this system is numerically integrated by applying the semi-implicit algorithm outlined in Appendix A.3. As the photon-life time in the absorber cavity is more than a magnitude lower than in the photon life-time in the gain ($\kappa_q^{-1} \ll \kappa_g^{-1}$) [SCH19b], the electric field equation for the absorber is adiabatically eliminated in all calculations presented in this work. A further reasoning is given in the course of the next section.

5.4.2 Model Discussion

The reason why the DAE model is more feasible to analyse third-order dispersion effects than the DDE system, lies within the relative contributions of diffusive and dispersive effects of different order in the two systems [SCH19b, SCH20d]. As discussed in Reference [SCH19b], a first estimate of the different contributions in the two models can be drawn from reducing them to the simplest possible partial differential equation (PDE) model. This corresponds to only investigating the electric field equations without losses and charge carrier contributions, i.e. an "empty cavity" limit. From this starting point, the two systems can

be transformed into Haus master PDE systems, directly unravelling the magnitude of the different dissipative and dispersive effects as they appear directly as derivatives of different order [HAU00, BOY08].
For the DDE system, the most simplified version reads

$$\gamma E(t) = \gamma E(t-T) - \frac{dE}{dt}, \tag{5.45}$$

where γ is the spectral filtering given by the gain bandwidth and/or the resonator, i.e. the distributed Bragg reflectors surrounding the active section in the micro-cavities. Following the steps given in Appendix A.2, the DDE model can be transformed into the following simple PDE [SCH20d]

$$\frac{\partial}{\partial\theta}E(\theta,\sigma) = \left[-\frac{1}{\gamma}\frac{\partial}{\partial\sigma} + \frac{1}{2\gamma^2}\frac{\partial^2}{\partial\sigma^2} - \frac{1}{3\gamma^3}\frac{\partial^3}{\partial\sigma^3}\right]E(\theta,\sigma), \tag{5.46}$$

where θ is the slow time scale referring to changes from round-trip to round-trip and σ is the fast time scale corresponding to alterations within one round-trip. As discussed for the Haus master equation model derived in section 4.3.3, the magnitude of the second-order contribution[13] ∂_σ^2 corresponds to the losses induced by the limited gain bandwidth/gain curvature [HAU00, SCH20d, HAU20a]. Following the general definition of third-order dispersion (see chapter 13 of Reference [BOY08]), its contribution is given by the third-order derivative term (∂_σ^3). Consequently, its magnitude can be approximated by $1/\left(3\gamma^3\right)$ for the DDE system [SCH20d]. Relating the magnitude of the TOD and the dissipative contribution gives the fraction $m = \frac{2}{3\gamma}$. Thus, the magnitudes are only of similar order if $\gamma \to \infty$ or $\gamma \to 1$. At an infinitely broad gain, the response of the system reduces to $E(t) = E(t-T)$, corresponding to a lossless pulse propagation through the cavity, with period $\tau_p = T$. Consequently, the dissipation dominates over the third-order dispersion, if γ is set to realistic values. This was outlined in References [SCH19b, SCH20d].
In order to obtain a simple PDE expression for the DAE model, a similar approach is followed. In the case of two resonant micro-cavities ($\omega_0 = 0$) with neglected charge carrier interaction ($n = 0$, $N = 0$), the DAE system reduces to

$$\frac{1}{\kappa_g}\frac{d}{dt}E_\pm(t) = -E_\pm(t) + h_g Y_\pm(t), \tag{5.47}$$

$$\frac{1}{\kappa_q}\frac{d}{dt}e(t) = -e(t) + h_q y(t), \tag{5.48}$$

$$y(t) = E_+(t-\tau_2) - Y_+(t-\tau_2), \tag{5.49}$$

$$Y_-(t) = e(t-\tau_2) - y(t-\tau_2), \tag{5.50}$$

$$Y_+(t) = \eta\big[E_-(t-2\tau_1) - Y_-(t-2\tau_1)\big]. \tag{5.51}$$

In this scenario, a single micro-cavity acts as a Gires-Tournois interferometer (GTI) [GIR64], inducing only third-order dispersion if no detuning is considered and the reflectivity of the

[13] The difference of the appearance of the filtering contribution in the DDE and PDE models stems from the two time scale representation. In the initial derivation of the Haus Master equation, the second derivative with respect to the fast time scale results from the assumption of a Lorentzian shaped gain determining the amplification of the axial modes in frequency space. The Lorentzian is then expanded, which is based on the assumption that the lasing frequency is close to resonance. In the following, an inverse Fourier transform ($i\omega \to \partial_\sigma$) is applied to arrive at the final PDE [HAU00] with the fast time scale σ.

bottom mirror is close to unity ($h_{g,q} = 2$) [SCH19b]. To arrive at a PDE, that directly indicates the magnitude of the dispersion and diffusion effects of different order, the functional mapping approach presented in Reference [SCH18f, SCH19b] is applied. It is based on relating the Fourier transform of the electric field profile $\tilde{E}_{\pm}(n,\omega)$ in round-trip (n) to that of the prior round-trip $(n-1)$. This is similar to the technique used to find the Haus master equation of mode-locking [HAU00], which focuses on determining the changes in the spectral mode amplitudes from round-trip to round-trip. Applying a Fourier transformation to the electric field equations (5.47)-(5.48) and denoting the round-trip by the integer superscript (n) leads to

$$-i\omega\kappa_g^{-1}\tilde{E}_{\pm}^{(n)}(\omega) = -\tilde{E}_{\pm}^{(n)}(\omega) + h_g\tilde{Y}_{\pm}^{(n)}(\omega)\,, \tag{5.52}$$

$$-i\omega\kappa_q^{-1}\tilde{e}^{(n)}(\omega) = -\tilde{e}^{(n)}(\omega) + h_q\tilde{y}^{(n)}(\omega). \tag{5.53}$$

Rewriting the pre-factor $\omega_i := \omega\kappa_i^{-1}$ for simplicity and rearranging for $\tilde{E}_{\pm}^{(n)}(\omega)$ and $\tilde{e}^{(n)}(\omega)$ yields the following relationship between the injected- and intracavity fields in round-trip n

$$\tilde{E}_{\pm}^{(n)}(\omega) = \frac{h_g}{1-i\omega_g}\tilde{Y}_{\pm}^{(n)}(\omega)\,, \tag{5.54}$$

$$\tilde{e}^{(n)}(\omega) = \frac{h_q}{1-i\omega_q}\tilde{y}^{(n)}(\omega). \tag{5.55}$$

To incorporate the external cavity geometry, the mapping approach is further applied to the delayed algebraic equations, which gives

$$\tilde{y}^{(n)}(\omega) = \tilde{E}_{+}^{(n)}(\omega_{\tau_2}) - \tilde{Y}_{+}^{(n)}(\omega_{\tau_2})\,, \tag{5.56}$$

$$\tilde{Y}_{-}^{(n)}(\omega) = \tilde{e}^{(n)}(\omega_{\tau_2}) - \tilde{y}^{(n)}(\omega_{\tau_2})\,, \tag{5.57}$$

$$\tilde{Y}_{+}^{(n)}(\omega) = \eta\left[\tilde{E}_{-}^{(n)}(\omega_{2\tau_1}) - \tilde{Y}_{-}^{(n)}(\omega_{2\tau_1})\right]. \tag{5.58}$$

The subscript of ω denotes the initial delay so that $\tilde{E}(\omega_\tau) = \mathcal{F}[E(t-\tau)](\omega)$ and n again accounts for the round-trip number. Inserting eq. (5.54) into eq. (5.58) then gives

$$\tilde{Y}_{+}^{(n)}(\omega) = \eta\left(\frac{h_g}{1-i\omega_g} - 1\right)\tilde{Y}_{-}^{(n)}(\omega_{2\tau_1}). \tag{5.59}$$

Iteratively inserting the delay algebraic equations finally leads to an expression mapping the Fourier transformed fields of the previous round-trip $(n-1)$ to that of the subsequent round-trip (n)[14]

$$\tilde{Y}_{+}^{(n)}(\omega) = \eta\left(\frac{h_g}{1-i\omega_g} - 1\right)\left(\frac{h_q}{1-i\omega_q} - 1\right)\left[\tilde{E}_{+}^{(n-1)}(\omega) - \tilde{Y}_{+}^{(n-1)}(\omega)\right]. \tag{5.60}$$

[14] Here, it is used that in case of an infinitely long, periodic signal the time can be shifted by the small time τ

$$\mathcal{F}\Big[E(t)\Big](\omega) = \mathcal{F}\Big[Y(t)\Big](\omega),$$
$$\Rightarrow \mathcal{F}\Big[E(t-\tau)\Big](\omega) = \mathcal{F}\Big[Y(t-\tau)\Big](\omega).$$

Where it is used that a delay of one cavity round-trip time $T = 2\tau_1 + 2\tau_2$ corresponds to a change in n according to: $\mathcal{F}[E(t-T)](\omega) = \tilde{E}^{(n-1)}(\omega)$. As a final step eq. (5.54) can be used again to find an expression only depending on $\tilde{Y}_+^{(n)}(\omega)$. This results in the following functional mapping equation for the changes experienced by the injected electric field $\tilde{Y}_+^{(n-1)}(\omega)$ in the frequency domain during one cavity round-trip

$$\tilde{Y}_+^{(n)}(\omega) = \eta r(\omega)\tilde{Y}_+^{(n-1)}(\omega)\,. \tag{5.61}$$

$$\tilde{Y}_+^{(n)}(\omega) = \eta \left(\frac{1+i\frac{\omega}{\kappa_g}}{1-i\frac{\omega}{\kappa_g}}\right)^2 \left(\frac{1+i\frac{\omega}{\kappa_q}}{1-i\frac{\omega}{\kappa_q}}\right) \tilde{Y}_+^{(n-1)}(\omega)\,, \tag{5.62}$$

where $h_i = 2$ is used in order to model a GTI regime, and the normalisation of the pre-factor is reintroduced. From the mapping equation, it is possible to define the reflectivity of the coupled micro-cavity setup according to $r = \exp(4i\Theta(\frac{\omega}{\kappa_g}) + 2i\Theta(\frac{\omega}{\kappa_q}))$ with $\Theta(\omega) = \arctan(\omega)$. As the empty cavity regime is considered, it is assumed that a linear PDE with linear operator $\mathcal{L}(\omega)$ exists that models the changes of the Fourier transformed electric field on the slow time scale θ

$$\frac{\partial}{\partial\theta}\tilde{Y}_+(\omega,\theta) = \mathcal{L}(\omega)\tilde{Y}_+(\omega,\theta). \tag{5.63}$$

Integrating this PDE from round-trip n to round-trip $n+1$, assuming that $\mathcal{L}$ is independent of θ (see Appendix A.2 for details), and comparing the results with the found functional mapping equation (5.61) yields the following expression for the linear PDE operator

$$\mathcal{L}(\omega) = \ln(\eta r(\omega)) \approx \ln(\eta) + 2i\omega\left(\frac{2}{\kappa_1} + \frac{1}{\kappa_q}\right) - \frac{2}{3}i\omega^3\left(\frac{2}{\kappa_g^3} + \frac{1}{\kappa_q^3}\right) + \mathcal{O}(\omega^5). \tag{5.64}$$

The expansion is reasoned by the fact that the response of the cavity is investigated close to resonance. Fourier transforming back to the time domain ($i\omega \to \partial_\sigma$), leads to the PDE modelling the V-shaped external cavity system in the empty cavity regime

$$\frac{\partial}{\partial\theta}Y_+(\theta,\sigma) = \left(\ln(\eta) - 2\left(\frac{2}{\kappa_1} + \frac{1}{\kappa_q}\right)\frac{\partial}{\partial\sigma} - \frac{2}{3}\left(\frac{2}{\kappa_g^3} + \frac{1}{\kappa_q^3}\right)\frac{\partial^3}{\partial\sigma^3}\right) Y_+(\theta,\sigma), \tag{5.65}$$

where σ corresponds to the fast time scale referring to changes within one round-trip. It is immediately noticeable, that there is no second-order diffusive term left in the PDE[15]. Therefore, the third-order dispersion effect is not overwhelmed in this system, as opposed to the DDE system[16]. From the PDE, it further becomes evident that the DAE system is conservative, if $\eta = 1$. Physically this corresponds to the situation of no light being coupled out of the external cavity. In Reference [SCH19b], an eigenvalue analysis of the fixed-point solution underlined the conservative nature of the DAE system in this situation. The analysis revealed that in the DAE system all eigenvalues have a zero real-part $\mathrm{Re}(\lambda) = 0$, if $\eta = 1$. Thus, perturbations to the system are conserved. Opposing, the distribution of the

[15] It has to be noted that this is only true for the empty cavity regime in perfect resonance. In a system of not perfectly resonant micro-cavities ($\omega_0 \neq 0$), a second-order diffusion (GVD) term occurs [SCH19b].

[16] Strictly speaking, the most simplified version of the DDE model and the corresponding PDE do not necessarily refer to an empty cavity, as the filtering is still included, which approximates the influence of the gain-bandwidth. However, empty cavity here primarily refers to the neglection of the charge-carrier equations and the most simplified versions of the systems.

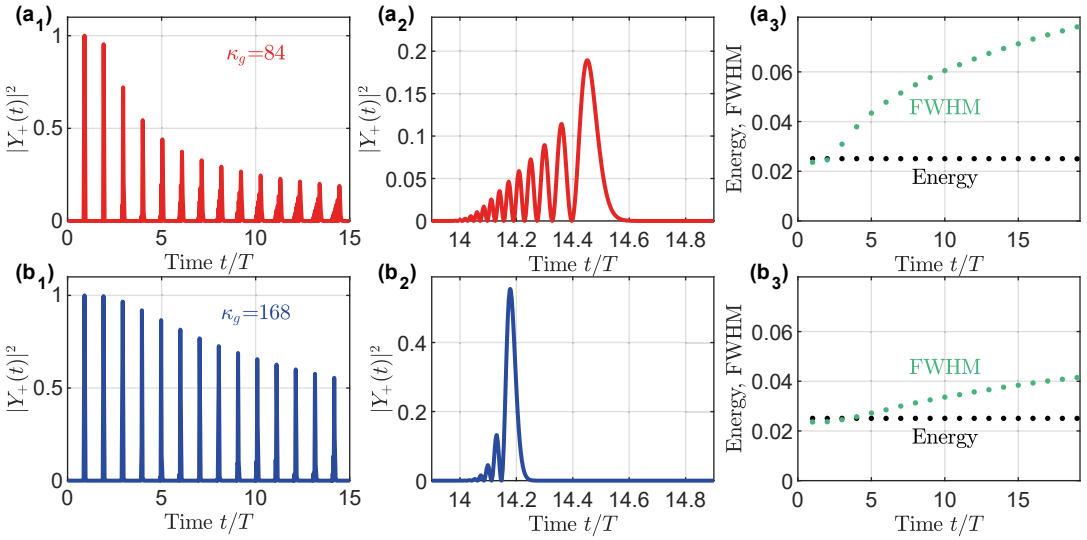

Figure 5.15.: V-shaped DAE with empty cavity: (a_1)-(b_1) Intensity time-series of the electric field $Y_+(t)$ incident on the gain micro-cavity (c.f. Fig. 5.14) in the empty cavity regime described by eq. (5.47)-(5.51). A Gaussian pulse with FWHM = 0.023 and amplitude $Y_0 = 1$ is utilised as the initial condition.(a_2)-(b_2) Close-up of the intensity dynamics in one round-trip. (a_3)-(b_3) Full width half maximum (FWHM) of the largest pulse in one round-trip and the total energy (area of all pulses in one round-trip) confined in the cavity. The photon decay rate in the gain micro-cavity is $\kappa_g = 84$ for sub-panels (a) and $\kappa_g = 168$ for panels (b), both scaled to a round-trip time of $T = 625\,\mathrm{ps}$. The absorber micro-cavity is adiabatically eliminated.

eigenvalues in the DDE system along the real and imaginary axes follows a parabolic shape and consequently eigenvalues with $\mathrm{Re}(\lambda) < 0$ exist, which lead to a damping of applied perturbations. As expected, a comparison of eq. (5.65) and the PDE derived for a single micro-cavity in an external cavity setup [SCH19b], points out that the additional influences of the second gain pass and the second micro-cavity in the setup just occur as additive terms in the final PDE.

In order to illustrate the effect of the third-order dispersion contribution and the conservative nature of the DAE system, the response of the reduced V-shaped DAE model eq. (5.47)-(5.51) to the injection of a Gaussian pulse is shown in Fig. 5.15. For the calculation of the time-series, the photon life-time in the absorber is assumed to be much smaller than in the gain $\kappa_q \to \infty$, which is in good agreement with experimental values [SCH19b].

Panels (a) and (b) of Fig. 5.15 demonstrate the response of the coupled cavity system at two different photon life-times κ_g^{-1} in the gain micro-cavity. The effect of the third-order dispersion contribution is embodied by the emerging satellite pulses as pointed in Reference [SCH19b]. These satellites result from the partial reflection of the main pulse at the micro-cavity surface, while the transmitted part is delayed by the interaction with the micro-cavity. As expected from the corresponding PDE eq. (5.65), the influence of the third-order dispersion strongly increases when κ_g is reduced, i.e. the photon life-time is increased. Vice versa, the delayed outcoupling induced by the micro-cavity interaction vanishes, if the photon life-time is infinitesimally small (far below the pulse width). This means that no satellites would appear [SCH19b]. Furthermore, the energy confined in the cavity is calculated by integrating the intensity over one round-trip. The result for both photon life-times is indicated in sub-panels (a_3) and (b_3). As expected from the conservative nature of the system

(if $\eta = 1$), the total energy stays constant over all round-trips. Additionally, the full width at half maximum (FWHM) of the maximum (initial) pulse is plotted in the same panels. This quantity increases as a result of the third-order dispersion, which is a well known effect [CUR93, ZHO94, BRA93a].
To asses the role of third-order dispersion on the emerging dynamics/instabilities in the V-shaped VECSEL, it is feasible to compare the DAE to the DDE system. In the latter the TOD has a minor influence on the dynamics, as it is overwhelmed by the filtering losses [SCH19b, SCH20d]. Thus, it is crucial to find a correspondence between the different parameters included in both models. In the following, equations for parameter transformations between the two models are found for the pump parameter, unsaturated absorption, the gain bandwidth/curvature and the factor s, which is proportional to the ratio of the differential gain coefficients in gain and absorber.

Pump and Unsaturated Absorption

The method applied to arrive at a relationship between the pump parameter N_0 and the unsaturated absorption n_0 in the DAE system and the similar parameters G_0 and Q_0 in the DDE model, is based on finding an approximation for the reflectivity $r_{g,q}$ of the semiconductor gain and absorber chip in both models. These quantities can then be utilised to relate the magnitude of the gain/absorption provided by the system.
Starting with the DDE system, an equation for the reflectivity can be deduced from the boundary conditions given by eq. (3.16)-(3.17), which describe the amplification of the electric field in the active sections. Assuming a double pass of the absorber active section due to the reflection at the back-side DBR, the absorber effective reflectivity $r_{q,\mathrm{DDE}}$ close to the lasing threshold[17] of the continuous-wave solution in the DDE system is given by

$$r_{q,\mathrm{DDE}} = \exp\left([1 - i\alpha_q]\, Q_0\right), \tag{5.66}$$

where Q_0 is the unsaturated absorption/equilibrium carrier density of the absorber.
In the DAE system, the reflectivity of the chips can be calculated directly from the ratio of the input and output fields ($r = \frac{O(t)}{Y(t)}$). In order to arrive at a comparable expression, a continuous-wave solution of the form $y(t) = y\exp(i\omega t)$, $e(t) = e\exp(i\omega t)$ and $\dot{n} = 0$ is plugged into the absorber equations (5.40)-(5.41). This leads to the following two algebraic equations

$$0 = [(1 - i\alpha_q)n - 1]e + h_q y - \kappa_q^{-1} i\omega e, \tag{5.67}$$
$$0 = \gamma_q n_0 - (\gamma_q + s|e|^2)n. \tag{5.68}$$

Solving eq. (5.67) for n yields

$$n = \frac{e - h_q y + \kappa_q^{-1} i\omega e}{[1 - i\alpha_q]\, e}. \tag{5.69}$$

[17] A pump power in the vicinity of the lasing threshold is assumed so that the integrated carrier densities can be approximated by their equilibrium values $Q(t) = Q_0$.

Inserting this expression into (5.68) then leads to

$$0 = \gamma_q n_0 - \left(\gamma_q + s|e|^2\right) \frac{\left[e - h_q y + \kappa_q^{-1} i\omega e\right]}{\left[1 - i\alpha_q\right] e}, \tag{5.70}$$

$$h_q y = \left[\frac{j\left[1 - i\beta\right]}{1 + \gamma_q^{-1} s|e|^2} - 1 - \kappa_q^{-1} i\omega\right] e. \tag{5.71}$$

Utilising the definition of the output field $o(t) = e(t) - y(t)$, the effective reflectivity can be expressed as $r_{q,\mathrm{DAE}} = \frac{o(t)}{y(t)} = \frac{e(t)}{y(t)} - 1$. Combined with the previously found expression for $y(t)$ above, this is used to arrive at an expression for the effective reflectivity of the absorber chip

$$r_{q,\mathrm{DAE}} = \frac{h_q + n_0(1 - i\alpha_q) \cdot (1 + \gamma_q^{-1} s|e|^2)^{-1} - 1 - \kappa_q^{-1} i\omega}{-n_0(1 - i\alpha_q) \cdot (1 + \gamma_q^{-1} s|e|^2)^{-1} + 1 + \kappa_q^{-1} i\omega}. \tag{5.72}$$

As mentioned before, the laser system is investigated close to the CW lasing threshold for a better comparability. Consequently, one can assume a small electric field $e(t)$. Furthermore, the influence of α_q is negligible for small n_0 and only the resonant mode ($\omega = 0$) is considered. Therefore, the expression for the effective reflectivity of the absorber simplifies to

$$r_{q,\mathrm{DAE}} = \frac{h_q + n_0 - 1}{1 - n_0}. \tag{5.73}$$

Equating this with the expression for the reflectivity eq. (5.66) found for the DDE system (with $\alpha_q = 0$) leads to the relation

$$\begin{aligned} \frac{h_q - 1 + n_0}{1 - n_0} &= \exp\left(\left[1 - i\alpha_q\right] Q_0\right), \\ \Rightarrow Q_0 &= \log\left(\frac{h_q - 1 + n_0}{1 - n_0}\right) \approx 2n_0, \end{aligned} \tag{5.74}$$

where $h_q = 2$ is used to find the linear approximation.
Making use of the same procedure for the gain equations (5.38)-(5.39), the following term for the effective reflectivity of the gain $r_{g,\mathrm{DAE}}$ can be acquired

$$r_{g,\mathrm{DAE}} = \frac{h_g + \frac{J(1 - i\alpha_g) \cdot (1 - \varepsilon_c |E_\mp|^2)}{1 + \gamma_g^{-1}(|E_+|^2 + |E_-|^2)} - 1 - i(\kappa_g^{-1}\omega - \omega_0)}{\frac{-N_0(1 - i\alpha_g) \cdot (1 - \varepsilon_c |E_\mp|^2)}{1 + \gamma_g^{-1}(|E_+|^2 + |E_-|^2)} + 1 + i(\kappa_g^{-1}\omega - \omega_0)}. \tag{5.75}$$

Assuming a strong carrier diffusion ($\epsilon_c \to 0$), a small electric field near the threshold and setting $\alpha_g = 0$ then leads to a simplified expression

$$r_{g,\mathrm{DAE}} = \frac{h_g + N_0 - 1}{1 - N_0}. \tag{5.76}$$

Using $\omega = 0$ can be justified by the fact that the detuning between the micro-cavities is not of importance, as only a single cavity is investigated and furthermore the resonant CW mode is considered. When finding an expression for the reflectivity of the gain chip in the DDE model, it has to be noted that in the model derivation it is assumed that the active section of the gain is only passed once and not a second time after the reflection at the back-side

DBR as assumed for the absorber (see section 3.3). Thus, the reflectivity of the gain close to the CW lasing threshold is given by[18]

$$r_{g,\mathrm{DDE}} = \exp\left(\frac{[1 - i\alpha_q]\, G_0}{2}\right). \tag{5.77}$$

Equating this with the expression for the gain reflectivity found for the DAE model leads to the transformation equation

$$G_0 = 2\log\left(\frac{h_g - 1 + N_0}{1 - N_0}\right) \approx 4N_0. \tag{5.78}$$

To arrive at the expanded linear relationship, $h_g = 2$ is used. In contrast to the correspondence of the unsaturated absorption parameters, a further factor of 2 in the linear approximation has to be multiplied to the pump parameter, which results from the assumption of a single pass of the active sections in the gain.
From the simplified expressions of the reflectivities (eq. (5.76) and (5.73)), one can deduce two critical parameter values that arise due to the normalisation (see appendix A.1 for details). If $h_{g,q} = 2$, the gain and absorber chip are transparent ($r = 1$) at $N_0 = 0$ and $n_0 = 0$, which results from the fact that both quantities are defined relative to the transparency carrier densities. Secondly, at high absolute values of the pump parameters, i.e. $n_0 \to -1$ and $N_0 \to 1$, the reflectivities enter regimes not feasible for the investigation of the coupled external cavity laser. In the scenario of $N_0 \to 1$, the reflectivity of the gain diverges as $r_{g,\mathrm{DAE}} \to \infty$. The reason for that lies in a second threshold, that corresponds to the solitary lasing threshold of the gain micro-cavity. This threshold can be derived by plugging the same CW Ansatz into eq. (5.38)-(5.39). Assuming no external injection ($Y = 0$), neglecting α_g and rearranging for N_0, then leads to a threshold of $N_{0,\mathrm{th}} = 1$ for the resonant CW mode. Nonetheless, this regime is very far above the threshold of the coupled cavities and therefore not meaningful for reproducing experimentally observed dynamics.
In contrast, the absorber reflectivity approaches $r_{q,\mathrm{DAE}} \to 0$ for $n_0 \to -1$, which is experimentally very difficult to realise. At this point it has to be stressed, that the unintuitive values of $N_0 = 1$ and $n_0 = -1$, result from the normalisation and that the approach of a DAE model can be utilised to give good qualitative description of different phenomena, if the boundaries of the parameter values are considered correctly [MUL05a, SCH19c, SCH19e, SCH20d].

Threshold Current

In contrast to the DDE-, the DAE-model incorporates the complex nonlinear interplay between pump current and gain bandwidth[19]. Therefore, finding an analytic expression for the threshold current $N_0 = N_{\mathrm{th}}$, is feasible to compare the behaviour of the two models close to the threshold. Furthermore, it can be used to connect the photon life-time in the gain κ_g^{-1} and the gain bandwidth γ, which both have a similar, but not equal role in the models. This is analysed later in this section. In addition to that, an expression for the threshold current

[18] Accounting for a double gain depletion can be achieved by adding an additional boundary condition to the set of algebraic equations (3.19)-(3.27), embodying the additional gain pass. Ultimately, it would lead to a factor of two in front of all delayed gain contributions and a factor of $e^{G(t)}$ multiplied to the delayed electric field in the gain equation, elevating the gain experienced by the electric field.

[19] It has to be noted that in the DDE model the gain curve is elevated as the pump current is increased and therefore additional modes are amplified. However, the FWHM of the Lorentzian stays constant.

delivers the position of the most trivial bifurcation line in the system, i.e. the Andronov-Hopf/Pitch-Fork bifurcation leading to the emergence of the CW solution, which is worth comparing in the two models to asses the previously found parameter transformation for the pump parameters.
For $\alpha_{g,q} \neq 0$ and $\omega_0 \neq 0$, the derivation becomes very complex and one has to rely on numerical methods to obtain the threshold bifurcation line [HES21]. Consequently, the amplitude-phase coupling and the cavity detuning are neglected at this point. This is sufficient to find an analytical expression that allows to compare the two models in regimes without too rich dynamics.
The threshold is defined as the parameter value of N_0 at which the laser transitions from the *off* to the continuous-wave state, which is defined as

$$(0,0,0,0,0,0,N_{\mathrm{th}},n_0) \rightarrow (\mathcal{E}_+ e^{i\omega t}, \mathcal{E}_- e^{i\omega t}, \epsilon e^{i\omega t}, \mathcal{Y}_+ e^{i\omega t}, \mathcal{Y}_- e^{i\omega t}, \upsilon e^{i\omega t}, N_{\mathrm{th}}, n_0). \tag{5.79}$$

By definition, the carrier densities at the threshold equal the parameter values of the pump parameter N_0 and the unsaturated absorption n_0 as they can also be understood as the equilibrium carrier densities, i.e. $N(t) = N_0 = N_{\mathrm{th}}$ and $n(t) = n_0$. Plugging the CW Ansatz (5.79) into the DAE model eq. (5.38)-(5.44) and splitting the electric field equations into real and imaginary parts yields the condition $\omega = 0$. It is reasoned by the fact that no other phase effects are left due to $\alpha_g = \alpha_q = 0$. The choice of $\omega = 0$ corresponds to the maximum gain mode. The real parts of the electric field equations read (using $N(t) = N_{\mathrm{th}}$ and $n(t) = n_0$)

$$0 = (N_{\mathrm{th}} - 1)\mathcal{E}_\pm + h_g \mathcal{Y}_\pm, \tag{5.80}$$
$$0 = (n_0 - 1)\epsilon + h_q \upsilon, \tag{5.81}$$
$$\upsilon = \mathcal{E}_+ - \mathcal{Y}_+, \tag{5.82}$$
$$\mathcal{Y}_- = \epsilon - \upsilon, \tag{5.83}$$
$$\mathcal{Y}_+ = \eta\left[\mathcal{E}_- - \mathcal{Y}_-\right]. \tag{5.84}$$

Rearranging eqs.(5.80) and eq. (5.81) then leads to

$$N_{\mathrm{th}} = 1 - h_g \frac{\mathcal{Y}_+}{\mathcal{E}_+}, \tag{5.85}$$
$$\mathcal{E}_- = \frac{h_g}{1 - J_g}\mathcal{Y}_-, \tag{5.86}$$
$$\epsilon = \frac{h_q}{1 - J_q}\upsilon. \tag{5.87}$$

Plugging (5.87) and (5.82) into eq. (5.83) yields

$$\mathcal{Y}_- = (\mathcal{E}_+ - \mathcal{Y}_+)\left(\frac{h_q}{1 - J_q} - 1\right). \tag{5.88}$$

Inserting this into (5.86) then leads to

$$\mathcal{E}_- = j_g(j_q - 1)(\mathcal{E}_+ - \mathcal{Y}_+), \tag{5.89}$$

where $j_g := h_g/(1 - N_{\mathrm{th}})$ and $j_q := h_q/(1 - n_0)$ are introduced for simplicity. Inserting the expressions (5.88) and (5.89) into eq. (5.84) yields a relationship between $\mathcal{Y}_+$ and $\mathcal{E}_+$

$$\mathcal{Y}_+ = \eta \frac{(j_q - 1)(j_g - 1)}{1 + \eta(j_q - 1)(j_g - 1)}\mathcal{E}_+. \tag{5.90}$$

Finally, this can be substituted into (5.85), to arrive at an expression for the threshold carrier density/pump parameter N_{th} independent of the field amplitudes

$$N_{\mathrm{th}} = 1 - \frac{h_g}{1 \pm \left[\eta \left(\frac{h_q}{1-n_0} - 1\right)\right]^{-\frac{1}{2}}}, \tag{5.91}$$

where j_g and j_q are resubstituted. Evaluating this expression for N_{th} highlights several important properties. Firstly, two solutions for the threshold exist. Anyhow, for all parameter values only one of the solutions is purely real. Hence, the complex solution can always be ruled out by physical arguments. The role of the two solutions is reversed at the critical parameter value $n_0 = -1$, predicted by the analysis of the effective chip reflectivities[20]. At this parameter value, the absorber reflectivity tends to $r_{q,\mathrm{DAE}} \to 0$ and hence the threshold can be found at $N_{\mathrm{th}} \to 1$. This can be reasoned by the fact that for $N_0 = 1$, the gain reflectivity tends towards infinity ($r_{g,\mathrm{DAE}} \to \infty$) to compensate for the losses. As this situation is not physical, it limits the analysis of the model to $N_0 < 1$ and $n_0 > -1$ (for $h_{g,q} = 2$).
A comparison of the CW threshold curve found for the DAE (red) and DDE model (blue)[21] is illustrated in Fig. 5.16 with respect to the unsaturated absorption. For a simple comparability, the linear relationships between N_0 and G_0 as well as between n_0 and Q_0 are used. For low values of the unsaturated absorption (the value for the unsaturated absorption used in this work is indicated by a dashed line), the bifurcation lines match very well. Yet, in the DDE model the threshold depends linearly on the unsaturated absorption, whereas in the DAE model a nonlinear relationship is evident. This leads to severe differences at high values of the unsaturated absorption. It is interesting to note, that the threshold equation for the DAE model (5.91) can be recovered by substituting the logarithmic parameter transformations for N_0 and n_0 (eq. (5.74) and eq. (5.78)) into the threshold equation of the DDE model (4.9). For the models to have the same threshold, this correspondence then requires the condition

$$\eta = \sqrt{\kappa}. \tag{5.92}$$

If the logarithmic parameter transformations are used instead of the linear ones, the DDE threshold curve perfectly matches the DAE curve. Consequently, the comparison of the threshold lines delivers a first verification of the parameter transformations.
As mentioned at the start of this section, the threshold of the single-micro cavity without injection ($h_g = 0$) and neglected amplitude-phase coupling can be found at $N_0 = 1$. The fact that the threshold of the external cavity device is lower (see Fig. 5.16) than that of the single-microcavity can be explained by understanding the injection terms as an optical feedback term that also accounts for multiple reflections. From this point of view, the single micro-cavity equations read very similar to the Lang-Kobayashi equations describing a single-mode laser subject to optical feedback [LAN80b, SCH20d]. For these, it is well known that increasing the feedback (which would be very strong in the scenario investigated here) reduces the threshold current.

[20] It has to be noted that if $h_{g,q} < 2$, this situation emerges at lower absolute values of n_0, but is in accordance with the analysis of the reflectivity. Furthermore, $h_{g,q} = 2$ is used throughout this work, as the reflectivity of the bottom DBRs is sufficiently close to unity.

[21] The threshold of the maximum gain mode ($\omega = 0$) in the DDE model calculated in section 4.2.1 is

$$G_{\mathrm{th}} = -\frac{1}{2}\ln(\kappa) - Q_0.$$

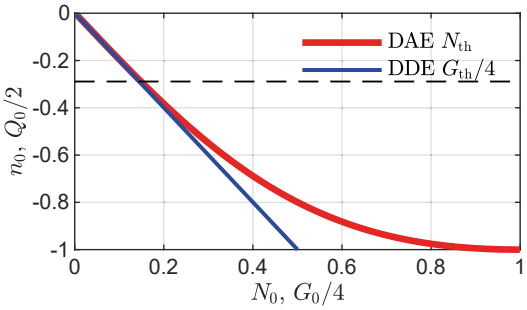

Figure 5.16: CW lasing threshold curve as a function of the unsaturated absorption n_0/Q_0 calculated for the DAE model eq. (5.91) (red) and for the DDE model (4.9) (blue). The parameter values of the DDE model are scaled according to the linear parameter relationships given by equations (5.78) and (5.74). The other parameters used here are $h_g = h_q = 2$ and $\eta = \sqrt{\kappa} = 0.995$.

Gain Bandwidth

A further influential quantity that cannot be compared directly in the two models is the gain bandwidth (or the limited bandwidth of the DBR mirrors of the cavity). In the DDE model, the effect of the limited gain bandwidth is taken into account by approximating it by a Lorentzian filter [VLA04, VLA05] of bandwidth γ following a lumped element approach (see section 3.3). In contrast, the bandwidths of the gain and absorber are embodied as two separate properties in the DAE model. These are related to the photon life-times in the micro-cavities $\kappa_{g,q}^{-1}$, but not solely dependent on them. This is discussed later in this section, by investigating the frequency dependent effective reflectivity (amplification) of the total external device. In experiments, the spectral width of the absorber is a lot broader than that of the gain, because the photon life-time in the absorber is usually a magnitude lower compared to the gain [SCH19b]. Therefore, it is focused on finding a relationship between γ and κ_g, as the curvature of the absorber has a negligible influence if the lasing frequency is close to resonance.
The approach followed in order to relate the spectral filtering in both models is similar to the one to determine the third-order dispersion contributions at the start of this section: Both models are transformed into a PDE, in which the magnitude of the filtering contribution (bandwidth of the gain) is embodied by the real pre-factor of the second-order derivative contribution (∂_σ^2) and is therefore directly comparable. Nonetheless, for this comparison the complete models (not excluding the charge carriers) have to be taken into account, to correctly account for the influence of the pump current.
The transformation of the DDE model is discussed in section 4.2.3, where a nonlocal Haus master PDE is found by applying a multiple time scale analysis. This leads to a filtering contribution of $1/(2\gamma^2)$, which is independent of the pump current [HAU00]. Furthermore, the FWHM of the effective reflectivity of the gain is 2γ, resulting from the assumption of a Lorentzian shaped gain spectrum [HAU00, VLA04].
In order to find a similar expression for the DAE system, the effective reflectivity of the coupled external cavity system r_{cav} is derived by combining the single chip reflectivities and the outcoupling losses η according to

$$r_{\mathrm{cav,DAE}}(\omega) = r_{g,\mathrm{DAE}}^2 \cdot r_{q,\mathrm{DAE}} \cdot \eta. \tag{5.93}$$

In the following, CW operation close to the lasing threshold is assumed to make use the expressions eq. (5.75) and eq. (5.72) for the reflectivities of the semiconductor chips. Fur-

thermore, close to threshold it is possible to neglect the electric field contributions. This leads to the following expression for the total external cavity reflectivity

$$r_{\mathrm{cav,DAE}}(\omega) = \left[\frac{h_g - 1 + N_0(1 - i\alpha_g) - i\left(\kappa_g^{-1}\omega - \omega_0\right)}{1 - N_0(1 - i\alpha_g) + i\left(\kappa_g^{-1}\omega - \omega_0\right)}\right]^2 \cdot \frac{h_q - 1 + n_0(1 - i\alpha_q) - i\kappa_q^{-1}\omega}{1 - n_0(1 - i\alpha_q) + i\kappa_q^{-1}\omega} \cdot \eta. \tag{5.94}$$

The effect of the different parameters on the absolute reflectivity in frequency space is illustrated in Fig. 5.17. Firstly, the pump parameter and the unsaturated absorption cause a similar adjustment of the reflectivity as shown in sub-panels (a) and (d). If the pump power (N_0) is enlarged, the reflectivity increases and the bandwidth is narrowed (see Fig. 5.17(a)). Adjusting the absolute value of the unsaturated absorption (n_0) leads to a reversed variation of the reflectivity (higher absorption - lower amplification), but has a minor influence on the bandwidth as visualised in Fig. 5.17(d). The photon life-time in the gain (κ_g^{-1}) does not impact the magnitude of the reflectivity, but strongly influences the bandwidth (see Fig. 5.17(b)), similar to the bandwidth parameter γ in the DDE model. A low photon life-time in the absorber (κ_q^{-1}) leads to a very broad reflectivity curve for the absorber compared to the gain. Hence, the total reflectivity almost remains unaffected in the regime close to the resonance when increasing κ_q, as indicated by overlapping blue and black lines in Fig. 5.17(e). Nevertheless, if the photon life-times in both micro-cavities are almost equal (red line in Fig. 5.17(e)), the absorption and gain cancel out each other and a very broad reflectivity curve with $|r_{\mathrm{cav,DAE}}(\omega)|^2 \approx 1$ remains. Furthermore, α_g and α_q each have a similar effect on the respective single reflectivity curves of gain and absorber micro-cavity, as they shift the central frequency. Nevertheless, α_g and α_q influence the total cavity reflectivity differently, due to the broad absorber curve and the differing magnitude of the prefactors of N_0 and n_0 (see eq. (5.94)) as indicated in Fig. 5.17(c). The absorber reflectivity curve is shifted strongly already at $\alpha_q = 2$. Thus, the gain curve is out of resonance with the absorber, which leads to a higher amplification at the central frequency due to the lower absorption at the gain maximum (see blue curve in Fig. 5.17(c)). In contrast, α_g only induces a comparably small shift of the gain reflectivity curve. Due to the broad absorber curve, this almost has no effect on the magnitude of the total reflectivity indicated by the black curve in Fig. 5.17(c).

Tuning the micro-cavity detuning ω_0 only shifts the gain reflectivity curve relative to that of the absorber (see Fig. 5.17(f)). In consequence, this leads to almost no visible changes in the magnitude of the reflectivity, in the investigated regime of a very broad absorber reflectivity. Therefore, a variation of ω_0 only induces a shift of the relative resonance frequency of the total effective reflectivity curve. It has to be noted that $\omega_0 = 1$ corresponds to a frequency shift of κ_g in the normalised spectrum. However, a strong alteration of the curve is evident at a very large detuning, because in that case the gain and absorber reflectivity (almost) do overlap each other and consequently a strong absorptive dip and a strong amplifying peak would be visible in the reflectivity curve. This scenario is usually prevented in experiments by a sophisticated semiconductor chip design. Yet, a slight detuning can be helpful to induce a certain amount of GVD optimising the pulse width [WAL16, SCH19b].

The expression for the effective external cavity reflectivity can now be further used to find a correspondence between the bandwidth parameter γ and the photon life-time κ_g^{-1}. The photon life-time in the absorber κ_q^{-1} is usually over a magnitude lower than in the gain chip

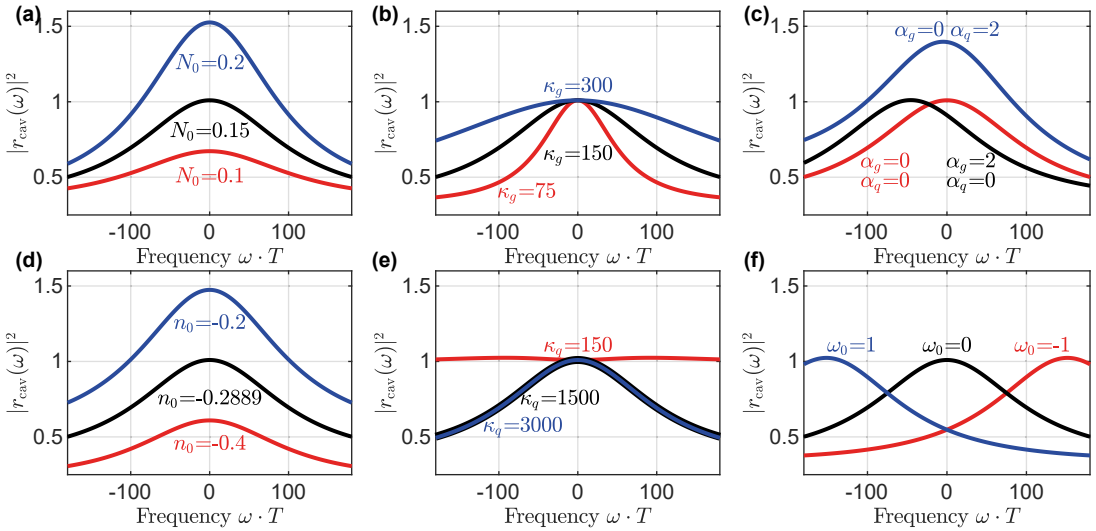

Figure 5.17.: Intensity reflectivity of the external cavity in the DAE model as a function of the frequency, normalised to the round-trip time T, calculated using eq. (5.94). The different subpanels illustrate the consequence of changing the indicated parameters. The other parameters (rates normalised to the round-trip time) are $h_g = h_q = 2$, $\eta = 0.995$, $\omega_0 = 0$, $N_0 = 0.15$, $n_0 = 0.2889$, $\kappa_g = 150$, $\kappa_q = 1500$, $\alpha_g = \alpha_q = 0$.

for the investigated devices [SCH19b]. Therefore, the approximation $\kappa_q \to \infty$ can be utilised, to further simplify the expression for the reflectivity. This approximation is further justified by the behaviour of the reflectivity shown in Fig. 5.17(e). The simplified effective external cavity reflectivity then reads

$$r_{\mathrm{cav,DAE}}(\omega) = \left[\frac{h_g - 1 + N_0(1 - i\alpha_g) - i\kappa_g^{-1}\omega}{1 - N_0(1 - i\alpha_g) + i\kappa_g^{-1}\omega}\right]^2 \cdot \frac{h_q - 1 + n_0(1 - i\alpha_q)}{1 - n_0(1 - i\alpha_q)} \cdot \eta. \tag{5.95}$$

As performed before in the empty cavity regime (see (5.96) and appendix A.2), it is now possible to apply a functional mapping by utilising the expression found for r_{cav} in combination with the functional mapping equation (5.61). Again, it is assumed that there is a linear PDE with operator $\mathcal{L}(\omega)$ describing the variations of the pulse spectrum $\tilde{Y}(\omega, \theta)$ from round-trip to round-trip time (on the slow time scale θ). The PDE is written as

$$\frac{\partial}{\partial\theta}\tilde{Y}_+(\omega,\theta) = \mathcal{L}(i\omega)\tilde{Y}_+(\omega,\theta). \tag{5.96}$$

Using a linear operator is valid in the vicinity of the threshold, because the nonlinear contributions of the charge carrier interactions are very small due to the small equilibrium carrier densities N_0 and n_0. Integrating the PDE over θ from round-trip $n-1$ to round-trip n and making use of eq. (5.61), relates the operator $\mathcal{L}(\omega)$ to the reflectivity via

$$\mathcal{L}(\omega) = \ln\left(r_{\mathrm{cav}}(\omega)\right). \tag{5.97}$$

Assuming a lasing close to resonance [HAU00, VLA04, SCH20d] and neglecting the amplitude-phase coupling ($\alpha_g = \alpha_q = 0$), one can expand the logarithm for small ω which yields

$$\ln\left(r_{\mathrm{cav}}(\omega)\right) \approx \frac{2ih_g\omega}{(N_0 - 1)(N_0 - 1 + h_g)} + \frac{\left(2h_g - h_g^2 - 2h_gN_0\right)\omega^2}{\kappa_g^2(N_0 - 1)^2(N_0 - 1 + h_g)^2} + \mathcal{O}(\omega^3). \tag{5.98}$$

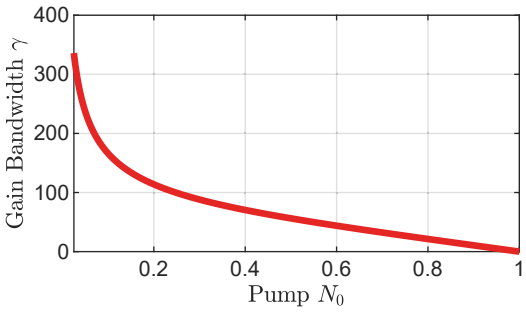

Figure 5.18: Gain bandwidth γ in dependence on the pump power according to eq. (5.100) with $\kappa_g = 150$. The x-axis minimum is set to $N = 0.025$ to obtain a better visibility.

From this expression one can already deduce that the second-order contribution $\mathcal{O}(\omega^2)$ is the one related to the spectral filtering, i.e. gain bandwidth (as this would transform to a second derivative in time when applying a Fourier transform). Consequently, one can equate it to the filtering coefficient $\frac{1}{2\gamma^2}$ found in the Haus master equation for the DDE model. With $h_g = 2$ this gives

$$\frac{1}{2\gamma^2} = \frac{4N_0}{\kappa_g^2 \left(1 - N_0^2\right)^2}. \tag{5.99}$$

Rearranging for γ leads to the following correspondence of the gain bandwidth between the two models

$$\gamma = \kappa_g \left(1 - N_0^2\right) \sqrt{\frac{1}{8N_0}}, \tag{5.100}$$

where it is used that $\gamma > 0$ from physical arguments and $N_0 < 1$. If lasing close to the threshold is investigated, one can substitute the threshold value $N_0 = N_{\text{th}}$ and hence determine κ_g from a given γ and Q_0. The general correspondence is indicated in Fig. 5.18. The plot indicates, that at higher pump powers the gain bandwidth (FWHM) in the DAE model becomes narrower. Consequently, lowering the bandwidth γ accordingly in the DDE model is required to obtain a comparable result. However, it has to be noted that despite the narrowing FWHM at large N_0, the number of modes experiencing an amplification grows due to the increased pump power.
To further illustrate the behaviour of the gain bandwidth in the two models, the reflectivity of the DDE model is calculated by combining the frequency independent single chip reflectivities eq. (5.66) and eq. (5.77), the Lorentzian filter modelling the gain bandwidth eq. (3.30) and the losses at the outcoupling facet. This yields the following expression for the reflectivity of the external cavity $r_{\text{cav,DDE}}(\omega)$

$$r_{\text{cav,DDE}}(\omega) = \sqrt{\kappa} \frac{\gamma}{\gamma + i\omega} \exp\left(\left[1 - i\alpha_q\right] G_0 + \left[1 - i\alpha_q\right] Q_0\right). \tag{5.101}$$

The intensity reflectivities obtained from both models close to the threshold at different values of the unsaturated absorption are presented in Fig. 5.19. For the pump power and the unsaturated absorption, the linear parameter transformations (eq. (5.78) and eq. (5.74)) are used, which is sufficient for low values of N_0 and n_0. Furthermore, κ_g is calculated from the pump power values (N_0), while using a bandwidth of $\gamma = 150$ for the DDE model (eq. (5.100)).
It is visible that across the central modes, both models lead to well matching results, if the parameter transformations are applied. Due to the fact that only the linear relationships

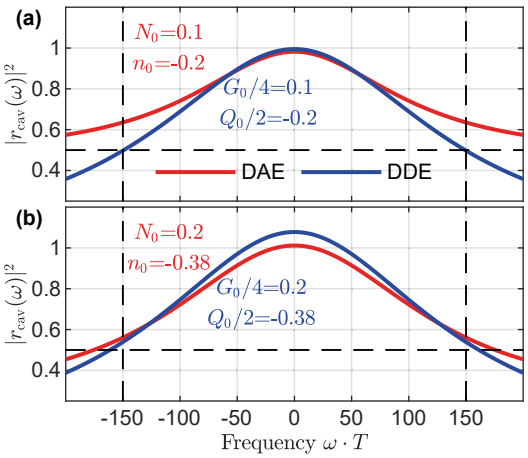

Figure 5.19: Intensity reflectivity of the external cavity depending on the frequency relative to the cavity resonance frequency scaled to a round-trip time of $T = 625$ ps. The reflectivity of the DAE (DDE) model is shown in red (blue). (a) and (b) indicate two different pairs of parameter values for the pump parameter and the unsaturated absorption, determined utilising the threshold equation of the DAE model (5.91). The values used for G_0 and Q_0 (DDE) are deduced by applying the linear parameter relationships given by eq. (5.78) and eq. (5.74). The gain bandwidth in the DDE model is set to $\gamma = 150$ and κ_g is calculated from the relationship (5.100). The dashed vertical lines mark the full width half maximum of the DDE reflectivity (FWHM $= 2\gamma$) and the horizontal dashed lines marks a value of $|r_{\mathrm{cav,DDE}}(\omega)|^2 = 0.5$.

between the equilibrium carrier densities are used, the reflectivity of the DDE model is slightly elevated for the chosen parameter set in (b). This can be further reasoned by the slightly lower CW threshold in the model DDE for higher Q_0 (see Fig. 5.16). From the dashed vertical lines, indicating the position of the FWHM of $r_{\mathrm{cav,DDE}}(\omega)$, it can be deduced that the values of G_0 and Q_0 do not influence the bandwidth in the DDE model. In opposition, n_0 and N_0 strongly impact the bandwidth in the DAE model (see Fig. 5.17(a) and (d)), despite the compensation introduced by adjusting κ_g according to eq. (5.100). Anyhow, a good agreement between the two models is found for the central modes when altering the pump and unsaturated absorption (see Fig. 5.16 (b)).

Ratio of the Differential Gain and Absorption

A last parameter that has to be compared is the normalisation factor s, which is proportional to the ratio of the differential gain coefficients in gain and absorber as well as to the ratio of the confinement factors. On that account, small carrier densities in the DDE model are assumed so that the exponentials in the absorber equation can be expanded. This simplification yields

$$\frac{d}{dt}Q(t) = Q_0\gamma_q - \gamma_q Q(t) - 2sQ(t) \mid E(t) \mid^2 . \tag{5.102}$$

In comparison, the equation in the DAE system reads

$$\frac{d}{dt}n(t) = \gamma_q \left[n_0 - n(t)\right] - sn(t)\,|e(t)|^2 . \tag{5.103}$$

From comparing the influence of the s parameters, it is possible to deduce $s_{DAE} = 2s_{DDE}$, which is related to the fact that a double pass of the absorber active section is assumed in the derivation of the DDE model.
All determined transformations are summarised in Table 5.1, which also includes the parameter values used for the further investigation of the DAE system.

Symbol	Value	Transformation
T	1	-
$\tau_{1,2}$	0.25	-
κ_g	168.5	$\gamma = \kappa_g \left(1 - N_0^2\right) \sqrt{\frac{1}{8N_0}}$
κ_q	$\kappa_q \to \infty$	-
N_0	$0 - 1$	$G_0 = 2\log\left(\frac{h_g - 1 + N_0}{1 - N_0}\right) \approx 4N_0.$
n_0	-0.289	$Q_0 = \log\left(\frac{h_q - 1 + n_0}{1 - n_0}\right) \approx 2n_0$
γ_g	0.625	-
γ_q	112.5	-
α_g	0	-
α_q	0	-
η	0.995	$\kappa = \eta^2$
s	4	$s_{DDE} = s_{DAE}/2$
$h_{g,q}$	2	-

Table 5.1.: Parameter values used for numerical integration of the V-shaped DAE model (5.38)-(5.44). All times and rates are normalised utilising a cavity round-trip time of $T = 625\,\mathrm{ps}$. Additionally, the transformation to the corresponding DDE parameter is given.

5.4.3 Comparison of DDE and DAE Systems

Fundamental Mode-Locking Instabilities

In order to obtain a more detailed overview of the influence of the micro-cavities and the related third-order dispersion effects on the stabilising dynamics, the DAE model is now compared to the DDE model. At first, this is done by means of path-continuation of the fundamental mode-locking solution. Although extensions of the DDE-biftool software for DAE systems are in development, its standard version is utilised due to the more convenient and well tested applicability [ENG02]. To be able to adequately include the DAE system into the software, it is required to transform the algebraic equations into differential equations. This can be done by adding a small differential contribution, which can be understood as a reverse adiabatic elimination. Introducing $\varepsilon \ll 1$ as a scaling parameter, the transformation of the algebraic equations exemplarily for the equation for $Y_-(t)$ reads

$$\varepsilon \frac{d}{dt} Y_-(t) = e(t - \tau_2) - y(t - \tau_2) - Y_-(t). \tag{5.104}$$

The other two algebraic equations (5.42)-(5.44) are transformed accordingly using the same value of ε.
As previously done in the bifurcation analysis of the DDE system (see section 4.2.3), the investigation is started at a low round-trip time of $T = 193$ ps. This is reasoned by the fact that not many multi-pulse states stabilise in this regime due to the broad pulse width relative to the round-trip time. Hence, a lower round-trip time serves as an excellent starting point to get a first overview of the dynamics. A 1D-bifurcation diagram of the FML solution (light blue) and the continuous-wave solution (orange) continued using the DAE system is shown in Fig. 5.20(a). It indicates the maximum electric field amplitude $\max(|E_+|)$ in dependence on the pump parameter N_0. Stable dynamics are indicated by thick lines and unstable dynamics by thin lines. For comparison, the 1D-bifurcation diagram of the FML and CW solution in

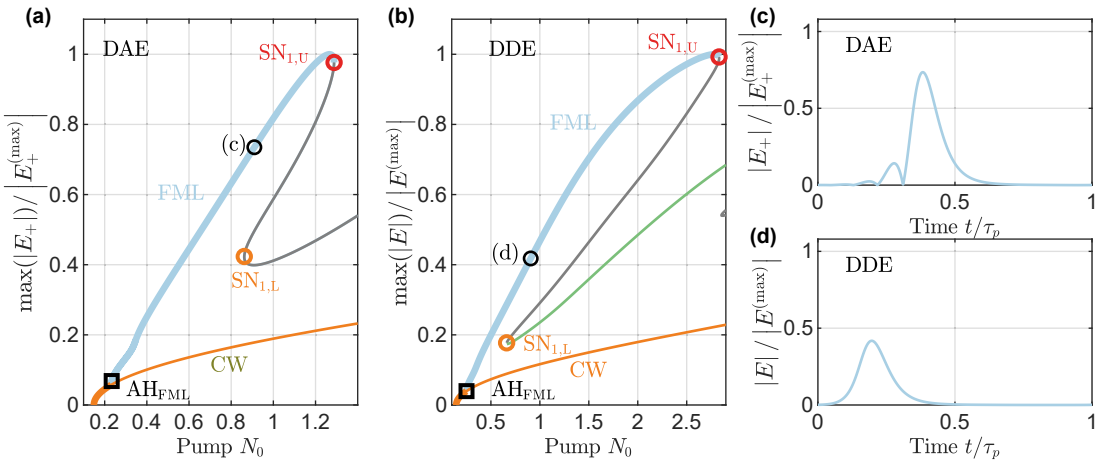

Figure 5.20.: 1D-Bifurcation diagrams showing the maximum electric field amplitude in one period of the solutions with respect to the pump parameter N_0 for (a) the DAE model and (b) the DDE model obtained using DDE-biftool. Light blue indicates the fundamental mode-locking solution along the branch, grey corresponds irregular pulse structure and green to the PC_2 solution. The continuous-wave steady state solution is plotted in orange. Thick (thin) lines denote stable (unstable) dynamics. The orange and red circles denote the lower ($SN_{1,L}$) and upper ($SN_{1,U}$) saddle-node bifurcations. (c)-(d) One period (τ_p) of the electric field dynamics at the points of the solution branches indicated by the black circles in (a)-(b). The round-trip time is set to $T = 193\,\mathrm{ps}$. The other laser parameters and the linear conversion used for the pump power G_0 are given in table 5.1 and $\varepsilon = 0.001$.

the DDE model is plotted in Fig. 5.20(b). To obtain an adequate comparability, the pump parameter G_0 from the DDE model is transformed to match the pump in the DAE model N_0 according to the linear conversion given in Table 5.1.

The fundamental periodic solution is born at the first Andronov-Hopf bifurcation along the continuous-wave branch (black square in Fig. 5.20(a)-(b)) in both models. After the bifurcation point ($N_0 > N_{\mathrm{HOPF}}$), the maximum electric field amplitude increases until a critical pump power and then a saddle-node bifurcation ($SN_{1,U}$) leads to a loop (fold) of the solution branch (red circles). In the following, the maximum pulse amplitude decreases and the branch stretches out to lower pump powers again. At a second saddle-node bifurcation ($SN_{1,L}$; orange circle), the branch loops once more and $\max(|E_+|)$ begins to increase again. Between the two saddle-node bifurcations (grey line) irregular pulse structures (many inequidistant satellite pulses with random amplitudes) exist, which are periodic at approximately the cold-cavity round-trip time, but unstable. Therefore, they would not be expected to be visible in experiments.

Although the 1D-bifurcation diagrams found for the two models are qualitatively similar (c.f. 5.20(a)-(b)), the solution along the branches differ after the $SN_{1,L}$ point. In the DDE model, a stabilisation of a PC_2 pulse-cluster solution appears (green), which destabilises as the branch loops again (not shown here, for details see section 4.2.3 and Fig. 4.9). In contrast, a periodic solution characterised by two very wide pulses (pulse width $\approx 0.2T$) with a distance of $\Delta \approx 0.25$ emerges for the DAE model. Nonetheless, this solution remains unstable and the branch just continues to higher pump powers without any further loops.

A possible explanation for the differing bifurcation scenario after the first loop can be found by investigating the pulse shape along the branches in more detail, of which a comparison is given in Fig. 5.20(c) and (d). It indicates, that in contrast to the DDE results, satellite pulses

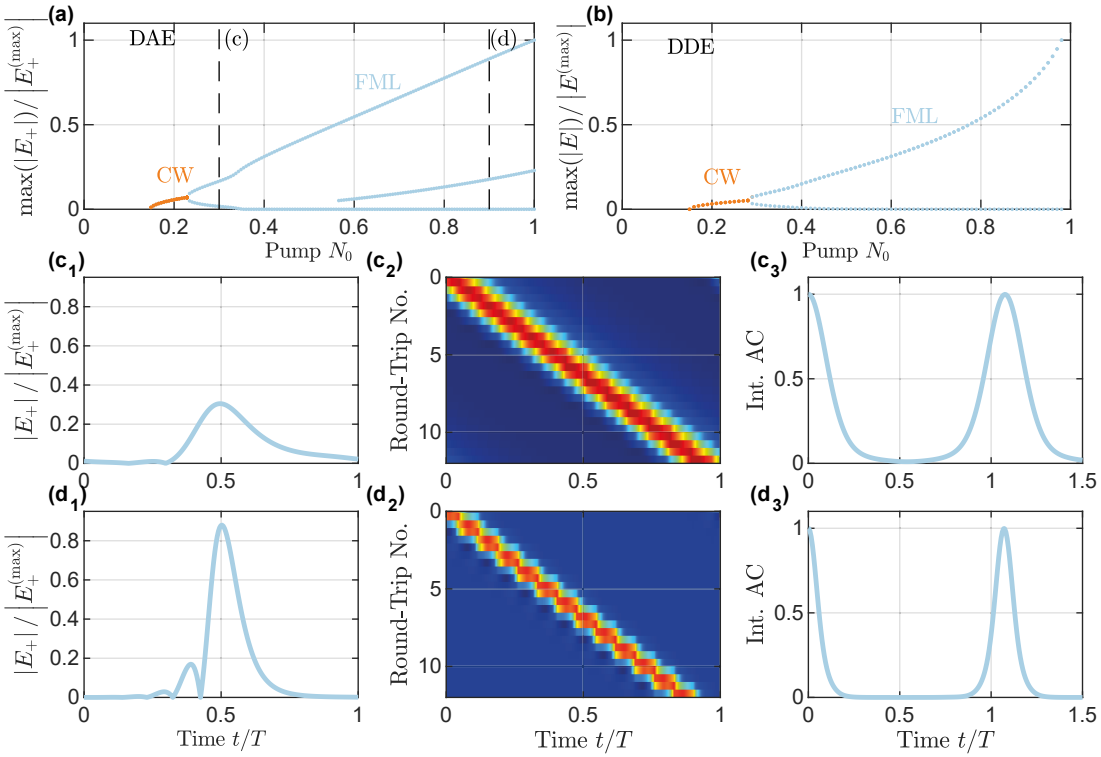

Figure 5.21.: (a)-(b) 1D-Bifurcation diagrams obtained applying direct numerical upsweep in the pump parameter N_0. Plotted are the unique maxima of the electric field amplitude found in 300 round-trips at different values of N_0 using (a) the DAE model and (b) the DDE model. (c)-(d) Electric field dynamics of the DAE model at the N_0 values marked by the vertical lines in (a). Panel 1 indicates the pulse shape, panel 2 corresponds to a pseudo space-time representation of the periodic dynamics (colour code indicates the electric field amplitude $|E_+|$) and panel 3 shows the intensity autocorrelation up the first maximum. The autocorrelation is calculated via the Wiener-Khinchin theorem using an intensity time-series of 1000 round-trips. The round-trip time is set to $T = 193\,\mathrm{ps}$. The other laser parameters and corresponding conversions are given in table 5.1.

at the leading edge of the main pulse emerge along the stable periodic FML solution in the DAE model. As discussed for the coupled micro-cavity system without gain and absorption (see Fig. 5.15), the satellites appear due to the partial reflection of the pulse at the surface of the micro-cavity. As this effect is not included into the DDE model, only a single pulse is evident in Fig. 5.20(d). Due to the combined influence of the gain and absorption, only a limited number of satellites is supported, in contrast to the empty micro-cavity system (see Fig. 5.15). Based on the transformation of the DAE system to a PDE system (eq. (5.65)), revealing the comparably strong third-order dispersion contribution, this can be interpreted as a third-order dispersion effect.

Due to the appearance of the satellites, the complete pulse structure becomes too broad in time with respect to the round-trip time for a PC_2 solution to stabilise. Therefore, the fat pulse solution occurs directly after the first loop of the solution branch. However, it does not turn stable in the investigated parameter regime. The sequence of pulsed solutions of different numbers can be interpreted similarly to the occurrence of higher-order pulse-cluster solutions observed in the DDE system. In that case, the PC_n solutions stabilise in additional loops along the branch which emerge at characteristic elevated round-trip times.

The higher round-trip times are required, to obtain a narrow pulse width combined with an increased available gain so that a pulse-cluster can be formed[22]. For the DAE system, these requirements are not met due to satellite pulses broadening the pulse structure and therefore circumventing the appearance of PC_n states at low round-trip times.
Despite the parameter conversion, the FML solution in the DAE system destabilises at lower values of the pump parameter. Possible reasons for this again lie in the broader pulse structure and the further amplification of the satellite pulses, which are a source of further instabilities, i.e. the stabilisation of quasi-periodic states. It has to be highlighted that pump powers $N_0 > 1$ are not necessarily physical[23] as the approximated reflectivity of the CW solution (5.94) diverges and the reversed logarithmic conversion for the pump power given in table 5.1 cannot be applied, as it converges to 1 for large G_0[24]. In consequence, values of $N_0 > 1$ are only used here to unravel the branch structure and G_0 is transformed according to the linear conversion equation $G_0 = 4N_0$ for all values.
On the account of exploring the impact of the third-order dispersion on the emergence of instabilities, the 1D-bifurcation diagram is calculated by means of direct numerical integration. An upsweep is performed in pump power N_0, which corresponds to utilising the stabilised dynamics at the previous parameter point as the initial condition for the next point in N_0. The unique maxima and minima of the electric field amplitude found in 300 round-trips are then plotted for each investigated parameter point. The resulting 1D-bifurcation diagrams for the DAE and DDE[25] system are plotted in Fig. 5.21(a)-(b). Once more, the round-trip time is set to $T = 193\,\mathrm{ps}$. Due to the divergence of the approximated continuous-wave reflectivity eq. (5.94) for $N_0 \to 1$, only the regime of $N_0 < 1$ is investigated.
As determined from the path-continuation result, the FML solution is born from the CW branch in both models and stays stable for $N_0 < 1$. The region of two maxima close to the CW branch refers to a regime of regular oscillations close to the Andronov-Hopf bifurcation point. When plotting all unique maxima, the satellite pulses occurring in the DAE system become visible in the 1D-bifurcation diagram as a second small maximum at each investigated pump power value (see Fig. 5.21(a)). The amplitude of the second maximum grows slower with respect to the pump power, because they bleach the absorber much less and therefore experience a lower net-gain [SCH20d]. Furthermore, the satellites experience a higher amount of gain and absorption as they pass both active sections prior to the main pulse. As discussed before, they do not occur in the DDE system (see Fig. 5.21(b)). It has to be noted that the increase of the pulse maxima in the DDE model appears much stronger in comparison to the branch determined using DDE-biftool. Nevertheless, this is just related to the fact that the full logarithmic conversion equation is used here.
The characteristics of the FML solution at two points along the branch in the DAE system, marked by dashed lines in Fig. 5.21(a), are presented in Fig. 5.21(c)-(d). The first panel

[22] A detailed discussion of the higher-order PC_n states can be found in section 4.2.3.
[23] As visible from the bifurcation diagram in Fig. 5.20, the calculations also lead to reasonable results for $N_0 > 1$. This can be reasoned by the simplification of assuming a small electric field $E_+ \approx 0$ used in the derivation of the reflectivity, which is not necessarily true in the investigated parameter regime far away from the lasing threshold. Furthermore, it has to be highlighted that the reflectivity is approximated for a CW solution and not a pulsed mode-locked solution. Thus, the reflectivity does not necessarily diverge for the FML solution and the system still leads to reasonable results. Nevertheless, a large value of $N_0 > 1$ leads to unrealistically high reflectivity and therefore is not investigated here, aside from the branch structure at low round-trip times.
[24] Vice versa it diverges for $N_0 \to 1$ when transforming $N_0 \to G_0$.
[25] The transformation of the pump parameter G_0 (DDE) to match N_0 (DAE) is performed according to the inverted logarithmic equation in table 5.1.

shows the pulse shape within one round-trip, the second panel indicates a pseudo space-time representation of the dynamics and the third panel indicates the normalised intensity autocorrelation. Comparing the pulse shapes in Fig. 5.21(c_1)-(d_1), one again notices that at small values of the pump parameter, the satellite is almost not visible (c_1), but its amplitude increases with the pump power (d_1). Due to the partial reflection at the upper surface of the micro-cavity, another pulse grows at the leading edge of the satellite at sufficiently high pulse amplitudes (see Fig. 5.21(d_1)).
The pseudo space-time representation in Fig. 5.21(c_2)-(d_2) demonstrates (exemplarily for 12 round-trips) how the satellites remains stable from round-trip to round-trip and do not lead to a destabilisation of the pulse train. Furthermore, it becomes evident that the temporal drift of the pulse structure is very pronounced, i.e. the period deviates strongly from the cold-cavity round-trip time due to the comparably large photon life-time κ_g^{-1} chosen for the investigation. Furthermore, the drift can be approximated from the PDE representation of the DAE model (5.65) in absence of gain and absorption (and $\kappa_q \gg 1$). In this case, the drift term is characterised by the first-order derivative with respect to σ, with a pre-factor of $4\kappa_g^{-1}$. Therefore, the period can be approximated by $\tau_p \approx T + 4\kappa_g^{-1}$. Opposing to that, the PDE representation of the DDE model leads to a drift contribution of γ^{-1}. Consequently, the period can be estimated by $\tau_p \approx T + \gamma^{-1}$, indicating a less pronounced drift (see Appendix A.2 for a derivation).
As expected from the approximation of the period, the intensity autocorrelation of the FML solution with satellite pulses exhibits clear maxima at $\tau_p \approx T + 4\kappa_g^{-1}$ for both investigated pump powers (see Fig. 5.21(c_3)-(d_3)). The intensity autocorrelation is calculated applying the Wiener-Khinchin using a time-series of 1000 round-trips. Due to the asymmetry of the pulse structure, the satellite pulses only lead to a broadening of the maxima (compared to a single pulse) and do not appear as distinguished structures in the autocorrelation trace. Furthermore, the maxima in each autocorrelation trace indicate a narrowing at elevated pump powers (see Fig. 5.21(c_3)-(d_3)), which has already been observed from the pulse shapes. This is related to the gain bandwidth changing with the increasing gain and the narrowing effect of the absorber.

Intermediate-Cavity Regime

After the initial discussion of the stable FML solution at low round-trip times, the parameter is now adjusted to match experimental realisations of the V-shaped VECSEL ($T = 625\,\mathrm{ps}$) [WAL16]. Again, the investigation of the dynamics is started with a path-continuation of the fundamental mode-locking solution in both models. The obtained 1D-bifurcation diagrams of the FML solution branch showing the maximum electric field amplitude in one period in dependence on the pump parameter N_0 are indicated in Fig. 5.22(a)-(b). Plotted in (a) is the result for the DAE system and in (b) for the DDE system[26]. Again, the grey parts of the branch indicate unstable, irregular periodic pulse structures.
As discussed in detail for the DDE system in section 4.2.3, the FML solution detaches from the CW steady state and becomes a solitary branch at an elevated round-trip time. The stable FML regime then is enclosed by two saddle-node bifurcations ($SN_{1,U}$ and ($SN_{1,L}$), instead of the first Andronov-Hopf bifurcation along the CW branch at the lower boundary

[26]The transformation of the pump parameter G_0 (DDE) to match N_0 (DAE) is performed according to the inverted logarithmic equation in table 5.1 for all following results. Furthermore, it has to be noted that only the detached FML branch is presented for comparison. For the full 1D bifurcation scenario see Fig. 4.9.

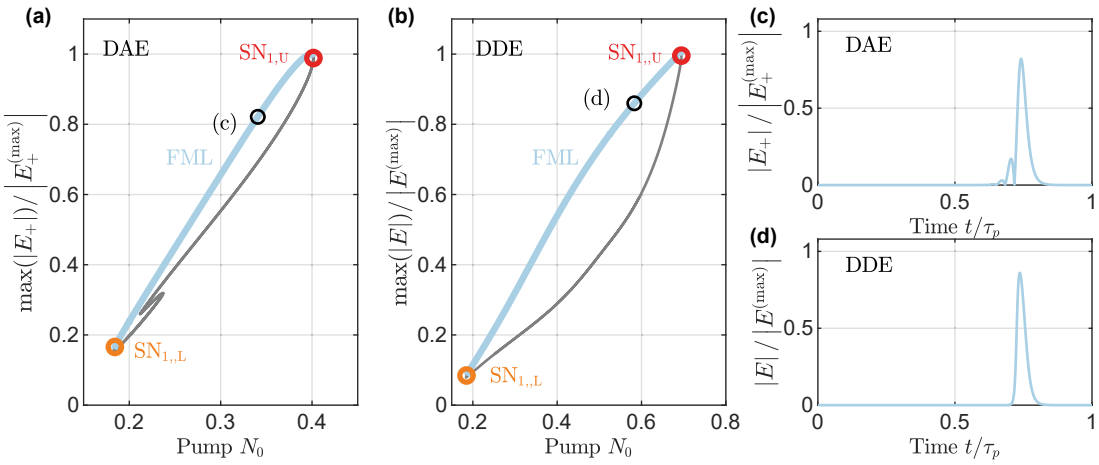

Figure 5.22.: 1D-Bifurcation diagrams showing the maximum electric field amplitude with respect to the pump parameter N_0 for (a) the DAE model and (b) the DDE model. Blue denotes the fundamental mode-locking solution regime, while grey corresponds to an irregular pulse structure. Thick (thin) lines denote stable (unstable) dynamics. The orange and red circles denote saddle-node bifurcations. (c)-(d) Pulse shape at the points of the solution branches indicated by the black circles in (a)-(b). The round-trip time is set to $T = 625\,\mathrm{ps}$. The other laser parameters and corresponding conversions are given in table 5.1 and $\varepsilon = 0.001$.

(see Fig. 5.22(b)). Interestingly, the same bifurcation scenario appears for the DAE system. As shown in Fig. 5.22(a), the FML solution branch is detached from the CW solution at elevated round-trip times. Furthermore, the stable FML region is bound by two saddle-node bifurcations ($\mathrm{SN}_{1,\mathrm{L}}$ and $\mathrm{SN}_{1,\mathrm{U}}$), embodying the upper and lower loop (fold) of the branch. Although an additional loop along the FML branch in the DAE system can be found at low N_0, it does not lead to the stabilisation of further solutions.

The position of the $\mathrm{SN}_{1,\mathrm{L}}$ point in N_0 is quantitatively similar for both models, if the parameter conversion is applied. Yet, the destabilising bifurcation point $\mathrm{SN}_{1,\mathrm{U}}$ is found at lower pump powers for the DAE model. This can again be reasoned by the additional satellite pulses emerging in the DAE system. An exemplary plot of the electric field amplitude in one period of the solution close to the upper bifurcation point is visualised in Fig. 5.22(c)-(d) for both models. The shape of the main pulse remains very similar, while the satellite pulses only appear in the DAE system.

Although the path-continuation results in qualitatively very similar branches across the models, the 1D-bifurcation diagrams obtained by direct numerical integration unravel the strong destabilising influence of the third-order dispersion contributions. The numerical upsweeps in N_0 are plotted in Fig. 5.23(a)-(b), and are calculated as before.

The lower electric field maxima in the FML regime (blue dots) again indicate that the satellite pulses are only present in the DAE model and that their amplitude increases with the pump current. At a pump power of $N_0 \approx 0.38$, the FML solution destabilises[27] and the system transitions to a quasi-periodic pulsed state (MP_1, pink dots). A characterisation of the quasi-periodic solution at the pump values indicated by the vertical dashed lines in (a)

[27] When comparing the position of FML upper stability boundary obtained using DDE-biftool and the direct numerical integration, slight deviations appear. These can be related to the alteration of the model, required for the application of the DDE-biftool software. Furthermore, the temporal resolution used in DDE-biftool is limited, due to the high memory and computational requirements, caused by the high number of system variables.

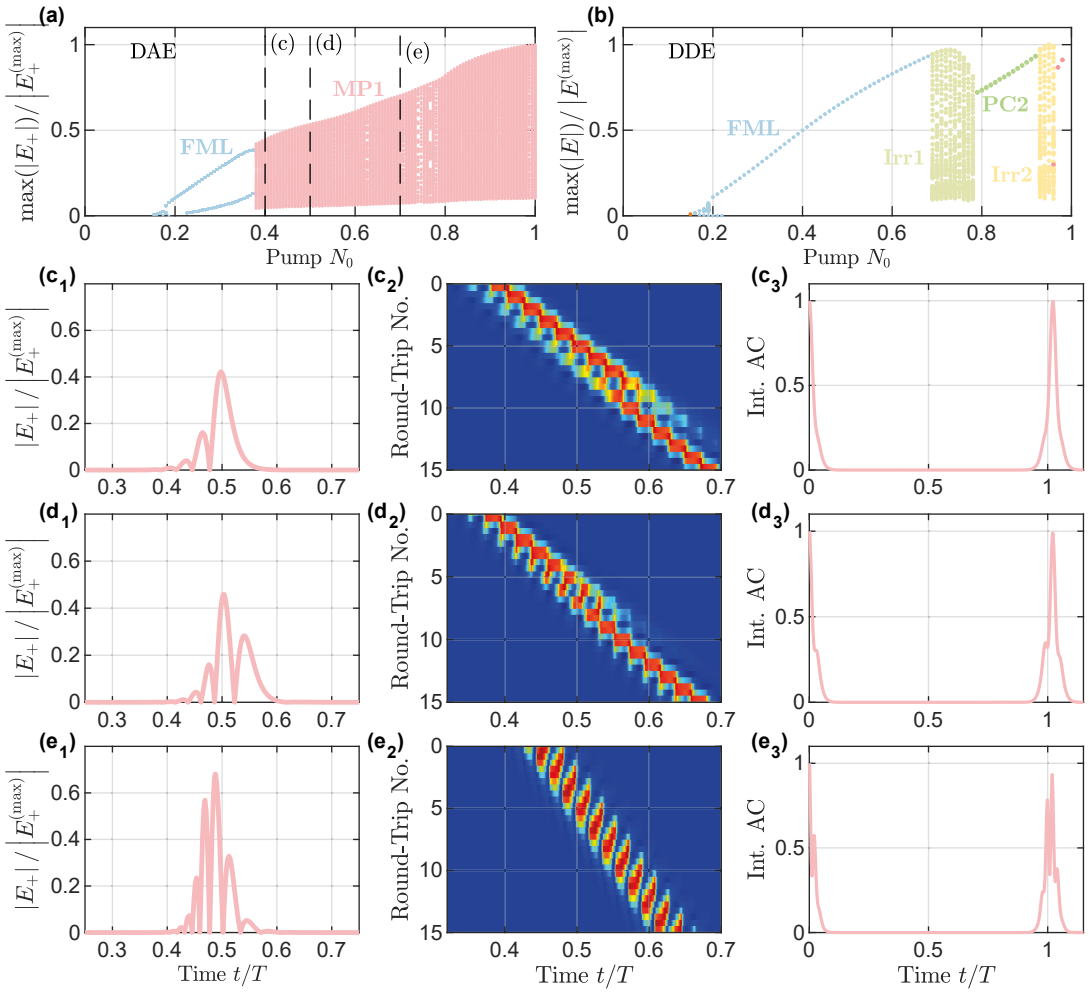

Figure 5.23.: (a)-(b) 1D-Bifurcation diagrams obtained applying direct numerical integration. Plotted are the unique maxima and minima of the electric field amplitude found in 300 round-trips at different values of the pump parameter N_0 (up-sweep) using (a) the DAE model and (b) the DDE model. (c)-(e) Electric field dynamics (DAE) at the N_0 values marked by the vertical lines in (a). Panel 1 indicates a representative pulse shape of the quasi-periodic dynamics, panel 2 corresponds to a pseudo space-time representation of the quasi-periodic dynamics (colour code indicates the electric field amplitude $|E_+|$) and panel 3 shows intensity autocorrelation up to the first maximum. The round-trip time is set to $T = 625\,\mathrm{ps}$. The other laser parameters and corresponding conversions are given in table 5.1.

is given in the panels (c)-(e). The exemplary illustrations of the pulse shapes in (c_1)-(e_1) evidence that the number of satellite pulses contributing to the pulse structure grows with increasing pump power, as found for the stable FML solution. However, at an intermediate round-trip time the satellite pulses at the leading edge become strong enough to create an instability similar to the case of the quasi-periodic temporally localised states discussed in Reference [SCH20d]. As visible in the pseudo space-time plots in Fig. 5.23(c_2)-(e_2), the satellite pulse in front of the main pulse continuously grows in amplitude until the gain is depleted so strongly that the main pulse does not experience enough gain to compensate the losses. Therefore, it decreases over several round-trips and eventually vanishes. In the mean time, the satellite pulse becomes the new main pulse. This process repeats in a quasi-periodic fashion. Due to the higher number of satellite pulses and a stronger amplification, the exchange of the main pulse occurs at a higher frequency for an increased pump power (see Fig. 5.23(e_2)).
The temporal drift of the pulses appears less pronounced in the pseudo space-time plots as well as in the traces of the intensity autocorrelation compared to the short cavity case. This can be reasoned by the lower photon life-time relative to the round-trip time, resulting from the enlarged cavity. Despite the quasi-periodic appearance of the solutions, the intensity autocorrelation exhibits distinct maxima at $\approx T + 4\kappa^{-1}$. Together with the number of unique maxima in the time trace, the autocorrelation can be utilised to identify the satellite instabilities in an automatised way from the numeric results.
Similar instabilities, driven by third-order dispersion were reported for temporally localised states in alike systems in References [SCH19b, SCH20d]. These instabilities are based on the growth of a satellite, which ultimately steals all the gain form the main pulse. Furthermore, a wiggling instability was reported in Reference [HES21], which is characterised by an oscillation of the pulse position. It is however not present in the investigated parameter regime discussed in this work. Although the quasi-periodic states can lead to the occurrence of side-pulses in the autocorrelation trace (see 5.23), their appearance strongly depends on the length of the determined time-series. Therefore, it is unlikely that the experimentally determined instabilities in the high-performance mode-locking regime reported in Reference **??** are driven by third-order dispersion effects. This is further supported by the low reflectivity at the gain-chip surface, since it is antireflection coated.
In the DDE system (see Fig. 5.23(b), the FML solution destabilises as an additional net-gain window opens at the position of the second gain pass of the pulse with increasing pump power. This leads to the emergence of a new small pulse, depleting the gain at this position. As the small pulse is further amplified, it collects all the gain, causing a disappearance of the initial pulse (light orange region in Fig. 5.23(b)). A pseudo space-time plot of this type of instabilities can be found in section 4.2.3 (see Fig. 4.6, a detailed discussion of this type of instabilities caused by the cavity geometry is given in Reference [MEI21a]. In contrast to the DAE system, the TOD contribution is overwhelmed by the filtering contribution in the DDE system and therefore the system can stabilise onto periodic pulse-cluster solutions at elevated pump powers (green and red dots in Fig. 5.23(b)). These destabilise in a cavity related instability. As the cavity features are also included in the DAE system, it is possible that a combination of the two instabilities (cavity geometry and third-order dispersion) could arise.

Influence of the Unsaturated Absorption

In order to obtain a broader overview of the arising instabilities, the laser dynamics are evaluated in the 2D parameter plane of the pump power and the unsaturated absorption (N_0, n_0). The 2D-bifurcation diagrams are obtained by performing 1D upsweeps in pump power for varied values of the unsaturated absorption[28]. For each parameter pair, the stabilised dynamics are evaluated according to the characteristic features of the time-series. The resulting 2D-bifurcation diagrams are shown in Fig. 5.24 for (a) the DAE system and (b) the DDE system. The dashed black line corresponds to the n_0 value used for the priorly discussed 1D-bifurcation diagrams. Again, the first characterisation is performed at a low round-trip time of $T = 193\,\mathrm{ps}$

For both models, the CW region denoted in orange is strongly pronounced, especially for high absolute values of the unsaturated absorption. At the low round-trip times investigated here, a continuous bleaching of the absorber is favoured, unless the pump power is drastically increased so that it compensates the losses and enables the emission of a broad pulse. The black line at the lower boundary of the CW regime corresponds to the analytically determined value of the lasing threshold eq. (5.91). It matches the numerically determined boundary very well and hence serves as a verification of the numerical method. The analytic threshold is in accordance with the numerical results of the DDE system (see Fig. 5.24), validating the applied parameter conversions for the pump parameter, the unsaturated absorption and the losses η.

The teal region at the border of the CW regime corresponds to regular sinusoidal oscillations with a very broad maximum and the minimum not stretching to a zero intensity. These occur directly after the first Andronov-Hopf bifurcation along the CW branch (c.f. Fig. 5.20), as the system slowly transitions from the CW to a pulsed state. Due to the width of the maxima, these oscillations are classified in the "fat" pulse category (minimum pulse width of $0.2T$). The shading of the FML region illustrates the pulse width (normalised to a pulse width of $0.2T$), with broad pulses represented by dark blue. As discussed before, the pulses become narrower when the pump is increased, at each value of the unsaturated absorption. This is related to the incomplete bleaching of the absorber in the investigated parameter regime, which leads to a narrowing effect as the leading edge of the pulse is absorbed [MEI21a].

At low values of n_0, the FML solution destabilises at lower pump powers for both models. In the DDE case (see Fig. 5.24(b)), the previously mentioned quasi-periodic cavity related instabilities occur (see Fig. 4.6) at lower pump powers (Irr_1; light orange), because the additional net-gain window opens as the absorption is decreased. In contrast, the grey region in the DAE results (see Fig. 5.24(a)) corresponds to very irregular dynamics, which are either quasi-periodic or chaotic, but cannot be clearly distinguished or asserted to a satellite instability. As discussed before (see Fig. 5.20), the upper stability boundary of the FML solution is given by a saddle-node bifurcation. The corresponding bifurcation line in the 2D parameter plane is indicated in red in Fig. 5.24(a) and is in accordance with the result of the direct numerical integration. A characterisation of the dynamics in the (N_0, n_0) parameter plane at an elevated round-trip time ($T = 625\,\mathrm{ps}$) is indicated in the 2D-bifurcation diagrams in Fig. 5.25. Once more, the DAE results are presented in (a) and the DDE results in (b). The round-trip time does not influence the threshold current in both systems and therefore

[28] The unsaturated absorption and pump parameters of the DDE model Q_0 and G_0 are transformed according to the inverse logarithmic equations given in Table 5.1.

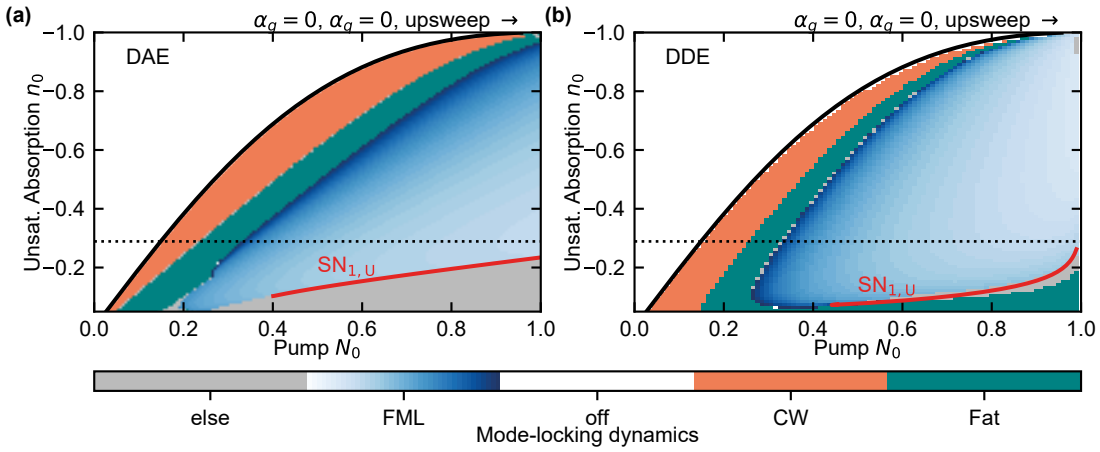

Figure 5.24.: 2D-bifurcation diagrams in the 2D parameter plane of pump parameter and unsaturated absorption (N_0, n_0) obtained by means of directly integrating the (a) DAE and (b) DDE model. For the DDE model, the parameters G_0 and Q_0 are converted to match the DAE model according to Table 5.1. The colour code distinguishes the dynamic regimes: fundamental mode-locking (blue); continuous-wave lasing (orange); fat pulses (teal); unclassified dynamics (grey); The shading of the blue region corresponds to the pulse width, normalised to a width of $0.2T$. The red line corresponds to the upper ($SN_{1,U}$) saddle-node bifurcation (see Fig. 5.20). The black dashed lines corresponds to the value of the unsaturated absorption used in the 1D-Scans in Fig. 5.20 and Fig. 5.21. The round-trip time here is set to $T = 193\,\mathrm{ps}$. The other laser parameters are given in table 5.1.

the analytic expression (black line) again matches the numerical results very well. The CW region is less pronounced in both cases (small orange region after the threshold) in comparison to the short cavity regime. This is reasoned by the photon life-time and gain bandwidth γ being much lower relative to the round-trip time, which leads to narrower pulses. Hence, the pulsed solution is energetically favourable to a continuous bleaching of the gain and absorber.

As known from the detailed investigation of the DDE system presented in section 4.2.3, higher-order pulse-cluster solutions (PC_n) emerge at elevated round-trip times. In an upsweep, these are separated by regions of a corresponding quasi-periodic instability resulting from the cavity geometry (Irr_{1-5}; light orange shading).

In contrast, the FML solution destabilises to a quasi-periodic satellite instability (light pink; MP_1) in the DAE system for a large region of unsaturated absorption values. This was already visible in the previously indicated 1D-bifurcation diagram in Fig. 5.23(a) while the characteristics of the solution are shown in Fig. 5.23(c)-(e). As the unsaturated absorption is increased, the boundary between FML and MP_1 shifts to higher pump powers, because the higher absorption suppresses the destabilising influence of the satellites.

The path-continuation of the FML branch for both system unravelled that the upper and lower stability boundaries of the FML solution are represented by a pair of saddle-node bifurcations $SN_{n,L}$ and $SN_{n,U}$ (see Fig. 5.22). Their bifurcation lines in the (N_0, n_0) plane are indicated in orange and red in Fig. 5.25(a) and (b) and are in accordance with the numerical result. Slight deviations of the bifurcation points found using the DAE system can be reasoned by the adjustments necessary to implement the system into DDE-biftool (equation (5.104)). In both models, the bifurcations collide at low absolute values of n_0 and the FML solution vanishes below that point. Thus, one can conclude that the bifurcation scenario of

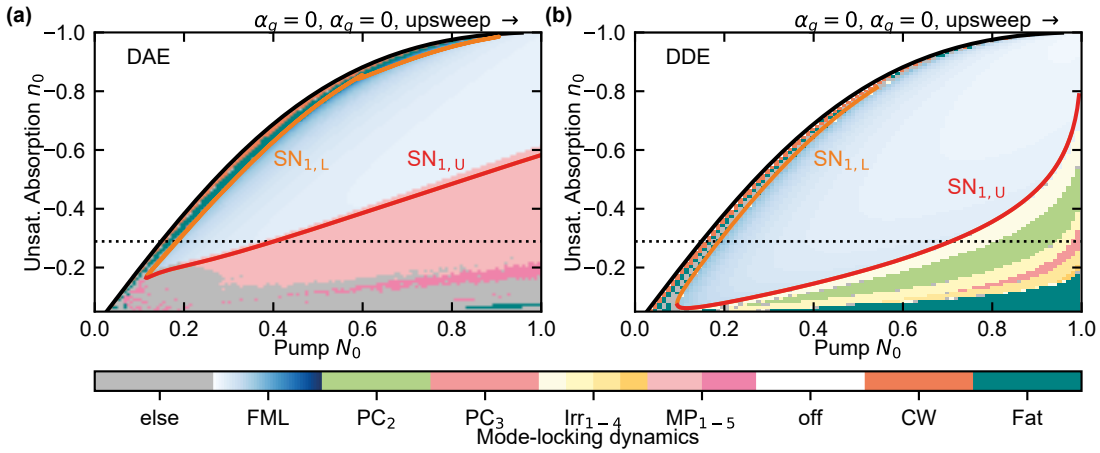

Figure 5.25.: 2D-bifurcation diagrams in the 2D parameter plane of pump parameter and unsaturated absorption (N_0, n_0) obtained by means of directly integrating the (a) DAE and (b) DDE model. For the DDE model, the parameters G_0 and Q_0 are converted to match the DAE model according to Table 5.1. The colour code distinguishes the dynamic regimes: fundamental mode-locking (blue); continuous-wave lasing (orange); fat pulses (teal); unclassified dynamics (grey); pulse-clusters with two (light green), three (light red), four (yellow) and five (purple) pulses; irregular quasi-periodic pulse-clusters (orange shading) and multi-pulsed states resulting from the influence of third-order dispersion (pink shading). Dynamics corresponding to the multi-pulse state MP_1 is indicated in Fig. 5.21(c)-(e) and to MP_2 in Fig. 5.26. The orange lines correspond to the lower saddle-node bifurcation ($SN_{1,L}$) and the red line to the upper ($SN_{1,U}$) saddle-node bifurcation (see Fig. 5.22). The black dashed lines corresponds to the value of the unsaturated absorption used in the 1D-Scans in Fig. 5.22 and Fig. 5.23. The round-trip time is set to $T = 625\,\mathrm{ps}$. The other laser parameters are given in table 5.1.

the FML solution is very similar across the two models in the discussed parameter regime. Despite the enlarged round-trip time, no regular PC_n solutions become stable in the DAE system in the investigated parameter regime[29]. This can be reasoned by the large influence of the satellite pulses (i.e. third-order dispersion), broadening the pulse structure and leading to instabilities. Nonetheless, a PC_2 satellite instability (MP_2) can be found at low unsaturated absorption values and is indicated by the dark pink region (MP_2) in Fig. 5.25(a).
The characteristics of the solution are visualised in Fig. 5.26. The temporal distance of the two pulse structures is given by $\approx T/4$ as visible from the exemplary electric field dynamics in one round-trip, illustrated in Fig. 5.26(a). The non-equidistant temporal separation of the pulses results from the double gain pass in the V-shaped cavity, which causes the pulses to adjust their distance so that the gain is depleted equidistantly, i.e. in the energetically most favourable way (for a detailed explanation see section 4.2.2).
As discussed for the FML instabilities, the satellite pulses of the PC_2 structure grow in amplitude from round-trip to round-trip. Hence, the main (largest) pulse experience less gain due to the stronger depleted gain and vanishes within several round-trips. As visible from the pseudo space-time representation in Fig. 5.26(b), the growth and disappearance of the pulses happens at the same frequency for the two pulse structures within one cluster, but not simultaneously. Hence, the autocorrelation trace only indicates a small maximum at the position of the second pulse structure ($t \approx T/4$), although the number of pulses and the

[29] Stable PC_2 solutions can be found at $N_0 > 2$ and $n_0 = -0.29$. However, this regime is not investigated here due to the excessively high pump powers.

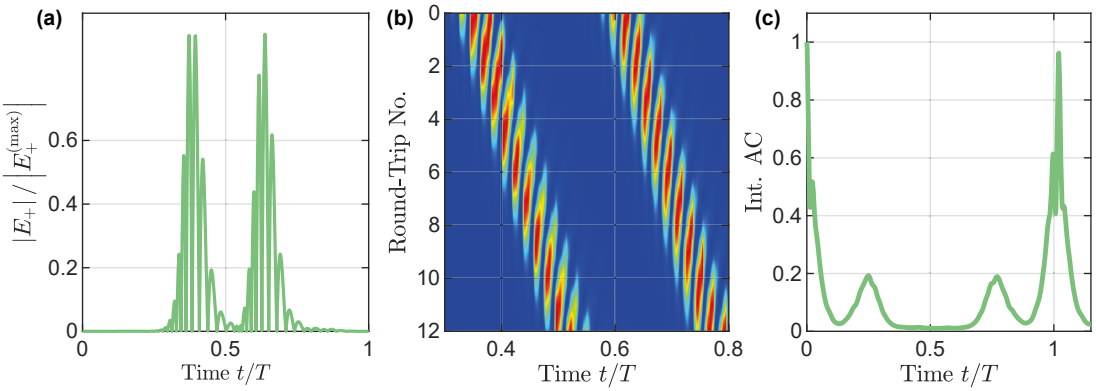

Figure 5.26.: Electric field characteristics of an irregular PC_2 (MP_2) solution. (a) indicates the pulse shape, (b) corresponds to a pseudo space-time representation of the quasi-periodic dynamics (colour code indicates the electric field amplitude $|E_+|$) and (c) shows the intensity autocorrelation. The unsaturated absorption is set to $n_0 = 0.177$, the pump to $N_0 = 0.9$ and the round-trip time to $T = 625\,\mathrm{ps}$. The other laser parameters and corresponding conversions are given in table 5.1.

general appearance of the two pulse structures appears similar at a first glance. However, the small maxima in the autocorrelation trace can be utilised to clearly distinguish the MP_2 from the MP_1 instability in the automated evaluation of the dynamics.
If the pulse width or the influence of the third-order dispersion (number of satellites) is reduced, an MP_3 instability can occur. This can be achieved by enlarging the round-trip time or reducing the photon life-time κ_g^{-1}.
In contrast to the DDE system, which transitions to a state characterised by wide pulses (teal region in Fig. 5.25(b)) at high pump powers and low n_0, the DAE system exhibits chaotic dynamics (grey area in Fig. 5.25(a)) that are not further classified here as no correlations between the states are found from the investigated properties of the time-series[30]. The chaotic dynamics are related to a strong amplification of the satellite pulses at low values of the unsaturated absorption and the additional influence of the V-shaped cavity geometry allowing for pulses to collide in the gain.
It is possible to conclude that the FML region as well as the CW steady state follow a very similar bifurcation scenario in both models. Yet, the strong influence of the third-order dispersion leads to the emergence of further instabilities, circumventing the stabilisation of regular multi-pulse states. It is to say that the chosen photon life-time is very high compared to experimental values. Hence, a decrease of κ_g^{-1} could potentially reduce the influence of the third-order dispersion (c.f. pre-factor in the TOD contribution eq. (5.65)) compared to the other contributions and enable the stabilisation of PC_2 states at realistic pump powers. Anyhow, the satellite instabilities still occur at very low κ_g^{-1} as found for temporally localised states in References [SCH19b, SCH20d].

[30] A possibility to distinguish chaotic and quasi-periodic dynamics would be the analysis of Poincare maps (return maps). These are characterised by plotting the amplitude of pulse n in the time-series with respect to the amplitude of pulse $n+1$. For chaotic dynamics, the resulting 2D map would then be continuously filled, whereas in the case of quasi-periodic dynamics it would only fill in certain characteristic for the quasi-periodic solution.

5.5 Summary

In this chapter, the influence of dispersion on the dynamics of a passively mode-locked VECSEL with a V-shaped cavity geometry was discussed.
On the account of investigating the impact of second-order dispersion (group-velocity dispersion), a generalisation of the Haus master equation was introduced. It enabled the application of the Haus master equation approach in the previously inaccessible regime of strong gain modulations, while the gain relaxation time is of the same magnitude as the round-trip time, typical for mode-locked VECSELs. The generalisation consisted of a dynamical boundary condition, connecting the gain value at the end of one round-trip to the value at the start of the next round-trip. The boundary condition was formulated as an ordinary differential equation, in order to be able to perform a path-continuation of the partial differential Haus master equation system and to circumvent the inconveniences of an asymmetric map boundary condition.
The generalised Haus master equation system was verified by comparing the results in different dynamical regimes to the well known ring delay differential equation model of mode-locking, from which the Haus model can be derived. Of most importance were the quasi-periodic QSML regime and the transition between harmonic mode-locking states, which cannot be modelled using a standard Haus model. A good agreement was found between the 2D-bifurcation lines in different parameter planes ((G_0, Q_0) and (G_0, γ_g)) in both dynamical regimes. On that basis, a first investigation of the role of dispersion on the boundary between QSML and fundamental mode-locking in the ring DDE was performed. It unravelled that, if no amplitude-phase effects are present ($\alpha_g = \alpha_q = 0$), positive and negative dispersion symmetrically shift the bifurcation lines to higher pump currents. This was reasoned by the varied pulse-shaping mechanism, induced by the additional dispersion contribution, which hinted at higher losses due to the excess bandwidth and the interaction with the absorber. Including non-zero line-width enhancement factors lead to a strong asymmetry of the bifurcation lines with respect to the point of zero dispersion, due to the complex nonlinear interplay of the phase effects. In this case, the lowest pump power at which the fundamental solution exists and exhibits the highest pulse energy can be found at positive values of the dispersion parameter.
Motivated by the successful application to the ring model, the generalisation (boundary condition) was applied to the nonlocal Haus master equation model, derived for the V-shaped system in the previous chapter, with the aim of investigating the impact of the GVD on the pulse-cluster solution discussed in section 4.2. The extension was again verified by comparing the accordance of the characteristic bifurcation points of the FML and PC_n solutions in models in the (G_0, Q_0) and (G_0, γ_g) parameter planes. The comparison lead to a good qualitative agreement.
At zero amplitude-phase coupling, the second-order dispersion parameter δ leads to a symmetric broadening and decrease of the pulse power around $\delta = 0$ at the upper bifurcation boundary of the FML and PC_2 solution and therefore it is shifted to lower pump powers. In contrast, the lower bifurcation boundary remains almost unaffected. Furthermore, an introduction of non-zero α-factors leads to an asymmetric shift of the upper bifurcation boundary to higher pump powers with the highest pump powers found at $\delta > 0$. The pulse width and pulse shape are strongly affected by the nonlinear interplay of the α-factors and the GVD. Hence, their combination does not necessarily lead to the best result in terms of the pulse width and pulse amplitude. Nevertheless, in accordance with experiments [WAL16], it could

be concluded that a slight amount of dispersion can be beneficial to achieve better performance figures and increase the pump power interval of stable operation. In further works, it could be interesting to include the system into the path-continuation software PDE2Path and unravel in detail how the bifurcation structure is changed by the influence of the GVD.

In the second part of this chapter, the influence of third-order dispersion was investigated. On that account, a delay differential equation (DAE) system for the V-shaped VECSEL was derived. It is based on treating the VECSEL setup as two coupled micro-cavities (gain and absorber chip). In recent works, it was discussed that in a DAE system the third-order dispersion contribution is not overwhelmed by filtering losses as in the DDE model and therefore TOD related instabilities can be studied [SCH19b, SCH20d, HES21]. In order to be able to sufficiently compare the results of the DAE and the DDE model of the V-shaped VECSEL, conversions for the unsaturated absorption, pump parameter, cavity losses and bandwidth parameter were found. A further advantage of the DAE system is the more realistic alteration of the gain bandwidth, if the pump power is adjusted. In the DDE system, the gain bandwidth is determined by the fixed parameter γ.
Making use of the parameter conversions, the laser dynamics was compared applying direct numerical integration techniques as well as a path-continuation of the fundamental mode-locking branch at low and intermediate-cavity lengths ($T = 193\,\mathrm{ps}$ and $T = 625\,\mathrm{ps}$). Interestingly, the path-continuation results lead to a very similar branch structure for both models. For low round-trip times, the direct numerical integration showed that the FML solution stays stable in a regime of realistic pump powers. Nonetheless, the third-order dispersion effects in the DAE system lead to the appearance of satellite pulses at the leading edge of the main FML pulse. At intermediate round-trip times, these pulses are amplified strong enough to generate satellite instabilities, in which the satellite increasingly depletes the gain at the leading edge of the pulse structure so that the main pulse disappears.
A further study of the destabilising influence of the TOD is performed by comparing the 2D-bifurcation diagrams in the parameter plane of pump power and unsaturated absorption for both models. The numerical results are tested by finding an analytical expression for the threshold current. At low round-trip times, the stabilising dynamics are very similar for both models. The only difference lies in the very chaotic dynamics at low unsaturated absorption values in the DAE model. Furthermore, in the DAE model no pulse-cluster solutions stabilise as the round-trip time is increased. Nevertheless, a satellite instability of the PC_2 solution can be found. In further works, it could be interesting to perform a comparison at lower (more realistic) photon life-times and lower absorption values. Due to the resulting narrow pulse-width this yet requires very long computation time and a high memory capacity. Additionally, the influence of the α-factors could be studied, as they can have a counter-acting influence on the TOD driven instabilities.

The results of this chapter indicate that second and third-order dispersion can strongly influence the bifurcation boundaries as well as the occurring instabilities. The presented models allow for reasonable computation times, while being complex enough to include the most important time scales. However, to further verify the influence of the dispersion effects, it would be interesting to compare the results to the calculations performed using a fully microscopic model as suggested in References [MCL20, MCL21]. This could allow for a detailed calculation of the different relaxation rates and especially deliver a valid approximation of the α-factors. Furthermore, it could be interesting to include a third-order dispersion con-

tribution into the Haus master equation, which can be phenomenologically done by adding a third-order derivative term to the electric field equation. The resulting influence of the TOD could then be compared to the results of the DAE model.
Furthermore, the DAE model allows to study the influence of a carrier grating, induced by the interference at the surface of the gain chip, caused to the non-normal incidence of the light. Additionally, a more in-depth bifurcation analysis could be performed, applying the newly developed DAE extensions of the DDE-biftool software.

6 Gain Effects

6.1 Introduction

Next to altering the cavity geometry or controlling dispersive influences, a widely used technique to improve vertical external cavity surface-emitting laser setups is to alter the composition of the active gain chip [KEL06, GAA16, GUI17]. The most established organisation of the gain chip consists of a back-side distributed Bragg reflector, a topside anti reflection coating and an active section characterised by multilayered quantum well structures [GAA16, KEL06, GUI17]. Typically, a similar structure is added as a saturable absorber to establish a mode-locked laser device [WAL16] (see section 3.2 for details).
The sought improvements aim at various characteristics of the laser device. Most importantly, the strive to enhance the maximum output power has to be mentioned, which can already be adjusted by optimising the details of the QW arrangement, QW material composition as well as the positioning of barriers [GUI17]. For mode-locked devices, the most important performance figures are an optimal interplay of pulse amplitude and pulse width [KEL06, WAL16, GAA16], while maintaining minimum fluctuations of both quantities. Enhancing the performance of the laser often is achieved by increasing the effective pump power, while maintaining a stable emission state. Hence, different destabilisation mechanisms have to be overcome when pushing the maximum possible pump power to higher levels. Especially heat management becomes a critical factor. A possibility to resolve this issue, is presented in References [KAH16, BEK17a, KAH19], where the gain chip is reduced to a thin semiconductor membrane containing several QW layers, which greatly eases heat transfer. Further destabilisation mechanisms that becomes important at higher pump powers are spatial and spectral hole burning, leading to a saturation of the gain [KIL16, ALF17, MCL20]. Furthermore, the technique of self mode-locking was pursued to possibly simplify the setup of VECSEL devices [BEK17a, CHI20]. These investigations however did not lead to comparable performance figures of standard mode-locked devices so far.
Alternative to the refinement of the QW layers in the gain and absorber chip, a possibility to adjust the final laser properties at the stage of the epitaxial growth process is the further reduction of the dimensionality of the active semiconductor sections. As already performed in one dimension for quantum wells (2D structure), the spatial extension of the active material is reduced the order of the de Broglie wavelength in one further dimension to achieve a spatial localisation of the electron/hole states [LIN15b]. Specifically, a reduction to a 1D semiconductor hetero structure can be exploited to construct nano-wire lasers, which greatly profit from their integrability to nanophotonic devices [LI12, MAY13, MAY17, ZAP19]. More important for mode-locked VECSEL structures is the reduction of the gain media to zero-dimensional localisation centres for the charge-carriers (0D), namely semiconductor quantum dots (for a more detailed introduction see section 2.1) [GRU02, LUE11a, CHO13a, JAH12, LIN16, LIN15b].

In monolithic laser diodes or VCSELs, quantum dots provide a large material gain, high thermal stability and a fast gain recovery which is required for ultrafast data transmission utilising direct modulation [SKO04, BER04a, LED07, GOM08]. In external cavity lasers aiming at a high power CW output, they enable a fine tailoring of the emission wavelength via an adjustment of their size (shifting the discrete quantum dot state energies) as well as a wide wavelength tunability [GER08a, SCH09h, NEC19]. With regard to mode-locked VECSELs, especially their strong inhomogeneous broadening (InAs QD system) is appealing, which can be exploited to reduce the pulse width [HOF08a, HOF11a]. Implementing quantum dots in the active section of the semiconductor saturable absorber mirror (SESAM) also profits from the possibility to finely regulate the absorption wavelength [FIN20]. Additionally, the fast carrier recovery is beneficial for the generation of ultra-short pulses [MAL06d, WIL09], which makes QD SESAMs interesting candidates for solid-state mode-locked lasers [LUM09]. The quantum dot area density can be altered conveniently during the growth process (up to a certain limit determined by the growth process), which can be used to tailor the modulation depth of the absorber. Equal to the gain structures, the inhomogeneous broadening leads to a feasible broad absorption linewidth [FIN20].
The most established technique to obtain quantum dot structures, is the so-called Stranski-Krastanov growth [STR37, STR38, LED96a, RAM97a]. In this technique, slightly above one monolayer of the quantum dot material is deposited on a substrate with a differing bandgap. At a critical thickness, quantum dots (pyramidal structures) form as a result of the lattice mismatch [PET03a], which are then overgrown to finalize the device. Although this technique is well-established and produces quantum dots well suited for laser applications [BIM97a, BHA99, GRI08a, GIE19, LIN15b], its downside is the low area density of the quantum dots that strongly limits the gain per unit length [ARS12, LIN16, HER16].
On the account of combining the fast gain recovery of Stranski-Krastanov grown quantum dots and the high gain of the well-established QW structures, a growth technique producing submonolayer quantum dots (SMLQDs) was developed [EGO94a, KRE99, KRE01, HAU21]. These are 0D localisation centres, but with slightly differing electrical and optical properties compared to Stranski-Krastanov grown quantum dots, due to the altered epitaxial growth process. Stacks of SMLQDs are produced by repeatedly depositing layers of a lower-band gap material (e.g. InAs) with a thickness below one mono-layer in between a higher bandgap material (e.g. GaAs). Due the lattice mismatch, quantum dots with a high area density form. These exhibit the advantageous properties of high gain and phase recovery as well as low degradation rates [ARS12, LIN16, HER15b, HAR16a, HER16, HAU21], while allowing for a high area density. Thus, they were successfully used as a gain medium in laser diodes [KRE01, XU04a, LED07] as well as in VECSELs [GER08a, DUD17] and in saturable absorber mirrors [ADD21].
However, recent experiments on coupling a gain chip composed of submonolayer quantum dots and a QW based saturable absorber have shown that instabilities can arise [ALF18]. In a simple approach, this was reasoned by the strong amplitude-phase coupling typical for SMLQD structures [HER16, ALF18].
In this section, an alternative approach is pursued to provide a first overview of the influence of submonolayers as the active medium and unravel improvements as well as potential instabilities. As the cavity geometry of the submonolayer VECSEL is very similar to the device discussed in section 3.2, the derivation of a suitable theoretical model is started at the DDE model for a V-shaped VECSEL with QWs in both active sections. Specifically, the V-shape DDE model is extended by dividing the gain dynamics into an equation for the

carrier dynamics in the 3D-bulk layer surrounding the active section and an equation for the occupation probability of the active submonolyer quantum dot states. To couple the adjusted carrier equations to the V-shape DDE model (see section 3.3), the phenomenological approach presented in [VIK06, VLA10] is followed. It is based on coupling the state occupation probability to the DDE system by finding an adequate gain factor that is multiplied by the population inversion. The description of the electric field and the field carrier interaction is adopted from the DDE system.
The chapter is structured as follows: In the first section 6.2 the V-shape DDE model is extended to model a laser device with an SMLQD gain medium and QW based saturable absorber as in [ALF18]. In the following section 6.3, the derived model is then used to perform a first comparison of how the coupling between the bulk layer and the active states can influence the dynamics. Especially the stability with regard to a strong amplitude-phase coupling, described by the α-factors, is investigated. The chapter closes with a summary and conclusive remarks 6.4.

6.2 Expanded Model

6.2.1 Phenomenological Derivation

In the previously discussed V-shape DDE model (3.48)-(3.51) (See section 3.3 for the full derivation), the charge-carrier dynamics in the active sections are solely described by means of the integrated carrier densities across the summed up quantum well stacks combined with a linear gain function. To incorporate more of the characteristics of a submonolayer based gain section, this model is adjusted here to be able to describe the mode-locked VECSEL experimentally realised in Reference [ALF18]. The device consists of a standard quantum well absorber chip and a gain chip with submonolayer quantum dots arranged in the standard disk laser geometry.
The SMLQD carrier dynamics are described by means of the phenomenological approach presented in References [HER16, LIN16]. In these works, the ultrafast microscopic carrier response of SMLQD devices to optical pulses was investigated and required a division of the SMLQDs into subgroups based on their confinement energy [HER16, LIN16]. However, the diffusive relaxation coupling among the subgroups, also responsible for a high damping [LIN16], acts on a time scale that is several magnitudes faster than the round-trip time of the VECSEL. Consequently, including the distinction of the subgroups and their coupling would lead to an immense increase of the computation time due to the long integration times required to adequately describe the VECSEL mode-locking states. This work focuses on the qualitative investigation of the mode-locking dynamics, therefore an average over the SMLQD subgroups is performed. The same approach was followed to successfully reproduce experimentally found locking effects in a SMLQD laser diode under optical feedback in Reference [HAU21]. It has to be mentioned that the effect of spectral hole burning is lost when averaging over all subgroups [HAU21]. However, the experimentally determined input-output curve behaved linearly not showing gain saturation effects to pump current values up to $J \approx 6J_{\mathrm{th}}$ [ALF18], which is the current range under investigation in this work. In consequence, a neglection of the gain saturation effects based on spectral hole burning can be justified. Nevertheless it has to be pointed out that for ultra-short pulses on the order of the scattering times spectral hole burning can become a very important effect.
As in the QW V-shape DDE model, the amplitude-phase coupling in the SMLQD device is modelled by constant α-factors. These also approximate the influence of the inactive

SMLQD states, which typically lead to a strong phase response [HER16, OWS20].
The submonolayer quantum dots states are not filled directly, but mainly via the scattering of electrons from the optically pumped 3D-bulk surrounding the SMLQDs [LIN16]. Thus, the gain dynamics are modelled by the mean occupation probability of the SMLQDs $\rho(t)$ and the charge-carrier densities $n(t)$ in the bulk reservoir. To adequately reproduce the amplification provided by the SMLQDs, the population inversion of the subgroups is multiplied by a gain factor g_g that can be approximated from the small signal response[1] of the gain chip [ALF18, LIN15b]. Following the approach presented in Reference [VIK06, VLA10] the dimensionless integrated carrier density $G(t)$ in the DDE model is therefore calculated from

$$G(t) = g_0 l_g \left[2\rho(t) - 1\right] = g_g \left[2\rho(t) - 1\right], \tag{6.2}$$

where g_0 is the small signal gain in m^{-1} and l_g is the length of the active section [VLA10]. The two quantities are summarised in the dimensionless small signal gain g_g. One could potentially calculate the gain parameter from microscopic calculations [MEI19].
Using the same equations for the occupation probability of the SMLQDs $\rho(t)$ and the charge-carrier densities $n(t)$ as introduced in [HAU21] and coupling them to the V-shape DDE model as done for the ring DDE model in [VIK06, VLA10] one obtains the following set of equations for the V-shaped VECSEL with SMLQD gain

$$\frac{d}{dt}E(t) = -\gamma E(t) + \gamma E(t-T)R(t-T), \tag{6.3}$$

$$\begin{aligned}\frac{d}{dt}\rho(t) = &-\gamma_\rho \rho(t) + R\left[\rho_{\mathrm{eq}}(t, n_g(t)) - \rho(t)\right] - \left[e^{G(t)} - 1\right] \\ &\times \left[\mid E(t) \mid^2 + \mid E(t-2\tau_2) \mid^2 e^{2Q(t-2\tau_2)+G(t-2\tau_2)}\right],\end{aligned} \tag{6.4}$$

$$\frac{d}{dt}n_g(t) = \frac{J_g}{h_{\mathrm{bulk}}} - \gamma_n n_g(t) - 2\frac{n_{\mathrm{SML}}}{h_{\mathrm{bulk}}} R\left[\rho_{\mathrm{eq}}(t, n_g(t)) - \rho(t)\right], \tag{6.5}$$

$$\frac{d}{dt}Q(t) = J_q - \gamma_q Q(t) - s\left[e^{2Q(t)} - 1\right] e^{G(t)} \mid E(t) \mid^2, \tag{6.6}$$

$$R(t-T) = \sqrt{\kappa} e^{\frac{1-i\alpha_g}{2}[G(t-2\tau_1)+G(t-T)]+(1-i\alpha_q)Q(t-T)}. \tag{6.7}$$

Here, the electric field and absorber equation are exactly the same as in the QW V-shape model (3.48)-(3.51). Importantly, γ_n and γ_ρ describe the carrier relaxation rates of the 3D-bulk and the SMLQD states respectively, which can differ strongly. Other new parameters are the SMLQD area density n_{SML} and the effective bulk reservoir thickness h_{bulk}. If a dimensionless formulation is required, $n_g(t)$ can be normalised to the thickness of the bulk section and the areal density of the SMLQDs according to $n_g(t) = n^*(t)h_{\mathrm{bulk}}/n_{\mathrm{SML}}$. The other parameters are defined as before, but the pump current is defined as a pump current density. An overview of the symbols and the used parameter values is given in Table 6.1.

[1] The amplification of the electric field during one round-trip T when passing the gain once can be approximated by

$$E(t) = rE(t-T) = e^{\ln(r)}E(t-T) \approx e^{G(t)}E(t-T) = e^{(2\rho(t)-1)g_g}E(t-T), \tag{6.1}$$

where r is the small signal reflectivity of the gain chip. A mean occupation probability of $\rho \approx 0.7 - 0.8$ is assumed, which corresponds to an intermediate pumping level well above the threshold. The same expression can be found from the electric field equation of the DDE model (3.48) in the situation of an unlimited bandwidth $\gamma \to \infty$ and therefore can be understood as the amplification of the maximum gain mode. Thus, the gain factor is approximated by $g_g = \ln(r)/(2\rho - 1)$.

Another differing parameter is the normalisation factor s that is mainly determined by the ratio of the differential gain and absorption coefficients in the QW model. As the gain equation is not modelled by an integrated carrier density here, the factor s has a different definition[2], but is of the same order of magnitude. The relaxation rates are chosen according to the fit performed in [HAU21].
The coupling between the 3D-bulk and the SMLQD states is mediated by the SMLQD quasi-equilibrium occupation probability $\rho_{\mathrm{eq}}(t,n)$ and the scattering rate R. The latter is dependent on the pump current according to

$$R = R_0 \left(\frac{J_g}{J_{\mathrm{tr}}}\right)^2, \tag{6.9}$$

where R_0 is the scattering rate at transparency and J_{tr} is the transparency pump current density (i.e. the pump current value at which the reflectivity of the chip is unity). The quadratic influence of J on the coupling rate is motivated by the quadratic relationship between charge-carrier scattering rates (from the 3D-bulk reservoir into the 0D SMLQD states) and the carrier density [WIL12b, LIN16, HAU21].
The SMLQD quasi-equilibrium occupation probability $\rho_{\mathrm{eq}}(t,n)$ is modelled by a Fermi-function of which the quasi-equilibrium Fermi level E_{F}, depends on the charge-carrier density $n(t)$. The Fermi-function reads

$$\rho_{\mathrm{eq}}(t,n_g) = \left[\exp\left(\frac{\bar{\varepsilon}_{\mathrm{SML}} - E_{\mathrm{F}}(t,n_g)}{k_{\mathrm{B}}T_L}\right) + 1\right]^{-1}, \tag{6.10}$$

where $\bar{\varepsilon}_{\mathrm{SML}}$ is the mean SMLQD confinement energy with respect to the bulk reservoir band edge, m^* is the effective mass, T_L is the lattice temperature. Importantly E_{F} is determined via the Pade approximation given in [COL95]:

$$E_{\mathrm{F}}(t,n_g) = k_{\mathrm{B}}T_L\{\ln[\tilde{n}_g(t)] + A_1\tilde{n}_g(t) + [K_1\ln[1+K_2\tilde{n}_g(t)] - K_1K_2\tilde{n}_g(t)]\}, \tag{6.11}$$

with $\tilde{n}_g(t) = n_g(t)/n_{\mathrm{C}}$ and the effective density of states n_{C} is given by

$$n_{\mathrm{C}} = 2\left(\frac{m^* k_{\mathrm{B}}T_L}{2\pi\hbar^2}\right)^{3/2}. \tag{6.12}$$

The coefficients to approximate the 3D Fermi integral are $A_1 = 1/\sqrt{8}$, $A_2 = -4.95009 \times 10^{-3}$, $K_1 = 4.7$ and $K_2 = \sqrt{2|A_2|/K_1}$ and are taken from [COL95]. In the final system the electron scattering between the optically pumped bulk layer to the active states depends on the carrier density. The inclusion of this physical effect is important to describe the higher damping typical for submonolayer or Stranski Krastanov quantum dots [LIN13, ROE15a, LIN15b, LIN16, HAU21]. Here, the carrier exchange between the 3D-bulk and active states is mediated by the quasi-equilibrium occupation probability characteristic for submonolayer quantum dots [LIN16, HAU21].

[2]The conversion factor s for the SMLQD model can be written as

$$s = g_q\Gamma_q\Delta z_g n^{(\mathrm{QD})}, \tag{6.8}$$

where g_q is the differential gain of the absorber, Δz_g is the thickness of the gain section, Γ_q is the confinement factor in the absorber section and $n^{(\mathrm{QD})}$ is the area density of the quantum dots in the gain. The initial normalisation leading to the definition of s in the QW model is presented in section 3.2 starting at equations (3.42)-(3.43). A rigorous derivation of the V-shape model with an arbitrary gain function can be found in Reference [MEI21a] chapter 5.2.

Symbol	Value	Normalised	Meaning
T	0.625 ns	1	Cold cavity round-trip time
$\tau_{1,2}$	0.15625 ns	0.25	Length of the cavity arms
γ	$3200\,\mathrm{ns}^{-1}$	2000	Gain/filter Bandwidth
J_g	$240 \cdot 10^{11}\,\mathrm{ns}^{-1}\,\mathrm{cm}^{-2}$	$150\,\mathrm{cm}^{-2}$	Gain pump current density
J_q	$-16\,\mathrm{ns}^{-1}$	-10	Pump rate in the absorber
γ_ρ	$24\,\mathrm{ns}^{-1}$	15	Relaxation rate active SMLQD states
γ_N	$0.528\,\mathrm{ns}^{-1}$	0.33	Relaxation rate 3D-bulk
γ_q	$500\,\mathrm{ns}^{-1}$	312.5	Absorber Non-radiative relaxation rate
R_0	$240\,\mathrm{ns}^{-1}$	150	3D-SMLQD coupling rate at transparency
α_g	0	0	Gain line-width enhancement factor -gain
α_q	0	0	Absorber line-width enhancement factor
κ	0.98	0.98	Intensity losses at the output coupler
s	2	2	Normalisation factor
g_g	0.05	0.05	Gain factor
m^*	$0.07m_e$	$0.07m_e$	Effective mass
$\bar{\varepsilon}_{\mathrm{SML}}$	60 meV	60 meV	SMLQD confinement energy
T_L	300 K	300 K	Lattice Temperature
h_{bulk}	53.0 nm	53.0 nm	effective bulk reservoir thickness

Table 6.1.: Parameter values used for numerical calculations. The applied normalisation is with respect ot the cold-cavity round-trip time so that the time is dimensionless. Parameters chosen to adapt the experimental values in [HAU21, ALF18]. Here, m_e denotes the electron mass.

Discussion of the Model

The derived model offers the possibility to study the dynamics of different mode-locking states in a mode-locked VECSEL with a SMLQD-based gain chip. It further allows an investigation of the role of the coupling between the 3D-bulk reservoir and the active SMLQD states. However, several simplifications have to be kept in mind when interpreting the results in the following.

Firstly, one could model the charge-carrier dynamics of the absorber similar to the gain as already introduced for a monolithic quantum dot device in References [VIK06, VLA10]. However, the absorber relaxation rates are several magnitudes faster than in the gain, which is why the description of the absorber remains unchanged with regard to the well-established integrated charge-carrier description in the DDE model [VLA04, VLA05, VLA09, HAU19]. Nevertheless, describing the usage of a SMLQD absorber would make the transformation necessary [ADD21].

As before, the influence of the gain bandwidth is modelled by a Lorentzian filter, which limits the distinction between the luminescence features of Stranski-Krastanov (SK) quantum dots, SMLQDs and QWs. Electro-luminescence and photo-luminescence spectra of amplifying devices based on the two types of quantum dots were investigated in References [LIN16, ALF18, HER19], which unravelled strong differences due to the different density of states. Including the frequency dependence of the gain by taking into account the different recombination energies across the SMLQD subgroups would allow to model spectral hole burning, which can be a limiting factor for QW based VECSELs [ALF18]. Reintroducing the distinguished modelling of the subgroups would either require the dynamic description

of the polarisation or a more complex treatment of the susceptibility, if the polarisation is adiabatically eliminated. Furthermore, it would enable the investigation of varied scattering rates across the subgroups[3]. However, the Lorentzian filter approximation is still appealing as it allows to obtain a first overview of the dynamics at pulse widths in the ps range while maintaining reasonable computation times.
Furthermore, the averaging over the subgroups and neglection of the inactive states makes the introduction of an α-factor necessary to approximate the phase response of the system. When choosing parameter values for α_g and α_q, which are typically high in SMLQD devices, one has to keep mind that in the DDE model all modes experience the same α-factor. Therefore the influence of $\alpha_{g,q}$ can quickly be overestimated [HER16].
As previously discussed, all transverse effects are neglected here as the laser is assumed to operate in a flat, single Gaussian transverse mode. Taking into account the transverse dimension together with a microscopic approach would be necessary for a detailed investigation of spatial hole-burning effects [MCL20, MCL21]. Nevertheless, the further inclusion of microscopic effects would greatly increase the complexity and computational demands. Consequently, it would not allow for the investigation of the mode-locking dynamics in the intermediate or long cavity regime over several thousand round-trips.
Finally, it has to be pointed out that a similar approach to the one presented here could be pursued to find a model which takes into account the confinement and scattering of the charge carriers in QW based devices in more detail. Important differences are that in contrast to the case of SMLQDs, the spatial localisation of the electron/hole states is only in one dimension in QW structures. Therefore, one does not obtain discrete states and the band structure is continuous. Furthermore, one would have to model the characteristic details of the coupling between the 3D reservoir and the 2D quantum well states as suggested in References [ROS11a, ALF17].

6.3 Influence of the 3D-Bulk to SMLQD Coupling Rate

One of the most critical differences between the model derived in this chapter (6.3)-(6.7) and the previously discussed QW model (3.48)-(3.51) is the introduction of the scattering between the pumped 3D-bulk and the active states, mediated by the scattering rate R_0. If the scattering rate is very large ($R_0 > 1600\,\mathrm{ns}^{-1}$), the filling of the active states occurs almost instantly and hence it approximates the situation of directly pumped active states. In this case, the SMLQD model becomes very similar to the QW model, as the bulk states lose their influence, it is referred to as QW-like in rest of this section. In contrast, the scattering for the SMLQD case is approximated by a value of $R_0 = 240\,\mathrm{ns}^{-1}$. This value is based on the theoretical reproduction of feedback experiments based on a SMLQD laser diode in Reference [HAU21] and is in accordance with the values determined in other works on SMLQD devices [LIN16].
The strong influence of the coupling can firstly be understood when investigating the relaxation oscillations (ROs) in the turn on dynamics of a simple SMLQD laser diode using the model outlined in [HAU21]. Relaxation oscillations are defined as oscillations in the electric field amplitude and the carrier frequency, occurring during the relaxation of the system towards a stable fixed-point solution after experiencing a perturbation or in the turn on process of the laser [LIN15b]. Their damping Γ_{RO} and frequency ω_{RO} of the os-

[3] A detailed overview of how the subgroups can be included separately is given in chapter 2 of Reference [LIN15b] for SK quantum dots.

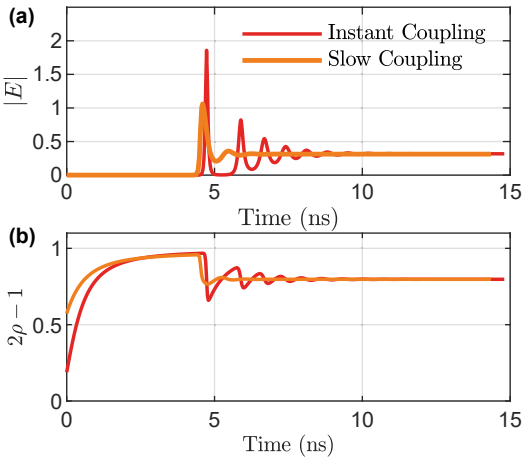

Figure 6.1: Relaxation oscillations of a SMLQD-based edge emitting laser diode as presented in [HAU21]. (a) Electric field dynamics (b) Dynamics of the population inversion, calculated from the occupation probability of the SMLQD states $\rho(t)$. The red line corresponds to an instantaneous coupling between 3D-bulk and SMLQD states and the orange line to a slow (SMLQD typical) coupling. The parameters and model are the same as in Reference [HAU21] and $J = 400\,\mathrm{ns}^{-1}$.

cillations are determined by the characteristic time-scales of the laser systems. External injection of the laser device can lead to strong alterations of the relaxation osciallations [KEL12a]. Furthermore, when the laser is subject to optical feedback, especially the oscillation frequency becomes of high relevance. If the ω_{RO} lies close to the feedback frequency, limit cycle solutions oscillating at approximately the RO frequency can become undamped and destabilise the CW fixed-point solution, ultimately leading to a chaotic output [MOR92, HEL90b, RIT93a, TYK16, KEL17b, HAU21].
The influence of the scattering rate R_0 on the ROs of a SMLQD diode is indicated in Fig. 6.1, where the orange line corresponds to $R_0 = 240\,\mathrm{ns}^{-1}$ and the red line to $R_0 = 1600\,\mathrm{ns}^{-1}$. The calculations are performed utilising the model and parameters introduced in Reference [HAU21]. Plotted in (a) is the dynamics of the electric field amplitude and in (b) the population inversion. One notices that the damping is strongly increased for lower scattering times with respect to an almost intermediate coupling between 3D-bulk and active states. The stronger damping is typical for quantum dot devices [LUE08, LUE11a][4]. In contrast, the frequency of the relaxation oscillation is lower for low scattering rates ($f_{\mathrm{RO}} \approx 0.7\,\mathrm{ns}^{-1}$) compared to the case of a direct coupling ($f_{\mathrm{RO}} \approx 0.9\,\mathrm{ns}^{-1}$). The lower damping at high scattering rates can be reasoned by the direct coupling between the 3D-bulk and active states, which leads to a direct transfer of perturbations from the SMLQD states to the reservoir [LIN15b]. In this case, one could adiabatically eliminate the reservoir dynamics and a single equation for the carriers would suffice to describe the dynamics [LIN15b]. For lower R_0, the scattering delays the transfer of perturbations from the active states to the reservoir, which leads to an increased damping. Hence, this simple example already indicates the strong influence of the scattering rate on the laser dynamics and the reaction to perturbations. A thorough investigation of the turn on dynamics of quantum dot lasers can be found in References [LUE11a, OTT13, LIN15b]. Here, the attention is now turned to the role of the coupling rate in the V-shaped VECSEL setup.
The dynamics in the fundamental mode-locking regime of a V-shaped VECSEL for different scattering rates R_0 is shown in Fig. 6.2. The plotted time-series are obtained by direct numerical integration of the V-shape SMLQD model (6.3)-(6.7) for different values of R_0,

[4] It has to be mentioned that the strong damping also relies on microscopic scattering effects and different relaxation rates of electrons and holes not included into the relatively simple model used here. For details on the modelling of quantum dots, see References [LUE11a, OTT13, LIN15b]. Furthermore, it has to be distinguished between Stranski-Krastanov QDs and SMLQD [LIN16, HER16, OWS20], which however both show a much higher damping than lasers based on bulk active sections.

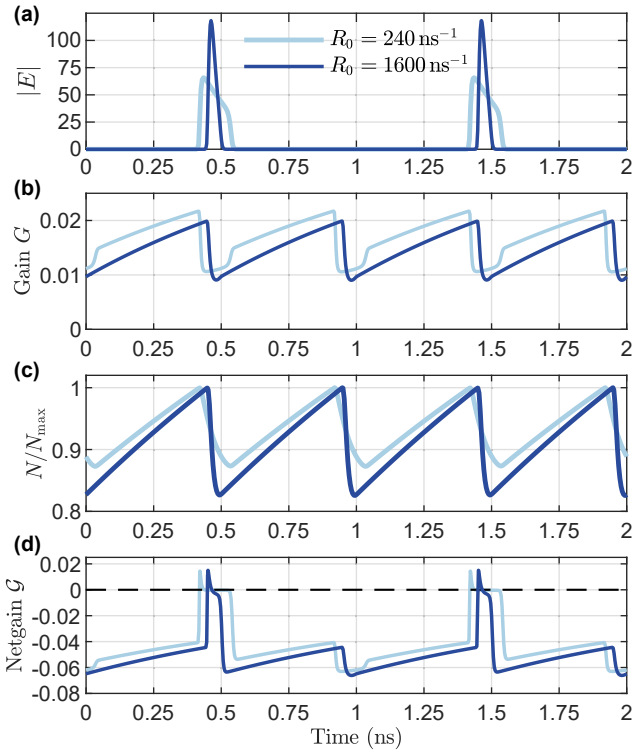

Figure 6.2: Dynamics in the regime of fundamental mode-locking found for the SMLQD-based V-shaped VECSEL by applying the model (6.3)-(6.7). (a) Dynamics of the electric field amplitude (b) Gain Dynamics (c) Dynamics of the charge-carrier density in the bulk (normalised to the maximum) and (d) Dynamics of the net-gain according to eq. (6.13). The different coloured lines correspond to the different scattering rates R_0 given in the legend (dark blue - fast coupling, light blue - slow coupling). The other laser parameters are given in Table 6.1 and $J_g = 110$.

depicted by the different colours. In the electric field dynamics in Fig. 6.2(a), one notices the strong influence of the scattering rate on the pulse width as well as on the pulse amplitude. In case of a slow scattering, the pulses are much wider than in case of a fast scattering. The reason for this lies in the recovery of the gain (population inversion of the active states), which is plotted in Fig. 6.2(b). If the carriers transition almost instantly from the 3D-bulk into the active states (dark blue), the gain directly enters a state of exponential recovery after a depletion. In contrast, the gain stays depleted for a longer period of time, if the scattering is slow (light blue). Following a short interval of a steep recovery, the dynamics transitions to the usual exponential relaxation. The altered course of the gain relaxation can be reasoned by the slow scattering and the fact that only the active states are depleted as the charge carriers in the reservoir do not interact with the electric field. Hence, the 3D reservoir is only depleted as the active states are refilled after the pass of a pulse. The slow scattering leads to delayed onset of the 3D-bulk depletion and therefore to a delayed onset of its exponential recovery (see Fig. 6.2(c)). The short phase of steep gain relaxation corresponds to the onset of the recovery of the 3D-bulk (end of the depletion).
A quantity that often is used to classify the mode-locking stability, is the so-called (intensity) net-gain [NEW74, HAU00, JAU17a]. It is defined by the summed up gain and losses at each point in time during one round-trip. In case of the DDE model, one obtains the following expression for the net-gain $\mathcal{G}(t)$ when taking into account the gain and loss terms resembling the field carrier interaction terms in the electric field equation

$$\mathcal{G}(t) = G(t - 2\tau_1) + G(t - T) + 2Q(t - T) + \ln(\kappa). \tag{6.13}$$

If the net-gain is positive, small perturbations can be amplified and therefore lead to a destabilisation of the system. In contrast, if the net-gain is negative, perturbations die out. As already visible from Fig. 6.2(d) a mode-locked pulse is accompanied by an open net-gain

window ($\mathcal{G} > 0$) [NEW74, HAU00]. It results from the saturation of the absorber, which leads to the gain being larger than the accumulated losses[5]. The course of the net-gain indicates that there is only enough gain to support one pulse in the cavity (for one net-gain window to open), characteristic for the FML regime.
For an almost instantaneous coupling (see Fig. 6.2(d) dark blue curve), the net-gain window only opens for a short time interval, and as it closes the net-gain value decreases substantially as the absorber recovers from the saturation. If the coupling between 3D-bulk and active states is slower compared to the instantaneous case (see Fig. 6.2(c,d) light blue curve), the net-gain window remains close to 0 after the initial gain-pulse interaction. This results from an interval of an almost constant gain after the initial depletion (see Fig. 6.2(b), light blue curve) combined with the bleaching of the absorber. Thus, the broader net-gain window leads to a broader pulse. However, one could understand the open net-gain window in a reversed way, i.e. to be resulting from a broad pulse that saturates the absorber for a longer period of time. In both cases, one can conclude that the pulse shape and form of the net-gain window behave in the energetically most favourable way with regard to the net amplification of the pulse, depending on the critical time-scales of gain and absorber. In case of the slow scattering rate, it is energetically favourable for the pulse to broaden to experience more gain, which leads to a decrease in amplitude compared to the fast scattering at the same pump level.

6.3.1 Comparison of Fast and Slow Coupling

In order to further investigate the role of the scattering between 3D-bulk and active states in a V-shaped VECSEL setup, a direct numerical integration of the model (6.3)-(6.7) for varied parameter values is applied, followed by an analysis of the resulting time-series. At first, the pump parameter is investigated, as it is the most easily tunable parameter in an experiment.
A 1D-bifurcation diagram for scattering rates of $R_0 = 240\,\mathrm{ns}^{-1}$ (light blue) and $R_0 = 1600\,\mathrm{ns}^{-1}$ (dark blue), is shown in Fig. 6.3(a). Plotted are all unique maxima of the electric field amplitude, detectable in 60 cavity round-trips. From an experimental point of view the bifurcation diagram can be understood to be similar to an input-output curve. As the system is highly multi-stable, fundamental mode-locking solutions (FML), stable at $J_g/J_{\mathrm{tr}} = 2.25$ for $R_0 = 240\,\mathrm{ns}^{-1}$ and $J_g/J_{\mathrm{tr}} = 3.25$ for $R_0 = 1600\,\mathrm{ns}^{-1}$ are used as the initial condition of the integration at each parameter point. Here, J_{tr} is the pump current at transparency, which can be approximated as the point at which the population inversion is reached, i.e. $\rho_{\mathrm{tr}} = 0.5$[6]. The stable solutions are determined at different pump powers in order to start the integrations at similar pulse amplitudes for both scattering rates.
The 1D-bifurcation diagrams depict that the maximum electric field amplitude[7] relatively increases much faster for the faster relaxation rate at lower pump currents ($J_g/J_{\mathrm{tr}} < 4$. This

[5] Here, one has to note that the charge-carrier equations are shifted in time as introduced at the end of section 3.3. In an experiment, the gain and absorber chip are well separated, but the mechanism of an open net-gain window resulting from the saturation of the absorber can still be applied.

[6] For $R_0 = 240\,\mathrm{ns}^{-1}$, a transparency pump current of $J_{\mathrm{tr}} = 79.2 \cdot 10^{11}\,\mathrm{ns}^{-1}\,\mathrm{cm}^{-2}$ is found and for $R_0 = 1600\,\mathrm{ns}^{-1}$ a transparency pump current of $J_{\mathrm{tr}} = 76.8 \cdot 10^{11}\,\mathrm{ns}^{-1}\,\mathrm{cm}^{-2}$.

[7] Please note that a normalisation with respect to the maximum pulse amplitude E_{sat} at the saturation for $R_0 = 1600\,\mathrm{ns}^{-1}$ is performed here to obtain a better comparability of the increase. However, the pulse amplitude saturates to an almost identical value for $R_0 = 240\,\mathrm{ns}^{-1}$. A discussion of the absolute pulse energy is presented in the next subsection.

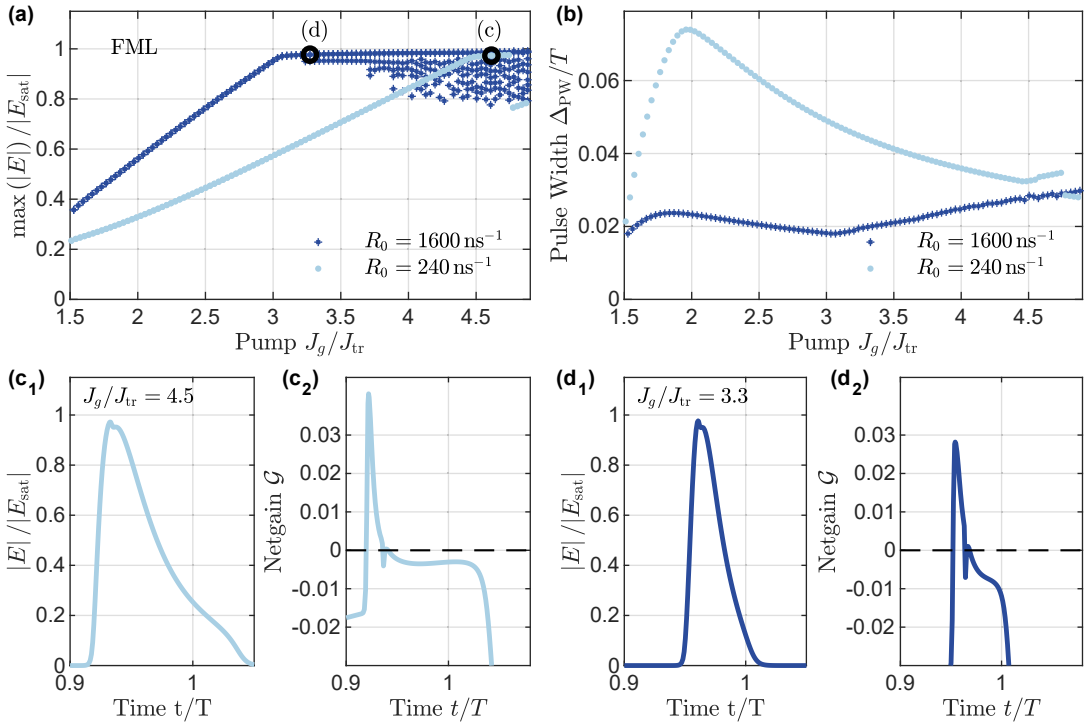

Figure 6.3.: (a) 1D-bifurcation diagrams obtained by direct numerical integration showing the behaviour of the unique maxima of the electric field amplitude (in 60 round-trips) with respect to the pump J_g. The amplitudes are normalised to the saturated global maximum amplitude found in the current interval E_{sat} for $R_0 = 240\,\mathrm{ns}^{-1}$, which is almost equal for both R_0. The different colours refer to different scattering rates as given by the legend. The bifurcation diagram is obtained by seeding a stable FML solution at every point in J_g. (b) Same bifurcation diagram, but with pulse width (FWHM) on the y-axis. (c_{1-2}) and (d_{1-2}) indicate a zoom of the pulses and the respective net-gain in the saturated FML regime for different R_0 at the parameter points marked by the black circles in (a). The laser parameters are given in Table 6.1.

is connected to the gain relaxation scenario and the broader pulse shape (longer open net-gain window) discussed before. Furthermore, it is evident that the FML solution destabilises at lower pump currents, if the relaxation rate is increased. The destabilisation is accompanied by a second local maximum occurring in the pulse shape, as indicated in Fig. 6.3(c_1). These local maxima begin to oscillate as the pump power is further increased, which leads to a high number of unique maxima in the diagram obtained for $R_0 = 1600\,\mathrm{ns}^{-1}$ (see Fig. 6.3(a), dark blue). In contrast, the system stabilises on a pulse-cluster with two pulses (PC_2), if the scattering rate is at $R_0 = 240\,\mathrm{ns}^{-1}$. However, it is important to say that the unstable FML solution is also found for the lower scattering rate and therefore the different bifurcation scenario results from the PC_2 attractor lying closer to the FML initial condition than the unstable FML solution.

At pump powers slightly below the destabilisation point of the FML solution, the maximum pulse amplitude saturates in both cases. This can be connected to the interplay of pulse width and the full saturation of the absorber. As depicted in Fig. 6.3(b) the pulse width rises until a critical point in J_g and then decreases to a local minimum. This local minimum in pulse width coincides with the onset of the saturation of the pulse maximum. For both R_0, the local minimum can be found at the point at which the absorber is completely saturated

and hence it is energetically favourable for the pulse to broaden than to grow in amplitude. The same behaviour of the pulse width exhibiting a local minimum at the point at which the absorber is fully saturated was found in an investigation of the QW DDE model in Reference [MEI21a] Chapter 5.3.2.
As the pulse amplitude increases slower with respect to the pump current for lower R_0, the absorber saturation point is reached at a higher point in pump power in comparison to the almost direct scattering. This can again be reasoned by the broader pulse shape, caused by the delayed depletion of the 3D reservoir as explained before (see Fig. 6.2(c)). The net-gain and the pulse amplitude in the vicinity of the pulse maximum at a pump value above the saturation (marked by black circles Fig. 6.3(a)) for both scattering rates are indicated in Fig. 6.3(c_1)-(d_1). The phase of quick gain recovery while the absorber is saturated causes a short second interval of positive net gain. The second open net-gain window leads to a second local maximum along the pulse as visualised in the close-ups of the pulses in Fig. 6.3(c_1)-(d_1). As discussed before, the effect is more pronounced if the scattering rate is lower and the reservoir experiences a delayed depletion. The second maximum causes the destabilisation of the FML solution, leading to a transition to the PC_2 solution in case of low R_0 and to oscillating side maxima in case of high R_0.
The saturation with respect to the pulse amplitude is more pronounced for the SMLQD model than found for the QW model as described in reference [MEI21a] and in section 4.2. This can firstly be reasoned by the different time-scales of gain and absorber used here and secondly by the fact that the scattering into the active states is reduced as it is mediated by the term (ρ_{eq}-ρ), which decreases as the occupation number grows ($\rho_{\text{eq}} \approx 1$ due to the strong pumping).

Unsaturated Absorption

On the account of obtaining a broader overview of the interplay of gain and absorption at different values of R_0, the dynamics are determined in the 2D parameter plane of the pump power and the unsaturated absorption (J_g, J_q). Due to the high multi-stability, different initial conditions of the direct numerical integration are chosen, to cleanly determine the different stability boundaries in the (J_g, J_q)-plane. Namely, the initial conditions are the stable fundamental mode-locking solution and the pulse-cluster solutions with two (PC_2) and three pulses in the cavity (PC_3). The electric field dynamics of the pulse-cluster solutions emerging for the SMLQD system qualitatively look exactly the same as for the QW system discussed in section 3.3. For each initial condition, the direct numerical integration is performed for a transient time of $1.5 \cdot 10^4$ round-trips at varied parameter points in the (J_g, J_q) plane and the stabilised state is evaluated from the following 60 round-trips. This leads to the 2D-bifurcation diagrams presented in Fig. 6.4. The upper row indicates the results for $R_0 = 1600\,\text{ns}^{-1}$ and the lower row for $R_0 = 240\,\text{ns}^{-1}$. The sub panels in each row correspond to the varied initial conditions (from left to right: FML, PC_2 and PC_3). An explanation of the colour code is given in the figure caption. It has to be noted that all colours are defined as in the other sections of this work, but the irregular regimes (orange shading) also comprise the irregular pulse structures shown in Fig. 6.3(c_1)-(d_1). These solutions are periodic at first but at higher pump powers the local maxima start to oscillate, leading to quasi-periodic solutions. This effect occurs similarly for the FML as well as for the PC_n solutions (all pulses show a similar irregular shape)
As discussed for the 1D scan before, the upper stability boundary of the FML solution shifts to lower pump powers if R_0 is enlarged as visible from the transition between the blue and

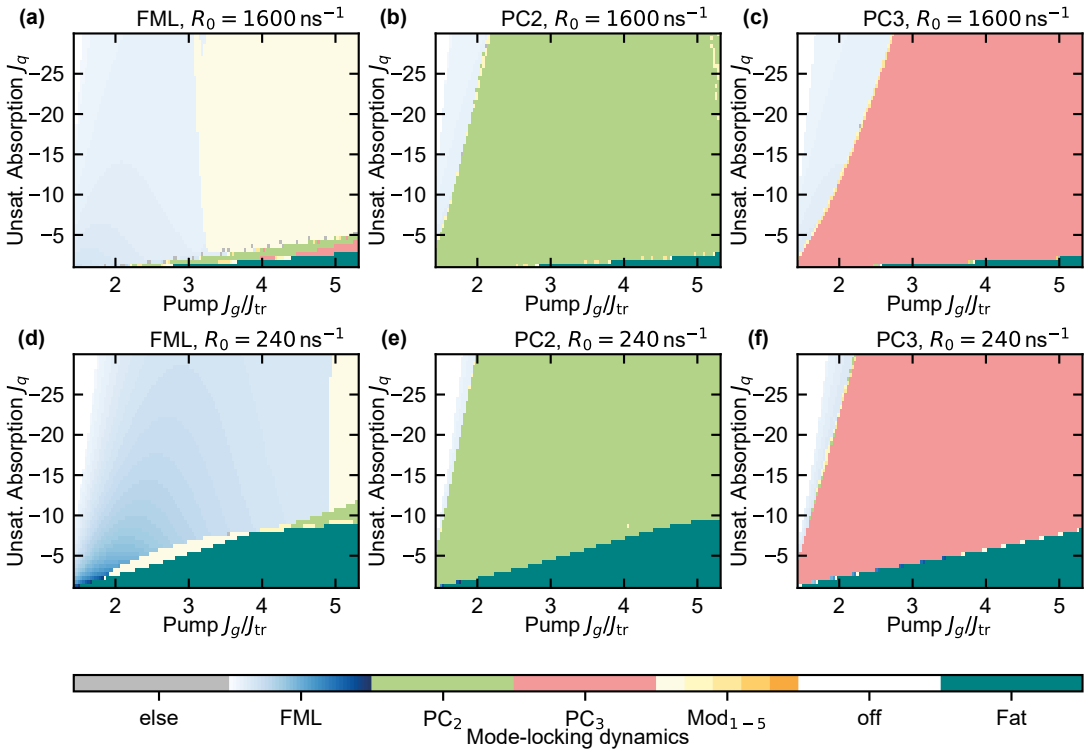

Figure 6.4.: 2D-bifurcation diagrams in the parameter plane of the pump power and the unsaturated absorption for the V-shaped laser with SMLQD-based gain. The upper panels (a)-(c) refers to the dynamics obtained using $R_0 = 1600\,\mathrm{ns}^{-1}$ and the lower panel (d)-(f) to $R_0 = 240\,\mathrm{ns}^{-1}$. The colour code distinguishes between fundamental mode-locking (FML; blue), pulse-cluster solutions (PC_n) and irregular pulse-cluster solutions with n pulses (Mod_n; orange shading). The white coloured region represents the laser *off*-state and the teal coloured region indicates pulses with a width of $PW > 0.2T$. The shading of the FML solution refers to the pulse width normalised to a pulse width of $PW = 0.2T$. At each parameter pair (J_g, J_q) a stable solution is utilised as the initial condition of the direct numerical integration (15000 round-trips). The utilised solutions are (a)-(d) FML and (b)-(e) PC_2 and (c)-(f) PC_3 and are indicated in the headline of each panel. The initial conditions are found as the stable solutions after $3 \cdot 10^4$ transient round-trips at the parameter pairs: FML (J_g/J_{tr}, J_q) = (2.24, −10) and (3.23, −10), PC_2 (2.85, −10) and (4.04, −10), PC_3 (3.47, −10) and (4.44, −10). The laser parameters are given in Table 6.1.

light orange regions in Fig. 6.4(a)-(c). The destabilisation (emergence of irregular pulses as shown in Fig. 6.3(c_1)-(d_1)) is connected to the full saturation of the absorber and the resulting formation of an unstable pulse structure. An increase of the absolute value of the unsaturated absorption leads to a shift of the upper stability boundary to lower pump currents. This is connected to the narrowing effect of the absorber that leads to a lower pulse energy, but an increased pulse maximum, which is illustrated in the 1D scans in Fig. 6.5. Plotted from left to right are the pulse width, the pulse maxima and pulse energy for differing values of J_q in the FML regime. The upper row depicts the results for $R_0 = 1600\,\mathrm{ns}^{-1}$ and the lower row for $R_0 = 240\,\mathrm{ns}^{-1}$. For both scattering rates, it is evident that the pulse amplitude necessary to saturate the absorber is reached at lower pump powers, if the unsaturated absorption is increased and therefore the destabilisation point is shifted accordingly. The shift of the upper stability boundary with varied J_q is less pronounced for the lower scattering rate presented in (d), because the pulses initially have a much lower maximum

(c.f. Fig. 6.5(b)-(e)). Therefore, the absorber is much further away from a full saturation and a shift of the absorption level has a less severe influence.
In comparison to the course of the bifurcation boundaries found from the QW DDE system (see Fig. 4.5), the behaviour of the upper bifurcation boundary is reversed[8], due to the additional irregular pulse structures resulting from the coupling between 3D-bulk and reservoir. In case of the QW model, the dominant effect leading to the shift of the upper bifurcation boundary is the increase of the losses, which prevents the net-gain window to open far enough for the emergence of quasi-periodic irregular solutions. Hence, an increased $|J_q|$ allows the regular FML and PC_n solutions to be stable at higher pump powers. It has to be pointed out that in the investigation of the QW model in section 3.3 a much higher absolute value of the unsaturated absorption ($J_q = -65$) and much lower value of the gain bandwidth ($\gamma = 150$) is used and therefore a full saturation of the absorber does not occur. However, in chapter 5.3 of Reference [MEI21a] it was shown that the respective adjustment of both quantities does not change the qualitative behavior of the bifurcation lines in the DDE QW model.
For the lower stability boundaries of the FML, PC_2 and PC_3 solutions one obtains the same behavior as found for the QW system (see Fig. 4.5): The bifurcation points shift approximately linearly to higher pump currents for an elevated $|J_q|$. This qualitative trend can be reasoned by the higher amount of gain necessary for the pulse patterns to stabilise, if the absorption is increased. In the picture of the net-gain, a higher amount of gain is required for an additional net-gain window to open as a stronger absorber depletion is required.
Comparing the upper and lower sub panels of Fig. 6.4, it becomes evident that the shift of the lower bifurcation boundary is less pronounced for lower scattering rates $R_0 = 240\,\mathrm{ns}^{-1}$. The reason for this may lie in the steeper increase of the pulse energy with pump power at lower scattering rates (see Fig. 6.5(c) and (f)). It hints at lower total losses experienced by the broader pulse, although the absorption is higher compared to the narrow pulses at $R_0 = 1600\,\mathrm{ns}^{-1}$. In consequence, the lower filtering losses for broader pulses and the affected nonlinear pulse shaping mechanism probably counteract the shift of the bifurcation line (in J_g) with increasing unsaturated absorption compared to narrow pulses ($R_0 = 240\,\mathrm{ns}^{-1}$).
Another difference in the 2D-bifurcation diagrams for different R_0 in Fig. 6.4, is the emergence of a regime of fat pulses. As the pulses are broader for lower scattering rates, the absorber has to deliver a stronger attenuation for the pulses in one cluster to remain well separated. Thus, the regime of fat pulses (teal region in Fig. 4.5) emerges at higher absolute values of the unsaturated absorption values for $R_0 = 240\,\mathrm{ns}^{-1}$.

Cavity Round-Trip Time

The same technique of direct numerical integration starting from different initial conditions is used to obtain 2D-bifurcation diagrams in the parameter plane of the pump power and the cold-cavity round-trip time (J_g, T). The only difference is that, for both scattering rates the same initial conditions of narrow pulses is applied, due to the strong influence of the round-trip time on the relative pulse width. The results are shown in Fig. 6.6, with the upper panels (a)-(c) referring to an almost instant scattering rate of $R_0 = 1600\,\mathrm{ns}^{-1}$ and the lower panels (d)-(e) correspond to a scattering rate of $R_0 = 240\,\mathrm{ns}^{-1}$.
Although the multi-stability is more pronounced in comparison to the QW DDE model (see Fig. 4.10), the general course of the upper stability boundaries remains the same. As the

[8] In the QW DDE system, the boundary shifts to higher pump currents at higher absolute J_q, see Fig. 4.5.

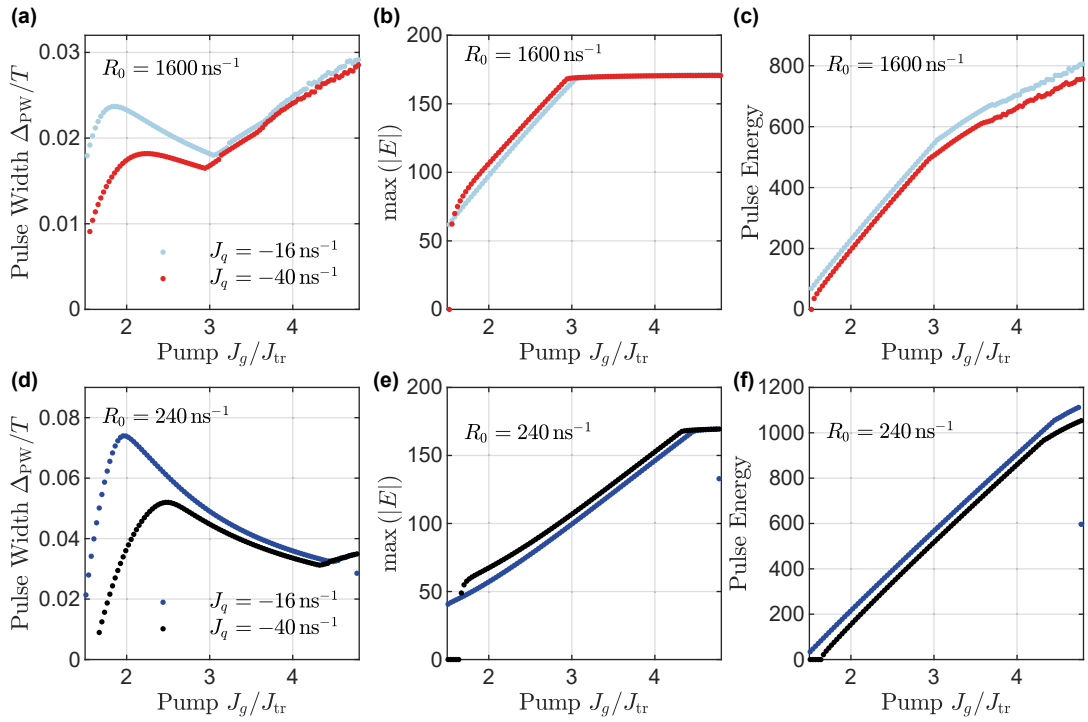

Figure 6.5.: 1D-bifurcation diagrams in pump power J_g obtained by direct numerical integration starting from the stable FML solution. Plotted from left to right are the pulse width, maximum pulse amplitude max($|E|$) and pulse energy (integration over the intensity). The quantities are evaluated as an average value from the pulses within 60 round-trips. The different line-styles represent the results for different J_q as given in the legend. The different colours refer to different scattering rates as given in the subpanels. The other laser parameters are given in Table 6.1.

round-trip time is increased, especially the upper stability boundaries of all solutions shift to lower pump powers. As discussed in detail in section 4.2.2, the higher round-trip time leads to a longer period of gain-recovery between pulse passes. Hence, the amplification is increased, leading to an earlier destabilisation due to the additional opening net-gain windows resulting from the excess gain.
In comparison to high scattering rates, the destabilisation of the regular solutions is shifted to higher pump powers for lower R_0 (lower panel in Fig. 6.6), because the pulse maxima grow slower as the pump current is increased (see Fig. 6.3). Therefore, the point at which the absorber is fully saturated, which defines the onset of the destabilisation, is reached at higher J_g as discussed before. Consequently, a larger stable region for the FML and the PC_n solutions can be found for the lower scattering rates in the investigated parameter regime in the (J_g, T) plane. Apart from this, the different scattering rates to not lead to qualitative differences in the 2D-bifurcation diagrams.

6.3.2 Influence of the Amplitude-Phase Coupling

Utilising submonolayer quantum dot (SMLQD) based gain chips in experiments can lead to occurrence of mode-locking instabilities as presented in Reference [ALF18]. In this reference, instabilities were determined by means of measuring the autocorrelation traces at different pump powers as well as optical and micro-wave spectra. In the measurements of

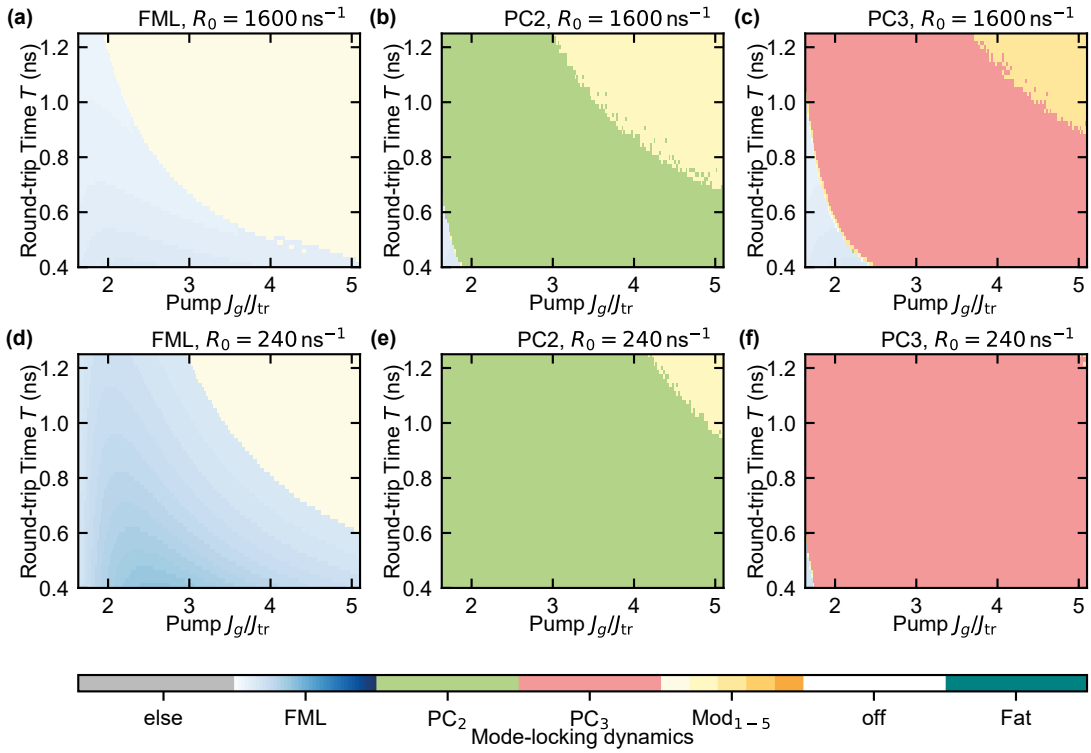

Figure 6.6.: 2D-bifurcation diagrams in the parameter plane of the pump power and the cold-cavity round-trip time (J_g, T). The upper panels (a)-(c) refers to the dynamics obtained using $R_0 = 1600\,\mathrm{ns}^{-1}$ and the lower panels (d)-(f) to $R_0 = 240\,\mathrm{ns}^{-1}$. The colour code and the numerical integration using stable initial conditions is the same as in Fig. 6.4. However for both R_0 the stable FML solution found for $R_0 = 240\,\mathrm{ns}^{-1}$ is used. The scattering rates are indicated as a headline of each panel. The laser parameters are given in Table 6.1.

the autocorrelation, the instabilities manifested as pulse shapes with irregular asymmetric modulations, which in combination with the micro-wave spectra hinted at quasi-periodic dynamics. The quasi-periodic behaviour and the irregular autocorrelation traces at higher pump powers were reasoned by the large amplitude-phase coupling, described by the factors α_g and α_q in the SMLQD model, typical for this type of gain media [HER16].
To investigate the role of the amplitude-phase coupling in the derived SMLQD model, compared to the case of instant coupling typically used to model QW devices, the stabilisation of the previously discussed dynamics are determined in two different 2D parameter spaces. Firstly, only the amplitude-phase coupling of the gain and its effect on the stability boundary with respect to the pump J_g is explored. On that account, again a direct numerical integration from the FML, PC_2 and PC_3 initial conditions is applied. The resulting 2D numerical bifurcation diagrams are presented in Fig. 6.7, with the upper panels (a)-(c) referring to an almost instant scattering and the lower panels to scattering rates typical for SMLQDs.
When comparing the stability boundaries of all three stable solutions for different R_0, it becomes evident that at fast scattering rates the system is much more robust against the destabilising influence of the amplitude-phase coupling in the gain. In contrast, the stable solutions all destabilise at much lower $\alpha_g \approx 1$ for $R_0 = 240\,\mathrm{ns}^{-1}$.
The reason for that can be found by taking a closer look at how the amplitude-phase coupling is included in the electric field equation (6.3). As the influence of the amplitude-phase

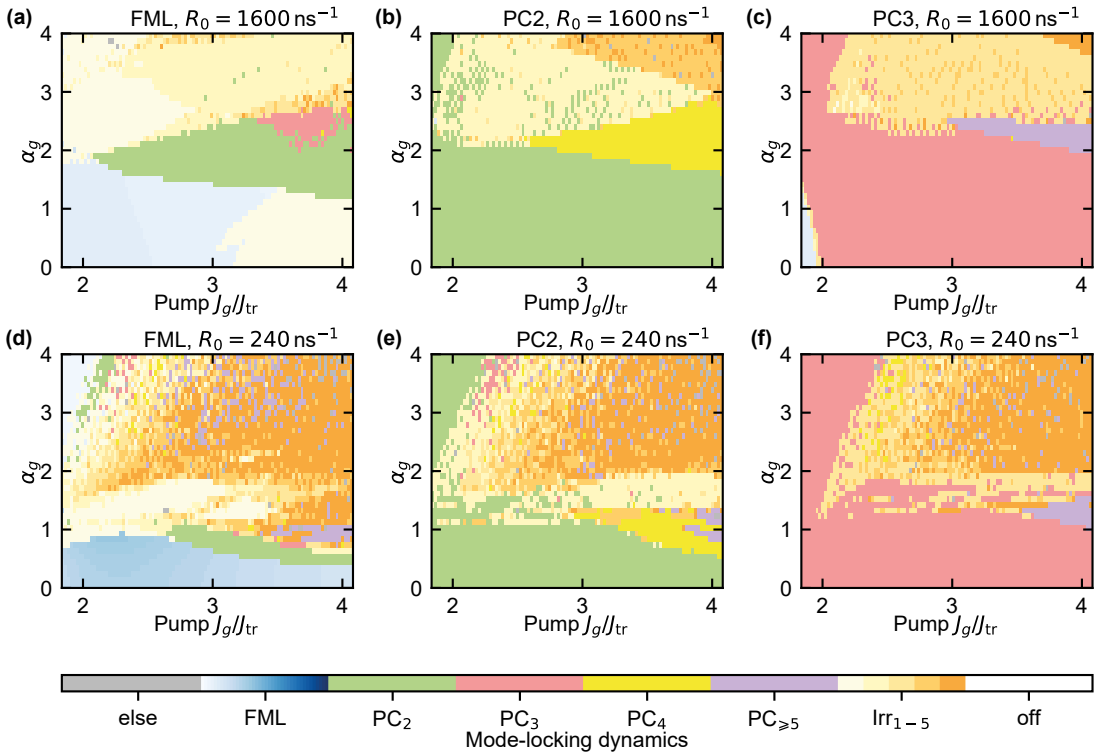

Figure 6.7.: 2D-bifurcation diagrams in the parameter plane of the pump power and amplitude-phase coupling of the gain (J_g, α_g) for the V-shaped SMLQD laser. The upper panels (a)-(c) refers to the dynamics obtained using $R_0 = 1600\,\mathrm{ns}^{-1}$ and the lower panels (d)-(f) to $R_0 = 240\,\mathrm{ns}^{-1}$. The colour code and the numerical integration using stable initial conditions the same as in Fig. 6.1, with additional higher-order pulse-cluster solutions. Which solution is used as an initial condition is indicated as a headline of each panel. The laser parameters are given in Table 6.1.

coupling is described via the product of the gain (absorption) and α_g (α_q), a larger gain leads to a much stronger influence of the amplitude-phase coupling (i.e. a higher carrier density leads to a more pronounced shift of the refractive index [HEN83]). If the contributions of gain $G(t)$ and absorption $Q(t)$ are approximately equal and $\alpha_g = \alpha_q$, the different α-factors can cancel out each other and the mode-locking solution (and especially CW solution) may stay stable [VLA04, VLA05]. However, for the 2D-bifurcation diagrams presented in Fig. 6.7, $\alpha_q = 0$ is chosen, because typically the condition $\alpha_q < \alpha_g$ is fullfilled for the combination of a SMLQD-based gain medium and a QW-based absorber [WAL16, ALF18]. Consequently, the absorber has no influence on the phase and is sufficient to interpret the more severe influence of α_g at lower R_0 by just investigating the gain dynamics. As already visible from the exemplary time-trace in Fig. 6.2, the gain is higher in the vicinity of the pulse for a longer period of time, if R_0 is small due to the altered gain relaxation. Thus, the product $i\alpha_g G(t)$ in the exponential is larger compared to the case of almost instant scattering. More importantly, the phase of a fast gain relaxation resulting from the slow scattering leads to a strong variation of the impact of the $i\alpha_g G(t)$ factor. Thirdly, a broader pulse leads to a longer interaction time of charge carriers and electric field in the gain. Therefore, already a smaller α_g leads to a severe influence on the phase and to destabilising effects as visible in Fig. 6.7. The different instabilities comprise irregular pulse shapes as well as quasi-periodic dynamics (orange shading). The destabilising mechanism is the same across all investigated

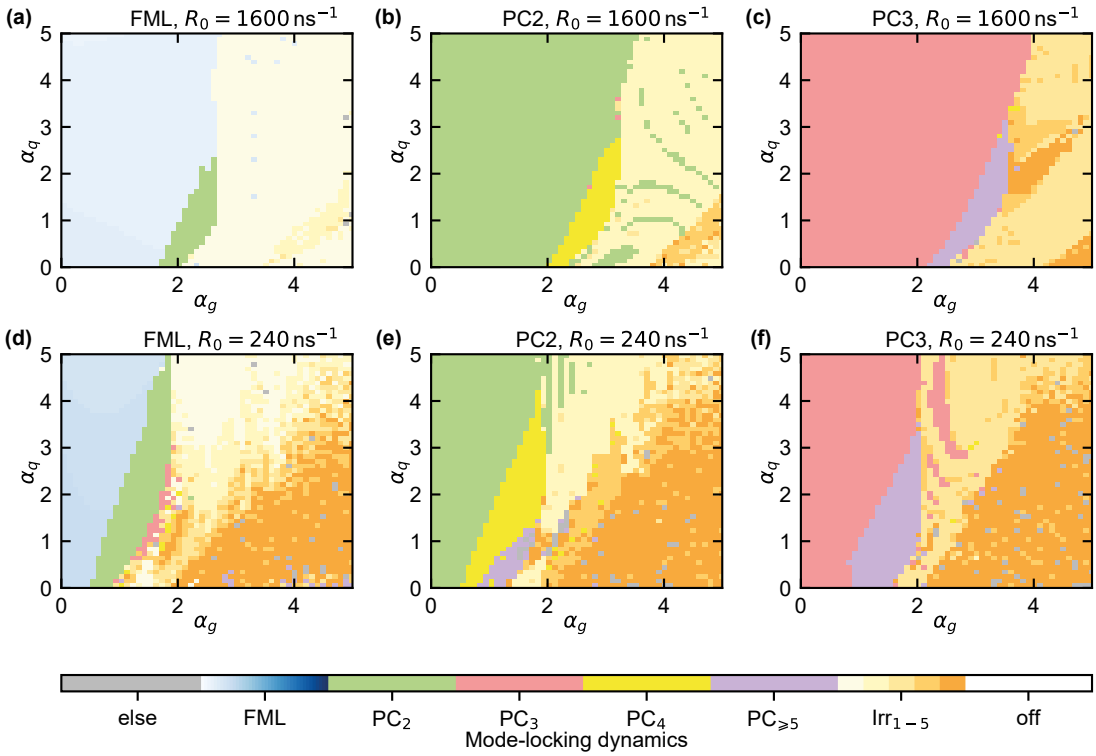

Figure 6.8.: 2D-bifurcation diagrams in the parameter plane of the α-factor in the gain and absorber section respectively (α_g, α_q). The upper panels (a)-(c) refers to the dynamics obtained using $R_0 = 1600\,\mathrm{ns}^{-1}$ and the lower panels (d)-(f) to $R_0 = 240\,\mathrm{ns}^{-1}$. The colour code and the numerical integration using stable initial conditions the same as in Fig. 6.1, with additional higher-order pulse-cluster solutions. Which solution is used as an initial condition is indicated as a headline of each panel. The laser parameters are given in Table 6.1.

solutions as discussed before. As more pulses are inside the cavity, a higher value of α_g is required to destabilise the solutions. If n pulses are present in the cavity, the amplitude is decreased in comparison to the $n-1$ pulses case at constant pump powers. Hence, the influence of the interaction term $Ee^{i\alpha_g}G$ is less severe, due to the lower pulse amplitude and the lower average gain level caused by the additional depletion.
When investigating the interplay of the amplitude-phase coupling induced by both active sections one finds a similar influence of the scattering rates as shown in Fig. 6.8. Plotted are 2D-bifurcation diagrams in the parameter plane of the α-factor in the gain and absorber section respectively (α_g, α_q). The upper panels again are obtained using $R_0 = 1600\,\mathrm{ns}^{-1}$ and for the lower panels $R_0 = 240\,\mathrm{ns}^{-1}$ is chosen. It has to be noted the pump current is left fixed at approximately the central value of J_g between the upper and lower stability value for the respective solution. From all panels it is possible to deduce that the inclusion of a non-zero α_q shifts the onset of the destabilisation to higher values of α_g.
An explanation for this can again be found by investigating the contributions in the exponential term in the gain equation (6.3). As outlined before, the influence on the phase induced by α_g and α_q roughly cancels out, if $\alpha_g G(t) = \alpha_q Q(t)$ [VLA05]. Thus, stable mode-locking can be maintained if both α-factors are increased simultaneously, if the gain and absorber integrated carrier densities are of a similar magnitude and their dynamics are similar.
However α_q has a much less destabilising effect on the dynamics compared to α_g. This can

be reasoned by the fact that in the investigated regime the absorber recovers completely on a much faster time-scale than the gain. Secondly, each pulse only interacts with the absorber once per round-trip. In contrast, the gain dynamics (especially for $R_0 = 240\,\mathrm{ns}^{-1}$) exhibits a more complex behaviour and therefore α_g destabilises the system more strongly.
When comparing the upper and lower panels of Fig. 6.8, it becomes evident that the system destabilises at lower values of α_g, if R_0 is increased. Once more, the reason lies in the elevated gain for lower R_0, which causes a stronger influence of the factor $\alpha_g G(t)$ in the exponential. The probably most important difference again is the different gain relaxation for small R_0 (see Fig. 6.2(b)). As the gain relaxes in two stages, the influence of α_g is much different than that of α_q which relaxes exponentially. In consequence, α_q does not compensate the induced irregular phase rotation of α_g as well as for large R_0. Furthermore, the pulses are much broader for low R_0 and therefore experience a longer interaction with the gain, i.e. are more strongly influenced by α_g.
In conclusion, it is to say that the qualitative influence of the amplitude-phase coupling does not change, if the scattering rate between the 3D-bulk and the active states is varied. However, at lower scattering rates the mode-locking solutions are destabilised at already very low values of α_g due to the elevated gain and the broader pulse shape. Therefore, the amplitude-phase coupling in the absorber does not have a strong stabilising influence, if the scattering rate is low. However, it has to be pointed out that due to the multi-mode characteristic of the model and the neglection of other phase effects such as dispersion, the α-factor might be strongly overestimated. A possibility to verify the results presented here would be to perform similar calculations using a fully microscopic model or at least use this type of models to determine a realistic α-factor that already includes counter-acting effects [MCL20, MCL21].

6.4 Summary

In this chapter, an extension of the delay differential equation system (DDE) used to investigate a passively mode-locked VECSEL with V-shaped cavity geometry was discussed. Namely, the modelling of the charge-carrier dynamics in the gain was adjusted from the original quantum well based approach so that it is suitable to describe a gain chip based on submonolayer quantum dots (SMLQDs). This was done by combining the charge-carrier equations used to successfully describe the dynamics of submonolayer based amplifiers in References [LIN16, HAU21] and the DDE quantum dot model in [VIK06, VLA10]. The charge-carrier dynamics in the gain were characterised by means of an equation modelling the charge-carrier density in the 3D semiconductor bulk surrounding the SMLQDs and the occupation probability of the SMLQD states as well as their charge-carrier density dependent coupling. In turn, the electric field and absorber equations remained equal to the model derived in chapter 3.
In the following, the role of the scattering rate, mediating the coupling between 3D-bulk and SMLQD states was investigated in detail. The results demonstrated that a slow coupling rate leads to a broadening of the pulses, as only the SMLQD states interact with the electric field and therefore the depletion and refilling of the pumped 3D-bulk is delayed.
Performing 1D scans in the pump current for a SMLQD typical coupling and an instant coupling, used in the DDE model to describe quantum wells, it was found that the fundamental mode-locking solution remains stable for a larger pump power interval at lower scattering rates. However, the general bifurcation scenario stays the same as the FML so-

lution destabilises as a result of the complete saturation of the absorber and a reopening of the net-gain window in the vicinity of the pulse due to the scattering between SMLQD and 3D-bulk states.
On the basis of 2D parameter scans in different regimes, it was possible to deduce that a pronounced multi-stability of the FML as well as pulse-cluster solutions of different order exists regardless of the scattering rate between 3D-bulk and active states. In the parameter plane of the pump power and unsaturated absorption (J_g, J_q), it was observed that the larger stability interval with regard to the pump power, is maintained for the lower scattering rates, regardless of the unsaturated absorption. The same behaviour was found in the (J_g, T) parameter plane, with the upper bifurcation lines shifting in a qualitative similar way for both scattering rates.
When investigating the role of the amplitude-phase coupling, it was found that for the lower scattering rates, the α-factor of the gain has a much higher destabilising influence on the FML as well as the PC_2 and PC_3 solution. All three solutions destabilised at a much lower value of α_g in case of a lower scattering rate. It was reasoned by the higher value of the gain in the vicinity of the pulse in case of lower R_0, which lead to a stronger influence of α_g. The same reasoning was expedient to explain the results of the stability analysis in the α_g, α_q parameter plane. For both scattering rates, α_q counteracts the effect of α_g and therefore the stability boundary of the solutions shifts to higher α_g. However, this effect is much more pronounced for higher scattering rates.
At the end of the chapter it has to be noted that the introduced model is not necessarily tailored to describe submonolayer quantum dots. With an adjustment of the parameters it could also serve to investigate Stranski Krastanov quantum dots, due to abstract inclusion of the active states and the 3D-bulk. In future works, the model could be extended to describe the distinct influence of the quantum dot subgroups and their different scattering and therefore include the features of either devices in more detail. As submonolayer based saturable absorber chips are currently under investigation in experiments [ADD21], an extension of the charge-carrier equations of the absorber could be of interest to investigate the resulting dynamics. Once more, a comparison to microscopic models could be of interest to asses the limitations of the model in detail.

7 Conclusion and Outlook

This thesis was dedicated to the theoretical analysis of passively mode-locked semiconductor lasers with V-shaped external cavity geometries. These disk lasers have been realised in various experiments, on the strive of obtaining a pulsed output suitable for applications such as frequency comb generation, optical metrology, two photon microscopy, eye surgery or material processing. However, compared to the well-established solid-state lasers, the semiconductor counterparts still are subject to intense research in order to improve the pulse width and amplitude as well as to stabilise the timing jitter. On that account, a detailed physical understanding of the various contributing physical processes leading to different instabilities and influencing the characteristics of the pulsed output is of high relevance. Yet, it is impractical to perform an investigation of the long term dynamics at a wide range of system parameters (e.g. cavity length or pump power) utilising fully microscopic laser models, due to the limitations of modern computational hardware. Therefore, it is necessary to perform purposeful simplifications, which have to be chosen according to the detailed device setup and the operation regime of interest, to arrive at a physically and computationally reasonable laser model. This work focused on introducing several mathematical models for passively mode-locked V-shaped VECSELs on a semiconductor basis that are then used to examine different forms of dynamical regimes and physical effects.

Motivated by the successful application of the ring delay differential equation model of mode-locking, which enabled an investigation of various operation regimes of monolithic- and external-cavity mode-locked devices, a delay differential equation (DDE) system for the V-shaped VECSEL was derived in Chapter 3. It is based on first principles and importantly includes the effect of the backwards travelling field inside the cavity.

Based on this DDE model, the experimentally observed emergence of pulse-cluster solutions was theoretically examined. The cluster states are characterised as a periodic repetition of temporally non-equidistant pulses packages. At first, their appearance was discussed in the regime of high performance mode-locking, i.e. at intermediate-cavity lengths. The formation of the pulse-cluster states was traced back to the characteristics of the V-shaped cavity: Each pulse passes the gain twice per round-trip in the V-shaped cavity and therefore leads to two depletions of the gain. In order to maintain the energetically favourable situation of twice as many equidistant gain depletions as pulses in the cavity during one round-trip time T, the n pulses form clusters with a temporal pulse distance of $\Delta = T/2n$, instead of harmonic mode-locking solutions (in a symmetric cavity arrangement).
Using direct numerical integration, the influence of different parameters on the stability boundaries of the pulse-cluster solutions was revealed. It was shown that enlarging the cavity length can lead to a stabilisation of higher order pulse-clusters and furthermore, the pulse-cluster solutions are supported at lower pump powers due to the increased gain relax-

ation time in between pulses and the decreased relative pulse width. Consequently, a very similar bifurcation scenario was found when investigating the impact of the gain relaxation rate. By means of path-continuation techniques, it was possible to show that the pulse-cluster solutions are all born along the fundamental mode-locking solution branch. The mechanism leading to their emergence at critical pump powers are cusps of saddle-node bifurcations. Changing the cavity geometry, i.e. the relative length of the cavity arms, revealed that a slight asymmetry can cause an extension of the stable fundamental mode-locking as well as pulse-cluster solutions to higher pump powers.
Motivated by recent experiments on localised states in mode-locked external cavity lasers, the V-shaped setup was investigated in the long-cavity regime. At cavity lengths at which the gain relaxation time is much lower than the cold cavity round-trip time, so-called localised pulsed states (dissipative solitons) can be observed. Their characteristic features are a multi-stability with the laser *off* state (below the lasing threshold) and a vanishing interaction of the pulses via the exponential tails of the gain relaxation.
In the localised state regime, it was found that the branch structure of the harmonic mode-locking and pulse-cluster solutions appear to be very similar to previously investigated case of linear cavity configurations. However, an analysis of the stabilising dynamics in the parameter plane of the (sub-threshold) pump power and the cavity asymmetry revealed that the harmonic mode-locking solutions do not stabilise at certain characteristic cavity configurations. At these configurations, the pulses in the equidistant harmonic mode-locking pulse train collide in the gain due to the second pass in the V-shaped cavity, which is energetically not favourable in terms of the maximum pulse amplification. These findings were supported by a bifurcation analysis, unravelling a discontinuity of the stabilising torus bifurcations in pump power at the critical cavity configurations. Vice versa a local minimum in pump power of the bifurcation lines (lower stability boundary) stabilising the FML and HML_n solutions could be found in the situation of the maximum distance between the gain depletions, i.e. maximum obtainable amplification.
In the long-cavity regime PC solutions stabilise as localised structures. It further became evident, that an alteration of the cavity arms causes a variation of the temporal distance of the pulses within one cluster so that the optimum pulse amplification is maintained. Deriving a nonlocal Haus master equation for the V-shaped system, it was possible to find an analytic expression for the temporal distance of the pulses. The analytic expression only depended on the cavity asymmetry, the gain relaxation rate and the cold cavity round-trip time and showed an excellent agreement with the numerical path-continuation results.
Interestingly, a Floquet analysis of the PC solutions unravelled that these are locally independent in the long-cavity regime. Nevertheless, due to the characteristics of the second gain pass in the V-shaped cavity, the pulses are still globally bound: A single pulse always remains trapped between the two gain passes of the preceding pulse. Despite the global binding mechanism, the phase difference of the pulses exhibits a random walk, making it possible to define the clusters as phase incoherent photonic molecules.

Further effects of importance, when optimising the output of a mode-locked VECSEL, are second and third-order dispersion. To examine the influence of second-order dispersion, the Haus master equation (HME) has proven to be an useful tool, since the dispersion of different orders simply occur as additional derivative terms of the respective order in the electric field equation. Yet, an application of the standard HME system in a regime of incomplete gain recovery and strong gain modulations was not possible, because long term carrier memory

was not adequately included. Thus, a dynamical boundary condition to adequately model the long term carrier dynamics was derived. The boundary condition was first tested using a ring HME and comparing its results to the well known ring DDE model of mode-locking. In a second step, the comparison of the generalised V-shape HME and the V-shape DDE showed an excellent agreement.
In the following, it was possible to show that the group velocity dispersion exhibits a strong interplay with the amplitude-phase coupling in the ring as well as in the V-shape models. In the case of no amplitude-phase coupling, the stability boundaries shifted symmetrically in pump power around the point of zero dispersion for all investigated dynamical regimes. Anyhow, an introduction of non-zero α-factors leads to a breaking of this symmetry. In the V-shaped system, a positive group velocity dispersion causes an extension of the upper stability boundary of the fundamental mode-locking and the pulse-cluster solutions to higher pump powers at non-zero α-factors compared to the influence of a negative dispersion factor. Nonetheless, the lower stability boundaries remained almost unaffected by the dispersion. A detailed interpretation was given by analysing the pulse energy as well as the pulse width.
The influence of third-order dispersion was studied by means of delay algebraic equation systems, since in contrast to the DDE counterparts the filtering effect of the gain bandwidth does not overwhelm its effect. On that account, a delay algebraic equation model for the V-shaped VECSEL was derived. Potentially, it would allow the study of interference effects at the gain chip, i.e. the formation of a carrier grating.
To enable a direct comparison of the DAE model to the DDE model, a detailed correspondence between the parameters in the different models was determined. In the following comparison, it was shown that the bifurcation structure of the DAE and DDE model for the FML solution is very similar. A direct numerical integration revealed that the third-order dispersion leads to the occurrence of satellite instabilities that prevent the emergence of stable pulse-cluster solutions in the investigated regimes.

In the last part of this work a variation of the gain chip configuration was elaborated. In detail, the V-shaped DDE model was adjusted to describe the inclusion of submonolayer quantum dots (SMLQD) as the active semiconductor medium in the gain. This comprised a separate description of the occupation probability of the active SMLQD states and the pumped 3D semiconductor bulk as well as their coupling. In the following, the role of the newly introduced scattering between the active states and 3D-bulk was examined in detail. It was shown that a slow coupling can increase the pulse width. Additionally, a slow scattering leads to a larger current interval in which the FML and PC_n solutions are stable. Furthermore, an investigation of the amplitude-phase coupling showed, that devices with a fast scattering could be more robust against the destabilising influence of high α-factors.

Outlook

Although it was shown that the influence of the gain bandwidth has a marginal effect on the bifurcation boundaries in pump power, it could be of interest to investigate the dynamics at realistic values of the bandwidth. In the DAE model, this would correspond to a decrease of the photon life-time in the micro-cavities. Especially with regard to dispersion effects, this could have an additional influence due to the reduced pulse width. Additionally, the influence of the line-width enhancement factors could be studied in more detail with regard to the emergence of further instabilities and their effect on the pulse shaping as well as the

bifurcation scenario. In future works, a more detailed investigation of the dispersion effects in the Haus master equation models as well as the DAEs could be conducted by applying path-continuation techniques based on the software pde2path or DAE extension of DDE-biftool.
Despite the fact that the different modelling schemes introduced in this work are all justified by their successful application to reproduce certain laser dynamics, their common weakness lies within the inclusion of certain effects as single adjustable parameters. Hence, certain physics such as e.g. the charge carrier dependence of the amplitude-phase coupling as well as of the dispersion and their interplay is lost due to the applied simplifications. Furthermore, finding a good estimate for the parameter values can be cumbersome, as other counteracting influences might be not included in the model. In future research, it would hence be interesting to specify the results of this work by firstly collecting more detailed experimental data with regard to the parameter dependencies of certain dynamical regimes to help adjust the parameter values and further asses the predictions of the bifurcation analysis. Secondly, fully microscopic models could serve as a starting point to translate the influence of the microscopic effects into effective parameter values (e.g. for dispersion or amplitude-phase coupling) to deliver a more precise estimate. Alternatively, the used models could be extended by a more complex description of the charge carrier effects, similar to the approach followed in the last chapter or the polarisation could be modelled dynamically. In combination, this could allow for a more detailed description of instabilities in mode-locked VECSELs and therefore could be of great use to improve future device generations.

A Appendix: Third Order Dispersion

A.1 Normalisation of the Delay Algebraic Equations

The non normalised electric field equation describing the electric field propagation in a single micro-cavity resulting from applying the proper boundary conditions to Maxwell's wave equation reads[1]

$$\left(r_u r_l \frac{2L_e}{v}\right)\frac{\partial \mathcal{E}(t)}{\partial t} = i\frac{\omega_0 \Gamma W}{2n\varepsilon_0 c}P(t) - (1 - r_u r_l)\,\mathcal{E}(t) + \left(i r_u r_l \frac{\tilde{L}_e}{q_0} + \tilde{\mathcal{R}}\right)\Delta_\perp \mathcal{E}(t) + (-1)^m t'_u e^{\frac{i\phi_u}{2}}\,(1 + r_l)\,Y(t), \tag{A.1}$$

where r_u and r_l are the amplitude of the complex reflectivities $\rho_{u,l} = r_{u,l}e^{i\phi_{u,l}}$ of the upper (u) and lower (l) distributed Bragg reflector (DBR) and t'_u is the transmissivity of the injected field as indicated in Fig. 5.13. Furthermore, Γ is the confinement factor and W the width of the quantum wells ($W \ll \lambda$). The effective cavity length L_e includes the variation of the phase induced by the DBR with respect to the optical frequency. Additionally, the effective length $\tilde{L}_e$ contains the phase variation with respect to the transverse wave-vector angle. The factor $\tilde{\mathcal{R}}$ represents the variations of the reflectivity with varying angle of incidence, n is the refractive index, c the speed of light, ε_0 the vacuum permittivity, ω_0 the carrier frequency, the velocity of the electric field is defined as $v = \frac{c}{n}$, and the wavenumber as $q_0 = \frac{m\omega_0}{v}$, finally m is an integer resulting from the resonance condition. The variable $\mathcal{E}(t)$ describes the electric field inside the micro-cavity and the variable $Y(t)$ corresponds to the electric field injected into the micro-cavity. Furthermore, $P(t)$ represents the macroscopic polarisation
One can now define the round-trip time in the microcavity as

$$\tau_c = \frac{2L_e}{v}, \tag{A.2}$$

the photon life-time κ in the micro-cavity as

$$\kappa = \frac{1}{\tau_c}\frac{1 - r_u r_l}{r_l r_u}, \tag{A.3}$$

the diffraction length l as

$$l = \sqrt{\frac{\tilde{L}_e}{q_0}\frac{r_l r_u}{1 - r_u r_l}}, \tag{A.4}$$

[1] The derivation was originally done by Julien Javaloyes and Svetlana V. Gurevich and transfered to the author in April 2019. Parts of it have been published in [MAR15b].

and finally the field diffusion coefficient referring to the influence of the angle of incidence on the cavity losses

$$d = \frac{q_0 \tilde{\mathcal{R}}}{r_l r_u \tilde{L}_e}. \tag{A.5}$$

Furthermore, the polarisation can be approximated by an adiabatic elimination as discussed in section 3.3 and described in References [MAR15c]

$$P(t) = \varepsilon_0 g_n (\alpha - i) \left(n - n^{tr}\right) \mathcal{E}(t), \tag{A.6}$$

where g_n is the material gain coefficient, resulting from the linear fit of the gain curve, α the line-width enhancement factor, and n^{tr} is the transparency carrier density. Inserting all newly defined parameters and complementing the electric field equation with a standard description of the carrier densities [MAR15c] in the active section yields the following equations

$$\frac{1}{\kappa}\frac{\partial \mathcal{E}(t)}{\partial t} = \left[a g_n (1 - i\alpha)\left(n - n^{tr}\right) - 1 + (i + d)\,\Delta_\perp\right]\mathcal{E}(t) + \tilde{h} Y(t), \tag{A.7}$$

$$\frac{\partial n(t)}{\partial t} = j - \gamma_n n(t) - 2 g_n \left(n(t) - n^{tr}\right)|\mathcal{E}(t)|^2 + \mathcal{D}\Delta_\perp n(t), \tag{A.8}$$

where the transverse dimensions are normalised to the diffraction length l, j is the current density, $\mathcal{D}$ is the carrier diffusion coefficient normalised to the diffraction length, γ_n is the non-radiative carrier recovery and the injection strength $\tilde{h}$ and the factor a are defined as follows

$$a = \frac{\omega_0 \Gamma W}{2\,(1 - r_u r_l)\, nc} \tag{A.9}$$

$$\tilde{h} = (-1)^m t'_u e^{\frac{i\phi_u}{2}} \frac{1 + r_l}{(1 - r_u r_l)}. \tag{A.10}$$

The electric field at the output of the micro-cavity is given by the superposition of the reflected injection field and the transmitted intracavity field

$$O(t) = t_u L_-(t) + r'_u Y(t), \tag{A.11}$$

where $L_-(t)$ is the upward propagating field in the upper part (above the QW) of the microcavity [2]. Making use of the boundary conditions of the intracavity fields, assuming a situation close to resonance and using Stokes relations, the expression for the output field can be transformed into

$$O(t) = \eta \mathcal{E}(t) - Y(t), \tag{A.13}$$

$$\eta = \frac{(-1)^m t_1}{1 + r_u}. \tag{A.14}$$

[2] In the upper ($0 < z < l$) and lower part ($l < z < L$) of the micro-cavity the field can be decomposed into up and downward propagating fields according to:

$$\mathcal{E} = \begin{cases} L_+ e^{iQz} + L_- e^{-iQz}, \text{ if } 0 < z < l \\ R_+ e^{iQz} + R_- e^{-iQz}, \text{ if } l < z < L \end{cases} \tag{A.12}$$

with the longitudinal wave vector $Q(q_\perp, \omega) = \sqrt{\frac{\omega^2}{v} - q_\perp^2}$, and the distance from the top to the QW active section given by l and the distance between QW and bottom of the microcavity defined by L. A detailed description of the boundary conditions is given in Reference [MUL05a] an appendix I of Reference [MAR15c].

where the negative sign in front of Y occurs due to the phase change following the reflection. Utilizing the factor η to normalise the injection strength ($\eta\tilde{h} = h$) and the electric field ($E = \eta\mathcal{E}$) then leads to the full set of DAE equations for a single microcavity

$$\frac{1}{\kappa}\frac{\partial E(t)}{\partial t} = [(1 - i\alpha)\, N(t) - 1 + (i + d)\, \Delta_\perp]\, E(t) + hY(t), \tag{A.15}$$

$$\frac{\partial N(t)}{\partial t} = \gamma_n\,(J - N(t)) - \frac{2g_n}{|\eta|^2} N(t)\,|E(t)|^2 + \mathcal{D}\Delta_\perp N(t), \tag{A.16}$$

$$O(t) = E(t) - Y(t), \tag{A.17}$$

with the carrier density normalised according to $N(t) = g_n a(n(t) - n^{tr})$ and the pump according to $J = g_n a \gamma_n (j - n^{tr})$. The normalised injection strength reads:

$$\tilde{h}\eta = h = \frac{(1 + \rho_l)\,(1 - \rho_u)}{1 - \rho_u \rho_l}. \tag{A.18}$$

As shown by the the sketch in Fig. 5.13, the coupling of two cavities can be described by the injection of the delayed output field of the one cavity into the other cavity. This yields the following expression for the injection fields at the two cavities

$$y(t) = t_{\mathrm{bs}} O(t - \tau) = t_{\mathrm{BS}}\big[E(t - \tau) - Y(t - \tau)\big], \tag{A.19}$$

$$Y(t) = t_{\mathrm{bs}} o(t - \tau) = t_{\mathrm{BS}}\big[e(t - \tau) - y(t - \tau)\big]. \tag{A.20}$$

The electric fields connected to the gain micro-cavity are denoted with the capital letters $Y(t), O(t), E(t)$ and the fields related to the absorber are given by the lower case letters $y(t), o(t), e(t)$. The delay τ in the output fields stems from the propagation time from the one to the other micro-cavity and the transmittance t_{bs} describes the outcoupling losses caused by a beam-splitter (or potentially from an output facet/lens). The equation system for the intracavity fields and charge carriers for the second micro-cavity read exactly the same, with the parameters adjusted to the distinct properties of each semiconductor chip. However, it is useful to normalise all fields to $2g_g\eta_g^{-1}$, with the outcoupling constant of the gain intracavity field η_g according to equation (A.13) and the differential gain g_g from the adiabatic elimination of the polarisation eq. (A.6). After the renormalisation the factor s can be introduced

$$s = \frac{g_q}{|\eta_q|^2}\frac{|\eta_q|^2}{g_g}, \tag{A.21}$$

which is referred to as the saturation parameter and can be understood as the ratio of differential gain and absorber. For mode-locking $s > 1$ is required, as the gain has to become

transparent at lower energies as the absorber [JAU17]. This then leads to the equation system already given in chapter 5.3:

$$\frac{1}{\kappa_g}\frac{d}{dt}E(t) = \left[(1-i\alpha_g)N(t) - 1 + i\omega_0 + (i+d_g)\,\Delta_\perp\right]E(t) + h_g Y(t), \tag{A.22}$$

$$\frac{d}{dt}N(t) = \gamma_g(N_0 - N(t)) - N(t)|E(t)|^2 + \mathcal{D}_g\Delta_\perp N(t), \tag{A.23}$$

$$\frac{1}{\kappa_q}\frac{d}{dt}e(t) = \left[(1-i\alpha_q)n(t) - 1 + (i+d_q)\,\Delta_\perp\right]e(t) + h_q y(t), \tag{A.24}$$

$$\frac{d}{dt}n(t) = \gamma_q(n_0 - n(t)) - sn(t)|e(t)|^2 + \mathcal{D}_q\Delta_\perp n(t), \tag{A.25}$$

$$y(t) = t_{\mathrm{bs}}O(t-\tau) = t_{\mathrm{BS}}\left[E(t-\tau) - Y(t-\tau)\right], \tag{A.26}$$

$$Y(t) = t_{\mathrm{bs}}o(t-\tau) = t_{\mathrm{BS}}\left[e(t-\tau) - y(t-\tau)\right]. \tag{A.27}$$

A.2 Third Order Dispersion in the DDE system

For an empty cavity without outcoupling losses, i.e. neglected charge carrier contributions, the delay differential equation system (3.48) reads

$$\gamma E(t) = \gamma E(t-T) - \frac{dE(t)}{dt}. \tag{A.28}$$

A Fourier transform can be applied to this equation to express the alteration of the electric field from round-trip $n-1$ to round-trip n in Fourier space. This yields

$$\gamma\tilde{E}_n(\omega) - i\omega\tilde{E}_n(\omega) = \gamma\tilde{E}_{n-1}(\omega). \tag{A.29}$$

Here $\tilde{E}_n(\omega)$ can be understood as the Fourier transformation of one periodically expanded pulse in round-trip n. Rearranging for $\tilde{E}_n(\omega)$ leads to

$$\tilde{E}_n(\omega) = \frac{1}{1 - i\gamma^{-1}\omega}\tilde{E}_{n-1}(\omega) = M(\omega)\tilde{E}_{n-1}(\omega), \tag{A.30}$$

where $M(\omega)$ is an operator describing the changes in the electric field from round-trip $n-1$ to round-trip n.
It can now be assumed that the evolution of the electric field can be expressed in terms of a fast time-scale σ referring to changes within one round-trip and a slow time-scale θ related to changes from round-trip to round-trip $E(t) \to E(\sigma,\theta)$. Further it can be assumed that a linear PDE exists, which describes the evolution of the field in the Fourier space of σ according to [SCH20d]

$$\partial_\theta\tilde{E}(\theta,\omega) = \mathcal{L}(i\omega)\tilde{E}(\theta,\omega). \tag{A.31}$$

Here $\mathcal{L}(i\omega)$ is a linear operator. The existence of this PDE is proven by the derivation of the Haus master equation model utilising a multiple time-scale approach in section 4.3.3. Integrating both sides over θ from $n-1$ to n using the separation of variables method and exploiting that $\mathcal{L}(i\omega)$ is not depending on θ leads to

$$\ln\frac{\tilde{E}_n(\omega)}{\tilde{E}_{n-1}(\omega)} = \mathcal{L}(i\omega). \tag{A.32}$$

As this equation has the same form as eq.(A.30) one can find an expression for the operator $\mathcal{L}(i\omega)$ by equating the two equations, which yields

$$\ln \frac{\tilde{E}_n(\omega)}{\tilde{E}_{n-1}(\omega)} = -\ln(1 - i\omega\gamma^{-1}) = \mathcal{L}(i\omega). \tag{A.33}$$

Applying the Taylor expansion for the natural logarithm for small $\omega\gamma^{-1}$ then gives

$$\mathcal{L}(i\omega) \approx i\frac{1}{\gamma}\omega + \frac{1}{2\gamma^2}i^2\omega^2 + \frac{1}{3\gamma^3}i^3\omega^3. \tag{A.34}$$

Inserting this expression into the PDE (A.31) and applying the inverse Fourier transform ($-i\omega \to \partial_\sigma$) [HAU00], then gives the final PDE corresponding to the simple DDE

$$\partial_\theta E(\sigma,\theta) = \left[-\frac{1}{\gamma}\partial_\sigma + \frac{1}{2\gamma^2}\partial_\sigma^2 - \frac{1}{3\gamma^3}\partial_\sigma^3\right] E(\sigma,\theta). \tag{A.35}$$

A.3 Semi-Implicit Numerical Algorithm for the DAE System

To illustrate the semi-implicit numerical algorithm, the following simplified DAE equation model is integrated:

$$\frac{1}{\kappa}\frac{dE}{dt} = -E + G\cdot E + h\cdot Y, \tag{A.36}$$

$$\frac{1}{\gamma}\frac{dG}{dt} = G_0 - G - G|E|^2, \tag{A.37}$$

$$Y(t) = \eta[E(t-\tau) - Y(t-\tau)]. \tag{A.38}$$

As a starting point a history array, containing all variable values for the time-steps between $-\tau$ to 0, is filled with the desired initial condition. The aim of the algorithm is to calculate the next step in the time series corresponding to $E_{\Delta t}$ in the electric field. The central idea of the semi-implicit algorithm is to integrate E on the time grid $0, \Delta t, 2\Delta t, ...$ and G over the shifted grid $\frac{1}{2}\Delta t, \frac{3}{2}\Delta t, ...$ This approximation gives good results if Δt is small. In the algorithm at first an approximation for $E_{\Delta t}$ is found and then for $G_{\frac{3}{2}\Delta t}$.
Integrating eq.(A.36) over t from 0 to Δt yields:

$$\frac{1}{\kappa}\int_0^{\Delta t}\frac{dE}{dt} = -\int_0^{\Delta t} E + \int_0^{\Delta t} G\cdot E + \int_0^{\Delta t} h\cdot Y. \tag{A.39}$$

Applying the trapezoidal rule to solve the integral over the electric fields Y and E then leads to:

$$\frac{1}{\kappa}(E_{\Delta t} - E_0) = -\Delta t\frac{E_{\Delta t} + E_0}{2} + \int_0^{\Delta t} G\cdot E + \frac{h}{2}\Delta t(Y_0 + Y_{\Delta t}). \tag{A.40}$$

To find a solution for the integral over the non-linear contribution one makes use of the trick of integrating G on a slightly shifted time. As G is integrated over another grid it is possible to approximate

$$\int_0^{\Delta t} G\cdot E \approx \int_0^{\Delta t} G_{\Delta t/2}\cdot E \approx G_{\Delta t/2}\cdot\frac{E_{\Delta t} + E_0}{2}\Delta t + O(\Delta t^2). \tag{A.41}$$

Substituting this into (A.40) then yields

$$\frac{1}{\kappa}(E_{\Delta t} - E_0) = -\Delta t\frac{E_{\Delta t} + E_0}{2} + G_{\Delta t/2} \cdot \frac{E_{\Delta t} + E_0}{2}\Delta t + \frac{h}{2}\Delta t(Y_0 + Y_{\Delta t}). \tag{A.42}$$

This can be rearranged with respect to $E_{\Delta t}$ and therefore an expression for the next step in the time-series of the electric field can be determined

$$E_{\Delta t}(\frac{1}{\kappa} + \frac{\Delta t}{2} - \Delta t\frac{G_{\Delta t/2}}{2}) = E_0(\frac{1}{\kappa} - \frac{\Delta t}{2} + \Delta t\frac{G_{\Delta t/2}}{2}) + \frac{h}{2}\Delta t(Y_0 + Y_{\Delta t}). \tag{A.43}$$

To find an expression for the next step in the time-series of the charge carriers dynamics, the same approximations are applied starting from the gain equation (A.37). Integrating the charge carrier equation from $\frac{1}{2}\Delta t$ to $\frac{3}{2}\Delta t$ and applying the trapezoidal rule for the linear terms leads to

$$\frac{1}{\gamma}(G_{\frac{3}{2}\Delta t} - G_{\frac{1}{2}\Delta t}) = G_0\Delta t - \frac{\Delta t}{2}(G_{\frac{3}{2}\Delta t} + G_{\frac{1}{2}\Delta t}) - \int_{\frac{1}{2}\Delta t}^{\frac{3}{2}\Delta t} GI. \tag{A.44}$$

The non-linear contribution can be approximated using the same technique as before

$$\int_{\frac{1}{2}\Delta t}^{\frac{3}{2}\Delta t} GI \approx \frac{\Delta t}{2} I_{\Delta t}(G_{\frac{3}{2}\Delta t} + G_{\frac{1}{2}\Delta t}) + O(\Delta t^2). \tag{A.45}$$

Substituting in the approximation leads to

$$\frac{1}{\gamma}(G_{\frac{3}{2}\Delta t} - G_{\frac{1}{2}\Delta t}) = G_0\Delta t - \frac{\Delta t}{2}(G_{\frac{3}{2}\Delta t} + G_{\frac{1}{2}\Delta t}) - \frac{\Delta t}{2} I_{\Delta t}(G_{\frac{3}{2}\Delta t} + G_{\frac{1}{2}\Delta t}), \tag{A.46}$$

which can be rearranged to find the following expression for the next time-step in the time-series for G

$$G_{\frac{3}{2}\Delta t}(\frac{1}{\gamma} + \frac{\Delta t}{2} + \Delta t\frac{I_{\Delta t}}{2}) = G_0\Delta t - (-\frac{1}{\gamma} + \frac{\Delta t}{2} + \Delta t\frac{I_{\Delta t}}{2})G_{\frac{1}{2}\Delta t} \tag{A.47}$$

B Appendix: Haus Master Equation

B.1 Numerical Methods to Solve the Haus Master Equation

B.1.1 Time-Splitting of the Electric Field Equation

The method used for the direct numerical integration of the Haus master equation models in this work[1], a combination of the Euler method and time splitting is applied as published in Appendix 4 of Reference [GUR17]. Details on time-splitting methods can be found in Reference [BOY00].
The illustration of the integration is started at the Haus master equation for the ring cavity as given in section 5.2. It reads

$$\partial_\theta E(\theta,\sigma) = \frac{1}{2\gamma^2}\partial_\sigma^2 E(\theta,\sigma) + \frac{1}{2}[(1-i\alpha_q)G(\theta,\sigma) + (1-i\alpha_q)Q(\theta,\sigma) + \frac{1}{2}\log\kappa]E(\theta,\sigma), \quad \text{(B.1)}$$

$$\partial_\sigma G(\theta,\sigma) = \gamma_g G_0 - \gamma_g G(\theta,\sigma) - G(\theta,\sigma)|E(\theta,\sigma)|^2, \quad \text{(B.2)}$$

$$\partial_\sigma Q(\theta,\sigma) = \gamma_q Q_0 - \gamma_q Q(\theta,\sigma) - sQ(\theta,\sigma)|E(\theta,\sigma)|^2. \quad \text{(B.3)}$$

The different contributions in the electric field equation (B.1) of the Haus master equation (HME) PDE can be split into a linear operator $\mathcal{L}$ and a non-linear operator $\mathcal{N}$ according to

$$\mathcal{N} = \frac{1}{2}[(1-i\alpha_g)G + (1-i\alpha_q)Q + \frac{1}{2}\log\kappa], \quad \text{(B.4)}$$

$$\mathcal{L} = \frac{1}{2\gamma^2}\partial_\sigma^2. \quad \text{(B.5)}$$

Hence, the equation can be rewritten in the following generic simple form

$$\partial_\theta E(\theta,\sigma) = \mathcal{L}E(\theta,\sigma) + \mathcal{N}E(\theta,\sigma). \quad \text{(B.6)}$$

Where it has to be noted that writing the linear operator as $\mathcal{N}$ is sufficient for the analysed system, but in general it would be $\mathcal{N}(E)$.
An (exact) solution of the system can be found integrating the system from θ_n to $\theta_n + \delta\theta$ using a separation of variables and utilising that the operators do not depend on θ (the dynamical equations for the charge carriers only the derivative with respect to σ appears)

$$E(\theta_n + \delta\theta, \sigma) = e^{\mathcal{L}\delta\theta + \mathcal{N}\delta\theta} E(\theta_n, \sigma). \quad \text{(B.7)}$$

However, it is much simpler to find the solutions of the two contributions separately. This can be done according to

$$\partial_\theta E(\theta,\sigma) = \mathcal{L}E(\theta,\sigma) \Rightarrow E(\theta_n + \delta\theta,\sigma) = e^{\mathcal{L}\delta\theta}E(\theta_n,\sigma) \quad \text{(B.8)}$$

$$\partial_\theta E(\theta,\sigma) = \mathcal{N}E(\theta,\sigma) \Rightarrow E(\theta_n + \delta\theta,\sigma) = e^{\mathcal{N}\delta\theta}E(\theta_n,\sigma). \quad \text{(B.9)}$$

[1] It has to be noted that here only the ring model is used for the demonstration, but the method can be followed analogously for the V-shaped system derived in section 4.3.3.

Which combined give the solution:

$$E(\theta_n + \delta\theta, \sigma) = e^{\mathcal{L}\delta\theta} e^{\mathcal{N}\delta\theta} E(\theta_n, \sigma). \tag{B.10}$$

However, this solution is only an approximation as the the operators generally do not commute and one would have to include an additional commutator term according to

$$e^{\mathcal{L}\delta\theta + \mathcal{N}\delta\theta} = e^{\mathcal{L}\delta\theta} e^{\mathcal{N}\delta\theta} e^{-[\mathcal{L}\delta\theta, \mathcal{N}\delta\theta]}. \tag{B.11}$$

However, as the operators scale with $\delta\theta$, the commutator is of order $O(\delta\theta^2)$. Therefore, the time splitting gives a good first-order approximation, especially if $\delta\theta$ is small.
As the two operators do not commute it is questionable which operator is multiplied first to the electric field term $E(\theta = n, \sigma)$. To take this into account, the influence of the non-linear operator is split into two contributions, which are multiplied before and after the contribution of the linear operator. Hence the integration method is adapted in the following way

$$E(\theta_n + \delta\theta, \sigma) = e^{\mathcal{N}\frac{\delta\theta}{2}} e^{\mathcal{L}\Delta t} e^{\mathcal{N}\frac{\delta\theta}{2}} E(\theta_n, \sigma) \tag{B.12}$$

To take the difference between an implicit and an explicit Euler method into account, the first non-linear exponential is approximated by the explicit Euler method and the second one by the implicit Euler method (see Appendix B.1.2). This yields

$$E(\theta_n + \delta\theta, \sigma) = \frac{1}{1 - \frac{\Delta t}{2}\mathcal{N}} e^{\mathcal{L}\delta\theta} (1 + \mathcal{N}\frac{\delta\theta}{2}) E(\theta_n, \sigma) \tag{B.13}$$

Calculating the second-order derivative with respect to σ in time-space can be computationally very demanding. In contrast, it is a simple multiplication of $-q_\sigma^2$ in Fourier-space. Hence a forward an backward Fourier transform is utilised to be able to apply the operator in Fourier-space. The resulting integration scheme then reads

$$E(\theta_n + \delta\theta, \sigma) = \frac{1}{1 - \frac{\delta\theta}{2}\mathcal{N}} \mathcal{F}^{-1}\mathcal{F}\{e^{\mathcal{L}\delta\theta} (1 + \mathcal{N}\frac{\delta\theta}{2}) E(\theta_n, \sigma)\} \tag{B.14}$$

which finally leads to

$$E(\theta_n + \delta\theta, \sigma) = \frac{1}{1 - \frac{\delta\theta}{2}\mathcal{N}} \mathcal{F}^{-1}\{e^{\tilde{\mathcal{L}}\delta\theta} \mathcal{F}[(1 + \mathcal{N}\frac{\delta\theta}{2}) E(\theta_n, \sigma)]\} \tag{B.15}$$

where the Fourier transformed linear operator $\tilde{\mathcal{L}}$ can be written as

$$e^{\tilde{\mathcal{L}}\delta\theta} = e^{-\frac{1}{2\gamma^2}\delta\theta q_\sigma^2} \tag{B.16}$$

Additional to the multiplication of this exponential, the factor $\exp(iv_0 q_\sigma \delta\theta)$ is multiplied in Fourier-space. Here q_σ is the wave-vector calculated from $q_\sigma = \frac{2\pi n}{T}$ with the number of the integer grid point in σ given by n, the drift correction v_0 and the 0 frequency component shifted to the center of the array. As v_0 suggests, this term is used to account for the fact that the integration domain does not perfectly match the round-trip time of the pulse $t\tau_p$ (period of the fundamental solution), due to the time-lag induced by the non-linear interactions and the Lorentzian filter. Hence v_0 is defined as $\tau_p = T + \frac{1}{\gamma} + v_0$. It is updated every round-trip according to

$$v_0 = v_0 + dv_n \tag{B.17}$$

with the adjustment calculated from

$$dv_n = \frac{\sum_i^N \left(I_i^{(n)} - I_i^{(n-1)}\right)\left(\frac{\partial I}{\partial \sigma}\right)_i}{\sum_i^N \left(\frac{\partial I^{(n)}}{\partial \sigma}\right)_i^2} \tag{B.18}$$

where n is referring to the round-trip number and i is the index over the array with N grid points in σ. How v_0 can be included into the boundary conditions discussed in section 5.2 is given in Appendix B.2.

B.1.2 Euler Methods for the Carrier Equations.

The aim of this section is to shortly introduce the integration steps used for the charge carrier equations in the Haus master equation model. Hence, the implicit an explicit Euler methods are presented shortly.
Considering only the non-linear part of the electric field equation as given in the previous section characterised by the operator $\mathcal{N}$, one can solve the equation by integrating over θ from θ_n to $\theta_n + \delta\theta$. This gives

$$\partial_\theta E(\theta, \sigma) = \mathcal{N} E(\theta, \sigma), \tag{B.19}$$

$$\Rightarrow \int_{\theta_n}^{\theta_n+\delta\theta} \partial_\theta E(\theta, \sigma) = \int_{\theta_n}^{\theta_n+\delta\theta} \mathcal{N} E(\theta, \sigma). \tag{B.20}$$

Instead of performing a separation of variables, the integral on the right-hand side can be approximated (assuming $\mathcal{O}$ does not depend on time) by either $E(\theta_n, \sigma)\delta\theta$ or $E(\theta_n+\delta\theta, \sigma)\delta\theta$, which is known as the difference between the implicit and explicit Euler methods. The prior gives

$$E(\theta_n + \delta\theta, \sigma) = (1 + \mathcal{N}\delta\theta) E(\theta_n, \sigma). \tag{B.21}$$

The latter gives

$$E(\theta_n + \delta\theta, \sigma) = \frac{E(\theta_n, \sigma)}{(1 - \mathcal{N}\delta\theta)}, \tag{B.22}$$

which leads to the approximations given in the integration scheme B.15.
The equations for the carriers do not depend on the slow time-scale. Therefore, they can be integrated using the intensity profile of the previous round-trip before again applying the integration scheme for the field equation outlined in the previous section. On that account, a semi-implicit method is used for the charge carrier equations. Staring from the gain equation

$$\partial_\sigma G(\theta, \sigma) = J_g - \gamma_g G(\theta, \sigma) - G(\theta, \sigma)|E(\theta, \sigma)|^2, \tag{B.23}$$

and integrating on both sides from σ_n to $\sigma_n + \delta\sigma$ one obtains

$$\begin{aligned} G(\theta, \sigma_n + \delta\sigma) - G(\theta, \sigma_n) =& J_g\delta\sigma - \gamma_g \frac{G(\theta, \sigma_n + \delta\sigma) + G(\theta, \sigma_n)}{2}\delta\sigma \\ & - \frac{G(\theta, \sigma_n + \delta\sigma)|E(\theta, \sigma_n + \delta\sigma)|^2 + G(\theta, \sigma_n)|E(\theta, \sigma_n)|^2}{2}\delta\sigma. \end{aligned} \tag{B.24}$$

Rearranging for $G(\theta, \sigma_n + \delta\sigma)$ then gives

$$G(\theta, \sigma_n + \delta\sigma)\left[1 + \frac{\delta\sigma}{2}\left[|E(\theta, \sigma_n + \delta\sigma|^2) + \gamma_g\right]\right] = J_g\delta\sigma + \left[1 - \frac{\delta\sigma}{2}[\gamma_g + |E(\theta, \sigma_n)|^2]\right] G(\theta, \sigma_n). \tag{B.25}$$

and finally yields

$$G(\theta, \sigma_n + \delta\sigma) = \frac{J_g\delta\sigma + \left\{1 - \frac{\delta\sigma}{2}\left[\gamma_g + |E(\theta, \sigma_n)|^2\right]\right\} G(\theta, \sigma_n)}{1 + \frac{\delta\sigma}{2}\left[|E(\theta, \sigma_n + \delta\sigma)|^2 + \gamma_g\right]}. \tag{B.26}$$

Performing the same steps for the absorber one obtains for $Q(\theta, \sigma_n + \delta\sigma)$

$$Q(\theta, \sigma_n + \delta\sigma) = \frac{J_q\delta\sigma + \left\{1 - \frac{\delta\sigma}{2}\left[\gamma_q + 2s|E(\theta, \sigma_n)|^2\right]\right\} Q(\theta, \sigma_n)}{1 + \frac{\delta\sigma}{2}\left[2s|E(\theta, \sigma_n + \delta\sigma)|^2 + \gamma_q\right]}. \tag{B.27}$$

The same steps can be performed for the non-local Haus master equation, where the non-locality is treated as a delay and a T periodicity is assumed on that account.

B.2 Second-Order Boundary Condition and Drift

In order to account for the fact that during the direct numerical integration of the Haus master PDE the period of the solution does not exactly match the round-trip time (the length of the integration domain $\tau_{In} = T + \frac{1}{\gamma}$ does not completely equal the period), one can introduce an additional artificial drift correction v_0 into the fast time-scale[2] σ. The value of the correction is defined as v_0, and the actual delayed round-trip time of a pulse then can be defined as $\tau_p = T + \frac{1}{\gamma} + v_0$. The inclusion of the $\frac{1}{\gamma}$ term is reasoned by the drift induced by the Lorentzian filter (see Appendix A.2). This additional drift correction v_0 is then calculated once per round-trip, during the direct numerical integration. Here the introduction of the drift into the Haus master equation as well as into the boundary condition is discussed. Furthermore, it is outlined, how the boundary condition can be extended to second-order.
Firstly the coordinate transformation $y[\theta, \sigma] = \sigma - v_0\theta$ is introduced. Furthermore, the variables are transformed according to

$$E(\theta, \sigma) \to \tilde{E}(\theta, y[\theta, \sigma]), \tag{B.28}$$

$$G(\theta, \sigma) \to \tilde{G}(\theta, y[\theta, \sigma]). \tag{B.29}$$

The derivatives with respect to θ and σ then are transformed by using the chain rule

$$\frac{\partial E}{\partial \sigma} = \frac{\partial y}{\partial \sigma}\frac{\partial \tilde{E}}{\partial y} = \frac{\partial \tilde{E}}{\partial y}, \tag{B.30}$$

$$\frac{\partial E}{\partial \theta} = \frac{\partial \tilde{E}}{\partial \theta} + \frac{\partial y}{\partial \theta}\frac{\partial \tilde{E}}{\partial y} = \frac{\partial \tilde{E}}{\partial \theta} - v_0\frac{\partial \tilde{E}}{\partial y}. \tag{B.31}$$

Inserting the transformed variables, derivatives and coordinates into the Haus master equation (5.5)-(5.7), one obtains an additional derivative with respect to y in the electric field

[2] The idea of the following derivation was proposed by Julien Javaloyes, UIB, Palma and Svetlana V. Gurevich, WWU Münster.

equation. However, in the direct numerical integration using the Fourier split-step method outlined in B.1 this just leads to a further multiplication of the factor $\exp(iv_0 q_n \delta\theta)$ in Fourier-space. Here q_σ is the wave-vector calculated from $q_\sigma = \frac{2\pi n}{T}$ with n being the number of integer grid points in σ, $\delta\theta$ is the resolution with respect to θ and the 0 frequency component shifted to the center of the array. The calculation of v_0 and its application in the integration scheme is outlined in B.1. The transformed systems of PDEs then reads (neglecting the α-factors):

$$\partial_\theta \tilde{E}(\theta, y) - v_0 \partial_y \tilde{E}(\theta, y) = \frac{1}{2\gamma^2}\partial_y^2 \tilde{E}(\theta, y) + \frac{1}{2}[\tilde{G}(\theta, y) - \tilde{Q}(\theta, y) - k]\tilde{E}(\theta, y), \tag{B.32}$$

$$\partial_y \tilde{G}(\theta, y) = \gamma_g G_M - \gamma_g \tilde{G}(\theta, y) - \tilde{G}|\tilde{E}(\theta, y)|^2, \tag{B.33}$$

$$\partial_y \tilde{Q}(\theta, y) = \gamma_q Q_M - \gamma_q \tilde{Q}(\theta, y) - \tilde{s}\tilde{Q}(\theta, y)|\tilde{E}(\theta, y)|^2. \tag{B.34}$$

Additionally, the transformation of the map boundary condition (5.8) leads to

$$G(\theta, 0) = G(\theta - 1, 1), \tag{B.35}$$

$$\Rightarrow \tilde{G}(\theta, y[\theta, 0]) = \tilde{G}(\theta - 1, y[\theta - 1, 1]), \tag{B.36}$$

$$\Rightarrow \tilde{G}(\theta, -v_0\theta) = \tilde{G}(\theta - 1, 1 - v_0(\theta - 1)). \tag{B.37}$$

From point, one applies the same steps as in the main text section 5.2 in order to arrive at two ODEs with respect to θ, modelling the variation of the gain at the start of each roundtrip $\mathcal{G}(\theta)$. In the next step one applies a Taylor expansion of the charge-carrier variable G with respect to small v_0, which always holds as v_0 is only a small correction ($\tau_p = T + \frac{1}{\gamma} + v_0$). The boundary condition can be shifted in time as the origin is irrelevant. This can be done in two ways and therefore leads to two equations, which however lead to the same result in the direct numerical integration. The first approach reads

$$\tilde{G}(\theta - 1, 1) = \tilde{G}(\theta, 0) - v_0 \partial_y \tilde{G}(\theta, 0), \tag{B.38}$$

or the second reads

$$\tilde{G}(\theta, 0) = \tilde{G}(\theta - 1, 1) + v_0 \partial_y \tilde{G}(\theta - 1, 1). \tag{B.39}$$

In the following approach only the first option is used, but the second can be applied analogously.
The integration over one round-trip with respect to the new variable y of the transformed gain equation (B.33) reads

$$\int_0^1 \partial_y \tilde{G}(\theta, y) dy = \tilde{G}(\theta, 1) - \tilde{G}(\theta, 0) = D(\theta), \tag{B.40}$$

where $D(\theta)$ represents the integrated right hand side of the gain equation. Now the asynchronous boundary condition can be used to only keep terms depending on $\sigma = 0$ (or $\sigma = 1$ for the second variant). Therefore, boundary condition (B.38) is adjusted to:

$$\tilde{G}(\theta, 1) = \tilde{G}(\theta + 1, 0) - v_0 \partial_y \tilde{G}(\theta + 1, 0). \tag{B.41}$$

Equation (B.41) can now be equated to the expression found for the left hand side of the integrated gain equation (B.40). Thus, one obtains (defining $\mathcal{G}(\theta) = \tilde{G}(\theta, 0)$)

$$\tilde{G}(\theta + 1, 0) - \tilde{G}(\theta, 0) = D(\theta) + v_0 \partial_y \tilde{G}(\theta + 1, 0), \tag{B.42}$$

$$\Rightarrow \mathcal{G}(\theta + 1) - \mathcal{G}(\theta) = D(\theta) + v_0 \partial_y \tilde{G}(\theta + 1, 0). \tag{B.43}$$

To transform this intermediate result into an ODE, one approximates the difference on the left hand side using the Taylor expansion. This step is justified by the slow evolution of $\mathcal{G}(\theta)$. The approximation to second-order reads

$$\mathcal{G}(\theta+1)-\mathcal{G}(\theta)\approx\frac{d}{d\theta}\mathcal{G}(\theta)+\frac{1}{2}\frac{d^2}{d\theta^2}\mathcal{G}(\theta). \tag{B.44}$$

Furthermore, the right hand side of the integrated gain equation is inserted for $D(\theta)$ and the approximation $v_0\partial_y\tilde{G}(\theta+1,0)\approx v_0\partial_y\tilde{G}(\theta,0)$ is used to find the same θ for all terms. The latter is justified by the slow change of the gain at the start of each round-trip. This yields

$$\frac{d}{d\theta}\mathcal{G}(\theta)+\frac{1}{2}\frac{d^2}{d\theta^2}\mathcal{G}(\theta)=\Gamma\left[G_0-\int_0^1\tilde{G}(\theta,y)dy\right]-\int_0^1\tilde{G}(\theta,y)|\tilde{E}(\theta,y)|^2dy+v_0\partial_y\tilde{G}(\theta,0). \tag{B.45}$$

The final boundary condition is determined by inserting eq. (B.33) with $y=0$ into the last term on the right-hand side. The final second-order ODE representing the dynamical change of the gain at the start of each round trip reads

$$\begin{aligned}\frac{d}{d\theta}\mathcal{G}(\theta)+\frac{1}{2}\frac{d^2}{d\theta^2}\mathcal{G}(\theta)=&\Gamma\left[G_0-\int_0^1\tilde{G}(\theta,y)dy\right]-\int_0^1\tilde{G}(\theta,y)|\tilde{E}(\theta,y)|^2dy\\&+v_0\left\{\Gamma[G_0-\mathcal{G}(\theta)]-\mathcal{G}(\theta)|\tilde{E}(\theta,0)|^2\right\}.\end{aligned} \tag{B.46}$$

By introducing the new variable $\phi=\frac{d}{d\theta}\mathcal{G}$ the found equation can be transformed into two first-order differential equations, which are solvable by applying the simple Euler method.

C Non-Zero α-factor in the Localised Regime

A 2D bifurcation diagram across the (J_g,τ_1) parameter plane in the localised regime is indicated in Fig. C.1. In (a) the PC_2 solution is used as a initial condition, whereas in (b) the PC_3 solution is used. The difference to the bifurcation diagram presented in section 4.3.4 is the usage of non-zero linewidth enhancement factors, i.e. $\alpha_g = 1.5$ and $\alpha_q = 0.5$. However, the general bifurcation structure is not strongly influenced. Furthermore, the adjustment of the pulse distance with changing cavity geometry is maintained.

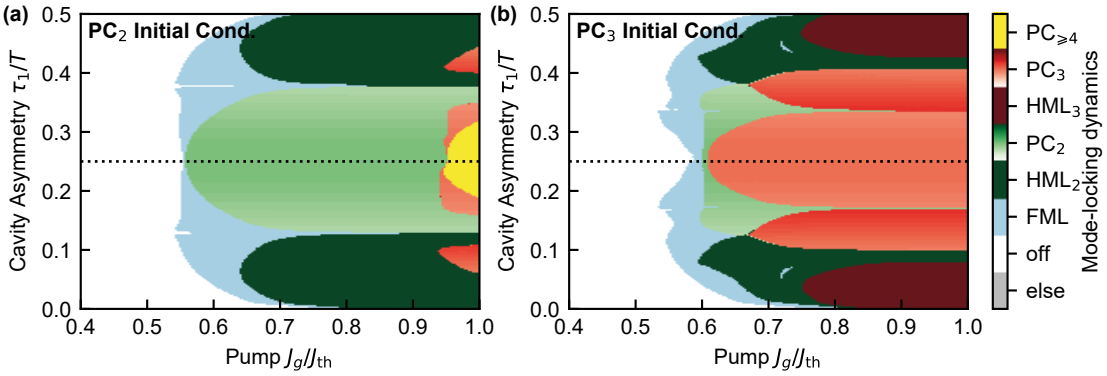

Figure C.1.: 2D Bifurcation diagrams across the (J_g,τ_2) parameter plane in the localised regime. The cavity asymmetry was varied, while maintaining a constant round-trip time, which was assured by fulfilling the boundary condition $T = 2\tau_1 + 2\tau$. The color-code distinguishes between fundamental mode-locking (FML), pulse cluster solutions (PC_n) and harmonic mode-locking solutions (HML_n) with n referring to the number of pulses. The white colored region represents the laser *off* state. At each parameter pair (J_g,τ_2) a stable solution was utilised as the initial condition of the direct numerical integration. The utilised solutions were (a) PC_2 and (b) PC_3. They were found as the stable solutions after transient 10^4 round-trips at a symmetric cavity configuration (black dashed line) and $J_g/J_{th} = 0.7$. The shading of the red and green color-code represents the distance between the pulses in the PC solution, with the darkest region corresponding the the maximum possible distance (transition to HML solution). Laser parameters according to Table 4.1 with $\alpha_g = 1.5$ and $\alpha_q = 0.5$. Figure adapted from [HAU20].

D Additional Figures - GVD

This section indicates two additional Figures for the discussion of the influence of the second-order dispersion. Figure D.1 indicates a plot of the pulse energy and the pulse width (FWHM) in the parameter plane of the pump power and the group velocity dispersion (G_0, δ) obtained by direct numerical integration of the Haus master PDE (upsweep in G_0). The used α-factors are $\alpha_g = 0.25$ and $\alpha_q = 0$. Furthermore, Fig. D.2 indicates the influ-

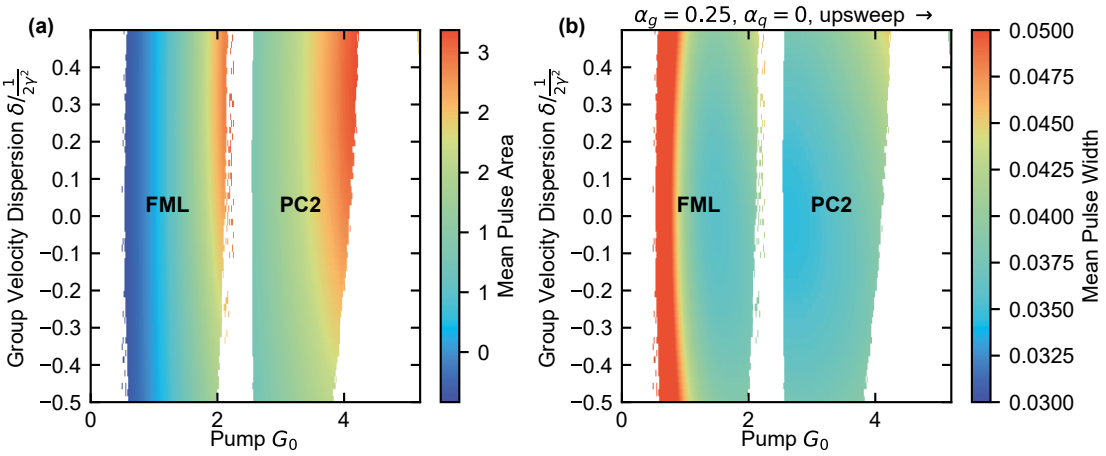

Figure D.1.: Additional information for non-zero linewidth enhancement (a) Mean pulse width in the parameter plane of the pump power and the group velocity dispersion (G_0, δ) obtained by direct numerical integration of the Haus master PDE (upsweep in G_0). (b) Mean Pulse width in the same parameter plane. Both quantities are shown only for the fixed point solutions (white indicates a (quasi-)periodic solution). The underlying dynamics is plotted in Fig. 5.10 and given by the labels. Laser parameters as given in Table 3.1, with $J_q = -39.375$ ($Q_0 = -0.35$) and $\alpha_g = 0.25$, $\alpha_q = 0.0$

ence on the stabilizing dynamics, when using a down-sweep instead of an up-sweep (for zero αfactors). As discussed in section 4.2.3 the irregular states do not stabilise and the lower bifurcation boundaries are not influence by the group velocity dispersion.

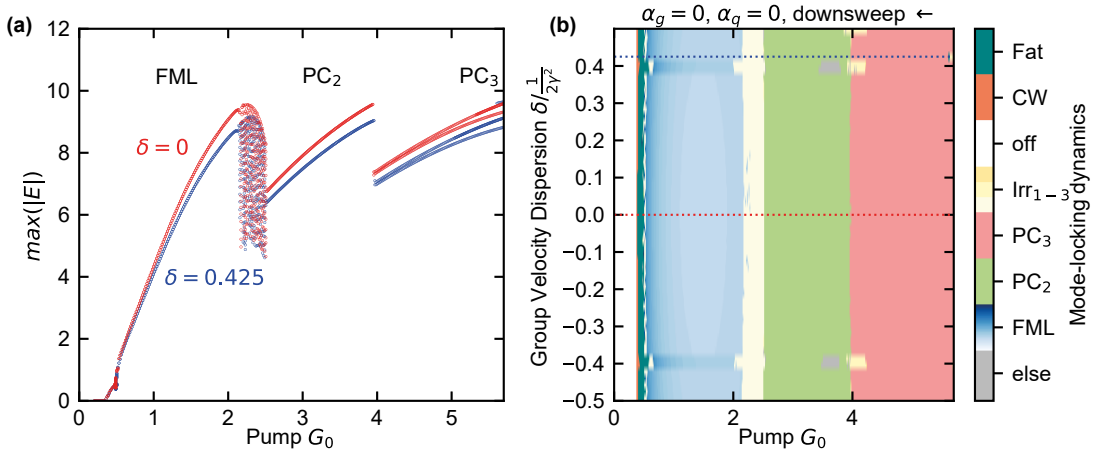

Figure D.2.: Downsweep: (a) 1D Bifurcation diagram in pump power G_0 showing all unique pulse maxima (max $(|E|)$) obtained in 500 round-trips in the regime of fundamental (FML) and pulse cluster mode-locking (PC_n). The blue dots correspond to a group velocity dispersion of $\delta/\frac{1}{2\gamma^2} = 0.425$ and the red dots to $\delta/\frac{1}{2\gamma^2} = 0$. (b) 2D Bifurcation diagram in the parameter plane of the the pump power and the group velocity dispersion (G_0, δ) obtained by direct numerical integration of the generalised non-local Haus master PDE (upsweep in G_0). The different colors refer to the same dynamics as in Fig. 5.6. Laser parameters as given in Table 3.1, with $J_q = -39.375$ ($Q_0 = -0.35$).

List of Figures

List of Tables

List of Acronyms

Acronym	Meaning
AC	autocorrelation
CW	continuous-wave (lasing)
DAE	Delay algebraic equation
DBR	distributed Bragg reflector
DDE	delay-differential equation
FML	fundamental mode-locking
FWHM	full width at half maximum
GaAs	gallium arsenide
GVD	Group-velocity dispersion
HME	Haus master equation
HML	harmonic mode-locking
InAs	indium arsenide
MP	multi-pulse quasi-periodic mode-locking structures
ODE	ordinary-differential equation
PC	pulse-cluster mode-locking
PDE	partial-differential equation
QD	quantum dot
QSML	Q-switched mode-locking
QW	quantum well
RO	relaxation oscillation
SESAM	semiconductor saturable absorber mirror
SMLQD	Submonolayer quantum dot
SN	Saddle-node bifurcation
T	Torus bifurcation
TOD	Third-order dispersion
VECSEL	vertical-external-cavity surface-emitting laser

List of Publications

1. J. Hausen, S. Meinecke, B. Lingnau, and K. Lüdge: *Pulse cluster dynamics in passively mode-locked semiconductor vertical-external-cavity surface-emitting lasers*, Phys. Rev. Appl. **11**, 044055 (2019)

2. J. Hausen, S. Meinecke, J. Javaloyes, S. V. Gurevich, and K. Lüdge: *Phase-incoherent photonic molecules in V-shaped mode-locked vertical-external-cavity surface-emitting semiconductor lasers*, Phys. Rev. Appl. **14** (2020)

3. J. Hausen, K. Lüdge, S. V. Gurevich, and J. Javaloyes: *How carrier memory enters the haus master equation of mode-locking*, Opt. Lett. **45**, 6210–6213 (2020)

4. J. Hausen, B. Herzog, A. Nelde, S. Meinecke, N. Owschimikow, and K. Lüdge: *Feedback induced locking in semiconductor lasers with strong amplitude-phase coupling*, Phys. Rev. A **103**, 043511 (2021)

5. J. Hausen, S. Meinecke, and K. Lüdge: *Bifurcation scenario leading to multiple pulse emission in VECSELs*, Proc. SPIE **10901**, 109010F (2019)

6. S. Meinecke, L. Kluge, J. Hausen, B. Lingnau, and K. Lüdge: *Optical feedback induced oscillation bursts in two-state quantum-dot lasers*, Opt. Express **28**, 3361–3377 (2020)

Bibliography

[ACK09] T. Ackemann, W. J. Firth, and G. L. Oppo: *Fundamentals and Applications of Spatial Dissipative Solitons in Photonic Devices*, in *Advances in Atomic Molecular and Optical Physics*, edited by (Academic Press, 2009), vol. 57 of *Advances In Atomic, Molecular, and Optical Physics*, chapter 6, pp. 323–421.

[ADD21] S. J. Addamane, A. Laurain, C. W. Baker, T. J. Rotter, J. Watt, J. L. Reno, G. Balakrishnan, and J. V. Moloney: *Submonolayer quantum-dot based saturable absorber for femtosecond pulse generation*, J. Electron. Mater. **50** (2021).

[AVI11a] R. Aviles-Espinosa, G. Filippidis, C. Hamilton, G. Malcolm, K. J. Weingarten, T. Südmeyer, Y. Barbarin, U. Keller, S. I. C. O. Santos, D. Artigas, and P. Loza-Alvarez: *Compact ultrafast semiconductor disk laser: targeting gfp based nonlinear applications in living organisms*, Biomed. Opt. Express **2**, 739 (2011).

[AGR89] G. P. Agrawal and N. A. Olsson: *Self-phase modulation and spectral broadening of optical pulses in semiconductor laser amplifiers*, IEEE J. Quantum Electron. **25**, 2297–2306 (1989).

[AGR91] G. P. Agrawal: *Effect of gain dispersion on ultrashort pulse amplification in semiconductor laser amplifiers*, IEEE J. Quantum Electron. **27**, 1843–1849 (1991).

[AGR93a] G. P. Agrawal and C. M. Bowden: *Concept of linewidth enhancement factor in semiconductor lasers: its usefulness and limitations*, IEEE Photon. Technol. Lett. **5**, 640–642 (1993).

[AGR01] G. P. Agrawal: *Nonlinear Fiber Optics* (Academic Press, 3 edition, 2001).

[AHL02] V. Ahlers and A. Pikovsky: *Critical properties of the synchronization transition in space-time chaos*, Phys. Rev. Lett. **88**, 254101 (2002).

[AHL04] A. Ahlborn and U. Parlitz: *Stabilizing unstable steady states using multiple delay feedback control*, Phys. Rev. Lett. **93**, 264101 (2004).

[AHL06] A. Ahlborn and U. Parlitz: *Chaos control using notch feedback*, Phys. Rev. Lett. **96**, 034102 (2006).

[AHM08] F. R. Ahmad and F. Rana: *Fundamental and subharmonic hybrid mode-locking of a high-power (220 mw) monolithic semiconductor laser*, IEEE Photon. Technol. Lett. **20**, 1308–1310 (2008).

[AHN90] D. Ahn and S. L. Chuang: *Optical gain and gain suppression of quantum-well lasers with valence band mixing*, IEEE J. Quantum Electron. **26**, 13–24 (1990).

[AKH98] N. N. Akhmediev, A. Ankiewicz, and J. M. Soto-Crespo: *Stable soliton pairs in optical transmission lines and fiber lasers*, J. Opt. Soc. Am. B **15**, 515 (1998).

[AKH05] N. N. Akhmediev and A. Ankiewicz: *Dissipative Solitons*, vol. 1 of *Lecture Notes in Physics* (Springer Berlin Heidelberg, 2005).

[AKH08] N. N. Akhmediev and A. Ankiewicz: *Dissipative Solitons: From Optics to Biology and Medicine*, vol. 751 (Springer, 2008).

[AKH09] N. N. Akhmediev, A. Ankiewicz, J. M. Soto-Crespo, and P. Grell: *Dissipative solitons: Present understanding, applications and new developments*, Int. J. Bifurc. Chaos Appl. Sci. Eng. **19**, 2621–2636 (2009).

[ALB11] F. Albert, C. Hopfmann, S. Reitzenstein, C. Schneider, S. Höfling, L. Worschech, M. Kamp, W. Kinzel, A. Forchel, and I. Kanter: *Observing chaos for quantum-dot microlasers with external feedback*, Nat. Commun. **2**, 366 (2011).

[ALF69] Z. I. Alferov, A. D. Andreev, V. I. Korolkov, E. L. Portnoi, and D. N. Tretyakov: *Injection properties of N-AlxGa1-XAs-P-GaAs heterojunctions.*, Sov. Phys. Semicond. **2**, 843 (1969).

[ALF96] Z. I. Alferov: *The history and future of semiconductor heterostructures from the point of view of a russian scientist*, Physica Scripta **T68**, 32 (1996).

[ALF17] C. G. E. Alfieri, D. Waldburger, S. M. Link, E. Gini, M. Golling, G. Eisenstein, and U. Keller: *Optical efficiency and gain dynamics of modelocked semiconductor disk lasers*, Opt. Express **25**, 6402–6420 (2017).

[ALF18] C. G. E. Alfieri, D. Waldburger, R. Nürnberg, M. Golling, L. C. Jaurigue, K. Lüdge, and U. Keller: *Modelocking instabilities for high-gain semiconductor disk lasers based on active submonolayer quantum dots*, Phys. Rev. Appl. **10**, 044015 (2018).

[ALS96] P. M. Alsing, V. Kovanis, A. Gavrielides, and T. Erneux: *Lang and Kobayashi phase equation*, Phys. Rev. A **53**, 4429–4434 (1996).

[ALN09] K. Al-Naimee, F. Marino, M. Ciszak, R. Meucci, and F. T. Arecchi: *Chaotic spiking and incomplete homoclinic scenarios in semiconductor lasers with optoelectronic feedback*, New J. Phys. **11**, 073022 (2009).

[ARA86] Y. Arakawa and A. Yariv: *Quantum well lasers – gain, spectra, dynamics*, IEEE J. Quantum Electron. **22**, 1887 (1986).

[ARA02] I. S. Aranson and L. Kramer: *The world of the complex Ginzburg-Landau equation*, Rev. Mod. Phys. **74**, 99 (2002).

[ARS12] D. Arsenijević, C. Y. Liu, A. Payusov, M. Stubenrauch, and D. Bimberg: *Temperature-dependent characteristics of single-mode inas submonolayer quantum-dot lasers*, IEEE Photon. Technol. Lett. **24**, 906–908 (2012).

[ASA84] M. Asada and A. Kameyama: *Gain and intervalence band absorption in quantum-well lasers*, IEEE J. Quantum Electron. **20**, 745–753 (1984).

[AST01] Y. A. Astrov and H. G. Purwins: *Plasma spots in a gas discharge system: Birth, scattering and formation of molecules.*, Phys. Lett. A **283**, 349–354 (2001).

[ATA03] F. M. Atay: *Distributed delays facilitate amplitude death of coupled oscillators*, Phys. Rev. Lett. **91**, 094101 (2003).

[AVR00] E. A. Avrutin, J. H. Marsh, and E. L. Portnoi: *Monolithic and multi-gigahertz mode-locked semiconductor lasers: Constructions, experiments, models and applications*, IEE Proc. Optoelectron. **147**, 251 (2000).

[AVR19] E. A. Avrutin and K. Panajotov: *Delay-differential-equation modeling of mode-locked vertical-external-cavity surface-emitting lasers in different cavity configurations*, Materials **12**, 3224 (2019).

[BAB02] N. Baba, A. Amann, E. Schöll, and W. Just: *Giant improvement of time-delayed feedback control by spatio-temporal filtering*, Phys. Rev. Lett. **89**, 074101 (2002).

[BAL95a] S. Balle: *Effective two-level-model with asymmetric gain for laser diodes*, Opt. Commun. **119**, 227 (1995).

[BAL98a] S. Balle: *Simple analytical approximations for the gain and refractive index spectra in quantum-well lasers*, Phys. Rev. A **57**, 1304–1312 (1998).

[BAN01] U. Bandelow, M. Radziunas, J. Sieber, and M. Wolfrum: *Impact of gain dispersion on the spatio-temporal dynamics of multisection lasers*, IEEE J. Quantum Electron. **37**, 183 (2001).

[BAR17a] S. Barland, S. Coen, M. Erkintalo, M. Giudici, J. Javaloyes, and S. Murdoch: *Temporal localized structures in optical resonators*, Adv. Phys. X **2**, 496–517 (2017).

[BEK17a] R. Bek, M. Großmann, H. Kahle, M. Koch, A. Rahimi-Iman, M. Jetter, and P. Michler: *Self-mode-locked AlGaInP-VECSEL*, App. Phys. Lett. **111**, 182105 (2017).

[BEN99c] C. M. Bender and S. A. Orszag: *Asymptotic Methods and Perturbation Theory*Advanced Mathematical Methods for Scientists and Engineers, (Springer, New York, NY, 1999), chapter 11, pp. 544–576.

[BER04a] T. W. Berg and J. Mørk: *Saturation and noise properties of quantum-dot optical amplifiers*, IEEE J. Quantum Electron. **40**, 1527–1539 (2004).

[BER15] M. Bertolotti: *Masers and Lasers: An Historical Approach* (CRC Press, Boca Raton, 2 edition, 2015).

[BHA99] P. Bhattacharya, K. K. Kamath, J. Singh, D. Klotzkin, J. Phillips, H. T. Jiang, N. Chervela, T. B. Norris, T. Sosnowski, J. Laskar, and M. R. Murty: *In(Ga)As/GaAs self-organized quantum dot lasers: DC and small-signal modulation properties*, IEEE Trans. Electron Devices **46**, 871–883 (1999).

[BIM97a] D. Bimberg, N. Kirstaedter, N. N. Ledentsov, Z. I. Alferov, P. S. Kop'ev, and V. Ustinov: *InGaAs-GaAs quantum-dot lasers*, IEEE J. Sel. Top. Quantum Electron. **3**, 196–205 (1997).

[BIM97] D. Bimberg, N. N. Ledentsov, M. Grundmann, and F. Heinrichsdorff: *Edge and surface emitting quantum dot lasers*, in *International Electron Devices Meeting. IEDM Technical Digest*, edited by 1997), pp. 381–384.

[BIM99] D. Bimberg, M. Grundmann, and N. N. Ledentsov: *Quantum Dot Heterostructures* (John Wiley & Sons Ltd., New York, 1999).

[BIM08a] D. Bimberg: *Semiconductor Nanostructures* (Springer-Verlag Berlin Heidelberg, Berlin, 1st edition, 2008).

[BIS95a] S. Bischoff, M. P. Sørensen, J. Mørk, S. D. Brorson, T. Franck, J. M. Nielsen, and A. Møller-Larsen: *Pulse-shaping mechanism in colliding-pulse mode-locked laser diodes*, Appl. Phys. Lett. **67**, 3877–3879 (1995).

[BIS97a] S. Bischoff, J. Mørk, T. Franck, S. D. Brorson, M. Hofmann, K. Fröjdh, L. Prip, and M. P. Sørensen: *Monolithic colliding pulse mode-locked semiconductor lasers*, Quantum Semiclass. Opt. **9**, 655–674 (1997).

[BLA04a] J. N. Blakely, L. Illing, and D. J. Gauthier: *Controling fast chaos in delay dynamical systems*, Phys. Rev. Lett. **92**, 193901 (2004).

[BLO56] N. Bloembergen: *Proposal for a new type solid state maser*, Phys. Rev. **104**, 324 (1956).

[BON12] C. Bonatto, B. Kelleher, G. Huyet, and S. P. Hegarty: *Transition from unidirectional to delayed bidirectional coupling in optically coupled semiconductor lasers*, Phys. Rev. E **85**, 026205–1 (2012).

[BOO04] H. J. Booth: *Recent applications of pulsed lasers in advanced materials processing*, Thin Solid Films **453-454**, 450 (2004).

[BOW95] C. M. Bowden and G. P. Agrawal: *Maxwell-Bloch formulation for semiconductors: Effects of coherent Coulomb exchange*, Phys. Rev. A **51**, 4132–4139 (1995).

[BOY00] J. P. Boyd: *Chebyshev and Fourier Spectral Methods*, Dover Books on Mathematics (Dover Publications, 2000).

[BOY08] R. W. Boyd: *Nonlinear Optics* (Academic Press, Inc., Florida, USA, 3 edition, 2008).

[BRA93a] T. Brabec and S. M. J. Kelly: *Third-order dispersion as a limiting factor to mode locking in femtosecond solitary lasers*, Opt. Lett. **18**, 2002–2004 (1993).

[BRA04] M. Brambilla, T. Maggipinto, G. Patera, and L. Columbo: *Cavity light bullets: Three-dimensional localized structures in a nonlinear optical resonator*, Phys. Rev. Lett. **93**, 203901 (2004).

[BUL79] R. K. Bullough, P. M. Jack, P. W. Kitchenside, and R. Saunders: *Solitons in laser physics*, Physica Scripta **20**, 364–381 (1979).

[CAL14] V. D. Calhoun, R. Miller, G. Pearlson, and T. Adali: *The chronnectome: time-varying connectivity networks as the next frontier in fMRI data discovery*, Neuron **84**, 262–274 (2014).

[CAM16] P. Camelin, J. Javaloyes, M. Marconi, and M. Giudici: *Electrical addressing and temporal tweezing of localized pulses in passively-mode-locked semiconductor lasers*, Phys. Rev. A **94**, 063854 (2016).

[CAM18] P. Camelin, C. Schelte, A. Verschelde, A. Garnache, G. Beaudoin, I. Sagnes, G. Huyet, J. Javaloyes, S. V. Gurevich, and M. Giudici: *Temporal localized structures in mode-locked vertical external-cavity surface-emitting lasers*, Opt. Lett. **43**, 5367–5370 (2018).

[CHA94] K. C. Chan and H. F. Liu: *Effect of third-order dispersion on soliton-effect pulse compression*, Opt. Lett. **19**, 49–51 (1994).

[CHE99c] Y. Chen, F. X. Kärtner, U. Morgner, S. H. Cho, H. A. Haus, E. P. Ippen, and J. G. Fujimoto: *Dispersion-managed mode locking*, J. Opt. Soc. Am. B **16**, 1999–2004 (1999).

[CHE10d] Y. K. Chembo, D. V. Strekalov, and N. Yu: *Spectrum and dynamics of optical frequency combs generated with monolithic whispering gallery mode resonators*, Phys. Rev. Lett. **104**, 103902 (2010).

[CHE16f] N. Cheemaa, S. A. Mehmood, S. T. R. Rizvi, and M. Younis: *Single and combined optical solitons with third order dispersion in kerr media*, Optik **127**, 8203–8208 (2016).

[CHI20] N. B. Chichkov, A. Yadav, A. V. Kovalev, S. V. Smirnov, M. Herper, K. A. Fedorova, E. A. Viktorov, and E. U. Rafailov: *Pulse dynamics in sesam-free electrically pumped VECSEL*, Opt. Express **28**, 13466 (2020).

[CHO84] Y. Cho and M. Umeda: *Chaos in laser oscillations with delayed feedback; numerical analysis and observation using semiconductor laser*, J. Opt. Soc. Am. B **1**, 497–498 (1984).

[CHO98a] W. W. Chow, A. Girndt, and S. W. Koch: *Calculation of quantum well laser gain spectra*, Opt. Express **2**, 119–124 (1998).

[CHO99] W. W. Chow and S. W. Koch: *Semiconductor-Laser Fundamentals* (Springer-Verlag Berlin Heidelberg, Berlin, 1st edition, 1999).

[CHO13a] W. W. Chow and F. Jahnke: *On the physics of semiconductor quantum dots for applications in lasers and quantum optics*, Prog. Quantum Electron. **37**, 109–184 (2013).

[CHO14b] W. W. Chow, F. Jahnke, and C. Gies: *Emission properties of nanolasers during the transition to lasing*, Light Sci. Appl. **3**, 1–8 (2014).

[CHO20b] W. W. Chow, Z. Zhang, J. C. Norman, S. Liu, and J. E. Bowers: *On quantum-dot lasing at gain peak with linewidth enhancement factor* $\alpha = 0$, APL Photonics **5**, 026101 (2020).

[CLA09] A. Clauset, C. R. Shalizi, and M. E. J. Newman: *Power-law distributions in empirical data*, SIAM Rev. **51**, 661–703 (2009).

[COD16] I. Coddington, N. Newbury, and W. Swann: *Dual-comb spectroscopy*, Optica **3**, 414–426 (2016).

[COI14] A. Coillet, J. M. Dudley, G. Genty, L. Larger, and Y. K. Chembo: *Optical rogue waves in whispering-gallery-mode resonators*, Phys. Rev. A **89**, 013835 (2014).

[COL95] L. A. Coldren and S. W. Corzine: *Diode Lasers and Photonic Integrated Circuits* (John Wiley and Sons, New York, 1995).

[COL12a] L. A. Coldren, S. W. Corzine, and M. Mashanovitch: *Diode Lasers and Photonic Integrated Circuits*, Wiley series in microwave and optical enginieering (Wiley & Sons, 2nd edition, 2012).

[COL12] J. J. Coleman: *The development of the semiconductor laser diode after the first demonstration in 1962*, Semicond. Sci. Technol. **27**, 090207 (2012).

[COU28] R. Courant, K. Friedrichs, and H. Lewy: *Über die partiellen differenzengleichungen der mathematischen physik*, Mathematische Annalen **100**, 32–74 (1928).

[COU87] P. Coullet, C. Elphick, and D. Repaux: *Nature of spatial chaos*, Phys. Rev. Lett. **58**, 431–434 (1987).

[CRO97a] S. M. Crook, G. B. Ermentrout, M. C. Vanier, and J. M. Bower: *The role of axonal delay in the synchronization of networks of coupled cortical oscillators*, J. Comput. Neurosci. **4**, 161–172 (1997).

[CHE18b] T. Chen Sverre, J. R. C. Woods, M. Polanik, P. Unger, A. C. Tropper, and V. Apostolopoulos: *Continuous repetition rate tuning from 960 mhz to 1.72 ghz of a sub-300 femtosecond mode-locked semiconductor disk laser*, Appl. Phys. Lett. **113**, 161106 (2018).

[COH66] C. Cohen-Tannoudji and A. Kastler: *I Optical Pumping*, in , edited by E. Wolf (Elsevier, 1966), vol. 5 of *Progress in Optics*, pp. 1–81.

[CUN01] S. T. Cundiff, J. Ye, and J. L. Hall: *Optical frequency synthesis based on mode-locked lasers*, Rev. Sci. Instrum. **72**, 3749–3771 (2001).

[CUR93] P. F. Curley, C. Spielmann, T. Brabec, F. Krausz, E. Wintner, and A. J. Schmidt: *Operation of a femtosecond ti:sapphire solitary laser in the vicinity of zero group-delay dispersion*, Opt. Lett. **18**, 54–56 (1993).

[DAV85] A. S. Davydov: *Solitons in Molecular Systems*, Mathematics and Its Applications (Springer, Dordrecht, 1 edition, 1985).

[DEK20] S. S. Deka, S. Jiang, S. H. Pan, and Y. Fainman: *Nanolaser arrays: toward application-driven dense integration*, Nanophotonics **10**, 149–169 (2020).

[DEM14] W. Demtröder: *Laser Spectroscopy 1: Basic Principles* (Springer, 2014).

[DEN94] M. L. Dennis and I. N. Duling: *Third-order dispersion in femtosecond fiber lasers*, Opt. Lett. **19**, 1750–1752 (1994).

[DID64] M. DiDomenico: *Small-signal analysis of internal (coupling type) modulation of lasers*, J. Appl. Phys. **35**, 2870 (1964).

[DID10] S. A. Diddams: *The evolving optical frequency comb*, JOSA B **27**, B51–B62 (2010).

[DIN74] R. Dingle, W. Wiegmann, and C. H. Henry: *Quantum states of confined carriers in very thin $Al_xGa_{1-x}As$-GaAs-$Al_xGa_{1-x}As$ heterostructures*, Phys. Rev. Lett. **33**, 827–830 (1974).

[DIN76] R. Dingle and C. H. Henry: *Quantum effects in heterostructure lasers.* United States Patent No. 3982207 (1976).

[DIN09] E. Ding and J. N. Kutz: *Operating regimes, split-step modeling, and the haus master mode-locking model*, J. Opt. Soc. Am. B **26**, 2290–2300 (2009).

[DUD17] V. V. Dudelev, N. A. Maleev, A. G. Kuz'menkov, S. A. Blokhin, V. Y. Myl'nikov, V. I. Kuchinskii, V. M. Ustinov, E. U. Rafailov, and G. S. Sokolovskii: *Peaking of optical pulses in vertical-cavity surface-emitting lasers with an active region based on submonolayer ingaas quantum dots*, Tech. Phys. Lett. **43**, 1099–1101 (2017).

[EGO94a] A. Y. Egorov, A. E. Zhukov, P. S. Kop'ev, N. N. Ledentsov, M. V. Maksimov, and V. M. Ustinov: *Growth of (in,ga)as/gaas quantum-well heterostructures through the deposition of "submonolayer" strained inas layers*, Semiconductors **28**, 363–366 (1994).

[EIC10] H. J. Eichler and J. Eichler: *Laser* (Springer, 7th edition, 2010).

[EIN16] A. Einstein: *Strahlungs-emission und absorption nach der quantentheorie*, Verhandlungen der Deutschen Physikalischen Gesellschaft **18**, 318–323 (1916).

[EIN17] A. Einstein: *Zur Quantentheorie der Strahlung*, Phys. Z. **18**, 121–128 (1917).

[ENG02] K. Engelborghs, T. Luzyanina, and D. Roose: *Numerical bifurcation analysis of delay differential equations using DDE-Biftool*, ACM Trans. Math. Softw. **28**, 1–21 (2002).

[ERN95a] T. Erneux, G. H. M. van Tartwijk, D. Lenstra, and A. M. Levine: *Determining lang and Kobayashi Hopf bifurcation points*, Proc. SPIE **2399**, 170–181 (1995).

[ERN00c] T. Erneux, P. Peterson, and A. Gavrielides: *The pulse shape of a passively q-switched microchip laser*, Eur. Phys. J. D **10**, 423 (2000).

[ERN10b] T. Erneux and P. Glorieux: *Laser Dynamics* (Cambridge University Press, UK, 2010).

[ERN17] T. Erneux, J. Javaloyes, M. Wolfrum, and S. Yanchuk: *Introduction to focus issue: Time-delay dynamics*, Chaos **27**, 114201 (2017).

[ERZ06] H. Erzgräber, B. Krauskopf, D. Lenstra, A. P. A. Fischer, and G. Vemuri: *Frequency versus relaxation oscillations in a semiconductor laser with coherent filtered optical feedback*, Phys. Rev. E **73**, 055201(R) (2006).

[FAI94] J. Faist, C. Sirtori, F. Capasso, L. Pfeiffer, and K. W. West: *Phonon limited intersubband lifetimes and linewidths in a two-dimensional electron gas*, Appl. Phys. Lett. **64**, 872 (1994).

[FAU90] S. Fauve and O. Thual: *Solitary waves generated by subcritical instabilities in dissipative systems*, Phys. Rev. Lett. **64**, 282–284 (1990).

[FIN20] T. Finke, J. Nürnberg, V. Sichkovskyi, M. Golling, U. Keller, and J. P. Reithmaier: *Temperature resistant fast $In_xGa_{1-x}As/GaAs$ quantum dot saturable absorber for the epitaxial integration into semiconductor surface emitting lasers*, Opt. Express **28**, 20954 (2020).

[FIO10] G. Fiol, D. Arsenijević, D. Bimberg, A. G. Vladimirov, M. Wolfrum, E. A. Viktorov, and P. Mandel: *Hybrid mode-locking in a 40GHz monolithic quantum dot laser*, Appl. Phys. Lett. **96**, 011104 (2010).

[FIS04] A. P. A. Fischer, M. Yousefi, D. Lenstra, M. W. Carter, and G. Vemuri: *Filtered optical feedback induced frequency dynamics in semiconductor lasers*, Phys. Rev. Lett. **92**, 023901 (2004).

[FLE68] J. A. Fleck: *Emission of pulse trains by q-switched lasers*, Phys. Rev. Lett. **21**, 131–133 (1968).

[FLY04] M. B. Flynn, L. O'Faolain, and T. F. Krauss: *An experimental and numerical study of q-switched mode-locking in monolithic semiconductor diode lasers*, IEEE J. Quantum Electron. **40**, 1008–1013 (2004).

[FON83] J. Fontaine, W. Dietel, and J. C. Diels: *Chirp in a mode-locked ring dye laser*, IEEE J. Quantum Electron **19**, 1467–1469 (1983).

[FOR03] T. M. Fortier, D. J. Jones, J. Ye, and S. T. Cundiff: *Highly phase stable mode-locked lasers*, IEEE J. Sel. Top. Quantum Electron. **9**, 1002–1010 (2003).

[FOR07] T. Fordell and A. M. Lindberg: *Experiments on the linewidth-enhancement factor of a vertical-cavity surface-emitting laser*, IEEE J. Quantum Electron. **43**, 6–15 (2007).

[NOB98] N. Foundation: *Nobel Lectures Physics 1963-1970* (World Scientific Publishing Co. Pte. Ltd., Singapore, 1998).

[GAA16] M. A. Gaafar, A. Rahimi-Iman, K. A. Fedorova, W. Stolz, E. U. Rafailov, and M. Koch: *Mode-locked semiconductor disk lasers*, Adv. Opt. Photonics **8**, 370–400 (2016).

[GAR02] C. W. Gardiner: *Handbook of stochastic methods for physics, chemistry and the natural sciences* (Springer, Berlin, 2002).

[GAR15] B. Garbin, J. Javaloyes, G. Tissoni, and S. Barland: *Topological solitons as addressable phase bits in a driven laser*, Nat. Commun. **6**, 5915 (2015).

[GOM08] J. Gomis-Bresco, S. Dommers, V. V. Temnov, U. Woggon, M. Lämmlin, D. Bimberg, E. Malić, M. Richter, E. Schöll, and A. Knorr: *Impact of Coulomb scattering on the ultrafast gain recovery in InGaAs quantum dots*, Phys. Rev. Lett. **101**, 256803 (2008).

[GEN08] P. Genevet, S. Barland, M. Giudici, and J. Tredicce: *Cavity soliton laser based on mutually coupled semiconductor microresonators*, Phys. Rev. Lett. **101**, 123905 (2008).

[GER08a] T. D. Germann, A. Strittmatter, J. Pohl, U. W. Pohl, D. Bimberg, J. Rautiainen, M. Guina, and O. G. Okhotnikov: *High-power semiconductor disk laser based on inas-gaas submonolayer quantum dots*, Appl. Phys. Lett. **92**, 101123 (2008).

[GIA96] G. Giacomelli and A. Politi: *Relationship between delayed and spatially extended dynamical systems*, Phys. Rev. Lett. **76**, 2686 (1996).

[GIE19] C. Gies and S. Reitzenstein: *Quantum dot micropillar lasers*, Semicond. Sci. Technol. **34**, 073001 (2019).

[GIR64] F. Gires and P. Tournois: *Interferometre utilisable pour la compression d'impulsions lumineuses modulees en frequence*, C. R. Acad. Sci. Paris **258**, 6112–6115 (1964).

[GMA01] C. Gmachl, F. Capasso, D. L. Sivco, and A. Y. Cho: *Recent progress in quantum cascade lasers and applications*, Rep. Prog. Phys. **64**, 1533 (2001).

[GOE83] E. O. Göbel, H. Jung, J. Kuhl, and K. Ploog: *Recombination enhancement due to carrier localization in quantum well structures*, Phys. Rev. Lett. **51**, 1588–1591 (1983).

[GOL99] D. Golomb and G. B. Ermentrout: *Continuous and lurching traveling pulses in neuronal networks with delay and spatially decaying connectivity*, Proc. Natl. Acad. Sci. **96**, 13480–13485 (1999).

[GOR54] J. P. Gordon, H. J. Zeiger, and C. H. Townes: *Molecular microwave oscillator and new hyperfine structure in the microwave spectrum of NH_3*, Phys. Rev. **95**, 282–284 (1954).

[GOR55] J. P. Gordon, H. J. Zeiger, and C. H. Townes: *The maser - new type of microwave amplifier, frequency standard, and spectrometer*, Phys. Rev. **99**, 1264–1274 (1955).

[GRE12b] P. Grelu and N. N. Akhmediev: *Dissipative solitons for mode-locked lasers*, Nat. Photonics **6**, 84–90 (2012).

[GRE13d] J. A. Greer: *History and current status of commercial pulsed laser deposition equipment*, J. Phys. D **47**, 034005 (2013).

[GRI08a] F. Grillot, B. Dagens, J. G. Provost, H. Su, and L. F. Lester: *Gain compression and above-threshold linewidth enhancement factor in* $1.3\mu m$ *InAs/GaAs quantum-dot lasers*, IEEE J. Quantum Electron. **44**, 946–951 (2008).

[GRI09] F. Grillot, C. Y. Lin, N. A. Naderi, M. Pochet, and L. F. Lester: *Optical feedback instabilities in a monolithic InAs/GaAs quantum dot passively mode-locked laser*, Appl. Phys. Lett. **94**, 153503 (2009).

[GRO20] M. Großmann, R. Bek, M. Jetter, and P. Michler: *Stable fundamental and dual-pulse mode locking of red-emitting VECSELs*, Laser Phys. Lett. **17**, 065001 (2020).

[GRU02] M. Grundmann: *Nano-Optoelectronics: Concepts, Physics and Devices* (Springer, Berlin, 2002).

[GUC83] J. Guckenheimer and P. Holme: *Nonlinear Oscillations, Dynamical Systems, and Bifurcations of Vector Fields* (Springer, Berlin, 1983).

[GUI17] M. Guina, A. Rantamäki, and A. Härkönen: *Optically pumped VECSELs: review of technology and progress*, J. Phys. D **50**, 383001 (2017).

[GUR17] S. V. Gurevich and J. Javaloyes: *Spatial instabilities of light bullets in passively-mode-locked lasers*, Phys. Rev. A **96**, 023821 (2017).

[GUR19] S. V. Gurevich, C. Schelte, and J. Javaloyes: *Impact of high-order effects on soliton explosions in the complex cubic-quintic ginzburg-landau equation*, Phys. Rev. A **99**, 061803 (2019).

[GUS15] F. Gustave, L. Columbo, G. Tissoni, M. Brambilla, F. Prati, B. Kelleher, B. Tykalewicz, and S. Barland: *Dissipative phase solitons in semiconductor lasers*, Phys. Rev. Lett. **115**, 043902 (2015).

[HAB14] T. Habruseva, D. Arsenijević, M. Kleinert, D. Bimberg, G. Huyet, and S. P. Hegarty: *Optimum phase noise reduction and repetition rate tuning in quantum-dot mode-locked lasers*, Appl. Phys. Lett. **104**, 1–4 (2014).

[HAD99] J. Hader, J. V. Moloney, and S. W. Koch: *Microscopic theory of gain, absorption, and refractive index in semiconductor laser materials-influence of conduction-band nonparabolicity and coulomb-induced intersubband coupling*, IEEE J. Quantum Electron. **35**, 1878–1886 (1999).

[HAD04] J. Hader, J. V. Moloney, and S. W. Koch: *Structural dependence of carrier capture time in semiconductor quantum-well lasers*, Appl. Phys. Lett. **85**, 369–371 (2004).

[HAK85] H. Haken: *Light : Volume PII : Waves, Photons, Atoms* (North-Holland, Amsterdam, 1985).

[HAK86] H. Haken: *Laser Light Dynamics*, vol. II (North Holland, 1st edition edition, 1986).

[HAL62] R. N. Hall, G. E. Fenner, J. D. Kingsley, T. J. Soltys, and R. O. Carlson: *Coherent light emission from GaAs junctions*, Phys. Rev. Lett. **9**, 366–368 (1962).

[HAR64] L. E. Hargrove, R. L. Fork, and M. A. Pollack: *Locking of He-Ne laser modes induced by synchronous intracavity modulation*, Appl. Phys. Lett. **5**, 4–5 (1964).

[HAR72] S. Haroche and F. Hartmann: *Theory of saturated-absorption line shapes*, Phys. Rev. A **6**, 1280–1300 (1972).

[HAR83] C. Harder, K. Vahala, and A. Yariv: *Measurement of the linewidth enhancement factor α of semiconductor lasers*, Appl. Phys. Lett. **42**, 328–330 (1983).

[HAR05] P. Harrison: *Quantum Wells, Wires and Dots: Theoretical and Computational Physics of Semiconductor Nanostructures* (John Wiley & Sons, Chichester, 2005).

[HAR16a] S. Harrison, M. P. Young, P. D. Hodgson, R. J. Young, M. Hayne, L. Danos, A. Schliwa, A. Strittmatter, A. Lenz, U. W. Pohl, and D. Bimberg: *Heterodimensional charge-carrier confinement in stacked submonolayer InAs in GaAs*, Phys. Rev. B **93**, 085302 (2016).

[HAS89] A. Hasegawa: *Optical solitons in fibers* (Springer Berlin Heidelberg, Berlin, Heidelberg, 1989).

[HAU75] H. A. Haus: *A theory of forced mode locking*, IEEE J. Quantum Electron. **11**, 323–330 (1975).

[HAU75b] H. A. Haus: *Theory of mode locking with a fast saturable absorber*, J. Appl. Phys. **46**, 3049–3058 (1975).

[HAU75a] H. A. Haus: *Theory of mode locking with a slow saturable absorber*, IEEE J. Quantum Electron. **11**, 736 (1975).

[HAU93a] H. A. Haus and A. Mecozzi: *Noise of mode-locked lasers*, IEEE J. Quantum Electron. **29**, 983 (1993).

[HAU93b] H. A. Haus, J. D. Moores, and L. E. Nelson: *Effect of third-order dispersion on passive mode locking*, Opt. Lett. **18**, 51–53 (1993).

[HAU95] H. A. Haus, K. Tamura, L. E. Nelson, and E. P. Ippen: *Stretched-pulse additive pulse mode-locking in fiber ring lasers: theory and experiment*, IEEE J. Quantum Electron. **31**, 591 (1995).

[HAU00] H. A. Haus: *Mode-locking of lasers*, IEEE J. Sel. Top. Quantum Electron. **6**, 1173–1185 (2000).

[HAU13] A. Hause and F. Mitschke: *Higher-order equilibria of temporal soliton molecules in dispersion-managed fibers*, Phys. Rev. A **88**, 063843 (2013).

[HAU19] J. Hausen, S. Meinecke, B. Lingnau, and K. Lüdge: *Pulse cluster dynamics in passively mode-locked semiconductor vertical-external-cavity surface-emitting lasers*, Phys. Rev. Appl. **11**, 044055 (2019).

[HAU19x] J. Hausen, S. Meinecke, and K. Lüdge: *Bifurcation scenario leading to multiple pulse emission in VECSELs*, Proc. SPIE **10901**, 109010F (2019).

[HAU20a] J. Hausen, K. Lüdge, S. V. Gurevich, and J. Javaloyes: *How carrier memory enters the haus master equation of mode-locking*, Opt. Lett. **45**, 6210–6213 (2020).

[HAU20] J. Hausen, S. Meinecke, J. Javaloyes, S. V. Gurevich, and K. Lüdge: *Phase-incoherent photonic molecules in V-shaped mode-locked vertical-external-cavity surface-emitting semiconductor lasers*, Phys. Rev. Appl. **14** (2020).

[HAU21] J. Hausen, B. Herzog, A. Nelde, S. Meinecke, N. Owschimikow, and K. Lüdge: *Feedback induced locking in semiconductor lasers with strong amplitude-phase coupling*, Phys. Rev. A **103**, 043511 (2021).

[HEA16] C. R. Head, A. Hein, A. P. Turnbull, M. Polanik, E. A. Shaw, T. C. Sverre, P. Unger, and A. C. Tropper: *High-order dispersion in sub-200-fs pulsed VECSELs*, in *Vertical External Cavity Surface Emitting Lasers (VECSELs) VI*, edited by K. G. Wilcox (SPIE, 2016), vol. 9734, pp. 15–24.

[HEC01] E. Hecht: *Optik* (Oldenbourg, München, 3. edition, 2001).

[HEC10] J. Hecht: *Short history of laser development*, Opt. Eng. **49**, 1 (2010).

[HEI98c] T. Heil, I. Fischer, and W. Elsäßer: *Coexistence of low-frequency fluctuations and stable emission on a single high-gain mode in semiconductor lasers with external optical feedback*, Phys. Rev. A **58**, 2672 (1998).

[HEL90b] J. Helms and K. Petermann: *A simple analytic expression for the stable operation range of laser diodes with optical feedback*, IEEE J. Quantum Electron. **26**, 833 (1990).

[HEL03] E. Hellstrom, H. Sunnerud, M. Westlund, and M. Karlsson: *Third-order dispersion compensation using a phase modulator*, J. Light. Technol. **21**, 1188–1197 (2003).

[HEN80] C. H. Henry: *Theory of defect-induced pulsations in semiconductor injection lasers*, J. Appl. Phys. **51**, 3051–3061 (1980).

[HEN82] C. H. Henry: *Theory of the linewidth of semiconductor lasers*, IEEE J. Quantum Electron. **18**, 259–264 (1982).

[HEN83] C. H. Henry: *Theory of the phase noise and power spectrumof a single mode injection laser*, IEEE J. Quantum Electron. **19**, 1391–1397 (1983).

[HER65] M. Hercher: *Single-mode operation of a q-switched ruby laser*, Appl. Phys. Lett. **7**, 39 (1965).

[HER78] J. P. Heritage and R. K. Jain: *Subpicosecond pulses from a tunable cw mode-locked dye laser*, Appl. Phys. Lett. **32**, 101–103 (1978).

[HER14b] T. Herr, V. Brasch, J. D. Jost, C. Wang, N. Kondratiev, M. Gorodetsky, and T. Kippenberg: *Temporal solitons in optical microresonators*, Nat. Photonics **8**, 145–152 (2014).

[HER15b] B. Herzog, N. Owschimikow, J. H. Schulze, R. Rosales, Y. Kaptan, M. Kolarczik, T. Switaiski, A. Strittmatter, D. Bimberg, U. W. Pohl, and U. Woggon: *Fast gain and phase recovery of semiconductor optical amplifiers based on submonolayer quantum dots*, Appl. Phys. Lett. **107**, 201102 (2015).

[HER16] B. Herzog, B. Lingnau, M. Kolarczik, Y. Kaptan, D. Bimberg, A. Maaßdorf, U. W. Pohl, R. Rosales, J. H. Schulze, A. Strittmatter, M. Weyers, U. Woggon, K. Lüdge, and N. Owschimikow: *Strong amplitude-phase coupling in submonolayer quantum dots*, Appl. Phys. Lett. **109**, 201102 (2016).

[HER19] B. Herzog, B. Lingnau, M. Kolarczik, S. Helmrich, A. Achtstein, K. Thommes, F. Alhussein, D. Quandt, A. Strittmatter, U. W. Pohl, O. Brox, M. Weyers, U. Woggon, K. Lüdge, and N. Owschimikow: *Broadband semiconductor light sources operating at 1060 nm based on InAs:Sb/GaAs submonolayer quantum dots*, IEEE J. Sel. Top. Quantum Electron. **25**, 1900310 (2019).

[HES96a] O. Hess and T. Kuhn: *Maxwell-Bloch equations for spatially inhomogeneous semiconductor lasers. I. Theoretical formulation*, Phys. Rev. A **54**, 3347–3359 (1996).

[HES21] D. Hessel, S. V. Gurevich, and J. Javaloyes: *Wiggling instabilities of temporal localized states in passively mode-locked vertical external-cavity surface-emitting lasers*, Opt. Lett. **46**, 2557–2560 (2021).

[HO78] P. T. Ho, L. A. Glasser, E. P. Ippen, and H. A. Haus: *Picosecond pulse generation with a cw gaalas laser diode*, Appl. Phys. Lett. **33**, 241–242 (1978).

[HOF08a] M. Hoffmann, Y. Barbarin, D. J. H. C. Maas, M. Golling, I. L. Krestnikov, S. S. Mikhrin, A. R. Kovsh, T. Südmeyer, and U. Keller: *Modelocked quantum dot vertical external cavity surface emitting laser*, Appl. Phys. B **93**, 733–736 (2008).

[HOF11a] M. Hoffmann, O. D. Sieber, V. J. Wittwer, I. L. Krestnikov, D. A. Livshits, Y. Barbarin, T. Südmeyer, and U. Keller: *Femtosecond high-power quantum dot vertical external cavity surface emitting laser*, Opt. Express **19**, 8108–8116 (2011).

[HOH95] A. Hohl, H. J. C. van der Linden, and R. Roy: *Determinism and stochasticity of power-dropout events in semiconductor lasers with optical feedback*, Opt. Lett. **20**, 2396–2398 (1995).

[HOL80] M. B. Holbrook, W. E. Sleat, and D. J. Bradley: *Bandwidth-limited picosecond pulse generation in an actively mode-.locked gaalas diode laser*, Appl. Phys. Lett. **37**, 59–61 (1980).

[HOO00] S. Hoogland, S. Dhanjal, A. C. Tropper, J. S. Roberts, R. Häring, R. Paschotta, F. Morier-Gemoud, and U. Keller: *Passively mode-locked diode-pumped surface-emitting semiconductor laser*, IEEE Photon. Technol. Lett. **12**, 1135–1137 (2000).

[HUE91a] G. Hüpper and E. Schöll: *Dynamic Hall effect as a mechanism for self-sustained oscillations and chaos in semiconductors*, Phys. Rev. Lett. **66**, 2372 (1991).

[IKE79] K. Ikeda: *Multiple-valued stationary state and its instability of the transmitted light by a ring cavity system*, Opt. Commun. **30**, 257–261 (1979).

[INN03] E. Innerhofer, T. Südmeyer, F. Brunner, R. Häring, A. Aschwanden, R. Paschotta, C. Hönninger, M. Kumkar, and U. Keller: *60-w average power in 810-fs pulses from a thin-disk yb:yag laser*, Opt. Lett. **28**, 36 (2003).

[IPP80] E. P. Ippen, D. J. Eilenberger, and R. W. Dixon: *Picosecond pulse generation by passive mode locking of diode lasers*, Appl. Phys. Lett. **37**, 267–269 (1980).

[IPP94] E. P. Ippen: *Principles of passive mode locking*, Appl. Phys. B **58**, 159–170 (1994).

[JAH12] F. Jahnke: *Quantum Optics with Semiconductor Nanostructures* (Woodhead, 2012).

[JAN15] J. K. Jang, M. Erkintalo, S. Coen, and S. G. Murdoch: *Temporal tweezing of light through the trapping and manipulation of temporal cavity solitons*, Nat. Commun. **6**, 7370 (2015).

[JAN18a] Y. S. Jang and S. W. Kim: *Distance measurements using mode-locked lasers: A review*, Nanomanufacturing and Metrology **1**, 131–147 (2018).

[JAU16] L. C. Jaurigue, O. Nikiforov, E. Schöll, S. Breuer, and K. Lüdge: *Dynamics of a passively mode-locked semiconductor laser subject to dual-cavity optical feedback*, Phys. Rev. E **93**, 022205 (2016).

[JAU17a] L. C. Jaurigue: *Passively Mode-Locked Semiconductor Lasers: Dynamics and Stochastic Properties in the Presence of Optical Feedback* (Springer, Cham, springer thesis edition, 2017).

[JAU17] L. C. Jaurigue, B. Krauskopf, and K. Lüdge: *Multipulse dynamics of a passively mode-locked semiconductor laser with delayed optical feedback*, Chaos **27**, 114301 (2017).

[JAV61] A. Javan, W. R. Bennett, and D. R. Herriott: *Population inversion and continuous optical maser oscillation in a gas discharge containing a He-Ne mixture*, Phys. Rev. Lett. **6**, 106–110 (1961).

[JAV09] J. Javaloyes and S. Balle: *Emission directionality of semiconductor ring lasers: A traveling-wave description*, IEEE J. Quantum Electron. **45**, 431–438 (2009).

[JAV10] J. Javaloyes and S. Balle: *Mode-locking in semiconductor Fabry-Pérot lasers*, IEEE J. Quantum Electron. **46**, 1023–1030 (2010).

[JAV10a] J. Javaloyes and S. Balle: *Quasiequilibrium time-domain susceptibility of semiconductor quantum wells*, Phys. Rev. A **81**, 062505 (2010).

[JAV11] J. Javaloyes and S. Balle: *Anticolliding design for monolithic passively mode-locked semiconductor lasers*, Opt. Lett. **36**, 4407–4409 (2011).

[JAV12] J. Javaloyes and S. Balle: *Multimode dynamics in bidirectional laser cavities by folding space into time delay*, Opt. Express **20**, 8496–8502 (2012).

[JAV16] J. Javaloyes: *Cavity light bullets in passively mode-locked semiconductor lasers*, Phys. Rev. Lett. **116**, 043901 (2016).

[JAV17] J. Javaloyes, M. Marconi, and M. Giudici: *Nonlocality induces chains of nested dissipative solitons*, Phys. Rev. Lett. **119**, 033904 (2017).

[JIA93a] W. Jiang, M. Shimizu, R. P. Mirin, T. E. Reynolds, and J. E. Bowers: *Electrically pumped mode-locked vertical-cavity semiconductor lasers*, Opt. Lett. **18**, 1937–1939 (1993).

[JIA01] L. A. Jiang, M. E. Grein, H. A. Haus, and E. P. Ippen: *Noise of mode-locked semiconductor lasers*, IEEE J. Sel. Top. Quantum Electron. **7**, 159 (2001).

[JON95b] D. J. Jones, L. M. Zhang, J. E. Carroll, and D. Marcenac: *Dynamics of monolithic passively mode-locked semiconductor lasers*, IEEE J. Quantum Electron. **31**, 1051–1058 (1995).

[JUH99] T. Juhasz, F. H. Loesel, R. M. Kurtz, C. Horvath, J. F. Bille, and G. Mourou: *Corneal refractive surgery with femtosecond lasers*, IEEE J. Sel. Top. Quantum Electron. **5**, 902–910 (1999).

[KAH16] H. Kahle, C. M. N. Mateo, U. Brauch, P. Tatar-Mathes, R. Bek, M. Jetter, T. Graf, and P. Michler: *Semiconductor membrane external-cavity surface-emitting laser (mecsel)*, Optica **3**, 1506–1512 (2016).

[KAH19] H. Kahle, J. P. Penttinen, H. M. Phung, P. Rajala, A. Tukiainen, S. Ranta, and M. Guina: *Comparison of single-side and double-side pumping of membrane external-cavity surface-emitting lasers*, Opt. Lett. **44**, 1146 (2019).

[KAI07b] R. Kaiser and B. Hüttl: *Monolithic 40-ghz mode-locked mqw dbr lasers for high-speed optical communication systems*, IEEE J. Sel. Top. Quantum Electron. **13**, 125–135 (2007).

[KAL08] V. L. Kalashnikov, A. Fernández, and A. Apolonski: *High-order dispersion in chirped-pulse oscillators*, Opt. Express **16**, 4206–4216 (2008).

[KAR94] J. R. Karin, R. J. Helkey, D. J. Derickson, R. Nagarajan, D. S. Allin, J. E. Bowers, and R. L. Thornton: *Ultrafast dynamics in field-enhanced saturable absorbers*, Appl. Phys. Lett. **64**, 676–678 (1994).

[KAE95] F. X. Kärtner and U. Keller: *Stabilization of solitonlike pulses with a slow saturable absorber*, Opt. Lett. **20**, 16–18 (1995).

[KEL92] U. Keller, D. A. B. Miller, G. D. Boyd, T. H. Chiu, J. F. Ferguson, and M. T. Asom: *Solid-state low-loss intracavity saturable absorber for Nd:YLF lasers: an antiresonant semiconductor fabry–perot saturable absorber*, Opt. Lett. **17**, 505 (1992).

[KEL96] U. Keller, K. J. Weingarten, F. X. Kärtner, D. Kopf, B. Braun, I. D. Jung, R. Fluck, C. Hönninger, N. Matuschek, and J. Aus-der Au: *Semiconductor saturable absorber mirrors (SESAM's) for femtosecond to nanosecond pulse generation in solid-state lasers*, IEEE J. Sel. Top. Quantum Electron. **2**, 435 (1996).

[KEL03] U. Keller: *Recent developments in compact ultrafast lasers*, Nature **424**, 831–838 (2003).

[KEL06] U. Keller and A. C. Tropper: *Passively modelocked surface-emitting semiconductor lasers*, Phys. Rep. **429**, 67–120 (2006).

[KEL12a] B. Kelleher, S. P. Hegarty, and G. Huyet: *Modified relaxation oscillation parameters in optically injected semiconductor lasers*, J. Opt. Soc. Am. B **29**, 2249–2254 (2012).

[KEL17a] B. Kelleher and G. Quinn: *Mutual coherence enhancement in coupled lasers*, IET Optoelectron. **11**, 86–90 (2017).

[KEL17b] B. Kelleher, M. J. Wishon, A. Locquet, D. Goulding, B. Tykalewicz, G. Huyet, and E. A. Viktorov: *Delay induced high order locking effects in semiconductor lasers*, Chaos **27**, 114325 (2017).

[KER16] C. Kerse, H. Kalaycioglu, P. Elahi, B. Cetin, D. K. Kesim, O. Akcaalan, S. Yavas, M. D. Asik, B. Öktem, H. Hoogland, R. Holzwarth, and F. Ilday: *Ablation-cooled material removal with ultrafast bursts of pulses*, Nature **537**, 84 (2016).

[KIL16] I. Kilen, S. W. Koch, J. Hader, and J. V. Moloney: *Fully microscopic modeling of mode locking in microcavity lasers*, J. Opt. Soc. Am. B **33**, 75–80 (2016).

[KIL17] I. Kilen, S. W. Koch, J. Hader, and J. V. Moloney: *Non-equilibrium ultrashort pulse generation strategies in VECSELs*, Optica **4**, 412–417 (2017).

[KIL18] I. Kilen, S. W. Koch, J. Hader, and J. V. Moloney: *Vecsel design for high peak power ultrashort mode-locked operation*, App. Phys. Lett. **112**, 262105 (2018).

[KIL19] I. Kilen, S. W. Koch, J. Hader, and J. V. Moloney: *Mode-locking in vertical external-cavity surface-emitting lasers with type-ii quantum-well configurations*, Appl. Phys. Lett. **114**, 252102 (2019).

[KIM07] J. Kim, J. Chen, J. Cox, and F. X. Kärtner: *Attosecond-resolution timing jitter characterization of free-running mode-locked lasers*, Opt. Lett. **32**, 3519–3521 (2007).

[KLA08] C. A. Klausmeier: *Floquet theory: A useful tool for understanding nonequilibrium dynamics*, Theor. Ecol. **1**, 153–161 (2008).

[KLE14] A. Klenner, S. Schilt, T. Südmeyer, and U. Keller: *Gigahertz frequency comb from a diode-pumped solid-state laser*, Opt. Express **22**, 31008 (2014).

[KLO11a] P. Klopp, U. Griebner, M. Zorn, and M. Weyers: *Pulse repetition rate up to 92 GHz or pulse duration shorter than 110 fs from a mode-locked semiconductor disk laser*, Appl. Phys. Lett. **98**, 071103 (2011).

[KOD94] Y. Kodama, M. Romagnoli, S. Wabnitz, and M. Midrio: *Role of third-order dispersion on soliton instabilities and interactions in optical fibers*, Opt. Lett. **19**, 165–167 (1994).

[KOL06] T. Kolokolnikov, M. Nizette, T. Erneux, N. Joly, and S. Bielawski: *The q-switching instability in passively mode-locked lasers*, Physica D **219**, 13 (2006).

[KRE99] I. Krestnikov, M. Straßburg, M. Caesar, A. Hoffmann, U. W. Pohl, D. Bimberg, N. Ledentsov, P. S. Kop'ev, Z. I. Alferov, D. Litvinov, A. Rosenauer, and D. Gerthsen: *Control of the electronic properties of cdse submonolayer superlattices via vertical correlation of quantum dots*, Phys. Rev. B **60**, 8695 (1999).

[KRE01] I. L. Krestnikov, N. N. Ledentsov, A. Hoffmann, and D. Bimberg: *Arrays of two-dimensional islands formed by submonolayer insertions: Growth, properties, devices*, Phys. Status Solidi A **183**, 207–233 (2001).

[KRU11] V. Kruglov, C. Aguergaray, and J. Harvey: *Propagation and breakup of pulses in fiber amplifiers and dispersion-decreasing fibers with third-order dispersion*, Phys. Rev. A **84**, 023823 (2011).

[KRU17b] K. Krupa, K. Nithyanandan, U. Andral, P. Tchofo-Dinda, and P. Grelu: *Real-time observation of internal motion within ultrafast dissipative optical soliton molecules*, Phys. Rev. Lett. **118**, 243901 (2017).

[KUE17] M. Kues, C. Reimer, B. Wetzel, P. Roztocki, B. E. Little, S. T. Chu, T. Hansson, E. A. Viktorov, D. J. Moss, and R. Morandotti: *Passively mode-locked laser with an ultra-narrow spectral width*, Nat. Photonics **11**, 159–162 (2017).

[KUN07a] M. Kuntz, G. Fiol, M. Lämmlin, C. Meuer, and D. Bimberg: *High-speed mode-locked quantum-dot lasers and optical amplifiers*, Proc. IEEE **95**, 1767–1778 (2007).

[KUR19] F. Kurtz, C. Ropers, and G. Herink: *Resonant excitation and all-optical switching of femtosecond soliton molecules*, Nat. Photon. **14**, 9–13 (2019).

[KUZ98a] Y. A. Kuznetsov and L. Sirovich: *Elements of Applied Bifurcation Theory*, Applied Mathematical Sciences (Springer-Verlag, New York, USA, 2 edition, 1998).

[LAG05] A. A. Lagatsky, E. U. Rafailov, W. Sibbett, D. A. Livshits, A. E. Zhukov, and V. M. Ustinov: *Quantum-dot-based saturable absorber with p-n junction for mode-locking of solid-state lasers*, IEEE Photon. Technol. Lett. **17**, 294–296 (2005).

[LAN80b] R. Lang and K. Kobayashi: *External optical feedback effects on semiconductor injection laser properties*, IEEE J. Quantum Electron. **16**, 347–355 (1980).

[LAU17] A. Laurain, R. Rockmore, H. T. Chan, J. Hader, S. W. Koch, A. R. Perez, W. Stolz, and J. V. Moloney: *Pulse interactions in a colliding pulse mode-locked vertical external cavity surface emitting laser*, J. Opt. Soc. Am. B **34**, 329–337 (2017).

[LAU18] A. Laurain, I. Kilen, J. Hader, A. Ruiz Perez, P. Ludewig, W. Stolz, S. Addamane, J. Balakrishnan, S. A. Koch, and J. V. Moloney: *Modeling and experimental realization of modelocked VECSEL producing high power sub-100 fs pulses*, Appl. Phys. Lett. **113**, 121113 (2018).

[LED96a] N. N. Ledentsov, V. A. Shchukin, M. Grundmann, N. Kirstaedter, J. Böhrer, O. Schmidt, D. Bimberg, V. M. Ustinov, A. Y. Egorov, A. E. Zhukov, P. S. Kop'ev, S. V. Zaitsev, N. Y. Gordeev, Z. I. Alferov, A. I. Borovkov, A. O. Kosogov, S. S. Ruvimov, P. Werner, U. Gösele, and J. Heydenreich: *Direct formation of vertically coupled quantum dots in stranski-krastanow growth*, Phys. Rev. B **54**, 8743 (1996).

[LED98] N. N. Ledentsov, V. M. Ustinov, V. A. Shchukin, P. S. Kop'ev, Z. I. Alferov, and D. Bimberg: *Quantum dot heterostructures: fabrication, properties, lasers (review)*, Semiconductors **32**, 343–365 (1998).

[LED99a] M. J. Lederer, B. Luther-Davies, H. H. Tan, C. Jagadish, N. N. Akhmediev, and J. M. Soto-Crespo: *Multipulse operation of a ti:sapphire laser mode locked by an ion-implanted semiconductor saturable-absorber mirror*, J. Opt. Soc. Am. B **16**, 895 (1999).

[LED07] N. N. Ledentsov, D. Bimberg, F. Hopfer, A. Mutig, V. A. Shchukin, A. V. Savel'ev, G. Fiol, E. Stock, H. Eisele, M. Dähne, D. Gerthsen, U. Fischer, D. Litvinov, A. Rosenauer, S. S. Mikhrin, A. R. Kovsh, N. D. Zakharov, and P. Werner: *Sub-monolayer quantum dots for high speed surface emitting lasers*, Nanoscale Res. Lett. **2**, 417–429 (2007).

[LEE94] K. J. Lee, W. D. McCormick, J. E. Pearson, and H. L. Swinney: *Experimental observation of self-replicating spots in a reaction-diffusion system*, Nature (London) **369**, 215–218 (1994).

[LEL07] F. Lelarge, B. Dagens, J. Renaudier, R. Brenot, A. Accard, F. van Dijk, D. Make, O. L. Gouezigou, J. G. Provost, F. Poingt, J. Landreau, O. Drisse, E. Derouin, B. Rousseau, F. Pommereau, and G. H. Duan: *Recent advances on InAs/InP quantum dash based semiconductor lasers and optical amplifiers operating at* $1.55\mu m$, IEEE J. Sel. Top. Quantum Electron. **13**, 111 (2007).

[LEO10] F. Leo, S. Coen, P. Kockaert, S. P. Gorza, P. Emplit, and M. Haelterman: *Temporal cavity solitons in one-dimensional kerr media as bits in an all-optical buffer*, Nat. Photonics **4**, 471–476 (2010).

[LEO13a] F. Leo, A. Mussot, P. Kockaert, P. Emplit, M. Haelterman, and M. Taki: *Nonlinear symmetry breaking induced by third-order dispersion in optical fiber cavities*, Phys. Rev. Lett. **110**, 104103 (2013).

[LI03] H. Li and K. Iga: *Vertical-Cavity Surface-Emitting Laser Devices*, Springer Series in Photonics (Springer, Berlin, Heidelberg, 1 edition, 2003).

[LI09] G. Li: *Recent advances in coherent optical communication*, Adv. Opt. Photonics **1**, 279 (2009).

[LI12] Q. Li, J. B. Wright, W. W. Chow, T. S. Luk, I. Brener, L. F. Lester, and G. T. Wang: *Single-mode gan nanowire lasers*, Opt. Express **20**, 17873–17879 (2012).

[LIN12b] B. Lingnau, K. Lüdge, W. W. Chow, and E. Schöll: *Failure of the α-factor in describing dynamical instabilities and chaos in quantum-dot lasers*, Phys. Rev. E **86**, 065201(R) (2012).

[LIN13] B. Lingnau, W. W. Chow, E. Schöll, and K. Lüdge: *Feedback and injection locking instabilities in quantum-dot lasers: a microscopically based bifurcation analysis*, New J. Phys. **15**, 093031 (2013).

[LIN14] B. Lingnau, W. W. Chow, and K. Lüdge: *Amplitude-phase coupling and chirp in quantum-dot lasers: influence of charge carrier scattering dynamics*, Opt. Express **22**, 4867–4879 (2014).

[LIN15b] B. Lingnau: *Nonlinear and Nonequilibrium Dynamics of Quantum-Dot Optoelectronic Devices*, Springer Theses (Springer International Publishing, Switzerland, 2015).

[LIN15] B. Lingnau: *Nonlinear and Nonequilibrium Dynamics of Quantum-Dot Optoelectronic Devices*, Ph.D. thesis, TU Berlin (2015).

[LIN16] B. Lingnau, K. Lüdge, B. Herzog, M. Kolarczik, Y. Kaptan, U. Woggon, and N. Owschimikow: *Ultrafast gain recovery and large nonlinear optical response in submonolayer quantum dots*, Phys. Rev. B **94**, 014305 (2016).

[LIN17e] S. M. Link, D. J. H. C. Maas, D. Waldburger, and U. Keller: *Dual-comb spectroscopy of water vapor with a free-running semiconductor disk laser*, Science **356**, 1164 (2017).

[LIU09] X. Liu: *Numerical and experimental investigation of dissipative solitons in passively mode-locked fiber lasers with large net-normal-dispersion and high nonlinearity*, Opt. Express **17**, 22401 (2009).

[LIU10b] X. Liu, E. U. Rafailov, D. Livshits, and D. Turchinovich: *Quantum well saturable absorber mirror with electrical control of modulation depth*, Appl. Phys. Lett. **97**, 051103 (2010).

[LUE08] K. Lüdge, M. J. P. Bormann, E. Malić, P. Hövel, M. Kuntz, D. Bimberg, A. Knorr, and E. Schöll: *Turn-on dynamics and modulation response in semiconductor quantum dot lasers*, Phys. Rev. B **78**, 035316 (2008).

[LUE11a] K. Lüdge: *Modeling Quantum Dot based Laser Devices*, in *Nonlinear Laser Dynamics - From Quantum Dots to Cryptography*, edited by K. Lüdge (WILEY-VCH Weinheim, Weinheim, 2012), chapter 1, pp. 3–34.

[LUG87] L. A. Lugiato and R. Lefever: *Spatial dissipative structures in passive optical systems*, Phys. Rev. Lett. **58**, 2209–2211 (1987).

[LUG03] L. A. Lugiato: *Introduction to the feature section on cavity solitons: An overview*, IEEE J. Quantum Electron. **39**, 193–196 (2003).

[LUM09] M. P. Lumb, E. Clarke, E. Harbord, P. Spencer, R. Murray, F. Masia, P. Borri, W. Langbein, C. G. Leburn, C. Jappy, N. K. Metzger, C. T. A. Brown, and W. Sibbett: *Ultrafast absorption recovery dynamics of 1300 nm quantum dot saturable absorber mirrors*, Appl. Phys. Lett. **95**, 041101 (2009).

[LUZ02] T. Luzyanina and K. Engelborghs: *Computing floquet multipliers for functional differential equations*, Int. J. Bifurc. Chaos **12**, 2977–2989 (2002).

[MAI60] T. H. Maiman: *Stimulated optical radiation in ruby*, Nature **187**, 493–494 (1960).

[MAI61] T. H. Maiman, R. H. Hoskins, I. J. D'Haenens, C. K. Asawa, and V. Evtuhov: *Stimulated optical emission in fluorescent solids. II. spectroscopy and stimulated emission in ruby*, Phys. Rev. **123**, 1151 (1961).

[MAK96a] T. Makino: *Analytical formulas for the optical gain of quantum wells*, IEEE J. Quantum Electron. **32**, 493–501 (1996).

[MAL06d] D. B. Malins, A. Gomez-Iglesias, S. J. White, W. Sibbett, A. Miller, and E. U. Rafailov: *Ultrafast electroabsorption dynamics in an InAs quantum dot saturable absorber at 1.3 μm*, Appl. Phys. Lett. **89**, 171111 (2006).

[MAR83] D. Marcuse: *Computer model of an injection laser amplifier*, IEEE J. Quantum Electron. **19**, 63–73 (1983).

[MAR84] O. E. Martinez, R. L. Fork, and J. P. Gordon: *Theory of passively mode-locked lasers including self-phase modulation and group-velocity dispersion*, Opt. Lett. **9**, 156–158 (1984).

[MAR85a] O. E. Martinez, R. L. Fork, and J. P. Gordon: *Theory of passively mode-locked lasers for the case of a nonlinear complex-propagation coefficient*, J. Opt. Soc. Am. B **2**, 753–760 (1985).

[MAR14c] M. Marconi, J. Javaloyes, S. Balle, and M. Giudici: *How lasing localized structures evolve out of passive mode locking*, Phys. Rev. Lett. **112**, 223901 (2014).

[MAR15c] M. Marconi, J. Javaloyes, S. Balle, and M. Giudici: *Passive mode-locking and tilted waves in broad-area vertical-cavity surface-emitting lasers*, IEEE J. Sel. Top. Quantum Electron. **21**, 85–93 (2015).

[MAR15d] M. Marconi, J. Javaloyes, S. Barland, S. Balle, and M. Giudici: *Vectorial dissipative solitons in vertical-cavity surface-emitting lasers with delays*, Nat. Photonics **9**, 450–455 (2015).

[MAR15b] M. Marconi, J. Javaloyes, P. Camelin, D. C. González, S. Balle, and M. Giudici: *Control and generation of localized pulses in passively mode-locked semiconductor lasers*, IEEE J. Sel. Top. Quantum Electron. **21**, 30–39 (2015).

[MAY13] B. Mayer, D. Rudolph, J. Schnell, S. Morkötter, J. Winner, J. Treu, K. Müller, G. Bracher, G. Abstreiter, G. Koblmüller, and J. J. Finley: *Lasing from individual GaAs-AlGaAs core-shell nanowires up to room temperature*, Nat. Commun. **4:2931** (2013).

[MAY15a] A. S. Mayer, A. Klenner, A. R. Johnson, K. Luke, M. R. E. Lamont, Y. Okawachi, M. Lipson, A. L. Gaeta, and U. Keller: *Frequency comb offset detection using supercontinuum generation in silicon nitride waveguides*, Opt. Express **23**, 15440–15451 (2015).

[MAY17] B. Mayer, A. Regler, S. Sterzl, T. Stettner, G. Koblmüller, M. Kaniber, B. Lingnau, K. Lüdge, and J. J. Finley: *Long-term mutual phase locking of picosecond pulse pairs generated by a semiconductor nanowire laser*, Nat. Commun. **8** (2017).

[MCC65] F. McClung and D. Weiner: *Longitudinal mode control in giant pulse lasers*, IEEE J. Quantum Electron. **1**, 94 (1965).

[MCL20] S. McLaren, I. Kilen, and J. V. Moloney: *Microscopic modeling of transverse mode instabilities in mode-locked vertical external-cavity surface-emitting lasers*, Appl. Phys. Lett. **116**, 031102 (2020).

[MCL21] S. McLaren, I. Kilen, and J. V. Moloney: *Microscopic modeling of non-normal incidence vertical external cavity surface-emitting laser cavities*, Appl. Phys. Lett. **118**, 121103 (2021).

[MEE14] J. K. Mee, R. Raghunathan, J. B. Wright, and L. F. Lester: *Device geometry considerations for ridge waveguide quantum dot mode-locked lasers*, J. Phys. D **47**, 233001 (2014).

[MEI19] S. Meinecke, L. Drzewietzki, C. Weber, B. Lingnau, S. Breuer, and K. Lüdge: *Ultra-short pulse generation in a three section tapered passively mode-locked quantum-dot semiconductor laser*, Sci. Rep. **9**, 1783 (2019).

[MEI20] S. Meinecke, L. Kluge, J. Hausen, B. Lingnau, and K. Lüdge: *Optical feedback induced oscillation bursts in two-state quantum-dot lasers*, Opt. Express **28**, 3361–3377 (2020).

[MEI21a] S. Meinecke: *Spatio-Temporal Modeling and Device Optimization of Passively Mode-Locked Semiconductor Lasers*, Ph.D. thesis, TU Berlin (2021).

[MEL65] I. Melngailis: *Longitudinal injection-plasma laser of insb*, Appl. Phys. Lett. **6**, 59 (1965).

[MES16] C. Mesaritakis, A. Kapsalis, A. Bogris, and D. Syvridis: *Artificial neuron based on integrated semiconductor quantum dot mode-locked lasers*, Sci. Rep. **6**, 39317 (2016).

[MEY20] J. T. Meyer, M. L. Lukowski, C. Hessenius, E. M. Wright, and M. Fallahi: *High peak power, sub-ps green emission in a passively mode locked W-cavity VECSEL*, Opt. Express **28**, 5794 (2020).

[MIL14b] C. Milián and D. V. Skryabin: *Soliton families and resonant radiation in a micro-ring resonator near zero group-velocity dispersion*, Opt. Express **22**, 3732–3739 (2014).

[MIT16] F. Mitschke, A. Hause, and C. Mahnke: *Soliton molecules for advanced optical telecommunications*, Eur. Phys. J. Spec. Top. **225**, 2453–2464 (2016).

[MOC65] H. W. Mocker and R. J. Collins: *Mode competition and self-locking effects in a q-switched ruby laser*, Appl. Phys. Lett. **7**, 270 (1965).

[MOR88] J. Mørk, B. Tromborg, and P. L. Christiansen: *Bistability and low-frequency fluctuations in semiconductor lasers with optical feedback: a theoretical analysis*, IEEE J. Quantum Electron. **24**, 123–133 (1988).

[MOR92] J. Mørk, B. Tromborg, and J. Mark: *Chaos in semiconductor lasers with optical feedback-Theory and experiment*, IEEE J. Quantum Electron. **28**, 93–108 (1992).

[MOR10a] J. A. Mores, G. N. Malheiros-Silveira, H. L. Fragnito, and H. E. Hernández-Figueroa: *Efficient calculation of higher-order optical waveguide dispersion*, Opt. Express **18**, 19522–19531 (2010).

[MOS87] E. Moses, J. Fineberg, and V. Steinberg: *Multistability and confined traveling-wave patterns in a convecting binary mixture*, Phys. Rev. A **35**, 2757–2760 (1987).

[MUL05a] J. Mulet and S. Balle: *Mode-locking dynamics in electrically driven vertical-external-cavity surface-emitting lasers*, IEEE J. Quantum Electron. **41**, 1148–1156 (2005).

[MUL06] J. Mulet and J. Mørk: *Analysis of timing jitter in external-cavity mode-locked semiconductor lasers*, IEEE J. Quantum Electron. **42**, 249 (2006).

[NAG09] Z. Nagy, A. Takacs, T. Filkorn, and M. Sarayba: *Initial clinical evaluation of an intraocular femtosecond laser in cataract surgery*, J. Refract. Surg. **25**, 1053–1060 (2009).

[NAM97] S. Namiki, E. P. Ippen, H. A. Haus, and C. X. Yu: *Energy rate equations for mode-locked lasers*, J. Opt. Soc. Am. B **14**, 2099–2111 (1997).

[NAT62] M. I. Nathan, W. P. Dumke, G. Burns, J. F.H. Dill, and G. Lasher: *Stimulated emission of radiation from GaAs p-n junctions*, Appl. Phys. Lett. **1**, 62–64 (1962).

[NEC19] K. Nechay, A. Mereuta, C. Paranthoën, G. Brévalle, C. Levallois, M. Alouini, N. Chevalier, M. Perrin, G. Suruceanu, A. Caliman, M. Guina, and E. Kapon: *InAs/InP quantum dot VECSEL emitting at 1.5 μm*, Appl. Phys. Lett. **115**, 171105 (2019).

[NEW74] G. New: *Pulse evolution in mode-locked quasi-continuous lasers*, IEEE J. Quantum Electron. **10**, 115 (1974).

[HOL62] J. N. Holonyak and S. F. Bevacqua: *Coherent (visible) light emission from $Ga(As_{1-x}P_x)$ junctions*, Appl. Phys. Lett. **1**, 82–83 (1962).

[NIE91] E. Niebur, H. G. Schuster, and D. M. Kammen: *Collective frequencies and metastability in networks of limit-cycle oscillators with time delay*, Phys. Rev. Lett. **67**, 2753 (1991).

[NIK16] O. Nikiforov, L. C. Jaurigue, L. Drzewietzki, K. Lüdge, and S. Breuer: *Experimental demonstration of change of dynamical properties of a passively mode-locked semiconductor laser subject to dual optical feedback by dual full delay-range tuning*, Opt. Express **24**, 14301–14310 (2016).

[NOR19] J. C. Norman, D. Jung, Z. Zhang, Y. Wan, S. Liu, C. Shang, R. W. Herrick, W. W. Chow, A. C. Gossard, and J. E. Bowers: *A review of high-performance quantum dot lasers on silicon*, IEEE J. Quantum Electron. **55**, 1–11 (2019).

[OHT99] J. Ohtsubo: *Feedback induced instability and chaos in semiconductor lasers and their applications*, J. Opt. Rev. **6**, 1–15 (1999).

[OHT08] J. Ohtsubo: *Semiconductor Lasers: Stability, Instability and Chaos* (Springer-Verlag Berlin Heidelberg, 2 edition, 2008).

[OLI06] M. Olivier, V. Roy, and M. Piché: *Third-order dispersion and bound states of pulses in a fiber laser*, Opt. Lett. **31**, 580–582 (2006).

[ORS04] L. Orsila, L. A. Gomes, N. Xiang, T. Jouhti, and O. G. Okhotnikov: *Mode-locked ytterbium fiber lasers*, Appl. Opt. **43**, 1902–1906 (2004).

[ORT07] B. Ortaç, M. Plötner, T. Schreiber, J. Limpert, and A. Tünnermann: *Experimental and numerical study of pulse dynamics in positive net-cavity dispersion mode-locked yb-doped fiber lasers*, Opt. Express **15**, 15595 (2007).

[ORT10] B. Ortac, A. Zaviyalov, C. Nielsen, O. Egorov, R. Iliew, J. Limpert, F. Lederer, and A. Tünnermann: *Generation of soliton molecules with independently evolving phase in a mode-locked fiber laser*, Opt. Lett. **35**, 1578–80 (2010).

[OTT12a] C. Otto, K. Lüdge, A. G. Vladimirov, M. Wolfrum, and E. Schöll: *Delay induced dynamics and jitter reduction of passively mode-locked semiconductor laser subject to optical feedback*, New J. Phys. **14**, 113033 (2012).

[OTT13] C. Otto: *Dynamics of Quantum Dot Lasers: Effects of Optical Feedback and External Optical Injection*, Ph.D. thesis, TU Berlin (2013).

[OTT14] C. Otto: *Dynamics of Quantum Dot Lasers – Effects of Optical Feedback and External Optical Injection*, Springer Theses (Springer, Heidelberg, 2014).

[OTT14b] C. Otto, L. C. Jaurigue, E. Schöll, and K. Lüdge: *Optimization of timing jitter reduction by optical feedback for a passively mode-locked laser*, IEEE Photonics J. **6**, 1501814 (2014).

[OWS20] N. Owschimikow, B. Herzog, B. Lingnau, K. Lüdge, A. Lenz, H. Eisele, M. Dähne, T. Niermann, M. Lehmann, A. Schliwa, A. Strittmatter, and U. W. Pohl: *Submonolayer Quantum Dots, Springer, ISBN 978-3-030-35655-2* (Springer Series in Solid-State Sciences, 2020), vol. 194 of *Semiconductor Nanophotonics*, chapter 2, p. Chapter 2, Booktitle: Semiconductor Nanophotonics.

[PAL99] S. L. Palacios, A. Guinea, J. M. Fernández-Diaz, and R. D. Crespo: *Dark solitary waves in the nonlinear schrödinger equation with third order dispersion, self-steepening, and self-frequency shift*, Phys. Rev. E **60**, R45–R47 (1999).

[PAN16e] M. Pang, W. He, X. Jiang, and P. S. J. Russell: *All-optical bit storage in a fibre laser by optomechanically bound states of solitons*, Nat. Photon. **10**, 454 (2016).

[PAS21] R. Paschotta: *The rp photonics encyclopedia, article on chromatic dispersion.* Website (2021), Dispersion.

[PED08] F. Pedaci, G. Tissoni, S. Barland, M. Giudici, and J. R. Tredicce: *Mapping local defects of extended media using localized structures*, Appl. Phys. Lett. **93**, 111104 (2008).

[PEN92] A. Penzkofer, M. Wittmann, W. Bäumler, and V. Petrov: *Theoretical analysis of contributions of self-phase modulation and group-velocity dispersion to femtosecond pulse generation in passive mode-locked dye lasers*, Appl. Opt. **31**, 7067 (1992).

[PEN19a] J. Peng, S. Boscolo, and H. Zhao: *Breathing dissipative solitons in mode-locked fiber lasers*, Sci. Adv. **5** (2019).

[PER99] A. Perot and C. Fabry: *On the Application of Interference Phenomena to the Solution of Various Problems of Spectroscopy and Metrology*, Astrophys. J. **9**, 87 (1899).

[PER20] A. M. Perego, B. Garbin, F. Gustave, S. Barland, F. Prati, and G. J. de Valcárcel: *Coherent master equation for laser modelocking*, Nat. Commun. **11**, 311 (2020).

[PET03a] P. M. Petroff: *Epitaxial Growth and Electronic Structure of Self-Assembled Quantum Dots* (Springer, 2003).

[PIC91] E. Picholle, C. Montes, C. Leycuras, O. Legrand, and J. Botineau: *Observation of dissipative superluminous solitons in a brillouin fiber ring laser*, Phys. Rev. Lett. **66**, 1454–1457 (1991).

[PIE01] D. Pieroux, T. Erneux, B. Haegeman, K. Engelborghs, and D. Roose: *Bridges of periodic solutions and tori in semiconductor lasers subject to delay*, Phys. Rev. Lett. **87**, 193901 (2001).

[PIM13] A. S. Pimenov, A. G. Vladimirov, S. V. Gurevich, K. Panajotov, G. Huyet, and M. Tlidi: *Delayed feedback control of self-mobile cavity solitons*, Phys. Rev. A **88**, 053830 (2013).

[PIM14] A. S. Pimenov, E. A. Viktorov, S. P. Hegarty, T. Habruseva, G. Huyet, D. Rachinskii, and A. G. Vladimirov: *Bistability and hysteresis in an optically injected two-section semiconductor laser*, Phys. Rev. E **89**, 052903 (2014).

[PIM17] A. S. Pimenov, S. Slepneva, G. Huyet, and A. G. Vladimirov: *Dispersive time-delay dynamical systems*, Phys. Rev. Lett. **118**, 193901 (2017).

[PIM19] A. S. Pimenov and A. G. Vladimirov: *Dynamics of an inhomogeneously broadened passively mode-locked laser*, Eur. Phys. J. B **92**, 114 (2019).

[PIM20] A. S. Pimenov, S. Amiranashvili, and A. G. Vladimirov: *Temporal cavity solitons in a delayed model of a dispersive cavity ring laser*, Math. Model. Nat. Phenom. **15**, 47 (2020).

[PAR14] P. Parra-Rivas, D. Gomila, F. Leo, S. Coen, and L. Gelens: *Third-order chromatic dispersion stabilizes kerr frequency combs*, Opt. Lett. **39**, 2971–2974 (2014).

[PRE07] W. H. Press, B. P. Flannery, S. A. Teukolsky, and W. T. Vettering: *Numerical Recipes (3rd ed.)* (Cambridge University Press, Cambridge, 2007).

[PER10d] A. Pérez-Serrano, J. Javaloyes, and S. Balle: *Bichromatic emission and multimode dynamics in bidirectional ring lasers*, Phys. Rev. A **81**, 043817 (2010).

[PYR92] K. Pyragas: *Continuous control of chaos by self-controlling feedback*, Phys. Lett. A **170**, 421 (1992).

[RAC06] D. Rachinskii, A. G. Vladimirov, U. Bandelow, B. Hüttl, and R. Kaiser: *Q-switching instability in a mode-locked semiconductor laser*, J. Opt. Soc. Am. B **23**, 663–670 (2006).

[RAD11a] M. Radziunas, A. G. Vladimirov, E. A. Viktorov, G. Fiol, H. Schmeckebier, and D. Bimberg: *Pulse broadening in quantum-dot mode-locked semiconductor lasers: Simulation, analysis, and experiments*, IEEE J. Quantum Electron. **47**, 935–943 (2011).

[RAF07] E. U. Rafailov, M. A. Cataluna, and W. Sibbett: *Mode-locked quantum-dot lasers*, Nat. Photonics **1**, 395–401 (2007).

[RAG13] R. Raghunathan, M. T. Crowley, F. Grillot, Y. Li, J. K. Mee, V. Kovanis, and L. F. Lester: *Pulse characterization of passively mode-locked quantum-dot lasers using a delay differential equation model seeded with measured parameters*, IEEE J. Sel. Top. Quantum Electron. **19**, 1100311 (2013).

[RAM97a] T. R. Ramachandran, A. Madhukar, I. Mukhametzhanov, R. Heitz, A. Kalburge, Q. Xie, and P. Chen: *Nature of stranski–krastanow growth of InAs on gaas (001)*, J. Vac. Sci. Technol. B **16**, 1330 (1998).

[REI99b] J. Reichert, R. Holzwarth, T. Udem, and T. W. Hänsch: *Measuring the frequency of light with mode-locked lasers*, Opt. Commun. **172**, 59–68 (1999).

[REM94] M. Remoissenet: *Waves Called Solitons* (Springer, Berlin, Heidelberg, 1 edition, 1994).

[RID90] W. Rideout, B. Yu, J. LaCourse, P. K. York, K. J. Beernink, and J. J. Coleman: *Measurement of the carrier dependence of differential gain, refractive index, and linewidth enhancement factor in strained-layer quantum well lasers*, Appl. Phys. Lett. **56**, 706–708 (1990).

[RIT93a] A. Ritter and H. Haug: *Theory of laser diodes with weak optical feedback. ii. limit-cycle behavior, quasi-periodicity, frequency locking, and route to chaos*, J. Opt. Soc. Am. B **10**, 145–154 (1993).

[ROH12a] P. Rohrmann, A. Hause, and F. Mitschke: *Solitons beyond binary: Possibility of fibre-optic transmission of two bits per clock period*, Sci. Rep. **2** (2012).

[ROH13] P. Rohrmann, A. Hause, and F. Mitschke: *Two-soliton and three-soliton molecules in optical fibers*, Phys. Rev. A **87**, 043834 (2013).

[ROE15a] A. Röhm, B. Lingnau, and K. Lüdge: *Understanding ground-state quenching in quantum-dot lasers*, IEEE J. Quantum Electron. **51**, 2000211 (2015).

[ROS75a] N. N. Rosanov: *Kinetics of a solid-state laser with an additional moving mirror*, Sov. J. Quant. Electron. **4**, 1191–1193 (1975).

[ROS11g] R. Rosales, K. Merghem, A. Martinez, A. Akrout, J. P. Tourrenc, A. Accard, F. Lelarge, and A. Ramdane: *Inas/inp quantum-dot passively mode-locked lasers for 1.55 μm applications*, IEEE J. Sel. Top. Quantum Electron. **17**, 1292–1301 (2011).

[ROS11a] D. P. Rosin, K. E. Callan, D. J. Gauthier, and E. Schöll: *Pulse-train solutions and excitability in an optoelectronic oscillator*, Europhys. Lett. **96**, 34001 (2011).

[ROS11c] M. Rossetti, P. Bardella, and I. Montrosset: *Time-domain travelling-wave model for quantum dot passively mode-locked lasers*, IEEE J. Quantum Electron. **47**, 139 (2011).

[ROS11f] M. Rossetti, T. Xu, P. Bardella, and I. Montrosset: *Modelling of passive mode-locking in InAs quantum-dot lasers with tapered gain section*, Phys. Status Solidi C **9**, 286–289 (2011).

[ROS12a] R. Rosales, S. G. Murdoch, R. T. Watts, A. Martinez, F. Lelarge, A. Accard, L. P. Barry, and A. Ramdane: *High performance mode locking characteristics of single section quantum dash lasers*, Opt. Express **20**, 8649 (2012).

[ROT07] V. Rottschäfer and B. Krauskopf: *The ECM-backbone of the Lang-Kobayashi equations: A geometric picture*, Int. J. Bifurc. Chaos **17**, 1575–1588 (2007).

[RUD08] B. Rudin, A. Rutz, M. Hoffmann, D. J. H. C. Maas, A.-R. Bellancourt, E. Gini, T. Südmeyer, and U. Keller: *Highly efficient optically pumped vertical-emitting semiconductor laser with more than 20 W average output power in a fundamental transverse mode*, Opt. Lett. **33** (2008).

[SAK18] H. Sakaguchi, D. V. Skryabin, and B. A. Malomed: *Stationary and oscillatory bound states of dissipative solitons created by third-order dispersion*, Opt. Lett. **43**, 2688–2691 (2018).

[SAN90] S. Sanders, A. Yariv, J. Paslaski, J. E. Ungar, and H. A. Zarem: *Passive mode locking of a two-section multiple quantum well laser at harmonics of the cavity round-trip frequency*, Appl. Phys. Lett. **58**, 681–683 (1990).

[SOT97] J. M. Soto-Crespo, N. N. Akhmediev, V. V. Afanasjev, and S. Wabnitz: *Pulse solutions of the cubic-quintic complex ginzburg-landau equation in the case of normal dispersion*, Phys. Rev. E **55**, 4783–4796 (1997).

[SOT99] J. M. Soto-Crespo and N. N. Akhmediev: *Multisoliton regime of pulse generation by lasers passively mode locked with a slow saturable absorber*, J. Opt. Soc. Am. B **16**, 674–677 (1999).

[SCH58] A. L. Schawlow and C. H. Townes: *Infrared and optical masers*, Phys. Rev. **112**, 1940 (1958).

[SCH61] A. L. Schawlow and G. E. Devlin: *Simultaneous optical maser action in two ruby satellite lines*, Phys. Rev. Lett. **6**, 96 (1961).

[SCH88j] E. Schöll: *Dynamic theory of picosecond optical pulse shaping by gain-switched semiconductor laser amplifiers*, IEEE J. Quantum Electron. **24**, 435–442 (1988).

[SCH96n] M. Schell, M. Tsuchiya, and T. Kamiya: *Chirp and stability of mode-locked semiconductor lasers*, IEEE J. Quantum Electron. **32**, 1180–1190 (1996).

[SCH03i] T. R. Schibli, J. Kim, O. Kuzucu, J. T. Gopinath, S. N. Tandon, G. S. Petrich, L. A. Kolodziejski, J. G. Fujimoto, E. P. Ippen, and F. X. Kaertner: *Attosecond active synchronization of passively mode-locked lasers by balanced cross correlation*, Opt. Lett. **28**, 947–949 (2003).

[SCH09h] P. J. Schlosser, J. E. Hastie, S. Calvez, A. B. Krysa, and M. D. Dawson: *Inp/algainp quantum dot semiconductor disk lasers for cw tem00 emission at 716-755 nm*, Opt. Express **17**, 21782–21787 (2009).

[SCH10g] H. Schmeckebier, G. Fiol, C. Meuer, D. Arsenijević, and D. Bimberg: *Complete pulse characterization of quantum dot mode-locked lasers suitable for optical communication up to 160 Gbit/s*, Opt. Express **18**, 3415 (2010).

[SCH12c] A. Schliesser, N. Picque, and T. W. Hänsch: *Mid-infrared frequency combs*, Nat. Photonics **6**, 440–449 (2012).

[SCH18e] C. Schelte, J. Javaloyes, and S. V. Gurevich: *Dynamics of temporally localized states in passively mode-locked semiconductor lasers*, Phys. Rev. A **97**, 053820 (2018).

[SCH18f] C. Schelte, J. Javaloyes, and S. V. Gurevich: *Functional mapping for passively mode-locked semiconductor lasers*, Opt. Lett. **43**, 2535–2538 (2018).

[SCH19b] C. Schelte, P. Camelin, M. Marconi, A. Garnache, G. Huyet, G. Beaudoin, I. Sagnes, M. Giudici, J. Javaloyes, and S. V. Gurevich: *Third order dispersion in time-delayed systems*, Phys. Rev. Lett. **123**, 043902 (2019).

[SCH19e] C. Schelte, A. S. Pimenov, A. G. Vladimirov, J. Javaloyes, and S. V. Gurevich: *Tunable kerr frequency combs and temporal localized states in time-delayed gires-tournois interferometers*, Opt. Lett. **44**, 4925–4928 (2019).

[SCH19c] E. Schöll, A. Zakharova, and R. G. Andrzejak: *Editorial on the research topic: Chimera states in complex networks*, Front. Appl. Math. Stat. **5**, 62 (2019), doi: 10.3389/fams.2019.00062.

[SCH20d] C. Schelte, D. Hessel, J. Javaloyes, and S. V. Gurevich: *Dispersive instabilities in passively mode-locked integrated external-cavity surface-emitting lasers*, Phys. Rev. Appl. **13**, 054050 (2020).

[SHA74] C. Shank and E. P. Ippen: *Subpicosecond kilowatt pulses from a mode-locked cw dye laser*, Appl. Phys. Lett. **24**, 373–375 (1974).

[SHE02] O. Shefi, I. Golding, R. Segev, E. Ben-Jacob, and A. Ayali: *Morphological characterization of in vitro neuronal networks*, Phys. Rev. E **66**, 021905 (2002).

[SHT05] Shtaif and A. Mecozzi: *Modelling of polarization mode dispersion in optical communications systems*Polarization Mode Dispersion, (Springer New York, New York, 1 edition, 2005), chapter 2, pp. 34–51.

[SIE98] J. Sieber, U. Bandelow, H. Wenzel, M. Wolfrum, and H. J. Wünsche: *Travelling Wave Equations for Semiconductor Lasers with Gain Dispersion* (1998).

[SIE13b] O. D. Sieber, M. Hoffmann, V. J. Wittwer, M. Mangold, M. Golling, B. W. Tilma, T. Südmeyer, and U. Keller: *Experimentally verified pulse formation model for high-power femtosecond VECSELs*, Appl. Phys. B **113**, 133–145 (2013).

[SIE14a] J. Sieber, K. Engelborghs, T. Luzyanina, G. Samaey, and D. Roose: *DDE-BIFTOOL manual - bifurcation analysis of delay differential equations*, arXiv (2014).

[SIM14] C. Simos, H. Simos, C. Mesaritakis, A. Kapsalis, and D. Syvridis: *Pulse and noise properties of a two section passively mode-locked quantum dot laser under long delay feedback*, Opt. Commun. **313**, 248–255 (2014).

[SKO04] M. S. Skolnick and D. J. Mowbray: *SELF-ASSEMBLED SEMICONDUCTOR QUANTUM DOTS: fundamental physics and device applications*, Annu. Rev. Mater. Res. **34**, 181–218 (2004).

[SOR60] P. P. Sorokin and M. J. Stevenson: *Stimulated infrared emission from trivalent uranium*, Phys. Rev. Lett. **5**, 557 (1960).

[SOR61] P. P. Sorokin and M. J. Stevenson: *Solid-state optical maser using divalent samarium in calcium fluoride*, IBM J. Res. Dev. 5 **5**, 56 (1961).

[SPE91] D. E. Spence, P. N. Kean, and W. Sibbett: *60-fsec pulse generation from a self-mode-locked ti:sapphire laser*, Opt. Lett. **16**, 42 (1991).

[STI95] A. Stingl, M. Lenzner, C. Spielmann, F. Krausz, and R. Szipöcs: *Sub-10-fs mirror-dispersion-controlled ti:sapphire laser*, Opt. Lett. **20**, 602 (1995).

[STR37] I. N. Stranski and N. Weber: *Zur Theorie der orientierten Abscheidung von Ionenkristallen aufeinander*, Zeitschrift für Physikalische Chemie **146**, 797 (1937).

[STR38] I. N. Stranski and L. Krastanow: *Abhandlungen der Mathematisch-Naturwissenschaftlichen Klasse IIb*, Akad. Wiss. Wien **146**, 797–810 (1938).

[STR94a] S. H. Strogatz: *Nonlinear Dynamics and Chaos* (Perseus Books, Cambridge, MA, 1st edition, 1994).

[STR01a] S. H. Strogatz: *Exploring complex networks*, Nature **410**, 268–276 (2001).

[STR01] C. Strümpel, H. G. Purwins, and Y. A. Astrov: *Spatiotemporal filamentary patterns in a dc-driven planar gas discharge system.*, Phys. Rev. E **63(2)**, 026409 (2001).

[TAG94] A. A. Tager and K. Petermann: *High-frequency oscillations and self-mode locking in short external-cavity laser diodes*, IEEE J. Quantum Electron. **30**, 1553–1561 (1994).

[TAN08b] Y. Tanguy, T. Ackemann, W. J. Firth, and R. Jäger: *Realization of a semiconductor-based cavity soliton laser*, Phys. Rev. Lett. **100**, 013907 (2008).

[TER18] S. Terrien, B. Krauskopf, N. G. R. Broderick, L. C. Jaurigue, and K. Lüdge: *Q-switched pulsing lasers subject to delayed feedback: A model comparison*, Phys. Rev. A **98**, 043819 (2018).

[THO03] M. G. Thompson, C. Marinelli, K. T. Tan, K. A. Williams, R. V. Penty, I. H. White, I. N. Kaiander, R. L. Sellin, D. Bimberg, D. J. Kang, M. G. Blamire, F. Visinka, S. Jochum, and S. Hansmann: *10 ghz hybrid modelocking of monolithic ingaas quantum dot lasers*, Electron. Lett. **39**, 1121–1122 (2003).

[TIL15] B. W. Tilma, M. Mangold, C. A. Zaugg, S. M. Link, D. Waldburger, A. Klenner, A. S. Mayer, E. Gini, M. Golling, and U. Keller: *Recent advances in ultrafast semiconductor disk lasers*, Light Sci. Appl. **4** (2015).

[TLI10] M. Tlidi and L. Gelens: *High-order dispersion stabilizes dark dissipative solitons in all-fiber cavities*, Opt. Lett. **35**, 306–308 (2010).

[TLI17] M. Tlidi, K. Panajotov, M. Ferré, and M. G. Clerc: *Drifting cavity solitons and dissipative rogue waves induced by time-delayed feedback in kerr optical frequency comb and in all fiber cavities*, Chaos **27**, 114312 (2017).

[TRO94] B. Tromborg, H. E. Lassen, and H. Olesen: *Traveling wave analysis of semiconductor lasers: modulation responses, mode stability and quantum mechanical treatment of noise spectra*, IEEE J. Quantum Electron. **30**, 939 (1994).

[TYK16] B. Tykalewicz, D. Goulding, S. P. Hegarty, G. Huyet, T. Erneux, B. Kelleher, and E. A. Viktorov: *Emergence of resonant mode-locking via delayed feedback in quantum dot semiconductor lasers*, Opt. Express **24**, 4239–4246 (2016).

[UDE02] T. Udem, R. Holzwarth, and T. W. Hänsch: *Optical frequency metrology*, Nature **416**, 233–237 (2002).

[UEC14] H. Uecker, D. Wetzel, and J. Rademacher: *pde2path - a matlab package for continuation and bifurcation in 2d elliptic systems*, Numer. Math. Theor. Meth. Appl. **7**, 58–106 (2014).

[UKH04] A. A. Ukhanov, A. Stintz, P. G. Eliseev, and K. J. Malloy: *Comparison of the carrier induced refractive index, gain, and linewidth enhancement factor in quantum dot and quantum well lasers*, Appl. Phys. Lett. **84**, 1058–1060 (2004).

[UMB96] P. B. Umbanhowar, F. Melo, and H. L. Swinney: *Localized excitations in a vertically vibrated granular layer*, Nature (London) **382**, 793–796 (1996).

[VAN94] E. V. Vanin, A. I. Korytin, A. M. Sergeev, D. Anderson, M. Lisak, and L. Vázquez: *Dissipative optical solitons*, Phys. Rev. A **49**, 2806–2811 (1994).

[ZIE75] J. P. van der Ziel, R. Dingle, R. C. Miller, W. Wiegmann, and W. A. Nordland: *Laser oscillation from quantum states in very thin gaas-al$_{0.2}$ga$_{0.8}$as multilayer structures*, Appl. Phys. Lett. **26**, 463 (1975).

[ZIE81] J. P. van der Ziel, W. T. Tsang, R. A. Logan, R. M. Mikulyak, and W. M. Augustyniak: *Subpicosecond pulses from passively mode-locked gaas buried optical guide semiconductor lasers*, Appl. Phys. Lett. **39**, 525 (1981).

[VER96] F. Verhulst: *Nonlinear differential equations and dynamical systems* (Springer-Verlag Berlin Heidelberg, 2006), vol. 2, chapter 10, pp. 122–135.

[VIK00] E. A. Viktorov and P. Mandel: *Low frequency fluctuations in a multimode semiconductor laser with optical feedback*, Phys. Rev. Lett. **85**, 3157 (2000).

[VIK06] E. A. Viktorov, P. Mandel, A. G. Vladimirov, and U. Bandelow: *Model for mode locking of quantum dot lasers*, Appl. Phys. Lett. **88**, 201102 (2006).

[VIK14] E. A. Viktorov, T. Habruseva, S. P. Hegarty, G. Huyet, and B. Kelleher: *Coherence and incoherence in an optical comb*, Phys. Rev. Lett. **112**, 224101 (2014).

[VLA04a] A. G. Vladimirov and D. V. Turaev: *A new model for a mode-locked semiconductor laser*, Radiophys. Quantum Electron. **47**, 769–776 (2004).

[VLA04] A. G. Vladimirov, D. V. Turaev, and G. Kozyreff: *Delay differential equations for mode-locked semiconductor lasers*, Opt. Lett. **29**, 1221 (2004).

[VLA05] A. G. Vladimirov and D. V. Turaev: *Model for passive mode locking in semiconductor lasers*, Phys. Rev. A **72**, 033808 (2005).

[VLA09] A. G. Vladimirov, A. S. Pimenov, and D. Rachinskii: *Numerical study of dynamical regimes in a monolithic passively mode-locked semiconductor laser*, IEEE J. Quantum Electron. **45**, 462–46 (2009).

[VLA10] A. G. Vladimirov, U. Bandelow, G. Fiol, D. Arsenijević, M. Kleinert, D. Bimberg, A. S. Pimenov, and D. Rachinskii: *Dynamical regimes in a monolithic passively mode-locked quantum dot laser*, J. Opt. Soc. Am. B **27**, 2102 (2010).

[VLA11] A. G. Vladimirov, D. Rachinskii, and M. Wolfrum: *Modeling of passively mode-locked semiconductor lasers*, in *Nonlinear Laser Dynamics - From Quantum Dots to Cryptography*, edited by K. Lüdge (Wiley-VCH, Weinheim, 2011), Reviews in Nonlinear Dynamics and Complexity, chapter 8, pp. 183–213.

[VOI17] F. F. Voigt, F. Emaury, P. Bethge, D. Waldburger, S. M. Link, S. Carta, A. van der Bourg, F. Helmchen, and U. Keller: *Multiphoton in vivo imaging with a femtosecond semiconductor disk laser*, Biomed. Opt. Express **8**, 3213 (2017).

[TAR98a] G. H. M. van Tartwijk and G. P. Agrawal: *Laser instabilities: a modern perspective*, Prog. Quantum Electron. **22**, 43–122 (1998).

[VUJ15] V. Vujicic, C. Calo, R. Watts, F. Lelarge, C. Browning, K. Merghem, A. Martinez, A. Ramdane, and L. P. Barry: *Quantum dash mode-locked lasers for data centre applications*, IEEE J. Sel. Top. Quantum Electron. **21**, 53–60 (2015).

[WAL16] D. Waldburger, S. M. Link, M. Mangold, C. G. E. Alfieri, E. Gini, M. Golling, B. W. Tilma, and U. Keller: *High-power 100 fs semiconductor disk lasers*, Optica **3**, 844–852 (2016).

[WAL18] D. Waldburger, C. G. E. Alfieri, S. M. Link, S. Meinecke, L. C. Jaurigue, K. Lüdge, and U. Keller: *Multipulse instabilities of a femtosecond SESAM-modelocked VECSEL*, Opt. Express **26**, 21872–21886 (2018).

[WAL19] D. Waldburger, A. S. Mayer, C. G. E. Alfieri, J. Nürnberg, A. R. Johnson, X. Ji, A. Klenner, Y. Okawachi, M. Lipson, A. L. Gaeta, and U. Keller: *Tightly locked optical frequency comb from a semiconductor disk laser*, Opt. Express **27**, 1786 (2019).

[WAN07] J. Wang, A. Maitra, C. G. Poulton, W. Freude, and J. Leuthold: *Temporal dynamics of the alpha factor in semiconductor optical amplifiers*, J. Light. Technol. **25**, 891–900 (2007).

[WAN19e] Z. Wang, K. Nithyanandan, A. Coillet, P. Tchofo-Dinda, and P. Grelu: *Optical soliton molecular complexes in a passively mode-locked fibre laser*, Nat. Commun. **10**, 1 (2019).

[WAN20f] Z. Wang, K. Nithyanandan, A. Coillet, P. Tchofo-Dinda, and P. Grelu: *Buildup of incoherent dissipative solitons in ultrafast fiber lasers*, Phys. Rev. Research **2**, 013101 (2020).

[WEB15] C. Weber, L. Drzewietzki, M. Rossetti, T. Xu, P. Bardella, H. Simos, C. Mesaritakis, M. Ruiz, I. Krestnikov, D. Livshits, M. Krakowski, D. Syvridis, I. Montrosset, E. U. Rafailov, W. Elsäßer, and S. Breuer: *Picosecond pulse amplification up to a peak power of 42W by a quantum-dot tapered optical amplifier and a mode-locked laser emitting at 1.26μm*, Opt. Lett. **40**, 395–398 (2015).

[WEB18a] C. Weber, A. Klehr, A. Knigge, and S. Breuer: *Picosecond pulse generation and pulse train stability of a monolithic passively mode-locked semiconductor quantum-well laser at 1070 nm*, IEEE J. Quantum Electron. **54**, 1–9 (2018).

[WEB18] C. Weber, A. Klehr, A. Knigge, and S. Breuer: *Picosecond pulse generation and pulse train stability of a monolithic passively mode-locked semiconductor quantum well laser at 1070 nm*, IEEE J. Quantum Electron. **54** (2018).

[WEI09] A. Weiner: *Ultrafast Optics*, vol. 1 (John Wiley and Sons, Hoboken, New Jersey, 2009).

[WIL88a] J. Z. Wilcox, G. L. Peterson, S. Ou, J. J. Yang, M. Jansen, and D. Schechter: *Gain- and threshold-current dependence for multiple-quantum-well lasers*, J. Appl. Phys. **64**, 6564–6567 (1988).

[WIL09] K. G. Wilcox, M. Butkus, I. Farrer, D. A. Ritchie, A. C. Tropper, and E. U. Rafailov: *Subpicosecond quantum dot saturable absorber mode-locked semiconductor disk laser*, Appl. Phys. Lett. **94**, 251105 (2009).

[WIL12b] A. Wilms, D. Breddermann, and P. Mathe: *Theory of direct capture from two- and three-dimensional reservoirs to quantum dot states*, Phys. Status Solidi C **9**, 1278–1280 (2012).

[WIL13b] K. G. Wilcox, A. C. Tropper, H. E. Beere, D. A. Ritchie, B. Kunert, B. Heinen, and W. Stolz: *4.35 kW peak power femtosecond pulse mode-locked VECSEL for supercontinuum generation*, Opt. Express **21**, 1599 (2013).

[WIL17b] M. Wilczek, W. Tewes, S. Engelnkemper, S. V. Gurevich, and U. Thiele: *Sliding drops: Ensemble statistics from single drop bifurcations*, Phys. Rev. Lett. **119**, 204501 (2017).

[WOO18] R. I. Woodward: *Dispersion engineering of mode-locked fibre lasers*, J. Opt. **20**, 033002 (2018).

[WU84] J. Wu, R. Keolian, and I. Rudnick: *Observation of a nonpropagating hydrodynamic soliton*, Phys. Rev. Lett. **52**, 1421–1424 (1984).

[WUN00] K. Wundke, S. Pötting, J. Auxier, A. Schülzgen, N. Peyghambarian, and N. F. Borrelli: *Pbs quantum-dot-doped glasses for ultrashort-pulse generation*, Appl. Phys. Lett. **76**, 10–12 (2000).

[XU04a] Z. Xu, D. Birkedal, M. Juhl, and J. M. Hvam: *Submonolayer InGaAs/GaAs quantum-dot lasers with high modal gain and zero-linewidth enhancement factor*, Appl. Phys. Lett. **85**, 3259–3261 (2004).

[YAC96] A. Yacoby, H. L. Stoermer, N. S. Wingreen, L. N. Pfeiffer, K. W. Baldwin, and K. W. West: *Nonuniversal conductance quantization in quantum wires*, Phys. Rev. Lett. **77**, 4612 (1996).

[YAM85] M. Yamada, S. Ogita, M. Yamagishi, and K. Tabata: *Anistropy and broadening of optical gain in a gaas/algaas multiquantum-well laser*, IEEE J. Quantum Electron. **21**, 640–645 (1985).

[YAN10] S. Yanchuk and M. Wolfrum: *A multiple time scale approach to the stability of external cavity modes in the Lang–Kobayashi system using the limit of large delay*, SIAM J. Appl. Dyn. Syst. **9**, 519 (2010).

[YAN17b] S. Yanchuk and G. Giacomelli: *Spatio-temporal phenomena in complex systems with time delays*, J. Phys. A **50**, 103001 (2017).

[YAO12] Y. Yao, A. J. Hoffman, and C. Gmachl: *Mid-infrared quantum cascade lasers*, Nat. Photonics **6**, 432–439 (2012).

[YAP15] C. Y. Yap, C. K. Chua, Z. L. Dong, Z. H. Liu, D. Q. Zhang, L. E. Loh, and S. L. Sing: *Review of selective laser melting: Materials and applications*, Appl. Phys. Rev. **2**, 041101 (2015).

[YAR65] A. Yariv: *Internal modulation in multimode laser oscillators*, J. Appl. Phys. **36**, 388–391 (1965).

[YAR97] A. Yariv: *Optical Electronics in Modern Communications* (Oxford University Press, 1997).

[YE03] J. Ye, H. Schnatz, and L. Hollberg: *Optical frequency combs: from frequency metrology to optical phase control*, IEEE J. Sel. Top. Quantum Electron. **9**, 1041–1058 (2003).

[YI18] X. Yi, Q. F. Yang, K. Y. Yang, and K. Vahala: *Imaging soliton dynamics in optical microcavities*, Nat. Commun. **9**, 3565 (2018).

[YOU17a] M. Younis, U. Younas, S. ur Rehman, M. Bilal, and A. Waheed: *Optical bright-dark and gaussian soliton with third order dispersion*, Optik **134**, 233–238 (2017).

[YUS14] O. V. Yushko, A. A. Redyuk, M. P. Fedoruk, and S. Turitsyn: *Coherent soliton communication lines*, J EXP THEOR PHYS **119**, 787 (2014).

[ZAP19] M. Zapf, T. Sidiropoulos, and R. Röder: *Tailoring spectral and temporal properties of semiconductor nanowire lasers*, Adv. Optical Mater. **2019**, 1900504 (2019).

[ZAV09] A. Zavyalov, R. Iliew, O. Egorov, and F. Lederer: *Dissipative soliton molecules with independently evolving or flipping phases in mode-locked fiber lasers*, Phys. Rev. A **80**, 043829 (2009).

[ZEB21] K. Zeb, Z. Lu, J. Liu, Y. Mao, G. Liu, P. J. Poole, M. Rahim, G. Pakulski, P. Barrios, W. Jiang, and X. Zhang: *InAs/InP quantum dash buried heterostructure mode-locked laser for high capacity fiber-wireless integrated 5G new radio fronthaul systems*, Opt. Express **29**, 16164–16174 (2021).

[ZHO94] J. Zhou, G. Taft, C. P. Huang, M. M. Murnane, H. C. Kapteyn, and I. P. Christov: *Pulse evolution in a broad-bandwidth ti:sapphire laser*, Opt. Lett. **19**, 1149–1151 (1994).

[ZHO05] S. Zhou, L. Kuznetsova, A. Chong, and F. W. Wise: *Compensation of nonlinear phase shifts with third-order dispersion in short-pulse fiber amplifiers*, Opt. Express **13**, 4869–4877 (2005).

[ZOU20] J. Zou, C. Dong, H. Wang, T. Du, and Z. Luo: *Towards visible-wavelength passively mode-locked lasers in all-fibre format*, Light Sci. Appl. **9**, 61 (2020).